第八届“空间信息网络”学术论坛

The 8th Space Information Networks Symposium

会议论文集

浙江·杭州

2024 年 10 月

目 录

Joint Beamforming Design for Reconfigurable Intelligent Surface-Assisted LEO Satellite Constellation Communication

YAO Wenfei[1], Chen Xiaoming[2], WANG Qi[3]

Abstract — Low earth orbit (LEO) satellite constellation, as a typical non-terrestrial network (NTN), can provide ubiquitous connectivity for sixth generation (6G) wireless networks with low transmission delay. However, satellite communications (SATCOM) are still hampered by challenges such as scarcity of spectrum resources and significant path losses. In this paper, reconfigurable intelligent surfaces (RISs) are deployed to enhance the performance of long-distance satellite-terrestrial communication. Further, by exploring inter-satellite links, a joint active beamforming at satellites and passive beamforming at RISs design algorithm is proposed to improve the weighted sum rate (WSR) of satellite-terrestrial communication in the presence of inter-satellite interference due to spectrum sharing. Specifically, we adopt alternating optimization (AO) method to split the original problem into two sub-problems and then solve them step by step. Firstly, given passive beamforming at RISs, we solve the active beamforming design problem with a closed-form solution. Secondly, given the active beamforming, we design passive beamforming for RISs through the alternating direction method of the multipliers. Theoretical analysis and extensive numerical simulations demonstrate the effectiveness of our proposed algorithm in RIS-assisted LEO satellite constellation communications.

Keywords—6G, LEO satellite constellation, reconfigurable intelligent surface, beamforming design

College of Information Science and Electronic Engineering, Zhejiang University, Hangzhou 310007, China.

I. INTRODUCTION

Nowadays, the fifth generation (5G) wireless network has entered the commercial stage and has been deployed and applied globally [1]. However, 5G solely encompasses densely populated regions, leaving a substantial portion of the earth's surface without network coverage, such as oceans, deserts, and remote mountainous areas [2]. Given the substantial expenses associated with establishing base stations and backhauls in these remote environments, satellite communication (SATCOM) network has been widely recognized as the non-terrestrial network (NTN) of future sixth generation (6G) systems, aiming to provide ubiquitous but low-cost communications. As of now, there have been numerous satellite projects, e.g., Starlink and OneWeb [3].

Amidst the array of satellite types orbiting at different altitudes, low earth orbit (LEO) satellites

have become a focal point because of their superior signal strength, shorter transmission delays, and greater cost-effectiveness in contrast to satellites positioned at higher orbits. Since LEO satellite moves very fast, a massive number of satellites forming a constellation provides continuous communications. For instance, Starlink will contain a total of 42000 LEO satellites. These satellites exchange data via inter-satellite links from one satellite to another and finally to the user equipments (UEs), and achieve continuous coverage of a specific area through satellite handover. This approach enables internet connectivity in remote or underserved areas all the time [4].

However, satellite-terrestrial communication still faces many challenges. For instance, in satellite-terrestrial communication, the path loss with long propagation distance is still much higher than that of terrestrial communications. Moreover, the channels between satellite and terrestrial UEs are affected by weather and obstacles seriously, which makes the communication quality susceptible to small-scale channel fading. In particular, the non-line of sight (NLoS) link experiences significant degradation in urban areas, [6]. To mitigate the effect of small-scale channel fading on the transmitted signal, channel equalization technologies, such as linear equalization [7] and least square equalization [8] are commonly used in SATCOM. In addition, SATCOM faces the challenge of scarce frequency resources, especially with the increasing number of satellites. To bolster spectral efficiency, the aggressive full frequency reuse (FFR) scheme [9] has been introduced into LEO satellite constellation communications. Notably, an aggressive utilization of frequency reuse will unavoidably lead to significant interference, thus requiring the use of interference management techniques, such as beamforming [10] and precoder [11]. However, these techniques can not completely eliminate interference. Fortunately, the recently emerged reconfigurable intelligent surface (RIS) is a possible technique that can overcome these challenges.

RIS, as a 6G candidate technology, has garnered significant attention. Specifically, RIS is a metasurface formed by numerous independent and controllable passive reflective elements. Every element can autonomously adjust phase shifts of the incident signals via a control board [12]. RIS has the potential to transform wireless communication by enabling the manipulation of electromagnetic signals to enhance communication reliability [13], coverage [14], efficiency [15], and so on [16], [17]. The challenges faced by LEO SATCOM can be further solved by applying RIS to LEO SATCOM. On the one hand, RIS compensates for path loss by adjusting the shape and direction of the signal beam to improve signal coverage and quality. On the other hand, RIS efficiently manages spectrum utilization by controlling signal reflection and transmission, enhancing spectrum efficiency, and enabling greater data transmission within limited frequency resources. Specifically, by reasonably designing the active beamforming of the satellites, the transmitted signals can be better beamed to the UE and cope with the interference. Further, by designing the passive beamforming of the RISs, the incident signal of the RIS can be well reflected to the UE, thus further enhancing the desired signal and suppressing the interference.

Recently, some academic works have introduced RIS into SATCOM systems to enhance communication performance. In contrast to terrestrial communication, SATCOM employs RIS in two manners. The first one deploys RIS on satellites. For instance, the authors in [18] investigated the cooperative communication performance in a RIS-assisted SATCOM. In [19], RIS

was used to compensate for the significant path loss inherent in very high-frequency carriers, resulting in significantly improved error rate performance in massive swarms of LEO SATCOM. In particular, the authors in [20] proposed a novel strategy to maximize the LEO satellite coverage range by leveraging RIS into the LEO satellite network. The second one deploys RIS on the ground. For instance, the authors in [21] proposed a beamforming design scheme in the blocked RIS-assisted hybrid satellite-terrestrial relay network, exploiting RIS to minimize the total power of both satellite and base station (BS) while guaranteeing users' rate requirements. The work in [22] designed an energy-efficient RIS-aided non-orthogonal multiple access (NOMA) communication network for LEO SATCOM. The authors in [23] considered hardware impairments and interference, and then examined the effectiveness of RIS-assisted integrated satellite-unmanned aerial vehicle (UAV)-terrestrial networks, particularly in scenarios where a direct link is unavailable. In particular, the work in [24] designed a medium earth orbit satellite-to-ground network to simultaneously serve ground users' navigation and communication by adopting the NOMA technique and RIS. Feng et al. [25] proposed a RIS-assisted multiple satellites cooperative downlink transmission scheme to enhance communication by jointly optimizing beamforming vectors at satellites and phase shift optimization at RIS. Moreover, some studies advocate the deployment of RIS at both satellite and ground. The authors in [26] investigated the security of double RIS-assisted space-ground networks.

Despite the works [18]-[26] have introduced RIS into SATCOM to enhance performance, most of them only considered simple scenarios involving a single satellite. In satellite constellation communications, inter-satellite interference often occurs among adjacent satellites [27]. Hence, mitigating interference is a crucial issue to ensure seamless coverage and high transmission rates. In this context, some effective interference cancellation techniques have been applied, i.e., resource allocation [28], channel allocation [29], power control [30], and beam management [31]. However, their systems did not consider the RIS technology. As far as the authors are aware, there is presently no research that applies RIS to alleviate interference and enhance communication in LEO satellite constellation communications. Therefore, We propose a RIS-assisted LEO satellite constellation communication framework, which aims to enhance satellite constellation communications through the joint beamforming design of satellites and RISs. The major contributions of this work can be summarized as follows:

- We propose a RIS-assisted LEO satellite constellation communication framework that leverages the cooperative nature of multiple satellites and RISs to improve the quality and efficiency of ubiquitous connectivity.
- To maximize the weighted sum rate (WSR) of UEs within the power constraints of LEO satellites, a WSR maximization problem is formulated to jointly optimize the active beamforming at satellites and passive beamforming at RISs. To get a feasible solution, we decompose the original problem into two subproblems: active beamforming design and passive beamforming design. Given the passive beamforming of RISs, a closed-form solution for satellite active beamforming is obtained. This not only reduces the computational complexity but also improves the practicability of the algorithm. Given the active beamforming of satellites, the ADMM method is used to solve the non-convex unit module constraints. Compared with the common semidefinite relaxation

algorithm which cannot guarantee the feasible rank one solution, our proposed algorithm can achieve a near-optimal solution.

• We delve into the convergence and complexity attributes of the proposed algorithm. Extensive numerical simulations further validate the superiority of the proposed algorithm, demonstrating significant performance improvements over existing benchmark algorithms as well as existing related works.

The subsequent sections of this paper are structured as follows. Section II introduces the model of LEO satellite constellation communication and formulates the optimization problem of joint beamforming design. Then, Section III designs a joint beamforming design algorithm by solving the formulated optimization problem. Section IV validates the proposed algorithm's effectiveness through simulation results. Lastly, Section V provides the conclusion of this paper.

Notations: $\mathbb{C}^{M\times N}$ denotes a complex matrix of size $M \times N$. Bold uppercase and lowercase letters represent matrices and column vectors, respectively. $\odot$ represents the Hadamard product. $\mathcal{N}(\mu,\sigma^2)$ denotes the complex Gaussian distribution with μ being the mean and σ^2 being the variance. $|\cdot|$ and $\|\cdot\|$ denote a scalar's absolute value and a vector's L2 norm, respectively. $(\cdot)^{\mathrm{T}}$ and $(\cdot)^{\mathrm{H}}$ denote the transpose and conjugate transpose, respectively. $\Re\{\cdot\}$ represents the real part of a complex number. $[\cdot]_{kk}$ represents the k-th diagonal element of the matrix. $\mathrm{diag}(\cdot)$ denotes the process of diagonalization. $(\cdot)^*$ and $(\cdot)^\dagger$ denote the conjugate and pseudo inverse,respectively.

II. SYSTEM MOEEL AND PROBLEM FORMULATION

A. SYSTEM MODEL

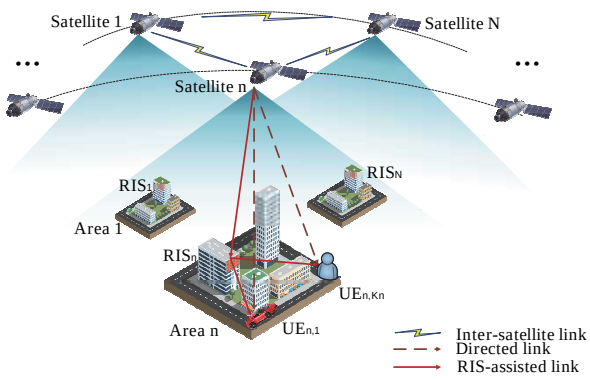

Figure 1 System model of RIS-assisted LEO satellite constellation communication

Let us consider a RIS-assisted LEO satellite constellation, which consists of a massive number of LEO satellites equipped with N_s antennas, communicate with UEs on the ground, as illustrated in Fig. 1. Within the constellation, there are N adjacent satellites providing service to the total K UEs. All UEs are randomly distributed in N ground areas, each served by one satellite. Specifically, the n-th area contains K_n UEs served by the n-th satellite with the multi-beam technique. Due to the long propagation path and the FFR scheme adopted in the whole constellation, the received signals of UEs suffer from significant attenuation and interference from adjacent satellites. Thus, one RIS equipped with N_r reflecting elements per area is used to improve communication quality, which is strategically deployed on the building surface while ensuring that the line of sight (LoS) link exist between RIS and UEs. In other words, the UE receives signals from both the satellite and the RIS. For brevity, let LEO_n and RIS_n represent the LEO satellite and the RIS serving the n-th area, respectively, while $\mathrm{UE}_{n,k}$ denotes the k-th UE located in the n-th area.

During each time slot, the channels remain constant and fade independently from slot to slot. At the beginning of each time slot, the system acquires channel state information (CSI), which is then shared among all LEO satellites via inter-satellite links. Based on the obtained CSI, all LEO satellites collaboratively design active beamforming for satellites and passive

beamforming for RISs to mitigate co-channel interference and enhance overall system performance. With the active beamforming at each satellite, LEO_n constructs a transmitted signal as

$$\mathbf{x}_n = \sum_{k=1}^{K_n} \mathbf{w}_{n,k} s_{n,k},$$

where $\mathbf{w}_{n,k}$ is the N_s -dimensional active beamforming vector designed for $\mathrm{UE}_{n,k}$, $s_{n,k}$ is the transmitted symbol for $\mathrm{UE}_{n,k}$, which satisfying $\mathbb{E}\{s_{n,k}s_{n,k}\} = 1$ and $\mathbb{E}\{s_{n,k}s_{n',k'}\} = 0, \forall (n',k') \neq (n,k)$. Then the signal is sent over the downlink channel, and then arrives at the UEs via the direct link and the RIS-assisted link.

For the direct link, in light of the signal propagation traits within LEO SATCOM [32], the channel between LEO_l and $\mathrm{UE}_{n,k}$ can be expressed as

$$\mathbf{h}_{l,n,k} = \sqrt{C_{l,n,k}}\mathbf{b}_{l,n,k}^{\frac{1}{2}} \odot \mathbf{r}_{l,n,k},$$

where $C_{l,n,k}$ is the large-scale fading factor, which is given by

$$C_{l,n,k} = \left(\frac{c}{4\pi f d_{l,n,k}}\right)^2 \frac{G_{n,k}}{\kappa B T},$$

with c being the speed of light, B being the carrrier bandwidth, f being the carrier frequency, T being the receive noise temperature, κ being the Boltzmann constant, $G_{n,k}$ being the receive gain of $\mathrm{UE}_{n,k}$ and $d_{l,n,k}$ being the propagation distance between LEO_l and $\mathrm{UE}_{n,k}$. In addition, $\mathbf{b}_{l,n,k}$ represents the N_s-dimensional satellite antenna gain vector of LEO_l, which of its mth element is expressed as

$$[\mathbf{b}_{l,n,k}]_m = \varpi_l \left(\frac{J_1(u_m)}{2u_m} + 36\frac{J_3(u_m)}{u_m^3}\right),$$

where ϖ_l is the maximum satellite launch gain of LEO_l and $u_m = 2.07123\left(\sin(\chi_{m,l,n,k})/\sin(3\chi_l^{3dB})\right)$ with $\chi_{m,l,n,k}$ being the angle between the m th antenna of LEO_l and $\mathrm{UE}_{n,k}$, χ_l^{3dB} being the 3dB angle, J_1 and J_3 are the first order and third order Bessel functions of the first kind, respectively. Moreover, $\mathbf{r}_{l,n,k} = r_{l,n,k}e^{j\boldsymbol{\varrho}_{l,n,k}}$ is the rain attenuation vector between LEO_l and $\mathrm{UE}_{n,k}$ with $\boldsymbol{\varrho}_{l,n,k}$ being a phase vector whose elements follow uniform distribution from 0 to 2π, and $r_{l,n,k}$ being the rain attenuation gain, which has a dB form $r_{l,n,k}^{dB} = 20\log_{10} r_{l,n,k}$ with log-normal distribution $\ln(r_{l,n,k}^{dB}) \sim \mathcal{N}(\mu_r, \sigma_r^2)$.

For the RIS-assisted link, it comprises two subchannels, i.e., the subchannel between LEO satellite and RIS and the subchannel between RIS and UE. In general, there exist LoS components in RIS-assisted channels. In this context, the subchannel between LEO_l and RIS_n is denoted as (1)

$$\mathbf{G}_{l,n} = \mathcal{P}_{l,n}\left(\sqrt{\frac{\mathcal{K}_{l,n}}{\mathcal{K}_{l,n}+1}}\mathbf{G}_{l,n}^{\mathrm{LoS}} + \sqrt{\frac{1}{\mathcal{K}_{l,n}+1}}\mathbf{G}_{l,n}^{\mathrm{NLoS}}\right),$$

where $\mathcal{P}_{l,n}$ denotes the channel gain between LEO_l and RIS_n, given by

$$\mathcal{P}_{l,n} = \sqrt{C'_{l,n}}\mathbf{b}'^{\frac{1}{2}}_{l,n} \odot \mathbf{r}'_{l,n}.$$

Similar to the direct channel, $\sqrt{C'_{l,n}}$, $\mathbf{b}'_{l,n}$ and $\mathbf{r}'_{l,n}$ denote the large-scale fading, transmit antenna gain and rain attenuation of the subchannel between LEO_l and RIS_n, respectively. In addition, $\mathcal{K}_{l,n}$ is the Rician factor, $\mathbf{G}_{l,n}^{\mathrm{LoS}} \in \mathbb{C}^{N_r \times N_s}$ and $\mathbf{G}_{l,n}^{\mathrm{NLoS}} \in \mathbb{C}^{N_r \times N_s}$ are the LoS and NLoS constituent parts of the subchannel between LEO_l and RIS_n, respectively. In particular, the elements of $\mathbf{G}_{l,n}^{\mathrm{NLoS}}$ adhere to $\mathcal{N}(0,1)$, and $\mathbf{G}_{l,n}^{\mathrm{LoS}}$ is specified as (2)

$$\mathbf{G}_{l,n}^{\mathrm{LoS}} = \mathbf{a}_{N_r}^{\mathrm{H}}(\Phi'_{l,n})\mathbf{a}_{N_s}(\Phi_{l,n}),$$

where $\mathbf{a}_{N_s}(\Phi_{l,n})$ and $\mathbf{a}_{N_r}^{\mathrm{H}}(\Phi'_{l,n})$ are the array response of LEO_l and RIS_n, respectively. Specifically, $\mathbf{a}_{N_s}(\Phi_{l,n})$ and $\mathbf{a}_{N_r}^{\mathrm{H}}(\Phi'_{l,n})$ with half-wavelength antenna spacing can be formulated as [33] (3)

$$\mathbf{a}_{N_s}(\Phi_{l,n}) = \left[1, e^{j\pi sin(\Phi_{l,n})}, \cdots, e^{j(N_s-1)\pi sin(\Phi_{l,n})}\right],$$

and

$$\mathbf{a}_{N_r}(\Phi'_{l,n}) = \left[1, e^{j\pi sin(\Phi'_{l,n})}, \cdots, e^{j(N_r-1)\pi sin(\Phi'_{l,n})}\right]^{\mathrm{T}} \quad (4)$$

where $\Phi_{l,n}$ and $\Phi'_{l,n}$ are the angle of depature (AoD) at LEO_l and the angle of arrive (AoA) at RIS_n of the signal from LEO_l to RIS_n, respectively.

The phase of the signal arrived at the RIS is adjusted by the reflecting elements. Through careful design of these phase shifts, the signal reflected by RIS can amplify the desired signal and alleviate the inter-satellite interference, namely passive beamforming at RIS. Let $\theta_{n,m}$ denotes the phase shift of the mth reflecting element of RIS_n, the passive beamforming matrix of RIS_n is given by

$$\boldsymbol{\Theta}_{\boldsymbol{n}} = \mathrm{diag}\{e^{j\theta_{n,1}}, e^{j\theta_{n,2}}, \ldots, e^{j\theta_{n,N_r}}\}.$$

Finally, $\mathrm{UE}_{n,k}$ receives the reflected signal through the subchannel between RIS_n and $\mathrm{UE}_{n,k}$, which is represented as

$$\mathbf{g}_{n,k} = \mathcal{P}'_{n,k}\left(\sqrt{\frac{\mathcal{K}'_{n,k}}{\mathcal{K}'_{n,k}+1}}\mathbf{g}_{n,k}^{\mathrm{LoS}} + \sqrt{\frac{1}{\mathcal{K}'_{n,k}+1}}\mathbf{g}_{n,k}^{\mathrm{NLoS}}\right),$$

where $\mathcal{P}'_{n,k}(dB) = 128.1 + 27.6\log_{10}\varsigma_{n,k}$ denotes the distance dependent large-scale channel fading factor with the distance $\varsigma_{n,k}(\mathrm{km})$ between RIS_n and $\mathrm{UE}_{n,k}$, $\mathcal{K}'_{n,k}$ is the Rician factor of the subchannel between RIS_n and $\mathrm{UE}_{n,k}$, $\mathbf{g}_{n,k}^{\mathrm{LoS}} \in \mathbb{C}^{N_r \times 1}$ and $\mathbf{g}_{n,k}^{\mathrm{NLoS}} \in \mathbb{C}^{N_r \times 1}$ are the LoS and NLoS constituent parts of the subchannel between RIS_n and $\mathrm{UE}_{n,k}$, respectively. Each element of $\mathbf{g}_{n,k}^{\mathrm{NLoS}}$ obeys $\mathcal{N}(0,1)$, and $\mathbf{g}_{n,k}^{\mathrm{LoS}}$ is given by

$$\mathbf{g}_{n,k}^{\mathrm{LoS}} = a_{N_r}(\Phi''_{n,k}),$$

where $a_{N_r}(\Phi''_{n,k})$ is the array response of RIS_n and $\Phi''_{n,k}$ is the AoD of the reflected signal with respect to $\mathrm{UE}_{n,k}$. In this context, the equivalent channel between LEO_l and $\mathrm{UE}_{n,k}$ can be represented as $\tilde{\mathbf{h}}_{l,n,k}^{\mathrm{H}} = \mathbf{h}_{l,n,k}^{\mathrm{H}} + \mathbf{g}_{n,k}^{\mathrm{H}}\mathbf{\Theta}_n\mathbf{G}_{l,n}$[1].

Due to the high mobility of LEO satellites, the communication between LEO satellites and UEs are affected by severe Doppler frequency shifts. To enhance the communication quality, the compensation of the Doppler frequency shift should be carried out. It is reasonably assumed that the Doppler frequency shift can be estimated perfectly, and then pre-compensation at LEO satellites and post-compensation at UEs are jointly performed [34]. In this way, the Doppler frequency shifts can be effectively eliminated. Thus, the received signal at $\mathrm{UE}_{n,k}$ can be represented as

$$y_{n,k} = \sum_{l=1}^{N}\tilde{\mathbf{h}}_{l,n,k}^{\mathrm{H}}\mathbf{x}_l + \Omega_{n,k}$$

$$= \underbrace{\tilde{\mathbf{h}}_{n,n,k}^{\mathrm{H}}\mathbf{w}_{n,k}s_{n,k}}_{\text{desired signal}} + \underbrace{\tilde{\mathbf{h}}_{n,n,k}^{\mathrm{H}}\sum_{j=1,j\neq k}^{K_n}\mathbf{w}_{n,j}s_{n,j}}_{\text{intra-areainterference}}$$

$$+ \underbrace{\sum_{l=1,l\neq n}^{N}\sum_{j=1}^{K_l}\tilde{\mathbf{h}}_{l,n,k}^{\mathrm{H}}\mathbf{w}_{l,j}s_{l,j}}_{\text{inter-areainterference}} + \underbrace{\Omega_{n,k}}_{\text{noise}},$$

In this context, the attainable data rate for $\mathrm{UE}_{n,k}$ can be computed as

$$R_{n,k} = \log_2(1+\Gamma_{n,k}), \tag{11}$$

where $\Gamma_{n,k}$ is the signal to interference plus noise ratio (SINR) of $y_{n,k}$, given by

$$\Gamma_{n,k} = \frac{|\tilde{\mathbf{h}}_{n,n,k}^{\mathrm{H}}\mathbf{w}_{n,k}|^2}{\sum_{l=1}^{N}\sum_{\substack{m=1,\\(l,m)\neq(n,k)}}^{K_l}|\tilde{\mathbf{h}}_{l,n,k}^{\mathrm{H}}\mathbf{w}_{l,m}|^2+\sigma_{n,k}^2}.$$

B. PROBLEM FORMULATION

Considering the limited power of LEO satellites, our goal is to maximize the WSR of all UEs under power constraints by jointly designing the active beamforming of LEO satellites and the passive beamforming of RISs. Therefore, the mathematical formulation of the optimization problem is given by

$$\max_{\mathbf{W},\mathbf{\Theta}} \sum_{n=1}^{N}\sum_{k=1}^{K_n}\alpha_{n,k}R_{n,k} \tag{12}$$

$$s.t.\ \sum_{k=1}^{K_n}\|\mathbf{w}_{n,k}\|^2 \leq P_n^{\max}, \forall n \in N,$$

$$0 \leq \theta_{n,m} < 2\pi, \forall n \in N, \forall m \in N_r,$$

where $\mathbf{W} = \{\mathbf{w}_{n,k}, \forall k \in K_n, \forall n \in N\}$ and $\mathbf{\Theta} = \{\mathbf{\Theta}_n, \forall n \in N\}$ represent the collections of optimization variables. For problem (16), the objective function (16) corresponds to the WSR of all UEs, with $\alpha_{n,k} \in (0,1)$ representing the priority coefficient for $\mathrm{UE}_{n,k}$. In particular, a larger $\alpha_{n,k}$ means a higher priority for the UE. Constraint (17) denotes the power restriction for each LEO satellite, with $P_n^{\max}$ representing the maximum transmit power of LEO_n. In addition, constraint (18) imposes the unit modulus constraint on each RIS reflecting coefficient. Deriving an optimal solution for problem (16) within polynomial time is challenging because of the coupled optimization variables $\mathbf{W}$ and $\mathbf{\Theta}$ in the objective function (16), as well as the non-convex constraint (18). To address this, we propose a suboptimal but effective algorithm.

III. JOINT OPTIMIZATION ALGORITHM DESIGN

[1] In general, since the distances between different areas are long, the signals reflected by the RIS to other areas can be neglected.

In this section, we focus on the design of a joint beamforming algorithm for RIS-assisted LEO satellite constellation communications by solving the optimization problem (16). Consider the two optimization variables, the active beamforming $\mathbf{W}$ impacts the beamforming at satellites, while the passive beamforming $\mathbf{\Theta}$ influences the equivalent channels. Both of them can affect the received signal quality at the UEs. When one of them is given or fixed, we can adjust the other to achieve improved performance. Specifically, we transform the objective function (16) containing fractional and logarithmic terms into a convex form of each variable. Subsequently, we adopt the alternating optimization (AO) approach to decompose the optimization variables and iteratively tackle the two resulting beamforming optimization sub-problems. In the following, we solve the optimization problem in detail.

A. OBJECTIEV FUNCTION TRANSFORM

Herein, we transform the objective function (16). Firstly, upon introducing the receivers $v_{n,k}$ for resultant signal $y_{n,k}$ at $\mathrm{UE}_{n,k}$, the mean square error (MSE) of $y_{n,k}$ is computed as (17) at the beginning of the following page, where

$$\vartheta_{n,k} = \sum_{l=1}^{N} \sum_{j=1}^{K_l} (\tilde{\mathbf{h}}_{l,n,k}^{\mathrm{H}} \mathbf{w}_{l,j} \mathbf{w}_{l,j}^{\mathrm{H}} \tilde{\mathbf{h}}_{l,n,k}) + \sigma_{n,k}^2.$$

It is evident that the minimization of $\mathrm{MSE}_{n,k}$ occurs only when $v_{n,k} = \mathbf{w}_{n,k}^{\mathrm{H}} \tilde{\mathbf{h}}_{n,n,k} \vartheta_{n,k}^{-1}$ as derived from (17). In this way, the minimum MSE (MMSE) of $\mathrm{UE}_{n,k}$

$$\begin{aligned}\mathbf{MSE}_{n,k} &= \mathbb{E}\left[\left(v_{n,k} y_{n,k} - s_{n,k}\right)^{*}\left(v_{n,k} y_{n,k} - s_{n,k}\right)\right] \\ &= v_{n,k}\vartheta_{n,k} v_{n,k}^{\mathrm{H}} - v_{n,k}\tilde{\mathbf{h}}_{l,n,k}^{\mathrm{H}}\mathbf{w}_{n,k} - \mathbf{w}_{n,k}^{\mathrm{H}}\tilde{\mathbf{h}}_{l,n,k} v_{n,k}^{\mathrm{H}} + 1 \\ &= \left(v_{n,k} - \mathbf{w}_{n,k}^{\mathrm{H}}\tilde{\mathbf{h}}_{n,n,k}\vartheta_{n,k}^{-1}\right)\vartheta_{n,k}\left(v_{n,k} - \mathbf{w}_{n,k}^{\mathrm{H}}\tilde{\mathbf{h}}_{n,n,k}\vartheta_{n,k}^{-1}\right)^{\mathrm{H}} + 1 - \mathbf{w}_{n,k}^{\mathrm{H}}\tilde{\mathbf{h}}_{n,n,k}\vartheta_{n,k}^{-1}\tilde{\mathbf{h}}_{n,n,k}^{\mathrm{H}}\mathbf{w}_{n,k},\end{aligned} \tag{17}$$

be experssed as

$$\begin{aligned}e_{n,k} &= 1 - \mathbf{w}_{n,k}^{\mathrm{H}}\tilde{\mathbf{h}}_{n,n,k}\vartheta_{n,k}^{-1}\tilde{\mathbf{h}}_{n,n,k}^{\mathrm{H}}\mathbf{w}_{n,k} \\ &= \frac{\vartheta_{n,k} - \mathbf{w}_{n,k}^{\mathrm{H}}\tilde{\mathbf{h}}_{n,n,k}\tilde{\mathbf{h}}_{n,n,k}^{\mathrm{H}}\mathbf{w}_{n,k}}{\vartheta_{n,k}} \\ &= \frac{1}{1+\Gamma_{n,k}}.\end{aligned} \tag{19}$$

Therefore, by substituting (19) into (16), we can reformulate the objective function (16) as

$$\min_{\mathbf{W},\mathbf{\Theta}} \sum_{n=1}^{N} \sum_{k=1}^{K_n} \alpha_{n,k} \log_2(e_{n,k}^{-1}). \tag{20}$$

Note that the minimization of a MMSE function is the same as the minimization of a MSE function with the MMSE receiver. Furthermore, the $\mathrm{MSE}_{n,k}$ is convex to each optimization variable, facilitating the transformation of the objective function. Hence, we rewrite the objective function (20) as

$$\min_{\mathbf{W},\mathbf{\Theta},\mathbf{V}} \sum_{n=1}^{N} \sum_{k=1}^{K_n} \alpha_{n,k} \log_2\left(\mathrm{MSE}_{n,k}\right), \tag{21}$$

where $\mathbf{V} = \left\{v_{n,k}, \forall n \in N, \forall k \in K_n\right\}$ is the colloction of receivers. Unfortunately, the objective function (21) is still non-convex because of the logarithm term. Next, through the introduction of auxiliary variables $\boldsymbol{\beta} = \left\{\beta_{n,k}, \forall n \in N, \forall k \in K_n\right\}$, we convert the objective function (23) as [35]

$$\min_{\mathbf{V},\mathbf{W},\boldsymbol{\beta},\mathbf{\Theta}} \sum_{n=1}^{N} \sum_{k=1}^{K_n} \alpha_{n,k}(\beta_{n,k}\mathrm{MSE}_{n,k} - \log_2(\beta_{n,k})), \tag{22}$$

Upon computing the first derivative of the function (22) concerning $\beta_{n,k}$, the optimal $\beta_{n,k}$ can be obtained, i.e., $\beta_{n,k} = \mathrm{MSE}_{n,k}^{-1}$. Although there are more optimization variables in (22) than that in (16), we have successfully addressed the fractional and logarithmic terms. Furthermore, for a given active beamforming $\mathbf{W}$ or passive beamforming $\mathbf{\Theta}$, the function (22) is convex to the other when $\mathbf{V}$ and $\boldsymbol{\beta}$ are fixed. Thus, we adopt the AO approach to address the optimization problem in the following.

B. ACTIVE BEAMFORMING DESIGN

In this subsection, we focus on optimizing active beamforming $\mathbf{W}$ while keeping passive beamforming $\mathbf{\Theta}$ fixed. Thus, the active beamforming optimization sub-problem is simplified as

$$\min_{\mathbf{V},\mathbf{W},\boldsymbol{\beta}} \sum_{n=1}^{N} \sum_{k=1}^{K_n} \alpha_{n,k}(\beta_{n,k}\mathrm{MSE}_{n,k} - \log_2(\beta_{n,k}))$$

$$\text{s.t. (16b).} \tag{23}$$

This can be readily confirmed as a convex problem for each variable when the other variables are held constant and can be solved easily. Firstly, we calculate the variables $\mathbf{V}$ and $\boldsymbol{\beta}$. For the receiver $v_{n,k}$, it is equal to the MMSE receiver $\mathbf{w}_{n,k}^{\mathrm{H}}\tilde{\mathbf{h}}_{n,n,k}\vartheta_{n,k}^{-1}$. For the auxiliary variable $\beta_{n,k}$, it is should be $\mathrm{MSE}_{n,k}^{-1}$. Then, with obtained $\mathbf{V}$ and $\boldsymbol{\beta}$, the optimal active beamforming $\mathbf{w}_{n,k}$ can be derived by using the Lagrangian multiplier method, which is given by

$$\mathbf{w}_{n,k} = \alpha_{n,k}\Big(\sum_{l=1}^{N}\sum_{j=1}^{K_l} \alpha_{l,j}\beta_{l,j}|v_{l,j}|^2\tilde{\mathbf{h}}_{n,l,j}\tilde{\mathbf{h}}_{n,l,j}^{\mathrm{H}} + \gamma_n\mathbf{I}\Big)^{\dagger} \cdot \beta_{n,k}v_{n,k}\tilde{\mathbf{h}}_{n,n,k}, \tag{24}$$

where $\gamma_n \geq 0$ is the Lagrangian multiplier, and it should be chosen to ensure power constraint at LEO_n. With the active beamforming solution expression (24), the transmit power at LEO_n can be formulated as a function of γ_n, given by

$$\begin{aligned} p_n(\gamma_n) &= \sum_{k=1}^{K_n} \| \mathbf{w}_{n,k} \|^2 \\ &= \sum_{k=1}^{K_n} c_{n,k}(\tilde{\mathbf{h}}_{n,n,k}^{\mathrm{H}}[(\mathbf{S}_n + \gamma_n\mathbf{I})^{\dagger}]^{\mathrm{H}}(\mathbf{S}_n + \gamma_n\mathbf{I})^{\dagger}\tilde{\mathbf{h}}_{n,n,k}), \end{aligned} \tag{25}$$

where $c_{n,k} = |\alpha_{n,k}\beta_{n,k}v_{n,k}|^2$ and

$$\mathbf{S}_n = \sum_{l=1}^{N}\sum_{j=1}^{K_l} \alpha_{l,j}\beta_{l,j}|v_{l,j}|^2\tilde{\mathbf{h}}_{n,l,j}\tilde{\mathbf{h}}_{n,l,j}^{\mathrm{H}}.$$

Since the matrix $\mathbf{S}_n$ is a Hermitian matrix, it can be unitarily diagonalized. Upon applying the singular value decomposition (SVD) method, $\mathbf{S}_n$ can be decomposed as

$$\mathbf{S}_n = \mathbf{D}_n\Lambda_n\mathbf{D}_n^{\mathrm{H}}, \tag{26}$$

where Λ_n is a diagonal matrix containing $\tilde{r}_n$ positive eigenvalues and $N_s - \tilde{r}_n$ zero eigenvalues with $\tilde{r}_n$ being the rank of $\mathbf{S}_n$, $\mathbf{D}_n$ contains the singular vectors corresponding to the eigenvalues. Then, by substituting (27) into (25), the function (25) can be rewritten as

$$p_n(\gamma_n) = \sum_{m=1}^{N_s} \frac{[\boldsymbol{\Phi}_{\mathbf{n}}]_{mm}}{([\boldsymbol{\Lambda}_n]_{mm} + \gamma_n)^2},$$

where $\boldsymbol{\Phi}_n = \sum_{k=1}^{K_n} c_{n,k}\mathbf{D}_n^{\mathrm{H}}\tilde{\mathbf{h}}_{n,n,k}\tilde{\mathbf{h}}_{n,n,k}^{\mathrm{H}}\mathbf{D}_n$. It is clear that $p_n(\gamma_n)$ decreases consistently as γ_n increases. Therefore, if $\tilde{r}_n = N_s$ and $p_n(0) \leq P_n^{\max}$, the optimal γ_n is zero and the optimal solution of active beamforming is

$$\mathbf{w}_{n,k} = \sqrt{\frac{P_n^{\max}}{p_n(0)}}\alpha_{n,k}\beta_{n,k}v_{n,k}\mathbf{S}_{\mathbf{n}}{}^{\dagger}\tilde{\mathbf{h}}_{n,n,k}.$$

Else, the optimal γ_n should be determined within the search interval $(0, \gamma_n^{\mathrm{ub}})$, where the upper bound of the interval γ_n^{ub} is given by

$$\gamma_n^{\mathrm{ub}} = \sqrt{\frac{\sum_{m=1}^{N_s}[\Phi_n]_{mm}}{P_n^{\max}}}.$$

Upon using the bisection search method, the optimal multiplier γ_n^{opt} can be derived and the optimal solution of active beamforming can be obtained by substituting it into (24).

C. PASSIVE BEAMFORMING DESIGN

In this subsection, we focus on optimizating the passvie beamforming $\boldsymbol{\Theta}$. Due to the long distance between different service areas, the RIS only serves the UEs within its located area, and the signals from the RISs belonging to the other areas is negligible. In other words, RIS for each area can be optimized individually. Therefore, with fixed active beamforming $\mathbf{W}$, the problem (16) can be divided into N single RIS optimization problems, allowing for optimization in parallel at different satellites. In this context, the problem of passive beamforming optimization of RIS_n is denoted as

$$\min_{\mathbf{v}_n,\boldsymbol{\Theta}_n,\boldsymbol{\beta}_n} \sum_{k=1}^{K_n} \alpha_{n,k}(\beta_{n,k}\mathrm{MSE}_{n,k} - \log_2(\beta_{n,k}))$$

$$\text{s.t. } |\theta_{n,m}| = 1, \forall m \in N_r, \tag{27}$$

where $\mathbf{V}_n = \{v_{n,k}, \forall k \in K_n\}$ and $\boldsymbol{\beta}_n = \{\beta_{n,k}, \forall k \in K_n\}$ are the sets of receivers and auxiliary variables for the UEs in the n-th area, respectively. For convenience, the equivalent channel between LEO_l and $\mathrm{UE}_{n,k}$ is reformulated as

$$\tilde{\mathbf{h}}_{l,n,k}^{\mathrm{H}} = \mathbf{h}_{l,n,k}^{\mathrm{H}} + \boldsymbol{\varphi}_n^{\mathrm{H}}\mathrm{diag}(\mathbf{g}_{n,k}^{\mathrm{H}})\mathbf{G}_{l,n}, \tag{28}$$

where $\boldsymbol{\varphi}_n = [\varphi_{n,1}, \cdots, \varphi_{n,m}] = [[\boldsymbol{\Theta}_n]_{11}, \cdots, [\boldsymbol{\Theta}_n]_{MM}]$. Then, $\mathrm{MSE}_{n,k}$ in equation (17) with $\mathbf{W}_{l,j} = \mathbf{w}_{l,j}\mathbf{w}_{l,j}^{\mathrm{H}}$ can be expressed as

$$\mathrm{MSE}_{n,k} = \boldsymbol{\varphi}_n\boldsymbol{\Xi}_{n,k}\boldsymbol{\varphi}_n^{\mathrm{H}} + 2\Re\{\boldsymbol{\varphi}_n\boldsymbol{\Upsilon}_{n,k}\} + \delta_{n,k} + 1,$$

where

$$\boldsymbol{\Xi}_{n,k} = |v_{n,k}|^2 \sum_{l=1}^{N} \sum_{j=1}^{K_l} \operatorname{diag}\left(\mathbf{g}_{n,k}^{\mathrm{H}}\right)\mathbf{G}_{l,n}\mathbf{W}_{l,j}\mathbf{G}_{l,n}^{\mathrm{H}}\operatorname{diag}\left(\mathbf{g}_{n,k}\right),$$

$$\boldsymbol{\Upsilon}_{n,k} = |v_{n,k}|^2 \sum_{l=1}^{N} \sum_{j=1}^{K_l} \operatorname{diag}\left(\mathbf{g}_{n,k}^{\mathrm{H}}\right)\mathbf{G}_{l,n}\mathbf{W}_{l,j}\mathbf{h}_{l,n,k} - \operatorname{diag}\left(\mathbf{g}_{n,k}^{\mathrm{H}}\right)\mathbf{G}_{n,n}\mathbf{w}_{n,k}v_{n,k}$$

and

$$\delta_{n,k} = |v_{n,k}|^2 \sum_{l=1}^{N} \sum_{j=1}^{K_l} \mathbf{h}_{l,n,k}^{\mathrm{H}}\mathbf{W}_{l,j}\mathbf{h}_{l,n,k} + 2\Re\{v_{n,k}\mathbf{h}_{n,k}^{\mathrm{H}}\mathbf{w}_{n,k}\}.$$

By updating $\mathbf{V}_n$ and $\boldsymbol{\beta}_n$ in a manner similar to the active beamforming design and eliminating the constant terms, problem (31) is reduced as

$$\min_{\boldsymbol{\varphi}_n} \boldsymbol{\varphi}_n \boldsymbol{\Xi}'_n \boldsymbol{\varphi}_n^{\mathrm{H}} + 2\Re\{\boldsymbol{\varphi}_n \boldsymbol{\Upsilon}'_n\} \quad \text{s.t. } |\varphi_{n,m}| = 1, \forall m \in N_r,$$

where

$$\boldsymbol{\Xi}'_n = \sum_{k=1}^{K_n} \alpha_{n,k}\beta_{n,k}\boldsymbol{\Xi}_{n,k}$$

and

$$\boldsymbol{\Upsilon}'_n = \sum_{k=1}^{K_n} \alpha_{n,k}\beta_{n,k}\boldsymbol{\Upsilon}_{n,k}.$$

Because of the unit modulus constraint (37b), problem (37) remains non-convex. To this end, we adopt the ADMM to address it. Upon introducing dual variable $\boldsymbol{\xi}_n = [\xi_{n,1}, \xi_{n,2}, \ldots, \xi_{n,K}]$ and a penalty term $\frac{\rho}{2} \| \boldsymbol{\varphi}_n - \boldsymbol{\phi}_n \|^2$ into problem (37) to address the non-convex constraint (37b), we have

$$\min_{\boldsymbol{\varphi}_n, \boldsymbol{\xi}_N, \boldsymbol{\phi}_n} \boldsymbol{\varphi}_n \boldsymbol{\Xi}'_n \boldsymbol{\varphi}_n^{\mathrm{H}} + 2\Re\{\boldsymbol{\varphi}_n \boldsymbol{\Upsilon}'_n\} + \Re\{\boldsymbol{\xi}^{\mathrm{H}}(\boldsymbol{\varphi}_n - \boldsymbol{\phi}_n)\} + \frac{\rho}{2} \| \boldsymbol{\varphi}_n - \boldsymbol{\phi}_n \|^2$$

$$\text{s.t. } |\varphi_{n,m}| \le 1, \forall m \in N_r, \quad |\phi_{n,m}| = 1, \forall m \in N_r,$$

where $\boldsymbol{\phi}_n = [\phi_{n,1}, \cdots, \phi_{n,N_r}]$ are the auxiliary variables. It is evident that problem (40) is convex for each variable when the other two variables are fixed and can be addressed by alternately updating each variable until convergence, and the updating method of each variable is introduced in the following. Firstly, when $\boldsymbol{\xi}_N$ and $\boldsymbol{\phi}_n$ are fixed, the problem (40) is simplified as

$$\min_{\boldsymbol{\varphi}_n} \boldsymbol{\varphi}_n \boldsymbol{\Xi}'_n \boldsymbol{\varphi}_n^{\mathrm{H}} + 2\Re\{\boldsymbol{\varphi}_n \boldsymbol{\Upsilon}'_n\} + \Re\{\boldsymbol{\xi}^{\mathrm{H}}(\boldsymbol{\varphi}_n - \boldsymbol{\phi}_n)\} + \frac{\rho}{2} \| \boldsymbol{\varphi}_n - \boldsymbol{\phi}_n \|^2 \quad \text{s.t. (40b)}, \tag{34}$$

which is convex and can be readily addressed using mathematical toolboxes like CVX. For variable $\boldsymbol{\phi}_n$, with obtained $\boldsymbol{\varphi}_n$ and $\boldsymbol{\xi}_n$ from the last iteration and eliminating constant terms, problem (41) is simplified as

$$\min_{\boldsymbol{\phi}_n} \Re\{-(\boldsymbol{\xi}_n + \rho\boldsymbol{\varphi}_n)^{\mathrm{H}}\boldsymbol{\phi}_n\} \quad \text{s.t. } |\phi_{n,m}| = 1, \forall m \in N_r, \tag{36}$$

which has an optimal closed-form solution for $\boldsymbol{\phi}_n$, given by

$$\boldsymbol{\phi}_n = e^{j\angle(\xi_n + \rho\varphi_n)}. \tag{37a}$$

For variable $\boldsymbol{\xi}_n$, the optimal solution with obtained $\boldsymbol{\phi}_n$ and $\boldsymbol{\varphi}_n$ is expressed as (37b)

$$\boldsymbol{\xi}_n = \boldsymbol{\xi}_n + \rho(\boldsymbol{\varphi}_n - \boldsymbol{\phi}_n). \tag{38}$$

By iteratively optimizing the active beamforming and passive beamforming until convergence, we can maximize the WSR of RIS-assisted LEO satellite constellation communication under power constraints. In conclusion, the joint beamforming design is summarized in Algorithm 1 on this page. (39)

Table 1 The joint beamforming design algorithm

Algorithm 1: The joint beamforming design

Input: $\mathbf{h}_{l,n,k}, \mathbf{g}_{n,k}, \mathbf{G}_{l,n}, N, K_n, P_n^{\max}, T^{\max}, N_r, \sigma_{n,k}^2$

Output: $\boldsymbol{\Theta}_n, \mathbf{w}_{n,k}$

1: Initialize iteration index $i = 1$, convergence criteria $\Delta = 1$, feasible active beamforming $\mathbf{W}$, passive beamforming $\boldsymbol{\Theta}$, $\boldsymbol{\xi}_n$, $\boldsymbol{\phi}_n$ and set weighted sum rate $\mathrm{WSR}^{(1)} = 0$. (40a) (40b) (40c)

2: While $\Delta > 0.01$ and $i < T^{\max}$

3: Calculate $v_{n,k} = \mathbf{w}_{n,k}^{\mathrm{H}}\tilde{\mathbf{h}}_{n,n,k}\vartheta_{n,k}^{-1}$ and $\beta_{n,k} = \mathrm{MSE}^{-1}$.

4: For $n = 1{:}N$

5: Calculate the $p_n(0)$ according to (28);

6: if $p_n(0) \le P_n^{\max}$ then

7: Obtain $\mathbf{w}_{n,k}^{(i+1)}$ according to (29);

8: else

9: Get the γ_n^{opt} by the bisection search

method and then Obtain $\mathbf{w}_{n,k}^{(i+1)}$ by substituting γ_n^{opt} into (24)
10: end if
11: end for
12: For $n = 1{:}N$
13: Calculate Ξ'_n and Υ'_n according to (38) and (39);
14: Repeat
14: Calculate passive beamforming $\boldsymbol{\varphi}_n^{(i+1)}$ by solving problem (41);
15: Update $\boldsymbol{\phi}_n$ and $\boldsymbol{\xi}_n$ according to (43) and (44);
16: Until convergence
17: end for
18: Update $\tilde{\mathbf{h}}_{l,n,k}^{\mathrm{H}}$ according to (32);
19: Update $\mathrm{WSR}^{(i+1)} = \sum_{n=1}^{N}\sum_{k=1}^{K_n}\alpha_{n,k}R_{n,k}$;
20: Update $\Delta = \mathrm{WSR}^{(i+1)} - \mathrm{WSR}^{(i)}$;
21: Update $i = i + 1$;
22: end while

D. ALGORITHM ANALYSIS

Herein, we explore the convergence and complexity characteristics of the proposed joint beamforming design algorithm, respe

In Algorithm 1, the optimal solution of (16) is achieved by iteratively optimizing $\boldsymbol{\Theta}$ and $\mathbf{W}$. At ith iteration, let $\mathcal{F}(\mathbf{W}^{(i)}, \boldsymbol{\Theta}^{(i)})$ represent the value of the objective function (16a). To be specific, we start by solving the convex problem (23), which corresponds to the original problem (16a) with fixed $\boldsymbol{\Theta}^{(i)}$. After obtaining $\mathbf{W}^{(i+1)}$ from Step 3 to Step 11, we get

$$\mathcal{F}(\mathbf{W}^{(i+1)}, \boldsymbol{\Theta}^{(i)}) \geq \mathcal{F}(\mathbf{W}^{(i)}, \boldsymbol{\Theta}^{(i)}).$$

Then, with obtained $\boldsymbol{\Theta}^{(i+1)}$ from the Step 12-17 of Algorithm 1, we get

$$\mathcal{F}(\mathbf{W}^{(i+1)}, \boldsymbol{\Theta}^{(i+1)}) \geq \mathcal{F}(\mathbf{W}^{(i+1)}, \boldsymbol{\Theta}^{(i)}),$$

which holds true because problem (41) is the augmented Lagrangian problem of problem (37), and the convergence of these two problems is identical and can be guaranteed [36]. Finally, according to (45) and (46), we get

$$\mathcal{F}(\mathbf{W}^{(i+1)}, \boldsymbol{\Theta}^{(i+1)}) \geq \mathcal{F}(\mathbf{W}^{(i)}, \boldsymbol{\Theta}^{(i)}),$$

which indicates that the WSR is non-decresing after each iteration. Moreover, there is a definite upper bound of WSR under the given maximum transmit power constraints. Therefore, we can affirm that Algorithm 1 will converge, as per the monotone boundedness theorem [37]. Furthermore, we demonstrate the convergence under different power constraints in Fig. 2. Observably, Algorithm 1 converges after less than 10 iterations.

Next, we analyze the computational complexity of Algorithm 1. Since each UE has only one antenna, the major complexity of the active beamforming design comes from the multiplication of complex matrices and the SVD of matrices. Specifically, the complexity involved in computing matrix $\boldsymbol{\Phi}_n, \forall n \in N$ is $\mathcal{O}(N^2N_s^2)$. The complexity of the decomposition of matrix $\mathbf{S}_n, \forall n \in N$ is $\mathcal{O}(NN_s^3)$. The complexity of calculating the optimal active beamforming $\mathbf{W}$ for all UEs is $\mathcal{O}(KN_s^3)$. Thus, the overall complexity of active beamforming design is $\mathcal{O}(KN_s^3)$. For passive beamforming design, the primary complexity arises from resolving the problem (41), which encompasses N_r optimization variables and is subject to N_r linear matrix inequality (LMI) constraints concerning each variable. Hence, the overall complexity of passive beamforming design is $\mathcal{O}\left(2\sqrt{2}NN_r^{\frac{5}{2}}\right)$ [38]. Finally, the total computational complexity of Algorithm 1 is $\mathcal{O}\left(KN_s^3 + 2\sqrt{2}NN_r^{\frac{5}{2}}\right)$.

IV. NUMERICAL RESULT

This section performs extensive numerical simulations to evaluate

(45)

UEs are distributed according to the commonly adopted Poisson point process (PPP) within the circular area centered on the RIS with a specified radius. Unless otherwise stated, the parameters are

(46)

listed in Table 2. In particular, we compare the proposed algorithm to benchmark algorithms listed below:

• Without RIS: No RIS is deployed in the network. To be specific, we set the subchannels $\mathbf{G}_{l,n}$ and $\mathbf{g}_{n,k}$ in RIS-assisted link to zero matrices and only the active beamforming design is executed.

(47)

• Random RIS: RISs are deployed in the network with

random passive beamforming and only the active beamforming design is executed.

• Upper bound [39]: Relax the unit modulus constraint (41) to $|\varphi_{n,m}| \le 1$ and solve problem (31) to get the passive beamforming, while the active beamforming design is the same as the proposed algorithm.

• Convex-concave procedure (CCP) algorithm [40]: Implement passive beamforming design with the penalty CCP. Specifically, by rewriting the unit modulus constraint (41) as $1 \le |\varphi_{n,m}| \le 1$, we have two new inequality constraints. Then, the right-hand inequality $1 \le |\varphi_{n,m}|$ can be transformed into $1 \le 2\Re\left\{\varphi_{n,m}\varphi_{n,m}^{(i)}\right\} - |\varphi_{n,m}^{(i)}|^2$ by using the successive convex approximation (SCA) method, where $\varphi_{n,m}^{(i)}$ is the solution of $\varphi_{n,m}$ obtained from the i-th iteration. Upon introducing $2N_r$ slack variables $\{e_1, e_2, e_3, \ldots, e_{2N_r}\}$ and penalty term $\rho^{(i)}\sum_{m=1}^{2N_r} e_m$, the problem (31) can be reformulated as

$$\min_{\boldsymbol{\varphi}_n} \boldsymbol{\varphi}_n^{\mathrm{H}}\boldsymbol{\Xi}_n\boldsymbol{\varphi}_n + 2\Re\{\boldsymbol{\varphi}_n^{\mathrm{H}}\boldsymbol{\Upsilon}_n\} + \rho^{(i)}\sum_{m=1}^{2N_r} e_m \tag{48a}$$

$$\text{s.t. } |\varphi_{n,m}^{(i)}|^2 - 2\Re\left\{\varphi_{n,m}\varphi_{n,m}^{(i)}\right\} \le e_m = -1, \forall m \in N_r, \tag{48b}$$

$$|\varphi_{n,m}| \le 1 + e_{m+N_r}, \forall m \in N_r, \tag{48c}$$

where $\rho^{(i)}$ represents the penalty factor in the i-th iteration.

• Semidefinite relaxation (SDR) algorithm [41]: Implement passive beamforming design by adopting the SDR technique. Speci

$$\min_{\boldsymbol{\varphi}_n} \overline{\boldsymbol{\varphi}}_n \mathrm{F}_n \overline{\boldsymbol{\varphi}}_n^{\mathrm{H}} \tag{49a}$$

$$\text{s.t. } |\varphi_{n,m}| = 1, \forall m \in N_r, \tag{49b}$$

where $\overline{\boldsymbol{\varphi}}_n = [\boldsymbol{\varphi}_n, 1]$ and

$$\mathrm{F}_n = \begin{bmatrix} \boldsymbol{\Xi}'_n & \boldsymbol{\Upsilon}'_n \\ (\boldsymbol{\Upsilon}'_n)^{\mathrm{H}} & 0 \end{bmatrix}. \tag{50}$$

Finally, by defining $\boldsymbol{\Psi}_n = \overline{\boldsymbol{\varphi}}_n^{\mathrm{H}}\overline{\boldsymbol{\varphi}}_n$ and adopting the SDR technique, the problem can be rewritten as

$$\min_{\boldsymbol{\Psi}_n} \mathrm{tr}\{\boldsymbol{\Psi}_n \mathrm{F}_n\} \tag{51a}$$

$$\text{s.t. } [\boldsymbol{\Psi}_n]_{ii} = 1, \forall i \in (N_r + 1), \tag{51b}$$

$$\boldsymbol{\Psi}_n \succeq 0. \tag{51c}$$

which is a semidefinite programming (SDP) problem, and can be solved easily. Finally, the passive beamforming can be obtained from the solution of problem (51).

Table 2 PARAMETER SETUP

Parameter	Value
Propagation distance $d_{l,n}$	550 km
Carrier frequency f	30 GHz
Spectrum bandwidth B	25 MHz
Number of satellites N	3
Number of antennas N_s	32
Maximum transmit power $P_n^{\max}$	30 dBm
Number of RISs N	3
Number of UEs K	24
Priority coefficient of UEs $\alpha_{n,k}$	1
Number of reflecting elements of RIS N_r	100
Transmit gain to noise temperature G_k/T	34 dB/K
Satellite antenna gain b_k	20 dBi
Boltzmann constant κ	$1.38 \times 10^{-23} J/m$
Rain attenuation mean μ_r	-2.6 dB
Rain attenuation variance σ_r^2	1.63 dB
AWGN variance $\sigma_{n,k}^2$	-170 dBm
3dB angle χ_l	0.4°
AoD of signals at LEO_n $\Phi_{l,n}$	$[\pi/2, 3\pi/2]$
AoA of singal $\Phi'_{l,n}$	$[3\pi/4, 5\pi/4]$
AoD of singal at RIS_n $\Phi''_{l,n}$	$[0, 2\pi)$
Rician factor of $\mathbf{G}_{l,n}$ $\mathcal{K}$	8
Rician factor of $\mathbf{g}_{n,k}$ $\mathcal{K}$	10
Maximum iteration number $T^{\max}$	30

First, we show the convergence behavior of the proposed algorithm 1 under different maximum transmit power $P_n^{\max}, \forall n \in N$ in Fig. 2. It is clear that the WSR increases continuously during the iterations, with convergence achieved within 10 iterations across different maximum transmit power settings. Furthermore, the WSR improves accordingly as the maximum transmit power increases.

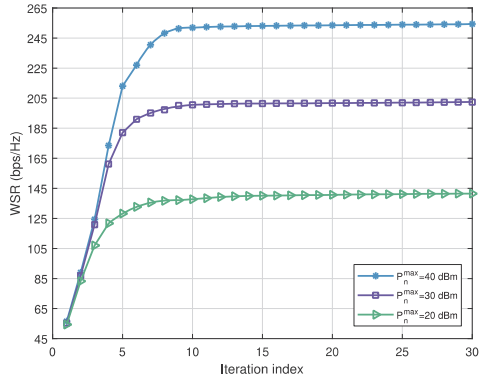

Figure 2 Convergence of the proposed Algorithm 1.

Secondly, in Fig. 3, we analyze the performance enhancement of the proposed algorithm in contrast to the benchmark algorithms at different maximum transmit power levels. The performance improvement achieved by “Random RIS" can be disregarded when compared to the scenario without RIS. Instead, by employing the proposed algorithm to design the passive beamforming, a significant performance improvement can be achieved, thus enhancing the quality of service (QoS) for UEs. This is because even though the signals reflected by the RISs with random passive beamforming have not been perfectly aligned towards UEs, UEs can still receive the signals through the direct link with the active beamforming at LEO satellites. On the contrary, the signals reflected by the RISs with the designed passive beamforming can further strengthen the desired signal, while suppressing the interference. Moreover, the observed performance improvement of the proposed algorithm exceeds that of CCP algorithm and SDR algorithm. This is because the results obtained by the CCP algorithm utilizing the SCA method to deal with the unit modulus constraints are more deviated from the optimal solution, while the SDR algorithm often fails to get a optimal rank-one solution to problem (51) and then requires additional steps to construct a feasible solution for passive beamforming, such as the Gaussian randomization technique. Furthermore, the effectiveness of the proposed algorithm is further demonstrated by the fact that the performance of the proposed algorithm is close to the “upper bound".

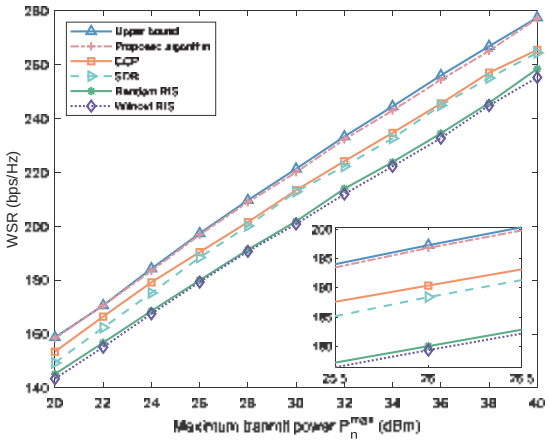

Figure 3 WSR versus the maximum tranmit power.

Next, we show in Fig. 4 how the number of reflecting elements in RISs influences the system performance. The performance of the proposed algorithm is improved by increasing the number of reflecting elements. The reasons are two-fold. On the one hand, since the RIS contains many passive reflective elements, an increment in the quantity of these elements results in an increment in the signal power received by RIS. On the other hand, incorporating more reflective elements provides additional channels from RIS to UEs, increasing spatial flexibility. This enables RIS to more effectively boost the desired signal and suppress interference with the enhanced passive beamforming capability. Nevertheless, escalating the amount of reflecting elements in RIS not only escalates deployment costs but also magnifies the algorithm’s computational complexity. Therefore, it is meaningful to strike a tradeoff between the performance and the quantity of reflecting elements when deploying RIS in practice. In addition, Fig. 4 also demonstrates that deploying RIS with random passive beamforming may lead to a worse performance compared to the scenario without deploying RIS, which indicates that properly configuring RIS is equally crucial.

Then, we demonstrated the influence of the distribution radius of UEs with respect to the RIS on the performance in each area, as shown in Fig. 5. The result indicates that the WSR decreases as the

distribution radius increases. When the distribution radius reaches 100 meters, the proposed algorithm performance approximates the scenario without RIS. This is because as the radius increases, the increased path-loss between the RIS and UE results in a weaker reflected signal received at the UE. Hence, it makes sense to deploy the RIS close to the UEs.

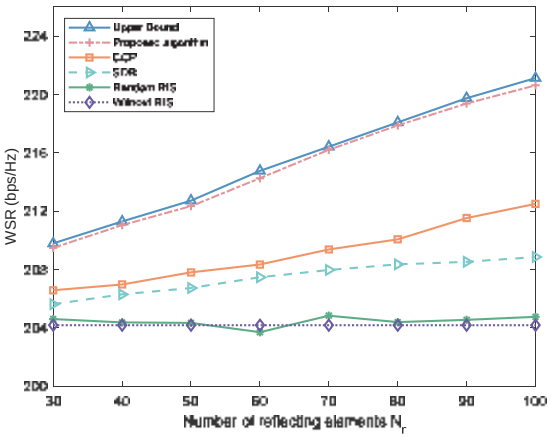

Figure 4 WSR versus the number of reflecting elements.

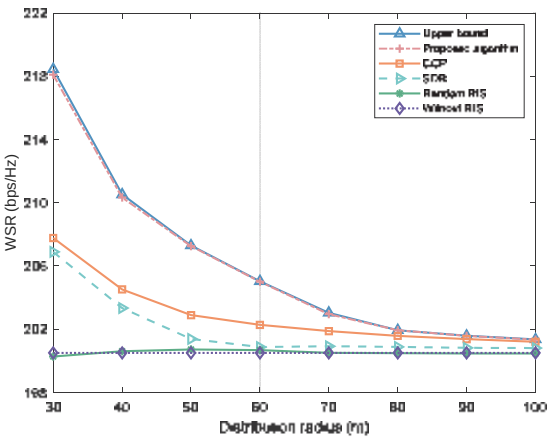

Figure 5 WSR versus the distribution radius.

In Fig. 6, the proposed algorithm's performance is assessed across orbital altitudes ranging from 300 to 2000 kilometers, revealing a reduction in WSR with ascending orbit altitudes. It is due to the increment in orbital altitude resulting in augmented path loss for both the direct and RIS-assisted channels. In addition, higher orbit altitude also results in higher transmission delay. As a result, both academia and industry are placing great emphasis on very LEO (VLEO) satellites as they have the potential to support the ultra-low latency and high throughput requirements of future 6G networks [42].

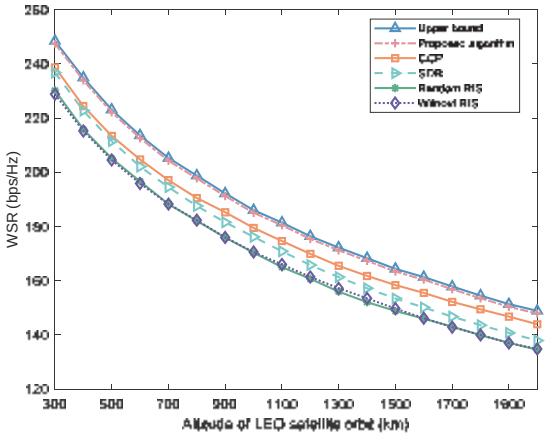

Figure 6 WSR versus the altitude of LEO satellites orbit.

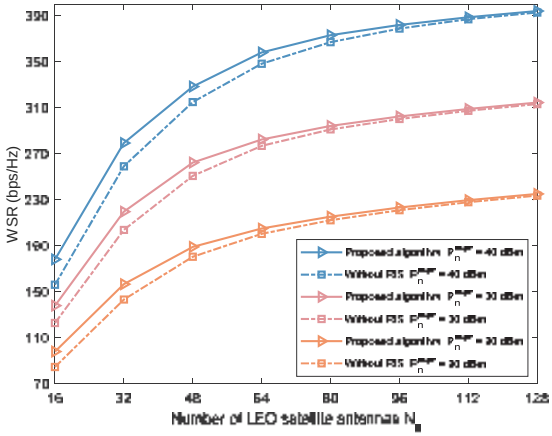

Figure 7 WSR versus the number of LEO satellite antennas.

In Fig. 7, we show the effect of varying numbers of LEO satellite antennas on performance. The WSR demonstrates an increase with a diminishing rate as the number of antennas rises. This trend can be attributed to the amplified array gain and increased freedom resulting from the augmented number of antennas on the LEO satellite, which notably enhances the direct channels between the satellite and UEs. However, the WSR will not infinitely increase with the growing

number of antennas, as there are limitations on maximum transmit power. However, equipping more antennas on the satellite leads to increased production costs and heightened computational complexity in the design of active beamforming. Hence, it is crucial to select an optimal number of antennas that strikes a balance between performance and the associated production and computational costs. Furthermore, Fig. 7 also indicates that the performance improvement achieved through optimizing passive beamforming at RISs diminishes as the number of satellite antennas increases. Thus, optimizing passive beamforming at RISs becomes essential for performance enhancement, especially when the antennas is few.

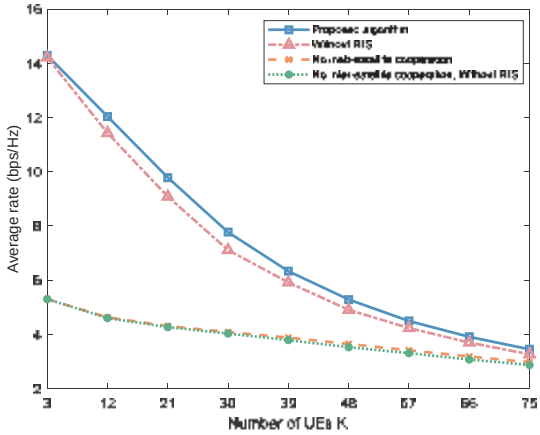

Figure 8 Average rate versus the number of UEs.

Finally, we depict the influence of joint beamforming design under different inter-satellite cooperation scenarios in Fig. 8. Here, “No inter-satellite cooperation" denotes that there doesn’t exist cooperation between satellites while each satellite designs the beamforming independently. In particular, the average rate is the result of dividing the WSR by the number of UEs, offering a better reflection on how the number of UEs influences system performance. The proposed algorithm surpasses the “No inter-satellite cooperation" obviously, especially in scenarios where the number of UEs is less. This occurs because the proposed algorithm maximizes the advantages derived from inter-satellite cooperation. Through inter-satellite cooperation, the shared CSI among satellites enables comprehensive consideration of all UEs when designing satellite active beamforming and RIS passive beamforming. Fig. 8 also demonstrates that the performance improvement achieved by optimizing RISs under the inter-satellite cooperation scenario exceeds that in the no inter-satellite cooperation scenario, highlighting the advantage of deploying and optimizing RISs in the inter-satellite cooperation scenario. Furthermore, inter-satellite cooperation enables higher capacity and faster data transmission rates due to the ability of satellites to exchange data with each other.

V. CONCLUSION

In this paper, we presented a RIS-assisted LEO satellite constellation communication framework to provide global coverage for ground UEs. By deploying the RISs in ground areas, the signals at UEs were significantly enhanced. To maximize the WSR of UEs while constraining the transmit power of the satellites, a non-convex optimization problem was formulated and solved. In particular, the active beamforming at satellites and the passive beamforming at RISs were jointly optimized by making use of inter-satellite links. Through the joint optimization of the beamforming, the inter-satellite interference is well suppressed and the communication quality is enhanced. Simulation results confirmed the effectiveness of the proposed joint beamforming design algorithm for RIS-assisted LEO satellite constellation communications.

Acknowledge

This work was supported by the Natural Science Foundation of China under Grant 62231009 and U21A20443.

References

[1] CHEN X M. Massive access for cellular internet of things theory technique [M]. Berlin, Germany: Springer, 2019.

[2] DING C, WANG J B, ZHANG H, et al. Joint optimization of transmission and computation resources for satellite and high altitude platform assisted edge computing [J]. IEEE Transactions on Wireless Communications, 2022, 21(2): 1362-1377.

[3] PAN X, ZHAN Y, ZENG G, et al. TT&C capacity analysis of mega-constellations: how many satellites can we support [C]// IEEE International Conference on Communications, Seoul, c2022: 2393-2398.

[4] HANDLEY M, Delay is not an option: Low latency routing in space [C]// Proceedings of the 17th ACM Workshop on Hot Topics in Networks, New York, c2018: 85-91.

[5] CHU J H, CHEN X M, ZHONG C J, et al. Robust design for NOMA-based multibeam LEO satellite Internet of Things [J]. IEEE Internet of Things Journal, 2021, 8(3): 1959-1970.

[6] FANG X R, FENG W, WEI T, et al. 5G embraces satellites for 6G ubiquitous IoT: Basic models for integrated satellite terrestrial networks [J]. IEEE Internet of Things Journal, 2021, 8(18): 14399-14417.

[7] CORSINOVI N, CIARDI R, PAGANI E, et al. Adaptive equalization as method for satellite communication channel characterization [C]//2023 IEEE 10th International Workshop on Metrology for AeroSpace, Milan, c2023: 580-584.

[8] AHMED W A, WU F L, BALOGUN B O, et al. Performance analysis of least square-based decision feedback equalization technique for mobile satellite communications [C]//IEEE International Conference on Signal Processing, Beijing, c2018: 722-726.

[9] SCHWARZ R T, DELAMOTTE T, STOREK K U, et al. MIMO applications for multibeam satellites [J]. IEEE Transactions on Broadcasting, 2019, 65(4): 664-681.

[10] LIN Z, LIN M, CHANPAPAGNE B, et al. Secrecy-energy efficient hybrid beamforming for satellite-terrestrial integrated networks [J]. IEEE Transactions on Communications, 2021, 69(9): 6345-6360.

[11] Qi C H, WANG X, Precoding design for energy efficiency of multibeam satellite communications [J]. IEEE Communications Letters, 2018, 22(9): 1826-1829.

[12] YOU X H, WANG C X, HUANG J, et al. Towards 6G wireless communication networks: vision enabling technologies and new paradigm shifts [J]. Science China Information Sciences, 2021, 64(1).

[13] LIN X Y, ZOU Y L LI B, et al. Security-reliability trade-off analysis of RIS-aided multiuser communications [J]. IEEE Transactions on Vehicular Technology, 2023 72(5): 6225-6237.

[14] HE M X, XU J D, XU W, et al. RIS-assisted quasi-static broad coverage for wideband mmWave massive MIMO systems [J]. IEEE Transactions on Wireless Communications, 2023, 22(4): 2551-2565.

[15] LIU S F, LIU R, LI M, et al. Joint BS-RIS-user association and beamforming design for RIS-assisted cellular networks [J]. IEEE Transactions on Vehicular Technology, 2023, 72(5): 6113-6128.

[16] PAN C H, REN H, WANG K Z, et al. Multicell MIMO communications relying on intelligent reflecting surfaces [J]. IEEE Transactions on Wireless Communications, 2020, 19(8): 5218-5233.

[17] HAN P B, ZHOU Z Y, WANG Z C, Joint user association and passive beamforming in heterogeneous networks with reconfigurable intelligent surfaces [J]. IEEE Communications Letters, 2021 25(9): 3041-3045.

[18] LEE J, SHIN W J, LEE J W, Performance analysis of IRS-assisted LEO satellite communication systems [C]// International Conference on Information and Communication Technology Convergence, Jeju Island, c2021: 323-325.

[19] TEKBIYIK K, KURT G K, EKTI A R, et al. Reconfigurable intelligent surfaces empowered THz communication in LEO satellite networks [J]. IEEE Access, 2022 10: 121957-121969.

[20] HASSAN S S, PARK Y M, TUN Y K, et al. SpaceRIS: LEO satellite coverage maximization in 6G sub-THz networks by MAPPO DRL and whale optimization [J]. 2024 IEEE Journal on Selected Areas in Communications, 2024, 42(5): 1262-1278.

[21] LIN Z, NIU H H, AN K, et al. Refracting RIS-aided hybrid satellite-terrestrial relay networks: Joint beamforming design and optimization [J]. IEEE Transactions on Aerospace and Electronic Systems, 2022, 58(4): 3717-3724.

[22] KHAN W U, LAGUNAS E, MAHMOOD A, et al. Energy-efficient RIS-enabled NOMA communication for 6G LEO satellite networks [C]//IEEE 97th Vehicular Technology Conference, Florence, c2023: 1-6.

[23] GUO K F, AN K, On the performance of RIS-assisted integrated satellite-UAV-terrestrial networks with hardware impairments and interference [J]. IEEE Wireless Communications Letters, 2022, 11(1): 131-135.

[24] HOU T W, LI A N, Performance analysis of NOMA-RIS aided integrated navigation and communication (INAC) networks [J]. IEEE Transactions on Vehicular Technology, 2023, 72(10): 13255-13268.

[25] FENG K, ZHOU T, XU T H, et al. Reconfigurable intelligent surface-assisted multisatellite cooperative downlink beamforming [J]. IEEE Internet of Things Journal, 2024, 11(13): 23222-23235.

[26] HOANG T M, XU C, VAHID A, et al. Secrecy-rate optimization of double RIS-aided space–ground networks [J]. IEEE Internet of Things Journal, 2023, 10(15): 13221-13234.

[27] DENG R Q, DI B Y, ZHANG H L, et al. Ultra-dense LEO satellite constellations: How many LEO satellites do we need? [J]. IEEE Transactions on Wireless Communications, 2021, 21(8): 4843 – 4857.

[28] TANG J Y, BIAN D M, LI G X, et al. Resource allocation for LEO beam-hopping satellites in a spectrum sharing scenario [J]. IEEE Access, 2021 9: 56468-56478.

[29] ZHANG B K, LIU J H, WEI Z L, et al. A deep reinforcement learning based approach for energy-efficient channel allocation in satellite internet of things [J]. IEEE Access, 2020 8: 62197 – 62206.

[30] HU J, LI G X, BIAN D M, et al. Optimal power control for cognitive LEO constellation with terrestrial networks [J]. IEEE Communications Letters, 2020, 24(3): 622-625.

[31] LIN Z Y, NI Z Y, KUANG L L, et al. Multi-satellite beam hopping based on load balancing and interference avoidance for NGSO satellite communication systems [J]. IEEE Transactions on Communications, 2023, 71(1): 282-295.

[32] YING M, CHEN X M, SHAO X D, Exploiting tensor-based Bayesian learning for massive grant-free random access in LEO satellite Internet of Things [J]. IEEE Transactions on Communications, 2023, 71(2): 1141-1152.

[33] HAN Y, TANG W K, JIN S, et al. Large intelligent surface-assisted wireless communication exploiting statistical CSI [J]. IEEE Transactions on Vehicular Technology, 2019, 68(8): 8238-8242.

[34] HAN S M, LEE W J, SHIN W J, et al. Adaptive beam size design for LEO satellite networks with doppler shift compensation [C]//IEEE VTS Asia Pacific Wireless Communications Symposium, Seoul, c2022: 26-30.

[35] SHI Q J, RAZAVIYAYN M; LUO Z Q, et al. An iteratively weighted MMSE approach to distributed sum-utility maximization for a MIMO interfering broadcast channel [C]//IEEE International Conference on Acoustics, Speech and Signal Processing, Prague, c2011: 4331-4340.

[36] MAGNUSSON S, WEERADDANDA P C, RABBAT M G, et al. Sindri Magnússon; Pradeep Chathuranga Weeraddana [J]. IEEE Transactions on Control of Network Systems, 2016 3(3): 296-309.

[37] BEZDEK J C, HATHAWAY R J. Convergence of alternating optimization [J]. Neural, Parallel & Scientific Computations, 2003, 11(4): 351-368.

[38] WANG K Y, SO A M, CHANG T H, et al. Outage constrained robust transmit optimization for multiuser MISO downlinks: Tractable approximations by conic optimization [J]. IEEE Transactions on Signal Processing, 2014, 62(21): 5690-5605.

[39] ZHANG Y, ZHONG C J, ZHANG Z Y, et al. Sum rate optimization for two way communications with intelligent reflecting surface [J]. IEEE Communications Letters, 2020, 24(5): 1090-1094.

[40] ZHOU G, PAN C H, REN H, et al. A framework of robust transmission design for IRS-aided MISO communications with imperfect cascaded channels [J]. IEEE Transactions on Signal Processing, 2020, 68: 5092-5106.

[41] WU Q Q, ZHANG R. Intelligent reflecting surface enhanced wireless network via joint active and passive beamforming [J]. IEEE Transactions on Wireless Communications. 2019, 18(11): 5394-5409.

[42] CHEN G Q, WU S H, DENG Y J, et al. VLEO stellite constellation design for regional aviation and marine coverage [J]. IEEE Transactions on Network Science and Engineering, 2024, 11(1): 1188-1201

About the authors

YAO Wenfei received the B.E. degree in Information Engineering from Zhejiang University, Hangzhou, China, in 2023. He is pursuing the M.sc. degree in the College of Information Science and Electronic Engineering, Zhejiang University, Hangzhou, China. His research interests include reconfigurable intelligent surface, Internet of Things, and satellite communications. (Email: yaowenfei@zju.edu.cn)

WANG Qi received the B.E. degree in Communication Engineering from Nankai University, Tianjin, China, in 2021. He is pursuing the Ph. D. degree in the College of Information Science and Electronic Engineering, Zhejiang University, Hangzhou, China. His research interests include integrated computing and communications, Internet of Things, and satellite communications. (Email: wang-qi@zju.edu.cn)

CHEN Xiaoming [corresponding author] received the B.Sc. degree from Hohai University in 2005, the M.Sc. degree from Nanjing University of Science and Technology in 2007 and the Ph. D. degree from Zhejiang University in 2011, all in electronic engineering. He is currently a Professor with the College of Information Science and Electronic Engineering, Zhejiang University, Hangzhou, China. His research interests mainly focus on 5G/6G key techniques, satellite-ground integrated networks, and smart communications. (Email: chen_xiaoming@zju.edu.cn)

热红外双向加密采样模式超分辨率方法研究

赵泉[1]，王密[1]，谢广奇[2]

摘　要：本文介绍了热红外载荷的双向加密采样的原理与方法，验证了该模式超分辨率的效果，提出了一种顾及硬件特性的最大后验概率（MAP）超分辨率方法。在双向加密采样的硬件基础上，引入了观测方程模型和MAP 方法实现影像超分辨率重建。资源一号 02E 卫星的热红外载荷是我国首个通过“双向加密采样”的方式支持影像超分辨率的遥感载荷。与 SPOT-5 通过 2 帧加密采样的模式类似，资源一号 02E 在 SPOT-5 加密采样模式的基础上，再获取仅在沿轨方向偏移 0.5 个像素与仅在垂轨方向偏移 0.5 个像素的 2 帧影像，即可以获取 4 帧存在半像素相对偏移的影像。本文使用资源一号 02E 的真实热红外加密采样模式数据进行了 2 倍超分辨率的验证分析，实验表明双向加密采样的硬件模式相比常规成像模式能够有效提高分辨率。本文算法分别优于仅考虑硬件特性的双向加密上采样与仅考虑软件算法的传统 MAP 超分辨率方法，是一种软硬件结合的有效超分辨率方法，获得的超分辨率图像目视清晰，在保持较高信噪比的同时重建了影像的高频细节信息。

关键词：热红外，资源一号 02E 卫星，双向加密采样，超分辨率，最大后验概率

A super-resolution method for thermal infrared bidirectional sub-pixel shifted sampling mode

ZHAO Quan[1], WANG Mi[1], XIE Guangqi[2]

Abstract: This paper describes in detail the principle and method of bidirectional overlapping sub-pixel shifted sampling of the thermal infrared camera of ZY-1 02E, verifies the effect of this mode of super-resolution, and proposes a super-resolution method that takes into account the hardware characteristics. Based on the hardware of bidirectional overlapping sub-pixel shifted sampling, the observation equation model and maximum a posteriori probability (MAP) method are introduced to realize the image super-resolution. The thermal infrared payload of ZY-1 02E satellite is the first remote sensing payload in China that supports image super-resolution by means of "bidirectional overlapping sub-pixel shifted sampling". Similar to the SPOT-5 mode, ZY-1 02E acquires 2 frames shifted by only 0.5 pixels in the along-track direction and then 0.5 pixels in the vertical direction additionally, i.e., it can acquire 4 frames with half-pixel relative shifts. In this paper, we use the thermal infrared overlapping sampling mode data of ZY-1 02E to validate and analyze super-resolution, and the experiments show that the hardware mode of bidirectional encrypted sampling can effectively improve the resolution compared with the

conventional imaging mode. The method proposed in this paper outperforms the bidirectional overlapping upsampling considering only hardware characteristics and the conventional MAP super-resolution method considering only software algorithms, respectively, and is an effective super-resolution method combining hardware and software, and the super-resolution images obtained are visually clear and reconstruct the high-frequency detail information of the image while maintaining a high signal-to-noise ratio.

Key words: thermal infrared remote sensing, ZY-1 02E satellite, super resolution, bidirectional overlapping sampling, sub-pixel shifted, maximum a posteriori probability (MAP)

1. 引言

空间分辨率是遥感卫星对地观测的重要指标，衡量了遥感影像对地观测获取信息的能力。更高的分辨率意味着更强的信息获取能力，遥感卫星对于提高分辨率的需求始终迫切。

根据物理机理，提高卫星影像分辨率的几种方式包括：减小传感器探元尺寸、降低卫星高度、增大镜头焦距。但显然，这些方法都是极大受制于传感器制造工艺、大气损耗、卫星体积，并且由于卫星传感器分辨率逐渐接近光学系统衍射极限，单纯从上述硬件改善角度出发，无法有效地提升卫星影像分辨率。

法国国家空间研究中心（CNES）从 1991 年开始研究一种基于“半像素错位”加密采样的新型成像模式和相应的超分辨率方法，并成功应用到了 SPOT-5 卫星的研制中[00]。该方法将两条线阵 CCD 在排列时在沿轨与垂轨方向各偏移 0.5 个像素，在推扫过程中，能够获取具有相对偏移的 2 景影像，以达到加密采样的效果。通过一次成像获得多幅存在已知的“亚像素错位”的影像，这样十分有利于后续利用亚像素位移信息的互补来实现影像超分辨率，这种模式被称为“超模式”[0]。理论上 SPOT-5 的这种超模式影像的空间分辨率能够提升$\sqrt{2}$倍，SPOT-5 卫星也成功验证了超模式方法的有效性[0]，也有相关学者基于 SPOT-5 超模式数据进行了超分辨率研究[000]。

随着 SPOT-5 的成功，国内外各单位在此基础上也提出了“高模式”的概念[0]，其核心思想是在超模式的基础上，再获取仅在沿轨方向偏移 0.5 个像素与仅在垂轨方向偏移 0.5 个像素的两景影像，即可以获取 4 景存在相对偏移的影像。中国科学院西安光学精密机械研究所曾以面阵 CCD 做过类似的实验，实验表明高模式超分的空间分辨率能够提升至原来的 2 倍[0]。CNES 对这种通过多帧“亚像素错位”影像融合得到更高分辨率影像的技术在全世界范围内申请了专利，并长期维持了技术优势。国内研究者虽然也很早就注意到了这一技术的重大应用潜力，但早期的研究多集中于用模拟图像来验证原理的正确性，由于缺乏遥感卫星实际工程应用的支撑，国内的相关研究已经很长时间趋于停滞[0]。

2022 年中国资源卫星应用中心发射了资源一号 02E 卫星（编号 ZY-1F）。资源一号 02E 是我国首颗对

高模式超分辨率进行实验验证的卫星，其搭载可见近红外载荷、高光谱载荷与热红外载荷。资源一号 02E 作为资源一号 02C、02D 的后续星，其所搭载的可见近红外载荷、高光谱载荷与资源一号 02D 基本一致，为资源环境等遥感研究提供了国产数据支撑 [00]。资源一号 02E 卫星搭载的热红外载荷，光谱覆盖范围为 $7.7\mu m$~$10.5\mu m$，常规成像模式空间分辨率为 $15m$。该热红外载荷的最大的特点是支持“高模式”超分辨率成像功能，其能够在沿轨和垂轨两个方向加密采样，并且在两个方向上分别偏移 0.5 个像素，构成了超分辨率的 4 帧影像，根据加密采样硬件设计可以直接进行交错上采样实现即可实现影像的超分辨率。

另一批研究者们希望从软件处理的角度来改善影像分辨率，恢复影像截止频率之外的高频信息。这一类超分辨率技术的概念最早在上世纪 60 年代，由 Harris[0] 和 Goodman[0] 提出。超分辨率重建技术具有进一步提升遥感卫星影像空间分辨率的潜力。该技术可以通过对同一场景的单帧或多帧低分图像进行处理来获取对应的高分图像。依据原理的不同，超分辨率算法可以被大致分为重构类算法与学习类算法两类。Tasi 和 Huang 等人提出首个频率域重构方法 [0]，Stark 提出的凸集投影 POCS 算法 [0] 和 Schultz 等人提出的最大后验概率 MAP 算法 [0] 则是空间域重构类算法的代表。近年来学习类方法也在超分辨率重建领域取得了较好的效果，从 Dong 等人提出 SRCNN[0] 开始，学习类超分辨率方法发展出了基于 CNN 的方法（如 EDSR[0]、CRN[0]）、基于 GAN 的方法（如 SRGAN[0]、ESRGAN[0]）、基于 Transformer 的方法（如 SwinIR[0]、DSSTSR[0]）等分支。超分辨率技术的原理在于多帧低分辨率影像序列中包含的亚像素位移信息可以进行互补来实现超分辨率重建。然而无论是重构类还是学习类超分辨率算法大多仅适用于常规成像模式，往往需要先通过运动估计和帧间匹配获得各帧空间位置对齐的影像，而双向加密采样的 4 帧影像如果想要空间位置对齐就需要进行额外的重采样，会造成信息损失和影像模糊。因此这些常规算法无法兼容双向加密采样的特殊硬件模式，必须设计针对性的超分算法。

仅仅对双向加密采样的 4 帧影像进行交错上采样能考虑到硬件特性，但其超分辨率效果远远不够。而常见的超分辨率算法研究又无法兼容双向加密采样的特殊硬件模式，难以直接应用于“亚像素错位”的影像，否则会造成信息损失和影像模糊。因此需要结合硬件模式和算法研究，提出最适用于“亚像素错位”模式的超分辨率方法，即一种软硬件结合的超分方法。本文的主要贡献包括：

1）验证“亚像素错位”模式实现影像超分辨率的可行性，分析该模式相比于常规成像模式的优势；

2）提出结合资源一号 02E 热红外“亚像素错位”硬件特性的超分辨率基本处理框架，并基于观测方程和最大后验概率理论，提出一种针对该硬件特性的新型超分辨率方法；

3）利用资源一号 02E 热红外双向加密采样的 4 帧真实数据验证本文方法效果，在高频细节信息恢复和噪声抑制两个维度取得了综合最优。

2. 原理与方法

2.1. 资源一号 02E 热红外载荷双向加密采样原理

资源一号 02E 热红外载荷由 2 个芯片共 8 片红外线阵 CCD 探测器构成。红外探测器的芯片②为芯片①的超分采样模组，位置关系如图 1 所示，即芯片②与芯片①在垂轨方向偏移 0.5 个像素以便在垂轨方向进行加密采样。

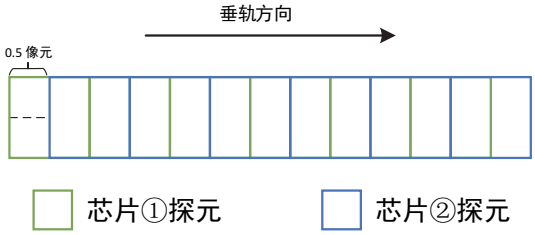

图 1 垂轨方向加密采样示意图

而在沿轨 TDI 方向上，资源一号 02E 热红外传感器采用新的 TDI 技术。为了在沿轨道方向加密采样，它改变了奇偶行的积分开始时间，使它们相差 $T_i/2$，T_i 为积分时间，如图 2 所示。对单个芯片影像的奇偶行进行分离既可获得沿轨方向上偏移 0.5 个像素的两幅影像，又避免了积分时间除以 2 造成的信噪比降低。

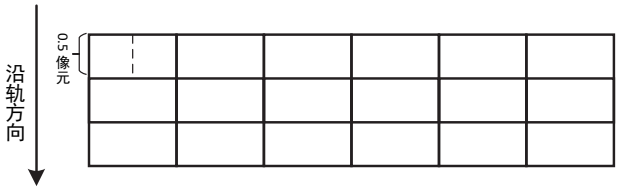

图 2 单个芯片在沿轨方向加密采样示意图

因此对于资源一号 02E 热红外相机而言可以获得垂轨与沿轨两个方向上各偏移 0.5 个像素的原始分辨率影像。如图 3 所示即为双向加密采样示意图。在该模式下，相机能够获得垂轨、沿轨方向上各偏移 0.5 个像素的 4 帧高模式加密采样模式的影像。

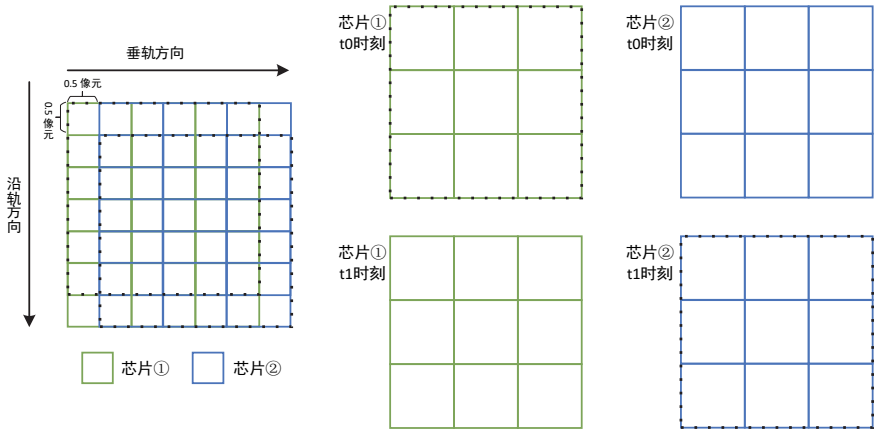

图 3 双向加密采样示意图

2.2. “亚像素错位”模式图像超分辨率流程

“亚像素错位”模式图像由多帧具有亚像素错位的图像组成，要将它们融合并超分辨率，需要通过两步处理：1）加密上采样：最终的影像格网（7.5m 分辨率）是由原始格网（15m 分辨率）得到的，但其采样间隔为原始格网的一半，因此首先需要将多帧图像融合并上采样成为同一张图像才能继续处理，称为多帧加密上采样；2）超分辨率重建：基于上采样结果，可以将原始多帧图像作为序列输入，加密上采样结果作为初值，运用多帧序列影像超分辨率重建方法进行处理。处理流程图如图 4 所示。

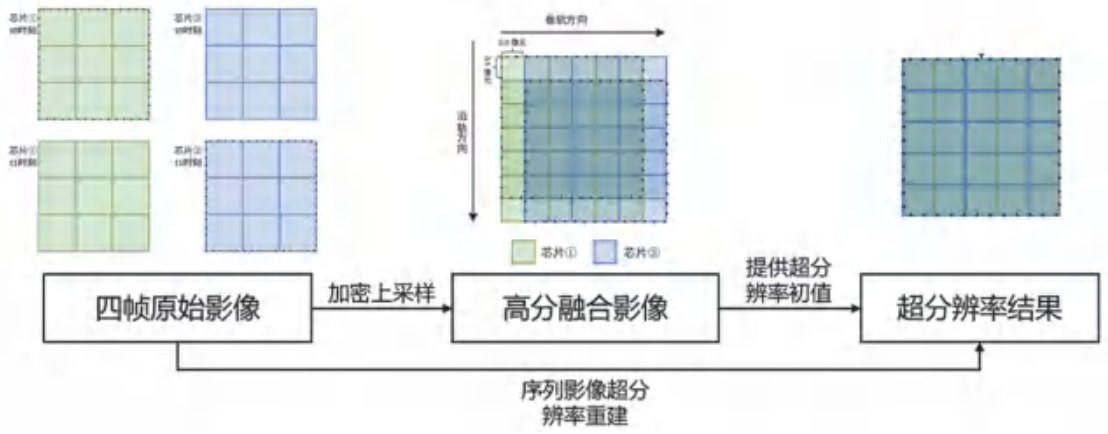

图 4 “亚像素错位”模式图像超分辨率处理流程图

多帧加密上采样是将多帧图像的信息融合，并且进行上采样。一类方法是基于内插的方法，即基于帧间“半像素错位”的固定位移关系进行内插和帧间平均 [0]。一类则是根据这类特殊采样模式设计机理模型进行处理。本文提出一种基于观测方程的多帧融合方法，基于高分辨率和低分辨率网格之间的灰度映射关系，列出观测方程，从而重建高分辨率像素 DN 值。

多帧序列超分辨率是以第一步加密上采样的结果作为高分辨率图像的估计初值，基于原始具有亚像素错位的图像进行超分辨率，主要采用 POCS、MAP 等空间重构超分辨率方法。普通采样模式获取的序列影像，其帧间亚像素错位关系是随机和不可控的，与之相比高模式加密采样模式获取的序列影像则拥有确定的亚像素错位关系，因此必须对常规序列影像超分辨率方法进行一定的改进。

2.3. 多帧加密上采样方法

（1）基于内插的上采样方法

对于半像素错位模式的影像，需要解决的一个关键问题是如何从多帧相互错位的影像得到一帧更高分辨率的影像。对于资源一号 02E 卫星的红外载荷，获取的四帧原始分辨率影像（15m）分别记为 A、B、C、D，它们在 X、Y 方向分别有着 0.5 个像素的错位，如图 5。而 $A_{m,n}$ 表示在第 m 行第 n 列处的像素 DN 值。待重建的高分辨率影像记为 H。

最简单的方法是使用帧间直接平均法，例如图 5 的阴影部分正好是四帧原始分辨率影像的公共部分，一种直接的估计方法是取四帧的平均值作为正中间高分辨率网格的灰度值。以待重建的高分辨率影像 H 的奇数行奇数列为例，计算公式如下：

$$H_{2m-1,2n-1}=\frac{1}{4}\left(A_{m,n}+B_{m-1,n}+C_{m,n-1}+D_{m-1,n-1}\right) \quad (1)$$

显然，正中间的高分辨率网格的灰度值分别只与 A、B、C、D 中的最邻近的一个像素有关，因此该方法的感受野是很小的，受噪声影响较大。

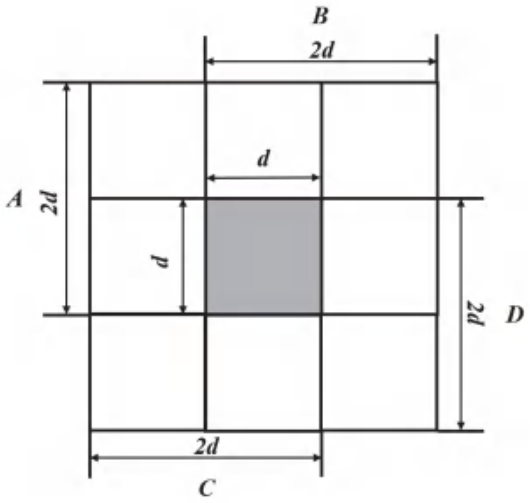

图 5 四帧半像素错位模式的帧间关系图

为了利用更大感受野的信息，更充分地利用邻域灰度信息和几何关系，下面结合采样过程中的观测方程提出一种新型的多帧融合重采样方法。

（2）基于观测方程的上采样方法

先考虑一维方向上的半像素错位，如下图 6。设 H 为待重建的高分辨率采样图像，每个像素宽度为 d；A、B 为实际获得的具有半像素错位的低分辨率影像，每个像素宽度为 2d，它们在空间上有宽度为 d 的重叠，低分辨率影像一行排列总共有 N 个像素。

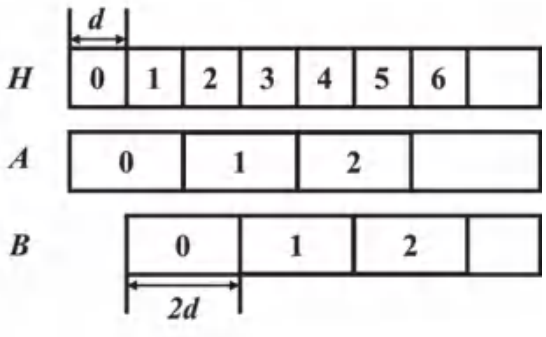

图 6 一维形式半像素错位的排列方式模型

在无像素间混叠的理想条件下，低分辨率影像的每一个像素可以由对应的高分辨率像素采样得到，即

$$A_n = \frac{H_{2n} + H_{2n+1}}{2} \tag{2}$$

$$B_n = \frac{H_{2n+1} + H_{2n+2}}{2} \tag{3}$$

其中$\left(n = 0,1,2,\ldots,N-1\right)$。上式可以看作一组观测方程，因为式子右边 H 为待求参数部分，式子左边为实际观测的低分辨率像素 DN 值。将上式移项得到

$$H_{2n+1} = 2A_n - H_{2n} \tag{4}$$

$$H_{2n+2} = 2B_n - H_{2n+1} \tag{5}$$

再加上初值$H_0 = A_0$，即得到一种基于观测方程的递推迭代方法。这种方法从 H_0 开始依次进行奇偶项递推，直至计算出最后一项 H_{2N-1}。

将上述方法拓展到二维形式，即影像 X、Y 方向均有半像素错位时如下：

$$H_{2m+1,2n+1} = 4A_{m,n} - H_{2m,2n} - H_{2m+1,2n} - H_{2m,2n+1} \tag{6}$$

$$H_{2m+2,2n+1} = 4B_{m,n} - H_{2m+1,2n} - H_{2m+2,2n} - H_{2m+1,2n+1} \tag{7}$$

$$H_{2m+1,2n+2} = 4C_{m,n} - H_{2m,2n+1} - H_{2m+1,2n+1} - H_{2m,2n+2} \tag{8}$$

$$H_{2m+2,2n+2} = 4D_{m,n} - H_{2m+1,2n+1} - H_{2m+2,2n+1} - H_{2m+1,2n+2} \tag{9}$$

通过将最邻近的低分辨率像素平均值赋给 H 的第一行和第一列作为初值，同样可以通过递推重建出整张高分辨率影像。

上述方法原理简单，能够唯一确定高分辨率像素值，但是问题在于计算误差引入的噪声很大，而且这些噪声在递推计算的过程中不断累积和传递 0。

基于以上理论，考虑到取帧间平均能够稳定地抑制噪声，本文提出的多帧加密上采样方法如下：1）先用基于内插的直接平均法估计高分辨率影像初值 H。2）分别利用四帧低分辨率影像列出观测方程，计算当前待求高分辨率影像像素，例如对于奇数行奇数列的像素 $H_{2m+1,2n+1}$，在四帧中分别计算的公式如下

$$H^{A}_{2m+1,2n+1} = 4A_{m,n} - H_{2m,2n} - H_{2m+1,2n} - H_{2m,2n+1} \tag{10}$$

$$H^{B}_{2m+1,2n+1} = 4B_{m,n} - H_{2m,2n+1} - H_{2m+1,2n+2} - H_{2m,2n+2} \tag{11}$$

$$H^{C}_{2m+1,2n+1} = 4C_{m,n} - H_{2m+1,2n} - H_{2m+2,2n} - H_{2m+2,2n+1} \tag{12}$$

$$H^{D}_{2m+1,2n+1} = 4D_{m,n} - H_{2m+1,2n+2} - H_{2m+2,2n+1} - H_{2m+2,2n+2} \quad (13)$$

即分别由四帧低分辨率原始影像估计出四帧高分辨率影像 H^A、H^B、H^C、H^D。

3）取同一像素在四帧高分辨率影像的平均值作为最终高分辨率像素 $H_{2m+1,2n+1}$ 的灰度值，即

$$H_{2m+1,2n+1} = \frac{H^{A}_{2m+1,2n+1} + H^{B}_{2m+1,2n+1} + H^{C}_{2m+1,2n+1} + H^{D}_{2m+1,2n+1}}{4} \quad (14)$$

2.4. 顾及硬件特性的 MAP 超分辨率重建

根据最大后验概率（MAP）超分辨率理论，对于一般成像过程，可以认为观测获得的 N 帧低分辨率图像是由同一幅高分辨率图像经过一系列的降质过程产生的。设原始高分辨率图像为 x，通过观测得到的第 k 帧低分辨率图像为 $\{y_k, k=1,2,\cdots N\}$，则图像退化模型可表示为

$$y_k = DB_k M_k x + n_k \quad (15)$$

中 D 为下采样矩阵，B_k 为光学模糊矩阵，M_k 为运动矩阵，n_k 表示加性噪声。如果将上述三个矩阵合并成一个退化矩阵 A_k，那么低分辨率图像的像素就可以看作是相应高分辨率图像像素的加权平均，其权系数由矩阵 A_k 决定。一般来说，如果进一步把对应于 N 帧低分辨率图像的观测方程进行合并，得到

$$y = Ax + n \quad (16)$$

最大后验估计（MAP）超分辨率重建的涵义是在已知低分辨率图像序列的前提下，使高分辨率图像出现的后验概率达到最大，即

$$\hat{x}_{MAP} = \arg\max_x \left[\Pr\{x|y\} \right] \quad (17)$$

由贝叶斯公式得到

$$\hat{x}_{MAP} = \arg\max_x \left[\frac{\Pr\{y|x\}\Pr\{x\}}{\Pr\{y\}} \right] \quad (18)$$

只考虑上式的分子部分，并取对数得

$$\hat{x}_{MAP} = \arg\max_x \left[\log\Pr\{y|x\} + \log\Pr\{x\} \right] \quad (19)$$

上式表明极大验后估计值由条件概率模型和先验概率模型共同决定，因此 MAP 方法能够有效引入先验信息，帮助恢复图像高频成分。

在具体求解方法上，文献 0 等假定影像噪声为均值为 0、方差为 σ^2 的高斯噪声，给出了条件概率密度函数 $\Pr\{y|x\}$ 的表达式。先验概率 $\Pr\{x\}$ 的估计方法则是对影像进行平滑约束，即对影像上差异较

大的邻近像元进行惩罚。同时假定各影像具有相同的噪声方差，利用正则化方法，最终化简为求解下列优化问题：

$$\hat{x}_{MAP} = \arg\min_{x}\left[\|y - Ax\|^2 + \alpha\|Qx\|^2\right] \quad (20)$$

其中 A 为退化矩阵，Q 为线性高通滤波算子，本文取二阶拉普拉斯算子，α 为正则化参数，根据文献 0 的方法自适应计算得到。

根据取得最值的必要条件，上式对 x 的微分为 0，得到

$$\left(A^T A + \alpha Q^T Q\right)x = A^T y \quad (21)$$

给出对目标高分图像 x 进行迭代求解的公式为

$$x_{k+1} = x_k + \left[A^T y - \left(A^T A + \alpha Q^T Q\right)x_k\right] \quad (22)$$

直至重建图像差异小于设定的阈值 d

$$\|x_{k+1} - x_k\|^2 / \|x_k\|^2 \le d \quad (23)$$

本文假设低分影像的退化函数为二维高斯函数，表示为：

$$A\left(u, v \middle| u', v'\right) = e^{-\frac{(u-u')^2+(v-v')^2}{2}} \quad (24)$$

上式中，u, v 为待求像素坐标值，u', v' 是退化函数的中心点坐标值。则 5×5 范围内的退化函数 PSF 可以离散表示为：

表 1 退化函数离散表示

0.0183	0.0821	0.1353	0.0821	0.0183
0.0821	0.3679	0.6065	0.3679	0.0821
0.1353	0.6065	1.0000	0.6065	0.1353
0.0821	0.3679	0.6065	0.3679	0.0821
0.0183	0.0821	0.1353	0.0821	0.0183

3. 实验与分析

3.1. 实验数据

本文实验数据选用资源一号 02E 热红外超分模式数据，成像时间为 2022 年 3 月 6 日，拍摄地点为山东烟台定标场，该景影像既能用于超分辨率实验也可用于后续的辐射定标等工作，左上角坐标为：120.942E，38.124N。在超分模式下共获取 4 帧常规分辨率（15m）的影像，在垂轨、沿轨方向各偏移 0.5 个像元，如图 7 所示。

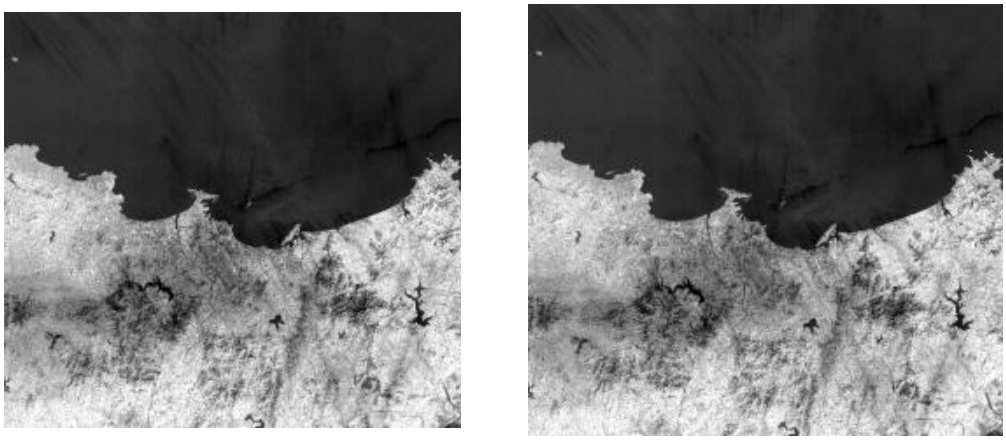

（a） （b）

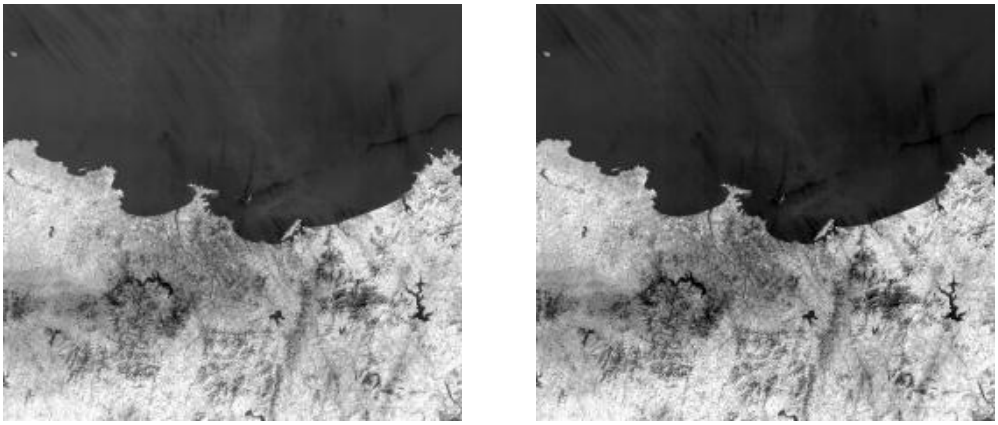

（c） （d）

图 7 资源一号 02E 热红外超分模式原始影像。
(a) 芯片 1 t_0 时刻，(b) 芯片 2 t_0 时刻，(c) 芯片 1 t_1 时刻，(d) 芯片 2 t_1 时刻

3.2. 评价指标

3.2.1. 平均梯度

平均梯度反映的是图像的细节与纹理变化程度，可以表示图像的清晰度，平均梯度越大，表明图像越清晰。平均梯度定义为：

$$AG = \frac{1}{(M-1)(N-1)} \sum_{i=1}^{M-1} \sum_{j=1}^{N-1} \sqrt{\left[\left(f(i,j) - f(i+1,j) \right)^2 + \left(f(i,j) - f(i,j+1) \right)^2 \right] / 2} \quad (25)$$

上式中，M、N 是图像的长度与宽度，$f(i,j)$ 是待测图像第 (i,j) 的像素值。

3.2.2. 信息熵

信息熵表示图像的信息量，信息熵越高，则表明图像蕴含的信息越丰富。信息熵定义为：

$$IE = -\sum_{i=min}^{max} p_i \log p_i \qquad (26)$$

上式中，p_i 表示灰度值 i 的像素数量占整幅图像的比例，min、max 分别表示图像中最小和最大灰度值。

3.2.3. 信噪比

信噪比表示图像中信息量与噪声的比值，信噪比越大，则表明图像抗噪性能越好，本文采用局部平均值与标准差计算信噪比[00]。信噪比的计算方法如下：

1） 计算整张图像的灰度平均值 M；

2） 对图像进行分块，计算每块的局部标准差 STD；

3） 得到局部标准差最大的值 STD_{max}；

4） 求解信噪比：

$$SNR = \frac{M}{STD_{max}} \qquad (27)$$

3.3. 实验分析

为了验证本文方法的有效性，找到最适用于加密采样成像模式的超分辨率方法。本文分别选用第一帧双线性上采样影像、基于内插的四帧双向加密上采样影像、基于观测方程的四帧双向加密上采样影像、传统 MAP 算法超分辨率影像与本文提出的顾及硬件特性的 MAP 算法超分辨率影像进行的对比。上述实验均相对原始影像进行了 2 倍上采样，即由 15 米地面分辨率采样至 7.5 米。

图是超分辨率结果的目视对比，对比子图(a) (b)可以看出第一帧双线性上采样影像的清晰度最低，比较模糊，基于内插的双向加密上采样的清晰度次之，但是因为融合了多帧信息，可以明显改善图像噪声提升，说明了加密过采样成像模式相比于普通成像模式在抑制噪声方面上更具优势。

对比图 8 (b) (c)可以看到，基于观测方程的双向加密上采样相比于基于内插的方法，在影像细节增强上取得了明显的效果，有些不明显的地物纹理、边缘等经过处理后变得容易辨认，目视效果显著改善。但缺点是在细节信息增强的同时导致了边缘锯齿效应加重和噪声放大。

图 8 (d)的传统 MAP 算法由于未能有效利用四帧间固有的半像素错位关系，因此造成了一定的影像模糊，效果并不理想。而图 8 (e)本文算法的目视效果综合细节清晰度和噪声水平这两个方面，取得了最优效果。

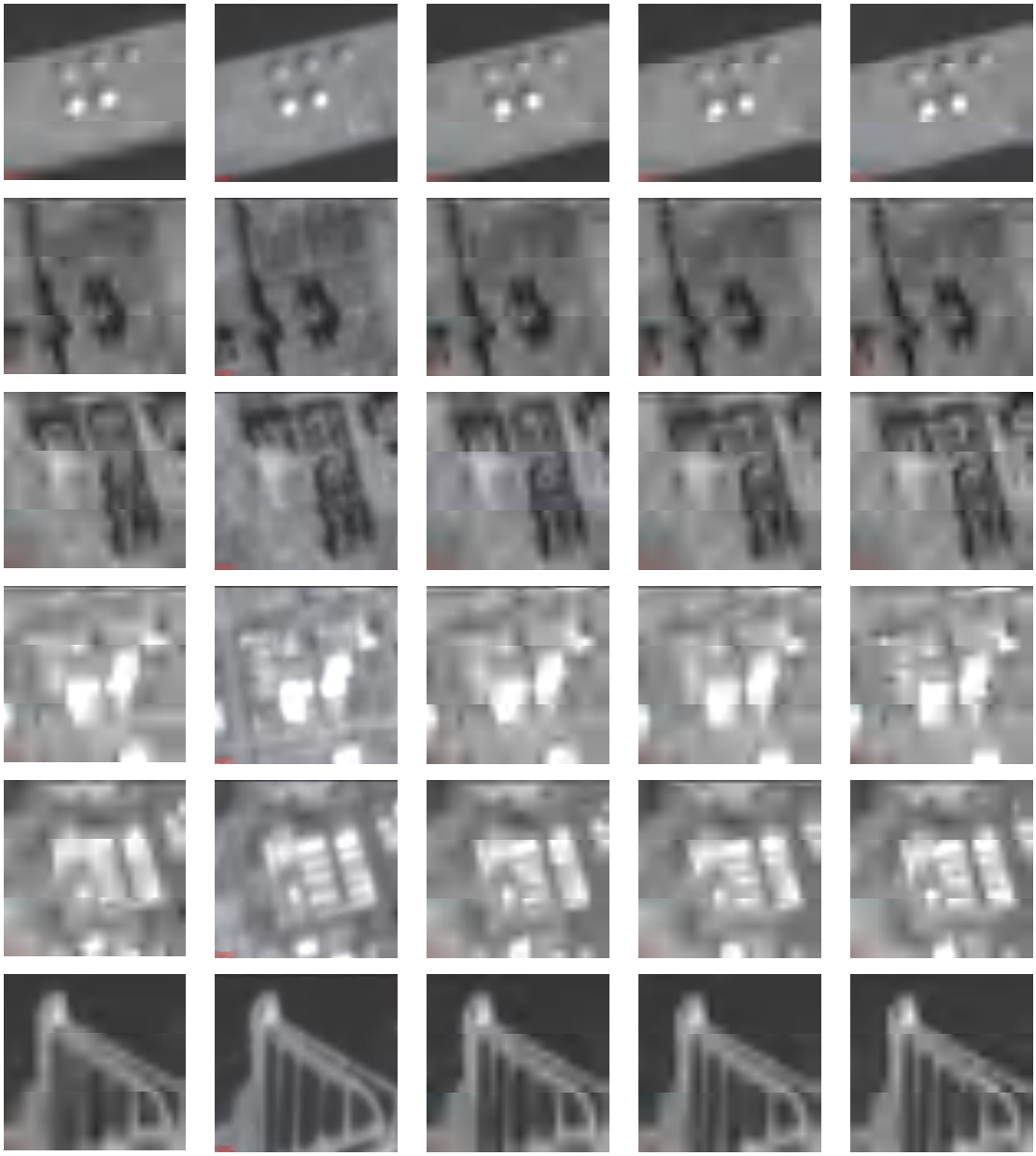

(a) (b) (c) (d) (e)

图 8 超分辨率结果对比(a) 第一帧双线性上采样，(b) 基于内插的双向加密上采样，(c) 基于观测方程的双向加密上采样，(d) 传统 MAP 算法，(e) 本文算法

表 2 超分辨率结果定量评价

	双线性上采样	基于内插的双向加密上采样	基于观测方程的双向加密上采样	MAP	本文算法
平均梯度	2.258	2.052	2.343	2.287	2.648
信息熵	5.038	5.033	5.037	5.037	5.042
信噪比	6.829	13.166	10.616	11.446	9.205

超分辨率定量评价结果如表 2 所示，平均梯度指标反应图像的清晰度与细节的丰富程度，信息熵能够体现影像的信息量，信噪比则用于评价影像的噪声水平。对比五种超分辨率方法，第一帧双线性上采样的结果作为基准，基于内插的双向加密上采样的平均梯度最低，为 2.052，但是达到了最高的信噪比，为 13.166，这说明该方法主要通过四帧之间的固定关系来消除影像噪声，但对影像的细节进行了模糊。基于观测方程的双向加密上采样方法的平均梯度与信息熵略低于本文算法，但信噪比较之本文算法较优，表明其牺牲了一定清晰度，但获取了较高的信噪比。传统 MAP 方法的三项指标均介于基于内插和基于观测方程的双向加密上采样之间，更好地取得了细节与噪声的平衡。本文方法由于综合了观测方程和最大后验概率原理，相比传统 MAP 方法，在信息熵大致相等的情况下，平均梯度指标更高，为 2.648，说明影像的高频细节信息得到了更有效的增强。总而言之，本文方法取得了最大的平均梯度和信息熵，分别达到 2.648 和 5.042，同时信噪比略低，为 9.205，表明其在增强影像的细节的同时，虽然在一定程度上放大了影像噪声，但是有效地增强了影像的细节，实现了超分辨率的目的。

综合以上三个定量评价指标，本文提出的顾及双向加密硬件特性的 MAP 方法的综合细节清晰度和噪声水平这两个方面是最优的。在以上对比实验中，相比于本文方法，基于内插和基于观测方程的双向加密上采样仅考虑了硬件特性，可以较好地融合四帧“半像素错位”的图像信息，并且一定程度上提升图像信噪比，但因为无法重建复杂的图像退化过程，导致对图像高频细节信息的恢复能力有限。传统 MAP 方法仅从软件算法理论出发，能够复原更多的图像细节，但由于没有较好地利用双向加密采样的硬件特性，导致亚像素位移信息未得到有效利用。而本文方法能够综合双向加密采样的硬件特性和最大后验概率的理论模型，实现了软硬件结合的超分辨率。

以上实验表明，资源一号 02E 热红外载荷的双向加密采样模式相比常规模式能够有效提高影像空间分辨率，本文算法在顾及硬件特性的情况下结合观测方程和最大后验概率原理，提出了一种新的针对性超分辨率算法，能够取得更优的超分辨率效果。

4. 结论

本文研究了资源一号 02E 顾及硬件特性的热红外影像超分辨率重建方法，根据资源一号 02E 红外载荷特殊的“半像素错位”双向加密采样超分辨率模式特点，利用观测方程和最大后验概率模型进行超分辨率重建，得到了一幅分辨率提升 2 倍的高分辨率影像。实验表明本文提出的算法能够有效提升资源一号 02E 的红外载荷的分辨率，能够得到更加丰富的影像细节信息，清晰度提高的同时信噪比并没有明显的降低。这种双向加密采样的模式，能够在不改变传感器原始分辨率的基础上，通过预先设计的“半像素错位”排

列方式由 4 帧影像综合为 1 帧分辨率达提高到原始分辨率 2 倍的影像。此外本文方法仍然存在一些值得研究与改进的方面，例如研究改进深度学习方法使其适用于加密采样这种非常规的成像模式，卫星震颤等因素导致 4 帧加密采样模式影像的相对位置不满足严格的“半像素错位”关系对本文方法的影响等，后续还需要进一步分析。

参考文献

[1] LATRY C, ROUGE B. SPOT5 THR mode[C]. Earth Observing Systems III. SPIE 3439, 1998: 480–491.

[2] LATRY C, VADON H, LEFEVRE M J, et al. SPOT5 THX: a 2.5m fused product[C]. 2nd GRSS/ISPRS Joint Workshop on Remote Sensing and Data Fusion over Urban Areas, 2003: 87–89.

[3] 谭兵, 邢帅, 徐青, 等. SPOT5 超模式数据处理技术研究[J]. 遥感技术与应用, 2004(04): 249–252. Tan Bing, Xing Shuai, Xu Qing, et al. A research on SPOT5 supermode image processing [J]. Remote Sensing Technology and Application, 2004(04): 249-252.

[4] 周峰, 乌崇德. 提高航天传输型 CCD 相机地面像元分辨率方法研究[J]. 航天返回与遥感, 2002(03): 35–42. Zhou Feng, Wu Chongde. A method for improving GSD of space real-time transmission CCD camera [J]. Spacecraft Recovery & Remote Sensing, 2002(03): 35-42.

[5] DHERETE P, ROUGE B. Image de-blurring and application to SPOT5 THR satellite imaging[C]. 2003 IEEE International Geoscience and Remote Sensing Symposium. Proceedings, 2003(1): 318–320.

[6] LATRY C, ROUGE B. Super resolution: quincunx sampling and fusion processing[C]. 2003 IEEE International Geoscience and Remote Sensing Symposium. Proceedings (IEEE Cat. No.03CH37477). 2003(1): 315–317.

[7] LEGER D, VIALLEFONT F, HILLAIRET E, 等. In-flight refocusing and MTF assessment of SPOT5 HRG and HRS cameras[C]. Sensors, Systems, and Next-Generation Satellites VI. SPIE 4881, 2003: 224–231.

[8] 尹志达, 周春平. 超分辨率采样模式中的高模式和超模式对比研究[J]. 首都师范大学学报(自然科学版), 2015, 36(01): 77–80. YIN Zhida, ZHOU Chunping. Comparative study of two super-resolution sampling modes: hipermode and supermode[J]. Journal of Capital Normal University (Natural Science Edition), 2015, 36(1): 77-80.

[9] 吴琼,田越,周春平,等.遥感图像超分辨率研究的现状和发展[J].测绘科学, 2008, 33(6):5. Wu Qiong, Tian Yue, Zhou Chunping, et al. Review of super-resolution in remote-sensing image[J]. Science of Surveying and Mapping, 2008, 33(6):5.

[10] 杨博, 王密. 资源一号 02C 卫星全色相机在轨几何定标方法[J]. 遥感学报, 2013, 17(05): 1175–1190. Yang Bo, Wang Mi. On-orbit geometric calibration method of ZY-1 02C panchromatic camera[J]. National Remote Sensing Bulletin, 2013, 17(05): 1175-1190.

[11] 刘瑶, 李俊生, 肖晨超, 等. 资源一号 02D 高光谱影像内陆水体叶绿素 a 浓度反演[J]. 遥感学报, 2022, 26(01): 168–178. Liu Y，Li J S，Xiao C C，Zhang F F and Wang S L. 2022. Inland water chlorophyll-a retrieval based on ZY-1 02D satellite hyperspectral observations. National Remote Sensing Bulletin, 26(1): 168-178

[12] Harris J L. Diffraction and Resolving Power[J]. Journal of the Optical Society of America (1917-1983), 1964, 54:931-933.

[13] Goodman J W, Cox M E. Introduction to Fourier optics[M]. McGraw-Hill, 1968.

[14] Tsai R Y, Huang T S. Multiframe image restoration and registration[C]. Advances in computer vision and image processing. 1984.

[15] Stark H, Oskoui P. HR image recovery from image-plane arrays, using convex projections[J]. Journal of the Optical Society of America A Optics & Image Science, 1989, 6(11): 1715.

[16] Schultz R R, Stevenson R L. A Bayesian approach to image expansion for improved definition.[J]. IEEE Transactions on Image Processing A Publication of the IEEE Signal Processing Society, 1994, 3(3): 233.

[17] Dong C , Loy C C , He K , et al. Learning a Deep Convolutional Network for Image Super-Resolution[C]. European Conference on Computer Vision, 2014.

[18] Lim B , Son S , Kim H , et al. Enhanced Deep Residual Networks for Single Image Super-Resolution[J]. 2017.

[19] Lan R S, Sun L, Liu Z B, et al. Cascading and enhanced residual networks for accurate single-image super-resolution[J]. IEEE Transactions on Cybernetics, 2021, 51(1): 115-125

[20] Ledig C , Theis L , Huszar F , et al. Photo-Realistic Single Image Super-Resolution Using a Generative Adversarial Network[J]. 2016.

[21] Wang X, Yu K, Wu S, et al. ESRGAN: enhanced super-resolution generative adversarial networks[C]. European Conference on Computer Vision. Munich: Springer, 2018: 63-79.

[22] Liang J Y, Cao J Z, Sun G L, et al. SwinIR: image restoration using swin transformer[C]. IEEE/CVF International Conference on Computer Vision Workshops. Montreal: IEEE, 2021: 1833-1844.

[23] Long Y Q, Wang X, Xu M, Zhang S Y, et al. Dual Self-Attention Swin Transformer for Hyperspectral Image Super-Resolution[J]. IEEE Transactions on Geoscience and Remote Sensing, 2023, 61: 1-12.

[24] 胡燕,胡莘,王昱.半像元错位图像的超分辨率重建方法[J].测绘科技, 2004, 24(1):9-13. HU Yan, HU Xin, WANG Yu. Method for Reconstructing a Single Super-resolution Image from Two Images with Half Pixel Offset[J]. Geomatic Science and Engineering, 2004, 24(1):9-13.

[25] 黄战华,蔡怀宇,张以谟,等.基于半像素错位的多幅图像重建高分辨率图像技术研究[J].光学技术, 2002, 28(5):4. HUANG Zhanhua, CAI Huaiyu, ZHANG Yimu, et al. One method of super-resolution image rebuilding using multi-images of half pixel offset [J]. Optical Technique, 2002, 28(5):4.

[26] 沈焕锋, 李平湘, 张良培. 一种自适应正则 MAP 超分辨率重建方法[J]. 武汉大学学报(信息科学版), 2006, 031(011):949-952. Shen Huanfeng, Li Pingxiang, Zhang Liangpei. Adaptive Regularized MAP Super-Resolution Reconstruction Method [J]. Geomatics and Information Science of Wuhan University, 2006, 031(011):949-952.

[27] Shen Huanfeng, Li Pingxiang, Zhang Liangpei and Zhao Yindi. A MAP algorithm to super-resolution image reconstruction[C]. Third International Conference on Image and Graphics, 2004: 544-547.

[28] 吴琼. 可见光图像超分辨率客观评价方法研究[D]. 2009. WU Qiong. Research on objective evaluation method of super-resolution in visible light images [D]. 2009.

[29] 陈强, 傅鹏, 孙权森, 等. 一种遥感图像信噪比评估和度量准则[J]. 测绘学报, 2013, 42(04): 559－567.
CHEN Qiang, FU Peng, SUN Quan-Sen, et al. A Method of SNR Estimation and Comparison for Remote Sensing Image[J]. Acta Geodaetica et Cartograghica Sinica, 2013, 42(04): 559-567.

[作者简介]

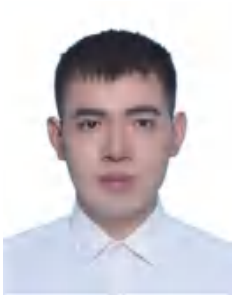

赵泉，1999 年生，男，博士研究生，研究方向为光学遥感影像辐射处理与智能分析。

王密，1974 年生，男，教授，研究方向为高分辨率光学遥感影像高精度处理与智能服务。

谢广奇，1992 年生，男，工学博士，研究方向为多源序列遥感影像时空谱一体化融合超分辨率的理论、方法与应用。

基于双流注意力网络的光学和 SAR 影像水体提取方法

朱睿哲[1]，潘俊[2]*，周清华[3]，宋浩[3]

（1.武汉大学资源与环境科学学院， 湖北 武汉 430079；

2.武汉大学测绘遥感信息工程国家重点实验室， 湖北 武汉 430079；

3.中铁工程设计咨询集团有限公司，北京 100055）

摘　要：现有铁路项目勘测大部分沿用传统的人工勘察设计方法，效率低下且难以满足现代工程建设的需求，结合遥感技术能够有效提升外业勘测效率，提升智能化水平。遥感水体提取方法常使用以光学影像为主的单模态数据，但由于其受光照、天气、云雾、阴影等因素影响，造成成像质量下降，可能出现“同物异谱，同谱异物”现象。而合成孔径雷达 SAR 不易受天气影响，能穿透云雾，实现全天时、全天候的地表目标观测。结合光学和 SAR 影像能够有效解决单模态信息获取地表信息方面的不足，提升图像解译精度。本文提出了一种双流注意力网络 DAT-Net（Dual Stream Attention Network, DAT-Net），网络采用双分支编码器结构，分别提取光学影像和 SAR 影像的特征，并通过基于注意力机制的跨模态注意力模块 CMAM（Cross modal attention module, CMAM）实现不同模态之间的通信，以融合获取有效信息。选取公开数据集 WHU-OPT-SAR 进行实验，选取五种水体提取网络（U-Net、HR-Net、CMTFNet、SFAFMA、MCA-Net）进行对比。相较于对比网络，DAT-Net 的平均交并比 mIoU 提升约 1%-2.6%，水体交并比 IoU 提升约 1.5%-4.5%，表现最优。此外，本文将双流注意力网络应用于铁路桥梁项目勘测，以四川省内某铁路数据为例，实现了铁路沿线水体交叉点的智能化、高精度提取。

关键词：深度学习；水体提取；多模态； 注意力机制；铁路勘测

Optical and SAR Image Water Extraction Method Based on Dual Stream Attention Network

Zhu Ruizhe[1], Pan Jun[2*], Zhou Qinghua[3], Song Hao[3]

基金项目： 国家重点研发计划（2022YFB3902300），国家自然科学基金（62371352），中铁工程设计咨询集团有限公司科技开发课题（研 2023-数字-3）

第一作者： 朱睿哲（2000—），男，硕士研究生，研究方向为遥感图像语义分割。 邮箱: 2019302050012@whu.edu.cn

通讯作者： 潘俊（1979—）， 男， 研究方向为遥感影像智能处理与质量改善。 邮箱: panjun1215@whu.edu.cn

1. School of Resource and Environmental Sciences, Wuhan University, Hubei Wuhan, 430079 China；

2. State Key Laboratory of Information Engineering in Surveying, Mapping and Remote Sensing, Wuhan University, Hubei Wuhan, 430079 China；

3. China Railway Engineering Design and Consulting Group Co., Ltd, Beijing, 100055 China

Abstract: Most of the existing railway project surveys use traditional manual survey and design methods, which are inefficient and difficult to meet the needs of modern engineering construction. Combining remote sensing technology can effectively improve the efficiency of field surveys and enhance the level of intelligence. Remote sensing water extraction methods often use single-mode data mainly based on optical images, but due to factors such as lighting, weather, clouds, shadows, etc., the imaging quality may decrease, and the phenomenon of "same object, different spectrum, same spectrum foreign object" may occur. Synthetic Aperture Radar (SAR) is not easily affected by weather and can penetrate clouds and fog, achieving all-weather and all-weather observation of surface targets. Combining optical and SAR images can effectively solve the shortcomings of single modal information acquisition of surface information and improve image interpretation accuracy. This article proposes a dual stream attention network DAT Net (DAT Net), which adopts a dual branch encoder structure to extract features from optical and SAR images, and achieves communication between different modalities through a cross modal attention module (CMAM) based on attention mechanism to fuse and obtain effective information. Select the publicly available dataset WHU-OPT-SAR for experiments, and compare five water extraction networks (U-Net, HR Net, CMTFNet, SFAFMA, MCA Net). Compared to the comparison network, DAT Net showed an average intersection rate improvement of about 1% -2.6% compared to mIoU, and a water intersection rate improvement of about 1.5% -4.5% compared to IoU, demonstrating the best performance. In addition, this article applies the dual stream attention network to the survey of railway bridge projects, using data from a railway in Sichuan Province as an example, to achieve intelligent and high-precision extraction of water intersections along the railway.

Key words: Deep learning, Water extraction, Multimodal, Attention mechanism, Railway survey

1 引言

铁路沿水体的工程识别是目前外业勘测任务中的一大挑战，虽然近年来一些新技术如无人机勘察、遥感技术等在工程勘察设计中的应用逐渐增多，但总体来看，技术应用水平仍然较低[1]。许多工

程项目仍然沿用传统的勘察设计方法，效率低下且难以满足现代工程建设的需求，存在着数据解译严重依赖技术人员经验、地质信息表达精细度不高等问题。基于遥感技术的空天勘察数据的智能解译和地质信息快速获取技术能够有效提升铁路勘测的智能化程度，提升勘测效率和质量[2]。

利用卫星遥感数据，可以高效地提取水体的位置、面积、形状和河宽等参数。水体提取的方法经历了从目视解译到自动分类[1][4]，再到结合光谱与空间信息的多阶段发展。传统的阈值法和分类器法在水体提取中应用广泛，但对细小水体的提取效果有限。面向对象的自动提取方法则利用影像的光谱、纹理和空间特征，提高了提取精度。近年来，深度学习方法在水体提取中显示出巨大潜力，能够自动从数据中学习特征，实现高精度的自动化提取[1][4]。

基于深度学习的水体提取方法由于无需人工特征选择，避免了特征提取的主观性和不确定性，也极大提升了识别效率，因此逐渐被广泛应用。光学遥感影像由于其分辨率较高，地物细节更丰富，因此被用作深度学习水体提取方法中的主要数据来源。何等人[5]结合归一化水体指数（Normalized Difference Water Index，NDWI）与卷积神经网络实现了水体提取，准确度达到 94%；郑[6]等人利用 GF-6 数据构建了四种卷积神经网络并进行水体提取，并优化了 U-Net 网络，增强了小面积水体的识别精度；Guo[7]等人提出了一种多尺度水体提取卷积神经网络，性能优于 U-Net 等经典网络；Yu[8]等人设计了一种自关注胶囊特征金字塔网络，结果表明其在不同场景下，对于不同形状、大小的水体的提取表现优于全卷积神经网络（Fully Convolutional Networks, FCN）、U-Net 等方法。随着合成孔径雷达(Synthetic Aperture Radar，SAR)成像空间分辨率的提升，基于 SAR 的水体提取方法也受到了学者的关注。徐[9]等人优化了 TransUNet 模型，设计了一种小样本数据集 SAR 影像水体提取模型。提取精度优于传统卷积模型。陈[10]等人面向多源 SAR 图像设计出了一种多级特征注意力水体提取网络，实现了多源 SAR 图像水体的高精度自动提取。

基于深度学习的水体提取算法极大提升了提取精度与模型泛化能力，但是对于复杂的地理环境仍然难以满足实际需求。单源图像在表征信息方面自身的固有缺陷是影响精度提升的重要原因。光学影像通过被动遥感的方式获取辐射信息，因此成像质量受到天气影像，云雾遮挡、弱光照等情况都可能影响最终的图像解译效果。合成孔径雷达影像能够全天时全天候监测地表信息，不受云雾、阴影等自然条件的影响，但是斑块噪声等问题也增加了其解译难度。研究表明，联合光学和 SAR 影像的互补信息有利于提升遥感影像解译的精度。由于两者的成像机理不同，现有的基于光学 SAR 遥感影像解译研究主要基于特征级融合，Li[15]等人基于非局部网络(Non-Local Neural Network)的思想，设计了多模态交叉注意力模块，用于整合光学 SAR 图像特征，Ren[14]等人通过压缩-激励模块将 SAR

图像特征整合到光学影像特征，提升了整体的图像解译精度。但目前的研究方法主要都是通过卷积神经网络（Convolutional Neural Network, CNN）网络作为提取网络主干，无法获得有效的影像全局信息，分割精度仍然存在提升空间。针对上述问题，本文基于光学 SAR 影像互补信息以及全局特征关注的思想，通过渐进式特征融合的方式，不断优化特征信息，设计了一种双流注意力网络 DAT-Net，实现了多源遥感影像的高精度水体提取。此外，本文还提出了基于 DAT-Net 的铁路沿线水体交叉点识别技术路线，并基于 GF-1 和 GF-3 影像、以四川省内某铁路数据为例，实现了铁路沿线水体交叉点的智能化、高精度提取。

2 双流注意力网路

高分辨率网络[16]（HR-Net）在网络的深层阶段保持高分辨率的特征表示，能够学习更精细的特征，从而提高模型的性能。对于水体提取这类密集型图像预测任务而言，细节信息有助于提升整体分类精度，因此本文基于保留高分辨率细节信息的思想，利用高分辨率网络作为基本主干，提出双流注意力网络 DAT-Net，实现联合光学 SAR 影像的高精度水体提取。网络结构如图 1 所示，通过两路并行的高分辨率网络编码器分别提取光学影像特征和 SAR 影像特征。光学影像具有更丰富的光谱信息、更细致的纹理信息，有助于实现更加精准的水体提取，因此将光学影像分支作为水体提取网络的主要分支，不断将 SAR 影像特征融合到该分支。SAR 影像中水体后向散射系数相对较低，在图像上通常表现为暗色，易与周围地物区分，能够提供有效的光谱特征辅助信息。此外，SAR 在多山地区，容易因为地形原因造成阴影与水体混淆，可以借助光学影像丰富的纹理特征得到改善。双流注意力网络 DAT-Net（Dual Stream Attention Network, DAT-Net）的具体实现是在每个阶段相同分辨率特征图之间，基于注意力机制[17]的思想，利用多模态特征融合模块 CMAM（Cross modal attention module, CMAM）自适应的关注 SAR 中细节与语义互补特征，并过滤掉噪声带来的冗余信息，实现渐进式的光学 SAR 特征信息融合，最终得到包含四种分辨率的融合影像特征。为进一步关注图像的全局信息，在网络中采用基于自注意力机制[13]的 Transformer 模块，以增强网络的全局上下文建模能力，进一步提取图像的深层特征。最终将光学高分辨率网络分支中的四个尺度特征进行上采样与通道拼接，通过卷积后输出最终的水体提取结果。

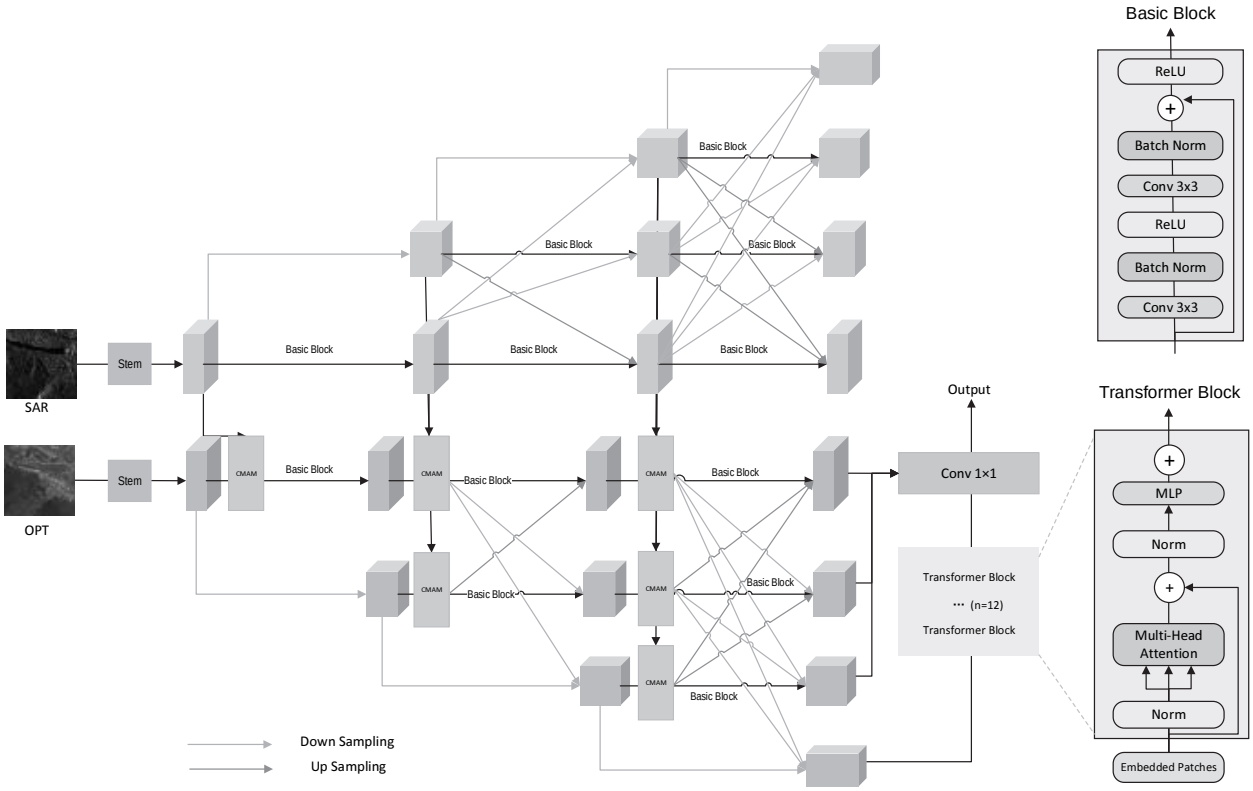

图1　双流注意力网络结构图

2.1　自注意力模块

自注意力机制[13]是通过捕捉序列内部不同位置之间的关系，实现元素之间的交互，进而实现全局上下文建模。视觉 Transformer（ViT）将自注意力机制应用于图像处理领域，和传统的卷积有较大区别。CNN 通过卷积层和池化层提取图像的局部特征，具有平移不变性，适合处理具有局部特征和尺度不变性的图像数据。ViT 则是通过自注意力机制捕捉图像的全局特征，不依赖于局部感受野。利用 CNN 的多尺度处理能力来提取不同分辨率的特征，并将这些特征输入到 ViT 中，能有效增强模型对不同尺度和细节的感知能力。

为了更好的建模图像的全局关系，在网络第四阶段结束后添加了 ViT 模块，进而获取图像的深层特征。为了弥补传统卷积网络造成的全局关系获取不充分，本文借鉴了 TransUnet[24]的 CNN-Transformer 混合架构。保留卷积神经网络部分作为模型的主体，通过卷积、池化等操作快速拟合，提升模型的学习效率。考虑到视觉 Transformer 在处理大规模的图像数据时可能需要占用大量的计算资源和内存，本文方法在特征分辨率最小的第四条分支中添加了 ViT 层，能够在提升模型全局建模能力的同时，保证了模型的计算效率。本文采用的 Transformer 编码器由 12 层多头自注意力(MSA)和多层感知机（MLP）模块组成，具体流程参考图 1。

2.2 跨模态特征融合模块

现有研究在处理光学 SAR 特征融合时采用的方法大致分为两类：基于卷积注意力的方法与基于非局部网络 Non Local[18]的方法。DDHR-Net[14]在处理光学 SAR 的多模态特征是基于卷积注意力的方法，将拼接后的特征通过通道注意力 SE[17]模块获得每个通道的权重信息，并调整通道数后与光学影像特征相加，从而得到融合后的影像。这种基于卷积注意力的特征融合方法，其优势在于快速关注特征重要信息，同时不会影像网络计算效率，但缺点在于对重要信息的关注不足，由于只使用最大池化或平均池化代替某一维度的特征，因此不具备较强的泛化性，很大程度受数据的限制。另一类基于 Non Local 的融合方法更多关注了像素的全局依赖关系，相比于卷积的局部运算可以聚合远距离特征，有助于更好的理解图中的复杂结构。但非局部操作需要计算输入特征图的每个元素与所有其他元素之间的关系，通常涉及大量的矩阵乘法操作，导致计算复杂度随着输入大小的增加而迅速增加。

受到非对称非局部网络[18]的启发，本文基于金字塔池[22]化与 Non Local 结合的思想设计了一种对称结构的跨模态特征融合模块 CMAM，在保留非局部操作的全局建模能力的同时，利用不同尺度的池化操作获得特征图的重要特征信息，降低了非局部运算对于网络计算效率的影响。模块的具体结构见图 2，以 SAR 分支的特征融合为例，首先利用卷积注意力模块 CBAM[20]初步提取光学重要特征，实现初步的特征融合，并将该结果作为后续非局部运算的 Query 值。参考下图 3，利用金字塔池化获取不同尺度的 SAR 特征，并展开成二维序列的采样点，作为非局部运算的 Key 和 Value 并与之前计算得到的 Query 进行 NL 计算，从而得到 SAR 影像增强特征。在光学特征分支中采用类似的运算获得光学影像增强特征。将增强后的影像与模块输入的光学 SAR 特征进行残差连接后输出最终的模态特征融合结果。

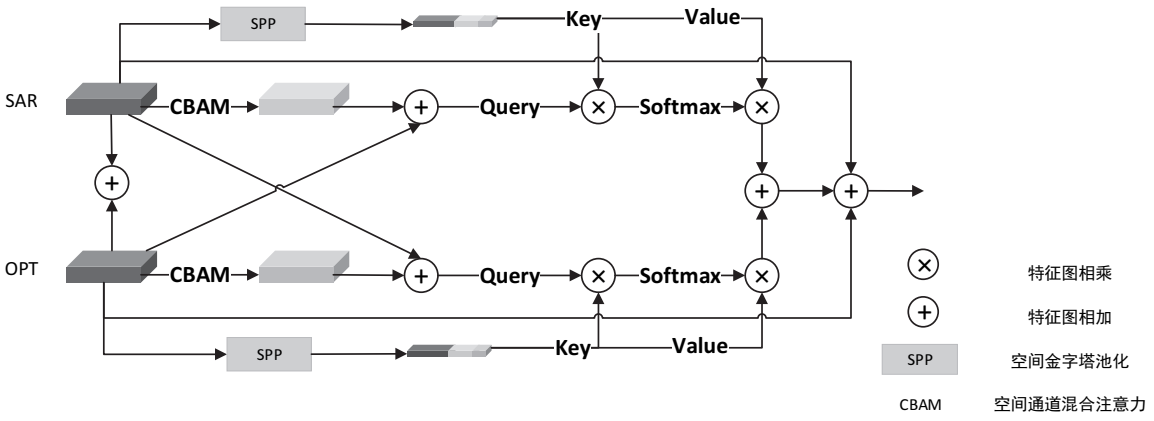

图2 跨模态特征融合模块CMAM结构图

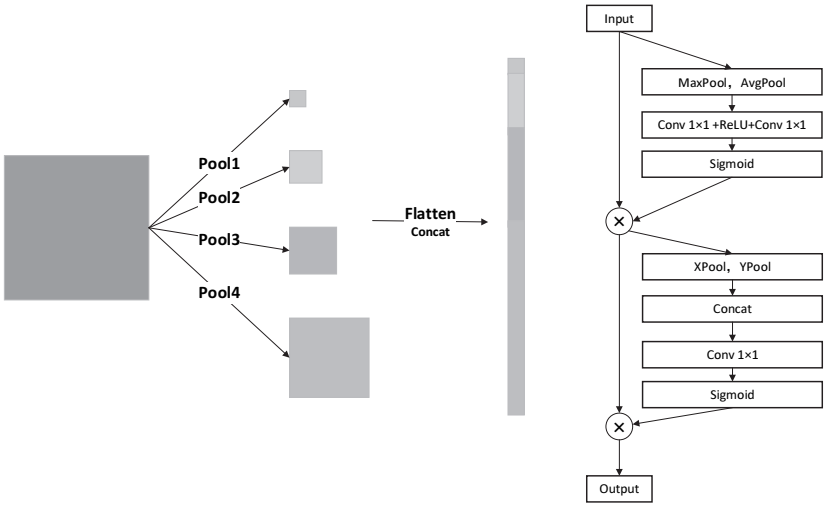

图3 空间金字塔池化和空间通道混合注意力示意图

3 数据集构建与实验

3.1 实验数据集

本文基于WHU-OPT-SAR[15]数据集进行实验，该数据覆盖区域为中国湖北省，覆盖面积约5000km^2，数据集包括高分辨率的光学影像和SAR影像，以及像素级的标注信息，分别来自GF-1和GF-3以及2017年全国土地变更调查数据。数据集包含5556×3704像素的光学和SAR影像共100对，二者空间分辨率均为5m，包含农田、水体等地物类别7类，其中水体类别的像素数占比约为14.20%。将数据中的影像统一裁剪至512×512像素共29400张，随机选取其中17640张作为训练集、5880张作为验证集、5880张作为测试集，并将非水体像素作为背景，对训练集使用翻转、旋转等数据增强方法。

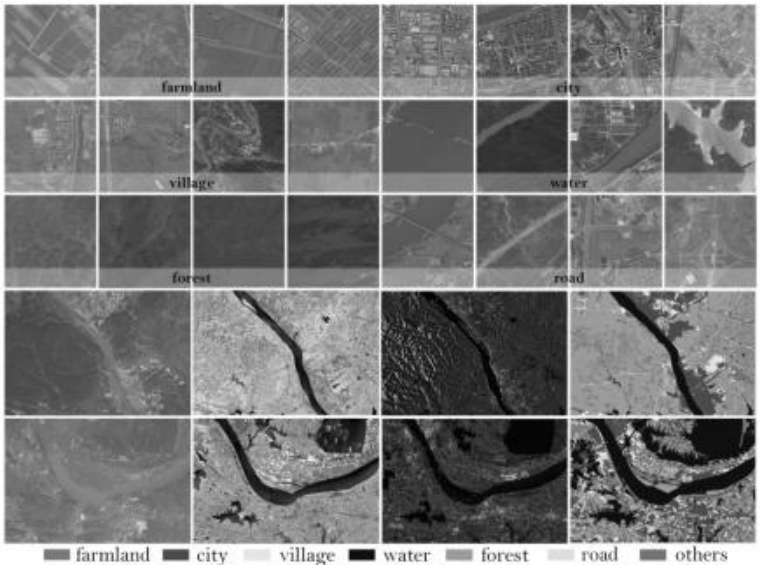

图4 WHU-OPT-SAR数据集

3.2 对比实验

本文选取三种经典的单模态语义分割模型（U-Net[25]、HR-Net[16]、CMTFNet[21]）作为对比模型，其中前两个为CNN网络，第三种为CNN—Transformer混合模型。此外，还选取了两种多模态模型（SFAFMA[22]、MCA-Net[15]）。对于单模态网络方法，将光学影像和SAR影像在通道维度拼接后作为网络的输入；对于多模态方法，分别将光学和SAR影像作为模型的输入。

实验基于深度学习框架Pytorch1.12.1，开发环境为两张TesIaP100（16G），Batch Size为32，损失函数为BCELoss，优化器采用AdamW，初始学习率为1e-3，共迭代120轮。对于实验的精度评价方面选取了六种典型的语义分割评价指标OA、mIoU[23]、IoU、Precision、Recall、Fscore。其中F1分数是准确率和召回率的调和平均数，能够整体衡量对于水体的提取效果。

对比实验的可视化结果如下图5，选取了测试集中的六张影像作为对比，其中包括了面积较大且形状不规则的自然水体、形状规则的人工水体以及光谱特征与水体接近的绿地场景等。六种方法对于水体提取的整体精度较高，主要差异体现在对于河流边缘、水体内部的非水体区域等细节信息的处理情况。在六种方法中，本文提出的DAT-Net表现整体最优，既能准确的保留水体结构信息，又能精准识别面积细小的人工水体，兼具了图像中的细节信息。

在三种单模态方法（U-Net、HR-Net和CMTFNet）中，CMTFNet表现最优，对于水体整体结构提取更为准确，同时能够兼具一定的细节提取能力，说明基于CNN-Transformer的混合架构能够有效建模全局信息，有利于捕捉图像的细节信息。在第一张影像的提取结果中U-Net和HR-Net将一部分的耕地识别为水体，说明单一的卷积网络结构在处理全局信息方面还存在不足，无法获取深层语义信息。在第三、四张影像的提取结果中，三种单模态方法均在一定程度上出现了地物细节缺失的问题，一些细长的小面积水体出现了错误识别。多模态模型的整体表现优于三种单模态的方法，这可能是由于光学影像和SAR影像成像机理存在差异，简单通道拼接的方式有可能导致不同模态特征之间的混淆和影响。然而，MCANet整体表现不佳，这可能是由于模型采用基于Non Local思想的特征融合方法，忽略了模型的通道信息。SFAFMA与本文提出的方法在六种方法中表现最优，并且两者均基于多模态特征的通道和空间信息实现了针对性的特征优化。此外， SFAFMA的特征融合模块仅通过卷积注意力的方法实现，对于特征的重要信息提取不充分，导致模型精度提升不明显。本文提出的CMAM模块采用基于非局部的计算可以实现长距离像素之间的关系建模，对于重要特征的提取更具备普遍性。通过图5中测试影像1和5可以发现，在一些细小像素上的识别处理上两者的效果还存在一定差距。如测试影像2，尽管河流的整体结构提取均较为出色，但本文方法在处理水体边缘的结果更加平滑，边缘提取效果与真实影像更接近。

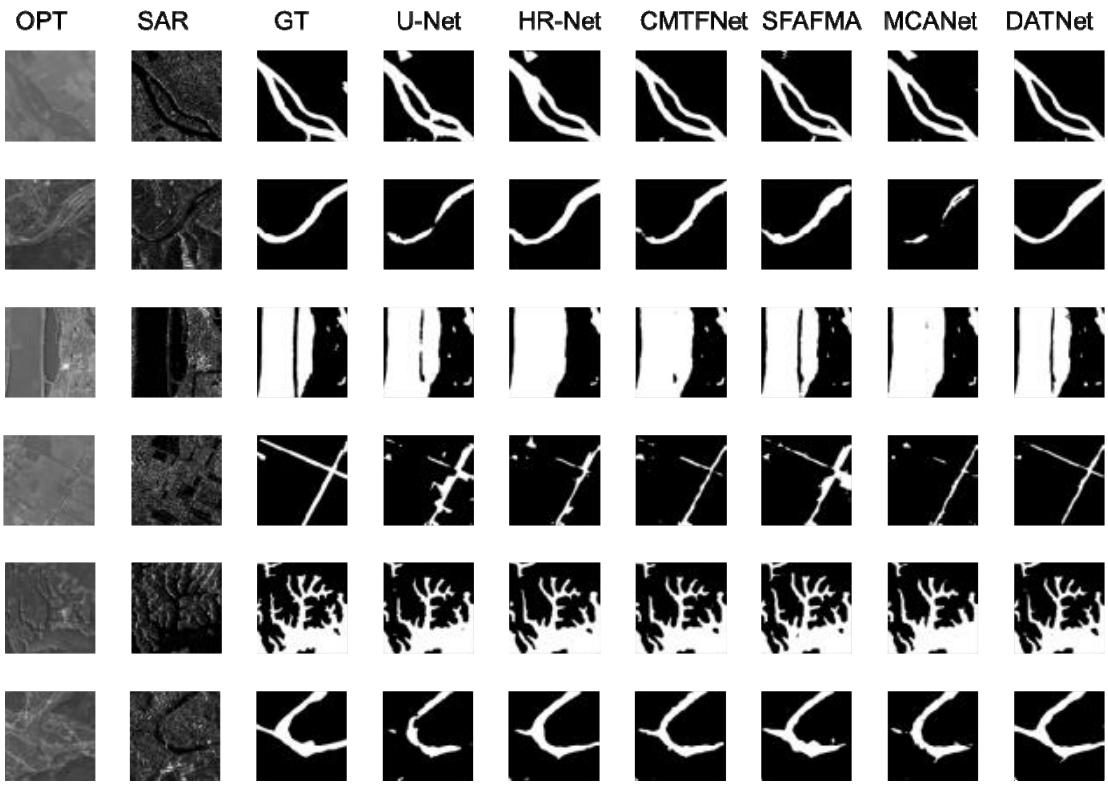

图5 模型对比实验可视化结果图

对比试验的定量结果如下表1，本文所提出的DAT-Net在六项指标中均表现最优，其次是SFAFMA-T，说明了多模态方法能够通过不同融合策略，更有效地整合不同模态数据，从而提高模型性能。并且相比于SFAFMA-T，本文方法在交并比指标提升约1.5%，证明了模型的有效性。CNN-Transformer混合架构的模型CMTFNet在单模态方法中表现最优，说明该模型采用的多尺度多头自注意力（M2SA）模块，能够有效结合CNN和Transformer的特征，提升语义分割准确性。

表1 模型对比试验精度评价结果

Network	OA	mIoU个	IoU	Pre	Rec	F1
U-Net	94.73%	80.85%	67.62%	84.47%	77.22%	80.69%
HR-Net	94.60%	80.40%	66.85%	84.38%	76.29%	80.14%
CMTFNet	94.72%	80.80%	67.54%	84.57%	77.04%	80.63%
SFAFMA-T	94.93%	81.48%	68.68%	85.23%	77.95%	81.43%
MCA-Net	94.40%	79.74%	65.76%	83.68%	75.43%	79.34%
DAT-Net	95.20%	82.40%	70.21%	85.88%	79.38%	82.50%

3.3 消融实验

为了证明模块的有效性进行消融实验，并采用水体分割的经典指标交并比IoU作为精度评价的标准。在消融实验中，共设置四组模型：基于HR-Net的单模态水体提取模型、只保留双编码器结构的方法F1、双

编码器基础上添加Transformer模块的方法F2、以及本文提出的模型DAT-Net。可视化结果见下图6。相比于HRNet，使用两个高分辨率网络作为编码器分别提取光学影像特征和SAR影像特征能够一定程度综合多模态之间的信息，提升水体提取的准确性。以下图6中测试影像3为例，在使用两个编码器独立提取光学SAR各自的模态特征后，原本的绿地与水体出现混淆的情况有所改善，形状细长的绿地部分被有效提取出来。在此基础上，引入自注意力机制能够进一步的提取到特征的深层语义信息。如图6测试影像1中，在F1方法下有部分绿地被识别为水体，但在F2下该部分像素错误识别的情况有所改善。本文提出的DAT-Net在F2的基础上，将模态信息直接相加改为利用多模态特征融合模块CMAM进行自适应的特征融合，利用非局部计算与金字塔池化运算提取特征的重要通道信息和空间信息，进一步优化水体提取准确性。以下图6的测试影像2、3为例，水体的轮廓特征更加平滑，更接近真实的影像数据。

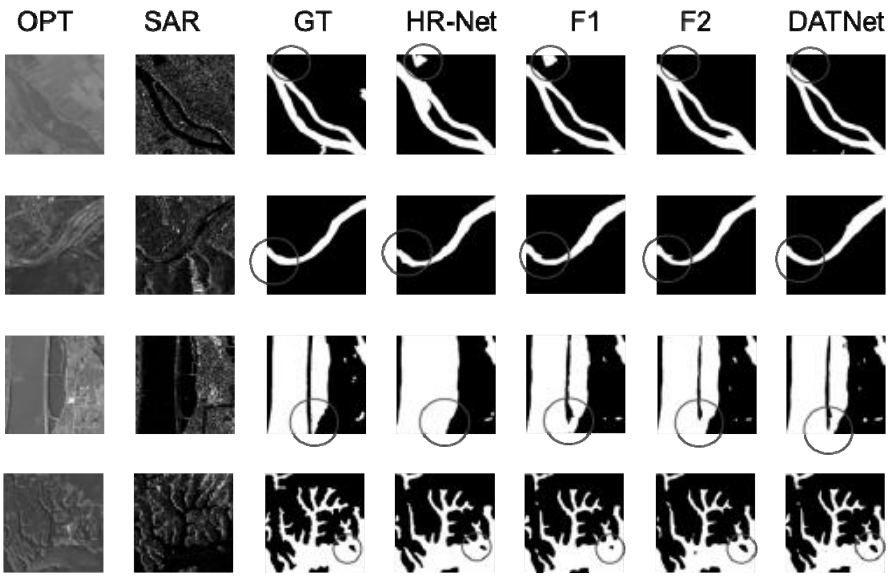

图6 模型消融实验可视化结果图

使用水体提取交并比IoU进行模型精度评价对比，具体的精度结果见下表2：相较于原始的高分辨率网络，双分支网络分别提取光学和SAR特征的方法使得水体交并比提升了约1.4%，说明使用双流注意力网络能够更好的综合两个模态的互补特征信息，避免简单堆叠造成的不同模态因为成像机制差异导致的特征提取影响。在此基础上，引入Transformer模块，模型的精度提升至69.10%，说明自注意力机制有助于图像的全局上下文建模以及深层特征的获取。CMAM模块的添加使得模型的精度提升至70.21%，相比于HR-Net模型提升了约3.4个百分点，实现了不同模态之间特征的有效融合，证明了模块添加的有效性。

表2 模型消融实验精度评价结果

Method	Without module	Transformer layer	CMAM	IoU
HR-Net				66.85%
F1	✓			68.20%
F2		✓		69.10%
DAT-Net		✓	✓	70.21%

4 铁路桥梁项目勘察设计中的应用

铁路桥梁项目勘察设计工作需获取沿线水体（河流、湖泊等）信息，精确测量线路与水体边界交叉点的位置信息，以确保桥梁设计方案的合理性、经济性和安全性。本文基于双流注意力网络 DAT-Net，实现对沿线地物的智能分类提取，利用基于拓扑关系的分类后处理以及矢量逻辑运算，实现交叉点的智能求解，具体技术路线如图 7：首先进行遥感影像预处理，将校正后的多光谱影像与全色影像进行影像融合，将 SAR 影像进行无控制点校正，并将光学 SAR 影像配准。基于本文提出的双流注意力网络 DAT-Net 获取多模态水体特征，并利用跨模态特征融合模块 CMAM 融合多模态特征，实现铁路沿线水体的智能提取；最后利用基于形态学的分类结果后处理与矢量逻辑运算求解得到铁路线路与水体边界的交叉点信息。

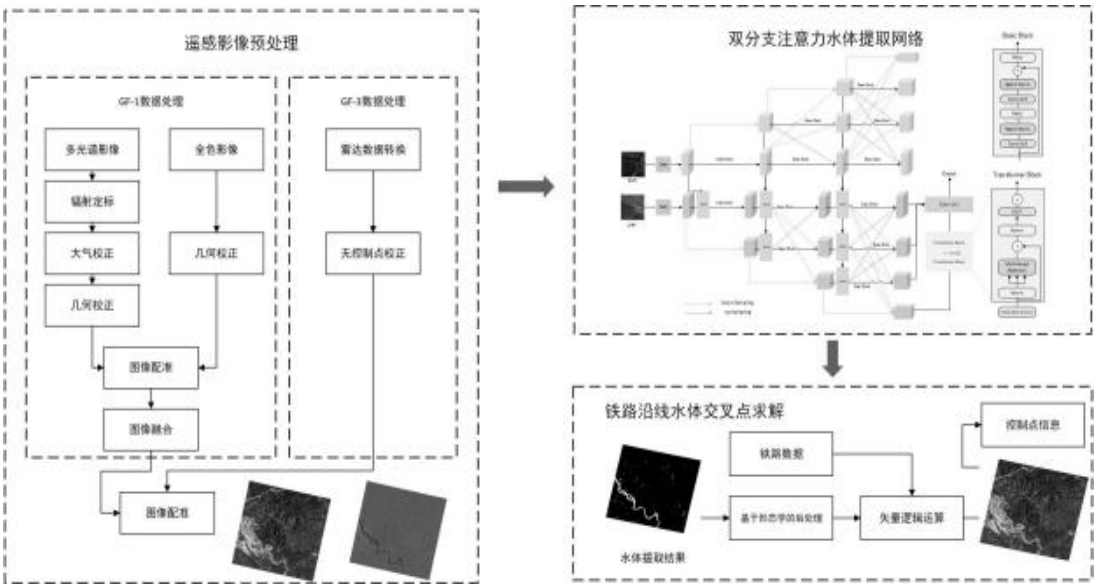

图7 铁路水体交叉点提取技术路线图

4.1 遥感影像预处理

本实验采用的光学和合成孔径雷达图像分别来自 GF-1 和 GF-3(FS II)。将 GF-1 的多光谱影像（RGB

波段）和全色影像分别校正后进行图像配准和融合，获得高分辨率的可见光影像；将 GF-3 影像进行校正后与光学影像进行图像配准。经过预处理后，光学图像的地面分辨率为 2 米，SAR 影像的地面分辨率为 5 米。将两者统一 WGS-84 坐标系，并使用双线性内插法将光学图像重采样到地面分辨率 5 米，以实现两者之间的逐个像素的对应。

4.2 遥感影像水体提取

将预处理后的光学影像和 SAR 影像裁剪至尺寸为 512×512 像素后，利用本文提出的 DAT-Net 实现水体提取，可视化结果如下图 8。使用本文方法在真实影像条件下的测试效果同样较为出色，以下图 8 中的局部 1 和局部 3 为例，对于水体整体的轮廓提取效果与真实水体接近，能够在正确识别大型水体的同时，保留细小水体的细节特征。通过联合光学、SAR 的水体识别能够识别出一些在单模态中容易识别出错的情况。以下图 8 中局部 2 为例，其中的水体面积相对较小，同时与相邻的农田、绿地等地物在光学影像上的光谱特征接近，容易出现漏检、错检的情况，本文方法能够较好的完成在该条件下的水体识别任务。

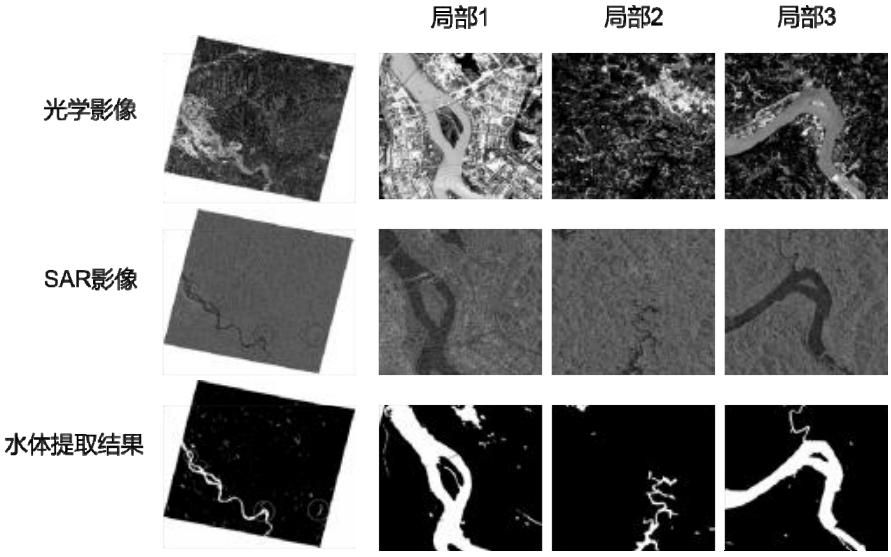

图8 试验区影像水体提取效果图

4.3 铁路沿线水体交叉点求解

在沿线水体交叉点识别中，输入数据包括两部分：基于DAT-Net获得的水体提取结果、铁路线路数据。交叉点的运算主要涉及到三个主要的步骤：地物分类结果的矢量化、基于拓扑运算的分类结果后处理与基于矢量逻辑运算的交叉控制点位置信息求解。最终求解出的铁路水体交叉信息，可用于计算交叉里程、角度等特征信息，进行后续的相关勘测设计工作。

根据交叉点识别技术路线，获得交叉点的具体经纬度坐标信息，输出交叉点的可视化结果如图9，其中黄色点为水体类型的交叉控制点。通过局部图可以看到，对于水体类型交叉控制点，不仅较好的区分了水体与陆地，同时识别到了河流中的陆地部分，精度较高。

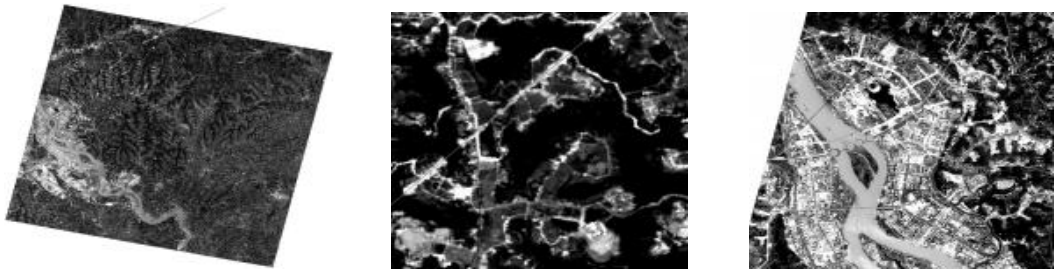

图 9 水体交叉点识别可视化结果图

5 总结

本文提出了一种联合光学SAR遥感影像的多模态水体提取网络DAT-Net，利用双分支编码器提取各模态的特征；基于非局部计算与多尺度池化提出多模态特征融合模块，实现多模态特征的自适应融合；基于自注意力机制进一步提取深层语义信息，实现像素间的长距离建模，最终实现精确的水体提取。本文方法在WHU-OPT-SAR数据集上进行的对比实验中，各项指标均表现最优。另外，为展示本文方法在工程项目中的应用，以四川省某铁路数据为例，本文利用DAT-Net实现了铁路水体交叉信息的智能提取。未来计划在此基础上进一步结合深度学习的域适应技术，提升模型的鲁棒性，增强泛化能力。

参考文献：

[1] 郑洪,谢浩,姚洪锡,等.陆路交通基础设施智能化勘察设计研究综述[J].铁道工程学报,2023,40(08):1-11.

[2] 王立兴.遥感信息技术在铁路勘察设计中的应用[J].测绘地理信息,2016,41(06):65-69. DOI:10.14188/j.2095-6045.2016.06.016.

[3] 冯思维,杨清华,贾伟洁,等.基于光学遥感的内陆地表水体提取综述[J/OL].自然资源遥感,1-16[2024-08-16]. http://kns.cnki.net/kcms/detail/10.1759.p.20240204.1538.006.html.

[4] 温泉,李璐,熊立,等.基于深度学习的遥感图像水体提取综述[J/OL].自然资源遥感,1-16[2024-08-16]. http://kns.cnki.net/kcms/detail/10.1759.p.20230830.1322.022.html.

[5] 何海清,杜敬,陈婷,等.结合水体指数与卷积神经网络的遥感水体提取[J].遥感信息,2017,32(05):82-86.

[6] 郑泰皓,王庆涛,李家国,等.基于深度学习的高分六号影像水体自动提取[J].科学技术与工程,2021,21(04): 1459-1470.

[7] Guo H, He G, Jiang W, et al. A multi-scale water extraction convolutional neural network (MWEN) method for GaoFen-1 remote sensing images[J]. ISPRS International Journal of Geo-Information, 2020, 9(4): 189.

[8] Yu Y, Yao Y, Guan H, et al. A self-attention capsule feature pyramid network for water body extraction from remote sensing imagery[J]. International Journal of Remote Sensing, 2021, 42(5): 1801-1822.

[9] 徐康,朱茂,贺秋华,等.一种基于 TransUNet 的 SAR 影像水体提取及洲滩面积变化监测应用[J].测绘科学,2024,49(02):55-64.DOI:10.16251/j.cnki.1009-2307.2024.02.006.

[10] 陈立福,龙凤琪,李振洪,等.面向多源 SAR 图像的多级特征注意力水体提取网络[J/OL].武汉大学学报(信息科学版),1-9[2024-08-16].https://doi.org/10.13203/j.whugis20230041.

[11] DONOHO D L. Compressed sensing[J]. IEEE Transactions on Information Theory, 2006, 52(4): 1289-1306.

[12] Wang X, Girshick R, Gupta A, et al. Non-local neural networks[C]//Proceedings of the IEEE conference on computer vision and pattern recognition. 2018: 7794-7803.

[13] Dosovitskiy A, Beyer L, Kolesnikov A, et al. An image is worth 16x16 words: Transformers for image recognition at scale[J]. arXiv preprint arXiv:2010.11929, 2020.

[14] Ren B, Ma S, Hou B, et al. A dual-stream high resolution network: Deep fusion of GF-2 and GF-3 data for land cover classification[J]. International Journal of Applied Earth Observation and Geoinformation, 2022, 112: 102896.

[15] Li X, Zhang G, Cui H, et al. MCANet: A joint semantic segmentation framework of optical and SAR images for land use classification[J]. International Journal of Applied Earth Observation and Geoinformation, 2022, 106: 102638.

[16] Wang J, Sun K, Cheng T, et al. Deep high-resolution representation learning for visual recognition[J]. IEEE transactions on pattern analysis and machine intelligence, 2020, 43(10): 3349-3364.

[17] Hu J, Shen L, Sun G. Squeeze-and-excitation networks[C]//Proceedings of the IEEE conference on computer vision and pattern recognition. 2018: 7132-7141.

[18] Zhu Z, Xu M, Bai S, et al. Asymmetric non-local neural networks for semantic segmentation[C]//Proceedings of the IEEE/CVF international conference on computer vision. 2019: 593-602.

[19] He K, Zhang X, Ren S, et al. Spatial pyramid pooling in deep convolutional networks for visual recognition[J]. IEEE transactions on pattern analysis and machine intelligence, 2015, 37(9): 1904-1916.

[20] Woo S, Park J, Lee J Y, et al. Cbam: Convolutional block attention module[C]//Proceedings of the European conference on computer vision (ECCV). 2018: 3-19.

[21] Wu H, Huang P, Zhang M, et al. CMTFNet: CNN and multiscale transformer fusion network for remote sensing image semantic segmentation[J]. IEEE Transactions on Geoscience and Remote Sensing, 2023.

[22] He X, Wang M, Liu T, et al. SFAF-MA: Spatial feature aggregation and fusion with modality adaptation for RGB-thermal semantic segmentation[J]. IEEE Transactions on Instrumentation and Measurement, 2023, 72: 1-10.

[23] Long J, Shelhamer E, Darrell T. Fully convolutional networks for semantic segmentation[C]//Proceedings of the IEEE conference on computer vision and pattern recognition. 2015: 3431-3440.

[24] Chen J, Lu Y, Yu Q, et al. Transunet: Transformers make strong encoders for medical image segmentation[J]. arXiv preprint arXiv:2102.04306, 2021.

[25] Ronneberger O, Fischer P, Brox T. U-net: Convolutional networks for biomedical image segmentation[C]//Medical image computing and computer-assisted intervention–MICCAI 2015: 18th international conference, Munich, Germany, October 5-9, 2015, proceedings, part III 18. Springer International Publishing, 2015: 234-241.

[作者简介]

朱睿哲（2000—），男，武汉大学地理信息科学学士学位，测绘工程硕士研究生在读，研究方向为遥感图像语义分割。

周清华(1989—)，男，硕士研究生，高级工程师，注册测绘师，《铁道勘察》审稿专家，主要研究方向为铁路工程勘察设计数字化。

潘俊（1979—），男，武汉大学地理信息科学学士学位和摄影测量与遥感硕士学位和博士学位，研究方向为遥感数据智能处理和图像质量提升。

宋浩（1993—），男，硕士研究生，工程师，主要从事桥梁设计与数字化研发工作。

多模态信息交互的零样本分类及其在火星探测场景的应用

席博博，檀晓萌*，薛长斌，李云松

摘　要：火星探测对于人类探索地外生命和地球起源等有着非常重要的意义。然而传统的以图像为主要的探测手段在面对火星复杂未知环境、未见类别频发的情况时表现不佳。为解决上述挑战，本文研究了多模态信息交互的零样本分类算法，并探索该算法向深空探测领域的迁移及优化。本文的研究内容主要分为两个方面，数据集构建和算法研究。在数据集构建方面，整合并重构了首个火星探测零样本分类数据集。在算法研究方面，提出了一种基于多模态特征交互的零样本场景分类算法，后结合知识蒸馏，对其进行了模型压缩优化，在保证零样本分类性能的同时，大幅降低了模型的参数量和复杂度。为验证本文算法的有效性，进行了大量对比实验和可视化分析，结果证明了本文算法的可行性和有效性。

关键词：火星探测；多模态学习；零样本学习

Zero-shot classification with multi-model information interaction and its application in Mars exploration scenarios

Bobo Xi, Xiaomeng Tan*, Changbin Xue

Abstract: Mars exploration is of great significance for human exploration of extraterrestrial life and the origin of the earth. However, traditional detection methods based on images do not perform well in the face of the complex and unknown environment of Mars and the frequent occurrence of unseen categories. To address the above challenges, this paper studies the zero-shot classification method of multimodal information interaction and explores the migration and optimization of the algorithm to the field of deep space exploration. The research content of this paper is mainly divided into two aspects: dataset construction and method research. In terms of dataset construction, the first zero-shot classification dataset for Mars exploration was integrated and reconstructed. For method research, a zero-shot scene classification network based on multi-modal feature interaction (MFINet) was proposed. Then combined with knowledge distillation, the model was compressed and optimized, which greatly reduces the number of parameters and complexity of the model while ensuring the performance of zero-shot classification. In order to verify the effectiveness of the methods in this paper, a large number of comparative experiments and visualization analysis were carried out, and the results proved the feasibility and effectiveness of the methods in this paper.

Key words: Mars exploration, multimodal learning, zero-shot learning

1　引言

深空探测是指对月球及以远的地外天体进行空间探测的活动[1]。它的科学目标是寻找地外宜居环境和

生命信号、预防太阳活动和小天体撞击对地球的灾害性影响、探究太阳系及其行星的起源和演化历史等等。具体的任务包括探索物质，如水、有机物、氧气等，识别天体形态、运行轨道，探测物质成分及矿产资源[2]。火星作为太阳系中与地球最为相似的行星，可能保存着太阳系生命起源的时间和行星演化中灾难性变化的最好记录，对研究地球起源与演化具有非常重要的比较意义，是探寻地外生命、探索生命起源与演化等重大科学问题最有价值的目标之一；而且火星距离地球较近，是人类有望率先登陆的地外行星，因此一直是国际行星探测的重点目标，是除月球外人类探索最多的地外天体。人类对火星的探索活动如图 1 所示。

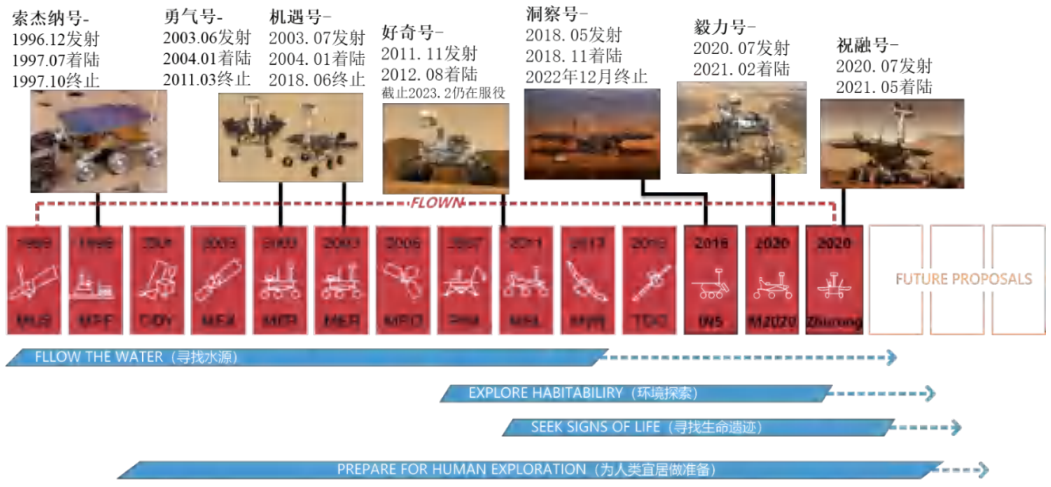

图1　人类对火星的探索活动

当前的深空探测模式需要探测器在接近目标过程中探测并传回数据，随后地面人员开展数据提取、建模和分析，并生成控制指令再回传给探测器。这种地面测控站+航天器的模式表现出了严重的不足，如较大的测控时延、传输数据量有限。此外，以火星探测为例，其表面地形多变，环境恶劣，沙尘暴频发，这意味着目标类别外观多变，并存在随时出现的未见场景。这些因素使得以图像为主要探测手段的火星探测任务的科学目标识别难、探测效率降低，也对能够适应复杂环境和任务的先进视觉处理算法提出了更为迫切的需求。

随着人工智能技术的发展，以机器学习/深度学习为代表的算法在视觉处理上展现出了优异的性能[3]。但这些先进视觉处理算法具有较大的参数量和较高的计算需求，如当前常用的视觉编码器 Vision Transformer（ViT）[4]，其不同变体的参数从 5.7 百万到 632 百万不等。即使有些变体做了参数量的简化，如数据高效的 DeiT 模型[5]，它的不同变体参数范围也在百万级别（5 百万~86 百万）。这种参数量级在传统探测模式下，当存在未知类别时，训练数据的下传、神经网络模型的上注与严格的通信和数据限制存在矛盾。

为缓解上述问题，本文将零样本学习算法引入火星探测领域，实现火星探测未见类别的识别。零样本学习算法作为当前图像探测技术的前沿热点之一[6]，可通过训练已见类别来获得推理未见类别的能力，以解决火星探测复杂环境未见类别的感知问题。值得注意的是，零样本学习模型在测试阶段可通过只上注文本知识来协助未见类别图像的识别。

2 相关工作

2.1 数据集调研

本文调研了国内外火星图像分类的数据集，常用的数据集有 MSL Surface Data Set[7]（简称 MSL 数据集）和 MSL Surface Data Set（v2）[8]（简称 MSL 数据集（v2）），如图 2 所示。目前的数据集都是视觉模态的数据集，仅支持基于监督学习范式的图像分类任务的验证，无法直接用于零样本学习任务。

（a）MSL数据集　　（b）MSL数据集（v2）

图2 火星图像分类数据集

2.2 算法的调研

本文的算法调研分为两个方面，一个是火星图像分类算法，另一个是零样本学习算法。下面来详细介绍以下这两方面的内容

1）火星图像分类算法

当前，将深度学习等图像处理方法用于火星图像分类领域已有较多的探索。Auld[9]等人针对火星高分辨率成像科学实验（HiRISE）图像研究了火星沟壑分类问题。Wagstaff[7]等人使用迁移学习获取基于 AlexNet 的火星图像分类网络 MSLNet。它验证了在地球图像上训练的卷积神经网络可以成功地进行微调以适应对火星图像进行分类。为提高分类器的准确性，Lu[10]等人在 Wagstaff[7]等人的基础上，修改了网络的微调方法，分析和分类了每个分类器在训练集和验证集中的常见错误，并采用分类器校准方法来提高分类器的可靠性。Wagstaff[8]等人在此前基础上，创建了新的标记 MSL 数据集（v2）来训练和评估最新版本的火星图像分类器，以应对 MSL 数据集图像的分类。为实现有效监督多类火星图像分类器识别，Nandi[11]等人结合迁移学习和集成方法得到一个动态路由模块，设计了一种新颖的轮询算法，在 MSL 数据集中达到了 88% 的测试精度。Lv[12]等人提出了一种基于视觉的高精度火星地形分类方法，通过分析火星地形特征，提取了专门针对地形分类的图像特征，使得火星车地形分类准确率超过了 90%。Vincent[13]等人为解决行星图像带注释训练数据缺乏以及当前模型由于域转移导致的归纳偏差的问题，提出了一种自监督学习框架，利用对比学习技术改进分类器的性能。

此外，针对现有火星分类模型在火星数据不平衡和失真的情况下表现不佳的问题，Wang[14]等人设计

了基于半监督对比学习的火星图像分类新框架，通过表示学习来开发鲁棒的视觉表示，通过改进对比学习方法，在标记数据上利用注释并忽略类内对，实现有监督的类间对比学习，在未标记数据上只最大化正样本对的相似性，不考虑负样本对的差异性，从而形成无监督的相似性学习。这种范式有效提高了算法的性能。随后 Wang[15]等人还研究了火星图像分割任务的半监督学习框架。

2）零样本学习算法

零样本，即无训练样本，零样本学习旨在让深度学习模型能够识别没有训练过的新类别，是指通过对已有标注样本训练加以其他辅助信息（通常为语义信息）来完成新类别或新概念的识别[16]。当前零样本学习算法的主流算法主要可分为三类，分别是基于嵌入模型的方法、基于生成网络的方法和基于预训练模型的方法。其中基于嵌入模型的方法研究最为广泛，也最为经典[17]。本节将重点介绍这类方法的研究进展。

基于嵌入模型的方法，根据嵌入空间的不同，可进一步分为基于基于语义空间嵌入的方法、基于视觉空间嵌入的方法和基于公共空间嵌入的方法。Socher 等人[18]引入了跨模态迁移思想，提出了基于空间嵌入的模型，极大促进了零样本学习算法的发展。随后，Frome 等人[19]提出了深度视觉-语义嵌入模型，利用已标记的图像和未标注的文本信息训练并识别图像，有效提升了零样本分类性能。此外，Akata 等人[20]提出了属性标签嵌入模型，将每一类都嵌入属性空间中，算法性能的提升充分证明了属性的重要性。

上述基于语义空间嵌入的算法使得零样本学习算法性能得到了较大的提高，但在距离度量过程中，可能会出现多个语义向量与映射后的图像距离最近的情况，即“枢纽点”问题。为解决该问题，有学者提出了将映射子空间改为视觉空间的方法，即基于视觉空间嵌入的算法。例如，Zhang 等人[21]提出了一种多模态融合方法，选取卷积神经网络输出的视觉特征空间为嵌入空间，将属性和词向量等语义特征映射到视觉空间，并采用循环神经网络实现语义空间表示的端对端学习。Sung 等人[22]在此基础上提出了关系网络，包含嵌入模块和关系模块两部分，嵌入模块将属性和词向量等语义特征嵌入到视觉空间，然后通过关系模块来判别类别。

此外，还有学者提出了将图像和类别标签同时映射到一个潜在公共空间中，即基于公共空间嵌入的算法，如 Reed 等人[23]提出的结构联合嵌入模型，通过端到端的训练在公共空间完成图像视觉特征和语义信息的匹配辅助分类。为增强图像和语义与分类的关联性，Tao 等人[24]提出了语义保留局部嵌入零样本算法，将图像和语义数据同时嵌入到派生空间进行分类，通过匹配跨域概念来执行子空间学习以提高性能。

3　研究方法

为实现零样本学习算法向深空探测领域的迁移，本文的研究主要分为数据集构建和算法研究两个方面在数据集构建方面，本文以火星探测为应用背景，构建用于零样本学习的火星探测数据集。在算法研究方面，本文进行了基于多模态特征交互的零样本场景分类算法及其轻量化设计研究。本节将依次介绍这两方面的研究内容。

3.1 数据集构建

首先，本文整理分析了火星探测数据集 MSL Surface Data Set[7]和 MSL Surface Data Set（v2）[8]，如 2.1 节所述。通过去掉特征增强的重复场景图像以及灰度图像，筛选适合于“岩石土壤”场景主题的类别图像，重构了数据集。在数据集类别定义方面，确定了如图 3 所示的 10 个类别，其类别的名称和对应的语义信息如图 4 所示。

图3 课题组构建的零样本火星场景分类数据集ZS-Mars

MARS SCENE CATEGORY LIST AND THE CORRECTED SENTENCE DESCRIPTION OF EACH MARS IMAGE SCENE CATEGORY.

Index	Category Names	Sentance Description
0	Martian Soil	Unconsolidated or poorly consolidated weathered materials on Mars, with a reddish color, will not form ridges due to the influence of terrain, and have relatively low fluidity.
1	Sands	The particulate matter composed of small rocks on Mars is generally formed by weathering and erosion of rocks, usually forming a ridge of windward and leeward slopes, with relatively strong fluidity.
2	Gravel	The particulate matter on Mars is generally formed by weathering and erosion of rocks, which are rougher than sand and smaller than rock particles, with average fluidity.
3	Light-Toned Veins	A landform on Mars composed of patches of gravel and rocks, with varying depths of veins/extensional stripes, usually dominated by rocks and covered by gravel.
4	Float Rocks	Small rocks that have fallen off the surface of Mars from large rocks, appearing in block or oval shape, with a strong and brittle texture, larger than the particles of gravel, and almost no gravel.
5	Igneous Rocks	A type of rock on Mars formed by magma ejecting from the surface or invading the crust, cooling and solidifying. It has obvious mineral crystal particles or pores, and the color of the rock is black with irregular shapes; Rocks have varying volumes and lack fluidity
6	Sedimentary Rocks	A type of rock on Mars that is formed by the consolidation of loose sediment in layers, usually with a certain layered texture; Not containing or containing a small amount of sand; The rock has a large volume and lacks fluidity; Sediment generally refers to loose debris, such as gravel, sand, clay, plaster, etc.
7	Tracks	The pattern left by the wheels of the Mars surface exploration vehicle after passing through soft soil or sand. The close-up image contains obvious wheel patterns, while the close-up image shows a blurry shape of the wheel patterns, showing long traces of heavy objects dragging.
8	Rover Components	Part of the structure present on a Mars rover or Mars cover.
9	Unkown	The distant images on Mars are mainly composed of soft soil, as well as some parts of the sky or hills, but it is difficult to distinguish the specific composition of the ground, and there are obvious light and dark layers between the regions.

图4 零样本火星场景分类数据集ZS-Mars中的类别标签及对应语义信息

3.2 算法的研究

在零样本学习算法向深空探测领域迁移的过程中，本文首先研究了基于多模态特征交互的零样本场景分类算法。此外，鉴于深空探测航天器存储和计算资源受限的特点，为使得零样本算法能适应星上环境，

本文随后研究了基于知识蒸馏的轻量化零样本场景分类算法。

1）基于多模态特征交互的零样本场景分类算法（MFINet）

本节提出的零样本图像场景分类算法 MFINet 主要由三部分构成，如图 5 所示：用于提取视觉特征的局部全局特征提取模块（Res-DeiT）、用于解释语义的语义编码器（Core-BERT） 信息，以及新颖的跨模态特征融合模块（CMFF）来交互地融合跨模态特征。

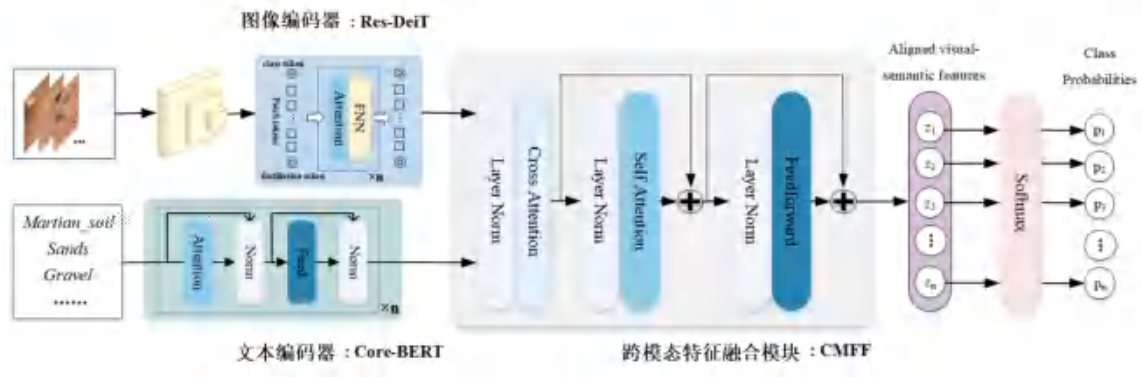

图5 基于多模态特征交互的零样本场景分类算法MFINet示意图[25]

与大多数现有的零样本学习嵌入模型相比，MFINet 的不同之处在于它将视觉特征提取模型、自然语言处理模型和视觉语义对齐模型集成到端到端训练过程中。这使得 MFINet 框架能够在视觉语义对齐模型的指导下提取更多语义上有意义的视觉特征和更多视觉信息丰富的语义信息。具体来说，在 Res-DeiT 模块中，采用了级联卷积神经网络和 Transformer 结构来获取图像的局部-全局联合视觉特征。对于语义提取方面，利用 Core-BERT 网络作为轻量化的语义编码器，继承了原始 BERT 网络的核心架构以实现语义信息提取，如图 6 所示。在 CMFF 模块中，跨模态注意力层可以促进视觉模态和语义模态之间的特征交互，有效地缓解两模态间的差距。

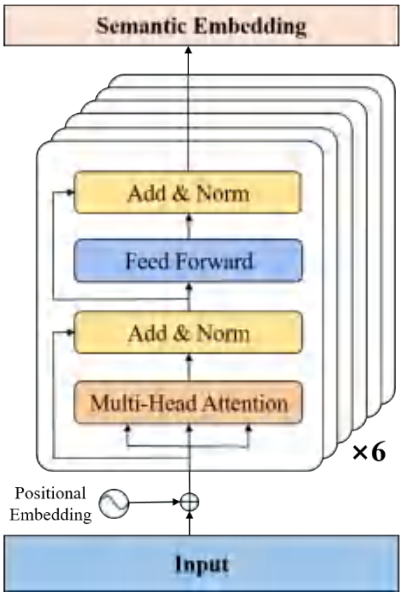

图6 基于多模态特征交互的零样本场景分类算法示意图

2）基于知识蒸馏的轻量化零样本场景分类算法（KDMSC）

基于知识蒸馏的轻量化零样本场景分类算法（KDMSC），如图 7 所示。该算法引入了知识蒸馏损失函数，由复杂教师模型和轻量化学生模型组成，利用教师模型最佳的预测结果来有效指导学生模型的优化过程。

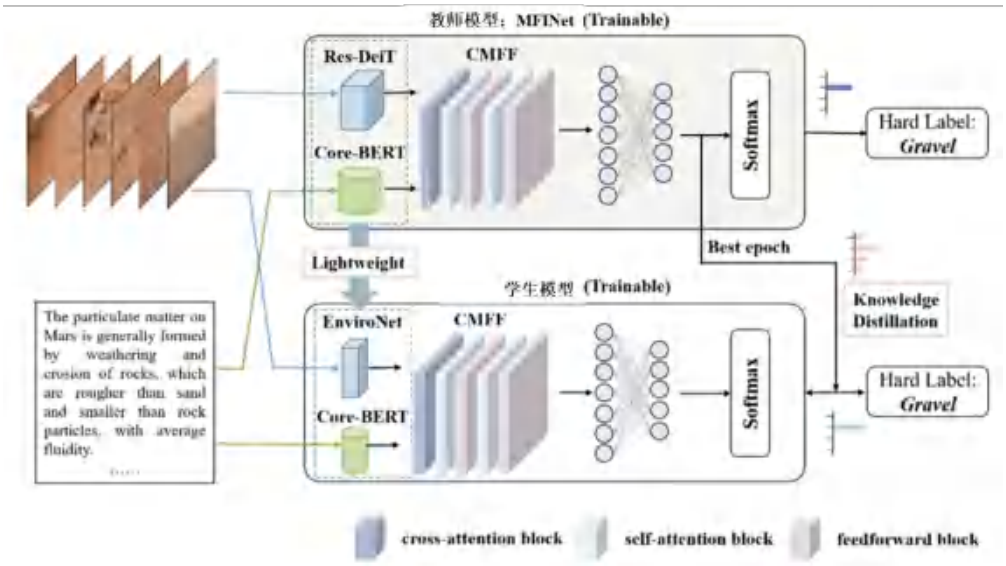

图7 基于知识蒸馏的轻量化零样本场景分类算法KDMSC示意图

教师模型沿用了 MFINet 网络。学生模型的语义编码器与教师模型一致，而在视觉编码器方面，学生模型通过引入上下文卷积构建了 EnviroNet 模型，可有效捕获图像的局部和全局特征，如图 8 所示。随后，同样利用 CMFF 模块，将两个模态的特征投影到同一潜在空间，实现视觉和语义特征间的匹配。

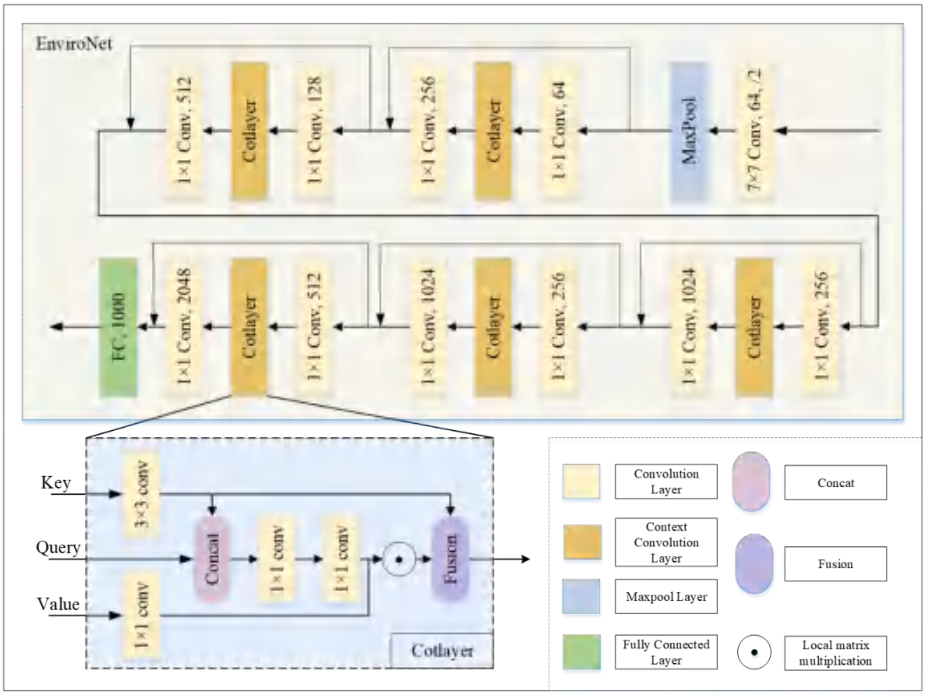

图7 轻量化图像特征提取网络EnviroNet示意图

3）损失函数的构建

MFINet 算法的损失函数 L_{MF} 由类回归损失 L_c 和交叉熵损失 L_r 两部分构成，它们的公式如下：

$$L_{MF} = L_c + \lambda \cdot L_r \tag{1}$$

式中，λ 为交叉熵损失 L_r 的权重。

类回归损失 L_c 和交叉熵损失 L_r 的计算公式分别为

$$L_c = \left\| X - y \right\|_2^2 \tag{2}$$

$$L_r = -\log\left(\frac{e^{X \cdot R}}{\sum_{\hat{c} \in l^s} e^{X \cdot R^{\hat{c}}}} \right) \tag{3}$$

式中，X, R 分别为由 CMFF 模块得到图像和文本特征；y 是图像对应的文本向量；$\hat{c}$ 是类别对应的文本信息；l^s 是图像的类别对应的未见类别文本描述信息。

KDMSC 算法中教师和学生模型均为 MFINet 算法的损失函数，此外，KDMSC 算法的总体损失函数额外添加了蒸馏损失函数。它的计算公式如下：

$$L_{KD} = L_{stu} + \lambda_{kd} \cdot L_{kd} \tag{4}$$

式中，L_{stu} 与 L_{MF} 函数一致；λ_{kd} 为蒸馏损失 L_{kd} 的权重；L_{kd} 的计算公式如下：

$$L_{KD} = KL\left(F_t\left(Z\left(X_1, Y \right) \right), F_s\left(Z\left(X_1, Y \right) \right) \right) \tag{5}$$

式中，KL 表示本文采用的 Kullback-Leibler 散度函数；$F_t(\cdot), F_s(\cdot)$ 分别代表教师和学生模型的输出 logits；$Z\left(X_1, Y \right)$ 为通过 CMFF 模块得到的特征；X_1, Y 分别为输入到 CMFF 模块的图像向量和文本向量。

4　实验分析

为充分证明所设计算法的可行性和有效性，本文分别利用词向量和语义向量两种语义信息，在 3 种可见/不可见比率下进行了对比实验和分类可视化结果的分析。

4.1　实验设置

1）设置细节

本文对零样本火星数据集的类别进行了 3 种可见/未见类别的划分，如表 1 所示。在 6/4 可见/不可见比率中，可见类别包含火壤（Martian Soil）、沙砾（Gravel）、浮石（Float Rocks）、火星车轨迹（Tracks）、火星车部件（Rover Components）、未知（Unknown）；未见类别为沙地（Sands）、脉络状沙石（Light-Toned Veins）、火成岩（Igneous Rocks）、沉积岩（Sedimentary Rocks）。在 7/3 可见/不可见比率中，可见类别包含 Martian Soil、Gravel、Float Rocks、Tracks、Rover Components、Igneous Rocks、Unknown，未见类别

为 Sands、Light-Toned Veins、Sedimentary Rocks。在 8/2 可见/不可见比率中，可见类别包含 Martian Soil、Gravel、Light-Toned Veins、Float Rocks、Igneous Rocks、Tracks、Rover Components、Unknown，未见类别为 Sands 和 Sedimentary Rocks。

表1 数据集可见/未见类别的划分

类型	可见/不可见比率		
	6/4	7/3	8/2
可见类	Martian Soil; Gravel; Float Rocks; Tracks; Rover Components; Unknown	Martian Soil; Gravel; Float Rocks; Igneous Rocks; Tracks; Rover Components; Unknown	Martian Soil; Gravel; Light-Toned Veins; Float Rocks, Igneous Rocks; Tracks; Rover Components; Unknown
未见类	Sands, Light-Toned Veins, Igneous Rocks, Sedimentary Rocks	Sands, Light-Toned Veins, Sedimentary Rocks	Sands, Sedimentary Rocks

2）评价指标

为充分说明算法的可行性和有效性，本文采用两种评价指标作为衡量标准，分别是总体准确率（Overall Accuracy，OA）和平均准确率（Average Accuracy，AA）。它们的计算公式如下：

$$OA = \frac{TP + TN}{TP + FN + FP + TN} \tag{6}$$

$$AA = \left(\frac{TP}{TP + FN} + \frac{TN}{FP + TN} \right) \Big/ 2 \tag{7}$$

式中，TP 表示分类器预测结果为正样本，实际也为正样本，即正样本被正确识别的数量；FP 表示分类器预测结果为正样本，实际为负样本，即误报的负样本数量；TN 表示分类器预测结果为负样本，实际也为负样本，即负样本被正确识别的数量；FN 表示分类器预测结果为负样本，实际为正样本，即漏报的正样本数量。

4.2 对比实验

为评估本文算法的性能，选取了 DeViSE[19]、ESZSL[26]、ALE[20]、SJE[23] 和 DUET[27]零样本算法来进行对比实验。OA 和 AA 的实验结果分别如表 2 和表 3 所示。表中的粗体为实验的最佳结果，斜体为次佳结果。

由表 2 可得，输入词向量时，KDMSC 算法 OA 结果在 6/4 可见/不可见比率下实现了最佳的分类效果，而在 7/3 和 8/2 可见/不可见比率下实现了次佳的分类结果。对应地，MFINet 算法 OA 结果在 6/4 可见/不可见比率下实现了次佳的分类效果，而在 7/3 和 8/2 可见/不可见比率下实现了最佳的分类结果。而在输入句子向量时，KDMSC 算法在 3 种比率下都取得了最佳的分类效果，MFINet 算法则在 6/4 和 7/3 可见/不可见

比率下实现了次佳的分类结果。值得注意的是，学生模型在 8/2 可见/不可见比率下实现了次佳的分类结果。

表2 对比实验的OA结果

语义向量	词向量			句子向量		
可见/不可见比率	6/4	7/3	8/2	6/4	7/3	8/2
DeViSE	36.6	47.5	65.3	17.3	34.0	71.7
ESZSL	34.0	46.8	71.6	21.9	27.2	50.3
ALE	37.9	46.1	60.6	17.8	32.7	67.9
SJE	34.8	45.1	56.9	18.0	38.4	69.7
DUET	37.9	61.9	82.9	32.4	43.2	57.9
MFINet	*45.1*	**64.8**	**99.1**	*39.1*	*54.9*	73.6
Student Model	44.8	59.1	95.9	37.0	50.6	*78.9*
KDMSC	**46.8**	*62.7*	*97.4*	**40.2**	**62.8**	**80.1**

表3 对比实验的AA结果

语义向量	词向量			句子向量		
可见/不可见比率	6/4	7/3	8/2	6/4	7/3	8/2
DeViSE	34.8	54.5	72.7	38.1	43.9	*77.1*
ESZSL	30.7	42.7	61.9	33.9	41.8	67.8
ALE	37.1	51.1	70.8	*38.6*	43.9	74.9
SJE	36.3	50.2	66.2	38.5	45.4	75.7
DUET	38.5	61.9	94.8	30.9	41.7	58.9
MFINet	41.1	**64.7**	**96.9**	34.2	44.9	67.9
Student Model	*44.8*	63.7	96.5	33.2	*48.2*	66.8
KDMSC	**45.3**	*63.7*	*96.7*	**39.6**	**54.9**	**77.9**

表 3 的结果表明，输入词向量时，KDMSC 算法 AA 结果在 6/4 可见/不可见比率下实现了最佳的分类效果，而在 7/3 和 8/2 可见/不可见比率下实现了次佳的分类结果。对应地，MFINet 算法 AA 结果在 6/4 可见/不可见比率下实现了次佳的分类效果，而在 7/3 和 8/2 可见/不可见比率下实现了最佳的分类结果。而在输入句子向量时，KDMSC 算法的 AA 结果依然在 3 种比率下都取得了最佳的分类效果，而学生模型仅在 7/3 可见/不可见比率下实现了次佳的分类结果。值得注意的是，ALE 算法在 6/4 可见/不可见比率下实现了次佳的分类结果，DeViSE 算法在 8/2 可见/不可见比率下实现了次佳的分类结果。上述的 OA 和 AA 结果都证明了本文所提算法可使得零样本分类算法在火星图像数据集上具有更好的零样本分类性能。

4.3 复杂度分析

在两种语义信息输入的情况下，MFINet、学生模型和 KDMSC 的参数量及复杂度等信息如表 4 所示。

表4 参数量及复杂度信息

模型	词向量			句子向量		
	复杂度（GFlops）	模型大小（MB）	参数量（M）	复杂度（GFlops）	模型大小（MB）	参数量（M）
MFINet	34.33	564.04	147.07	34.34	562.42	147.43
学术模型	3.33	269.85	70.74	3.33	271.23	71.10
KDMSC	3.33	269.85	70.74	3.33	271.23	71.10

由表 4 可得，本文设计的模型压缩优化方案在保证算法性能的情况下，有效降低了参数量和计算度。此外，对于句子向量和词向量输入的变化，这三个模型在复杂度上没有影响，而在模型大小和参数量上有一定影响。

4.3 可视化结果分析

为更为直观的查看零样本分类预测结果，本文将输入词向量时，6/4 可见/不可见比率下对于 4 种不可见类别的预测概率进行可视化，如图 8 所示。其中，图（a）、图（b）和图（c）分别为 MFINet 算法、学生模型和 KDMSC 算法的可视化结果。图 8 中的类 0~3 对应的数据集类别名称如表 5 所示。

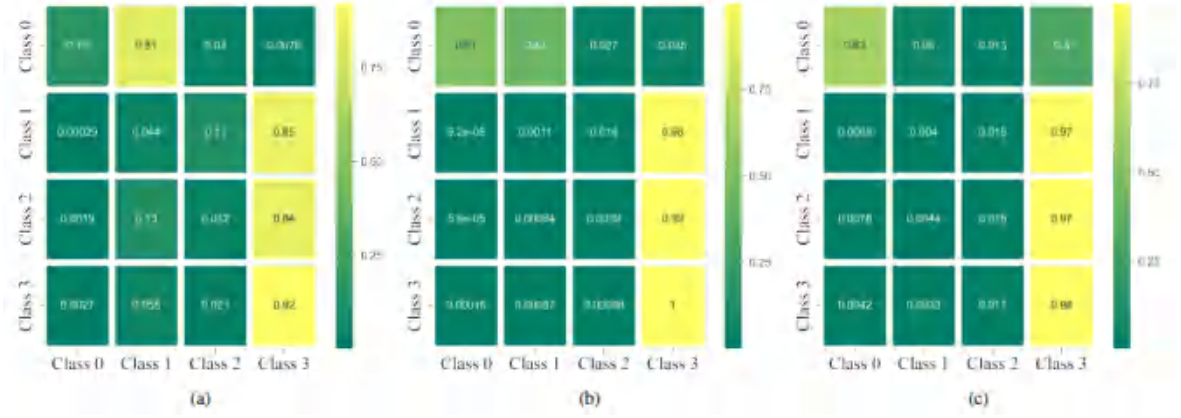

图8 类别分类结果的可视化结果。（a）MFINet；（b）学生模型；（c）KDMSC

表5 图8中类别对应的数据集类别名称

	标签
Class 0	Sands
Class 1	Light-Toned Veins
Class 2	Igneous Rocks
Class 3	Sedimentary Rocks

由图 8 可得，MFINet 算法仅能正确识别类别 3，在类别 0 的识别上实现了次高的预测概率。学生模型同样仅能正确识别类别 3，在类别 0 的识别上同样实现了次高的预测概率，但在这两类预测概率上都有了一定提高。KDMSC 算法则有效结合了这两类算法的优势，实现了类别 0 和类别 3 的有效识别。

5　结束语

为缓解火星图像分类任务科学目标识别难、探测效率低等问题，本文探索了多模态信息交互的零样本分类算法，构建了首个火星探测领域零样本分类数据集，提出了一种基于多模态特征交互的零样本场景分类算法，并结合知识蒸馏和轻量化模型设计，对该算法进行了模型压缩优化，在保证零样本性能的同时，实现了参数量和复杂度的大幅降低，更有利于进行实际设备的部署。为验证算法的有效性，本文进行了大量的对比实验，并对结果进行了可视化分析，实验结果证明了本文所提算法可实现优越的零样分类性能。

参考文献：

[1] 吴伟仁, 于登云. 深空探测发展与未来关键技术[J]. 深空探测学报(中英文）, 2014, 1(1): 5–17.
[2] 叶培建, 孟林智, 马继楠, 等. 深空探测人工智能技术应用及发展建议[J]. 深空探测学报, 2019, 6(4): 303-316+383.
[3] 于登云, 张哲, 泮斌峰, 等. 深空探测人工智能技术研究与展望[J]. 深空探测学报, 2020, 7(1): 11–23.
[4] Alexey Dosovitskiy, Lucas Beyer, Alexander Kolesnikov, et al. An Image is Worth 16x16 Words: Transformers for Image Recognition at Scale: arXiv:2010.11929[Z]. arXiv, 2021.
[5] Hugo Touvron, Matthieu Cord, Matthijs Douze, et al. Training data-efficient image transformers & distillation through attention[C]//Proceedings of the 38th International Conference on Machine Learning. PMLR, 2021: 10347–10357
[6] Weipeng Cao, Yuhao Wu, Yixuan Sun, et al. A review on multimodal zero-shot learning[J]. WIREs Data Mining and Knowledge Discovery, 2023, 13(2): e1488.
[7] Kiri L. Wagstaff, You Lu, Alice Stanboli, et al. Deep mars: CNN classification of mars imagery for the PDS imaging atlas[C]//Proceedings of the Thirty-Second AAAI Conference on Artificial Intelligence and Thirtieth Innovative Applications of Artificial Intelligence Conference and Eighth AAAI Symposium on Educational Advances in Artificial Intelligence. New Orleans, Louisiana, USA: AAAI Press, 2018: 7867–7872
[8] Kiri Wagstaff, Steven Lu, Emily Dunkel, et al. Mars Image Content Classification: Three Years of NASA Deployment and Recent Advances: 17[J]. Proceedings of the AAAI Conference on Artificial Intelligence, 2021, 35(17): 15204–15213.
[9] Katherine S. Auld, John C. Dixon. A classification of martian gullies from HiRISE imagery[J]. Planetary and Space Science, 2016, 131: 88–101.
[10] S. Lu, K. Wagstaff, J. Cai, et al. Content-based Classification of Mars Imagery for the PDS Image Atlas[J]. 2019, 2019: P43E-3509. .
[11] Arpan Nandi, Arjun Mallick, Arkadeep De, et al. Mars-TRP: Classification of Mars imagery using dynamic polling between transferred features[J]. Engineering Applications of Artificial Intelligence, 2022, 114: 105014.
[12] Fengtian Lv, Nan Li, Chuankai Liu, et al. Highly Accurate Visual Method of Mars Terrain Classification for Rovers Based on Novel Image Features[J]. Entropy, 2022, 24(9): 1304.
[13] Grace M. Vincent, Isaac R. Ward, Charles Moore, et al. CLOVER: Contrastive Learning for Onboard Vision-Enabled Robotics[J]. Journal of Spacecraft and Rockets, 2023, 0(0): 1–13.
[14] Wenjing Wang, Lilang Lin, Zejia Fan, et al. Semi-Supervised Learning for Mars Imagery Classification[C]//2021 IEEE International Conference on Image Processing (ICIP).
[15] Wenjing Wang, Lilang Lin, Zejia Fan, et al. Semi-supervised Learning for Mars Imagery Classification and

Segmentation[J]. ACM Transactions on Multimedia Computing, Communications, and Applications, 2023, 19(4): 144:1-144:23.

[16] 贾霄, 郭顺心, 赵红. 基于图像属性的零样本分类方法综述[J]. 南京大学学报(自然科学), 2021, 57(04): 531–543.

[17] Tan X, Xi B, Li J, et al. Review of Zero-Shot Remote Sensing Image Scene Classification[J]. IEEE Journal of Selected Topics in Applied Earth Observations and Remote Sensing, 2024: 1–16.

[18] R. Socher, M. Ganjoo, Christopher D. Manning, et al. Zero-Shot Learning Through Cross-Modal Transfer[Z]

[19] Andrea Frome, Greg S Corrado, Jon Shlens, et al. DeViSE: A Deep Visual-Semantic Embedding Model[J]. 2013. .

[20] Zeynep Akata, Florent Perronnin, Zaid Harchaoui, et al. Label-Embedding for Attribute-Based Classification[C]//2013 IEEE Conference on Computer Vision and Pattern Recognition.

[21] Li Zhang, Tao Xiang, Shaogang Gong. Learning a Deep Embedding Model for Zero-Shot Learning[C]//2017 IEEE Conference on Computer Vision and Pattern Recognition (CVPR).

[22] Flood Sung, Yongxin Yang, Li Zhang, et al. Learning to Compare: Relation Network for Few-Shot Learning[C]//2018 IEEE/CVF Conference on Computer Vision and Pattern Recognition.

[23] Scott Reed, Zeynep Akata, Honglak Lee, et al. Learning Deep Representations of Fine-Grained Visual Descriptions[C]//2016 IEEE Conference on Computer Vision and Pattern Recognition (CVPR).

[24] Shih-Yen Tao, Yi-Ren Yeh, Yu-Chiang Frank Wang. Semantics-Preserving Locality Embedding for Zero-Shot Learning[C]//Procedings of the British Machine Vision Conference 2017. London, UK: British Machine Vision Association, 2017: 3

[25] Tan X, Xi B, Xu H, et al. MFINet: A Novel Zero-Shot Remote Sensing Scene Classification Network Based on Multimodal Feature Interaction[J]. IEEE Journal of Selected Topics in Applied Earth Observations and Remote Sensing, 2024: 1–16.

[26] Anonymous. An embarrassingly simple approach to zero-shot learning[C]//Proceedings of the 32nd International Conference on Machine Learning.

[27] Zhuo Chen, Yufeng Huang, Jiaoyan Chen, et al. DUET: Cross-modal Semantic Grounding for Contrastive Zero-shot Learning[C]//Proceedings of the Thirty-Seventh AAAI Conference on Artificial Intelligence and Thirty-Fifth Conference on Innovative Applications of Artificial Intelligence and Thirteenth Symposium on Educational Advances in Artificial Intelligence. AAAI Press, 2023: 405–413

[作者简介]

席博博 (1994-)，男，博士，西安电子科技大学副教授。主要研究方向为高光谱图像处理、机器学习和深度学习。

檀晓萌 (1997-)，女，中国科学院大学在读博士生。主要研究方向为遥感图像处理、零样本学习、机器学习和深度学习。

薛长斌 (1972-)，男，博士，中国科学院国家空间科学中心研究员。主要研究方向为深空探测科学载荷全过程处理和仿真技术、机器学习和深度学习。

李云松（1974-），男，博士，西安电子科技大学教授，博导。主要研究方向为图像/视频处理、编码及传输、芯片设计和高性能计算。

手机直连高轨卫星语音解决方案及关键技术研究

张剑寅、尼凌飞、于天意、刘昱、王汉白、程锦霞、邓伟

（中国移动通信有限公司研究院，北京 100053）

摘　要：手机直连高轨卫星语音因覆盖区域广、全球可用性强等技术特点在远距离通信、紧急通信、广域监控等场景有显著优势。本文提出基于透明转发高轨卫星实现语音业务的解决方案，结合网络需求针对专用 QoS 保障、编解码简化、SIP 协议优化、紧急通信等关键技术开展研究，并通过基于高轨卫星的实验室与外场测试完成技术方案验证。最后分析潜在技术挑战并展望未来业务发展方向，希望为手机直连高轨卫星语音的研究、建设与应用提供参考。

关键词：手机直连卫星；星地融合网络；高轨卫星；语音服务

Solution and key technologies of direct-to-handset voice service based on GEO satellite

ZHANG jianyin, NI lingfei, YU tianyi, LIU yu, WANG hanbai, CHENG jinxia, DEN wei

China Mobile Research Institute, Beijing 100053, China

Abstract: Due to the characteristics of wide coverage area and strong global availability, direct-to-handset voice service based on GEO has significant advantages in remote communication, emergency communication, wide-area monitoring and other scenarios. This paper proposes a solution for voice service based on GEO satellite in the transparent forwarding pattern. According to the network requirements, some research work is conducted on the key technologies including dedicated QoS guarantee, codec simplification, SIP protocol optimization and emergency communication, etc. And the solution is verified by laboratory and field tests based on maritime high-orbit satellites. Finally, the potential technical challenges and the future development direction are analyzed so as to provide a reference for the research, construction and application of direct-to-handset voice service based on GEO satellite.

Key words: direct-to-handset, satellite-terrestrial integration network, GEO satellite, voice service

1　引言

在地面移动通信网络蓬勃发展的同时全球卫星通信的发展也在提速，随着越来越多泛在通信、星地通

信需求的凸显，地面与卫星通信产业生态系统正逐步走向融合形成卫星互联网。卫星互联网建设已成为大国竞争焦点，各国不断拓展近地轨道空间，加速大型甚至巨型星座化布局[1-2]。2022 年 2 月欧盟宣布推进建立欧盟卫星互联网（EU space-based secure connectivity system）并起草太空交通管理规则（Space Traffic Management）。美国星链（Starlink）作为在轨卫星数量最多的卫星系统截止 2022 年 10 月已发射卫星超过 3000 颗，服务用户分布在 39 个国家超 70 万人。2024 年 1 月 SpaceX 宣布通过星链（Starlink）卫星结合 T-Mobile 地面网络实现短消息发送并计划落地商用。我国同样出台多项发展卫星互联网的战略举措，将卫星互联网纳入“新基建”通信网络基础设施的范畴[3]。

卫星网络主要分为轨道海拔低于 2000 km 的低轨卫星（LEO）网络、轨道海拔在 2000 km 至 36000 km 之间的中轨卫星（MEO）网络、以及轨道海拔在 36000 km 的高轨卫星（GEO）网络。低轨卫星网络对地低通信延迟相对较低、信号质量较好，通信业务的实时性体验更好，但是由于其非同步特性导致网络需要频繁切换、链路接续困难；另外由于单星覆盖范围较小，组建覆盖广域区域的低轨卫星网络成本更高[4]。中轨卫星同样属于非同步卫星，组建卫星星座通常需要超过 20 颗卫星，并且由于轨道路径的多样性，地面天线、终端等设备与卫星的持续接续依然是接入侧的主要挑战。高轨卫星属于同步卫星，链路切换与接续的问题相对较小，并且由于单星覆盖范围大更适合嘴贱广域卫星网络，相应的星地时延更大、信号功率损失更严重。

本文将针对天地一体卫星互联网中手机直连高轨卫星语音场景进行需求与背景分析，提出基于透明转发透明转发的支持高轨卫星语音通话的星地融合组网架构，并针对此场景下的专用 QoS 保障、编解码简化、SIP 协议优化、紧急通信等关键问题提出解决方案，最后通过基于海事高轨卫星的实验室与外场测试进行技术方案验证。

2　高轨语音背景分析

高轨道卫星（GEO）移动通信因覆盖区域广、全球可用性等特征广泛应用于应急通信、自然监控、跨国通信等场景。高轨移动通信随着卫星技术发展逐步由传真、消息向话音、卫星电视服务演进，国内外高轨移动通信卫星根据有效载荷技术水平大致以8年为周期分为三代。第一代是以移动卫星通信（MSAT）和Inmarsat-3为代表的采用星上模拟载荷的移动通信卫星，对移动通信支持能力较弱，用户终端多为便携式终端。第二代是以 Thuraya和Inmarsat-4为代表的采用星上数字化载荷的移动通信卫星，星上具备处理交换能力，能够较好地支持手持终端和宽带移动接入。第三代是以TerreStar-1和天地通一号卫（Skyterra-1）为代表的采用地基波束形成技术的移动通信卫星，星上透明转发，能够广泛支持多种移动数据业务。高轨卫星技术在全球范围内一直是卫星通信领域的研究热点，2019年，Yang等人利用全球导航卫星系统（GNSS）

进行高轨卫星的导航和定位，通过测量伪距和多普勒频移，提升了高轨卫星的导航精度 [5]。2020年，Li和Chen提出了一种基于可观测性分析的优化导航滤波方法，大幅减少了高轨卫星的位置信息和速度估计误差 [6]。2021年，Lou等人开发了基于滤波方法的实时多GNSS精密轨道确定方法，提高了卫星轨道预测的精度和可靠性 [7]。2022年，Bo Yang、Fen Hu和Xi Zang提出了地球同步轨道合成孔径雷达（SAR）的概念，使得在各种天气条件下获取高分辨率图像成为可能，增强了高轨卫星的遥感能力[8]。在手机直连高轨卫星的研究方面，Xuan Huang等人提出了在6G架构下基于物联网非地面网络（IoT NTN）的语音服务解决方案，一种是基于OTT平台，采用AHELP语音编码和增强协议以适应IoT NTN的窄带和高延迟特性；另一种是基于改进的IMS，通过优化SIP信令和增强QoS机制，提供端到端的QoS保证 [9]。Starlink计划在2024年首先推出短信和消息服务，这将使用户能够在没有传统蜂窝覆盖的地方发送和接收短信和消息 [10]。

随着5G移动通信技术的成熟与广泛商用，手机直连卫星语音通信也成为高轨移动通信的研究热点。在国内外标准层面上，3GPP Release 17已制定NB-IoT与非地面网络（NB-IoT over NTN）架构与相关技术要求。ITU-T SG13已成立固定、移动、卫星融合（Fixed, mobile and satellite convergence）课题组，推进天地一体IMT-2020网络的需求、架构、网络技术、业务技术研究与标准制定。CCSA成立TC12航天通信技术组对航天通信网络系统与基础电信网络互通互联与融合的相关技术进行研究与标准制定。手机直连高轨卫星语音技术结合了地面移动通信终端接入便捷、业务多样灵活以及高轨卫星通信覆盖范围广、全球可用性强的优点，为远距离通信、紧急通信、偏远地区通信、广播通知、广域监控等场景提供解决方案。

现在高轨语音采用专用终端，用户需要切换终端才能使用卫星服务，并且只能与专用终端用户通话无法与移动、固定网络用户交互。基于NTN的通用手机直连高轨卫星语音技术支持用户采用手机终端直接使用卫星服务与卫星网络、移动网络与固定网络用户通话，但是此技术起步时间较晚、研究资料较少、技术方案欠缺，亟需进行研究。

3 高轨语音解决方案

伴随标准高轨语音技术演进，基于透明转发模式的高轨卫星并与IMS语音通信技术融合，形成高轨语音整体解决方案日益成为高轨卫星通信产业发展的热点和方向。面向手机直连高轨卫星语音通信服务的提供，3GPP在R18增加了GEO卫星支持NB-IoT接入技术，在R20启动高轨卫星支持语音通话研究，在今年6月的TR 22.887中增加了针对高轨卫星接入支持IMS语音通话的需求，重点围绕呼叫建立时间缩短、卫星低码率编解码和通信延时优化等开展分析和研究。

面向上述业务需求，本文提出了基于透明转发GEO卫星和IMS网络的语音通话组网架构（如下图1所

示）。

终端直连透明转发的GEO卫星，使用IoT-NTN空口通过卫星、信关站接入地面IoT-NTN基站，地面IoT-NTN基站使用S1-MME接口连接MME进行接入注册鉴权和移动性管理等处理，使用S1-U接口与SAE-GW相连实现语音信令媒体报文的传递，SAE-GW与SBC相连使用IMS网络提供卫星覆盖终端之间以及卫星覆盖下终端与地面4/5G手机之间的语音通话。

本文针对现有IoT-NTN不支持语音进行了突破，并针对IoT-NTN支持语音面临的带宽速率低(仅有1-2kbps)，时延大(1200字节报文单向传输延迟约10-15s)，以及高轨卫星单波束覆盖面积大(平均约5万平方千米-55万平方千米)等挑战形成解决方案。高轨卫星与手机通信距离远、通信带宽小，为了保障语音服务的实时通信质量，需要对无线进行增强、建立专用的无限载波部署模式、对星地融合网络配置支持语音专属承载的专用QoS保障。为了减小误码率保障语音数据包传输，需增强语音数据发送模型及无线调度方案。为了减小语音服务占用带宽，需要对语音编解码进行简化。为了在高时延环境减少网络内处理时长，需要对SIP协议进行优化。为了保障手机直连卫星下的紧急呼叫服务，紧急通信的呼叫建立、服务质量保障、就近呼叫中心路由等流程都需要打通。

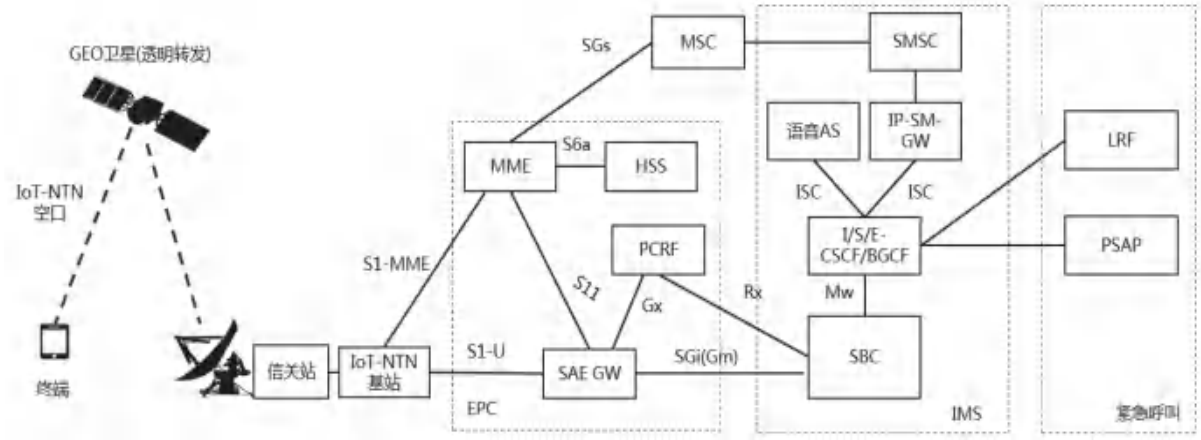

图1 基于透明转发GEO卫星和IMS网络的语音通话组网架构

4 高轨语音关键技术

上述高轨语音解决方案涉及终端、无线和核心网等专业领域，主要包括无线调度增强和IMS SIP信令优化等7大关键技术。

(1) 面向语音的无线特性增强方案

适配语音承载数据进行无线特性增强。基于UP模式，利用IoT-NTN中2个DRB建立2条承载，一条承载传输语音信令，一条承载传输语音媒体数据；面向实时语音中语音媒体数据承载，采用HARQ disable 和

RLC-UM技术，话音媒体数据无需重传，可满足话音传输时延要求；面向实时语音中语音媒体数据承载，其包头（IP+UDP+RTP）共40字节，通过RoHC理论上能压缩至1-3字节。

(2) 语音数据发送模型及无线调度方案

着重保障语音数据包在卫星侧的即时发送与接收。产业初期可考虑先采用大延时拼包方案，后续待标准和产业成熟后可考虑采用小延时拼包方案。大延时拼包方案指大量语音抽样拼包组成一个数据包发送（如采用500ms甚至1s来组成一个数据包），包头开销小，网络调度简单，可以在Anchor或Non-Anchor载波上进行发送；但该方案单向语音时延大，远超过ITU定义的单向语音时延400ms，再叠加核心网时延，有可能出现小对讲现象；目前在进行原型验证。小延时拼包方案单向语音时延小，可接近ITU定义的单向语音时延400ms，能够接近GMR-1性能（天通或海事），譬如可采用80ms，甚至更小，但该方案需要采用专用Non-Anchor语音载波，且需要无线调度增强标准化方案。

(3) 无线载波部署模式

着重关注语音并发用户容量，产业初期可考虑采用混合部署方案，后续待标准和产业成熟可考虑采用语音媒体数据独立载波部署方案。混合部署，即任何一路载波语音信令、语音媒体数据以及窄带数据混合部署。语音媒体数据独立载波部署，即语音媒体数据在non-anchor载波独立部署，可适用于小延时语音数据收发模型。

(4) 语音专属承载

语音专属承载方案旨在为IoT-NTN（物联网-非地面网络）语音通信提供专属的语音信令及语音媒体数据承载。首先，为了确保信令的高可靠性，定义了语音信令专属承载QCI。用户设备（UE）在IMS（IP多媒体子系统）注册前，通过IMS APN（接入点名称）建立PDN（分组数据网络）连接，策略控制与计费规则功能（PCRF）会下发卫星语音信令专属承载QCI。该QCI基于确认模式（AM），具有10^-5的包差错率，资源类型为非保证比特率（Non-GBR），并且具有最高的优先级。在UE成功完成IMS注册后，发起语音通话请求，核心网会为语音媒体资源进行分配，并下发卫星语音媒体数据专属承载QCI。该QCI基于无确认模式（UM），具有10^-2的包差错率，资源类型为保证比特率（GBR），优先级次高。该承载需要启用HARQ（混合自动重传请求）禁用、RLC UM（无线链路控制无确认模式）以及RoHC（鲁棒头压缩）等特性。

通过上述方案，确保了IoT-NTN环境下的语音通信在信令和媒体传输方面均能获得高效、可靠的服务保障。

(5) 低码率语音编解码转换

低码率语音编解码转换方案旨在解决IoT-NTN（物联网-非地面网络）卫星链路低速率场景下的语音码

率适配问题，特别是受限于IoT-NTN链路的承载能力，要求语音编解码速率应低于或等于1.2kbps。在该方案中，当IoT-NTN用户终端发起语音通话请求至核心网时，其会话描述协议（SDP）中会携带IoT-NTN语音编解码信息。核心网在接收到该请求后，若呼叫为IoT-NTN用户呼叫非IoT-NTN用户，将会将SDP中的IoT-NTN语音编解码信息修改为通用语音编解码，并将修改后的请求发送至被叫用户。

在媒体协商完成并建立通话后，核心网会根据协商结果对收到的媒体报文进行编解码转换后转发，从而实现双方的正常通话。相反，当核心网接收到对IoT-NTN用户终端的语音呼叫请求时，会检查该请求的SDP中是否携带IoT-NTN语音编解码信息。若未携带，则核心网会将其SDP修改为携带IoT-NTN语音编解码信息后发送至IoT-NTN用户终端。在媒体协商完成并建立通话后，核心网同样会根据媒体协商结果对收到的媒体报文进行编解码转换并转发，从而保证通话的正常进行。

该方案不仅有效解决了IoT-NTN链路低速率条件下的语音通话问题，同时保证了跨网络通话的兼容性和稳定性。通过低码率语音编解码的应用，不仅满足了IoT-NTN场景中的带宽限制要求，也在保障语音质量的前提下，提升了网络资源的利用效率。

(6) IMS SIP 信令优化简化

IMS SIP信令优化简化方案旨在降低SIP信令开销，减少IoT-NTN通话建立时延，并改善由于星地传输延迟导致的呼叫失败和通信体验差的问题。该方案包括SIP流程简化方案、SIP机制简化优化方案和SIP消息简化优化方案。SIP流程简化主要针对IoT-NTN用户设备（UE）与核心网之间的SIP流程进行优化，保留IMS注册、呼叫和短消息等基础通信流程，以及少量的补充业务流程如前转功能，而删减呼叫等待、呼叫保持、呼叫转移、多方会话、彩铃和彩印等增值业务流程，以减少UE与核心网的交互消息。SIP机制简化优化在保留IP通信路由和SIP/SDP Offer/Answer媒体协商机制的基础上，删减了资源预留、注册订阅通知机制，以及SIP over TCP及TLS等复杂机制；并优化了SIP协议定时器、SESSION TIMER和前传业务定时器的设置，调整定时器时长以适应星地通信的高延迟。SIP消息简化优化针对Gm接口的SIP信令消息方法、消息头域和消息体进行了简化和优化。消息方法方面，保留REGISTER、INVITE、ACK和BYE等基本方法，删减PUBLISH、INFO、REFER、UPDATE和OPTIONS等方法。消息头域方面，仅保留From、To、CALL-ID、CONTACT和VIA等必要头域，并对这些头域进行简写以缩短其长度。消息体方面，不支持多消息体，消息体仅保留SDP和IMS协议中必选的v行和c行，删减e行、k行和p行等不必要行，并优化精简媒体m行和相关a、b行，从而减少消息体长度。此外，为了进一步减少通话建立时间，还可以减小单个IMS消息的大小，例如省略SIP INVITE消息中的“contact”、“Supported”、“Allow”、“Max-forward”等字段，这些字段可以由P-CSCF恢复；跳过不必要的消息，如UPDATE和200(UPDATE)。通过该方案，显著降低了SIP信

令开销，减少了通话建立时延，提升了IoT-NTN环境下的语音通信质量。

IMS SIP消息	原始消息字节（Bytes）	简化消息字节（Bytes）
INVITE	2512	~1000
183	1706	~600
PRACK	1334	删除
200（PRACK）	815	删除
UPDATE	1928	删除
200（UPDATE）	1639	删除
180 RINGING	1046	~500
总大小	10980	~3200

在GEO卫星环境下，语音呼叫设置时间是从呼叫者发送第一个SIP INVITE消息到接收者听到振铃音或忙音的时间段。根据文献，语音呼叫设置时间受到IMS信令消息大小、信令数据速率以及传播时延等因素的影响。例如，在1kbps信令数据速率下，SIP INVITE消息大小为2512字节，整体SIP消息大小为10980字节，传播时延为285毫秒，此时语音呼叫设置时间约为93秒。然而，通过优化IMS消息大小和简化信令流程可以显著降低呼叫设置时间，包括省略SIP INVITE消息中的非必要字段如“contact”、“Supported”、“Allow”、“Max-forward”等，并由P-CSCF在必要时恢复，同时跳过不必要的信令消息如UPDATE和200(UPDATE)。优化后的信令数据速率为4kbps时，原始呼叫设置时间约为32秒，经过上述优化措施后，可减少到10至12秒，这与当前Tiantong GMR-2系统（如华为Mate 60 Pro）采用的类似电路交换呼叫信令的呼叫设置时间相近。这些优化措施包括减小IMS消息大小、跳过不必要的消息以及调整SIP协议定时器，以适应星地通信的高延迟特性，从而显著改善了GEO卫星环境下的语音呼叫设置时间，确保了在高延迟和低数据速率条件下的可靠语音通信。

(7) 卫星紧急呼叫

当IoT-NTN用户拨打紧急呼叫号码发起紧急呼叫时，核心网在收到用户终端发起的紧急呼叫请求后，会向无线网络获取接入网信息。这些信息包括用户终端所在的TA1、ECGI等位置信息。核心网根据这些位置信息确定相应的紧急呼叫中心号码，将被叫号码替换为紧急呼叫中心号码，并将呼叫请求路由到紧急呼叫中心以建立紧急呼叫通话。

为了进一步提升紧急呼叫的可靠性和及时性，基于卫星接入类型进行特别的QoS（服务质量）流区分

尤为关键。不同类型的卫星接入（如GEO、LEO或MEO卫星）由于其轨道高度和覆盖范围的差异，表现出不同的通信延迟和信道质量特性。为了确保紧急呼叫在网络资源紧张时仍能获得优先处理，核心网需要针对紧急呼叫设定更高优先级的QoS流。这一动态调整包括增加带宽、降低延迟和提高数据传输的可靠性，以适应不同卫星接入类型的特性，从而显著减少呼叫建立时延，提高紧急呼叫的成功率。

此外，用户高精度位置获取技术在卫星紧急呼叫服务中至关重要。传统基于小区ID的定位方式只能提供粗略的位置信息，在使用高轨卫星进行紧急呼叫的场景中，由于高轨卫星覆盖范围较广，小区范围较大，无法通过用户所处小区ID得出用户的精确地理位置信息。通过引入先进的定位技术，如全球导航卫星系统（GNSS）和地球观测系统（EOS），可以显著提高定位精度。GNSS利用多个卫星信号进行三角测量，提供高精度的地理位置数据，而EOS通过地面基站增强定位信号的稳定性和准确性，使得用户位置的确定更加精确和可靠。在接收到紧急呼叫请求后，核心网能够迅速整合来自GNSS和EOS的高精度位置信息，与用户终端的接入网信息相结合，进一步提升定位精度，为紧急呼叫中心提供精准的用户位置，从而大幅度提高紧急呼叫场景下的救援效率和成功率。这一综合方案不仅有效解决了IoT-NTN链路低速率条件下的语音通话问题，同时保证了跨网络通话的兼容性和稳定性。

5　高轨语音实验验证

本文基于透明转发模式高轨卫星和中国移动地面移动网络完成手机直连高轨卫星NB-IoT NTN语音功能验证。如下图所示，位于试验卫星波束覆盖下的上海浦东地区IoT-NTN手机终端直连高轨试验卫星，通过位于北京海淀上庄的地面信关站接入地面4/5G融合网络，语音通信信令与数据信息通过地面信关站路由至IoT-NTN基站。IoT-NTN基站通过专线与位于北京移动国际信息港的核心网相连。核心网主要包括用于管理用户接入与会话控制的4/5G融合核心网、提供语音和消息服务的IMS网络以及提供紧急呼叫服务的紧急呼叫中心。

图2. 手机直连高轨卫星NB-IoT NTN语音功能验证组网架构

本次测试验证了 IoT-NTN 增强支持实时语音通信能力具备技术可行性。在试验测试中，试验手机终端采用低于 1.2kbps 低码率语音编码，完成了高轨场景下 IoT-NTN 与 IoT-NTN 用户终端间的实时语音通话，以及 IoT-NTN 用户终端与地面移动通信网络中 VoLTE（Voice over Long-Term Evolution，4G 承载语音）与 VoNR（ Voice over New Radio，5G 承载语音）商用用户终端的实时语音通话，话音清晰流畅，在此基础上进一步验证了号码显示、前转等话音补充业务，同步验证了 IoT-NTN 手机终端支持收发 IMS/NAS 短消息的能力。在关键技术测试中，完成了 HARQ disable 、RLC-UM 和 RoHC 等无线特性增强、面向卫星语音信令及语音媒体数据的专属承载 QoS 保障、基于语音数据收发模型的无线资源调度、基于低码率语音编解码转换、SIP 协议简化优化和卫星紧急呼叫就近路由等关键技术方案测试。

本次测试验证了IoT-NTN手机直连高轨卫星提供语音通话、短消息等基础通信服务的技术可行，下一步将针对IoT-NTN语音通话性能、可靠性和通话质量进行分析优化，具体会从终端连接卫星的稳定性优化、编解码选择、信令优化简化、抗干扰等方面、无线网的调度优化、数据包拼包和专属承载QoS保障等方面、核心网的信令优化简化、语音编解码转换质量优化等方面进行研究。

6 高轨语音挑战和未来方向

虽然基于透明转发的星地融合组网架构项目组已经在海事高轨卫星的实验室与外场成功完成星地语音、短信的业务验证，但高轨语音依然有许多技术挑战与业务方向供业界探索。

在技术挑战上，高频段通信是无线侧正在探讨的技术焦点，NTN 计划在跨越传统的特高频 (UHF) 和超高频 (SHF) 波段的2-4千兆赫 (GHz) 的S波段频率上运行，然而更高的频率可能会影响全球卫星连接的5G服务质量、效率和可靠性，3GPP和ITU正在就解决频谱挑战及其对 NB-IoT 连接的影响进行讨论。空天地融合网络技术是网络演进讨论的焦点，高轨卫星网络与地面物联网、低空物联网、中低轨物联网等网络如何互联互通甚至合并融合。低消耗卫星终端是终端技术讨论的焦点，相比于地面通信卫星通信需要更高的功耗进行星地传输，但对于用户终端以及物联网终端，减少电池供电并支持低功耗运行是增强业务体检的关键。

在业务方向上，云计算依然是DICT产业的核心，基于物联网的高轨语音业务会产生大量数据，如何及时对数据进行收集、分析和存储是亟需解决的问题，构建卫星云在星上进行数据处理、或者构建星地融合云就近选择地面数据中心处理是未来可选择的方向。卫星专网是提高星地融合网络价值的重要方向，面向各类行业企业提供差异化、专业化网络服务是卫星互联网向B段落地的关键途径。卫星网络能力开放是打破网络管道化的关键，如何提炼、封装、编排组合星地网络、话音业务、云计算等各领域的能力是开放运

营商网络的关键。

参考文献：

[1] 汪春霆,翟立君,卢宁宁,等.卫星通信与 5G 融合关键技术与应用[J].国际太空,2018.DOI:CNKI:SUN:GJTK.0.2018-06-005.

[2] Jianyin ZHANG, Lingfei NI, Hanbai WANG, Shangming GU, Yu LIU, Jinglei LIU. Research on the enhancement and key technologies of 5G network for satellite-terrestrial integration[J]. Telecommunications Science, 2024, 40(6): 38-48.

[3] 姜奇平.2022,卫星互联网步入快车道[J].互联网周刊, 2023(1):6-6.

[4] 王健,范静,孙治国.高轨移动通信卫星发展现状与趋势分析[J].卫星应用,2019(11):6.DOI:10.3969/j.issn.1674-9030.2019.11.013.

[5] Mi W , Bo Y , Fen H ,et al.On-Orbit Geometric Calibration Model and Its Applications for High-Resolution Optical Satellite Imagery[J].Remote Sensing, 2014, 6(5):4391-4408.DOI:10.3390/rs6054391.

[6] Xiao Y , Zhou X , Wang J ,et al.Observability Analysis and Navigation Filter Optimization of High-Orbit Satellite Navigation System Based on GNSS[J].Applied Sciences, 2020, 10(21):7513.DOI:10.3390/app10217513.

[7] Lou Y , Dai X , Gong X ,et al.A review of real-time multi-GNSS precise orbit determination based on the filter method[J].Satellite Navigation, 2022, 3(1):1-15.DOI:10.1186/s43020-022-00075-1.

[8] Mi W , Bo Y , Fen H ,et al.On-Orbit Geometric Calibration Model and Its Applications for High-Resolution Optical Satellite Imagery[J].Remote Sensing, 2014, 6(5):4391-4408.DOI:10.3390/rs6054391.

[9] Huang X ,Qi W , Xia X , et al. IoT NTN for Voice Services: Architectures, Protocols, and Challenges[J]. IEEE Network, 2024, 3(20):40-47.DOI: 10.1109/MNET.2024.3379517.

[10] Len Rosen. Starlink Direct To Cell Service: Here's What We Know So Far. Starlink Insider. Retrieved from Starlink Insider[EB/OL].starlinkinsider.com,2022

[作者简介]

张剑寅（1974- ），男，博士，中国移动通信有限公司研究院主任研究员，高级工程师，主要研究方向为星地融合核心网、核心网演进、5G 专网等。

尼凌飞（1978- ），男，硕士，中国移动通信有限公司研究院研究员，高级工程师，主要研究方向为天地一体化网络、核心网演进、网络能力开放等。

于天意（1993- ），女，硕士，中国移动通信有限公司研究院研究员，主要从事星地融合关键技术研究，包括 NR NTN、IOT NTN 协议，高轨卫星语音技术，低轨天地一体融合技术等。

刘昱（1991- ），男，博士，中国移动通信有限公司研究院研究员，主要研究方向为星地融合通信、移动通信、能力开放等。

王汉白（1999- ），男，中国移动通信有限公司研究院研究员，主要研究方向为天地一体化网络、核心网演进等。

程锦霞（1981- ），女，博士，中国移动通信有限公司研究院研究员，高级工程师，CCSA TC13 WG1 副组长、IMT-2020 5G 应用工作组组长，主要研究方向为天地一体化、面向垂直行业的 5G 专网及 5G 工业互联网。

邓伟（1978-），男，硕士，中国移动通信有限公司研究院星地融合技术研究所所长，教授级高工，主要研究星地融合技术，通感一体技术。

星地融合网络支持服务功能的多路径传输机制

范晓静，郑涛，周王健，周华春

（北京交通大学电子信息工程学院，北京 100044）

摘　要：目前，地面用户流量如何接入卫星网络进行传输并在核心网域得到服务支持是亟待解决的问题。本文提出一种支持服务功能的多路径传输机制，该机制利用 DTN-MPTCP 方法将接入流量分割至空间网络与地面网络，基于 SFC 引导流量遍历空间核心网功能。考虑到服务功能多元化，以安全功能链为例，采用并行路径按序遍历卫星功能节点。基于多层卫星 Tr 星座搭建星地融合网络原型系统，实验结果表明，DTN-MPTCP 方法能够有效建立卫星网络与地面网络的连接。模拟包含三种类型应用不同流量比例的场景一和场景二，所提的 DTN-MPTCP 方法相比于 NTN-TCP 方法，能够分别降低 64.9%和 78.4%的时延、64.9%和 78.4%的丢包率，同时提升 14.1%和 5.7%的流完成度。在空间核心网中，相比于基准路径，SFC 并行传输方法能够降低 10.5%的总资源开销。

关键词：星地融合网络；多路径传输；DTN；卫星接入网关

Multipath Transmission Mechanism Supporting Service Functions in Integrated Space-Ground Networks

Xiaojing Fan, Tao Zheng, Wangjian Zhou, Huachun Zhou

(School of Electronic and Information Engineering, Beijing Jiaotong University, Beijing 100044, China)

Abstract: Currently, a critical challenge is determining how terrestrial user traffic can access satellite networks for transmission and receive service support within the core network domain. This paper proposes a multipath transmission mechanism that supports service functions by leveraging the DTN-MPTCP approach, which segments incoming traffic between space and terrestrial networks. Traffic is then guided through the space core network functions based on service function chains. Considering the diversity of service functions, the mechanism utilizes parallel paths to sequentially traverse satellite function nodes, using a security function chain as an example. A prototype system of an integrated space-ground network was built based on Tr constellation. Experimental results demonstrate that the DTN-MPTCP method effectively establishes connections between satellite and terrestrial networks. In both scenario one and scenario two, the proposed DTN-MPTCP method reduces latency by 64.9% and 78.4%, packet loss by 64.9% and 78.4%, and increases flow completion by 14.1% and 5.7% compared to the NTN-TCP method. Additionally, within the space core network, the SFC parallel transmission method reduces total resource consumption by 10.5% compared to the baseline path.

Key words: integrated space-ground network, multipath transmission, DTN, satellite access gateway

基金项目：国家自然科学基金资助项目（No. 62341102）；国家重点研发计划资助项目（No. 2018YFA0701604）
Foundation Items: The National Natural Science Foundation of China (No. 62341102); The National Key Research and Development Program（No. 2018YFA0701604）

1 引言

星地融合网络是 6G 的标志性发展方向，3GPP Release 17 明确提出将卫星通信作为地面网络的必要补充[1]。如何有效地将地面用户流量接入卫星网络进行传输，并在核心网域得到服务支持，成为亟待解决的问题。回顾 3GPP（3rd Generation Partnership Project，第三代合作伙伴计划）标准的发展历史以寻求该问题的解决方案。Release 15 建议使用非 3GPP 接入方式替代传统的 3GPP 接入。随后在 Release 16 中，引入 ATSSS（Access Traffic Steering-Switching-Splitting，接入流量引导-切换-分割）作为可选项[2]，支持 MPTCP（Multipath Transmission Control Protocol，多路径传输控制协议）作为 ATSSS 功能的关键组件之一，使多端口设备能够同时使用 3GPP 和非 3GPP 接入[3]。在星地融合网络中，地面卫星网关始终处于多颗卫星的覆盖范围内，可同时与多颗接入卫星建立连接，实现地面网络与空间网络的无缝集成，从而引导流量进入空间网络。

3GPP NTN（Non-Terrestrial Network，非地面网络）支持透明转发和星上再生两种架构模式，核心网方案分为无状态和有状态两大类。无状态方案中，UE（User Equipment，用户设备）存储与会话相关的状态，卫星仅执行数据转发功能[4]。有状态方案通过隧道建立会话，使用卫星集群内和集群间切换程序应对切换问题[5]。透明转发架构虽然有利于快速商业化，但在空间网络资源的灵活调度方面存在一定局限性。SDN（Software Defined Network，软件定义网络）和 NFV（Network Functions Virtualization，网络功能虚拟化）技术使服务和资源编排变得灵活。网络服务以功能链的形式提供，用户可以根据需求申请任意网络服务功能的组合，形成一个综合的集成服务。

目前在星地融合网络接入和核心网功能方面的主要研究有：SaT5G 将卫星作为一种新的接入方式，基于 ATSSS 功能组件将卫星无缝连接集成到地面网络，确保无处不在的 5G 接入[6]。文献[7]首次在 NS-2 中模拟低轨卫星网络以讨论 MPTCP 的可行性，提出一种支持多路径传输的路由方法。文献[8]针对动态 LEO（Low Earth Orbit，近地轨道）卫星网络中的服务功能链编排，提供一种低复杂度的启发式算法，以最大化服务接受度和负载公平性。文献[9]通过收集服务请求和相关的服务质量约束，实现服务编排功能，但该方案适用于准静态场景。上述研究在卫星网络接入和管理方面做出了重要贡献，但他们只关注接入网或核心网单一部分，多路径技术在 ATSSS 中的应用主要集中在地面域，空间多路径 VNF（Virtual Network Function，虚拟网络功能）的研究聚焦于服务功能编排优化问题，且缺少原型系统验证方法的实用性。

在本文，我们从星地融合网络的接入传输到核心网功能部署给出整套解决方案，提出一种支持服务功能的多路径传输机制。基于 ATSSS 功能组件研制多路径卫星接入网关，采用 DTN-MPTCP 方法引导流量接入。多种业务流量以 MPTCP 子流的形式被分割到地面和卫星网络，分割到地面域的流量被路由至不同的链路传输，分割到卫星网络的流量基于 DTN（Delay-Tolerant Network，时延容忍网络）[10]协议栈传输。在空间核心网域，使用虚拟化技术将计算、存储、感知、安全等功能组件以 SFC（Service Function Chain，服务功能链）的形式进行部署，基于 SFC 引导流量按需有序地经过功能节点。本文与上述研究的不同之处：

我们综合考虑了卫星接入和核心网服务部署问题，将卫星与地面基础设施均作为接入方式，流量并行引导至空间域和地面域。在空间核心网域，流量从一个网络功能通过多条路径到达另一个网络功能。此外，我们还搭建了原型系统并进行实验来验证所提方案。

2 研究方案的设计与实现

在本节，我们概述星地融合网络支持服务功能的多路径传输方案。其中，多路径卫星接入网关和空间域服务功能部署是核心内容。我们使用 DTN-MPTCP 方法将流量分割至空间域与地面域，在空间域，基于 SFC 引导流量按序遍历卫星功能节点。由于 MPTCP 在地面网络中的成熟研究和 DTN 对硬件要求较低，DTN-MPTCP 方法在兼容性和设备需求上具有明显优势。

2.1 总体方案

星地融合网络支持服务功能的多路径传输框架如图 1 所示，包含 MP SAG（Multipath Satellite Access Gateway，多路径卫星接入网关）、TCN（Terrestrial Core Network，地面核心网）和 SCN（Space Core Network，空间核心网）。MP SAG 实现卫星网络与地面网络的互联互通，采用 3GPP ATSSS 支持的 MPTCP 功能组件将卫星集成到地面网络。TCN 基于路由转发规则引导流量，SCN 基于 SFC 引导流量按需有序经过卫星服务功能。其中，使用卫星接入网关实现的多路径与空间核心网控制组件下发的路径策略可独立运行。

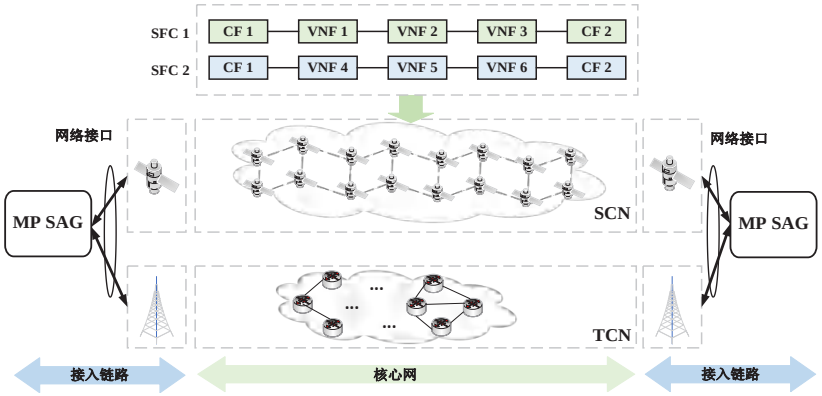

图 1 支持服务功能的多路径传输框架

MP SAG 聚合地面路由器和空间协议转换网关双功能，提供地面网络与卫星网络之间的接口，实现 TCP/IP 协议栈和 DTN 协议栈的转换。来自用户终端的流量经 MP SAG 使用 DTN-MPTCP 方法传输，一部分流量以多路径方式走空间网络，一部分流量以多路径方式走地面网络。MP SAG 能够实时感知每条子流的往返时延、丢包率等链路质量信息。这些实时感知能力使 MPTCP 能够在动态多路径环境中智能地分配和调度业务流量，最大化传输性能并减少延迟和数据丢失。当地面网络质量较差或中断时，MP SAG 会将业务流量调度到卫星网络传输，反之，则通过地面互联网传输。SCN 的控制组件下发路径策略，对于单一 SFP（Service Function Path，服务功能路径），用户流量以串行顺序从一个 VNF 经过多条路径到达另一个 VNF。对于并行服务路径，用户流量以并行顺序从一个 VNF 经过多条路径到达另一个 VNF。控制组件包含四种路径策略，分别是基准路径、SFC1、SFC2 和 SFC 并行路径。TCN 用户流量经由 DTN-MPTCP 将

一部分流量引导至地面网络，按照路由转发规则到达接收端 MP SAG。

2.2　多路径卫星接入网关

A.　MP SAG 结构

MP SAG 结构如图 2 所示。BP（Bundle Protocol，Bundle 协议）[11]使用一个或多个 EID（Endpoint Identifier，端点标识符）表示 DTN 网络中的实体[12]。地面 MPTCP 用户终端向 MP SAG 发送包含源 IP 和目的 IP 的数据包。MP SAG 将流量分成两部分，一部分从 a 口转发至地面互联网，另一部分进入空间网络。对于进入空间域的流量，MP SAG 首先提取目的 IP 地址，在 IP 与 EID 映射表中查找对应的下一跳卫星节点。然后，提取应用层数据，重新封装为 Bundle 报文，从 b 口将数据转发至下一跳卫星节点。为适应星地融合网络的协议环境，IP 数据包在入口卫星网关处作为 DTN 数据包的有效载荷，通过空间隧道传输。图 2 中的 mapping 指的是 IP 地址与 EID 之间的解析关系，此时网络层的路由功能简化，数据直接转发到与 EID 解析绑定的下一跳 IP 地址的卫星节点。

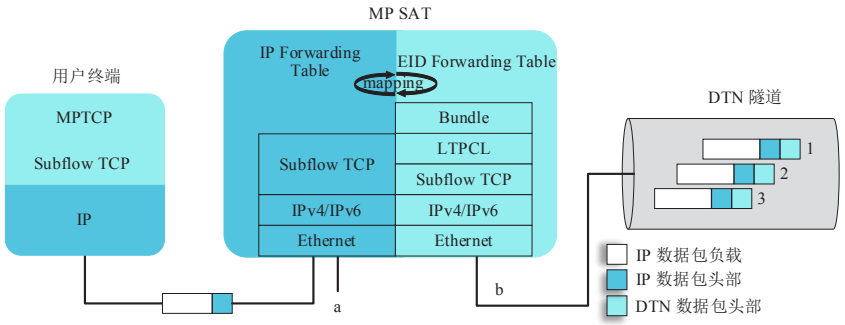

图 2　多路径卫星接入网关结构图

B.　工作模式

MP SAG 适用于地面网络、非地面网络和星地融合网络，支持四种工作模式，如表 1 所示。四种模式分别为地面网络 TCP 传输（TN-TCP）、地面网络 MPTCP 传输（TN-MPTCP）、空间网络 TCP 传输（NTN-TCP）和星地融合网络 MPTCP 传输（DTN-MPTCP）。在 TN-TCP 模式下，MPTCP 未开启，数据通过 a 口传输；在 TN-MPTCP 模式下，开启 MPTCP，数据通过 a 口传输；在 NTN-TCP 模式下，MPTCP 未开启，数据通过 b 口传输；在 DTN-MPTCP 模式下，开启 MPTCP，数据通过 a 口和 b 口同时传输。

表 1　MP SAG工作模式

工作模式	MPTCP	路径数量	逻辑接口	作用域
TN-TCP	关闭	单条	a	地面网络
TN-MPTCP	开启	多条	a	地面网络
NTN-TCP	关闭	单条	b	空间网络
DTN-MPTCP	开启	多条	a&b	地面&空间网络

C.　DTN-MPTCP 算法

基于 DTN-MPTCP 方法实现地面网络与卫星网络的集成，实现过程如算法 1 所示。基于 BP 协议建立 IP 数据包传输隧道，ION-DTN 提供 API 实现 BP 协议栈功能。通过创建和配置 TUN 设备，从用户空间读

取和写入 IP 数据包，并利用 BP 协议在 DTN 网络中进行数据传输。子进程负责从 TUN 设备读取 IP 数据包，通过 BP 协议发送到至目的 EID。父进程负责从本地接收端接收 BP 协议数据包，将其解封为 IP 数据包，并通过 TUN 设备发送到本地网络。从而实现 IP 数据在 DTN 网络中的传输。

算法中的 ***BpArg*** 结构体用于配置 DTN，包含 TUN 接口文件描述符、本地 DTN 节点的 EID、目的 DTN 节点的 EID、服务接入点 SAP、存储数据参考 SDR 等。***Role*** 用于标识实例的角色（客户端或服务器端）。***TUN_device*** 则指代用于读取和写入 IP 数据包的 TUN 接口设备。MP SAG 的 a 口对应代码中的“*a_port*”。而 b 口则是 TUN 接口的数据出口。TUN 接口负责将数据包封装，并通过 DTN 隧道发送给目的空间节点，此传输路径通过“*b_port*”进行的。

Algorithm 1: DTN-MPTCP

Input: *BpArg structure, role, TUN_device*
Output: *None*

```
1: function ipOverDtn(arg)
2:     Initialize buffer, BpSAP, Sdr, and other variables from arg
3:     while true do
4:         ip_packet ← read(TUN_device)   //从 TUN 设备读取 IP 数据包
5:         tunnel_bpsend(ip_packet)   //使用 DTN 隧道发送 IP 数据包
6:     end while
7:     return
8: end function

9: function ipOutDtn(arg)
10:    while state.running do
11:        register_signal_handler(SIGINT)
12:        delivery_result ← bp_receive()   //接收 DTN 数据包并返回接收结果
13:        if delivery_result = BpPayloadPresent then   //如果接收到有效负载
14:            start_sdr_transaction()   //开始 SDR 处理
15:            buffer ← receive_ZCO_data(get_payload_length(ZCO))   //接收 ZCO 数据并存储到缓冲区
16:            end_sdr_transaction()
17:            send2DataLink(buffer)   //将缓冲区数据发送到数据链路层
18:        end if
19:        bp_release_delivery()   //释放接收到的 DTN 数据包
20:    end while
21:    return
22: end function

23: if role = "client" then
24:    thread_dtn ← create_thread(ipOverDtn, BpArg_structure)   //创建并启动 ipOverDtn 线程
25: else if role = "server" then
26:    thread_dtn ← create_thread(ipOutDtn, BpArg_structure)
27: end if
28: mptcp_socket ← create_mptcp_socket()   //创建 MPTCP 套接字
29: add_subflow_to_mptcp(mptcp_socket, a_port)
30: add_subflow_to_mptcp(mptcp_socket, b_port)
```

2.3　空间服务功能部署

在空间核心网域，用户流量通过 SFC 进行引导和拆分，按序遍历各个服务功能组件。图 3 展示了空间核心网域服务功能的部署方案，发送方和接收方主机通过 MP SAG 进入空间服务功能域。卫星转发节点内部署服务功能组件，负责用户流量数据的路由、存储、计算、感知等功能。高轨控制器向转发节点下发路径策略，转发节点接收路径策略并对流量进行服务功能模块组合。本文在图 3 中选用计算、安全和存储功能作为服务功能示意。LEO 层卫星链路切换频繁，可见时间短，因此将多元化服务功能组件部署在 MEO（Medium Earth Orbit，中地球轨道）节点，将控制组件部署在 GEO（Geosynchronous Earth Orbit，地球同步轨道）节点。

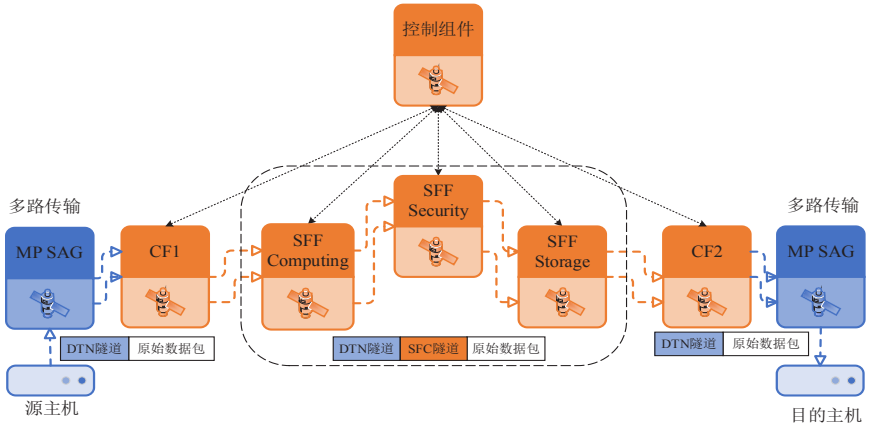

图 3　SCN服务功能部署

A.　服务功能组件

服务功能组件对应图 3　SCN 服务功能部署的 SFF（Service Function Forwarder，服务功能转发器）卫星节点。3GPP 对 NTN 环境提出了与地面互联网相同的安全性要求[13]，我们通过在空间环境部署安全功能组件，构建入侵检测系统来抵御 DDoS（Distributed Denial of Service，分布式拒绝服务）攻击。使用 Open vSwitc[14]作为服务功能链的分类器和转发器，实现流量沿服务路径的转发。服务功能组件通过 Docker[15]实现虚拟化部署。转发脚本将进入 SFF 的流量根据预定义的规则转发到相应的功能组件。基于 Docker 实现反射型 DDoS 攻击检测模块、网络层 DDoS 攻击检测模块、低速率 DDoS 攻击检测模块、应用层 DDoS 攻击检测模块、僵尸网络检测模块和防火墙模块。其中，各类型 DDoS 检测模块基于智能化检测算法保证正常流量的转发，同时拦截对应类型的恶意流量。

卫星节点接收到数据包后，去除 DTN 首部，接着 SFC 代理接收并解析数据包，去除 NSH（Network Service Header，网络服务头），将原始数据包发送至安全功能组件。SFC 代理根据路径判断流量是否进入该 VNF，若进入，则将数据包 NSH 首部中的 SI（Service Index，服务索引）减 1，并将数据包封装发送至 SFF。

B.　控制器组件

使用 Opendaylight[16]作为功能链控制器，部署在 GEO 卫星。Opendaylight 使用 RESTful API 作为北

向接口，配置服务功能组件的类型和 IP、绑定服务功能和转发器、配置服务功能链路径和获取服务功能链路信息，通过 HTTP 请求和响应进行通信。控制器使用 Openflow 协议作为南向接口，向分类器和转发器下发流表并配置路径。其中，控制组件包含四种 SFP 策略：基准路径、SFC1、SFC2 和 SFC 并行路径。如图 4 所示。基准路径是本文的参考路径，确保所有流量依次经过所有类型的安全功能模块。SFC1 针对反射型 DDoS 和低速率 DDoS 攻击检测场景。SFC2 针对网络层 DDoS 和僵尸网络 DDoS 攻击检测场景。SFC 并行路径将流量分流到不同路径上，该策略使系统可以同时应对所有类型攻击。通过流表的 NSP（Network Service Path，网络服务路径）项区分 SFP。

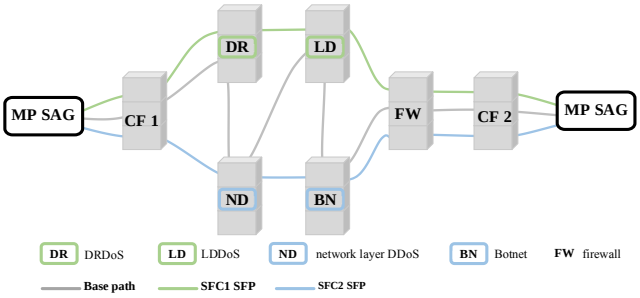

（a）单一路径 single service function path

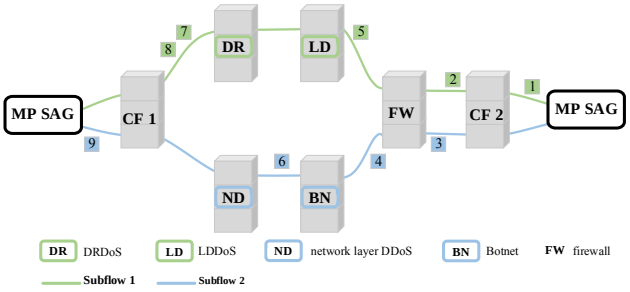

（b）SFC并行路径

图 4 SCN路径策略

3 实验

为验证本文方法并评估其性能，我们基于 Tr 星座[17]搭建 Linux 原型系统。在本节，我们首先描述原型实现，然后定义性能指标，接着通过实验验证本文方案的可行性和原型系统的功能。

3.1 原型系统搭建

表 2 三层卫星星座参数

卫星	轨道高度/公里	运行周期/小时	卫星数量	轨道倾角/°
GEO 卫星	36000	24	1×3	0
MEO 卫星	10390	6	2×5	45
LEO 卫星	895.5	12/7	6×11	90

卫星网络业务类型多样，流量巨大，当网络负载较高时，三层星座的高带宽、多路径、高可靠性等性能优于单层星座，因此选择 LEO/MEO/GEO 三层 Tr 星座模型。星座参数如表 2 所示。采用 ION[18]（Interplanetary Overlay Network）作为 DTN 网络协议栈的一种实现应用。使用 STK（Satellite Tool Kit）[19]

对多层卫星网络建模输出星历信息。经由 Matlab 处理得到一系列由单位时间静态拓扑组成的有序快照集合。依照快照信息配置卫星节点的邻居机制、传输协议引擎参数、转发方案、LTP 参数和接触计划等信息，生成卫星节点管理文件，实现卫星节点配置。

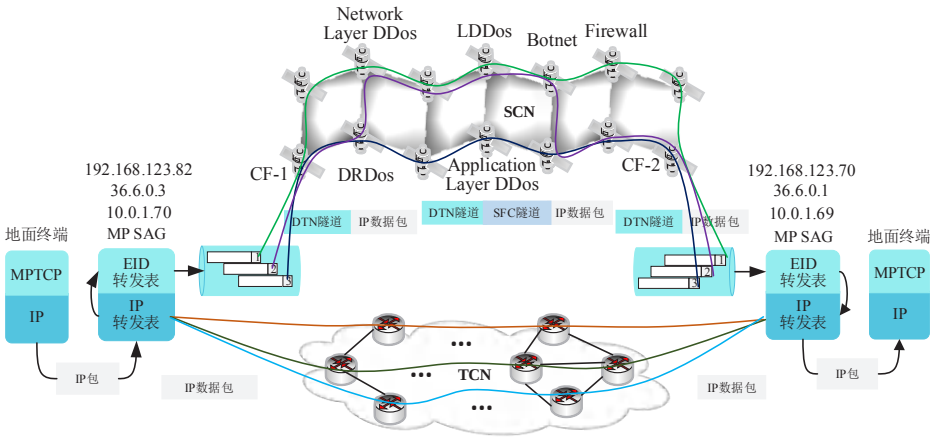

图 5　网络拓扑图

实验网络拓扑如图 5所示，实验参数如表 3所示。卫星接入网关基于linux 4.4.88内核、MPTCP v0.92实现DTN-MPTCP算法部署，采用fullmesh模式进行路径管理。使用Open vSwitch交换机和OpenDaylight控制器搭建服务功能链。使用Docker在部分MEO节点实现功能模块的虚拟化部署。其中，入口分类器和出口分类器分别部署在MEO-4和MEO-7卫星节点。DRDoS攻击检测模块和网络层DDoS攻击检测模块部署在MEO-10卫星节点。LDDoS攻击检测模块、应用层DDoS攻击检测模块和僵尸网络检测模块部署在MEO-6卫星。防火墙模块部署在MEO-9卫星节点。在地面节点模拟包含时敏应用、高吞吐量应用和尽力而为应用三种类型的持续on-off流量[20]，流量开关时间决定任意两个独立流之间的平均突发和空闲时间，均遵循帕累托分布。模拟场景一和场景二中三种类型应用的流量比例分别为{20%，30%，50%}、{30%，55%，15%}[21]。

表 3　实验参数设置

参数变量名称	数值
流量形状参数与尺度参数	1.5ms，500ms
通信时间	600ms
场景一、二流量比例	{20%，30%，50%}、{30%，55%，15%}
MPTCP 子流数量	3
业务流数量	120
调整系数	30
资源开销权重系数	1
单位带宽资源开销	1

3.2　性能指标

本文采用吞吐量、平均时延、丢包率、流完成度和总资源开销作为性能指标。

平均时延是所有成功传输的数据包的时延总和与数据包总数的比值，表示为式（1）：

$$\overline{AD}=\sum_{j=1}^{N_p}\sum_{k=1}^{f_j}\sum_{r=1}^{p_k}d_k\zeta_r \Big/ \sum_{j=1}^{N_p}\sum_{k=1}^{f_j}\sum_{r=1}^{p_k}\zeta_r \tag{式（1）}$$

平均丢包率是丢包数量与总数据包数量的比值，表示为式（2）：

$$\overline{APL}=1-\sum_{j=1}^{N_p}\sum_{k=1}^{f_j}\sum_{r=1}^{p_k}\zeta_r \Big/ \sum_{j=1}^{N_p}\sum_{k=1}^{f_j}p_k \tag{式（2）}$$

平均流完成度是成功传输的流数量与流总数的比值，表示为式（3）：

$$\overline{AFR}=1-\sum_{j=1}^{N_p}\sum_{k=1}^{f_j}\varpi_k \Big/ \sum_{j=1}^{N_p}f_j \tag{式（3）}$$

SFC 总资源开销定义为总节点计算资源开销与总链路带宽资源开销之和，表示为式（4）：

$$C=\psi_1\cdot C_{com}+\psi_2\cdot C_{ban} \tag{式（4）}$$

计算资源开销 C_{com} 包含实例化计算资源开销和运行资源开销，表示为式（5）：

$$C_{com}=\rho_{com}\cdot\Big(\sum_{v\in V}\sum_{n\in N}k_v\cdot w_n^v+\sum_{r\in R}\sum_{v_i^r\in V_r}\sum_{n\in N}\delta_{v_i^r}\cdot y_n^{v_i^r}\Big) \tag{式（5）}$$

链路带宽资源开销 C_{ban} 是链路用于传输业务流所需的带宽资源，表示为式（6）：

$$C_{ban}=\rho_{ban}\cdot\sum_{r\in R}\sum_{h_j^r\in H_r}\sum_{e_{m,n}\in E}f_{h_j^r}\cdot z_{e_{m,n}}^{h_j^r} \tag{式（6）}$$

设置单位计算资源开销 ρ_{com} 与两点间最小跳数平均值 π^{hop} 成正比，即 $\rho_{com}=\zeta_p\cdot\pi^{hop}$。其中，$\zeta_p$ 为调整系数。π^{hop} 由式（7）计算得出，π_{mn}^{hop} 表示网络中节点 m 和节点 n 之间的最小跳数。

$$\pi^{hop}=\frac{1}{|N|^2-|N|}\cdot\sum_{m\in N}\sum_{n\in N,n\neq m}\pi_{mn}^{hop} \tag{式（7）}$$

3.3 实验与分析

A. 星地融合网络多路径实验

MP SAG 实现融合网络空间域与地面域的多路并行传输。TCP 与 MPTCP 吞吐量性能如图 6 所示。MPTCP 由三条路径聚合形成，吞吐量均值由 100s 内的实时数据计算得到。图 6 显示 TN-TCP、TN-MPTCP、NTN-TCP 和 DTN-MPTCP 的吞吐量分别在 1.705 Gbit/s、7.111 Gbit/s、0.895 Gbit/s 和 5.781 Gbit/s 上下浮动。吞吐量均值依次为 NTN-TCP < TN-TCP < DTN-MPTCP < TN-MPTCP，其中 DTN-MPTCP 为 NTN-TCP 的 6.5 倍。在地面网络中，多路径传输的吞吐量显著高于单路径。然而，在空间网络中，多路径传输虽然优于 NTN 单路径，但效果不及 TN-MPTCP，且吞吐量波动较大，主要由于卫星链路不稳定导致数据包丢失

和重传增多。

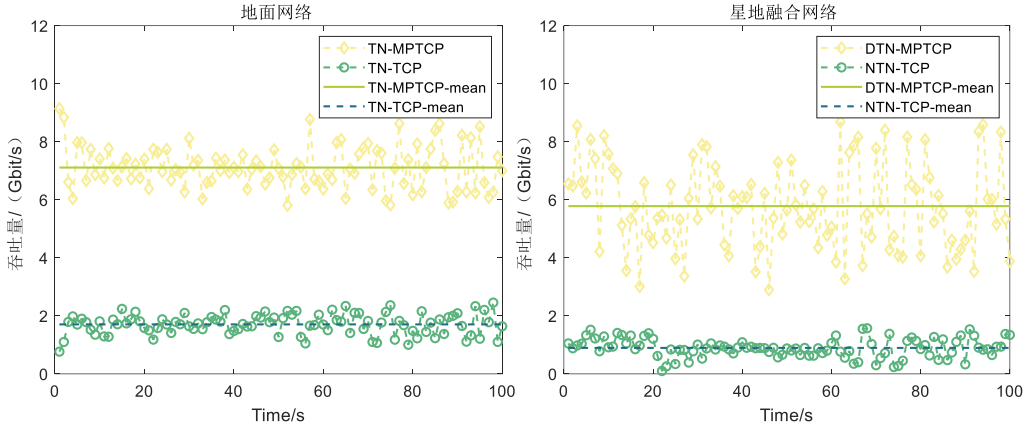

图 6　星地融合网络单/多路径吞吐量

B.　基于服务类型的传输实验

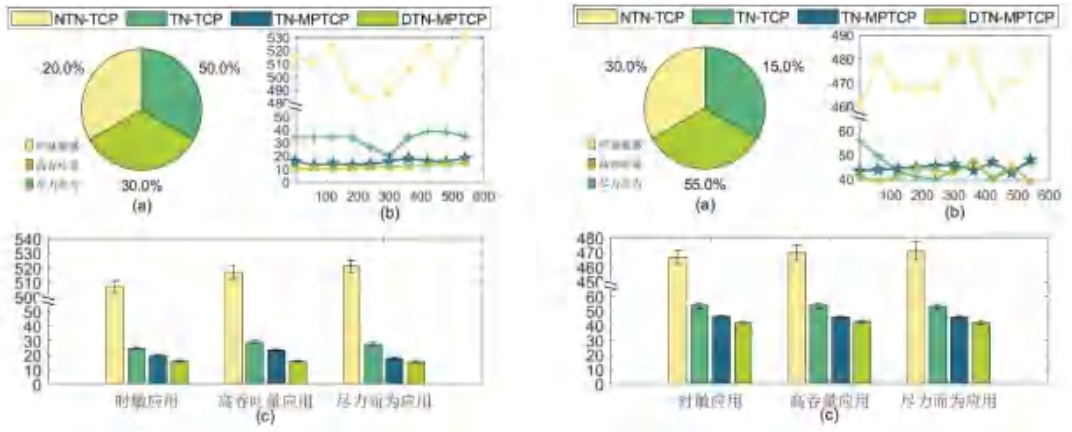

图 7　场景一、二每种应用的端到端时延

（a）表示场景一、二业务流量比例；（b）表示时敏应用在整个通信周期内的平均时延；（c）表示每种业务流量使用不同传输方案的端到端时延。

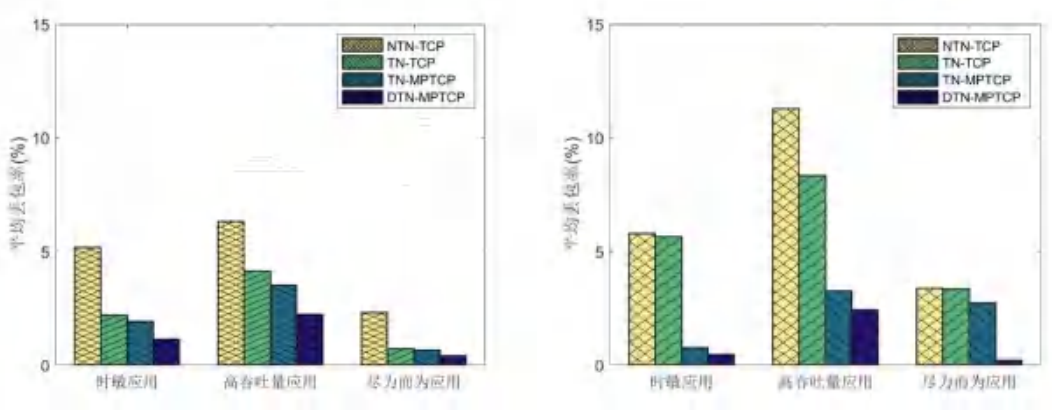

图 8　场景一、二每种应用的平均丢包率

图 7 展示了四种传输方法在不同业务应用下的时延性能。实验结果显示，DTN-MPTCP 方法在时敏应用中的平均时延性能最优。与 NTN-TCP、TN-TCP 和 TN-MPTCP 方法相比，DTN-MPTCP 在两种场景下

分别降低了 96.8%、36.2%、20.6%和 91.0%、21.3%、8.3%的平均时延。DTN-MPTCP 通过聚合面的多路径优势，实现了最优的时延性能。对比图 7 左右两幅图可知，改变应用流量比例对 DTN 的时延性能影响不大。

图 8显示了四种传输方法在不同业务应用下的丢包率性能。结果表明，DTN-MPTCP在高吞中的丢包率最低。与NTN-TCP、TN-TCP和TN-MPTCP相比，DTN-MPTCP在两种场景下的丢包率了64.9%、46.3%、36.7%和78.4%、70.7%、25.3%。DTN-MPTCP利用空间和地面多路径的优势，应对链路切换和拥塞问题，实现最优的丢包率性能。即使在场景二中高吞吐量应用流量增加，DTN 仍能显著降低丢包率。

图 9 表明 DTN-MPTCP 方法可以提升三种应用的平均流完成度。在场景二中，DTN-MPT NTN-TCP 和 TN-TCP 分别提升了 14.1%、16.8%、19.6%和 5.7%、13.9%、14.0%的流完成度；相比 TN- 提升了 2.3%、10.1%、7.9%。即使在尽力而为应用比例减少至 15%时，DTN-MPTCP 仍能保持较 成度。三种应用的流量特性不同导致平均流完成度不同。DTN-MPTCP 方法通过使用最大数量的 时敏应用数据的传输时延，通过占用多条链路带宽满足高吞吐量应用的高带宽需求。尽力而为应 和时延的要求最低，在网络资源有限的情况下被优先忽略，导致平均流完成度最低。

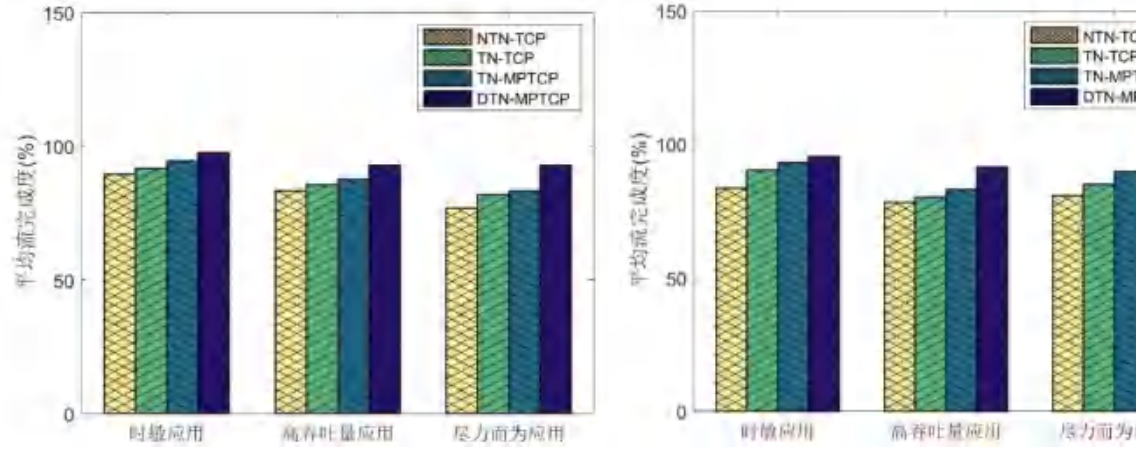

图 9 场景一、二每种应用的平均流完成度

C. 空间服务功能部署实验

针对不同源 IP（36.6.0.2 和 36.6.0.3）的服务请求，数据包在空间域经过不同的 SFC。如图 10 所示，NSP=45 和 NSP=58 分别表示 SFC1 和 SFC2，两条路径的 SI 在经过 DRDoS 和网络层 DDoS 检测模块后数值减 1。实验使用正常流量，故检测模块前后数据包数量相同。在功能节点 Docker 中，去掉 NSH 头部后解析源 IP 和目的 IP。

对比流量通过不同安全服务功能路径的端到端时延。如图 11 所示，基准路径的平均时延为 7.22s，SFC1 的平均时延为 4.63s，SFC2 的平均时延为 4.90s，SFC1 较基准路径平均时延下降 35.87%，SFC2 较基准路径平均时延下降 32.13%。由于空间环境链路特性，导致 SFP 端到端时延均处于秒钟级别。

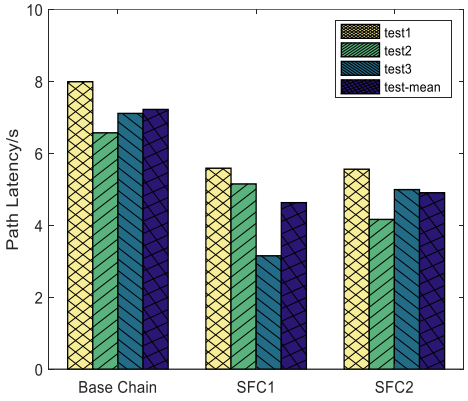

图 11　服务功能路径时延对比

为比较功能路径的网络资源开销，设置场景二业务流总数为 $r=120$。图 12 展示了 SFC 域内四种 SFP 运行状态下的节点计算资源和带宽资源开销。相较基准路径 MEO-10 和 MEO-6 两节点运行状态下的计算资源开销，SFC1 分别减少 58.3%和 53.8%，SFC2 分别减少 45.0%和 37.1%，SFC 并行路径分别减少 33.7%和 26.1%。这是因为 MEO-10 节点和 MEO-6 节点均包含两种虚拟功能，SFC1 路径和 SFC2 路径在每个卫星节点只消耗一个虚拟功能的开销，SFC 并行路径不涉及卫星节点内部虚拟功能之间转发处理的开销。对于带宽资源开销，除控制器外，SFC 并行路径节点所需带宽明显高于 SFC 基准路径、SFC1 和 SFC2，带宽消耗集中在 MEO-10、MEO-6 和 MEO-9 三个卫星功能节点。因此，当功能节点处理业务流时，SFC 并行路径方案能明显降低计算资源开销，但需消耗更多的带宽资源。

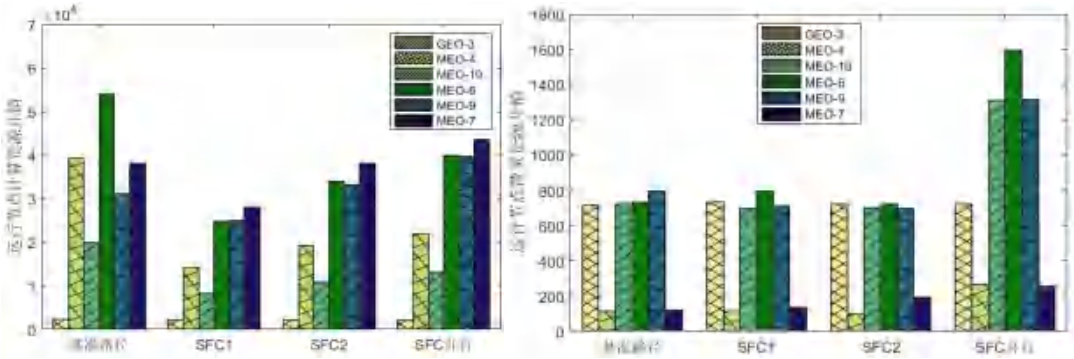

图 12　节点运行计算与带宽资源开销（$r=120$）

图 13 展示了四种 SFP 经过 SFC 域的总资源开销。SFC 并行机制在保证业务流经过所有服务功能的情

况下，在节省网络总资源开销方面表现最佳，能够降低 10.5%的总资源开销。在分类器开销、功能节点开销、控制器与收发节点开销、带宽开销四种资源开销中，功能节点开销占比最大，在四种路径方案中的比例分别为 51.4%、44.3%、46.9%和 46.3%。其中，基准路径和 SFC 并行路径是五种服务功能的开销、SFC1 和 SFC2 是三种服务功能的开销。因此，空间域 SFC 并行机制能明显降低功能节点开销在总资源开销中的占比，优化服务功能节点部署对星上资源受限的空间域网络意义重大。

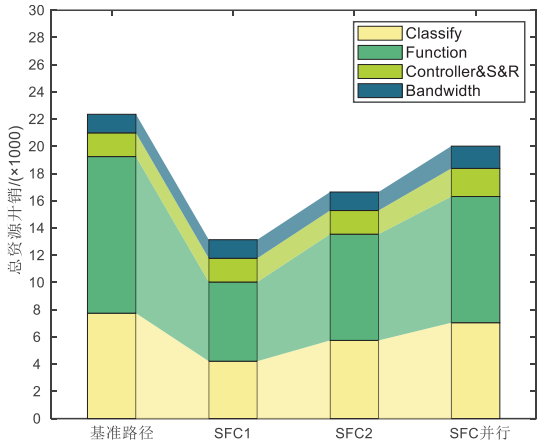

图 13　SFC域总资源开销（$r=120$）

4　结束语

在本文，我们提出一种支持服务功能的多路径传输机制。该机制使用 DTN-MPTCP 方法将接入流量分割至空间核心网与地面核心网，使用 SFC 引导流量遍历空间核心网功能。基于不同类型的业务流量，分析 DTN-MPTCP 方法的端到端时延、丢包率和平均流完成度性能。在空间域以安全服务功能为例，部署 SFC 并行传输机制，旨在降低路径时延和资源开销。最后，搭建星地融合网络原型系统，投放两种不同比例的业务流量进行性能测试。实验结果表明，DTN-MPTCP 方法能够有效实现空间网络与地面网络的连通。场景一和场景二中，相比于 NTN-TCP 方法，所提的 DTN-MPTCP 方法可以分别降低 64.9%和 78.4%的时延、降低 64.9%和 78.4%的丢包率、提升 14.1%和 5.7%的流完成度。在空间域网络中，相比于基准路径，SFC 并行传输机制能够降低 10.5%的总资源开销。本文验证了所提方法的实用性，未来将进一步研究空间域多元化服务功能部署问题，基于业务需求选择多条功能路径，以最小化时延、丢包率等链路属性作为优化目标，采用人工智能算法实现业务流量的多路径分割，进一步提高星地融合网络的智能化水平。

参考文献

[1] 3GPP, TR 28.808: Technical Specification Group Services and System Aspects Study on management and orchestration aspects of integrated satellite components in a 5G network[S]. 2021.

[2] 3GPP, TS 23.501：System Architecture for the 5G System[S]. 2020.

[3] Tessares 5G ATSSS. [EB/OL]. https://www.tessares.net/solutions/5g-atsss-solution.

[4] Li Y, Li H, Liu W, et al. A case for stateless mobile core network functions in space[C]//Proceedings of the ACM SIGCOMM 2022 Conference. 2022: 298-313.

[5] 王尚广,王超,马骁,等.星载 6G 核心网架构与网元功能设计及验证[J/OL].电信科学,1-19[2024-08-18].http://kns.cnki.net/kcms/detail/11.2103.TN.20240702.1811.005.html.

[6] SaT5G, Multi-link and Heterogeneous Transport - Analysis, Design and Proof of Concepts, Satellite and Terrestrial Network for 5G, May 2020.

[7] Du P, Li X, Lu Y, et al. Multipath TCP over LEO satellite networks[C]//2015 International Wireless Communications and Mobile Computing Conference (IWCMC). IEEE, 2015: 1-6.

[8] He J, Cheng N, Yin Z, et al. Service-Oriented Resource Allocation in SDN Enabled LEO Satellite Networks[C]//2023 IEEE 34th Annual International Symposium on Personal, Indoor and Mobile Radio Communications (PIMRC). IEEE, 2023: 1-6.

[9] Petrosino A, Piro G, Grieco L A, et al. On the optimal deployment of virtual network functions in non-terrestrial segments[J]. IEEE Transactions on Network and Service Management, 2023, 20(4): 4831-4845.

[10] Cerf V, Burleigh S, Hooke A, et al. Delay-tolerant networking architecture[R]. 2007.

[11] Scott K, Burleigh S. RFC 5050: Bundle protocol specification[J]. 2007.

[12] 徐琪,周华春,李光磊,等.天地一体化网关设计与实现[J].铁道学报,2016,38(10):69-77.

[13] 3GPP, TS 33.501: Security architecture and procedures for 5G System[S]. 2022.

[14] OpenvSwitch. [EB/OL]. [2019-04-18]. http://www. openvswitch.org/.

[15] Docker. [EB/OL]. [2019-04-10]. https://www.docker.com/.

[16] Medved J, Varga R, Tkacik A, et al. Opendaylight: Towards a model-driven sdn controller architecture[C]//Proceeding of IEEE international symposium on a world of wireless, mobile and multimedia networks 2014. IEEE, 2014: 1-6.

[17] Long F. Satellite network robust QoS-aware routing[M]. Springer Berlin Heidelberg, 2014.

[18] BURLEIGH S. ION: Interplanetany Overlay Network[DB/OL]. https://ion.ocp.ohiou.edu/.2014.

[19] Satellite Tool Kit (STK). [EB/OL]. [2018.3.22]. http://www.agi.com.

[20] Taleb T, Mashimo D, Jamalipour A, et al. Explicit load balancing technique for NGEO satellite IP networks with on-board processing capabilities[J]. IEEE/ACM transactions on Networking, 2008, 17(1): 281-293.

[21] Huang Y, Feng B, Tian A, et al. An Efficient Differentiated Routing Scheme for MEO/LEO-Based Multi-Layer Satellite Networks[J]. IEEE Transactions on Network Science and Engineering, 2023.

[作者简介]

范晓静（1999-），女，北京交通大学博士生，主要研究方向为星地融合网络、服务功能编排等。

郑涛（1983-），男，博士，北京交通大学副教授、博士生导师，主要研究方向为移动专用网络。

周王健（1999-），男，北京交通大学硕士生，主要研究方向为卫星网络、安全功能链。

周华春（1965-），男，博士，北京交通大学教授、博士生导师，主要研究方向为互联网架构、天空地一体化网络、智能通信网络、移动性管理、移动安全计算以及路由协议。

A Deep Reinforcement Learning Based Dynamic Resource Allocation Approach in Satellite Systems

ZHOU Junyang[1],WAN Yunxiao[1], LI Yurui[1],WANG Jian[1*]

Abstract—Recently, space information networks(SIN), especially satellites, have become crucial for providing global connectivity. Efficiently allocating resources in these networks remains a significant challenge due to constraints in bandwidth and power, particularly as user demand increases. Dynamic Channel Allocation (DCA) is an effective technology for improving spectrum utilization and service quality, and it has been studied in many research works on multi-beam satellite systems. However, little research considers multiple resource allocations while accounting for performance constraints in practical scenarios. This paper introduces a Deep Reinforcement Learning-based Dynamic Resource Allocation (DDRA) algorithm designed to enhance traffic satisfaction rates and reduce blocking rates in space information networks. The study employs simulations to evaluate the performance of the DDRA algorithm against traditional fixed resource allocation and greedy random allocation methods. The results demonstrate that the DDRA algorithm significantly outperforms the other methods, achieving lower blocking probabilities and higher traffic satisfaction rates.

[1]School of Electronic Science and Engineering, Nanjing University, Nanjing 210023, China

[*]Corresponding author

Keywords — satellite system, dynamic resource allocation, restricted resource, deep reinforcement learning

I. INTRODUCTION

The Space Information Network (SIN) is a networked system that utilizes space platforms (such as geostationary satellites, medium and low Earth orbit satellites, stratospheric balloons, aircraft, etc.) as carriers, in combination with ground network nodes, to accomplish the tasks of space information acquisition, preprocessing, transmission, and reprocessing. The Space Information Network primarily consists of various types of satellites, constellations, spacecraft, and other space-based infrastructures in different orbits, integrated with corresponding ground facilities. It forms a comprehensive space-ground information system through inter-satellite and satellite-to-ground links[1].

In recent years, due to the continuous expansion of Internet services and application demands, the gradual maturity of microsatellite technology, and the challenges of achieving global coverage with ground-based networks, the development of the Space Information Network has attracted increasing attention. [2].

The communication transmission network formed between satellites and ground users is the most typical example of a Space Information Network. As communication demands continue to grow and the Space Information Network rapidly develops, increasing the system's spectrum utilization, service quality, and the dynamic allocation of its schedulable resources has become a key research focus.

DCA (Dynamic Channel Allocation) is an effective technology for improving spectrum utilization and service quality, and it has been studied in many research works on multi-beam satellite systems. Reference [3] proposed two DCA algorithms based on predefined cost functions, which effectively reduce the blocking probability but have high algorithm complexity and computational overhead. Reference [4] addressed the problem of optimal power allocation and admission control in satellite networks using dynamic programming methods. However, the energy consumption of each user is generated based on a priori known probability distributions, while in reality, it is a random event and typically unknown beforehand. Reference [5] proposed low-complexity DCA algorithms based on interference measurement (IM-DCA) and user location (L-DCA), which can effectively reduce co-channel interference. References [6] and [7] improved the IM-DCA and L-DCA algorithms from the perspective of service quality by considering channel priority. These algorithms greedily allocate channels with the lowest interference levels to users but neglect the inherent temporal correlation in DCA sequence decisions, leading to reduced spectrum utilization. DCA algorithms need to consider beam traffic, terminal distribution, and the impact of subsequent allocation decisions, as well as constraints such as power and co-channel interference, making it a sequential decision problem in a complex environment. Deep reinforcement learning methods have shown great application potential in such problems and have been applied in many dynamic resource management issues [8]-[11]. These studies indicate that there is a certain research foundation on how to perform dynamic channel allocation or resource scheduling in satellite systems using deep reinforcement learning or DCA methods. However, there is still relatively little research that simultaneously considers multiple resource allocations while accounting for performance constraints in practical scenarios. In actual systems, allocating resources dynamically requires balancing between various users and services, and satellites have limited power, which must be efficiently allocated among various communication links. Due to delays, limited inter-satellite communication, and potential conflicts between resource demands, it is difficult to implement simulation algorithms efficiently. For simulation cases closer to actual systems, resource allocation models combined with intelligent algorithms will provide forward-looking support for the future development of satellite communication networks and space information networks.

The main contributions of this paper are as follows:

- This paper proposes a DDRA (DQN-based Dynamic Resource Allocation) under satellite communication systems that considers power and traffic constraints, aiming to improve traffic satisfaction rates and reduce user blocking rates.
- A simulation system based on ns3 simulation software was built in this paper. By comparing the changes in the proposed algorithm with two traditional system resource allocation methods under different user service request rates, the feasibility of the proposed method in this system is demonstrated.

II. SYSTEM MODEL AND PROBLEM FORMULATION

In this section, the system model of a Space Information Network composed of a multi-beam satellite and ground user terminals will be introduced, along with the formulation of the dynamic channel allocation problem.

A. SYSTEM MODEL

This paper primarily considers a Space Information Network system formed between a multi-beam satellite and ground user terminals, as shown in Figure 1. The solid-line circular area represents the coverage area of the satellite at a given time. To improve spectrum resource efficiency and avoid interference, the satellite's coverage area is divided into N beam coverage areas, represented by dashed circular regions. The set of all beams can be denoted as $\boldsymbol{B}_N = \{b_n | n = 1,2,\dots,N\}$; The distribution of user terminals is indicated by red triangles, with the density of user terminals in different beam coverage areas being randomly distributed.

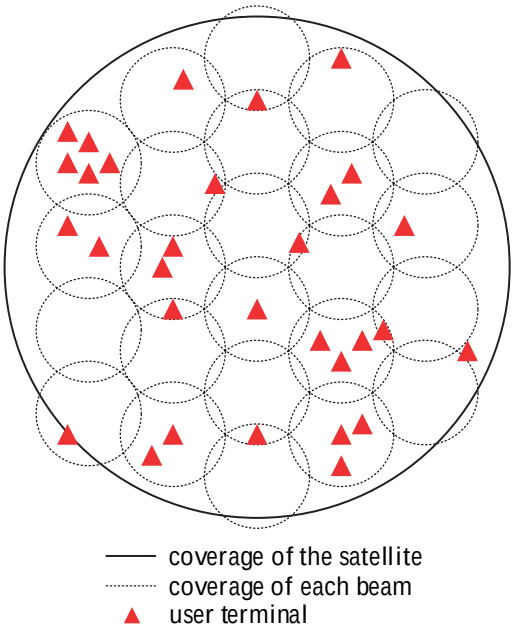

Figure 1 Multibeam satellite system

Let's assume the satellite system has a total of M available channels, which can be represented as the channel set $\boldsymbol{C}_M = \{c_m | m = 1,2,\dots,M\}$, with each channel c_m having a bandwidth of B_c. The total bandwidth of the satellite system is $B_{total} = MB_c$. Here, we consider that using the same channel at a sufficiently large distance will not cause significant interference, but using the same channel within the same beam will lead to mutual interference, reducing the transmission rate and degrading the quality of service (QoS) [12]. Therefore, it is stipulated that each channel can only serve a single user to ensure QoS.

We use the vector $\boldsymbol{p}_n = \{p_{n,1}, p_{n,2}, \dots, p_{n,M}\}$ to represent the power distribution of beam n when providing services to user terminals, where $p_{n,m}$ represents the power of beam n when using channel mmm. If $p_{n,m} > 0$, it indicates that the satellite is using channel m in the coverage area of beam n to provide service to users. The power distribution across all beams in the entire satellite coverage area can thus be represented by the matrix $\boldsymbol{P} = [\boldsymbol{p}_1, \boldsymbol{p}_2, \dots, \boldsymbol{p}_N]$.

Considering the satellite's actual power limitations, let's assume the maximum total output power of the satellite is P_{total}, the maximum power for any single beam b_n is P_b, and the maximum power for a single channel transmission is P_{cmax}. To simplify the system model and reduce the impact of interference and path loss in the environment, we assume that the minimum power required for using a single channel to serve users is P_{cmin}. If the remaining allocatable power is less than P_{cmin}, the satellite will refuse to provide service.

Next, we consider the scenario where the satellite provides services to users. Since users need to establish a connection with the satellite, they must send a request

to the satellite, which then decides whether to respond based on the schedulable beams and channels, ensuring that existing services are not affected. For these requests, we assume the number of users in each area is randomly distributed, and that these requests can be successfully transmitted to the satellite without loss. The traffic demand for service Q follows a normal distribution. To respond to users' requests and provide service, the satellite needs to allocate its power to ensure signal transmission and increase transmission rates to meet users' traffic demands.

To meet users' traffic demands, the satellite must allocate transmission bandwidth to balance the traffic needs of different users, thereby alleviating issues of insufficient available bandwidth and long user waiting times under high load conditions. The transmission rate when serving users on channel m of beam n can be defined as $v_{n,m}$. The bandwidth usage of beam n and the entire satellite coverage area can be represented by $\boldsymbol{v}_n = \{v_{n,1}, v_{n,2}, \dots, v_{n,M}\}$ and $\boldsymbol{V} = [\boldsymbol{v}_1, \boldsymbol{v}_2, \dots, \boldsymbol{v}_N]$, respectively. To ensure service quality, the transmission rate must be greater than v_{min}; otherwise, the satellite will consider it unable to provide service and will block the user request.

B. PROBLEM FORMULATION

The resource allocation problem in a multi-beam satellite system can be viewed as a decision-making problem in discrete time. Let's assume that each unit time step is t. Whenever a user sends a service request to the satellite, the satellite should make a decision to respond. The satellite needs to decide whether it can provide the requested service to the user based on the availability of channels and within its power limitations, while also striving to maintain the quality of other ongoing services. Assuming the request rate of all users is λ, and it follows a Poisson distribution, we can consider that within a fixed period, an average of λ service requests will be generated in the area. The duration of the service requested by users follows an exponential distribution with a mean of μ.

If the user's request cannot be fulfilled due to the satellite's power limitations and insufficient available channels, the request will be blocked; otherwise, the request will be accepted. Here, the ratio of the number of services the satellite is currently providing to the number of blocked user requests at a given time is defined as the service blocking rate at that time, denoted as $\phi_{blocked}$. The value of $\phi_{blocked}$ at any discrete time can be calculated using Eq.(1).

$$\phi_{blocked} = \frac{N_{blocked}}{N_{ut}} \#(1)$$

Here, $N_{blocked}$ represents the number of blocked service requests, and N_{ut} represents the total number of user service requests.

However, when the satellite's transmission bandwidth usage reaches its limit, the satellite must decide whether to block the user's request or to reduce the quality of other services within a certain range. Since reducing the quality of other services can lead to increased service time, this may cause the blocking rate to continue to increase. The unmet service demand (USD) is defined as the difference between the amount of traffic required by users and the amount of traffic provided by the satellite at a given time t:

$$USD_t = \sum_{n=1}^{N} max\left[D_{b_n,t} - Q_{b_n,t}, 0\right] \#(2)$$

Here, $D_{b_n,t}$ and $Q_{b_n,t}$ represent the demand traffic and the traffic provided by the satellite on beam b_n at time t, respectively. When the traffic provided by the satellite is greater than the demand,

the unmet service demand is 0.

Based on the above system modeling and problem setup, this paper aims to minimize the service blocking rate and unmet service demand over a period T. The objective is to provide high-quality service to as many users as possible while ensuring that the satellite's power meets the constraints, thus achieving a balance between resource utilization, service rate, and service quality. Considering the constraints related to power and traffic, the optimization problem can be modeled as Eq.(3) subject to Eq.(4)-(8).

$$minimize \sum_{t=1}^{T} \left[\phi_{blocked,t} + \beta USD_t\right] \#(3)$$

$$s.t. \sum_{n=1}^{N} P_{n,t} < P_{total} \#(5)$$

$$0 \le P_{b_n,t} \le P_b, \forall b_n \in B_N \#(4)$$

$$0 \le P_{c_m,t} \le P_{cmax}, \forall c_m \in C_M \#(6)$$

$$\sum_{n=1}^{N} \sum_{m=1}^{M} v_{n,m,t} \le Q_{total} \#(7)$$

$$v_{n,m,t} \ge v_{min} \#(8)$$

where Q_{total} and β respectively represent the total traffic for services that the system can provide and the normalization parameter for unmet service demand.

For the optimization problem in Eq.(3), constraint in Eq.(4) means total transmitting power should not exceed total transmitting power. Constraints in Eq.(5)-(6) mean that any beam power should not exceed the maximum beam power, and any channel power should not exceed the maximum channel power at any time. Constraint in Eq.(7) means the total traffic for services should not exceed the total traffic for services. Constraint in Eq.(8) means the transmission rate should exceed the minimum transmission rate to ensure the QoS of the service.

III. PROPOSED DDRA ALGORITHM

A. DDRA ARCHITECTURE

For the resource allocation problem in the aforementioned multi-beam satellite system, traditional decision-making methods rely on specific rules and prior information to make decisions, and they do not perform well in complex environments. In contrast, deep reinforcement learning-based methods allow the satellite agent to continuously interact with the environment, selecting actions based on environmental changes and reward feedback. This approach enables the agent to find the optimal actions within a specific system. The DQN based dynamic resource allocation architecture is illustrated in Figure 2

In Figure 2, the left side represents the communication system formed between the satellite and the user terminals. From this system, state information s and the current global feedback reward r are obtained and fed to the agent for learning. The right side illustrates the decision-making process based on deep reinforcement learning. According to the input state,
the required action is derived through the Q-network . The quadruple (s_t, a_t, r_t, s_{t+1}) which includes the current state s_t, selected action a_t, reward r_t, and the next state s_{t+1} are stored. At each step, a small batch of historical data is randomly sampled from the experience replay pool and combined with the target network to calculate the loss function, continuously updating the Q-network. After every c steps, the target network is updated.

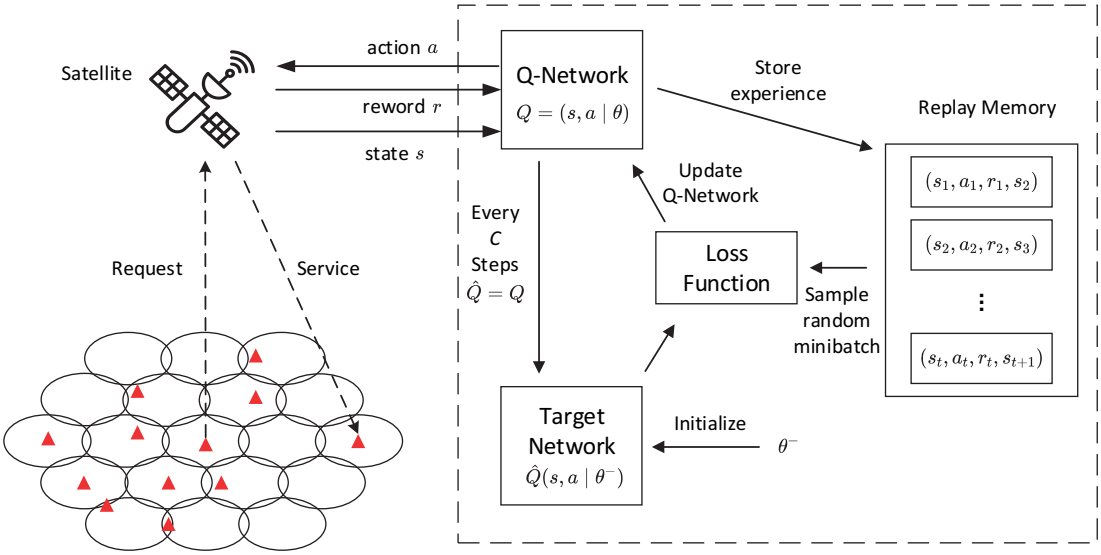

Figure 2 DDRA Architecture

B. MPD MODEL

Reinforcement learning tasks are often described using a Markov Decision Process (MDP), which is a mathematical method for solving sequential decision-making problems in discrete time. An MDP mainly consists of four key elements: states, actions, transition probabilities, and reward functions. The objective of the MDP is to maximize the long-term cumulative expected reward, i.e., to maximize $E[\sum_{k=0}^{\infty}\ \gamma^k r_{t+k}]$, where r_{t+k} represents the reward at time $t+k$, and $\gamma \in (0,1)$ is the discount factor. Based on the system modeling and optimization problem described above, the definitions of state, action, and reward for this system based on MDP are provided.

1. State

For the satellite to decide how to allocate schedulable resources at the next moment, it needs to consider the resources it has already allocated and the incoming requests at the current time, i.e., the known power and rate distribution across beams and channels, as well as the incoming request u_t,the request u_t includes the requested traffic volume Q_t, the service duration μ_t, and the beam area b_t, where the user is located, i.e. $u_t=[Q_t,\mu_t,b_t]$. Therefore, the state space can be expressed as:

$$s_t=[P,V,u_t]\#(9)$$

2. Action

The action involves how the satellite handles previously provided services and allocates channels, power, and traffic volume for new users. Given that each service request requires multiple resources to be allocated, the action space can become excessively large, making learning difficult. Therefore, the satellite must make several decisions to fulfill the service request.

First, the satellite must assign a channel $c_t \in \{0,C_M\}$ to the user. If a channel is available, it should select one from C_M for the user; otherwise, the user will be blocked. If a channel is assigned, the satellite will allocate traffic v_t to the user within the limits. If the power does not meet the constraints (4), (5), (6), the user will still be blocked. When the traffic reaches its limit, the satellite must decide whether to reduce the service quality of other ongoing services to free up bandwidth for the current service, while ensuring that constraints (7) and (8) are met. Therefore, the action space will include:

$$a_t=[c_t,v_t,d_t]\#(10)$$

where $d_t \in \{0,-1\}$ indicates whether to reduce the traffic of other nodes. If the traffic is not reduced, then $d_t=0$. If the traffic is reduced, it frees up v_t of traffic from the other users to meet the needs of the

current user.

3. Reward

The reward is the feedback the agent receives after taking an action. The agent primarily relies on the reward and the state to determine its actions, so the design of the reward function is crucial. The objective of this paper is to enable the satellite agent to provide as many high-quality services as possible under the constraints of power and traffic, thereby reducing user blocking rates and increasing user satisfaction with the allocated traffic. Therefore, the reward function in this paper is designed as follows:

$$r_t = \begin{cases} r_{blocked}, & blocked \\ r_{satisfied}, & otherwise \end{cases} \#(11)$$

When the agent's current choice successfully meets the new service request, it will receive a positive reward $r_{satisfied}$ based on the degree of satisfaction. Conversely, if the service is blocked, a negative reward $r_{blocked}$ will be given.

C. DDRA ALGORITHM

Based on the MDP model constructed above and the reinforcement learning framework, this paper introduces a Dynamic Resource Allocation algorithm (DDRA) based on the Deep Q-Network (DQN) algorithm. In the DQN-based algorithm, we use techniques such as exploration, experience replay, and a target network to improve the stability and convergence speed of the Q-network. For action selection, the ϵ-greedy algorithm is used for exploration. The exploration rate ϵ is initialized at ϵ_0 =0.99 and eventually converges to a minimum value of $\epsilon_{min} = 0.01$. The exploration value convergence strategy adopted here is:

$$\epsilon = \epsilon_{min} + (\epsilon_0 - \epsilon_{min}) * e^{-t/\epsilon_{decay}} \#(12)$$

Here, t represents the current elapsed time steps, and ϵ_{decay} is the decay rate.

According to the reinforcement learning framework shown in Figure 2, in this algorithm, the maximum memory capacity for experience replay is N_D. During each training process, newly generated tuples (s_t, a_t, r_t, s_{t+1}) are stored, and a small batch B is randomly sampled and input into the mean squared error loss function. The Q-network is then trained using stochastic gradient descent. The loss function is calculated as follows:

$$L = \frac{1}{|B|} \sum_{(s_t, a_t, r_t, s_{t+1}) \in B} \left[Q(s_t, a_t) - \left(r_t + \gamma \max_{a_t} \hat{Q}(s_{t+1}, a_t) \right) \right] \#(13)$$

Based on the above content, here provides the process flow of the DDRA algorithm:

Algorithm 1: DQN-based dynamic resource allocation

Initialize replay memory D to capacity N_D
Initialize action-value function Q with random weights θ
Initialize target action-value function $\hat{Q}$ with random weights θ^-
for $episode = 1, E$ do
  Initialize the system parameters $\boldsymbol{V}, \boldsymbol{P}, N_{blocked}, N_{ut} = 0$
  for $t = 1, T$ do
    Observe the arrival user u_t and generate the state s_t as (9)
    Update user nums $N_{ut} = N_{ut} + 1$
    Calculate the available channel set c_t by $\boldsymbol{P}$
    If $c_t = \emptyset$ do
      Update blocked users $N_{blocked} = N_{blocked} + 1$
      Calculate the reward $r_t = r_{blocked}$
    Else do
      Calculate the available choice set d_t by V
      If $d_t = \emptyset$ do
        Update blocked users $N_{blocked} = N_{blocked} + 1$
        Calculate the reward $r_t = r_{blocked}$
      Else do
        With probability ϵ select a random action a_t
        Otherwise select $a_t = \max_a Q(s_t, a; \theta)$
        Execute action a_t and observe the reward $r_t = r_{satisfied}$
        Observe the next state s_{t+1}
        Store transition(s_t, a_t, r_t, s_{t+1}) in D
        Sample random minibatch (s_j, a_j, r_j, s_{j+1}) from D
        Calculate the loss $L(\theta)$ by (13)
        Every c steps reset $\hat{Q} = Q$
      End If
    End If
  End for
End for

IV. SIMULATION RESULTS AND ANALYSIS

In this section, we present the simulation

experiments to validate the performance of the proposed model and deep reinforcement learning method in the system, and compare them with existing methods to demonstrate their superiority. First, the validation parameters used in the simulations are provided. Then, the training results of the algorithm in this system are presented and analyzed to demonstrate the feasibility of the algorithm. Finally, we analyze the variations in blocking rates and service satisfaction rates under different user service request rates in this system and compare them with traditional methods.

A. SIMULATION PARAMETERS

The simulation experiments in this paper are conducted using the ns-3 simulation platform, with the ns-3 and ns-3-ai modules employed to implement satellite communication simulations and the proposed algorithm. The simulation tests will be performed on a computer equipped with an Intel i7-9700K CPU and an RTX 2080Ti GPU for training and verification. The simulation parameters are listed in TABLE 1.

Table 1 Simulation Parameters

Parameters	Values
System parameters	
Number of beams N	19
Number of channels M	16
Total bandwidth B_{total}	5 MHz
Channel bandwidth B_c	312.5 kHz
Total transmission power P_{total}	23 dbW
Maximum beam power P_b	20 dbW
Maximum channel power P_{cmax}	0.35 dbW
Minimum channel power P_{cmin}	0.3 dbW
Traffic of requests for services Q	Gaussian distribution
Total traffic for services Q_{total}	20 Mbps
Minimum traffic for services v_{min}	500 kbps
Traffic arrival rate λ	Poisson distribution
Traffic duration μ	Exponential distribution
Total time steps T	1000
Algorithm parameters	
Replay memory size N_D	20000
Batch size B	64
Target update frequency c	100
Learning rate α	0.01
Initial epsilon ϵ_0	0.99
Minimum epsilon ϵ_{min}	0.01
Epsilon decay ϵ_{decay}	1000
Discount factor γ	0.99

To verify the feasibility of the proposed algorithm, two traditional fixed allocation methods are provided for comparison:

Fixed Resource Allocation Method: For service requests, channels are allocated in a fixed order, and a fixed amount of traffic and power are provided. The allocation does not change based on the current situation or past resource allocation.

Greedy Random Allocation Method: For service requests, the satellite randomly allocates channels to users and provides as much traffic and power as possible. This method does not reclaim or restrict resources that have already been allocated.

B. SIMULATION RESULTS

Firstly, the reward-episode curve as the training results of the proposed algorithm are shown in Figure 3. We can observe that, due to the longer training steps in each iteration and the extensive model adjustments, the network quickly adapts its channel allocation pattern within the first 10 iterations. The system then gradually stabilizes in subsequent iterations. It is important to note that during the training, the average user request frequency was set at 16 users per unit time, with an average service request time of 3 units. This implies that all bandwidth will be fully utilized, and the random positions of users will quickly push the system to the boundary between blocked and unblocked states. The algorithm initially focuses on maximizing user traffic satisfaction, indicated by higher rewards, and gradually converges to a balanced state between user traffic satisfaction and blocking rates, maintaining relative stability.

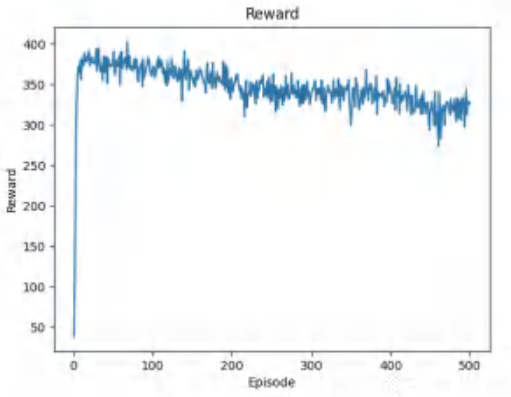

Figure 3 reward-episode curve of training

In the experimental validation, the comparison is based on variations in the system's blocking rate and traffic satisfaction levels under different user service request rates. These are compared with the fixed allocation strategy and the greedy random allocation strategy, as shown in Figure 4 and Figure 5

For both blocking rate and traffic satisfaction rate, it is evident that the current algorithm outperforms the other two methods across all traffic scenarios. When the user service request rate is approximately 20 requests per minute, the blocking rate is significantly lower compared to the fixed allocation and random strategy methods, and the traffic satisfaction rate is also notably higher than that of the fixed allocation method. When the number of user service requests is high, the differences between these methods diminish because the traffic constraints become very severe. This results in new user service requests being almost unable to be properly accommodated.

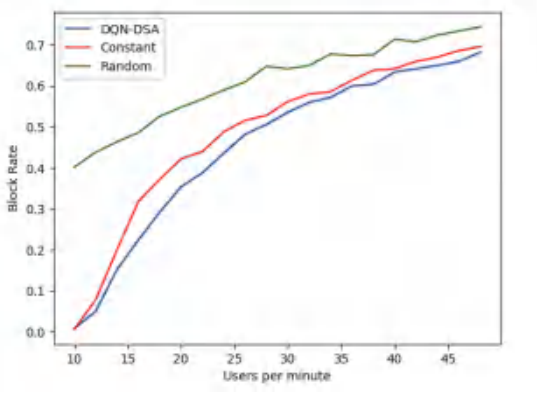

FIGURE 4 block rate curve under different user request rates

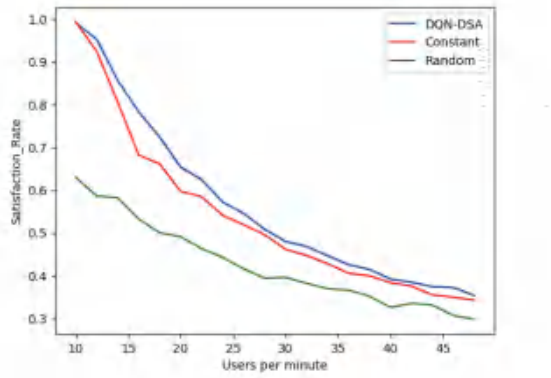

FIGURE 5 traffic satisfaction rate curve under different user request rates

V. CONCLUSION

This paper proposes a Deep Reinforcement Learning-based Dynamic Resource Allocation (DDRA) algorithm aimed at increasing traffic satisfaction rates and reducing blocking rates. The simulation results indicate that, compared to traditional fixed resource allocation strategies and greedy random allocation methods, the DDRA algorithm achieves lower blocking probabilities and higher traffic satisfaction rates. However, further research is needed to address channel and power limitations more effectively and to better reflect the impact of power allocation in the algorithm.

References

[1] Ren Y, Jiang C X, Du J, et al. Space information network architecture and applications

[2] Khuwaja A A, Chen Y, Zhao N, et al. A survey of channel modeling for UAV communications[J]. IEEE Communications Surveys & Tutorials, 2018, 20(4): 2804-2821.

[3] E. D. Re, R. Fantacci, and G. Giambene, ‘‘Efficient dynamic channel allocation techniques with handover queuing for mobile satellite networks,’’ IEEE J. Sel. Areas Commun., vol. 13, no. 2, pp. 397–405, Feb. 1995.

[4] A. C. Fu, E. Modiano, and J. N. Tsitsiklis, ‘‘Optimal energy allocation and admission control for communications satellites,’’ IEEE/ACM Trans. Netw., vol. 11, no. 3, pp. 488–500, Jun. 2003.

[5] M. Umehira and F. Naito, ‘‘Centralized dynamic channel assignment schemes for multi-beam mobile satellite communications systems,’’ in Proc. AIAA ICSSC, 2012, p. 15123.

[6] M. Umehira, S. Fujita, Z. Gao, and J.Wang, ‘‘Dynamic channel assignment based on interference measurement with threshold for multi-beam mobile satellite networks,’’ in Proc. 19th Asia–Pacific Conf. Commun. (APCC), Denpasar, Indonesia, Aug. 2013, pp. 688–692.

[7] M. Umehira, S. Fujita, Z. Gou, and J. Wang, ‘‘Location-based centralized dynamic channel assignment with channel segregation for multi-beam mobile satellite networks,’’ in Proc. 6th Int. Conf. Wireless Commun. Signal Process. (WCSP), Hefei, China, Oct. 2014, pp. 1–5.

[8] H. Mao, M. Alizadeh, I. Menache, and S. Kandula, ‘‘Resource management with deep reinforcement learning,’’ in Proc. ACM Workshop Hot Topics Netw., 2016, pp. 50–56.

[9] Z. Xu,Y.Wang, J. Tang, J.Wang, and M. C. Gursoy, ‘‘Adeep reinforcement learning based framework for power-efficient resource allocation in cloud RANs,’’ in Proc. IEEE Int. Conf. Commun. (ICC), Paris, France, 2017, pp. 1–6.

[10] N. Liu et al., ‘‘A hierarchical framework of cloud resource allocation and power management using deep reinforcement learning,’’ in Proc. IEEE 37th Int. Conf. Distrib. Comput. Syst. (ICDCS), Atlanta, GA, USA, Jun. 2017, pp. 372–382.

[11] J. Zhu, Y. Song, D. Jiang, and H. Song, ‘‘A new deep-Q-learning-based transmission scheduling mechanism for the cognitive Internet of Things,’’ IEEE Internet Things J., to be published.

[12] B. Zhao, J. Liu, Z. Wei and I. You, "A Deep Reinforcement Learning Based Approach for Energy-Efficient Channel Allocation in Satellite Internet of Things," in IEEE Access, vol. 8, pp. 62197-62206, 2020, doi: 10.1109/ACCESS.2020.2983437.

About the authors

Zhou Junyang received the B.E. degree in communication engineering from Nanjing University, Nanjing, China in 2023. He is currently pursuing M.S. degree in electronic and information engineering from Nanjing University (Email: tsukizhou@gmail.com)

面向人机友好的遥感图像编码多尺度框架

张真，肖晶*，王密

摘　要：随着遥感数据量的增加和机器协同解译的发展，遥感影像传输除了需要高效的压缩之外，还需要服务于人机视觉双重需求。然而现有的以像素表示为优化基础的压缩方法在面对下游的机器分析任务时会存在性能下降的问题。针对该问题，提出了一种特征域优化的人机友好的遥感影像压缩框架。设计一个紧凑的多尺度特征提取器，将图像变换到特征域，并对紧凑特征进行压缩以实现高效传输。解码时，将压缩后的特征直接用于机器分析，避免了人机视觉的权衡。为了重建视觉上令人愉悦的图像，我们利用任务间的协同作用，利用高级任务中的特征增强图像重建。在 AID 和 NWPU-RESISC45 数据集上的实验结果表明，在同等视觉效果的情况下，所提方法在分析性能上优于现有方法。

关键词：图像压缩；语义压缩；机器视觉；深度学习

A Multi-scale Framework Towards Human-machine Friendly Remote Sensing Image Coding

Zhen Zhang, Jing Xiao*, Mi Wang

Abstract: With the increase in the amount of remote sensing data and the development of machine collaborative interpretation, remote sensing image transmission need to serve both human and machine vision, in addition to high-efficient compression. However, existing compression methods optimized on pixel representation suffer performance degradation when confronted with downstream machine analysis tasks. To address this issue, we proposed a feature-domain-optimized human-machine friendly remote sensing image compression framework. We design a compact multi-scale feature extractor to transform images into feature domain, and compress the compact feature for efficient transmission. When decoding, the compressed feature is directly used for machine analysis, which avoid the trade-off between human and machine vision. To reconstruct visually pleasing images, we exploit synergy between tasks and enhance the image reconstruction with features from high-level task. Experimental results on both AID and NWPU-RESISC45 datasets demonstrate that our proposed method outperforms existing methods in terms of analytical performance with equivalent visual effects.

Key words: Image Compression, Semantic Compression, Machine Vision, Deep Learning

1 Introduction

The development of remote sensing imaging technology produced a huge amount of remote sensing data, which is impossible to fully interpretation and analysis by limited manpower. In contrast, the widespread application of deep learning in the field of remote sensing has significantly boosted the ability of machine to understanding remote sensing images. In the nearest future, human-machine collaborative understanding of remote sensing images will become a mainstream method. Therefore, efficient human-machine vision friendly image compression is an indispensable study to support the premium application of remote sensing data.

To achieve high-efficiency image transmission, many efforts have been made over decades of research ranging from predictive coding, transform coding to hybrid coding. Recently, with the development and expansion of neural networks, learning-based codecs [1, 2, 3] have rapidly evolved and attained promising performance. Nonetheless, the development of image compression efficiency is sluggish and limited, and it is challenging to achieve higher compression ratios by orders of magnitude to support the explosive growth of remote sensing data traffic. In addition image compression methods are usually designed for human vision and are independent of machine analysis. Since the principles of machine vision are different from human vision [4], the reconstructed images optimized by human vision may obtain sub-optimal analysis results. Particularly, the compression artifacts under low bit rates seriously affect the semantic analysis accuracy since feature fidelity is not considered.

In this paper, we proposed a human-machine vision friendly image compression framework to satisfy the requirements of human-machine collaborative understanding and high-efficiency compression. Rather than compressing and transmitting images directly, we tend to extract compact feature from the input image and compress the feature to ensure semantic fidelity. On the encoding side, we employ multi-scale dilated convolutions to extract features, which assists in alleviating the challenge of large scale discrepancies across remote sensing objects. On the decoding side, the compressed features are directly used in downstream tasks. We set up two branches to perform image reconstruction for human vision and machine analysis for machine vision using the reconstructed features. To address the challenge of downstream task performance degradation caused by feature distortion, we explore the inter-task relationships and employ high-level task features to enhance the low-level task performance. Specifically, we inject the intermediate features from the image classification branch into the image reconstruction branch, which are then aggregated with the compressed features and fed to the deconvolution decoder for image reconstruction.

In summary, the main contributions of this paper are:

1) We design a remote sensing image compression framework for both human and machine vision to support collaborative understanding of remote sensing images, which performs image classification and reconstruction from the compressed features.

2) We propose to extract compact multi-scale features by multi-scale dilate convolutions to facilitate both compression and downstream analysis, and leverage the synergy between tasks to enhance the low-level task with features from high-level task.

3) Our method achieves reconstruction quality comparable to the state-of-the-art in image compression, and outperforms classification methods from the decoded images in term of bit-accuracy on both two remote sensing image classification datasets.

2 Related Work

2.1 Image Compression

Image compression aims to reduce the storage volume and transmission bandwidth of images while retaining the important information as much as possible. Traditional hand-craft methods, such as JPEG [5], JPEG2000 [6], AVC [7], HEVC/H.265 [8], VVC/H.266 [9], remove signal redundancy and human imperceptible information with intra prediction, discrete cosine transformation or wavelet transformation, quantization, and entropy coding pipeline The development of deep learning significant facilitated learning-based codecs. Balle *et al.* [1] proposed the most widely used learning-driven lossy image compression model with auto-encoder. Zhou *et al.* [2] utilized a pyramidal encoder for fusing features of multiple scales to generate the latent representation of auto-encoder. Cheng *et al.* [3] proposed to use discretized Gaussian mixture likelihoods to parameterize the distributions of latent codes and achieved substantial performance improvement. Recently, Xie *et al.* [10] largely mitigate the information loss problem by introducing invertible neural network as enhanced encoder. However, these methods are optimized with pixel-level metrics that designed for visual fidelity, which is sub-optimal for machine vision.

2.2 Image Coding for Machine

Different from image compression for human visual perception, image coding for machines aims to compress and transmit source images to support the downstream machine analysis tasks. A naive solution is to jointly optimize the image compression models and the downstream intelligent tasks in the image domain. Based on task-oriented heuristic prior knowledge, [11], [12] and [13] proposed to utilize region of interest based bit allocation strategy to save transmission overhead. However, these methods imply a trade-off between semantic fidelity and pixel fidelity, leading to sub-optimal results for machine vision. Therefore, some methods compresses the features of corresponding tasks instead of original images for both coding efficiency and calculation load. Hu *et al.* [14] transmitted a compact edge map for machine vision tasks with the reference pixels as enhanced layer for human vision. Liu *et al.* [15] proposed to learn features with pyramid structure for scalable encoding to support multi-grained tasks. Feng *et al.* [16] extracted a compact omnipotent feature by contrastive learning for various downstream tasks. However, these methods are not optimized for the multi-scale characteristic of remote sensing images.

3 Proposed Method

3.1 Framework Overview

The structure of proposed framework is shown in Fig. 1. Given a image x with label y, we firstly extract its multi-scale compact feature z at the encoder side with the proposed multi-scale dilated convolution (MSDC) module. Subsequently, the feature z is fed into a lossy compression module with a hyper-prior module to facilitate transmission. At last, the compressed representation $\hat{z}$ is reconstructed at the decoder side and used to predict the label $\hat{y}$ and reconstruct the image $\hat{x}$ respectively. More specifically, we use standard Transform blocks to build the image classification branch and aggregate the features of the image classification branch for image reconstruction.

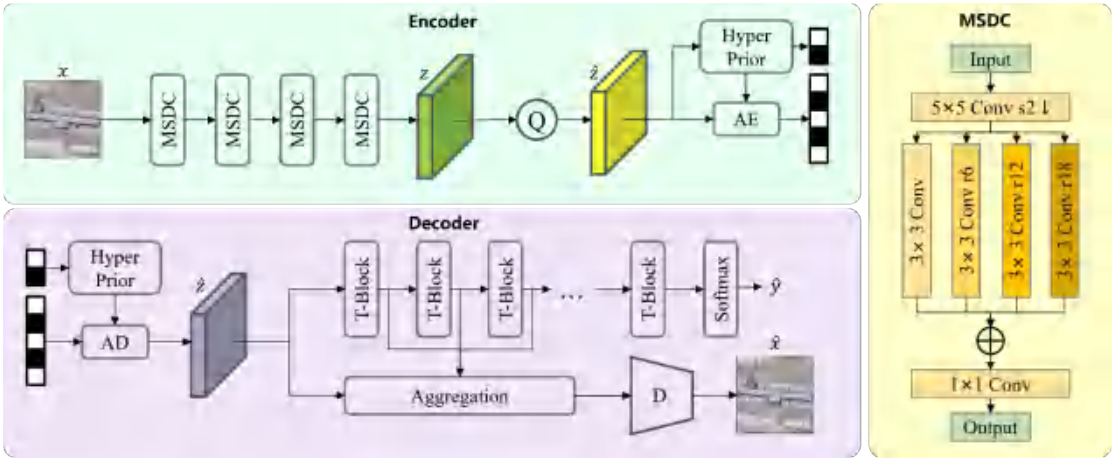

Fig. 1. Overview of proposed human-machine vision friendly remote sensing image compression framework. $\boldsymbol{s}$ and $\boldsymbol{r}$ in convolution layers represent stride and dilation rate respectively. $\boldsymbol{Q}$: Quantization. $\boldsymbol{AE}$: Arithmetic Encoder. $\boldsymbol{AD}$: Arithmetic Encoder. ***T-Block***: Transformer Block.

3.2 Feature Extraction and Compression

Considering the large scale discrepancies between remote sensing objects, we stack four MSDC modules to extract multi-scale compact representation and gradually reduce the spatial dimension. Specifically, the MSDC module employs a convolutional layer with stride of 2 to reduce the spatial resolution to half. Then, multiple dilated convolution layers with different dilation rate are utilized to capture features at different scales in parallel. At last, the features from all branches are concatenated in channel and then fed into a convolution layer for channel dimension reduction. The input image $x \in \mathcal{R}^{3\times w\times h}$, where w and h donate the width and height, respectively, is transformed into compact representation $z \in \mathcal{R}^{c\times\frac{w}{16}\times\frac{h}{16}}$ through by four MSDC modules, where c is the number of channels.

Since the value range of the feature z is continuous, we quantize it to the discrete-valued $\hat{z}$ before compressing it. A hyper-prior module [3] of learning-based image compression method is employed to estimate the hyper-prior conditional probability distribution for the entropy coding of $\hat{z}$. Note that the proposed modules on the encoding side are relatively lightweight, thus can be deployed on satellites with limited computational capacity.

3.3 Downstream Feature Application

The bitstream is restored to $\hat{z}$ on the decoding side, which is then sent to the machine analysis branch and image reconstruction branch respectively. In particular, we selected the image classification task as the machine analysis branch.

Classification Branch. Rather than reconstructing the image from $\hat{z}$ and then classifying it, we directly utilize $\hat{z}$ for inference. We employ the standard Transform blocks in ViT [17] to build our analysis branch. Following ViT, we adopt the learnable position embedding to maintain the spatial information, and the class embedding for classification. At the end, the transferred class embedding is fed to the classification head with a softmax activation function to predict class probabilities.

Reconstruction Branch. To reconstruct images with higher visual quality, we attempt to utilize the features of classification branch to enhance image reconstruction, motivated by the consideration that features of high-level vision tasks may assist low-level vision tasks. Transformers are able to extract global context information from the compressed features, which has been demonstrated to help improve compression performance in [18]. Therefore, we inject the intermediate layer features from the classification branch into reconstruction. Specifically, we aggregate the decompressed feature $\hat{z}$ with the features from the first three layers of classification branch. We concatenate these features in the channel dimension and employ convolution layers for information fusion. At last, the decoder utilizes the aggregated features to reconstruct the high-quality image.

3.4 Training Objectives

Our optimization objectives include image reconstruction quality, image classification accuracy, and feature compression bit rate. The L_2 loss between x and $\hat{x}$ constrains the reconstruction quality, and the cross-entropy loss is utilized for classification branch. The rate loss is expressed by the entropy of latent variable z. The entire loss function can be expressed as:

$$L_{total} = \alpha H(y, \hat{y}) + \beta \|x - \hat{x}\|_2^2 - \log p(\hat{z}), \tag{1}$$

where $H(\cdot,\cdot)$ denotes the cross entropy, α and β are the associated weights.

4 Experimental Results

4.1 Experimental Setup

Datasets. We evaluate our method on the AID dataset [19] and NWPU-RESISC45 dataset [20]. AID is a well-

known remote sensing image scene classification dataset containing 30 scene classes with 10,000 images. Its image resolution is 600×600, and the ground resolution ranges from 8 meters to half a meter. NWPU-RESISC45 is large-scale scene classification dataset containing 31,500 images, covering 45 scene classes with 700 images in each class. We split them equally into training set and validation set.

Implementation Details. We implement our method with Pytorch and optimize it using AdamW for 300 epochs. The initial learning rate is set to 0.0001 with a cosine decay learning rate scheduler. We set α/β to 100 and α to 0.1, 0.3, 0.6, 0.9, respectively to equip networks with different compression ratio.

Comparison Methods. We compare our method with the traditional codecs including JPEG, JPEG2000, BPG, and the learning-based image codecs including mbt [21] and GMM [3]. In addition, we take the decoded images as the input of images classification models to validate analytical performance. We select the CNN-based model, ResNet50 [22], and Transformer-based model, Swin-T [23] to compute the Top-1 accuracy.

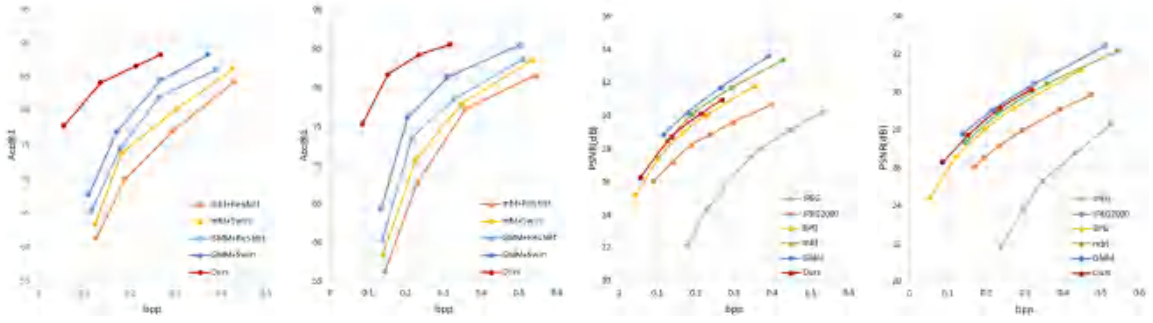

(a) Rate-accuracy Comparison (b) Rate-distortion Comparison

Fig. 2. Classification accuracy (a) and image reconstruction PSNR (b) under different bitrates. The results on AID and NWPU-RESISC45 are shown from left to right, respectively.

4.2 Effectiveness and Superiority

Image Classification. We report the rate-accuracy result of our model on both AID and NWPU-RESISC45 in Fig. 2 (a). We jointly trained the image compression and image classification networks for a fair comparison. Our method significantly surpasses ResNet50 and Swin-T applied to the reconstructed images. This is mainly due to the serious distortion of reconstructed images at low bit rates, which are not robust to machine analysis. However, our method performs compression in the feature domain, thus the semantically fidelity information can be transmitted at a lower bit rate.

Reconstruction Results. Fig. 2 (b) demonstrates the rate-distortion performance. The proposed method significantly outperforms the traditional image codecs, *i.e.*, JPEG and JPEG2000, and achieves performance comparable to the learning-based codecs, that is, the PSNR difference is no more than 1dB under the same bpp. We

also present the visual comparison of the reconstructed images in Fig. 3. At low bit rates, the proposed method retains more fidelity edge and texture and produces the most pleasing visual effects. All learning-based codecs are fine-tuned on remote sensing datasets for fair comparison.

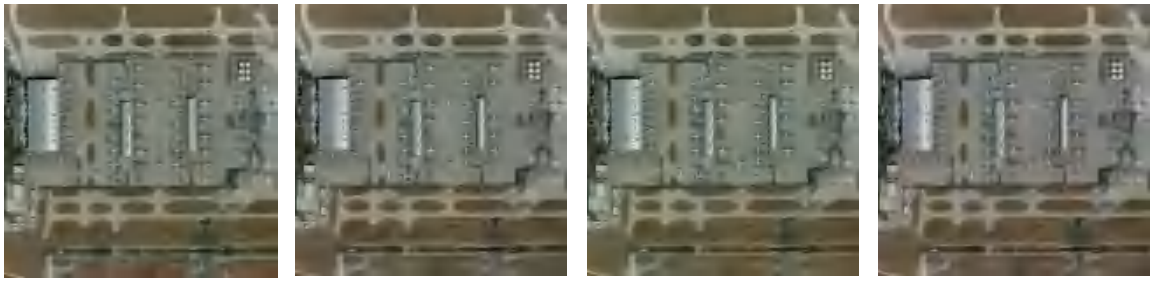

(a) Input/bpp/PSNR　(b) mbt/0.135/27.82dB　(c) GMM/0.120/28.48dB　(d) Ours/0.129/27.65dB

Fig. 3. Qualitative comparison on image compression methods. All images are controlled at similar bit rates for fair comparison. The reconstruction quality is measured by PSNR.

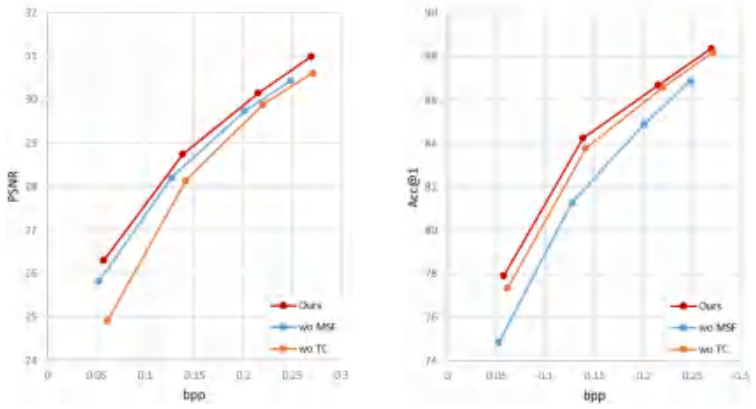

Fig. 4. The ablation study on multi-scale feature extraction and collaboration between tasks. The image reconstruction quality is on the left side, while the picture classification accuracy is on the right.

4.3 Ablation Studies

We validate the effectiveness of the proposed multi-scale feature extraction (MSF) and task-collaboration (TC). Fig. 4 shows the comparison of with and without MSF and TC on AID dataset. MSF results in a slight bit rate increase, but has a positive effect on both human and machine vision with richer information. Although TC is only applied to the human vision branch, it can help with both image classification and reconstruction by the optimization in Eq. 1. All designed modules promote the improvement of both rate-distortion and rate-accuracy performance.

5 Conclusion

In this paper, we proposed a novel framework to simultaneously tackle the needs of remote sensing picture compression for both human and machine vision. Instead of reconstructing the image from the code stream, we

extract and directly transmit the compact multi-scale features of remote sensing images for machine analysis. In addition, we exploit the features from classification branch to enhance the quality of image reconstruction. Experimental results demonstrate the effectiveness of the proposed method on both human and machine vision.

6 参考文献

[1] Johannes Ball´e, Valero Laparra, and Eero P Simoncelli, “End-to-end optimized image compression,” arXiv preprint arXiv:1611.01704, 2016.

[2] Lei Zhou, Chunlei Cai, Yue Gao, Sanbao Su, and Junmin Wu, “Variational autoencoder for low bit-rate image compression,” in CVPRW, 2018, pp. 2617–2620.

[3] Zhengxue Cheng, Heming Sun, Masaru Takeuchi, and Jiro Katto, “Learned image compression with discretized gaussian mixture likelihoods and attention modules,” in CVPR, 2020, pp. 7939–7948.

[4] Haohan Wang, Xindi Wu, Zeyi Huang, and Eric P Xing, “High-frequency component helps explain the generalization of convolutional neural networks,” in CVPR, 2020, pp. 8684–8694.

[5] Gregory K Wallace, “The jpeg still picture compression standard,” Commun. ACM, vol. 34, no. 4, pp. 30–44, 1991.

[6] Majid Rabbani and Rajan Joshi, “An overview of the jpeg 2000 still image compression standard,” Signal Process. Image Commun., vol. 17, no. 1, pp. 3–48, 2002.

[7] Thomas Wiegand, Gary J Sullivan, Gisle Bjontegaard, and Ajay Luthra, “Overview of the h. 264/avc video coding standard,” IEEE Trans. Circuits Syst. Video Technol., vol. 13, no. 7, pp. 560–576, 2003.

[8] Gary J Sullivan, Jens-Rainer Ohm, Woo-Jin Han, and Thomas Wiegand, “Overview of the high efficiency video coding (hevc) standard,” IEEE Trans. Circuits Syst. Video Technol., vol. 22, no. 12, pp. 1649–1668, 2012.

[9] Benjamin Bross, Ye-Kui Wang, Yan Ye, Shan Liu, Jianle Chen, Gary J Sullivan, and Jens-Rainer Ohm, “Overview of the versatile video coding (vvc) standard and its applications,” IEEE Trans. Circuits Syst. Video Technol., vol. 31, no. 10, pp. 3736–3764, 2021.

[10] Yueqi Xie, Ka Leong Cheng, and Qifeng Chen, “Enhanced invertible encoding for learned image compression,” in ACM MM, 2021, pp. 162–170.

[11] Qi Cai, Zhifeng Chen, Dapeng Oliver Wu, Shan Liu, and Xiang Li, “A novel video coding strategy in hevc for object detection,” IEEE Trans. Circuits Syst. Video Technol., vol. 31, no. 12, pp. 4924–4937, 2021.

[12] Zhimeng Huang, Chuanmin Jia, Shanshe Wang, and Siwei Ma, “Visual analysis motivated rate-distortion model for image coding,” in ICME. IEEE, 2021, pp. 1–6.

[13] Chen Dong, Haotai Liang, Xiaodong Xu, Shujun Han, Bizhu Wang, and Ping Zhang, “Semantic communication system based on semantic slice models propagation,” IEEE J. Sel. Areas Commun., vol. 41, no. 1, pp. 202–213, 2022.

[14] Yueyu Hu, Shuai Yang, Wenhan Yang, Ling-Yu Duan, and Jiaying Liu, “Towards coding for human and machine vision: A scalable image coding approach,” in ICME. IEEE, 2020, pp. 1–6.

[15] Kang Liu, Dong Liu, Li Li, Ning Yan, and Houqiang Li, “Semantics-to-signal scalable image compression with learned revertible representations,” Int. J. Comput. Vision, vol. 129, no. 9, pp. 2605–2621, 2021.

[16] Ruoyu Feng, Xin Jin, Zongyu Guo, Runsen Feng, Yixin Gao, Tianyu He, Zhizheng Zhang, Simeng Sun, and Zhibo Chen, “Image coding for machines with omnipotent feature learning,” in ECCV. Springer, 2022, pp. 510–528.

[17] Alexey Dosovitskiy, Lucas Beyer, Alexander Kolesnikov, Dirk Weissenborn, Xiaohua Zhai, Thomas Unterthiner, Mostafa Dehghani, Matthias Minderer, Georg Heigold, Sylvain Gelly, et al., “An image is worth 16x16 words: Transformers for image recognition at scale,” arXiv preprint arXiv:2010.11929, 2020.

[18] Yichen Qian, Zhiyu Tan, Xiuyu Sun, Ming Lin, Dongyang Li, Zhenhong Sun, Hao Li, and Rong Jin, “Learning accurate entropy model with global reference for image compression,” arXiv preprint arXiv:2010.08321, 2020.

[19] Gui-Song Xia, Jingwen Hu, Fan Hu, Baoguang Shi, Xiang Bai, Yanfei Zhong, Liangpei Zhang, and Xiaoqiang Lu, “Aid: A benchmark data set for performance evaluation of aerial scene classification,” IEEE Trans. Geosci. Remote Sens., vol. 55, no. 7, pp. 3965–3981, 2017.

[20] Gong Cheng, Junwei Han, and Xiaoqiang Lu, “Remote sensing image scene classification: Benchmark and state of the art,” Proc. IEEE Inst. Electr. Electron. Eng., vol. 105, no. 10, pp. 1865–1883, 2017.

[21] David Minnen, Johannes Ball´e, and George D Toderici, “Joint autoregressive and hierarchical priors for learned image compression,” NeurIPS, vol. 31, 2018.

[22] Kaiming He, Xiangyu Zhang, Shaoqing Ren, and Jian Sun, “Deep residual learning for image recognition,” in CVPR, 2016, pp. 770–778.

[23] Ze Liu, Yutong Lin, Yue Cao, Han Hu, Yixuan Wei, Zheng Zhang, Stephen Lin, and Baining Guo, “Swin transformer: Hierarchical vision transformer using shifted windows,” in ICCV, 2021, pp. 10012–10022.

Link-Cluster-Based Spectrum Sharing for Hybrid Satellite-UAV-Terrestrial Maritime Networks

Yanmin Wang[1], Wei Feng[2], Jue Wang[3,4], Shidong Zhou[2], and Cheng-Xiang Wang[5,6]
[1]School of Information Engineering, Minzu University of China, Beijing 100081, China
[2]Department of Electronic Engineering, Tsinghua University, Beijing 100084, China
[3]School of Information Science and Technology, Nantong University, Nantong 226019, China
[4]Nantong Research Institute for Advanced Communication Technology, Nantong 226019, China
[5]National Mobile Communications Research Laboratory, School of Information Science and Engineering, Southeast University, Nanjing 210096, China
[6]Purple Mountain Laboratories, Nanjing 211111, China
E-mail: wangyanmin@muc.edu.cn, fengwei@tsinghua.edu.cn, wangjue@ntu.edu.cn, zhousd@tsinghua.edu.cn, chxwang@seu.edu.cn

***Abstract*—Spectrum sharing among the satellite, unmanned aerial vehicle (UAV), and terrestrial components is crucial to alleviate spectrum scarcity in a hybrid maritime communication network (MCN). In the time domain, spectrum sharing optimization based on fine-grained time slices is widely envisioned. However, fine-grained time synchronization is rather challenging due to the large diversity in the link delay. In this paper, we focus on link-cluster-based spectrum sharing based on coordinated link scheduling in terms of subcarrier and time slice allocation. By link-cluster-based scheduling for the satellite links, time-slice-oriented spectrum sharing is realized with coarse time synchronization at time scales much larger than single time slice duration. Only large-scale channel state information (CSI) is utilized for saving cost. An NP-hard mixed integer programming (MIP) problem is formulated, and with the aid of link clustering, a suboptimal spectrum sharing scheme, with only a small performance gap to the optimal one, is proposed. Simulations show that a significant improvement in both energy efficiency and spectrum efficiency could be achieved by the proposed scheme.**

***Index Terms*—Maritime communication, hybrid network, spectrum sharing, time synchronization, channel state information (CSI)**

I. Introduction

Ubiquitous coverage is ranked among the top targets of the sixth generation (6G) network, for which enhanced maritime coverage is considered to be a key scenario [1], [2]. Since the terrestrial base stations (BSs), in general, are only suitable for off-shore coverage, the non-terrestrial network components, including satellites and unmanned aerial vehicles (UAVs), are indispensable for realizing broadband maritime communications [1]–[3]. With the ability to integrate the advantages of different networks together, the hybrid satellite-UAV-terrestrial maritime communication network (MCN) is considered to be a promising solution for 6G maritime coverage [3]. To counter spectrum scarcity in such hybrid MCN, spectrum sharing among different links is necessary [2], [5]–[8].

For efficient spectrum utilization, time slicing could be adopted together with subcarrier division in both the terrestrial and satellite components [3]. As the maritime users in a hybrid MCN are usually dispersively distributed in a large area, the links for different users are usually largely different in path loss and propagation delay [1]–[3]. Due to the high altitude of satellites, the difference between satellite links and UAV/terrestrial links is especially prominent. While the diversity in path loss of these links brings chances for opportunistic spectrum utilization, the difference in propagation delay makes it difficult to achieve fine-grained network-wide time synchronization, especially when the satellite, UAV, and terrestrial components are operated separately with limited information exchange [3], [4]. Thus, it is rather challenging to fully exploit the performance gains of cooperative spectrum sharing among all links in the time domain based on time-sliced subcarriers [3]. In previous research [5]–[7], spectrum sharing was mainly achieved through opportunistic coordination between satellite and UAV/terrestrial links in the frequency domain. Coordinated optimization in the time domain, e.g., across time slots, was either not considered or just considered for UAV/terrestrial links [5]–[7]. To the best of our knowledge, no spectrum sharing scheme has been designed for hybrid satellite-UAV-terrestrial networks based on opportunistic transmission across both the frequency and time domains.

In this paper, we focus on spectrum sharing for a hybrid satellite-UAV-terrestrial MCN, where UAV-to-vessel (U2V) and vessel-to-vessel (V2V) links reuse the same frequency band with vessel-to-satellite (V2S) links. With spectrum resource being utilized in terms of time-sliced subcarriers for all links, coordinated link scheduling in terms of subcarrier and time slice allocation is explored. To circumvent challenges brought by network-wide fine-grained time synchronization, the V2S links are dynamically grouped into *clusters* according to the inter-link interference. Then, the V2S link clusters, instead of individual links, are jointly scheduled with U2V and V2V links. By such V2S-link-cluster-based scheduling, successive time slices of each subcarrier could be grouped together and assigned adaptively to each of the V2S link clusters as a whole.

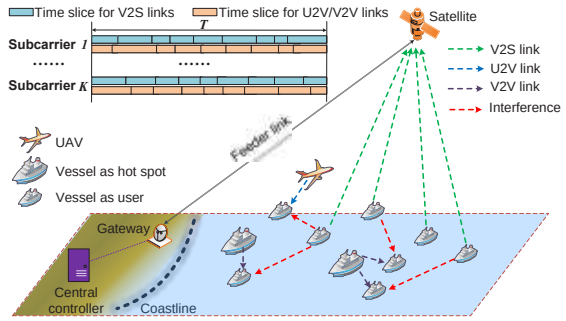

Fig. 1. Illustration of a hybrid satellite-UAV-terrestrial MCN.

With delicately-designed V2S link clusters, fine-grained time-slice-oriented coordination between V2S links and U2V/V2V links could be achieved with coarse time synchronization at time scales much larger than a single time slice. Besides, only large-scale channel state information (CSI) is utilized in the above procedure. Due to the slow varying of large-scale fading, the acquisition of large-scale CSI incurs a much reduced overhead and signaling cost compared to instantaneous CSI [4], [8].

II. System Model and Problem Formulation

A. System Model

Fig. 1 shows a hybrid satellite-UAV-terrestrial MCN. The satellite provides macro coverage for both service and signaling. The UAVs and some of the vessels with spare communication capabilities provide hot-spot access for coverage enhancement. The vessels as users could be served either directly by the satellite or via the UAV/vessel-based hot spots. Assume that there are M UAVs and N vessels. Set $\mathbb{N}_1 = \{1, ..., N_1\}$, $\mathbb{N}_2 = \{N_1+1, ..., N_1+N_2\}$, and $\mathbb{N}_3 = \{N_1+N_2+1, ..., N_1+N_2+N_3\}$, with $N = N_1+N_2+N_3$. N_1 of the vessels, indexed with $n_1 \in \mathbb{N}_1$, are served directly by the satellite in the uplink via V2S links, and N_2 of the vessels, indexed with $n_2 \in \mathbb{N}_2$, are served by the UAVs and the other N_3 vessels, indexed with $n_3 \in \mathbb{N}_3$, in the downlink via U2V and V2V links, with $N_2 \geq M + N_3$. For efficient spectrum utilization, the U2V and V2V links share the same frequency band with the V2S links, coordinated by a central controller.

Suppose that K ($K \leq N_1$) subcarriers, each with a bandwidth of B, are available. In a serving time duration of T, the V2S links serving the N_1 vessels $n_1 \in \mathbb{N}_1$ are scheduled in the subcarriers with time slicing, as illustrated in Fig. 1. The time slicing in each subcarrier could be even or uneven, according to the QoS requirements of the vessels. To avoid collision, at most one V2S link is active in each subcarrier at each specific moment. At the same time, the U2V and V2V links for the N_2 vessels $n_2 \in \mathbb{N}_2$ share the K subcarriers opportunistically. Time slicing is also adopted for the scheduling of the U2V and V2V links. To control interference, at most one U2V or V2V link is scheduled in each subcarrier at each specific moment. Besides, each of the vessels $n_1 \in \mathbb{N}_1$ and $n_2 \in \mathbb{N}_2$ can only be served in one subcarrier at each moment.

For spectrum sharing, the V2S links are firstly grouped into *clusters*, and then jointly scheduled with U2V and V2V links in terms of *link clusters* instead of individual links. With V2S link clusters, the scheduling of the V2S links and that of the U2V and V2V links are only coarsely synchronized at the time scale T, instead of the duration of a single time slice. Due to the downward pointing of the antennas on UAVs for the U2V links, as well as the down tilt of those on the vessels $n_3 \in \mathbb{N}_3$ for the V2V links, the interference from the U2V and V2V links to the V2S links is ignored [4]. The received signal of the V2S and U2V/V2V links can be written as

$$y_{n_1}^{(s)} = R_{n_1}^{(s)} h_{n_1}^{(s,v)} T_{n_1}^{(v)} x_{n_1}^{(v)} + z^{(s)}, \tag{1a}$$

$$y_{n_2}^{(v)} = R_{n_2}^{(v)} h_{n_2}^{(v,uv)} T_{n_2}^{(uv)} x_{n_2}^{(uv)} + \hat{R}_{n_2,\hat{n}_{n_2}}^{(v)} \hat{h}_{n_2,\hat{n}_{n_2}}^{(v,v)} \hat{T}_{n_2,\hat{n}_{n_2}}^{(v)} x_{\hat{n}_{n_2}}^{(v)} + z^{(v)}. \tag{1b}$$

$y_{n_1}^{(s)}$ denotes the received signal at the satellite from vessel n_1, and $y_{n_2}^{(v)}$ is that at vessel n_2 from the UAV or vessel that serves it. $|R_{n_1}^{(s)}|^2$, $h_{n_1}^{(s,v)}$, $|T_{n_1}^{(v)}|^2$, and $x_{n_1}^{(v)}$ are the receive antenna gain, the channel, the transmit antenna gain, and the transmit signal of the V2S link for vessel n_1, respectively, $|R_{n_2}^{(v)}|^2$, $h_{n_2}^{(v,uv)}$, $|T_{n_2}^{(uv)}|^2$, and $x_{n_2}^{(uv)}$ represent those of the U2V/V2V link for vessel n_2, and $|\hat{R}_{n_2,\hat{n}_{n_2}}^{(v)}|^2$, $\hat{h}_{n_2,\hat{n}_{n_2}}^{(v,v)}$, $|\hat{T}_{n_2,\hat{n}_{n_2}}^{(v)}|^2$, and $x_{\hat{n}_{n_2}}^{(v)}$ are those of the interference link from vessel $\hat{n}_{n_2}$ to n_2. $\hat{n}_{n_2} \in \mathbb{N}_1$ is the vessel served by the V2S link that interferes the U2V/V2V link serving vessel n_2. $z^{(s)}$ and $z^{(v)}$ denote the white Gaussian noise at the satellite and the vessels, respectively.

A composite channel model consisting of large-scale fading and small-scale fading, i.e., $h = \sqrt{l}w$, is adopted for all the links [4], [9]. l denotes the large-scale fading, and w is the small-scale fading, with $\mathbf{E}[|w|^2] = 1$. $\mathbf{E}$ is the expectation operator. The large-scale fading is mainly caused by path loss, and the small-scale fading could be Rayleigh or Rician [9]. To save cost, only large-scale CSI of the links is utilized for spectrum sharing. Without loss of generality, we assume the large-scale CSI of each link is the same in different subcarriers.

B. Problem Formulation

Let C_{V2S}, $1 \leq C_{V2S} \leq N_1$, denote the number of V2S link clusters. Set $\mathbb{K} = \{1, ..., K\}$ and $\mathbb{C} = \{1, ..., C_{V2S}\}$. Let $\delta_{n_1,c}$, $n_1 \in \mathbb{N}_1, c \in \mathbb{C}$, denote the cluster indicators for the V2S links. If the V2S link for vessel n_1 is in cluster c, $\delta_{n_1,c} = 1$, and otherwise $\delta_{n_1,c} = 0$. Further, let $\eta_{k,c}$ and θ_{k,n_2}, $k \in \mathbb{K}$, $c \in \mathbb{C}$, $n_2 \in \mathbb{N}_2$, represent the scheduling indicators for the V2S links clusters and the U2V/V2V links, respectively. If some link in the V2S link cluster c is scheduled in subcarrier k, then $\eta_{k,c} = 1$, and otherwise $\eta_{k,c} = 0$. Similarly, if the U2V/V2V link for vessel n_2 is scheduled in subcarrier k, then $\theta_{k,n_2} = 1$, and otherwise $\theta_{k,n_2} = 0$.

When only the large-scale CSI is available, the transmission rates of the V2S and U2V/V2V links can be expressed as

$$\mathcal{R}_{n_1} = B\mathbf{E}_w \log_2\left(1 + \frac{|R_{n_1}^{(s)}|^2 l_{n_1}^{(s,v)} |w_{n_1}^{(s,v)}|^2 |T_{n_1}^{(v)}|^2 p_{n_1}^{(v)}}{{\sigma^{(s)}}^2}\right), \tag{2}$$

$$\mathcal{R}_{n_2} = B\mathbf{E}_w \log_2(1 + \frac{|R_{n_2}^{(v)}|^2 l_{n_2}^{(v,uv)} |w_{n_2}^{(v,uv)}|^2 |T_{n_2}^{(uv)}|^2 p_{n_2}^{(uv)}}{\mathfrak{I}_{n_2} + {\sigma^{(v)}}^2}), \tag{3}$$

in which $\mathbf{E}_w$ denotes the expectation operator with respect to the small-scale channel fading. ${\sigma^{(s)}}^2$ and ${\sigma^{(v)}}^2$ are the power of $z^{(s)}$ and $z^{(v)}$, respectively. $\mathfrak{I}_{n_2}$ is the interference suffered by the U2V/V2V link for vessel n_2, and

$$\begin{aligned}\mathfrak{I}_{n_2} &= \mathbf{E}_w \left[|\hat{R}_{n_2,\hat{n}_{n_2}}^{(v)}|^2 \hat{l}_{n_2,\hat{n}_{n_2}}^{(v,v)} |\hat{w}_{n_2,\hat{n}_{n_2}}^{(v,v)}|^2 |\hat{T}_{n_2,\hat{n}_{n_2}}^{(v)}|^2 p_{\hat{n}_{n_2}}^{(v)} \right] \\ &= |\hat{R}_{n_2,\hat{n}_{n_2}}^{(v)}|^2 \hat{l}_{n_2,\hat{n}_{n_2}}^{(v,v)} |\hat{T}_{n_2,\hat{n}_{n_2}}^{(v)}|^2 p_{\hat{n}_{n_2}}^{(v)}.\end{aligned} \tag{4}$$

$p_{n_1}^{(v)} = \mathbf{E}[|x_{n_1}^{(v)}|^2]$, $p_{n_2}^{(uv)} = \mathbf{E}[|x_{n_2}^{(uv)}|^2]$, and $p_{\hat{n}_{n_2}}^{(v)} = \mathbf{E}[|x_{\hat{n}_{n_2}}^{(v)}|^2]$ are the transmit power of the corresponding links. When the U2V/V2V link for the vessel n_2 is scheduled in subcarrier k, i.e., $\theta_{k,n_2} = 1$, it can be determined that

$$\hat{n}_{n_2} \in \mathfrak{N}_k = \{n_1 | \eta_{k,c} = 1, \delta_{n_1,c} = 1, c \in \mathbb{C}, n_1 \in \mathbb{N}_1\}. \tag{5}$$

Correspondingly, when the U2V/V2V link for the vessel n_2 is scheduled in subcarrier k, we introduce a *worst-case* model to depict the interference and replace $\mathfrak{I}_{n_2}$ by its upper bounds $\tilde{\mathfrak{I}}_{n_2,k}$ in the spectrum sharing optimization, with

$$\tilde{\mathfrak{I}}_{n_2,k} = \begin{cases} \max\limits_{n_1 \in \mathfrak{N}_k} |\hat{R}_{n_2,n_1}^{(v)}|^2 \hat{l}_{n_2,n_1}^{(v,v)} |\hat{T}_{n_2,n_1}^{(v)}|^2 p_{n_1}^{(v)}, & \mathfrak{N}_k \neq \phi, \\ 0, & \mathfrak{N}_k = \phi. \end{cases} \tag{6}$$

Further, $\mathcal{R}_{n_2}$ given by (3) is replaced by its lower bound as

$$\underline{\mathcal{R}}_{n_2,k} = B\mathbf{E}_w \log_2(1 + \frac{|R_{n_2}^{(v)}|^2 l_{n_2}^{(v,uv)} |w_{n_2}^{(v,uv)}|^2 |T_{n_2}^{(uv)}|^2 p_{n_2}^{(uv)}}{\bar{\mathfrak{I}}_{n_2,k} + {\sigma^{(v)}}^2}). \tag{7}$$

To guarantee the QoS for the vessels $n_1 \in \mathbb{N}_1$ and $n_2 \in \mathbb{N}_2$, we assume that a minimum data volume $V_n^{QoS} > 0$, $n \in \mathbb{N}_1 \cup \mathbb{N}_2$, is required to be transmitted for vessel n within the time duration of T. With a serving time of $\tau_{n,k}$ for vessel $n \in \mathbb{N}_1 \cup \mathbb{N}_2$ in subcarrier k, the total energy consumption of the MCN for transmission can be written as

$$E_{total} = \sum_{n_1=1}^{N_1} p_{n_1}^{(v)} \sum_{k=1}^{K} \tau_{n_1,k} + \sum_{n_2=N_1+1}^{N_1+N_2} p_{n_2}^{(uv)} \sum_{k=1}^{K} \tau_{n_2,k}. \tag{8}$$

With the target of minimizing E_{total} while guaranteeing the QoS for the vessels, the spectrum sharing problem is formulated as (9), where $\mathfrak{k}_{n_1} = \{k | \delta_{n_1,c} = 1, \eta_{k,c} = 1, c \in \mathbb{C}, k \in \mathbb{K}\}$. (9b) and (9c) are for the QoS guarantees for the vessels $n_1 \in \mathbb{N}_1$ and $n_2 \in \mathbb{N}_2$, (9d) is to assure that each of the vessels can only be served in one subcarrier at each moment, and (9e) indicates that at most one V2S link and one U2V/V2V link are active in each subcarrier. Note that $\underline{\mathcal{R}}_{n_2,k}$ is a function of $\delta_{n_1,c}$ and $\eta_{k,c}$, as shown in (5)–(7).

$$\min_{\{C_{V2S}, \delta_{n_1,c}, \eta_{k,c}, \theta_{k,n_2}, \tau_{n_1,k}, \tau_{n_2,k}\}} E_{total} \tag{9a}$$

$$s.t.\ \ \mathcal{R}_{n_1} \sum_{k \in \mathfrak{k}_{n_1}} \tau_{n_1,k} \geq V_{n_1}^{QoS}, n_1 \in \mathbb{N}_1, \tag{9b}$$

$$\sum_{k=1}^{K} \theta_{k,n_2} \underline{\mathcal{R}}_{n_2,k} \tau_{n_2,k} \geq V_{n_2}^{QoS}, n_2 \in \mathbb{N}_2, \tag{9c}$$

$$\sum_{k=1}^{K} \tau_{n_1,k} \leq T,\ \sum_{k=1}^{K} \tau_{n_2,k} \leq T, \forall n_1, n_2, \tag{9d}$$

$$\sum_{n_1=1}^{N_1} \tau_{n_1,k} \leq T,\ \sum_{n_2=N_1+1}^{N_1+N_2} \tau_{n_2,k} \leq T, \forall k, \tag{9e}$$

$$1 \leq C_{V2S} \leq N_1, \tau_{n_1,k} \geq 0,\ \tau_{n_2,k} \geq 0, \forall k, n_1, n_2, \tag{9f}$$

$$\delta_{n_1,c} \in \{0,1\}, \eta_{k,c} \in \{0,1\}, \theta_{k,n_2} \in \{0,1\}, \forall n_1, n_2, k, c, \tag{9g}$$

III. Link-Cluster-based Spectrum Sharing

It can be seen from (9) and (5)-(7) that the formulated problem is a complicated NP-hard mixed integer programming (MIP) problem [11], and it is rather challenging to solve. In the following, the V2S links are firstly clustered, and then a suboptimal spectrum sharing scheme is proposed.

A. V2S Link Clustering

Consistent with the context that spectrum sharing between links is needed, the MCN is supposed to be in a full-load state for the V2S links, i.e., $(\sum_{n_1=1}^{N_1} V_{n_1}^{QoS}/R_{n_1})/T = K$. With the worst-case interference model in (6), it can be inferred that the V2S links could be grouped into $C_{V2S} = K$ clusters for interference coordination. Besides, to satisfy the QoS requirements of the vessel users $n_1 \in \mathbb{N}_1$, a single V2S link could belong to different V2S link clusters simultaneously.

Intuitively, the V2S links that may cause similar interference to the U2V and V2V links should be grouped together, so that the diversity in interference could be reserved and opportunistically utilized for spectrum sharing. Thus, to carry out V2S link clustering, we define a feature vector for each V2S link as

$$\mathcal{F}_{n_1} = \left[\frac{V_{N_1+1}^{QoS}}{\hat{\mathcal{R}}_{N_1+1}^{(n_1)}} p_{n_2}^{(uv)}, ..., \frac{V_{N_1+N_2}^{QoS}}{\hat{\mathcal{R}}_{N_1+N_2}^{(n_1)}} p_{n_2}^{(uv)} \right], \tag{10}$$

where $\hat{\mathcal{R}}_{n_2}^{(n_1)} = B\mathbf{E}_w[\log_2(1 + \gamma_{n_2}^{(n_1)})]$ with $\gamma_{n_2}^{(n_1)} = (|R_{n_2}^{(v)}|^2 l_{n_2}^{(v,uv)} |w_{n_2}^{(v,uv)}|^2 |T_{n_2}^{(uv)}|^2 p_{n_2}^{(uv)})/(\hat{\mathfrak{I}}_{n_2}^{(n_1)} + {\sigma^{(v)}}^2)$, is the transmission rate of the U2V/V2V link for vessel n_2 when it is scheduled in the same subcarrier with the V2S link for vessel n_1, and $\hat{\mathfrak{I}}_{n_2}^{(n_1)} = |\hat{R}_{n_2,n_1}^{(v)}|^2 \hat{l}_{n_2,n_1}^{(v,v)} |\hat{T}_{n_2,n_1}^{(v)}|^2 p_{n_1}^{(v)}$. Further, the similarity between the V2S link for vessel $n_1 \in \mathbb{N}_1$ and that for $n_1' \in \mathbb{N}_1$ is measured by

$$\mathcal{D}_{n_1,n_1'} = ||\mathcal{F}_{n_1} - \mathcal{F}_{n_1'}||_1 = \sum_{n_2 \in \mathbb{N}_2} \left| \frac{V_{n_2}^{QoS}}{\hat{\mathcal{R}}_{n_2}^{(n_1)}} - \frac{V_{n_2}^{QoS}}{\hat{\mathcal{R}}_{n_2}^{(n_1')}} \right| p_{n_2}^{(uv)}. \tag{11}$$

Algorithm 1 Proposed V2S link clustering algorithm

Set $C_{V2S}=K$, and allocate subcarrier k to the V2S link cluster $c=k$, $k=1,...,K$.
Select K feature vectors of the V2S links, i.e., $\mathcal{F}_{\acute{n}_i}$, $i=1...,K$, $\acute{n}_i \in \mathbb{N}_1$, as the initial centers for the V2S link clusters, i.e., $\mathfrak{c}_j$, $j=1,...,K$.
Let $\Phi_c, c=1,...,C_{V2S}$, represent the set of the V2S links in the C_{V2S} clusters, respectively.
Set $\delta=10^{-2}$, $\mathcal{D}_0^{sum}=0$, $\mathcal{D}_1^{sum}=\sum_{n_1=1}^{N_1}||\mathcal{F}_{n_1}||_1$.
while $|\mathcal{D}_0^{sum}-\mathcal{D}_1^{sum}|/\mathcal{D}_1^{sum}>\delta$ **do**
  Set $\mathcal{D}_0^{sum}=\mathcal{D}_1^{sum}$ and $\mathcal{D}_1^{sum}=0$.
  for $n_1=1,...,N_1$ **do**
    for $j=1,...,K$ **do**
      Calculate the distance between the V2S link for vessel n_1 and the center of the jth cluster based on (11), and denote it as $\hat{\mathcal{D}}_{n_1,j}=||\mathcal{F}_{n_1}-\mathfrak{c}_j||_1$.
    end for
  end for
  Let $\bar{\Phi}$ denote the set of the V2S links that wait to be clustered, and initialize $\bar{\Phi}=\{1,...,N_1\}$ and $\Phi_j=\phi, j=1,...,K$.
  Initialize the serving time for all the vessels n_1 in the K subcarriers as $\tau_{n_1,k}=0$, $n_1\in\mathbb{N}_1$, $k\in\mathbb{K}$.
  while $\bar{\Phi}\neq\phi$ **do**
    Find $\{n_1^*,j^*\}=\arg\min_{n_1,j}\hat{\mathcal{D}}_{n_1,j}$, and calculate the unoccupied time in the subcarrier allocated to the V2S cluster j^*, i.e., $\Delta t_{j^*}=T-\sum_{n_1=1}^{N_1}\tau_{n_1,j^*}$, to judge whether it is *unsaturated for the QoS guarantees*.
    if $\Delta t_{j^*}>0$ **then**
      Cluster the V2S link for vessel n_1^* into cluster j^*, and set $\Phi_{j^*}:=\Phi_{j^*}\cup\{n_1^*\}$, $\hat{\mathcal{D}}_{n_1^*,j^*}=+\infty$, and $\mathcal{D}_1^{sum}:=\mathcal{D}_1^{sum}+||\mathcal{F}_{n_1^*}-\mathfrak{c}_{j^*}||_1$.
      Calculate the serving time that could be allocated to the V2S link for vessel n_1^* in cluster j^*, i.e., $\tau_{n_1^*,j^*}:=\min\{V_{n_1^*}^{QoS}/\mathcal{R}_{n_1^*}-\sum_{k=1}^{K}\tau_{n_1^*,k},\Delta t_{j^*}\}$.
      if $\sum_{k=1}^{K}\tau_{n_1^*,k}=V_{n_1^*}^{QoS}/\mathcal{R}_{n_1^*}$ **then**
        Set $\bar{\Phi}:=\bar{\Phi}\setminus\{n_1^*\}$.
      end if
    end if
  end while
  Update the centers for the K V2S link clusters as $\mathfrak{c}_j=\frac{1}{|\Phi_j|}\sum_{n_1\in\Phi_j}\mathcal{F}_{n_1}$, $j=1,...,K$.
end while

Note that $\mathcal{F}_{n_1}$ and $\mathcal{D}_{n_1,n_1'}$ are defined based on the target utility of (9), i.e., the energy consumption of the MCN.

With $\mathcal{F}_{n_1}$ and $\mathcal{D}_{n_1,n_1'}$, we propose a V2S link clustering algorithm based on a modified K-means method [12], as illustrated in Algorithm 1. The fundamental idea is grouping the V2S links with close distance between their feature vectors into one cluster. Specially, the QoS requirement of the V2S links shown in (9b) is also considered in clustering. The main steps of Algorithm 1 are as follows.

1) Set $C_{V2S}=K$, and select K feature vectors of the V2S links as the initial centers of the clusters.
2) Calculate the distance between the feature vectors of all the V2S links and the centers of the K V2S link clusters, and following the *smallest-distance-first* principle, group each V2S link into the cluster that is *unsaturated for the QoS guarantees* and has the center that is closest to the feature vector of the V2S link.
3) Update the center of each V2S link cluster, and repeat 2)-3) until convergence.

Algorithm 2 Proposed spectrum sharing scheme for the MCN

Let $\hat{\mathbb{S}}=\{\hat{C}_{V2S},\hat{\delta}_{n_1,c},\hat{\eta}_{k,c},\hat{\theta}_{k,n_2},\hat{\tau}_{n_1,k},\hat{\tau}_{n_2,k}\,|\,c\in\hat{\mathbb{C}},n_1\in\mathbb{N}_1,n_2\in\mathbb{N}_2,k\in\mathbb{K}\}$ denote a solution for the problem in (9).
Randomly select K V2S links as the initial centers for the K V2S link clusters, i.e., $\mathcal{F}_{\acute{n}_i}$, $i=1...,K$, $\acute{n}_i\in\mathbb{N}_1$.
Form K V2S link clusters via Algorithm 1, and get $\hat{C}_{V2S}=K$, $\hat{\tau}_{n_1,k}$, $\hat{\delta}_{n_1,c}$, and $\hat{\eta}_{k,c}$, $n_1\in\mathbb{N}_1$, $k\in\mathbb{K}$, $c\in\hat{\mathbb{C}}$.
Schedule the U2V and V2V links in the K subcarriers by solving a linear programming problem derived from (9), and get $\hat{\tau}_{n_2,k}$ and $\hat{\theta}_{k,n_2}$, $n_2\in\mathbb{N}_2$, $k\in\mathbb{K}$.

The *smallest-distance-first* principle assures that the V2S links with a smaller distance to the cluster centers are always grouped first. Besides, a cluster c is judged as being *unsaturated for the QoS guarantees* when the subcarrier allocated to it, i.e., the subcarrier $k=c$, is not fully occupied in the time duration of T, i.e., $\sum_{n_1=1}^{N_1}\tau_{n_1,k}<T$. Note that the V2S link for the vessel n_1 may remain waiting to be clustered, i.e., $n_1\in\bar{\Phi}$, even if it has already been clustered into some of the K clusters, until the required time for the transmission of $V_{n_1}^{QoS}$, i.e., $V_{n_1}^{QoS}/\mathcal{R}_{n_1}$, is satisfied. That is each V2S link is allowed belong to multiple clusters simultaneously. Furthermore, $\tau_{n_1,k}$, $n_1\in\mathbb{N}_1$, $k\in\mathbb{K}$, are also obtained at the end of Algorithm 1.

B. Proposed Spectrum Sharing Scheme

Based on the V2S link clustering algorithm, we propose a suboptimal spectrum sharing scheme for the hybrid MCN, as shown in Algorithm 2.

By Algorithm 2, a solution can derived for (9) as $\hat{\mathbb{S}}=\{\hat{C}_{V2S},\hat{\delta}_{n_1,c},\hat{\eta}_{k,c},\hat{\theta}_{k,n_2},\hat{\tau}_{n_1,k},\hat{\tau}_{n_2,k}\,|\,c\in\hat{\mathbb{C}},n_1\in\mathbb{N}_1,n_2\in\mathbb{N}_2,k\in\mathbb{K}\}$, with $\hat{\mathbb{C}}=\{1,...,\hat{C}_{V2S}\}$ and $\hat{C}_{V2S}=K$. Specifically, after K V2S link clusters $\Phi_c, c\in\hat{\mathbb{C}}$, and $\hat{\tau}_{n_1,k}$, $n_1\in\mathbb{N}_1$, $k\in\mathbb{K}$, are obtained via Algorithm 1, we can get $\hat{\delta}_{n_1,c}$ and $\hat{\eta}_{k,c}$, $n_1\in\mathbb{N}_1$, $c\in\hat{\mathbb{C}}$, $k\in\mathbb{K}$, as

$$\hat{\delta}_{n_1,c}=\begin{cases}1, & n_1\in\Phi_c,\\ 0, & n_1\notin\Phi_c,\end{cases} \tag{12}$$

$$\hat{\eta}_{k,c}=\begin{cases}1, & k=c,\\ 0, & k\neq c.\end{cases} \tag{13}$$

Then based on the observation that $\theta_{k,n_2}=1$ if $\tau_{n_2,k}>0$ and $\theta_{k,n_2}=0$ if $\tau_{n_2,k}=0$, $\hat{\tau}_{n_2,k}$, $n_2\in\mathbb{N}_2$, $k\in\mathbb{K}$, can be obtained by solving a linear programming problem derived from (9), in which $C_{V2S},\delta_{n_1,c},\eta_{k,c},\tau_{n_1,k}$ are replaced by $\hat{C}_{V2S},\hat{\delta}_{n_1,c},\hat{\eta}_{k,c},\hat{\tau}_{n_1,k}$ and all θ_{k,n_2} are removed. Finally, we have $\hat{\theta}_{k,n_2}=1$ if $\hat{\tau}_{n_2,k}>0$ and $\hat{\theta}_{k,n_2}=0$ if $\hat{\tau}_{n_2,k}=0$.

IV. Simulations and Discussions

A. Settings for the hybrid MCN

In the simulations, we consider a hybrid satellite-UAV-terrestrial MCN with $M=5$, $N=205$, $N_1=100$, $N_2=100$, $N_3=5$, $K=10$, $f_c=2$GHz, and $B=1$MHz. Suppose that the satellite is deployed in an orbit with an altitude of 1000km, and the UAVs are deployed at the height of 200m. The UAVs

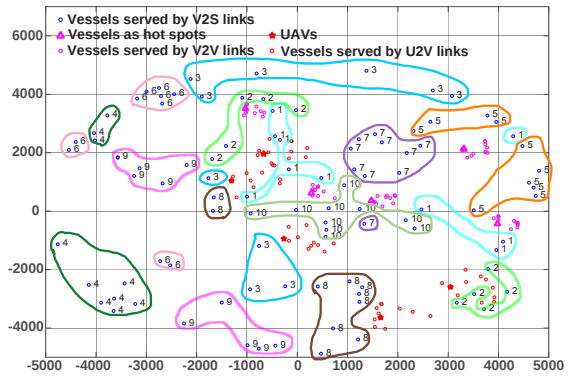

Fig. 2. A random topology for the hybrid MCN with V2S link clusters.

and the vessels are all assumed to be randomly distributed in a circular area $\mathcal{A}$ with a radius of 5km within the coverage area of the satellite. Each UAV serves 10 of the vessels $n_2 \in \mathbb{N}_2$ located in the circular area of a radius of 1000m around it, and each vessel $n_3 \in \mathbb{N}_3$ serves 10 of the vessels $n_2 \in \mathbb{N}_2$ located in the circular area of a radius of 500m around it. The serving time duration is set as $T = 10$s, during which the sub-satellite point is assumed to be located at $(125°E, 10°N)$, and the center of $\mathcal{A}$ is at $(110°E, 10°N)$.

A random topology for the hybrid MCN, with no indication of the position of the satellite, is shown in Fig. 2. The V2S link clusters formed based on Algorithm 1 are also presented. Different V2S link clusters are indicated by closed lines with different colors. The V2S links for vessels $n_1 \in \mathbb{N}_1$ circled by the line/lines with the same color belong to the same cluster. The number next to each of the vessel $n_1 \in \mathbb{N}_1$ indicates the index of the cluster its V2S link belongs to.

All the vessels $n_1 \in \mathbb{N}_1$ are supposed to be equipped with an antenna array with an aperture of 0.5m, the pattern of which follows the recommendation ITU-R S.465. Correspondingly, we have $|T_{n_1}^{(v)}|^2 = 18.5$dBi, and $|\hat{T}_{n_2,\hat{n}_{n_2}}^{(v)}|^2$ is dependent on the off-axis angle. Each vessel $n_2 \in \mathbb{N}_2$ is assumed to be equipped with a single omni antenna, and thus $|R_{n_2}^{(v)}|^2$ and $|\hat{R}_{n_2,\hat{n}_{n_2}}^{(v)}|^2$ are all 0dBi. Set $|R_{n_1}^{(s)}|^2 = 25$dBi, $|T_{n_2}^{(uv)}|^2 = 5$dBi, $p_{n_1}^{(v)} = 30$dBm for all $n_1 \in \mathbb{N}_1$, $p_{n_2}^{(uv)} \in [0, 20]$dBm for all $n_2 \in \mathbb{N}_2$, and ${\sigma^{(s)}}^2 = {\sigma^{(v)}}^2 = -114$dBm. The small-scale fading of the V2V links is assumed to follow the Rayleigh distribution, and that of the V2S and the U2V links is assumed to be Rician distributed, the K-factors of which are respectively set as 0.3 and 0.5. The large-scale fading of the V2S links is set as the free-space path loss with an extra atmospheric loss of 1dB, and that of the U2V and V2V links are obtained based on the channel models proposed in [13] and [14], respectively. The channel parameters for the U2V links are set as $a = 5.0188$, $b = 0.3511$, $\eta_{LOS} = 2.3$, and $\eta_{NLOS} = 34$ [13]. The antenna height of the vessels $n_1 \in \mathbb{N}_1$ and $n_2 \in \mathbb{N}_2$ is set as 10m, and that of the vessels $n_3 \in \mathbb{N}_3$ is set as 30m [14].

Without loss of generality, the QoS of the vessels is set in proportion to the transmission rates of the V2S, U2V and V2V links, i.e., $V_{n_1}^{QoS} = (KT/N_1)\mathcal{R}_{n_1}$ and $V_{n_2}^{QoS} = \min_{n_1} \hat{\mathcal{R}}_{n_2}^{(n_1)} + \alpha(\max_{n_1} \hat{\mathcal{R}}_{n_2}^{(n_1)} - \min_{n_1} \hat{\mathcal{R}}_{n_2}^{(n_1)})$, $n_1 \in \mathbb{N}_1$, $n_2 \in \mathbb{N}_2$. Note that larger α indicates more stringent QoS for the vessels n_2, and the problem (9) may be infeasible when $\alpha \in [0, 1)$ is too large for some MCN topologies. In the simulations, only feasible MCN topologies are considered for the selected α.

B. Performance of the Proposed Spectrum Sharing Scheme

Note that with fixed $p_{n_1}^{(v)}$ and $\sum_{n_1=1}^{N_1}\sum_{k=1}^{K}\tau_{n_1,k} = \sum_{n_1=1}^{N_1} KT/N_1 = KT$, the energy consumption of the V2S links, i.e., $\sum_{n_1=1}^{N_1} p_{n_1}^{(v)}\sum_{k=1}^{K}\tau_{n_1,k} = \sum_{n_1=1}^{N_1} p_{n_1}^{(v)} KT/N_1$, is a constant. Thus, only the energy consumption of the U2V and V2V links, i.e., $\hat{E}_{total} = \sum_{n_2=N_1+1}^{N_1+N_2} p_{n_2}^{(uv)}\sum_{k=1}^{K}\tau_{n_2,k}$, is demonstrated in the following.

The energy consumption with the proposed spectrum sharing scheme for $\alpha = 0, 2/3$ and $\mathcal{L}_s = (125°E, 10°N)$ is shown in Figs. 3–4. The energy consumption in Figs. 3–4 is obtained by averaging over 10 random topologies of the MCN. For comparison, performance of three benchmark schemes are also shown, which are denoted as the optimal scheme, Random-I scheme, and Random-II scheme, respectively. The optimal scheme is derived based on optimal spectrum sharing among individual V2S, U2V and V2S links with perfect time-slice-based network-wide time synchronization, which, however, is not achievable in practice. By considering each V2S link individually and with perfect fine-grained time synchronization, the optimal scheme can be obtained by linear programming. The Random-I scheme is obtained based on random clustering of the V2S links and optimal scheduling of the U2V and V2V links based on randomly-formed V2S link clusters. The Random-II scheme is a completely random scheme with both random clustering, of the V2S links, and random scheduling, of the U2V and V2V links. Note that in the Random-II scheme, the QoS is assured by adjusting the serving time for the U2V and V2V links, and when $T = 10$s is not enough, the serving time is extended until the required $V_{n_2}^{QoS}$ is transmitted. Further, when the Random-I scheme is not feasible for the QoS guarantees, the result achieved by the Random-II scheme is adopted instead.

It is shown by Figs. 3–4 that the proposed scheme achieves a significant performance gain in reducing the energy consumption compared to the Random-I and Random-II schemes, especially for large α. Furthermore, the proposed scheme has only a small performance gap from the lower bound achieved by the optimal spectrum sharing with the assumption of perfect fine-grained network-wide time synchronization. Note that the sudden turning point on the curve of the Random-I scheme in Fig. 4 is due to the variation of the feasibility of the scheme in ensuring the QoS for the U2V/V2V links along with the SNR. In some of the 10 topologies, the Random-I scheme is infeasible in the lower SNR region and feasible in the higher SNR region. Besides, since the transmission rate of the U2V/V2V links given in (7) is more sensitive to interference at low transmit power, a larger performance gain is observed in the low SNR region for the proposed scheme.

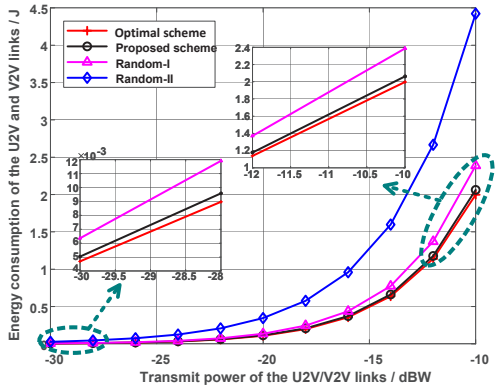

Fig. 3. Energy consumption for $\alpha = 0$, $\mathcal{L}_s = (125°E, 10°N)$.

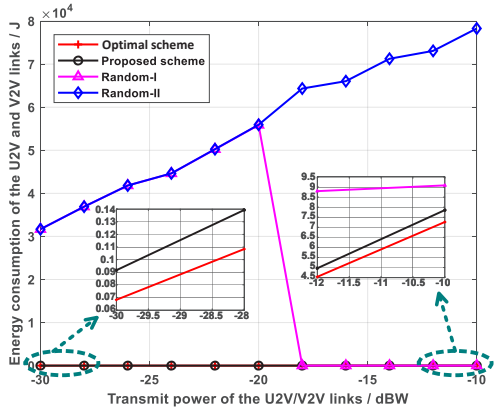

Fig. 4. Energy consumption for $\alpha = 2/3$, $\mathcal{L}_s = (125°E, 10°N)$.

The spectrum efficiency achieved by the proposed scheme, the Random-I scheme, and the Random-II scheme for $2/3$, $\mathcal{L}_s = (125°E, 10°N)$ is shown in Fig. 5. Note that the spectrum efficiency is calculated based on V_n^{QoS}, $n = n_1$ or n_2, and the practically-occupied transmission time by the links. The spectrum efficiency with only the V2S links is also presented for comparison. A prominent improvement in the spectrum efficiency is observed with the proposed scheme.

V. Conclusions

A link-cluster-based spectrum sharing scheme has been investigated for a hybrid satellite-UAV-terrestrial MCN based on large-scale CSI. With the target of minimizing the energy consumption, an NP-hard MIP problem is formulated. With the help of a novel V2S link clustering algorithm, a suboptimal spectrum sharing scheme is proposed, by which time-slice-oriented spectrum sharing can be carried out with coarse time synchronization at time scales much larger than single time slices. With the advantages of both low complexity and high flexibility, the proposed scheme is quite promising for practical applications.

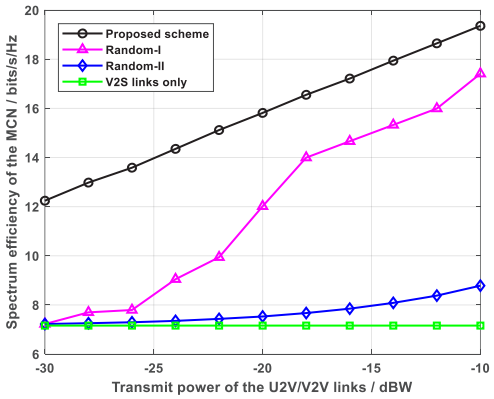

Fig. 5. Spectrum Efficiency for $\alpha = 2/3$, $\mathcal{L}_s = (125°E, 10°N)$.

References

[1] C.-X. Wang, X. You, X. Gao, et al., “On the road to 6G: Visions, requirements, key technologies and testbeds,” *IEEE Communications Surveys & Tutorials*, vol. 25, no. 2, pp. 905–974, Feb. 2023.

[2] W. Feng, Y. Wang, Y. Chen, N. Ge, and C.-X. Wang, “Structured Satellite-UAV-Terrestrial Networks for 6G Internet of Things,” *IEEE Network*, doi: 10.1109/MNET.2024.3380052, 2024.

[3] G. Varrall, “5G and satellite spectrum, standards, and scale”, *Artech House*, 2018.

[4] Y. Wang, and Z. Lu, “Coordinated resource allocation for satellite-terrestrial coexistence based on radio maps,” *China Communications*, Vol. 15, No. 3, pp. 149–156, Mar. 2018.

[5] P. K. Sharma, P. K. Upadhyay, D. B. da Costa, P. S. Bithas, and A. G. Kanatas, “Performance analysis of overlay spectrum sharing in hybrid satellite-terrestrial systems with secondary network selection,” *IEEE Transactions on Wireless Communications*, vol. 16, no. 10, pp. 6586–6601, Oct. 2017.

[6] Z. Lin, M. Lin, J. Wang, T. Cola, and J. Wang, “Joint beamforming and power allocation for satellite-terrestrial integrated networks with non-Orthogonal multiple access,” *IEEE Journal of Selected Topics in Signal Processing*, vol. 13, no. 3, pp. 657–670, Jun. 2019.

[7] F. Pervez, L. Zhao, and C. Yang, “Joint user association, power optimization and trajectory control in an integrated satellite-aerial-terrestrial network,” *IEEE Transactions on Wireless Communications*, vol. 21, no. 5, pp. 3279–3290, May 2022.

[8] Y. Ruan, Y. Li, C.-X. Wang, R. Zhang, and H. Zhang, “Energy efficient power allocation for delay constrained cognitive satellite terrestrial networks under interference constraints,” *IEEE Transactions on Wireless Communications*, vol. 18, no. 10, pp. 4957–4969, Oct. 2019.

[9] S. R. Saunders, A. Aragon-Zavala, “Antennas and propagation for wireless communication systems – second edition,” *John Wiley & Sons, Ltd*, 2007.

[10] Radio Communication Sector of International Telecommunication Union (ITU-R), “Propagation data required for the design of earth-space land mobile telecommunication systems”, *Recommendation ITU-R P.681-6*, 2019.

[11] W. Feng, Y. Wang, D. Lin, N. Ge, J. Lu, and S. Li, “When mmWave communications meet network densification: a scalable interference coordination perspective,” *IEEE Journal on Selected Areas in Communications*, vol. 35, no. 7, pp. 1459-1471, Jul. 2017.

[12] G. James, D. Witten, T. Hastie, and R. Tibshirani, “An introduction to statistical learning,” *Springer Berlin Heid*, 2022.

[13] A. Al-Hourani, S. Kandeepan, and S. Lardner, “Optimal LAP altitude for maximum coverage,” *IEEE Wireless Communications Letters*, vol. 3, no. 6, pp. 569–572, Dec. 2014.

[14] S. Jo and W. Shim, “LTE-maritime: high-speed maritime wireless communication based on LTE technology,” *IEEE Access*, vol. 7, pp. 53172–53181, 2019.

基于特征金字塔卷积神经网络的高分辨率遥感影像多尺度建筑物实例提取框架

陈鼎元[①②]，钟燕飞[②]，王超怡[①]，宋慧娜[①]，宋朝晖[①]

[①] 杭州电子科技大学空间信息研究院，杭州，310018

[②] 武汉大学测绘遥感信息工程国家重点实验室，武汉，430079

摘　要：基于高分辨率遥感影像进行建筑物提取已经被广泛应用于自动化测绘。近年来，实例分割算法引入到建筑物提取，通过先检测后分割的思路提取建筑物实例掩膜，相比于其他算法可以同时统计建筑物个数和面积。但在建筑物实例提取中，存在以下挑战：1）单幅遥感影像中存在多尺度的建筑物；2）相邻建筑物彼此遮挡导致无法区分。为了解决上述问题，本文提出特征金字塔卷积神经网络建筑实例提取框架。关于多尺度问题，构建特征金字塔卷积神经子网络，利用自底向上和自顶向下联合的多尺度特征来描述不同尺度的目标；关于遮挡问题，构建多尺度目标感知实例提取子网络，引入多尺度注意力机制来感知目标，提高模型的分辨能力，从而有效区分邻近建筑物。结果显示该模型具有良好的性能并在多尺度建筑物提取上有较好的鲁棒性。为验证模型的实用性，本文还将提出的方法应用于常州市建筑物提取，实验结果表明该模型在实际场景是有效的。

关键词：深度学习；实例分割；多尺度建筑物提取；高分辨率遥感影像

Feature Pyramid Convolution Neural Network Based Multi-Scale Building Extraction Framework in High Resolution Remote Sensing Imagery

Dingyuan Chen[①②], Yanfei Zhong[②], Huina Song[①], Zhaohui Song[①]

[①]Space Information Research Institute, Hangzhou Dianzi University, Hangzhou, 310018, P. R. China

[②]State Key Laboratory of Information Engineering in Surveying, Mapping and Remote Sensing, Wuhan University, Wuhan, 430079, P. R. China

Abstract: Building extraction based on high-resolution remote sensing imagery has been widely used in automatic surveying and mapping. Recently, the instance segmentation algorithm has been introduced to the building extraction, which extracts the building instance mask in a detection before segmentation way. Compared with other algorithms, it can calculate the number and area of buildings simultaneously. In building instance extraction, there are some challenges: 1) buildings with various scales exist in the imagery; 2) occlusion by other adjacent buildings. In this paper, to solve these problems, we propose a feature pyramid Convolution Neural

通讯作者：宋朝晖 E-mail：songzh@hdu.edu.cn

Network (CNN) building instance extraction framework for high spatial resolution remote sensing imagery. In order to solve the multi-scale problem, a feature pyramid CNN is proposed, which describes multi-scale objects by combining multi-scale features from both the bottom-up and top-down architectures. In order to solve the occlusion problem, a multi-scale object-aware instance proposal network is proposed. It introduces the multi-scale attention mechanism to aware objects as well as to improve the performance of the network, which effectively distinguishes neighbor buildings. The experiments conducted on a self-annotated dataset and two public datasets show that the proposed method can achieve an excellent performance and shows great robustness at different scales. To verify the practicality of the proposed model, it is applied to the building extraction in Changzhou city. The experimental results show that the model performs well in real applications.

Key words: Deep learning; instance segmentation; multiscale building extraction; high-resolution imagery

1 引言

随着 IKONOS、Worldview、国产的资源三号和高分一/二号等高分辨率遥感卫星影像的大量获取，基于高分辨率遥感影像进行精细地物感知和认知越来越普及。海量遥感数据中，地物类别相当丰富。遥感数据体系中，道路作为系统的骨架，建筑物是血肉，在地物要素中所占比重非常大。高分辨率遥感数据支持精细的建筑物语义信息表达，为基础测绘工作、地理国情监测、城市规划等相关部门精细化制图提供了数据基础。其中，本文选取常州市作为研究区，开展该地区的建筑物提取。为响应“四个全面”和“五位一体”战略布局，江苏省常州市积极推动城市经济建设和智能化的步伐。常州市建筑物作为民生的一大经济体，在满足实施区域发展总体战略的需求、政府科学管理和智慧江苏建设的需求、强化公共服务与改善民生的需求等方面有重要意义。

建筑物提取方法主要包括传统建筑物提取方法和基于深度学习的建筑物提取方法。传统建筑物提取方法主要包括：1）基于概率统计的建筑物提取。文献[1]在提取框架的前段采用支持向量机（SVM）进行建筑物与非建筑物区域的划分。2）基于面向对象的建筑物提取。文献[2]研究一种基于面向对象的建筑物提取方法，获得较好的提取效果。流程主要包括：多分辨率分割、基于对象的分类。3）基于辅助信息的建筑物提取。文献[3]针对太阳光照（方向、角度和辐射季节等属性）以及阴影信息（长度、范围等）建模，通过阴影信息反推建筑物的感兴趣区域，辅助建筑物提取。基于深度学习方法主要包括：1）基于语义分割方法。文献[4]最早提出基于 CNN 的语义分割方法 FCN，该方法用卷积层替换基于 CNN 分类模型的全连接层，并在编码网络的后端添加解码结构得到语义分割预测结果。文献[5]设计轻量级的 U 形编码-解码结构，融合深层和浅层信息以提升空间细节表达能力。文献[6]的思路与 FCN 类似，级联多层特征，但他们采用多路径优化、残差卷积单元（Residual Conv Unit，RCU）、链式残差池化（Chained Residual Pooling, CRP）等模块提升融合效果，通过对称解码结构融合多层卷积的特征。文献[7]采用空洞卷积和空洞空间金字塔池化(atrous spatial pyramid pooling，ASPP)增大感受野。文献[8]是目前基于特征金字塔结构的最好实现，成为众

多模型中的特征提取网络。2）基于目标检测方法。文献[9]是目前主流的 One-stage 目标检测方法提取模块、目标检测模块和非极大抑制（Non-maximum suppression，NMS）模块组成。文献[10]最到端的 two-stage 目标检测模型 Faster R-CNN。该模型由深度特征表达、感兴趣区域提取、感兴化和预测端（分类和矩形框坐标回归）构成。文献[11]基于 Faster R-CNN 提出 Cascade R-CNN 模多层级联的方式实现检测结果迭代优化，成为目前性能最佳的目标检测模型。上述深度学习方法的特征提取能力，但无法同时统计建筑物的个数和面积，难以适应实际的生产需求。

近年来，实例分割算法被提出，通过先检测后分割的思路提取目标实例掩膜。实例分割算法两类：第一类是 proposal-based 方法。文献[12]采用多任务级联实例分割框架赢得 2015 MS-COCO 挑战赛，但是他们没有考虑遮挡问题。文献[13]采用 position-sensitive 得分图解决目标间相互遮挡但提取结果存在锯齿化边缘。文献[14]在 Faster R-CNN 模型上增加一个语义分割分支，提出的 Ma可提取更加精细的边缘。之后，文献[15]基于 Mask R-CNN 提出 PAN 获得更好的性能。第二类是 pro方法。文献[16]引入判别损失函数将深度特征映射到一个新的特征空间以提取实例掩膜。文献[17]结习和种子点选取等方法生成可以代表该目标的掩膜。文献[18]通过组合语义分割掩膜和边缘检测图感影像中的车辆目标。文献[19]采用深度分水岭变换方法进行实例提取，将传统的分水岭变换用深取不同遮挡顺序的目标。

实例分割算法引入到建筑物提取，用于获取建筑物实例掩膜，统计建筑物个数和面积。但在遥感影像建筑物提取中依旧存在如下问题：

1）多尺度特性。常用的解决方案是影像金字塔（缩放影像得到多尺度输入）、多尺度特征（卷积核得到多尺度输出）等。文献[20]在模型前端共享 CNN 权重参数，最后一个卷积层采用多核多尺度特征并将特征进行融合，提升模型效率。文献[21]首先将多尺度影像输入平行的深度网络，学习做特征融合。文献[22]采用级联多层特征的方法提取建筑物，结合符号距离函数提升边缘精度

2）邻近建筑物遮挡。建筑物分布于三维空间，在遥感传感器探测方向上可能发生重叠和遮地籍数据库入库带来不便。文献[23]结合 GIS 中的建筑物实例数据和街景数据进行细粒度分类。文实例分割方法进行建筑物实例掩膜提取，引入可旋转矩形框获取建筑物最小外包矩形，解决密集率低的问题。这些方法考虑了遮挡问题，但只是从单一尺度上对目标加以区分，可区分性有限。

基于深度学习方法中的一些研究针对上述问题做了一定的工作：1）针对多尺度问题的深度2）提取建筑物实例的深度学习方法。虽然这些深度学习方法在一定程度上解决建筑物提取存在题，但仍然没能从本质上很好解决这些问题。

为了解决上述问题，本文提出特征金字塔卷积神经网络建筑实例提取框架。

关于遮挡问题，构建多尺度目标感知实例提取子网络，引入多尺度注意力机制来感知目标，将不同尺度目标映射到不同尺度的特征图上。这一映射机制将邻近建筑物稀疏化表达，提高模型的分辨能力，能很好区分邻近建筑物。

本文在两个公开的建筑物数据集和自主构建的常州建筑物数据集上开展实验，证明模型在实际应用中的可行性。

2　特征金字塔卷积神经网络建筑实例提取框架

本文中，提出特征金字塔卷积神经网络建筑实例提取框架提取高分辨率遥感影像中建筑物实例掩膜。这是一个端到端的模型，其中的建筑物目标检测和掩膜标记共享深度卷积特征。该模型由两个部分组成：特征金字塔卷积神经子网络、多尺度目标感知实例提取子网络，结构如图 1 所示。

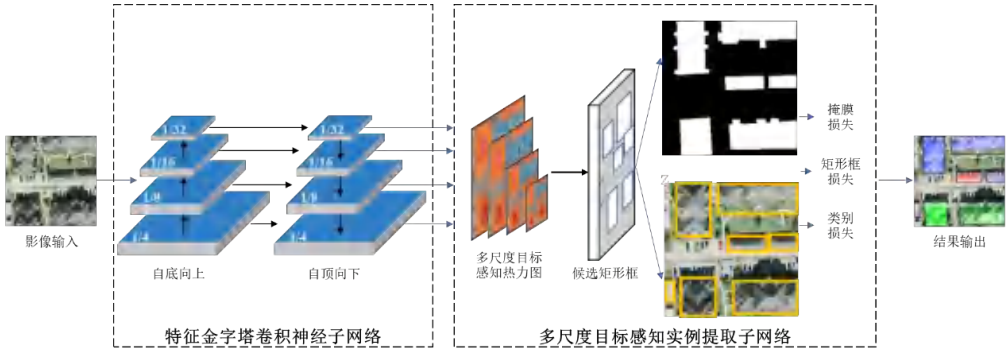

图1　特征金字塔卷积神经网络建筑实例提取框架图。由特征金字塔卷积神经子网络、多尺度目标感知实例提取子网络两个模块组成

首先，遥感影像输入特征金字塔卷积神经子网络学习多尺度特征。然后，采用多尺度目标感知实例提取子网络来提取建筑物实例。多尺度目标感知实例提取子网络引入注意力机制来提取建筑物矩形框，多尺度目标感知有助于解决重叠目标的遮挡问题。

2.1　特征金字塔卷积神经子网络

本文构建特征金字塔卷积神经子网络提取多尺度特征，该网络由自底向上和自顶向下两个模块组成，自底向上模块中每个单元都采用残差结构，即将输入 X 直接与卷积后的输出 F(X)相加。自顶向下模块将包含语义信息的深层特征和包含空间细节的浅层特征进行逐像素相加融合，并利用卷积和上采样恢复尺寸。最终，将不同尺度（原图尺寸 1/4、1/8、1/16、1/32）的特征图输出给多尺度目标感知实例提取子网络。

2.2　多尺度目标感知实例提取子网络

网络中的多尺度目标感知模块在多尺度卷积特征图上滑动3×3的小窗口，并对区域内特征进行卷积操作将其映射至低维特征向量，再输入给两个并行的1×1卷积层（边界框回归层和前背景分类层）进行目标感知。每个小窗滑动的位置对应原始影像的一系列区域，称为 Anchor，$k=12$，包括 4 种尺寸增益（4，8，16，32）和 3 种长宽比（1：1，1：2，2：1）。

为了训练该模块，需要为每个候选区域设定一个二值分类标签（建筑物或背景），其中正样本定义包含两种情况：与真实标签的 Intersection over Union（IoU）最大；与真实标签的 IoU 大于 0.7。负样本定义如下：与真实标签的 IoU 小于 0.3。其余样本不参与训练。为有效拟合模型参数，对候选区域坐标进行坐标参数化，具体形式如下：

$$\left.\begin{aligned} t_i^x &= (x - x_a)/w_a, t_i^y = (y - y_a)/h_a \\ t_i^w &= \log(w/w_a), t_i^h = \log(h/h_a) \end{aligned}\right\}$$

$$\left.\begin{aligned} t_i^{x^*} &= (x^* - x_a)/w_a, t_i^{y^*} = (y^* - y_a)/h_a \\ t_i^{w^*} &= \log(w^*/w_a), t_i^{h^*} = \log(h^*/h_a) \end{aligned}\right\}$$

其中，t_i^*, t_i^{*} 分别表示预测值与真实值的参数化坐标（x、y、w、h 分别表示中心坐标及长宽）。x_a, y_a, w_a, h_a 表示 Anchor 对应区域的位置信息。

利用上述模块提取候选矩形框后，对区域内特征进行池化，并输入三个并行卷积层，分别用于分类、矩形框坐标回归和掩膜提取，对应类别损失，矩形框损失和掩膜损失。类别损失定义如下：

$$L_{cls}(p_i, p_i^*) = -\log(p_i^* p_i + (1 - p_i^*)(1 - p_i))$$

其中，p_i, p_i^* 表示预测标签和真实标签。矩形框损失定义如下：

$$L_{bbox} = \sum_{s \in \{x,y,w,h\}} smooth_{L1}(t_i^s - t_i^{s^*})$$

$$smooth_{L1}(x) = \begin{cases} 0.5x^2 & if\ |x| < 1 \\ |x| - 0.5 & otherwise \end{cases}$$

掩膜损失定义如下：

$$L_{mask}(x_i, x_i^*) = -\log(x_i^* x_i + (1 - x_i^*)(1 - x_i))$$

其中，x_i, x_i^* 表示像素的预测标签和真实标签。基于三种损失求和得到总损失函数，如下：

$$L(\{p_i\}, \{t_i\}, \{x_j\}) = \alpha \frac{1}{N_{cls}} \sum_i L_{cls}(p_i, p_i^*) +$$

$$\beta \frac{1}{N_{bbox}} \sum_i p_i^* L_{cls}(t_i, t_i^*) + \gamma \frac{1}{N_{pixel}} \sum_j p_j^* L_{mask}(x_j, x_j^*)$$

通过上述过程，基于多尺度目标感知进行目标检测和掩膜提取，实现建筑物个数和面积统计。

3 基于特征金字塔卷积神经网络建筑实例提取框架的高分遥感建筑物提取

本节主要描述基于特征金字塔卷积神经网络建筑实例提取框架的高分遥感影像建筑物实例提取过程。

3.1 遥感影像数据预处理

为了能更好地表达遥感影像中的地物信息，在开始训练特征金字塔卷积神经网络建筑实例提取框架之前，需要对高分遥感影像进行数据预处理，以增加样本的多样性。首先，对一幅大图进行滑窗裁剪，得到大小的影像块，然后通过图像归一化算法，调整影像的对比度和亮度，减少光照对场景分类的噪声影响。

然后，采用水平翻转、随机抖动、高斯噪声等数据增强操作将数据集数量扩大为原来的 12 倍。

3.2 高分遥感影像建筑物实例提取

本文提出的特征金字塔卷积神经网络建筑实例提取框架是一种端到端的深度学习方法，由用于提取多分辨率多尺度深度卷积特征的特征金字塔卷积神经子网络模块、提取建筑物实例的多尺度目标感知实例提取子网络模块组成。

首先，影像输入特征金字塔卷积神经子网络模块，通过逐层卷积得到抽象语义特征。为了获取多尺度特征，将包含语义特征的深层网络和包含空间细节的浅层特征进行相加融合。

然后，深度卷积特征输入多尺度目标感知实例提取子网络模块，该模块通过对候选框进行前/背景判断及坐标回归生成代表目标实例的矩形框。在分类分支中，经过 Softmax 分类器输出 维的预测结果（经过样本数的正则化）以识别候选区域是前景/背景。在矩形框回归中，矩形框基于建筑物中心坐标，采用 Smooth L1 损失函数进行回归。最后，基于单个建筑物的感兴趣区域被感知。

最后，对生成的感兴趣区域进行精细化分类和坐标回归，得到最终的实例提取结果。在训练阶段，将批尺寸为 m 的影像块输入该端到端模型，每次迭代中，通过计算模型输出和真实标签的差值计算损失函数，通过梯度下降算法进行模型参数更新。在测试阶段，将原始影像裁剪成 的影像块，输入训练得到的模型，输出预测结果。

4 基于特征金字塔卷积神经网络建筑实例提取框架的建筑物提取实验及分析

为了有效地评估特征金字塔卷积神经网络建筑实例提取框架模型在高分遥感影像建筑物实例提取的性能，在两个有挑战性的建筑物遥感数据集上进行测评(ISPRS Vaihingen semantic labeling contest dataset 和 WHU aerial image dataset)。为了验证模型的实用性，特征金字塔卷积神经网络建筑实例提取框架在自主构建的常州市建筑物数据集上进行测评。

4.1 实验设置

特征金字塔卷积神经网络建筑实例提取框架基于 MXNet 深度学习框架进行训练和测试。为控制对比实验的变量，设定特征金字塔卷积神经网络建筑实例提取框架、FCIS 及 Mask R-CNN 的基准学习率为 0.004，batch 的大小为 4，weight decay rate 和 momentum 分别为 0.0001 和 0.9。模型采用随机梯度下降进行参数更新和优化。实验分别在 Tesla K40C 及 Titan X 两种型号的显卡上部署，每次实验均使用单块显卡，显卡内存为 12G。

公开的建筑物数据集：The ISPRS Vaihingen Semantic Labeling Contest Dataset 由近红外、红、绿波段组成，实验中这三个通道被转换为 RGB 通道得到彩色影像。该数据集由 33 个 像素的大图片块组成，其地面采样距离（ground sample distance，GSD）为 0.09m。其中，16 个图像块标有真实标签，并被随机裁剪成固定尺寸的 像素的样本。样本集按 5：3：2 的比例被随机分为训练、验证和测试子数据集。WHU Aerial Image Dataset 影像覆盖新西兰的 Christchurch 市 450 平方千米区域。该数据集的空间分辨率是 0.3 米。在

测试集中，包含 2416 幅 像素的影像切片（共计 42000 个建筑物实例）。

常州市建筑物数据集：常州市位于江苏省南部，影像范围：（119.75°E，31.58°N）至（120.00°E，31.71°N）。建筑物比较稀疏，拥有大面积农田，包含大面积水域——滆湖。原始影像为航飞数据，于 2016 年采集，包含 RGB 三波段，其空间分辨率为 0.3 米。采集的影像尺寸为 46281×79154，无重叠裁剪成 1024×1024 的样本，总共 3840 张。通过 ArcGis 软件人工标注建筑物的多边形轮廓，生产.shp 矢量文件。在输入模型训练前，对矢量文件栅格化，得到真实标签的掩膜。栅格文件中不同的建筑物多边形用不同 ID 表示，对邻近建筑物的边界加以区分。

4.2 ISPRS Vaihingen 数据集实验

在 ISPRS 数据集上测评的结果表明：特征金字塔卷积神经网络建筑实例提取框架模型在较大尺寸的建筑物提取上也有鲁棒的性能，实验结果见表 4.1。从表中可以看出，当 IoU 小于 0.5 时，本文提出的方法显著优于其他几种对比方法，说明该方法在提取 ISPRS 数据集中大尺寸建筑物的有效性。

表 4.1 在 ISPRS Vaihingen Semantic Labeling Contest 数据集上的对比实验

对比方法	mAP@0.3（%）	mAP@0.4（%）	mAP@0.5（%）
Mask R-CNN	95.35	94.15	94.98
FCIS	90.77	90.77	90.76
本文方法	96.62	95.84	95.17

4.3 WHU Aerial Image Dataset 数据集实验

为了验证特征金字塔卷积神经网络建筑实例提取框架模型的泛化性，本文对比了特征金字塔卷积神经网络建筑实例提取框架和 Mask R-CNN 在不同训练集和测试集上的泛化性能，测评结果见表 4.2。在自己标注的建筑物实例数据集上训练的模型直接在具有挑战性的 WHU aerial image dataset 上进行鲁棒性测试。正如表 4- 4 所示，特征金字塔卷积神经网络建筑实例提取框架在泛化能力上优于 Mask R-CNN，而且当 IoU=0.5 和 0.7 时，提出的特征金字塔卷积神经网络建筑实例提取框架模型的 mAP 分别超过 Mask R-CNN4.1%和 1.2%。通过对精度和召回率的分析发现，特征金字塔卷积神经网络建筑实例提取框架表现更好因为它可以召回更多建筑物实例正样本。

表 4.2 在 WHU aerial image 数据集上测试的对比实验

方法	IoU=0.5			IoU=0.7		
	mAP（%）	精度（%）	召回率（%）	mAP（%）	精度（%）	召回率(%)
Mask R-CNN	63.2	85.4	66.3	56.1	66.5	54.7
本文方法	67.3	86.1	71.2	57.3	64.3	55.2

4.4 常州市建筑物提取实验

为了验证本文提出的模型在实际场景的有效性，采用特征金字塔卷积神经网络建筑实例提取框架模型，对常州市建筑物提取开展实验。首先，将常州市研究区获取的 3840 景影像划分成训练集（3000 景）和测试集（840 景）。然后对训练集进行迭代训练，并在测试集上进行测试。实验结果表明：当 IoU=0.5 时，mAP 为 56%，验证了该模型在实际场景中的有效性。可视化结果如图 2 所示。

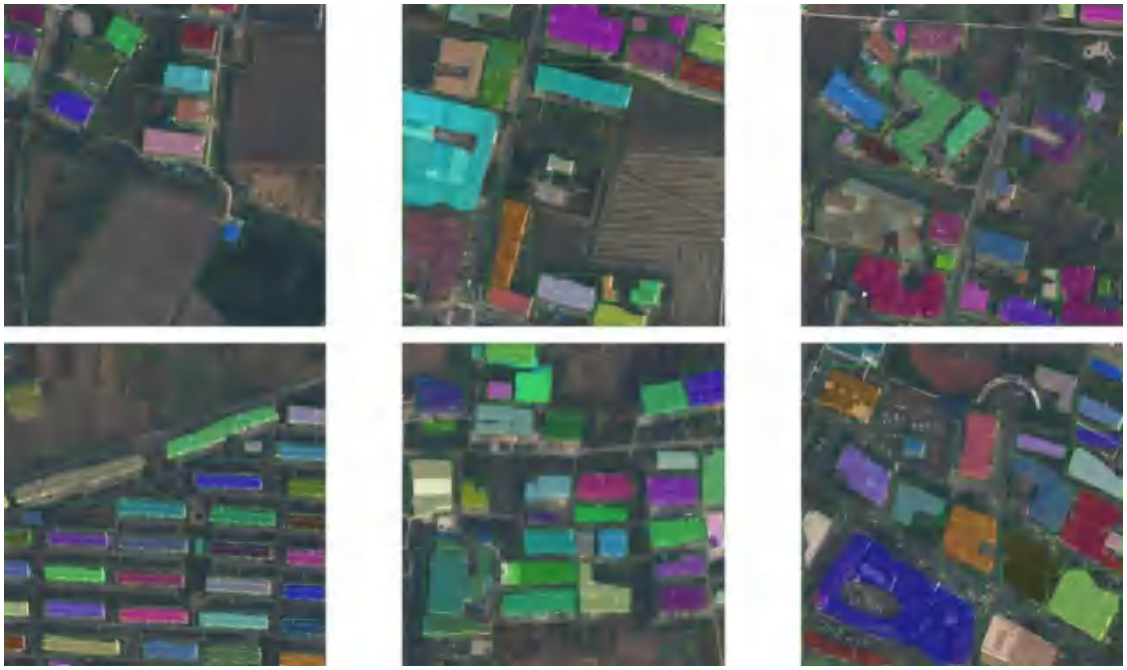

图2　常州市建筑物可视化结果（基于本文提出的算法）

5　结束语

本文将实例分割算法引入到建筑物提取，通过先检测后分割的思路提取建筑物实例掩膜，相比于其他算法可以同时统计建筑物个数和面积。但在建筑物实例提取中，存在以下挑战：1）单幅遥感影像中存在多尺度的建筑物；2）相邻建筑物彼此遮挡导致无法区分。为了解决上述问题，本文提出特征金字塔卷积神经网络建筑实例提取框架。针对多尺度问题，构建特征金字塔卷积神经子网络，利用自底向上和自顶向下联合的多尺度特征来描述不同尺度的目标；针对遮挡问题，构建多尺度目标感知实例提取子网络，引入多尺度注意力机制来感知目标，提高模型的分辨能力，从而有效区分邻近建筑物。

提出的特征金字塔卷积神经网络建筑实例提取框架方法在ISPRS Vaihingen semantic labeling contest dataset上与Mask R-CNN进行对比实验，结果显示：当IoU=0.5时，特征金字塔卷积神经网络建筑实例提取框架在两个数据集上的mAP比Mask R-CNN高0.19%。此外，在WHU aerial image dataset上进行鲁棒性测试，结果表明：当IoU=0.5时，特征金字塔卷积神经网络建筑实例提取框架的mAP超过Mask R-CNN4.1%。此外，特征金字塔卷积神经网络建筑实例提取框架模型还在常州市研究区开展实用性研究，实验结果表明：特征金字塔卷积神经网络建筑实例提取框架在实际场景中也有较好的适应性。

参考文献

[1] TURKER M, KOC-SAN D. Building extraction from high-resolution optical spaceborne images using the integration of support vector machine (SVM) classification, Hough transformation and perceptual grouping [J]. International Journal of Applied Earth Observations and Geoinformation, 2015, (34): 58-69.

[2] ATTARZADEH R, MOMENI M. Object-based building extraction from high resolution satellite imagery [J]. International Archives of the Photogrammetry, Remote Sensing and Spatial Information Sciences, 2012, 39: B4.

[3] OK A O, SENARAS C, YUKSEL B. Automated detection of arbitrarily shaped buildings in complex environments from monocular VHR optical satellite imagery [J]. IEEE Transactions on Geoscience and Remote Sensing, 2013, 51(3): 1701-1717.

[4] LONG J, SHELHAMER E, DARRELL T. Fully convolutional networks for semantic segmentation [C]. Proceedings of the Proceedings of the IEEE Conference on Computer Vision and Pattern Recognition, 2015: 3431-3440.

[5] RONNEBERGER O, FISCHER P, BROX T. U-net: Convolutional networks for biomedical image segmentation [C]. Proceedings of the International Conference on Medical Image Computing and Computer-assisted Intervention, Springer, 2015: 234-241.

[6] LIN G, MILAN A, SHEN C, REID I. Refinenet: Multi-path refinement networks for high-resolution semantic segmentation [C]. Proceedings of the Proceedings of the IEEE Conference on Computer Vision and Pattern Recognition, 2017: 1925-1934.

[7] CHEN L-C, ZHU Y, PAPANDREOU G, SCHROFF F, ADAM H. Encoder-decoder with atrous separable convolution for semantic image segmentation [C]. Proceedings of the Proceedings of the European Conference on Computer Vision, 2018: 801-818.

[8] LIN T-Y, DOLLáR P, GIRSHICK R, HE K, HARIHARAN B, BELONGIE S. Feature pyramid networks for object detection [C]. Proceedings of the Proceedings of the IEEE Conference on Computer Vision and Pattern Recognition, 2017: 2117-2125.

[9] REDMON J, DIVVALA S, GIRSHICK R, FARHADI A. You only look once: Unified, real-time object detection [C]. Proceedings of the Proceedings of the IEEE Conference on Computer Vision and Pattern Recognition, 2016: 779-788.

[10] REN S, HE K, GIRSHICK R, SUN J. Faster R-CNN: Towards real-time object detection with region proposal networks [C]. Proceedings of the Advances in neural information processing systems, 2015: 91-99.

[11] CAI Z, VASCONCELOS N. Cascade R-CNN: Delving into high quality object detection [C]. Proceedings of the Proceedings of the IEEE Conference on Computer Vision and Pattern Recognition, 2018: 6154-6162.

[12] DAI J, HE K, SUN J. Instance-aware semantic segmentation via multi-task network cascades [C]. Proceedings of the Proceedings of the IEEE Conference on Computer Vision and Pattern Recognition, 2016: 3150-3158.

[13] LI Y, QI H, DAI J, JI X, WEI Y. Fully convolutional instance-aware semantic segmentation [C]. Proceedings of the Proceedings of the IEEE Conference on Computer Vision and Pattern Recognition, 2017: 2359-2367.

[14] HE K, GKIOXARI G, DOLLáR P, GIRSHICK R. Mask R-CNN [C]. Proceedings of the Proceedings of the IEEE International Conference on Computer Vision, 2017: 2961-2969.

[15] LIU S, QI L, QIN H, SHI J, JIA J. Path aggregation network for instance segmentation [C]. Proceedings of the Proceedings of the IEEE Conference on Computer Vision and Pattern Recognition, 2018: 8759-8768.

[16] DE BRABANDERE B, NEVEN D, VAN GOOL L. Semantic instance segmentation with a discriminative loss function [Z]. 2017

[17] FATHI A, WOJNA Z, RATHOD V, WANG P, SONG H O, GUADARRAMA S, MURPHY K P. Semantic instance segmentation via deep metric learning [Z]. 2017

[18] MOU L, ZHU X X. Vehicle instance segmentation from aerial image and video using a multitask learning residual fully convolutional network [J]. IEEE Transactions on Geoscience and Remote Sensing, 2018, (99): 1-13.

[19] BAI M, URTASUN R. Deep watershed transform for instance segmentation [C]. Proceedings of the Proceedings of the IEEE Conference on Computer Vision and Pattern Recognition, 2017: 5221-5229.

[20] AUDEBERT N, LE SAUX B, LEFèVRE S. Semantic segmentation of earth observation data using multimodal and multi-scale deep networks [C]. Proceedings of the Asian Conference on Computer Vision, Springer, 2016: 180-196.

[21] LIU Q, HANG R, SONG H, LI Z. Learning multi-scale deep features for high-resolution satellite image classification [Z]. https://arxivorg/abs/161103591. 2016

[22] YUAN J. Learning building extraction in aerial scenes with convolutional networks [J]. IEEE transactions on pattern analysis and machine intelligence, 2018, 40(11): 2793-2798.

[23] KANG J, KöRNER M, WANG Y, TAUBENBöCK H, ZHU X X. Building instance classification using street view images [J]. ISPRS Journal of Photogrammetry and Remote Sensing, 2018, 145: 44-59.

[24] WEN Q, JIANG K, WANG W, LIU Q, GUO Q, LI L, WANG P. Automatic Building Extraction from Google Earth Images under Complex Backgrounds Based on Deep Instance Segmentation Network [J]. Sensors, 2019, 19(2): 333.

[作者简介]

陈鼎元，男，博士，副教授。主要研究方向为高分辨率遥感智能解译、多源遥感灾害应急。

钟燕飞，男，博士，教授。主要研究方向为智能化遥感数据提取分析与应用。

宋慧娜，女，博士，副教授。主要研究方向为深度学习 SAR 图像解译、InSAR 数据处理。

宋朝晖，男，博士，教授。主要研究方向为通信理论与系统、遥感信息处理。

FANETs in Low-Altitude Space: a Q-Learning Enabled Routing Algorithm with Visual Information

Haoran Shen[1], Jingzheng Chong[1], Zhihua Yang[1,2]

***Abstract*—Flying Ad Hoc Networks (FANETs) draw people's attention these years due to their wide range of civil and military applications. Due to the high mobility and limited battery capacity of Unmanned Aerial Vehicles (UAVs), it is difficult to exploit existing Ad Hoc network routing algorithms protocols in especially low-altitude complex environments with dense obstacles for FANETs. Therefore, this paper proposes a Q-learning based Visual Information assisted Routing algorithm (QVIR) for FANET in low altitude complex environments, which could make use of the imaged data collected by the onboard camera to reduce the influence of flight environment on the network. Simulation results show that compared with the classical FANETs routing algorithm, the QVIR algorithm has better performance with respects to lower delay, higher packet delivery ratio and better energy efficiency.**

***Keywords*—FANETs, Q Learning, Low Altitude, Routing**

I. INTRODUCTION

The field of Unmanned Aerial Vehicles (UAVs), which are also known as drones, has experienced rapid growth since the 21st century [1]. In recent years, the production of low-cost drones has started to become popular in view of the advances in the field of embedded systems and the scale of integration that can be achieved. Drones are suitable for formation flying. With the continuous development in technology, nowadays, drones can be easily equipped with various sensors such as cameras, radars, etc. These on-board sensors have brought great convenience to drones in carrying out their missions [2]. Researchers have proposed Flying Ad-Hoc Networks (FANETs) based on Mobile Ad-Hoc Networks (MANETs) and Vehicular Ad-Hoc Networks (VANETs) [3].

However, due to the limitation of the communication range of UAVs, it is difficult for each drone in the formation to communicate directly with the ground Base Station(BS). In this case, UAV-to-UAV communication is the solution to the problem [4]. UAVs can transmit the data to the BS through a multi-hop relay. Given the mobility and flexibility of UAVs, paths between nodes in FANETs can change rapidly. These rapid changes can leave the communication link in an unstable state. In addition, different numbers of UAV nodes may join or leave the network at any time while performing certain tasks. This leads to unpredictable topological changes and problems. Therefore, in order to make the communication between UAVs efficient and reliable, academia and industry have started to focus on the design of routing protocols in FANETs.

Before FANETs was proposed, there have been many topology-based routing protocols for Ad-Hoc networks. The researchers found that these traditional routing protocols are not well adapted to FANETs scenarios [5]. To solve these problems, location-based routing protocols gained popularity among researchers. But it is still difficult to solve problems such as void area problem. Therefore, to overcome these drawbacks, researchers have developed Q-learning based routing protocols with the help of techniques like Machine Learning (ML) and Artificial Intelligence (AI) [6].

However, we find that most of current Q-learning-based routing protocols make decisions by only considering the metrics of the UAVs, ignoring the impact of the real environment if deploying UAV formations in urban downtown, residen-

1. The Guangdong Provincial Key Laboratory of Aerospace Communication and Networking Technology, Harbin Institute of Technology, Shenzhen, China, 518055.

2. The Network Communication Department, Pengcheng Laboratory, Shenzhen.

This work is supported in part by the National Natural Science Foundation of China under Grant 62371158 and Grant 62027802 and the Major Key Project of PCL(PCL2024A01), Peng Cheng Laboratory.

tial neighbourhoods and other low-altitude complex environments. For example, a drone with excellent metrics is about to avoid many buildings in the next period of time. Under the traditional Q-learning-based protocol, this drone is likely to be selected as the next node for packet forwarding. However, it may lose contact with the UAV swarm in the next few seconds even minutes for avoiding buildings, or even crash due to excessive manoeuvres. This may cause problems to the network such as packet loss and restarting of the route search, deteriorating the performance of FANETs.

Therefore, We attempt to solve these challenges by considering load balancing to minimize the network failure and performance degradation via exploiting the visual information of surroundings of FANET. Contributions of this study are as follows:

- We develop a Q-learning-based Visual Information assisted Routing Algorithm (QVIR) for FANET in low-altitude complex environments, which could make use of the imaged data collected by the onboard camera to reduce the influence of flight environment on the network.
- We propose a simple and efficient environment evaluation method with modified YOLOv5 algorithm, in which the results of the evaluation are incorporated into the design of Q-learning to reduce the impact of dynamic and complex flight environments.
- The simulation results indicate that QVIR has lower delay, higher packet delivery ratio and energy efficiency compared with typical algorithm GPSR and QGeo.

The remain of this paper is ordered as follows. Section II describes the related work of this paper. In section III, we state the system model and formulate the problem. In section IV, the proposed algorithm is introduced in detail. In section V, the simulation results are presented to verify the efficiency of the proposed scheme. Finally, conclusions of this study is given in Section VI.

II. RELATED WORK

Due to the rapid development of FANETs, researchers have conducted many research on the design of routing protocol. Owing to the effects brought by the high dynamics of UAVs, some traditional routing protocols are not well suited for FANETs. Therefore, scholars have tried various approaches to solve the FANETs routing challenges. We briefly review the existing routing protocols along three lines: general topology-based routing, position-based routing, and Q-learning-based routing.

Topology based protocols can be further classified into three categories: proactive, reactive and hybrid [7]. Proactive routing protocols are those in which each node in the network maintains one or more tables containing routing information to each node in the network. Reactive routing protocols discover paths when data needs to be transmitted and usually determine paths by sending route requests and waiting for route replies. Waheed et al. [8] proposed a link-aware on-demand routing protocol LAOD, enabling the estimation of effective link lifetime. Hybrid routing protocols combine the characteristics of both proactive and reactive routing protocols. Zone Routing Protocol (ZRP) [9] uses the concept of zones for UAV swarms, effectively solves the scaling problem of UAV networks.

Considering drone characteristics, topology based protocols can not make the network performance optimal. Therefore, researchers have proposed to use location based routing information. In location based routing, the node's geographic location information is used for packet forwarding decisions. In [10] MPGR was proposed, where the mobility prediction scheme is merged with geographic routing mechanism in order to minimise the impact of high mobility of UAVs on routing performance.

As for Q-learning-based routing, a Q-learning-based geographic routing protocol (QGeo) is proposed in [11], which is designed to enhance the network performance of unmanned robotic networks, critical for remote control and monitoring of mobile robotic devices. QGeo uses a reinforcement machine learning algorithm to make distributed geographic routing decisions without global network knowledge and aims to reduce network overhead in high-mobility scenarios. Its performance evaluation indicates that QGeo has a higher packet delivery ratio and lower network overhead than existing methods.

In [12], the author introduces QMR protocol. It aims to provide low-latency and low-energy network services by adaptively adjusting Q-learning parameters to suit the highly dynamic nature of FANETs. A new exploration and exploitation mechanism is proposed to discover potential optimal routing paths while utilizing existing knowledge. Simulation results demonstrate the superior performance of the QMR protocol in terms of packet arrival ratio, reduced delay, and energy consumption compared to existing Q-learning based routing methods.

Recently, Hu et al. designed a Q-routing protocol based on fuzzy logic for FANETs (FQR) [13]. FQR uses a fuzzy logic approach to evaluate wireless link quality based on multiple metrics such as relative mobility, residual energy, and link quality. Simulations using a real UAV trajectory model show that the proposed approach outperforms traditional strategies in packet delivery ratio, end-to-end delay, and network lifetime.

III. SYSTEM MODEL AND PROBLEM FORMUALTION

A. System model

As shown in Figure 1, this paper constructs a FANET in a low-altitude complex environment. The drones set Ω can be denoted as $\Omega = \{u_1, u_2, ..., u_n\}$. For each node u_i, the neighbor set of u_i at time t can be denoted as $N_i(t)$. Every node can transmit the packet to their neighbors if the link is not broken. With the help of knowledge of graph theory, the network topology can be regarded as a graph $G(\Omega, E(t))$, where $E(t)$ is the set of edges, representing the connection between the UAVs at time t. Specifically, the link of the whole network can be further expressed using the matrix $\Phi(t)$, where $\Phi_{ij}(t)$ means whether a link between the UAV node u_i and u_j exists. If $\Phi_{ij}(t) = 1$, it means that there is a stable link between these two drones. Otherwise, it means the opposite.

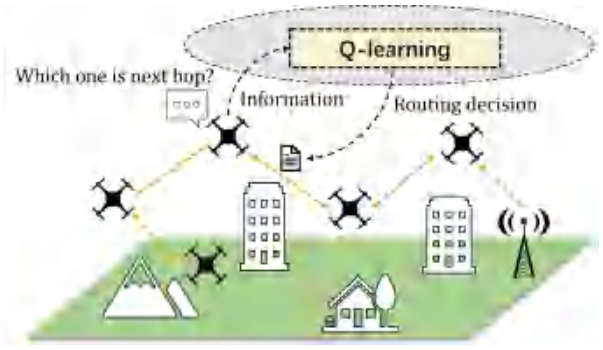

Figure 1 FANET model in low-altitude complex environment

• Energy Consumption Model: For each UAV node u_i, there is an initial energy capacity eng^i_{init}. The flying movement and packet transmission will consume the energy, denoted as eng^i_m and eng^i_t. So the residual energy eng^i_{res} can be expressed as follows:

$$eng^i_{res} = eng^i_{init} - eng^i_m - eng^i_t. \tag{1}$$

If eng^i_{res} is less than a threshold, it means that the drone can no longer fly and will leave the swarm later.

• Mobility Model: In this paper, all drones can obtain its location (x_i, y_i, z_i) and velocity $\boldsymbol{v}_i$ through some devices like GPS. A Gaussian Markov mobility model is adopted. According to this model, the position of a drone at time t can be updated according to equations below.

$$\boldsymbol{p}^t_i = \boldsymbol{p}^{t-1}_i + \boldsymbol{v}^{t-1}_i \times \Delta t, \tag{2}$$

where $\boldsymbol{p}_i = (x_i, y_i, z_i)$. Velocity at time t can be updated according as follows:

$$\boldsymbol{v}^t_i = \alpha \boldsymbol{v}^{t-1}_i + \boldsymbol{n}_v, \tag{3}$$

where α is the velocity autocorrelation coefficient and $\boldsymbol{n}_v$ is a random perturbation term obeying a zero-mean Gaussian distribution. In short, each increment of the components of the velocity in different directions as the drone moves obeys a Gaussian distribution and is not affected by the previous state.

• Flight Environment Model: Unlike usual airspace, low altitude one has many obstacles which may cause problems to the flight and packet transmission. Considering the limitations of the UAV, we build a very simple model of the surrounding environment for each drone. We consider that each UAV has an onboard camera, where You Only Look Once version 5 (YOLOv5) algorithm is implemented in its core. Through the camera, pictures of the front environment can be taken and analyzed. YOLOv5 is a real-time object detection system [14]. It is widely used for object detection tasks in images. With the help of YOLOv5, the drone u_i can easily sense the number of obstacles OBS_i such as buildings ahead by analyzing the picture. The number of obstacles can somewhat indicate whether the environment in which the UAV is currently located is safe and suitable for data transmission.

B. Problem Formulation

In this paper, we assume that a swarm of UAVs is performing a mission in a low altitude complex environment, where one UAV needs to deliver the collected mission data to another UAV close to the base station. The former is the source node u_s and the latter is the destination node u_d. We hope that the packet can be transmitted by muti-hop relay by using proposed routing algorithm QVIR which aims at ensuring the data to be successfully delivered from the source node to the end point with low latency and high delivery ratio. That means, for $\Phi(t)$, $\Phi_{si}(t), \Phi_{ij}(t), ..., \Phi_{jd}(t) = 1$. So, the problem above can be formulated as:

$$\Phi(t)^* = \arg\max_{\Phi(t)} R(\Phi(t), M), \tag{4}$$

where $R(\Phi(t), M)$ is an effectiveness function. This function, related to the effectiveness metric M, judges whether the route path can guarantee the low delay and high delivery ratio. M is the combination of some metric of the UAV itself, such as eng^j_{res} and the link between drones. The details will be shown in the next section.

The above equation is subject to the following constraints:

$$\Phi_{ij}(t) = \begin{cases} 1, & j \in N_i(t) \\ 0, & otherwise, \end{cases} \tag{5}$$

$$eng^j_{res} > threshold, j \in N_i(t). \tag{6}$$

It means that for node u_i, the next hop node can only be chosen from its neighbor set. In other word, u_s can not build connection with nodes out of its communication range. Also, the candidates must have enough energy.

IV. QVIR Algorithm

A. Overview

In this paper, the UAV nodes will make routing decisions based on information about their neighbors and themselves, so they will use HELLO packets to exchange their own information with neighbor nodes. Considering the complex low altitude environment, the drone will use the convenient and fast YOLOv5 algorithm to evaluate the environment and incorporate the results into the design of some metrics. Then, to solve the problem in section II, the Q-learning algorithm is adopted to calculate the matrix $\Phi(t)^*$.

B. Environment Evaluation

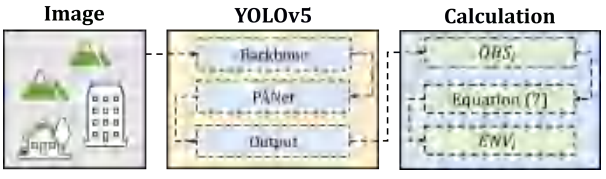

Figure 2 Environment evaluation process

In this study, according to environment model in section II, we evaluate the surrounding environment by the only using detection results.

The result of the evaluation is denoted as ENV_i. Moreover, considering that there is also certain randomness in the effect of the complex environment on the UAV, we use the random function. We use the following formula to obtain ENV_i.

$$ENV_i = \begin{cases} RAND(0,0.3), & 0 \le OBS_i \le 1 \\ RAND(0.3,0.6), & 2 \le OBS_i \le 3 \\ RAND(0.6,1), & OBS_i \ge 4. \end{cases} \tag{7}$$

The above equations mean that we regard the environment as safe if the number of obstacles is between 0 and 1, normal if it is between 2 and 3, and dangerous otherwise.

A low ENV_i indicates that the current surrounding environment is safe for flying and communication. While a node has a too high ENV_i, it may not regarded as candidates of data transmission node.

C. Neighbor Discovery

To get neighbors' information, each node performs neighbor discovery by sending HELLO messages periodically. The HELLO message packet contains each node's own geographic location, speed vector, residual battery energy, queuing delay, etc.

Each node also maintains a neighbor information table that stores the content of Hello messages sent by its neighbors, the message arrival time and the calculated Q-value. These information will be used in the Q-learning algorithm later. Apart from that, the neighbor information table also holds the current node's learning rate and discount factor. When an information entry exceeds the time limit, the neighbor information table removes that entry.

D. Q-learning Algorithm in QVIR

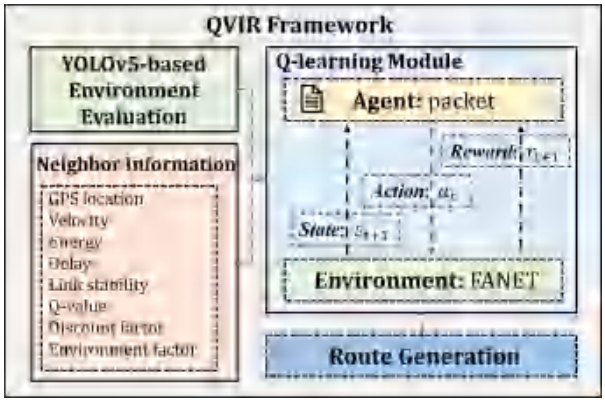

Figure 3 QVIR Algorithm framework

a. Basic Design

According to the problem in section II, we use Q-learning algorithm to get the matrix $\Phi(t)^*$. Q-learning is a model-free reinforcement learning algorithm that learns an action-value function, known as the Q-function, to assist an agent in choosing the best action in a given state [15].

Initially, the Q-table is initialized. At each time step, the agent selects an action and observes the outcome (the next state s_{t+1} and reward r_{t+1}). Then it updates the Q-table. Finally, the estimation of the Q-function will gradually converge to the optimal value, at which point the agent can choose the optimal action based solely on the Q-table. The update of the Q-table follows the rule below:

$$Q(s_{t+1},a_{t+1}) = Q(s_t,a_t) + \alpha[r_{t+1} + \gamma \max_{a_{t+1}} Q(s_{t+1},a_{t+1}) - Q(s_t, \tag{8}$$

Here, $Q(s_t,a_t)$ is the Q-value for the current state-action pair. α is the learning rate, which determines the speed at which new information overrides old information. γ is the discount factor, which determines the importance of future rewards relative to immediate rewards. $\max_{a_{t+1}} Q(s_{t+1},a_{t+1})$ is the maximum Q-value among all possible actions in the next state s_{t+1}.

In our proposed algorithm, a data packet travels from a source node to a destination node by a multi-hop relay. So,

Algorithm 1 Q-learning Algorithm

Initialize $Q(s,a)$ for all state-action pairs
Initialize parameters: step size $\alpha \in (0,1]$ and small $\varepsilon > 0$
repeat
    Choose an action a_t according to some policy(e.g., $\varepsilon-$ greedy policy)
    Take action and observe r_{t+1} and s_{t+1} from environment
    Update Q value in the Q-table using equation (8)
    Change to next state s_{t+1}
until s_{t+1} is the destination

we regard the whole network as an environment, and each data packet as an agent. Each state of the agent indicates a node which currently holds the packet.

For example, when a packet is at node u_i, the current state is s_i. An action a_{ij} means that the packet is to be forwarded from node u_i to its neighbor node u_j. After that, the state of the packet moves from s_i to s_j. At last, the packet gets a reward.

b. Delay

In the physical layer, the propagation delay is almost negligible in FANET. Considering the cache of the UAV node itself and the delay brought by the MAC layer, we define the delay metric as follows:

$$dealy_{ij} = delay\_mac_{ij} + delay\_que_{ij}, \tag{9}$$

$$delay\_mac_{ij} = t_{ACK} - t_{Send}. \tag{10}$$

According to the queuing theory:

$$delay\_queue_{i,j} = \frac{1}{sr_j} \times \frac{1}{1-util_j}, \tag{11}$$

where sr_j means service rate, $util_j$ means the resource utilization.

c. Energy

To balance the energy consumption of the forwarding nodes, we consider the residual energy of the neighbor nodes when selecting the next hop. To avoid the problem caused by running out of energy, we introduce an energy metric in our algorithm to represent the energy level. It is expressed as follows:

$$eng_i = \frac{eng\_res_i}{eng\_init_i}, \tag{12}$$

where eng_res_i is the residual energy and eng_init_i is the initial energy of node u_i.

d. Link Stability

We obtain a quantitative result by the calculating the predicted link maintenance time. The link stability can be expressed as follows:

$$LS_{ij} = \begin{cases} \frac{R+d_{ij}}{|\boldsymbol{v}_i - \boldsymbol{v}_j|} \times (1 - ENV_j), cosim_{ij} \geq 0 \\ \frac{R-d_{ij}}{|\boldsymbol{v}_i - \boldsymbol{v}_j|} \times (1 - ENV_j), cosim_{ij} \leq 0, \end{cases} \tag{13}$$

where d_{ij} is the distance between two nodes, $cosim_{ij}$ is the cosine similarity of v_i and v_j. They can be expressed as follows:

$$cosim_{ij} = \frac{\boldsymbol{v}_i \cdot \boldsymbol{v}_j}{\sqrt{\boldsymbol{v}_i{}^2 \times \boldsymbol{v}_j{}^2}}, \tag{14}$$

$$d_{ij} = \sqrt{(x_i - x_j)^2 + (y_i - y_j)^2 + (z_i - z_j)^2}. \tag{15}$$

e. Reward Function

To reduce the delay and energy consumption while maintaining delivery ratio, we jointly consider the delay, energy metric and link stability of the possible node in the reward function design. The reward function is defined as follows:

$$f_R(s_t, a_t) = \begin{cases} r_{\max}, s_{t+1}\ is\ the\ destination \\ r_{\min}, s_{t+1}\ is\ local\ minimum \\ a \times eng_j + b \times e^{-delay_{ij}} + \\ c \times \left(1 - e^{-LS_{ij}}\right), otherwise, \end{cases} \tag{16}$$

where a, b, c is the weight ($a+b+c=1$).

The above equations indicate that at current time t, the agent is a packet at node u_i, the state is s_i. Then the agent takes action at and the state changes to s_j. The reward will be different according to the next state.

If next hop is the destination, the agent (data packet) gets maximum reward. If next hop is local minimum, it indicates that all neighbor nodes are more far away from the destination than the current node. So, the agent will get little reward, indicating that the action is not good.

f. Adaptive Q-learning Parameters

Due to the dynamic nature of FANET, when the link between nodes becomes unstable, the learning rate should become larger, allowing the Q-value to be updated faster. Thus, we consider the link stability metric in order to adjust the learning rate. We first normalize the link stability:

$$LSnorm_{ij} = \frac{|LS_{ij} - \mu_{ij}|}{\sigma_{ij}}, \tag{17}$$

where μ_{ij} is the mean value and σ_{ij} is the variance of the link stability metric. Then, the learning rate α_{ij} can be expressed

as follows:

$$\alpha_{ij} = \begin{cases} e^{-LSnorm_{ij}}, \sigma_{ij} \neq 0 \\ 0.3, \qquad \sigma_{ij} = 0. \end{cases} \tag{18}$$

Apart from the learning rate, discount factor is another important parameter. We calculate the discount factor γ_i of node u_i as follows:

$$\gamma_i = (1 - ENV_i) \times \frac{N_i(t-1) \cap N_i(t)}{N_i(t-1) \cup N_i(t)}, \tag{19}$$

where $N_i(t)$ is current neighbor set and $N_i(t-1)$ is the previous neighbor set of node u_i.

g. Penalty Mechanism

To minimize the routing hole problem which will significantly increase the delay of the network, we introduce a penalty mechanism. This mechanism is applied under two circumstances. One circumstance is that node u_j detects a routing hole problem and inform node u_i. If the packet at node u_i wants to take action a_{ij}, it will get a minimum reward. Another circumstance is that node u_i does not receive the ACK packet within the expiration time, the agent will also get a minimum reward.

Algorithm 2 QVIR Algorithm

Input: UAV nodes, packet and related information
Output: route path

while $eposide \leq M$ **do**
  for $t = 1, 2, 3, ..., N$ **do**
    Each node executes environment evaluation
    Each node executes neighbor discovery
    if neighbor table of current node is empty **then**
      Initialize the Q-value of neighbor nodes
    end if
    The agent performs an action based on ε − greedy policy
    The agent calculates the reward of action
    The agent obtains the next state from the environment
    The agent updates the Q value in neighbor table
    if routing hole problem happens or packet is expired **then**
      Execute penalty mechanism
    end if
    $t = t + 1$
  end for
  $eposide = eposide + 1$
end while

E. Computation Complexity

We denote the number of neighbor nodes of u_i is N_i. For nieghbor discovery, there is not any for loop, so the time complexity is $O(1)$. For environment evaluation, node u_i needs to send the HELLO packets to all its neighbors one by one. That means the command will be repeated N_i times, so the time complexity is $O(N_i)$. For Q-learning-based routing in algorithm 2, there is a *while* loop and a for loop, so the time complexity is $O(MNN_i)$.

V. SIMULATION RESULT

Table 1 Simulation Parameters

Parameters	Settings
Number of drones	$20 \sim 100$
Velocity of drones	$10 \sim 40 m/s$
Space size	$2000m \times 2000m \times 200m$
Communication range	$200\ m$
MAC protocol	IEEE 802.11n
Transport protocol	UDP
Initial energy	100000 units
Hello interval	$250\ ms$
Mobility model	Gaussian Markov mobility model

Some important parameters are given in Table 1. We will evaluate the algorithm from three aspects: average end-to-end delay (E2E), packet delivery ratio (PDR), energy consumption and routing overhead.

According to Fig 4 and 5, for all algorithms, there is a noticeable increase in delay as the number of drones increases. This trend may results from the heightened communication and processing load as the network grows. However, our QVIR algorithm consistently shows the lowest delay across all numbers of drones compared with QGeo and GPSR. Delay in QVIR is about 25% and 50% lower than QGeo and GPSR respectively. As is shown in Fig 5, As the velocity of the drones increases, our QVIR also outperforms the QGeo and GPSR in delay, which is reduced around 18% and 42% respectively. The reason might be our more holistic consideration of some factors in the algorithm design which may influence the network delay performance.

PDR is defined as the ratio of the number of data packets successfully delivered to the destination to the total number of packets that were sent from the source. It is expressed as a percentage.

Fig 6 and Fig 7 indicate that all algorithms perform a decline in PDR as the velocity of drones increases, opposite to

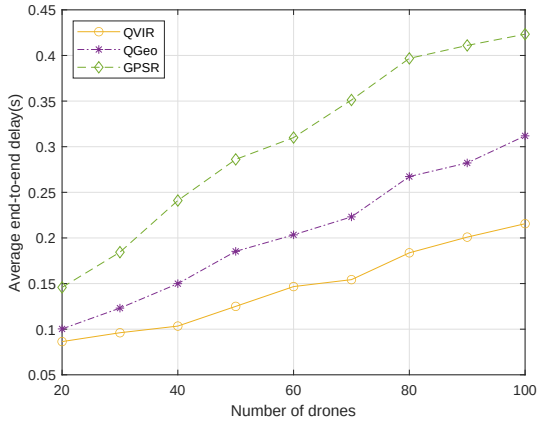

Figure 4 Average E2E delay at different number of drones

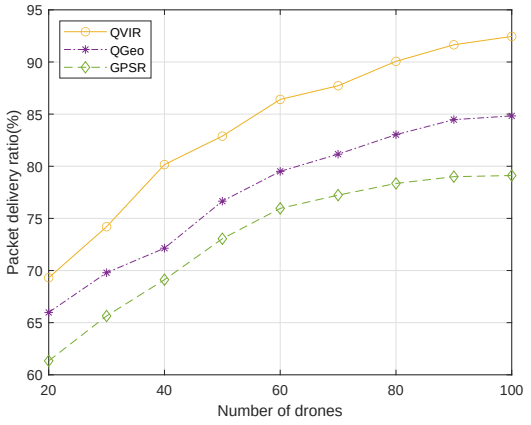

Figure 6 PDR at different number of drones

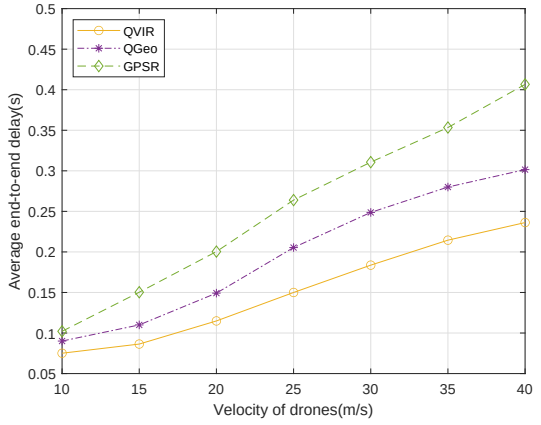

Figure 5 Average E2E delay at different velocity of drones

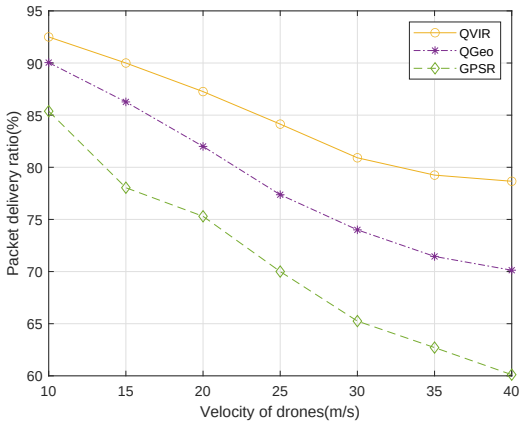

Figure 7 PDR at different velocity of drones

the situation when the changing factor is number of drones. Across both charts, the QVIR algorithm consistently demonstrates the highest PDR, reaching over 90% when the environment is good. It is probably due to the better Q-learning design and our decrease of routing hole problem which thanks to the environment evaluation method in some way.

Energy consumption in FANETs refers to the total amount of electrical energy used by UAVs for various operations, including communication.

Fig 8 and Fig 9 show that QVIR maintains the best energy efficiency across all tested velocities, consuming around 5% and 10% less energy than that in QGeo and GPSR as the node density increases.There is a similar situation when velocity of drones rises. The benefit of QVIR may result from our consideration of energy consumption and evaluation of surrounding environment, reducing extra packet retransmission.

Routing overhead refers to the additional resources, such as additional control packets, that are required to manage the routing of data packets through a network.

From Fig 10 and Fig 11, we can find that routing overhead increases as the number of drones becomes larger. A same trend can be seen as the velocity rises. Through all tests, QVIR has higher overhead than other two algorithms. The reason might be our larger HELLO packets which are sent to transmit the neighbor node information, including velocity, energy, environment metric and so on.

VI. CONCLUSION

The dramatic changes in FANET topology in low altitude and the limited energy of UAVs make it challenging to design a suitable FANET routing algorithm. In this paper, we propose QVIR algorithm, in which a modified YOLOv5 algorithm is added to the design of Q-learning. By taking into account latency and energy, we also dynamically adjust the learning rate and discount factor according to the link stability between UAVs and their neighbourhood changes. The simu-

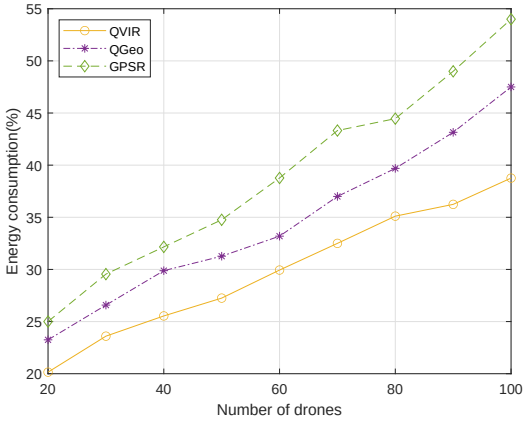

Figure 8 Energy consumption at different number of drones

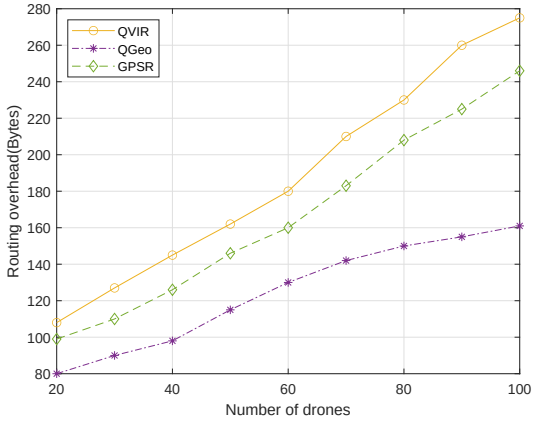

Figure 10 Routing overhead at different number of drones

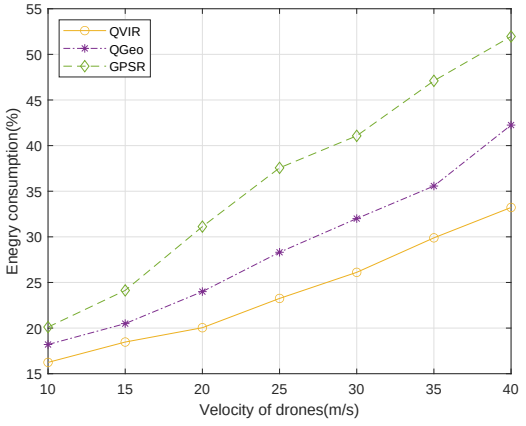

Figure 9 Energy consumption at different velocity of drones

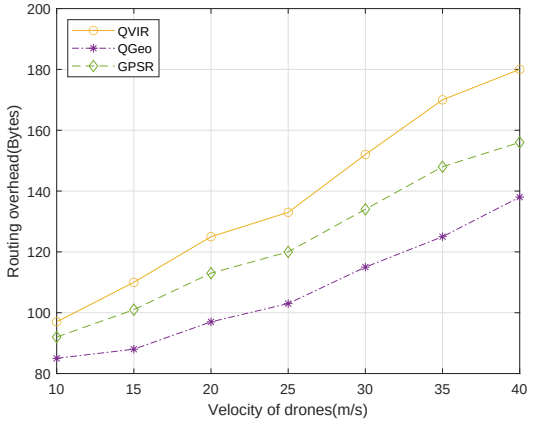

Figure 11 Routing overhead at different velocity of drones

lation results illustrate that QVIR performs better than QGeo and GPSR in terms of delay, packet delivery ratio, and energy efficiency, although QVIR has a larger routing overhead. In the future, with the further development of AI, how to design an efficient FANET routing algorithm that can performance better through AI may be an issue of interest.

References

[1] AHMED F, MOHANTA J, KESHARI A, et al. Recent advances in unmanned aerial vehicles: a review[J]. Arabian Journal for Science and Engineering, 2022, 47(7): 7963-7984.

[2] MENG K, WU Q, XU J, et al. Uav-enabled integrated sensing and communication: Opportunities and challenges[J]. IEEE Wireless Communications, 2023.

[3] KAUR M, VERMA S, et al. Flying ad-hoc network (fanet): challenges and routing protocols[J]. Journal of Computational and Theoretical Nanoscience, 2020, 17 (6): 2575-2581.

[4] SRIVASTAVA A, PRAKASH J. Future fanet with application and enabling techniques: Anatomization and sustainability issues[J]. Computer science review, 2021, 39: 100359.

[5] WHEEB A H. Flying ad hoc networks (fanet): Performance evaluation of topology based routing protocols. [J]. Int. J. Interact. Mob. Technol., 2022, 16(4): 137-149.

[6] REZWAN S, CHOI W. A survey on applications of reinforcement learning in flying ad-hoc networks[J]. Electronics, 2021, 10(4): 449.

[7] WHEEB A H, NORDIN R, SAMAH A, et al. Topology-based routing protocols and mobility models for flying

ad hoc networks: A contemporary review and future research directions[J]. Drones, 2021, 6(1): 9.

[8] WAHEED A, WAHID A, SHAH M A. Laod: Link aware on demand routing in flying ad-hoc networks[C]// 2019 IEEE International Conference on Communications Workshops (ICC Workshops). IEEE, 2019: 1-5.

[9] BEIJAR N. Zone routing protocol (zrp)[J]. Networking Laboratory, Helsinki University of Technology, Finland, 2002, 9(1): 12.

[10] LIN L, SUN Q, WANG S, et al. A geographic mobility prediction routing protocol for ad hoc uav network[C]// 2012 IEEE Globecom Workshops. IEEE, 2012: 1597-1602.

[11] JUNG W S, YIM J, KO Y B. Qgeo: Q-learning-based geographic ad hoc routing protocol for unmanned robotic networks[J]. IEEE Communications Letters, 2017, 21(10): 2258-2261.

[12] HU P, WANG J, HUANG Y, et al. A dynamic and local perspective: A reliable q-routing protocol based on fuzzy logic for fanets[C]//2023 IEEE/CIC International Conference on Communications in China (ICCC). IEEE, 2023: 1-6.

[13] BIOMO J D M M, KUNZ T, ST-HILAIRE M. An enhanced gauss-markov mobility model for simulations of unmanned aerial ad hoc networks[C]//2014 7th IFIP Wireless and Mobile Networking Conference (WMNC). IEEE, 2014: 1-8.

[14] WU W, LIU H, LI L, et al. Application of local fully convolutional neural network combined with yolo v5 algorithm in small target detection of remote sensing image[J]. PloS one, 2021, 16(10): e0259283.

[15] WATKINS C J, DAYAN P. Q-learning[J]. Machine learning, 1992, 8: 279-292.

About the Authors

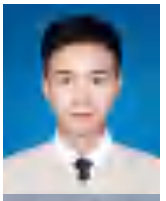

Haoran Shen received the B.Eng. degree from Harbin Institute of Technology, Shenzhen, China, in 2024, where he is currently pursuing the master's degree with the School of Electrical and Information Engineering, Shenzhen, HIT. His current research interests include flying ad hoc network (FANET) and Integrated Sensing and Communication (ISAC).

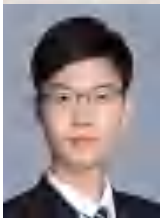

Jingzheng Chong received the M.Eng. degree from the Harbin Institute of Technology (HIT), Harbin, China, in 2021. He is currently working toward the Ph.D. degree with the School of Electrical and Information Engineering, Shenzhen, HIT. His research interests include flying ad hoc network (FANET), routing and MAC protocols.

Zhihua Yang received the Ph.D. degree in communication engineering from the Harbin Institute of Technology (HIT), Harbin, China, in 2010. He is currently an Associate Professor with the Department of Electrical and Information Engineering, Shenzhen, HIT. His current interests include air-to-space communications and networking, UAVs swarm control and wireless communications.

Joint Resource Allocation and Data Offloading for Closed-Loop Controls in Satellite-UAV Networks

Chengleyang Lei[1,2], Wei Feng[1,2], Peng Wei[3], Yunfei Chen[4], Ning Ge[1,2], and Shiwen Mao[5]

[1]Department of Electronic Engineering, Tsinghua University, Beijing 100084, China
[2]State Key Laboratory of Space Network and Communications, Tsinghua University, Beijing 100084, China
[3]National Key Laboratory of Science and Technology on Communications,
University of Electronic Science and Technology of China, Chengdu 611731, China
[4]Department of Engineering, University of Durham, DH1 3LE Durham, U.K
[5]Department of Electrical and Computer Engineering, Auburn University, Auburn, AL 36849, USA
Contact e-mail: fengwei@tsinghua.edu.cn

***Abstract*—To efficiently provide coverage for the machines and robots in remote areas, satellites and unmanned aerial vehicles (UAVs) can be utilized. In such scenarios, UAVs need to integrate different functions to support the control tasks of robots efficiently, while satellites can serve as backhaul to the cloud. To improve the overall performance of the closed-loop control tasks of robots, we jointly optimize the communication and computing resource allocation with data offloading. Specifically, we explore the linear quadratic regulator (LQR) cost to measure the control performance and formulate a sum LQR cost minimization problem. An iterative algorithm is proposed to solve the optimization problem. Simulation results are provided to demonstrate the superiority of the proposed scheme.**

***Index Terms*—Closed-loop control, linear quadratic regulator (LQR), satellite, unmanned aerial vehicle (UAV).**

I. Introduction

The future sixth generation (6G) networks are envisioned to facilitate the operation of machines and robots for their tasks [1]. When serving robots in post-disaster or remote areas where terrestrial infrastructures are unavailable, non-terrestrial infrastructures, such as satellites and unmanned aerial vehicles (UAVs), can be utilized [2]. Due to the limited capabilities of individual robots, extra devices should be deployed on UAVs to assist in task execution. For example, sensors are required to obtain environmental information, computing units are required to process data and formulate robotic actions, and communication modules are required for information exchanges. Therefore, UAVs can integrate sensors, base stations, and mobile edge computing (MEC) servers to efficiently support robots.

Due to the limited capacity of UAVs, the onboard resources are usually constrained [3]. Therefore, UAVs may need satellites to offload a portion of data to the cloud for processing. In such cases, the resource allocation and data offloading strategies should be meticulously designed to maximize resource utilization. In the literature, recent research efforts have focused on improving the communication performance by optimizing the resource allocation and data offloading. For example, Hu *et al.* investigated a UAV-aided MEC system and jointly optimized the UAV trajectory, the ratio of offloading tasks, and the user scheduling to minimize the total delays [4]. Authors in [5] maximized the energy efficiency of a space-air-ground integrated network by optimizing the UAV trajectory and resource allocation, while satisfying the quality-of-experience requirements. The above works are valuable for the satellite-UAV networks. However, most of these works focus on the communication performance only, such as latency or energy efficiency. When serving robots for their tasks, the communication systems are designed to enable control. Therefore, the control performance may be more important than merely optimizing communication performance.

Recently, several works have considered the control performance when designing communication systems. Yang *et al.* [6] optimized the power and time allocation to maximize the ratio of the remaining energy to the linear quadratic regulator (LQR) cost, where the LQR cost is a measure of the control performance. Reference [7] maximized the spectral efficiency of a wireless control system by optimizing the bandwidth and power allocation, while satisfying the control convergence rate requirement. These studies have made significant advances towards control-oriented communication system designs. However, the sensing, communication, and computing components in the system need to be jointly considered, as they cooperate closely to accomplish tasks. Furthermore, MEC should be integrated into the system to reduce the computation delay and enhance the control performance.

Motivated by the above issues, we investigate a satellite-UAV network that serves multiple robots simultaneously. The UAV is integrated with sensing, computing, and communication modules to support the control tasks of robots. The satellites offload a portion of the data. We utilize the LQR cost to evaluate the control performance, and formulate an optimization problem to minimize the sum LQR cost by optimizing the communication and computing resource allocation and the data partition. We propose an iterative algorithm to solve this optimization problem. Simulation results are provided to demonstrate the superiority of the proposed scheme

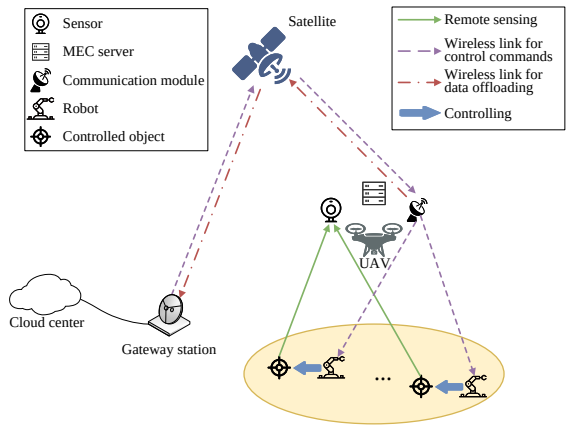

Fig. 1. Illustration of a closed-loop-control-oriented satellite-UAV network.

over the traditional communication-oriented schemes.

II. System Model and Problem Formulation

As shown in Fig. 1, we consider a satellite-UAV network that serves K robots to perform mission-critical tasks. The UAV is equipped with a sensor, an MEC server, and a communication module. Due to the limited computing capability of the UAV, some sensing data is offloaded to the cloud server through the satellite, as described in [8]. The satellite links provide backhaul to the powerful cloud center, while the UAV achieves edge capabilities such as sensing and controlling, thereby combining the wide coverage of satellites with the on-demand deployment capabilities of UAVs.

During the periodic control process, the onboard sensor monitors the state of the controlled object. Next, the acquired data is analyzed on the servers to generate control commands. The communication module then transmits these commands to robots to guide their actions. The whole process constitutes a closed loop of sensing, communication, computing, and control components, which is referred to as a sensing-communication-computing-control ($\mathbf{SC}^3$) loop. The system enables K $\mathbf{SC}^3$ loops to simultaneously serve K robots.

As described above, different components in the $\mathbf{SC}^3$ loop cooperate closely to accomplish tasks. Considering the coupling of the components, we propose treating the sensing, computing, and communication modules on the UAV as a unified entity. As a center of the task-related information, this entity can be referred to as an edge information hub (EIH) [9]. This allows us to comprehensively consider the influence of the components on the closed-loop performance. Next, we will present the model of the components within the $\mathbf{SC}^3$ loop.

In this paper, we model each robot and its corresponding object as a linear control system. Note that some complicated control systems can also be analyzed as linear systems by local linearization [10]. The discrete-time system equation of the k-th control system in cycle t is given by [11]

$$\mathbf{x}_{k,t+1} = \mathbf{A}_k \mathbf{x}_{k,t} + \mathbf{B}_k \mathbf{u}_{k,t} + \mathbf{v}_{k,t}, \tag{1}$$

where t denotes the cycle index, $\mathbf{x}_{k,t} \in \mathbb{R}^{n_k}$ and $\mathbf{u}_{k,t} \in \mathbb{R}^{m_k}$ represent the system state and the control input, n_k and m_k denote their dimensions, $\mathbf{v}_{k,t} \in \mathbb{R}^{n_k}$ denotes the Gaussian noise with mean zero and covariance $\mathbf{\Sigma}_k^{\mathrm{V}}$, and $\mathbf{A}_k$ and $\mathbf{B}_k$ are $n_k \times n_k$ and $n_k \times m_k$ parameter matrices, respectively.

We utilize the LQR cost to evaluate the control performance of the $\mathbf{SC}^3$ loop, which is formulated as [11]

$$l_k \triangleq \lim_{N\to\infty} \mathbb{E}\left[\frac{1}{N}\sum_{t=1}^{N}\left(\mathbf{x}_{k,t}^{\mathrm{T}}\mathbf{Q}_k\mathbf{x}_{k,t} + \mathbf{u}_{k,t}^{\mathrm{T}}\mathbf{R}_k\mathbf{u}_{k,t}\right)\right], \tag{2}$$

where $\mathbf{Q}_k$ and $\mathbf{R}_k$ are semi-positive definite weight matrices. The term $\mathbf{x}_{k,t}^{\mathrm{T}}\mathbf{Q}_k\mathbf{x}_{k,t}$ denotes the deviation of the system from zero state, and the term $\mathbf{u}_{k,t}^{\mathrm{T}}\mathbf{R}_k\mathbf{u}_{k,t}$ represents the control energy consumption. The LQR cost is a comprehensive measure of the state convergence and energy consumption. A small LQR cost indicates a good control performance.

The sensing process is also linear, and the observation equation can be written as

$$\mathbf{y}_{k,t} = \mathbf{C}_k \mathbf{x}_{k,t} + \mathbf{w}_{k,t}, \tag{3}$$

where $\mathbf{y}_{k,t} \in \mathbb{R}^{q_k}$ is the sensing output with q_k denoting its dimension, $\mathbf{C}_k \in \mathbb{R}^{q_k \times n_k}$ is the observation matrix, and $\mathbf{w}_{k,t} \in \mathbb{R}^{q_k}$ is the Gaussian sensing noise with mean zero and covariance $\mathbf{\Sigma}_k^{\mathrm{W}}$.

After the sensing process, the acquired data is analyzed by the computing modules to generate control commands. Due to the limited computing capability of the MEC server, some of these data is transmitted to the cloud server through the satellite. We assume that these data can be arbitrarily split into three parts: the first part is completely processed on the MEC server, the second part is pre-processed on the MEC server to extract semantic features and then sent to the cloud for further processing, and the third part is completely processed on the cloud. The data sizes of these three parts are denoted as $D_{k,1}$, $D_{k,2}$ and $D_{k,3}$ in bits. We have

$$D_{k,1} + D_{k,2} + D_{k,3} = D_k, \tag{4}$$

where D_k is the size of data in the k-th $\mathbf{SC}^3$ loop.

These three parts of data are processed in parallel as data streams. We next analyze the processing time of each data stream. The computing capabilities of the MEC server allocated to the first part and second part of data in $\mathbf{SC}^3$ loop k are denoted as $f_{k,1}$ and $f_{k,2}$, respectively. The backhaul rates from the UAV to the satellite for the second part and third part of data are denoted as $R_{k,2}$ and $R_{k,3}$, respectively. We have the following resource constraints

$$\sum_{k=1}^{K}\left(f_{k,1} + f_{k,2}\right) \le F_{\max}, \tag{5}$$

$$\sum_{k=1}^{K}\left(R_{k,2} + R_{k,3}\right) \le R_{\max}^{\mathrm{U2S}}, \tag{6}$$

where $F_{\max}$ denotes the computing capability of the MEC server, and $R_{\max}^{\mathrm{U2S}}$ denotes the satellite-backhaul rate constraint.

The computation time for the first part of data is

$$T_{k,1}^{\text{comp}} = \frac{\alpha D_{k,1}}{f_{k,1}}, \tag{7}$$

where α denotes the number of CPU cycles for processing the first part of data per bit.

Similarly, the time for pre-processing the second part of data is formulated as

$$T_{k,2}^{\text{proc}} = \frac{\beta D_{k,2}}{f_{k,2}}, \tag{8}$$

where β denotes the number of CPU cycles for pre-processing the second part of data per bit. We assume that the semantic compression ratio of the features-extracting process is ρ, i.e., $\rho D_{k,2}$-bits features will be sent to the cloud server for further processing. The transmission latency from the UAV to satellite is

$$T_{k,2}^{\text{trans}} = \frac{\rho D_{k,2}}{R_{k,2}}. \tag{9}$$

We assume that the downlink transmission latency from the satellite to the cloud and the computation time on the cloud server are negligible compared with $T_{k,2}^{\text{trans}}$ and $T_{k,2}^{\text{proc}}$, due to the typically large downlink transmission data rate and computing capability of the cloud. In addition, since the output data size is much smaller than the input data size, the transmission latency of the output data is also assumed negligible. In this case, the overall processing time of the second part of data is

$$T_{k,2}^{\text{comp}} = \begin{cases} 0, & \text{if } D_{k,2} = 0, \\ \max\left\{T_{k,2}^{\text{proc}}, T_{k,2}^{\text{trans}}\right\} + 4\tau, & \text{if } D_{k,2} > 0, \end{cases} \tag{10}$$

where τ is the propagation latency between the ground and the satellite. Since the pre-processing and transmission processes are in parallel, we consider the maximum of these times as the overall latency. When $D_{k,2} = 0$, the latency for the second part of data is 0.

Similarly, the time for processing the third part of data can be calculated by

$$T_{k,3}^{\text{comp}} = \begin{cases} 0, & \text{if } D_{k,3} = 0, \\ \dfrac{D_{k,3}}{R_{k,3}} + 4\tau, & \text{if } D_{k,3} > 0. \end{cases} \tag{11}$$

Based on the above analysis, the overall computation time is the maximum time for processing the three parts of data as

$$T_k^{\text{comp}} = \max\left\{T_{k,1}^{\text{comp}}, T_{k,2}^{\text{comp}}, T_{k,3}^{\text{comp}}\right\}. \tag{12}$$

After analyzing the data, control commands will be transmitted to the corresponding robots. The transmit data rate from the UAV to robot k can be calculated as

$$R_k^{\text{U2G}}(p_k) = \log_2\left(1 + \frac{g_k p_k}{\sigma^2}\right), \tag{13}$$

where p_k denotes the transmit power of $\mathbf{SC}^3$ loop k, g_k represents the channel power gain, and σ^2 denotes the channel noise power. The channels between the UAV and robots are assumed to be dominated by line-of-sight (LoS) links [12], so we have $g_k = \frac{\gamma_0}{d_k^2}$, where d_k denotes the distance between the UAV and robot k, and γ_0 is the reference channel power gain at a distance of one meter. Due to the limited onboard resources, we have

$$\sum_{k=1}^{K} p_k \le P_{\max}, \tag{14}$$

where $P_{\max}$ represents the transmit power constraint.

Denoting the transmission time for the control commands as T_k^{commu}, we have

$$T_k^{\text{comp}} + T_k^{\text{commu}} \le T_k, \tag{15}$$

where T_k is the time resource reserved for the computing and communication processes in each cycle of $\mathbf{SC}^3$ loop k.

To improve the control performance, we optimize the resource allocation and data offloading in the system. Next, we establish the relationship between the control performance and the communication capability. According to [11, Theorem 5], to achieve a certain LQR cost l_k, the average data throughput transmitted through channel k per cycle must satisfy the following constraint

$$BT_k^{\text{commu}} R_k^{\text{U2G}}(p_k) \ge \overline{e}_k(l_k), \tag{16}$$

where the left side of (16) denotes the information entropy transmitted per cycle, and

$$\overline{e}_k(l_k) \triangleq h_k + \frac{n_k}{2}\log_2\left(1 + \frac{n_k |\det \mathbf{N}_k \mathbf{M}_k|^{\frac{1}{n_k}}}{l_k - l_{\min,k}}\right) \tag{17}$$

denotes the minimum entropy to achieve the LQR cost l_k, $h_k \triangleq \log_2|\det \mathbf{A}_k|$ is the intrinsic entropy rate of object k, $l_{\min,k} = \text{tr}\left(\mathbf{\Sigma}_k^{\text{V}}\mathbf{S}_k\right) + \text{tr}\left(\mathbf{\Sigma}_k \mathbf{A}_k^{\text{T}} \mathbf{M}_k \mathbf{A}_k\right)$ denotes the lower bound of the LQR cost, $\mathbf{N}_k$, $\mathbf{M}_k$ and $\mathbf{S}_k$ are the solutions to the matrix equations shown in [11], which are related to the control parameters, i.e., $\mathbf{A}_k$, $\mathbf{B}_k$, $\mathbf{R}_k$, $\mathbf{Q}_k$, $\mathbf{\Sigma}_k^{\text{V}}$, and $\mathbf{\Sigma}_k^{\text{W}}$.

Using (16), we minimize the sum LQR costs of all $\mathbf{SC}^3$ loops by jointly optimizing the transmit power allocation $\mathbf{p} = \{p_k\}$, the computing capability allocation $\mathbf{f} = \{f_{k,1}, f_{k,2}\}$, the satellite transmission rate allocation $\mathbf{R} = \{R_{k,2}, R_{k,3}\}$, and the data partition $\mathbf{D} = \{D_{k,1}, D_{k,2}, D_{k,3}\}$. The optimization problem is formulated as

$$\min_{\mathbf{p},\mathbf{f},\mathbf{R},\mathbf{D},\mathbf{l}} \quad \sum_{k=1}^{K} l_k \tag{18a}$$

$$\textit{s.t.} \quad \sum_{k=1}^{K} p_k \le P_{\max}, \tag{18b}$$

$$D_{k,1} + D_{k,2} + D_{k,3} = D_k, \quad k = 1, 2, \cdots, K, \tag{18c}$$

$$\sum_{k=1}^{K} (f_{k,1} + f_{k,2}) \le F_{\max}, \tag{18d}$$

$$\sum_{k=1}^{K} (R_{k,2} + R_{k,3}) \le R_{\max}^{\text{U2S}}, \tag{18e}$$

$$T_k^{\text{comp}} + T_k^{\text{commu}} \le T_k, \quad k = 1, 2, \cdots, K, \tag{18f}$$

$$BT_k^{\text{commu}} R_k^{\text{U2G}}(p_k) \geq \overline{e}_k(l_k), \tag{18g}$$

where $\mathbf{l} = [l_1, l_2, \cdots, l_K]$. Problem (18) is difficult to solve due to the non-convex and non-continuous expression of T_k^{comp} as in (12). Next, we will recast this problem to a more tractable form and propose an iterative algorithm to solve it.

III. Joint Resource Allocation and Data Offloading

In this section, we will solve the optimization problem (18) by proposing an iterative algorithm based on the successive convex approximation (SCA) method.

A. Problem Simplification

From (18), we can find that the data partition parameters of each $\mathbf{SC}^3$ loop will be decoupled if the computing capability allocation and satellite-backhaul rate allocation are given. As l_k is monotonically decreasing with the transmission time T_k^{commu}, the optimal offloading scheme to minimize the LQR cost also minimizes the computing time. Therefore, the optimal data partition scheme in $\mathbf{SC}^3$ loop k, given the computing capability allocation and satellite-backhaul rate allocation, can be obtained by solving the following optimization problem

$$\min_{\mathbf{D}_k, \mathbf{f}_k, \mathbf{R}_k} \quad \max\left\{T_{k,1}^{\text{comp}}, T_{k,2}^{\text{comp}}, T_{k,3}^{\text{comp}}\right\} \tag{19a}$$

$$\text{s.t.} \quad D_{k,1} + D_{k,2} + D_{k,3} = D_k, \tag{19b}$$

$$f_{k,1} + f_{k,2} \leq f_k, \tag{19c}$$

$$R_{k,2} + R_{k,3} \leq R_k, \tag{19d}$$

where f_k and R_k denote the computing capability and satellite-backhaul rate allocated to $\mathbf{SC}^3$ loop k, respectively, and the variable vectors to be optimized are $\mathbf{D}_k = [D_{k,1}, D_{k,2}, D_{k,3}]$, $\mathbf{f}_k = [f_{k,1}, f_{k,2}]$ and $\mathbf{R}_k = [R_{k,2}, R_{k,3}]$.

Once the problem (19) is solved, the optimal resource allocation can be obtained via the following problem

$$\min_{\mathbf{p}, \mathbf{f}', \mathbf{R}', \mathbf{l}} \quad \sum_{k=1}^{K} l_k \tag{20a}$$

$$\text{s.t.} \quad \sum_{k=1}^{K} p_k \leq P_{\max}, \tag{20b}$$

$$\sum_{k=1}^{K} f_k \leq F_{\max}, \tag{20c}$$

$$\sum_{k=1}^{K} R_k \leq R_{\max}^{\text{U2S}}, \tag{20d}$$

$$T_k^{\text{comp},*}(f_k, R_k) + T_k^{\text{commu}} \leq T_k, \ k = 1, 2, \cdots, K, \tag{20e}$$

$$BT_k^{\text{commu}} R_k^{\text{U2G}}(p_k) \geq \overline{e}_k(l_k), \tag{20f}$$

where $\mathbf{f}' = \{f_k\}$ and $\mathbf{R}' = \{R_k\}$. The function $T_k^{\text{comp},*}(f_k, R_k)$ denotes the minimal computation time of loop k when f_k and R_k are given, which is solution to (19a).

To solve (20), we give the closed-form expression of $T_k^{\text{comp},*}(f_k, R_k)$ by solving (19) in the following proposition.

Proposition 1: *$T_k^{comp,*}(f_k, R_k)$ is given by the piece-wise function shown in* (21) *on the next page.*

Proof: If $f_k \geq \frac{\alpha D_k}{4\tau}$, we have $\frac{\alpha D_k}{f_k} < 4\tau$, indicating that the time to process all the data locally will be less than the propagation delay 4τ. In such a case, all the data should be processed on the MEC, and we have $T_k^{\text{comp}} = T_{k,1}^{\text{comp}} = \frac{\alpha D_k}{f_k}$.

On the contrary, if $f_k < \frac{\alpha D_k}{4\tau}$, we have

$$T_{k,1}^{\text{comp}} = T_{k,2}^{\text{comp}} = T_{k,3}^{\text{comp}}, \tag{22}$$

$$T_{k,2}^{\text{proc}} = T_{k,2}^{\text{trans}}. \tag{23}$$

Otherwise, we can adjust the data partition or the resource allocation within $\mathbf{SC}^3$ loop k, to keep the overall computing time non-increasing. In addition, as the latency is non-increasing with respect to $f_{k,1}$, $f_{k,2}$, $R_{k,1}$ and $R_{k,2}$, we have $f_{k,1} + f_{k,2} = f_k$ and $R_{k,2} + R_{k,3} = R_k$. Based on the above equations, we have $f_{k,1} = f_k - f_{k,1}$, $R_{k,2} = \frac{\rho}{\beta} f_{k,2}$, and $R_{k,3} = R_k - \frac{\rho}{\beta} f_{k,2}$. Substituting these variables into (19b) and (22), we can formulate T_k^{comp} as

$$T_k^{\text{comp}} = \frac{\alpha\beta D_k - 4\beta\tau f_k + 4\beta\tau f_{k,2}}{(\alpha - \alpha\rho - \beta) f_{k,2} + \beta f_k + \alpha\beta R_k} + 4\tau. \tag{24}$$

In (24), we formulate T_k^{comp} as a fractional linear function of $f_{k,2}$. Therefore, T_k^{comp} is monotonic with respect to $f_{k,2}$. If $4\beta\tau R_k - (\alpha - \alpha\rho - \beta) D_k + 4(1-\rho)\tau f_k \geq 0$, it can be proved that T_k^{comp} is increasing with respect to $f_{k,2}$. In such case, $f_{k,2} = 0$ must hold to minimize T_k^{comp}, and we have

$$T_k^{\text{comp}} = \frac{\alpha D_k - 4\tau f_k}{f_k + \alpha R_k} + 4\tau. \tag{25}$$

Similarly, if $4\beta\tau R_k - (\alpha - \alpha\rho - \beta) D_k + 4(1-\rho)\tau f_k \leq 0$, $f_{k,2}$ should be as large as possible. With the constraints $f_{k,1} \geq 0$ and $R_{k,3} \geq 0$, we can obtain the optimal value of $f_{k,2}$, and calculate the corresponding computing time, which completes the proof. More detailed proof can be found in our extended paper [9]. □

B. Iterative Algorithm to solve (19)

Although we recast the original problem (18) to a more tractable form (19), it is still difficult to solve it as it is a non-convex optimization problem. In this subsection, we propose an iterative algorithm to solve (19) based on the SCA method [13].

First, in order to address the non-convexity of constraint (20f), we include the communication time $\{T_k^{\text{commu}}\}$ as variables to be optimized, and rewrite (20) as

$$\min_{\mathbf{p}, \mathbf{f}', \mathbf{R}', \mathbf{l}, \mathbf{T}^{\text{commu}}} \quad \sum_{k=1}^{K} l_k \tag{26a}$$

$$\text{s.t.} \quad \sum_{k=1}^{K} p_k \leq P_{\max}, \tag{26b}$$

$$\sum_{k=1}^{K} f_k \leq F_{\max}, \tag{26c}$$

$$T_k^{\text{comp},*}(f_k,R_k)=\begin{cases} T_k^1(f_k,R_k)\triangleq\dfrac{\beta D_k}{\beta R_k+(1-\rho)f_k}+4\tau, \quad (f_k,R_k)\in\mathcal{S}_1\triangleq\left\{(f,R)\mid 0\le f\le\min\left\{\dfrac{(\alpha-\alpha\rho-\beta)D_k-4\beta\tau R}{4(1-\rho)\tau},\dfrac{\beta R}{\rho}\right\}\right\} \\ T_k^2(f_k,R_k)\triangleq\dfrac{\rho\alpha D_k-4\rho\tau f_k+4\beta R_k\tau}{\rho f_k+(\alpha-\beta)R_k}+4\tau,\ (f_k,R_k)\in\mathcal{S}_2\triangleq\left\{(f,R)\mid \dfrac{\beta R}{\rho}\le f\le\dfrac{(\alpha-\alpha\rho-\beta)D_k-4\beta\tau R}{4(1-\rho)\tau},R\ge 0\right\} \\ T_k^3(f_k,R_k)\triangleq\dfrac{\alpha D_k-4\tau f_k}{f_k+\alpha R_k}+4\tau,\ (f_k,R_k)\in\mathcal{S}_3\triangleq\left\{(f,R)\mid \dfrac{(\alpha-\alpha\rho-\beta)D_k-4\beta\tau R}{4(1-\rho)\tau}\le f\le\dfrac{\alpha D_k}{4\tau},f\ge 0,R\ge 0\right\} \\ T_k^4(f_k,R_k)\triangleq\dfrac{\alpha D_k}{f_k}, \quad (f_k,R_k)\in\mathcal{S}_4\triangleq\left\{(f,R)\mid f\ge\dfrac{\alpha D_k}{4\tau},R\ge 0\right\}\end{cases} \tag{21}$$

$$\sum_{k=1}^{K}R_k\le R_{\max}^{\text{U2S}}, \tag{26d}$$

$$T_k^{\text{comp},*}(f_k,R_k)+T_k^{\text{commu}}\le T_k,\quad k=1,2,\cdots,K, \tag{26e}$$

$$BR_k^{\text{U2G}}(p_k)\ge\frac{\overline{e}_k(l_k)}{T_k^{\text{commu}}},\quad k=1,2,\cdots,K, \tag{26f}$$

where $\mathbf{T}^{\text{commu}}=\{T_k^{\text{commu}}\}$. It can be shown that the function $\frac{\overline{e}_k(l_k)}{T_k^{\text{commu}}}$ is convex with respect to (l_k,T_k^{commu}). Therefore, constraint (26f) describes a convex set. Next, we handle the non-convexity of the function $T_k^{\text{comp},*}(f_k,R_k)$ in (26e).

To solve (26), we propose an iterative algorithm based on the SCA method. First, we introduce the following proposition in order to approximate $T_k^{\text{comp},*}(f_k,R_k)$.

Proposition 2: *For any $x>0$, $y>0$, $x_0>0$ and $y_0>0$, we have the following inequality*

$$\frac{1}{xy}\ge\frac{1}{x_0y_0}\left(3-\frac{x}{x_0}-\frac{y}{y_0}\right). \tag{27}$$

The equality holds when $x=x_0$ and $y=y_0$.

Proof: Using the Hessian matrix, it can be shown that $1/xy$ is convex with $x>0$, $y>0$. The inequality in (27) can be obtained immediately through the first-order condition of convex functions [14, Section 3.1.3]. □

Substituting $x=1/u, y=au+bv, x_0=1/u_0$, and $y_0=au_0+bv_0$ into (27), we have

$$\frac{u}{au+bv}\ge\frac{u_0}{au_0+bv_0}\left(3-\frac{u_0}{u}-\frac{au+bv}{au_0+bv_0}\right), \tag{28}$$

where $a>0$, $b>0$, $u>0$, and $v>0$. Based on (28), we approximate $T_k^{\text{comp},*}(f_k,R_k)$ by a convex function $\overline{T}_k^{\text{comp},*}(f_k,R_k|f_{k0},R_{k0})$, which is formulated as (29) on the next page. The functions $\overline{T}_k^2(f_k,R_k|f_{k0},R_{k0})$ and $\overline{T}_k^3(f_{k0},R_{k0})$ in (29) are two functions that approximate $T_k^2(f_k,R_k)$ and $T_k^3(f_k,R_k)$ based on (28), respectively, as shown in (30) and (32) on the next page.

The following proposition gives the properties of $\overline{T}_k^{\text{comp},*}$.

Proposition 3: *The function $\overline{T}_k^{comp,*}(f_k,R_k|f_{k0},R_{k0})$ shown in* (29) *is convex, and satisfies the following inequality*

$$\overline{T}_k^{comp,*}(f_k,R_k|\ f_{k0},R_{k0})\ge T_k^{comp,*}(f_k,R_k), \tag{34}$$

where f_{k0} and R_{k0} are non-negative constants, and the equality holds when $f_k=f_{k0}$, and $R_k=R_{k0}$.

Proof: First, as T_k^1, $\overline{T}_k^2$, $\overline{T}_k^3$ and T_k^4 are reciprocal functions of the linear combination of f_K and R_k, we can obtain the convexity of $\overline{T}_k^{\text{comp},*}(f_k,R_k|f_{k0},R_{k0})$.

Next, by comparing the values of $T_k^i(f_k,R_k)$ for $i\in[1,2,3,4]$, we can establish the relationship among the four functions when (f_k,R_k) is in different regions as

$$T_k^4(f_k,R_k)>T_k^3(f_k,R_k)>T_k^1(f_k,R_k),\ (f_k,R_k)\in\mathcal{S}_1, \tag{35a}$$
$$T_k^4(f_k,R_k)>T_k^3(f_k,R_k)\ge T_k^2(f_k,R_k),\ (f_k,R_k)\in\mathcal{S}_2, \tag{35b}$$
$$T_k^1(f_k,R_k)\ge T_k^2(f_k,R_k)\ge T_k^3(f_k,R_k),\ (f_k,R_k)\in\mathcal{S}_3, \tag{35c}$$
$$T_k^4(f_k,R_k)\ge T_k^3(f_k,R_k),\ (f_k,R_k)\in\mathcal{S}_3, \tag{35d}$$
$$T_k^2(f_k,R_k)\ge T_k^3(f_k,R_k)>T_k^4(f_k,R_k),\ (f_k,R_k)\in\mathcal{S}_4. \tag{35e}$$

Therefore, if $(f_{k0},R_{k0})\in\mathcal{S}_1\cup\mathcal{S}_2$, we have

$$\overline{T}_k^{\text{comp},*}(f_k,R_k|\ f_{k0},R_{k0}) \tag{36a}$$
$$=\max\left\{T_k^1(f_k,R_k),\overline{T}_k^2(f_k,R_k|f_{k0},R_{k0})\right\} \tag{36b}$$
$$\ge\max\left\{T_k^1(f_k,R_k),T_k^2(f_k,R_k)\right\} \tag{36c}$$
$$\ge T_k^{\text{comp},*}(f_k,R_k), \tag{36d}$$

where (36d) can be obtained from (35a)-(35e) by examining the cases separately where (f_k,R_k) belongs to different regions.

Following a similar procedure, it can be proven that $\overline{T}_k^{\text{comp},*}(f_k,R_k|\ f_{k0},R_{k0})\ge T_k^{\text{comp},*}(f_k,R_k)$ when $(f_{k0},R_{k0})\in\mathcal{S}_3$ and $(f_{k0},R_{k0})\in\mathcal{S}_4$.

Finally, since $\overline{T}_k^2(f_{k0},R_{k0}|f_{k0},R_{k0})=T_k^2(f_{k0},R_{k0})$ and $\overline{T}_k^3(f_{k0},R_{k0}|f_{k0},R_{k0})=T_k^3(f_{k0},R_{k0})$, the equality condition in **Proposition 3** is obtained. □

By approximating $T_k^{\text{comp},*}(f_k,R_k)$ to $\overline{T}_k^{\text{comp},*}(f_k,R_k|f_{k0},R_{k0})$, the approximate optimization problem of (26) is formulated as

$$\min_{\mathbf{p},\mathbf{f}',\mathbf{R}',\mathbf{l},\mathbf{T}^{\text{commu}}}\ \sum_{k=1}^{K}l_k \tag{37a}$$
$$s.t.\ \overline{T}_k^{\text{comp},*}\left(f_k,R_k|f_k^{(i-1)},R_k^{(i-1)}\right)+T_k^{\text{commu}}\le T_k,\quad k=1,2,\cdots,K, \tag{37b}$$
$$(26b)-(26d),(26f), \tag{37c}$$

$$\overline{T}_k^{\text{comp},*}\left(f_k, R_k | f_{k0}, R_{k0}\right) = \begin{cases} \max\left\{T_k^1\left(f_k, R_k\right), \overline{T}_k^2\left(f_k, R_k | f_{k0}, R_{k0}\right)\right\}, & \left(f_{k0}, R_{k0}\right) \in \mathcal{S}_1 \cup \mathcal{S}_2 \\ \overline{T}_k^3\left(f_k, R_k | f_{k0}, R_{k0}\right), & \left(f_{k0}, R_{k0}\right) \in \mathcal{S}_3 \\ T_k^4\left(f_k, R_k\right), & \left(f_{k0}, R_{k0}\right) \in \mathcal{S}_4 \end{cases} \tag{29}$$

$$\overline{T}_k^2\left(f_k, R_k | f_{k0}, R_{k0}\right) \triangleq \frac{\rho\alpha D_k}{\rho f_k + (\alpha-\beta) R_k} + 4\frac{\alpha\tau}{\alpha-\beta} - \frac{\frac{4\rho\alpha\tau}{\alpha-\beta} f_{k0}}{\rho f_{k0} + (\alpha-\beta) R_{k0}} \left[3 - \frac{f_{k0}}{f_k} - \frac{\rho f_k + (\alpha-\beta) R_k}{\rho f_{k0} + (\alpha-\beta) R_{k0}}\right] \tag{30}$$

$$\geq \frac{\rho\alpha D_k}{\rho f_k + (\alpha-\beta) R_k} + 4\frac{\alpha\tau}{\alpha-\beta} - \frac{\frac{4\rho\alpha\tau}{\alpha-\beta} f_k}{\rho f_k + (\alpha-\beta) R_k} = T_k^2\left(f_k, R_k\right) \tag{31}$$

$$\overline{T}_k^3\left(f_k, R_k | f_{k0}, R_{k0}\right) \triangleq \frac{\alpha D_k}{f_k + \alpha R_k} + 4\tau - \frac{4\tau f_{k0}}{f_{k0} + \alpha R_{k0}} \left[3 - \frac{f_{k0}}{f_k} - \frac{f_k + \alpha R_k}{f_{k0} + \alpha R_{k0}}\right] \tag{32}$$

$$\geq \frac{\alpha D_k}{f_k + \alpha R_k} + 4\tau - \frac{4\tau f_k}{f_k + \alpha R_k} = T_k^3\left(f_k, R_k\right) \tag{33}$$

Algorithm 1: Iterative algorithm for solving problem (26)

Input : System parameters $P_{\max}$, $F_{\max}$, $R_{\max}$, etc; the convergence tolerance ϵ.

Initialization: Calculate a feasible $\mathbf{f}'^0$ and $\mathbf{R}'^0$ based on (26c) and (26d), and set $i = 0$

repeat

  Set $i = i + 1$;

  Update $\mathbf{p}^i$, $\mathbf{f}'^i$ and $\mathbf{R}'^i$ by solving (37), denote the value of the objective function as L^t;

until $\frac{L^{i-1} - L^i}{L^{i-1}} < \epsilon$;

Output : The optimal resource allocation $\mathbf{p}^i$, $\mathbf{f}'^i$, $\mathbf{R}'^i$, and the sum LQR cost L^i.

where i is the iteration index, and $f_k^{(i-1)}$ and $R_k^{(i-1)}$ denote the solutions in the $(i-1)$-th iteration. As $\overline{T}_k^{\text{comp},*}\left(f_k, R_k | f_{k0}, R_{k0}\right)$ is a convex function, problem (37) is convex, which can be solved efficiently by convex optimization tools [14].

By solving (37) iteratively, **Algorithm 1** is proposed to solve (26). Denoting the optimal solution to problem (37) in the i-th iteration as $\left(\mathbf{p}^i, \mathbf{f}'^i, \mathbf{R}'^i, \mathbf{l}^i, \mathbf{T}^{\text{commu},i}\right)$, we have

$$\overline{T}_k^{\text{comp},*}\left(f_k^{(i-1)}, R_k^{(i-1)} | f_k^{(i-1)}, R_k^{(i-1)}\right) + T_k^{\text{commu}} \tag{38a}$$

$$= T_k^{\text{comp},*}\left(f_k^{(i-1)}, R_k^{(i-1)}\right) + T_k^{\text{commu}} \tag{38b}$$

$$\leq \overline{T}_k^{\text{comp},*}\left(f_k^{(i-1)}, R_k^{(i-1)} | f_k^{(i-2)}, R_k^{(i-2)}\right) + T_k^{\text{commu}} \tag{38c}$$

$$\leq T_k, \tag{38d}$$

where (38c) follows from (34), and (38d) holds because $\mathbf{f}'^{i-1}$ and $\mathbf{R}'^{i-1}$ are the optimal solutions to (37) in the $(i-1)$-th iteration and should satisfy the constraint (37b). Therefore, $\left(\mathbf{p}^{(i-1)}, \mathbf{f}'^{(i-1)}, \mathbf{R}'^{(i-1)}, \mathbf{l}^{(i-1)}, \mathbf{T}^{\text{commu},(i-1)}\right)$ is also feasible to the optimization problem (37) in the i-th iteration, indicating that the objective function is non-increasing during the iteration. Therefore, **Algorithm 1** converges.

IV. Simulation Results

In this section, simulation results are provided to evaluate the proposed joint resource allocation and data offloading scheme. We use the CVX toolbox to solve the convex optimization problem [14]. The number of robots is set as $K = 5$. The robots are assumed to be randomly distributed in a circular area with a radius of 5000 m, where the UAV is at the center of the circular area with a height of 100 m. We set $B = 5$ kHz, $\tau = 5$ ms, $\beta_0 = -60$ dB, and $\sigma^2 = -110$ dBm [15]. For the computing parameters, we set $D_k = 300$ Mb, $\rho = 0.2$, $\alpha = 100$ CPU cycles/bit, and $\beta = 50$ CPU cycles/bit. Unless otherwise specified, the resource constraints are set as $T_k = 70$ ms, $F_{\max} = 5$ GHz, $P_{\max} = 10$ dBW and $R_{\max}^{\text{U2S}} = 50$ Mbps.

The control parameters are set as follows. The state matrices $\mathbf{A}_k$ are assumed to be 50×50 diagonal matrices with diagonal elements randomly selected in $[-10, 10]$. The covariance matrices of the control system noise and sensing noise are $\mathbf{\Sigma}_k^{\text{V}} = \sigma_{\text{V},k}^2 \times \mathbf{I}_n$ and $\mathbf{\Sigma}_k^{\text{W}} = \sigma_{\text{W},k}^2 \times \mathbf{I}_n$, with $n = 50$, $\sigma_{\text{V},k}^2 = \sigma_{\text{V}}^2 = 0.01$, and $\sigma_{\text{W},k}^2 = \sigma_{\text{W}}^2 = 0.001$. The observation matrices and the LQR weight matrices are set as $\mathbf{C}_k = \mathbf{I}_n$, $\mathbf{Q}_k = \mathbf{I}_n, \mathbf{R}_k = \mathbf{0}$.

To evaluate the proposed algorithm, we compare it with the following benchmark schemes.

- Closed-loop-oriented power allocation: optimizing transmit power allocation to minimize the sum LQR cost as in [16], where the computing capability and the satellite-backhaul rate are allocated equally to the loops.
- Communication-oriented scheme: optimizing the computing capability allocation to minimize the sum computation time [17], where the satellite-backhaul rate is allocated equally to the loops, then the transmit power allocated is optimized to maximize the data throughput.

Fig. 2 shows the LQR cost achieved by the three schemes under different transmit power constraints. Note that the control system with the communication-oriented scheme is

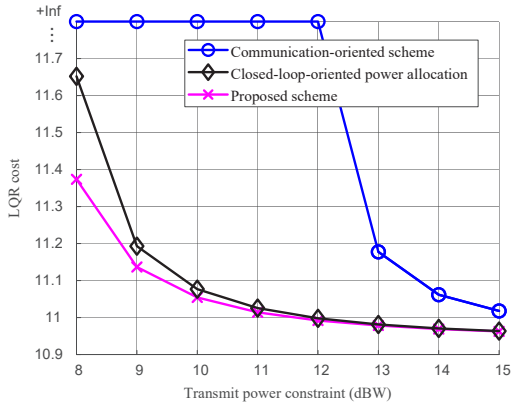

Fig. 2. LQR cost achieved by different schemes, varying with the transmit power constraint.

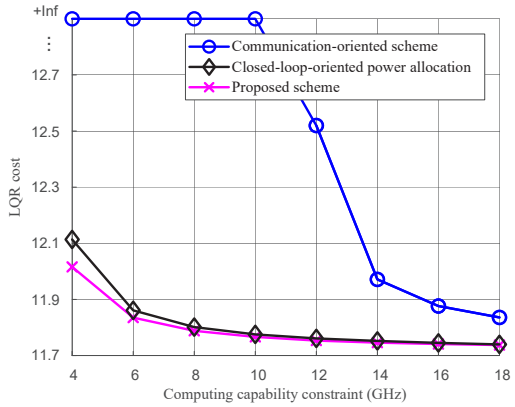

Fig. 3. LQR cost achieved by different schemes, varying with the computing capability constraint.

unstable when the power constraint is lower than 12 dBW, so the corresponding LQR cost is infinite. It is seen that the LQR cost decreases with increased power constraint. This is because more exact control commands can be transmitted as the transmit power increases, leading to an improved control performance. In addition, the proposed scheme achieves the lowest LQR cost among the three schemes, showing its superiority.

In Fig. 3, we show the LQR cost under different computing capability constraints. We can see that the proposed scheme achieves lower LQR cost than the benchmark schemes. Similar to Fig. 2, it is shown that the LQR cost decreases with increased $F_{\max}$, as the time available for communication increases with the increase of the computing capability.

V. Conclusion

In this paper, we have investigated a satellite-UAV network serving multiple robots to perform control tasks. In order to improve the overall performance of these control tasks, we have formulated a sum LQR cost minimization problem by jointly optimizing resource allocation and data offloading. We have recast the problem to a more tractable form and proposed an iterative algorithm to solve it. Simulation results have demonstrated the superiority of the proposed scheme.

References

[1] M. Giordani, M. Polese, M. Mezzavilla, S. Rangan and M. Zorzi, "Toward 6G networks: Use cases and technologies," *IEEE Commun. Mag.*, vol. 58, no. 3, pp. 55-61, Mar. 2020.

[2] W. Feng, Y. Wang, Y. Chen, N. Ge, and C.-X. Wang, "Structured satellite-UAV-terrestrial networks for 6G Internet of Things," *IEEE Netw.*, vol. 38, no. 4, pp. 48-54, Jul. 2024.

[3] W. Feng *et al.*, "Radio map-based cognitive satellite-UAV networks towards 6G on-demand coverage," *IEEE Trans. Cogn. Commun. Netw.*, vol. 10, no. 3, pp. 1075-1089, Jun. 2024.

[4] Q. Hu, Y. Cai, G. Yu, Z. Qin, M. Zhao and G. Y. Li, "Joint offloading and trajectory design for UAV-enabled mobile edge computing systems" *IEEE Internet Things J.*, vol. 6, no. 2, pp. 1879-1892, Apr. 2019.

[5] Z. Hu *et al.*, "Joint resources allocation and 3d trajectory optimization for uav-enabled space-air-ground integrated networks," *IEEE Trans. Veh. Technol.*, vol. 72, no. 11, pp. 14214-14229, Nov. 2023.

[6] H. Yang, K. Zhang, K. Zheng and Y. Qian, "Leveraging linear quadratic regulator cost and energy consumption for ultrareliable and low-latency IoT control systems," *IEEE Internet Things J.*, vol. 7, no. 9, pp. 8356-8371, Sep. 2020.

[7] B. Chang, L. Zhang, L. Li, G. Zhao, and Z. Chen, "Optimizing resource allocation in URLLC for real-time wireless control systems," *IEEE Trans. Veh. Tech.*, vol. 68, no. 9, pp. 8916-8927, Sep. 2019.

[8] X. Fang, W. Feng, T. Wei, Y. Chen, N. Ge and C. -X. Wang, "5G embraces satellites for 6G ubiquitous IoT: Basic models for integrated satellite terrestrial networks," *IEEE Internet Things J.*, vol. 8, no. 18, pp. 14399-14417, Sep. 2021.

[9] C. Lei *et al.*, "Edge information hub: Orchestrating satellites, UAVs, MEC, sensing and communications for 6G closed-Loop controls," arXiv preprint, arXiv:2403.06579, Mar. 2024.

[10] E. D. Sontag, *Mathematical Control Theory: Deterministic Finite Dimensional Systems.* New York, NY, USA: Springer Science & Business Media, 2013.

[11] V. Kostina and B. Hassibi, "Rate-cost tradeoffs in control," *IEEE Trans. Auto. Control*, vol. 64, no. 11, pp. 4525-4540, Nov. 2019.

[12] Y. Zeng, R. Zhang, and T. J. Lim, "Throughput maximization for UAV-enabled mobile relaying systems," *IEEE Trans. Commun.*, vol. 64, no. 12, pp. 4983-4996, Dec. 2016.

[13] Y. Sun, P. Babu and D. P. Palomar, "Majorization-minimization algorithms in signal processing, communications, and machine learning," *IEEE Trans. Signal Process.*, vol. 65, no. 3, pp. 794-816, Feb. 2017.

[14] S. Boyd and L. Vandenberghe, *Convex Optimization.* Cambridge, U.K.: Cambridge Univ. Press, 2004.

[15] M. Hua, Y. Wang, Z. Zhang, C. Li, Y. Huang, and L. Yang, "Power-efficient communication in UAV-aided wireless sensor networks," *IEEE Commun. Lett.*, vol. 22, no. 6, pp. 1264-1267, Jun. 2018.

[16] C. Lei *et al.* "Control-oriented power allocation for integrated satellite-UAV networks," *IEEE Wireless Commun. Lett.*, vol. 12, no. 5, pp. 883-887, May 2023.

[17] J. Ren, G. Yu, Y. He and G. Y. Li, "Collaborative cloud and edge computing for latency minimization," *IEEE Trans. Veh. Technol.*, vol. 68, no. 5, pp. 5031-5044, May 2019.

基于天基分布式计算的动态低轨星座接入任务调度

徐潇审[1]，罗俊波[1]，卢俊麒[1]，杜金艳[2]
（1.中国人民解放军 32039 部队，北京，102300;
2.中国联合网络通信集团有限公司，北京 100032）

摘　要：针对 LEO 星座中航天器接入和数据中继的波束资源调度难题，提出一种基于星载分布式计算的多波束源任务调度算法。航天器可以动态申请波束资源并获得准实时任务调度结果响应。在求解过程中，需要考虑任务的属性和资源的限制，如开始和结束时间、优先级、可见窗口和链路建立时间。因此，任务调度是一类复杂约束条件下的组合优化过程，需要大量计算资源。基于二维个体描述模型和单一父代遗传（遗传算法）的设计，旨在支持分布式计算，以提高星上应用的可行性和突破 LEO 卫星星载计算能力的限制。同时，分布式计算框架提升了系统和调度过程的鲁棒性。本文设计了由八个嵌入式设备组成的分布式集群，用于模拟 LEO 卫星分布式计算的场景。对算法流程、数学模型、触发策略、基于遗传算法的创新改进和分布式计算架构进行了研究和验证。仿真和实测结果表明，与传统的双链路遗传算法相比，所提算法在分配结果和响应时间上都有明显提升。

关键词: 波束源分配、分布式计算、LEO 星座、航天器接入、卫星任务调度

Dynamic LEO Constellation Scheduling Based on Space-based Distributed Computing

Xu Xiaoshen[1]，Luo Junbo[1]，Lu Junqi[1]，Du Jinyan[2]
(1.Unit 32039 of the People's Liberation Army, Beijing, 102300;
2. China United Network Communications Group Co., Ltd., Beijing 100032)

Abstract: Aiming at the problem of beam resource scheduling for spacecraft access and data relay in LEO constellation, a multi-beam source task scheduling algorithm based on spaceborne distributed computing is proposed. The spacecraft can dynamically apply beam resources and obtain near-real-time mission scheduling results. In solving the process, you need to consider the attributes of the task and resource constraints, such as start and end time, priority, visible window, and link establishment time. Therefore, task scheduling is a combinatorial optimization process under complex constraints, which requires a lot of computational resources. The design, based on a two-dimensional individual description model and single parent genetics (genetic algorithm), aims to support distributed computing to improve the feasibility of on-board applications and break through the limitations of on-board computing power on LEO satellites. At the same time, the distributed computing framework improves the robustness of the system and scheduling process. In this paper, a distributed cluster composed of eight embedded devices is designed to simulate the distributed computing scenario of LEO satellites. The algorithm flow, mathematical model, trigger strategy, innovative improvement based on genetic algorithm and distributed computing architecture are studied and verified. The simulation and experimental results show that compared with the traditional

dual-link genetic algorithm, the proposed algorithm has obvious improvement in both the distribution result and response time.

Keywords: beam source allocation, distributed computing, LEO constellation, spacecraft access, satellite mission scheduling

1 引言

随着通信、导航、遥测、遥感、载人航天和深空探测等空间应用的快速发展，航天器数量迅速增长。 传统的 GEO（地球同步轨道）数据中继卫星（DRS）系统存在卫星数量少、设备成本高、传输时延高、波束源有限等缺点，无法为大量航天器提供接入和数据中继服务。 高速发展的 LEO 通信和传输卫星星座基于相控阵天线和数字波束形成（DBF）技术，为航天器的接入和数据中继提供了更多机会。 低轨星座由大量 LEO 卫星组成，并提供低延迟和高容量的网状网络来连接航天器和地面站。 航天器通过通信和中继波束接入网络后，空间数据可以传输到任意目的地。 然而，LEO 卫星星座规模和航天器数量增加了波束源分配的难度[1,2]。

LEO 星座波束资源的任务调度应考虑更多的约束。 当航天器动态提交波束请求时，自主调度系统应尽快提供响应。 还考虑了 LEO 卫星与请求航天器之间的可见窗口、任务的开始和结束时间、通信链路建立时间等因素。 此外，服务体验还受到响应时间的影响。 在这种约束下，提供准实时的任务调度响应是一个困难[3]。针对传统 GEO DRS 的星载调度性能提出了很多研究，由于 LEO 技术正处于上升阶段，因此 LEO 卫星领域的研究较少。

星载任务调度的过程包括三个部分：（a）需求提交（b）触发判断（c）任务调度。 组合优化问题的范围更有吸引力，因此，大多数研究集中在第三步的性能提升上。 提出了许多算法和策略来最大化多目标函数，因为卫星波束任务调度是源约束下的类似优化问题。

2 低轨星座任务调度模型

1.1 任务调度场景与流程

图 1 给出了多卫星和多航天器的场景。 LEO 星座用于为来自航天器的各种波束请求提供准实时响应。LEO 星座轨道高度为 1000km，卫星数量为 RS。 每颗 LEO 卫星有 1~8 个可移动点波束，以满足航天器的要求。此外，每一个波束一次只能服务一个航天器。 航天器的轨道高度和数量分别为 500km 和 TS。

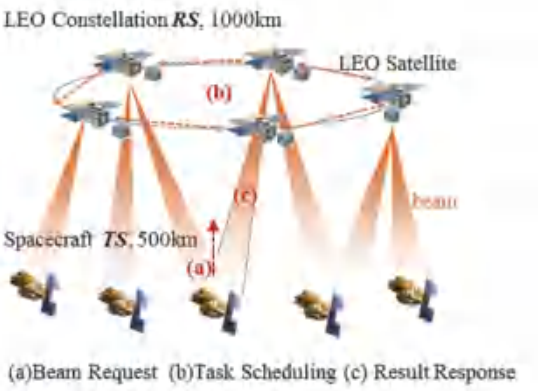

FIGURE 1. The multi-satellite and multi-spacecraft model

所有航天器都可以随机动态地向 LEO 星座提交他们的波束请求。星座应尽快给出基于需求和波束状态的波束资源任务调度响应。 大量的 LEO 卫星和航天器增加了任务调度计算难度的挑战[4,5]。

一个完整的任务调度过程的详细步骤包括三个部分： 1）收集航天器请求和波束资源状态的信息。 2） 检查触发条件。 3） 任务调度并获得优化结果。

Step 1: 信息收集

第一步，应将请求和波束状态收集到在 LEO 星座中起中心作用的卫星。 这意味着中心卫星知道任务调

度的所有必要信息。 然后，当满足触发条件时，可以根据波束需求将波束源分配给不同的航天器。

中心卫星表示为核心节点，其他卫星命名为正常节点，如图 2 所示。 所有节点都可以收集来自航天器的波束请求，并将请求信息传输到核心节点。 信息收集由分布式资源监控应用程序实现。

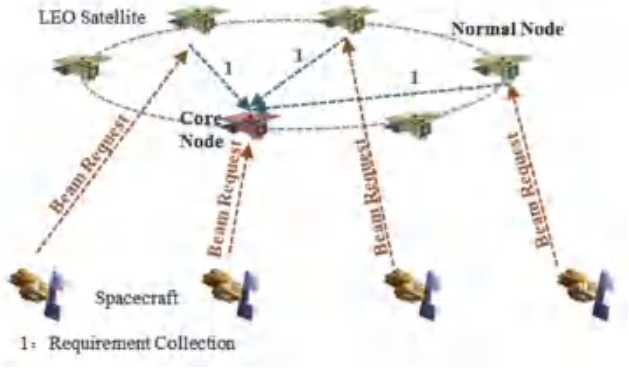

FIGURE 2. The different notes in the LEO constellation

Step 2: 触发条件判断

触发条件用于确定何时触发观察窗口的新任务调度。提出的触发条件由循环触发条件和动态触发条件两部分组成。

循环触发的周期设置为 3 分钟，以避免长时间没有触发任务调度。在这样的触发下，观察窗口可以继续向前移动。任务调度可以流式运行。

如果航天器的动态请求很紧急，而下一个周期触发太远，无法满足调度，任务就不会被满足。设置动态触发器以避免这种情况。如果任务队列中任务的开始时间距离当前时间小于 ts，则应该触发调度。本文将 ts 定义为 40s。

任务调度触发频率不能太频繁，因为调度过程需要时间。定时器用于记录触发新任务调度的时间，当任务调度被循环触发或动态触发触发时，定时器设置被更新。在这项工作中，两次关闭触发器之间的最小间隔设置为 20 秒。详细的时序图如图 3 所示。

如第一节所述，卫星波束源的任务调度是一个典型的优化问题，具有很多复杂的约束条件。本文采用改进的遗传算法对任务调度结果进行优化。

由于 LEO 卫星的计算能力有限，因此应考虑优化迭代产生的计算成本。受到广泛应用于地面云计算和边缘计算的分布式计算的启发。所提出的遗传算法旨在支持多卫星分布式计算集群。这意味着调度的计算任务可以由多颗卫星同时处理，以避免单一的功率约束，提高响应速度。分布式集群是基于资源虚拟化构建的。板载计算由资源池的形式提供，避免单颗 LEO 卫星的功率受限[6,7]。第三节和第四节给出了分布式计算的详细技术介绍。

Step 3: 分布式任务规划

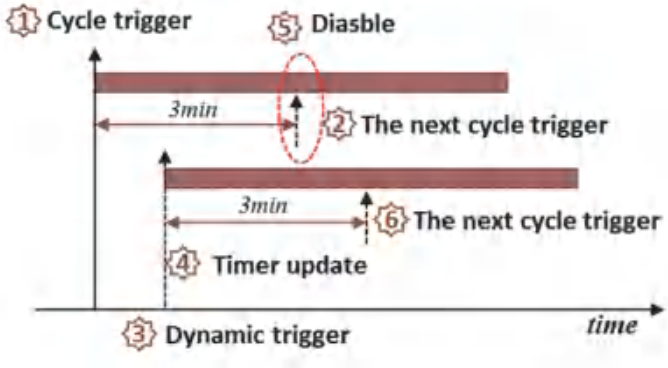

FIGURE 3. The proposed trigger sequence chart.

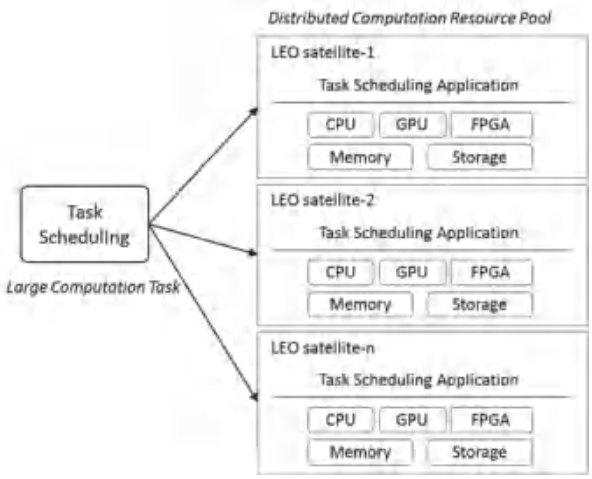

FIGURE 4. The distributed computation resource pool.

1.2 任务模型与资源模型

根据遗传算法设计，在任务调度的优化过程中，约束主要来自两个因素：任务请求和波束资源[8]。

波束请求（来自航天器）被认为是一个任务请求模型，它可以由一个向量表示，它有 10 个元素，表示如下：

$$BR=[TID, RTS, TSID, TSN, TP, TF, TS, TE, TD, TED]$$

其中 TID 为专属任务号，RTS 为任务状态，TSID 为提交该任务的航天器 ID 号，TSN 为补充参数，TP 表示任务的优先级，TF 表示是否可以将任务分解为 TS 和 TE 是任务可用窗口的开始时间和结束时间，TD 是时间窗口的长度，可以通过 TE-TS 计算，TED 是实际任务时间。

- TID：详细信息可以随时通过该 ID 在系统和数据库中进行索引，因此，TID 号应该是唯一的。
- RTS：不同的值表示任务的不同状态。 这 5 种状态包括：待提交、已提交、已调度、正在执行、已执行和失败。
- TSID, TSN：LEO 星座与请求航天器之间的可见窗口是根据轨道和天线信息计算得出的，这些信息可以通过 TSID 进行索引。 并且 TSN 可以加速索引过程。
- TP：优先级影响波束资源分配结果。 随着 TP 的增加，任务将更早地获得波束资源。
- TF：由于高速运动，LEO 卫星与航天器之间的可用时间窗可能不够长。 对于时间较长的任务，可能需要将任务分解为两部分以满足可用的时间窗口。 这意味着两束波束通过它们的合作来支持一个航天器的请求。
- TS, TE：可以执行任务的时间窗口的开始时间和结束时间。
- TD：时间窗口的长度和 TD 可以计算为 TE-TS。
- TED：任务的实际时间。 如果传感图像的大小为 5GB，一个波束的链路容量为 1Gbps，则 TED 可以预测为 40s。 例如 TS 是 8:00 am TE 是 8:30 am, TED 是 40s 表示任务调度系统应该在 8:00 和 8:30 之间提供一个超过 40s 的波束源来满足这个任务 是。 时间窗口 TD 是 30min，但实际任务时间只有 40s.

在这个模型中总结了一个任务的必要信息，并且足以被调度。 航天器可以随时随地向 LEO 星座提交这样的波束请求，星座会对其进行调度并尽快做出响应。

波束资源的信息作为数学模型给出如下

$$RS=[BID, BT, BD]$$

其中 BID 是唯一的波束编号，BT 是微波和激光等波束源的类型。 BD 是一个补充参数，用于补充 BT，如机械扫描和相位扫描。

此外，约束对于 LEO 卫星和航天器之间的链接非常重要。 该模型如下所示。

$$CP=[OED, RED, VED, BRT, LBT]$$

其中 OED 是观察时间窗口，RED 是可见时间窗口，VED 是可用可见时间窗口，BRT 是波束资源的状态。

- RED：RED 包括两个元素 RS 和 RE，即窗口的开始时间和结束时间。 LEO 卫星和航天器之间的可见时间窗口可以通过轨道和天线信息计算出来。 空间可视关系如图 5 所示。

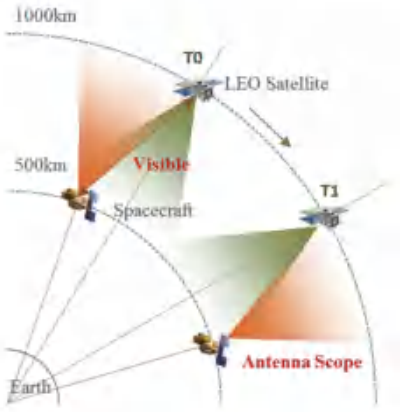

FIGURE 5. The visible relationship between moving satellite and spacecraft

- VED：VED 包括两个元素 VS 和 VE，它们是可用可见窗口的开始时间和结束时间。 可用的可见时间窗口是 RED 和 TD 之间的交集。 当两个约束同时满足时，星间链路是有效的。 图 6 给出了不同的时间窗口。

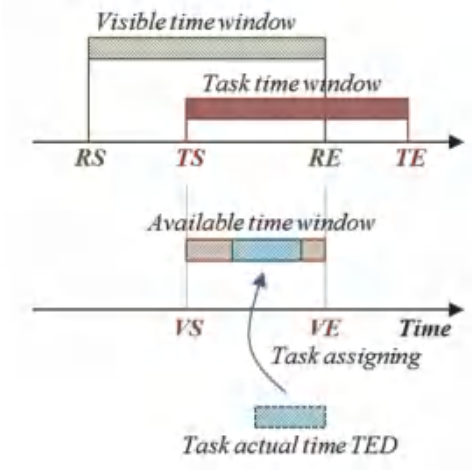

FIGURE 6. The different time windows

- BRT：只有未占用的波束资源可以分配给任务。 BRT 用于记录波束源的状态。
- LBT：LEO 卫星和航天器之间建立通信链路的时间成本。 典型值为 100 秒。

上面介绍的所有参数都用于描述场景和所提出算法的输入。不同的场景可以通过不同的参数设置进行设置。 所提出的算法具有更广泛的适用性[9]。

3 改进的 GA 算法

本节详细介绍改进的 GA 算法。 主要创新点分别是二维个体模型和不相关单父继承法。 该算法基于新的个体描述模型，不需要传统遗传算法中的基因编码和解码。 因此，提高了算法的效率。 同时，遗传过程仅与单个父系个体关联，以支持分布式计算。 与传统的集中式 GA 算法相比，基于这两个要点，最终优化任务调度结果的效益值得到提高，响应时间得到降低[10,11]。

3.1GA算法流程

所提出的 GA 算法有几个主要步骤。 首先，随机生成具有 CN 个体的初始种群。 个体由二维矩阵描述，每个个体是可用但不是最优的波束资源任务调度结果。 其次，父系个体可以通过基因操作产生子个体。 具有 CN 个体的新父系群体根据目标函数从老父系群体和子代群体中选出。 最后重复第二步，直到结果收敛或

满足结束条件，得到优化结果。 重要的是基因编码和解码过程不在流程图中操作，以提高算法效率。

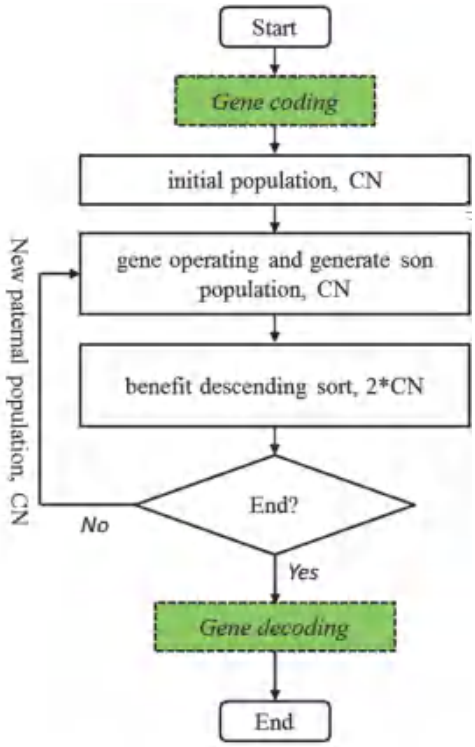

FIGURE 7. The flowchart of the proposed GA algorithm.

3.2 二维个体描述模型

波束资源状态、任务时间、航天器和 LEO 卫星等信息可以直接从甘特图中获取。 因此，最终优化的波束资源任务结果通常以甘特图的形式来描述。 受甘特图的启发，个体方法被设计为相同的二维矩阵形式，如图 8 和（4）所示。

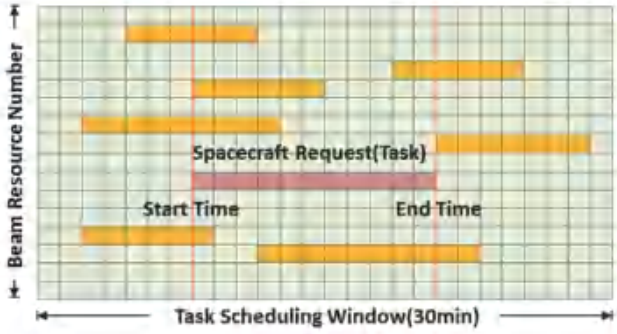

FIGURE 8. The flowchart of the proposed GA algorithm.

$$FMP = \begin{bmatrix} fmp_{11} & fmp_{12} & \cdots & fmp_{1j} \\ fmp_{21} & fmp_{22} & \cdots & fmp_{2j} \\ \cdots & \cdots & \cdots & \cdots \\ fmp_{i1} & fmp_{i2} & \cdots & fmp_{ij} \end{bmatrix} \quad (4)$$

在图 8 中，横轴任务调度窗口（30 分钟）被划分为 90 个相同长度的跨度（20 秒）。 纵轴是束资源编号。 有色矩形表示航天器请求的任务调度结果。 甘特图可以用 (4) 给出的矩阵来描述。 矩阵元素的值可以是 0 或任务 ID。 当元素值为 0 时，beam 资源可用。当元素值为任务 ID 时，beam 资源被占用。 总占用

时间可以通过被视为基因的连续任务 ID 来计算。并且可以通过下标 j 间接获得开始时间和结束时间信息。优化后的 FMP 就是最终的任务调度结果。 所提出算法中的个体模型使用这样的矩阵形式进行基因操作，避免了常规的基因编码和解码[12]。 效率得到提高。 第四节给出了详细的模拟、测量、比较和分析。

3.3 单一父代遗传

所提出的 GA 算法旨在应用于 LEO 卫星。应考虑板载计算能力的限制。一个大的计算任务应该根据所提出的算法分解成小的子任务，以支持分布式计算[10]。本文对基因操作和遗传方法进行了改进。

图 7 所示的基因操作有两个主要步骤。步骤 1：从矩阵 FMP 中取出一些调度的任务，如果有的话，这意味着一个父代个体释放被占用的 beam 资源。第二步：将所有未调度的任务放入矩阵中，采用随机、优先、顺序等策略，得到一个新的矩阵，即子代个体。此外，在这种情况下，子代个体的产生只与一个父代个体有关。该过程对于分布式计算很重要。

分布式计算的流程图如图 9 所示。在初始步骤中，将种群的大小设置为较大的值 CN*N，这有利于优化结果。为了避免无法忍受的计算成本，种群被分成 N 个大小为 CN 的子种群。这意味着子任务大小仅为初始任务的 1/N。优化的过程可以在不同的卫星上运行。

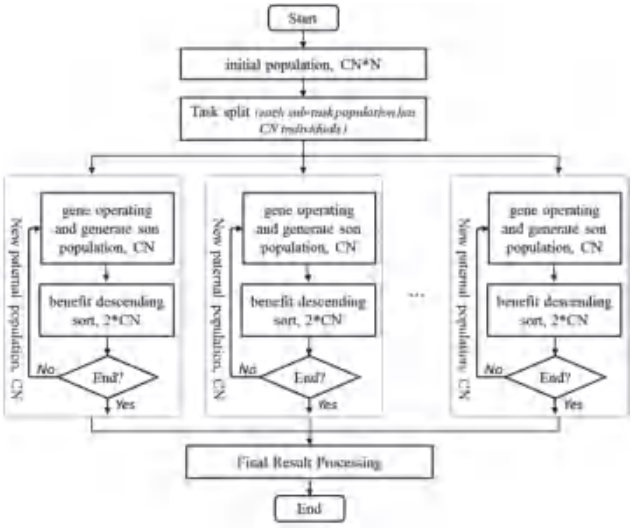

FIGURE 9. The distributed computing of proposed GA.

3.4 目标函数与结束条件

目标函数旨在评估个体的质量。 函数的输入是 FMP 得到的个体状态矩阵，输出是个体的收益值。 收益值越大，个体越好。

$$OF = \alpha \cdot \sum_{i=1}^{TN} PF_i + \beta \cdot \sum_{j=1}^{TN} I_j - \lambda \cdot \sum_{k=1}^{TN} SW_k \quad (5)$$

其中，TN 是计划任务的数量。 PF 是任务的优先级。 SW 是波束切换数。 当前两项较大时，结果对航天器有利。 这意味着更多的任务计划成功。 当第三项较小时，结果对卫星有利。 这意味着系统开销很小。

结束条件由收敛条件和最大迭代条件组成。 如果 OF 的升级率变小或迭代达到预设值（LX），将自动停止优化以节省计算时间.

4 仿真结果与讨论

在本节中，给出了三种数值模拟结果来说明所提出算法的可用性和性能。 首先给出改进 GA 的特征曲线结果来表明有效性。 然后，提供了不同方法之间的比较结果。 最后，提出的算法在 Docker 和 Kubernates (K8S) 中实现，以说明分布式计算的可用性。

4.1 算法有效性验证

为了验证所提出的算法，在 Matlab 中创建并模拟了一个多卫星和多航天器模型。 模拟设置的详细参数如表 I 所示。

TABLE I. PARAMEMTERS OF FIRST EXAMPLE

Index		Parameter	Value
1	RS	Number of LEO Satellite	25
2	BN	Beam Number of per LEO Satellite	4
3	TS	Number of spacecraft	100
4	OED	Observation time window(min)	30
5	LBT	Time of Link Build(s)	100
6	CN	The population size of i-GA	20
7	LX	The iteration limitation of i-GA	20

航天器任务甘特图如图 10 所示，其中横轴为时间，纵轴为航天器。 OED 创建期间共有 675 个任务，任务的 TS、TE 信息可以通过彩色矩形的位置间接表示。

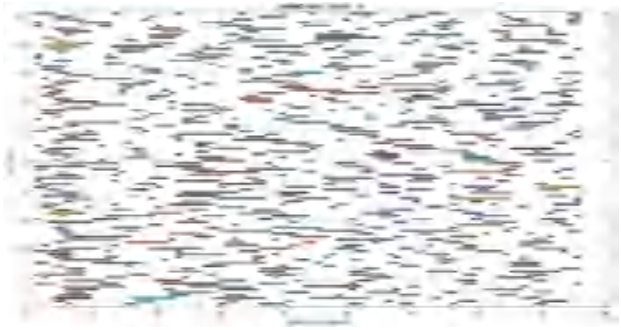

FIGURE 10. The Gantt chart result of the mission from spacecraft.

该优化在集中计算模型中运行以验证算法。 初始种群大小设置为 20，最大迭代次数设置为 20。优化结果如图 9 所示。 LEO 卫星与航天器之间的通信链路建立时间（LBT）设置为 100s。 这意味着每个任务添加一个 100s 的标题。 因此，图 11 中的任务长度看起来更长。

仿真耗时 9.23s，成功调度 674 个任务。 成功率为 99.85%。 特征曲线如图 12 所示。

FIGURE 11. The Gantt chart result of task scheduling (the time cost of link building is considered).

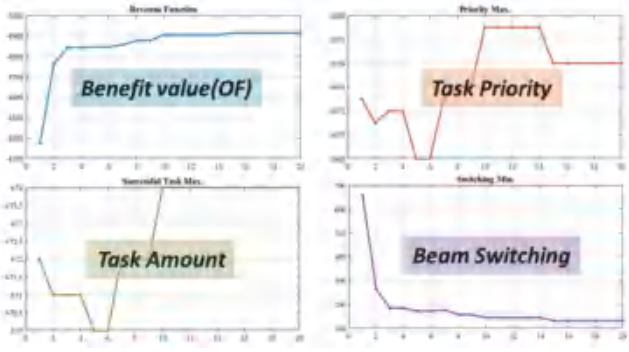

FIGURE 12. The characteristic carves calculated by objective function.

所提算法能快速得到收敛优化结果，对航天器和 LEO 卫星均有较好的效果。 验证了算法的有效性。

4.2 算法对比

给出了三个例子来说明与传统算法相比所提出的算法的改进。

Comparison Example 1: 稀缺束源情况下的性能分析。

本例中 TS 的值为[50:4:86]，RS 的值为[10:1:19]，BN 为 4。样本量为 100。特征值曲线、成功率和计算时间结果 如图 13-15 所示。

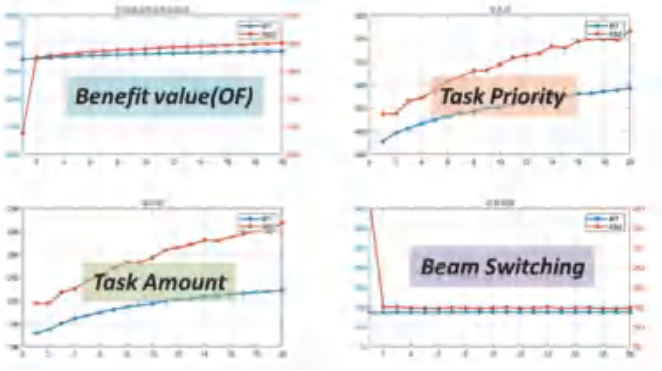

FIGURE 13. The characteristic carve comparison results.

结果由 20 次迭代中 100 个样本的平均值计算得出。 很明显，所提出的算法（红色）比传统算法（蓝色）具有更好的性能。

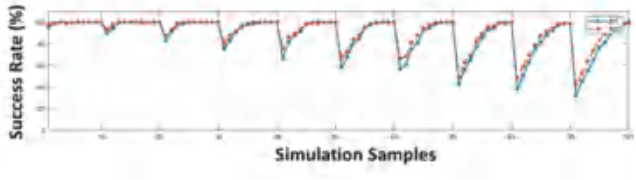

FIGURE 14. The comparison results of success rate.

由于波束资源不足，部分任务可能无法调度成功。 但是，所提出的算法（红色）仍然比传统算法（蓝色）具有更高的成功率。

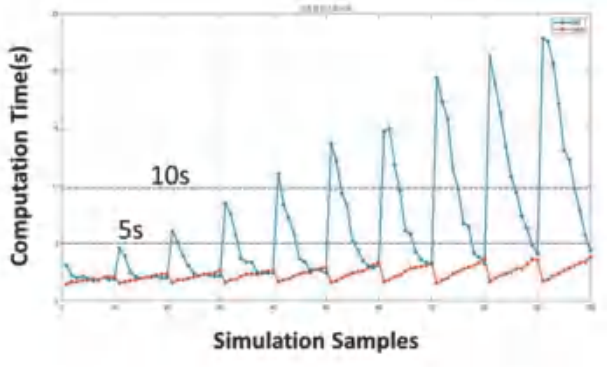

FIGURE 15. The comparison results of computation time.

很明显，传统算法（蓝色）的计算时间比提出的算法（红色）要长得多，尤其是在波束源明显较少的情况下。

Comparison Example 2: 足够束源情况下的性能分析。

本例中 TS 的值为[40:4:76]，RS 的值为[10:1:19]，BN 为 4。样本量为 100。特征雕刻、成功率和计算时间结果 如图 16-18 所示。

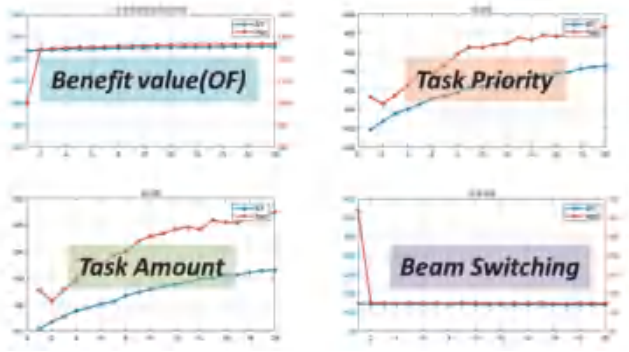

FIGURE 16. The characteristic carve comparison results.

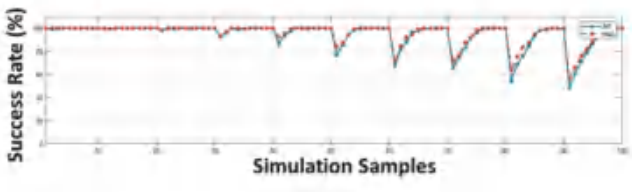

FIGURE 17. The comparison results of success rate.

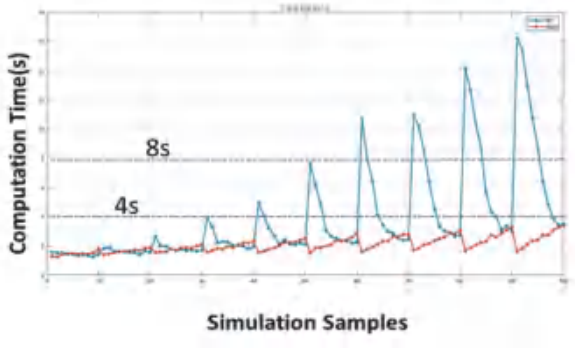

FIGURE 18. The comparison results of computation time.

这三个结果的结论与示例 1 相似，但优势越来越小。

Comparison Example 3: 波束资源充分情况下的性能分析。

本例中，TS 的值为[20:4:56]，RS 的值为[10:1:19]，BN 为 4。样本量为 100。特征雕刻、成功率和计算时间结果 如图 19-21 所示。

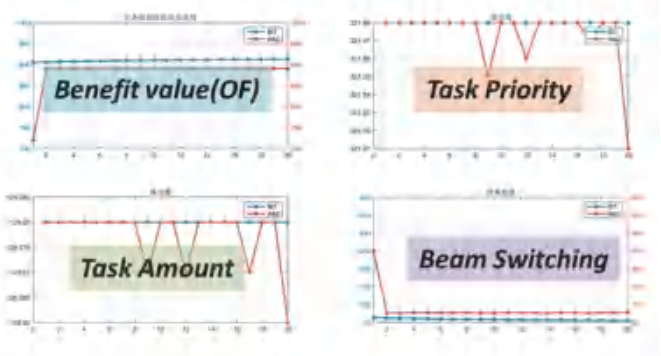

FIGURE 19. The characteristic carve comparison results.

结果由 20 次迭代中 100 个样本的平均值计算得出。 随着波束源的增加，传统算法（蓝色）与提出的算法（红色）相比具有狭窄的优势。

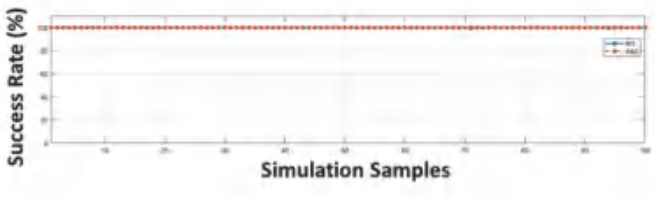

FIGURE 20. The characteristic carve comparison results.

当波束资源丰富时，两种算法的成功率相同。 航天器的所有任务都安排成功。

根据图 21 中的结果，所提出的算法（红色）具有更大的时间成本，因为在调度任务时会检查 FMP 中所有可用的波束资源。 当可用的波束资源更丰富时，检查过程产生时延导致优势会降低。

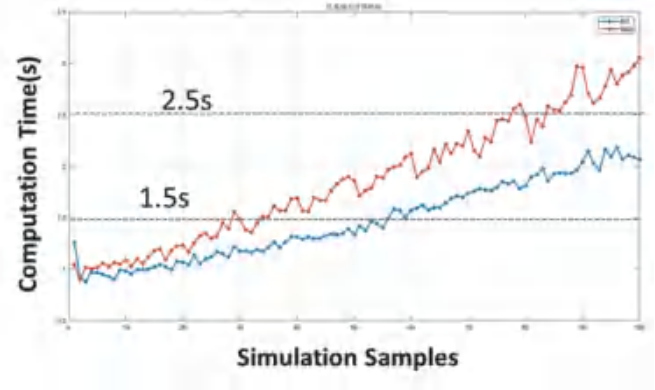

FIGURE 21. The comparison results of computation time.

这三个例子用于说明所提出的遗传算法在不同情况下的性能。该算法在真实场景的波速资源稀少时具有明显的优势。

4.3 分布式计算模型分析

随着LEO卫星规模的增大，动态任务调度的计算量越来越大。因此，受星上计算能力的限制，大规模计算任务仅靠一颗低轨卫星无法实时处理。受云计算技术启发，多卫星间分布式计算模型可用于LEO星座，利用云集群丰富的计算资源解决波束任务调度问题。换句话说，一个大型计算任务可以由多颗卫星同时处理，以减少处理时延。

实验室搭建了一个基于 Docker 和 Kubernetes（K8S）的原理验证分布式系统，如图 22 所示。由八个嵌入式设备用作卫星计算有效载荷的模拟器。基于Linux工具tc和netem模拟动态网络。容器引擎 Docker 和 K8S 集群组件安装在每台设备上。分布式架构可以将计算任务自动调度到设备中，实现多星协作。

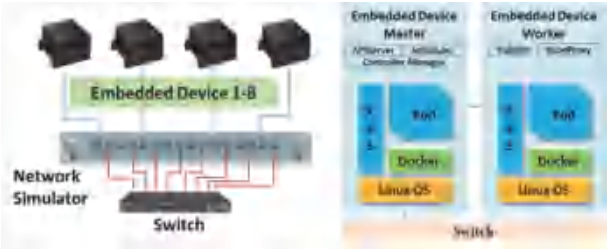

FIGURE 22. The principle proof distributed system.

波束资源的任务调度过程如图23所示，描述如下。第一步：波束资源任务调度应用的核心节点根据航天器的请求和LEO卫星的波束资源状态创建计算任务。第二步：然后，将计算任务划分为4-5个规模相同的子任务，分别提交给分布式计算集群。第三步：虚拟代理组件 KubeProxy 根据负载均衡策略将子任务放入不同的

集群节点。子任务独立处理，任务调度结果返回核心节点，如步骤1所述。 步骤4：子任务结果对比分析得到优化结果。换句话说，最终结果是从子任务的结果中选择出来的。

在这样的流程图中，大型计算任务被分成许多小的部分，作为不相关的子任务。如上所述，分布式计算由基于单父继承的改进遗传算法支持。在这种情况下，虽然任务调度结果的最大收益略有降低。由于计算任务规模的减小，计算时间显着减少。

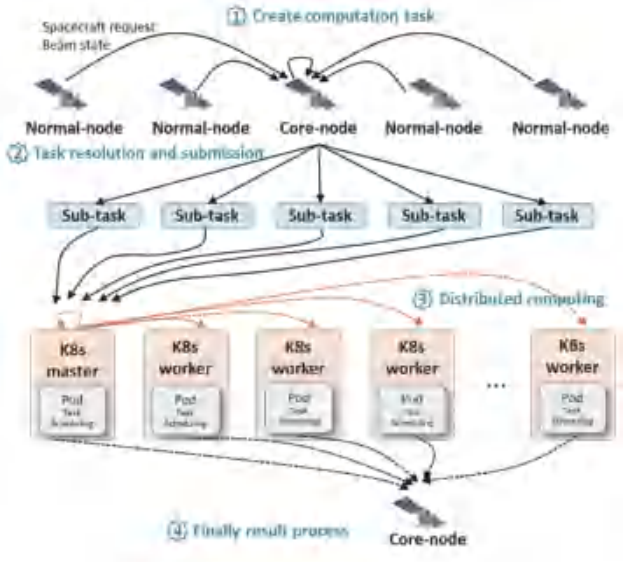

FIGURE 23. The flowchart of distributed task scheduling.

图 24 和图 25 给出了不同模拟样本的数值结果，以说明传统集中计算与提议的分布式计算之间的差异。

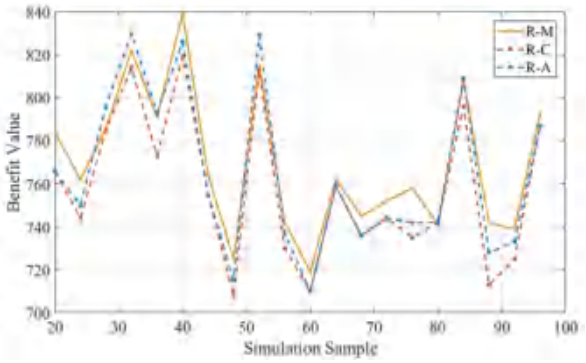

FIGURE 24. The flowchart of distributed task scheduling.

在图 24 中，R-M 表示集中计算结果的好处。 R-A 和 R-C 表示分布式计算结果的平均和最差收益。 结果表明，集中计算的效益值优于分布式计算结果，但差异不明显。

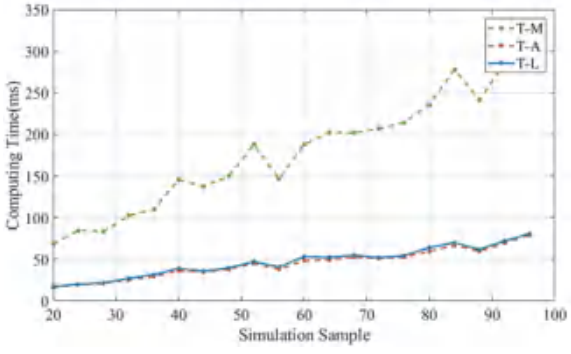

FIGURE 25. The flowchart of distributed task scheduling.

在图 25 中,T-M 表示集中计算结果的计算时间。T-A 和 T-L 表示分布式计算的平均和最长计算时间。如结果所示。 分布式计算时间明显少于集中式计算时间。

可以得出结论，分布式计算可以节省大量的计算时间，但代价是降低了收益。 如果考虑到不同卫星之间的典型时间延迟（17-30ms），在计算规模较大的情况下，结论仍然正确。

常规算法不支持分布式计算模型，因此进队提出算法进行分布式性能分析。

5 结论

针对LEO星座动态波束资源任务调度问题，提出了一种可运行于机载分布式计算系统的改进GA算法。 与传统算法相比，基于二维个体模型和不相关单父继承方法的收益和计算时间都有所提高。 给出了仿真结果来说明算法的有效性。 此外，构建了基于Docker和K8S的分布式计算原理证明系统，展现了计算时间相对于集中式计算的优势。

分布式计算集群虽然可以解决单颗卫星计算能力有限的问题，但在后续工作中仍需考虑时延和动态网络对星载分布式集群的影响。

参考文献

[1]Lei Wang, Chunxiao Jiang, Linling Kuang, et al.Mission Scheduling in Space Network with Antenna Dynamic Setup Times[J]. IEEE Transactions on Aerospace and Electronic Systems, 2018, Early Access, 1-13

[2]Fan Dandan, Li Benjin, Fei Li Gang, et al. Design of global emergency communication system based on geosynchronous TDRSS[J] 2015 International Conference on Wireless Communications & Signal Processing (WCSP),2015:1-4

[3]徐晓斌，王琪，范存群，等. 面向空天地一体化信息网络的边缘计算资源融合管理方法[J]. 计算机学报，2023,46(4):690-710.

[4]别灵臻. 基于大型低轨卫星星座的分布式路由算法研究[D]. 黑龙江: 哈尔滨工业大学，2022.

[5]费立刚,范丹丹,寇保华,等. 基于中继卫星的天地一体化信息网络综合集成演示系统研究[J].中国电子科学研究院学报,2015, 10(5),479-484.

[6]李学富，耿座学，王英伍，等. 基于延迟接受的低轨星座用户接入策略[J]. 航天器工程，2024,33(1):26-35

[7]王丰. 面向动态可持续的天地一体化融合通信关键技术研究[D]. 四川: 电子科技大学，2022.

[8]邵浩典，低轨星座网络用户行为及业务建模研究[D]. 四川:电子科技大学，2023.

[9]冯少栋，揭晓，李仰志，等.低轨星座系统业务建模与仿真[J]. 宇航学报，2010, 31(1):179-184.

[10]王磊，匡麟玲，黄惠明. 基于时空特征的中继卫星系统业务模型[J].清华学报 (自然科学版),2017, 57(1), 55-60.

[11]单长胜，李于衡，孙海忠. 中继卫星支持海量航天器在轨测控技术[J]. 中国空间科学技术，2017,37(1):89-96.

[12]朱至天等.太空互联网关键技术与应用分析[C]. 第十四届卫星通信学术年会论文集,2018:400-406.

【作者简介】

徐潇审，1985 年 8 月出生，男，博士，高级工程师，主要研究方向卫星通信与测控。

罗俊波，1993 年 7 月出生，男，学士，工程师，主要研究方向卫星通信与测控。

卢俊麒，1987 年 11 月出生，男，博士，工程师，主要研究方向卫星通信与算法研究。

杜金艳，1985 年 03 月出生，女，硕士，工程师，主要研究方向是通信网络及网络安全。

低轨通信星座覆盖性能仿真分析

刘二江，徐潇审，王良

（中国人民解放军 32039 部队，北京 102300）

摘　要：低轨通信星座具有广覆盖、高带宽、低时延等特点，成为未来航天和通信领域的重要发展方向，已受到世界各国的广泛关注。本文首先梳理了具有代表性的 6 个低轨星座研究现状，对各个星座系统功能和星座构型进行了总结。然后构建了一种混合星座，由 66 颗近极轨道卫星和 216 颗倾斜轨道卫星组成，并针对该星座构型的覆盖性能进行了全面分析，基于 STK 软件从星座全球覆盖性、典型位置覆盖性和区域覆盖性等多个维度进行仿真分析。仿真结果表明，本文所设计的星座可实现全球覆盖，在部分区域可实现多重覆盖。

关键词：低轨星座；STK 软件；覆盖性能；构型设计

Simulation analysis of LEO communication constellation coverage performance

Liu Erjiang, Xu Xiaoshen, Wang Liang

（Unit 32039 of the Chinese PLA, Beijing 102300, China）

Abstract: The low Earth orbit communication constellation has the characteristics of wide coverage, high bandwidth, and low latency, and is becoming an important development direction in the future aerospace and communication fields, receiving widespread attention from countries around the world. This article first reviews the current research status of six representative low Earth orbit constellations, and summarizes the functions and configurations of each constellation system. Then, a hybrid constellation is constructed, consisting of 66 near polar orbit satellites and 216 inclined orbit satellites. A comprehensive analysis is conducted on the coverage performance of the constellation configuration. Based on the STK software, simulation analysis is conducted from multiple dimensions including constellation global coverage, typical location coverage, and regional coverage of the constellation. The simulation results show that the constellation designed in this paper can achieve global coverage and multiple coverage in some areas.

Key words: low orbit constellation, STK simulation software, coverage performance, constellation design

1　引言

在当今数字化时代，高速、稳定且广泛覆盖的通信网络已成为社会发展和人们生活的关键需求。随着卫星模块化技术、批量部署技术和 5G 技术的发展，低轨通信星座应运而生，利用大量低成本微小卫星组建的巨型星座系统来为地面提供互联网等各类服务，成为未来航天和通信领域的重要发展方向。低轨通信

星座由成百上千甚至上万颗运行在低地球轨道上的卫星组成，与传统的地球同步轨道卫星相比，低轨通信星座具有带宽成本低、传输时延短、系统容量大、覆盖区域广等特点，可以实现全球范围内的稳定通信，具有巨大的发展潜力。此外，随着卫星批量化生产、一箭多星发射和火箭复用等技术的日益成熟，低轨星座的建设和部署成本得到了有效控制，Space X、Amazon、Oneweb、Telesat 等多家商业航天公司提出了多项星座部署计划并在加速建设中。

覆盖性能是衡量低轨通信星座有效性的关键指标之一，它直接关系到星座所能提供的服务地区以及服务质量。对低轨通信星座覆盖性能的准确评估与分析，不仅有助于星座构型的优化设计，提高资源利用率，同时也可为通信系统的规划和运营提供重要的决策依据。为此，本文针对低轨通信星座的覆盖性能分析问题开展研究，设计了一种混合星座，基于 STK 仿真软件对该星座的全球覆盖性、典型位置覆盖性、区域覆盖性进行了仿真对比分析。

2 低轨星座研究现状

2.1 星链星座

StarLink 星座系统[1]由 SpaceX 公司于 2015 年首次向 FCC 提交申请，计划发射和运营 4425 颗卫星，并于 2018 年 3 月通过审批。后续 SpaceX 公司又在 2018 年 11 月、2019 年 8 月、2020 年 4 月对该构型的星座进行了多轮修改。从 SpaceX 公司 2021 年 4 月公开申请的星链星座轨道构型可见，星链一期部署 11926 颗卫星，二期部署近 30000 颗卫星，工作在 328-614km 高度的 LEO（低地球轨道）和 VLEO（极低地球轨道）。截至 2024 年 4 月 12 日，SpaceX 公司共计发射 6189 颗“星链”卫星，其中 5721 颗在轨正常工作[2-4]。星链星座构型方案如表 1 所示。

表1 星链星座方案

实施阶段		轨道面数	每轨卫星数	轨道高度（km）	轨道倾角（°）	总数
一期	第一阶段	72	22	550	53	1584
	第二阶段	72	22	540	53.2	2824
		36	20	570	70	
		6	58	560	97.6	
		4	43	560	97.6	
小计		190	-	-	-	4408
一期	第三阶段	-	-	345.6	53	2547
		-	-	340.8	48	2478
		-	-	335.9	42	2493
小计		-	-	-	-	7518
二期		-	-	-	-	30000
总数		-	-	-	-	41926

2.2 “星盾”星座

2022 年 12 月 2 日， SpaceX 公司官方网站发布“星盾”（StarShield）计划，将“星盾”定义为服务于国家安全的卫星星座，区别于“星链”的商业化运行，“星盾”专为美军政部门服务，主要提供通信、遥感和载荷托管三方面服务，并且“星盾”在“星链”数据加密服务基础上使用额外加密技术来保证托管载荷数据处理安全性，以满足官方需求。2023 年 9 月 1 日，美太空系统司令部授予 SpaceX 公司首份价值 7000 万美元合同，用于采购“星盾”互联网服务。合同约束了端到端服务、用户终端、辅助设备、网络管理和其他相关服务。

从 SpaceX 官网公布信息来看，目前“星盾”系统的功能主要涉及三项：一是全球通信，“星盾”系统通过用户设备，为政府用户提供可靠的全球通信。SpaceX 公司已获得美国联邦通信委员会（FCC）批准发射 7500 颗二代“星链”卫星，其中部分卫星可能用于建设“星盾”卫星。“星盾”将继承“星链”星间激光通信链路天线和对地天线，实现与“星链”无缝组网。二是地球观测，“星盾”系统可发射带有遥感设备有效载荷的卫星，并将处理后的数据直接提供给用户。SpaceX 公司官方解释是带有传感器的卫星对地观测，不光局限于光学观测，还有红外等波段的遥感观测。三是搭载先进的传感器。“星盾”将打造能力更强的卫星平台，能集成多种有效载荷，满足军事用户最为苛刻的托管要求，帮助军方实现通信导航、侦察监视、态势感知、反导预警等多重能力。

2.3 铱星星座

Iridium 移动通信系统是美国于 1987 年提出的第一代卫星移动通信星座系统，主要提供话音和短数据服务。Iridium 系统主要采用星间微波链路组网实现互联互通，地面多个信关站分别独立管理不同区域的用户接入。1999 年 8 月宣布破产，并改组成立美国 Iridium 网络公司，美国国防部成为其最重要的政府用户。2010 年，第二代 Iridium 系统（Iridium Next）开始筹划建设[5, 6]，2017 年 1 月，Iridium Next 首批 10 颗卫星发射成功，拉开了 Iridium Next 系统的部署进程，2019 年 1 月，Iridium Next 最后 10 颗卫星的发射成功，标志着第二代铱星系统组网成功。目前，Iridium Next 星座有 66 颗卫星工作（不含在轨备份 9 颗、地面备份 6 颗），工作于极轨轨道，高度 780km，轨道倾角 86.4 度。Iridium Next 星座设有星间链路，每颗卫星与其前后左右相邻的四颗卫星建立连接。卫星配置 1 副 L 频段移动通信天线（120 个馈源形成 48 个波束）、4 副 Ka 频段星间链路天线以及 2 副 Ka 频段馈电链路天线，支持 Ka 频段宽带通信（馈电复用 1 个波束），搭载导航增强载荷和航空航海监视载荷，支持 GPS 全球连续监测、全球安全定位授时。

2.4 OneWeb 星座

2014 年，OneWeb 公司提出了部署数百颗 LEO 卫星组成的宽带通信星座计划，采用 716 颗卫星构成星座，提供 3G、LTE、5G 和 WIFI 覆盖的用户终端，通过空中、海上和陆地在全球范围向个人用户内

提供高速接入服务[7-11]。2017 年 6 月底，美国联邦通信委员会（FCC）正式授权 OneWeb 公司，批准其在美国使用 OneWeb 星座提供互联网接入服务。OneWeb 星座采用开放式架构，可在原有系统基础上通过增加卫星以提升星座整体容量。OneWeb 计划发展的星座将分为两个阶段部署，第一阶段发射约 716 颗卫星，实现全球范围的无缝覆盖服务，星座将具有约 5～6Tbps 的容量；第二阶段完成后续卫星的增补、扩充在轨容量等工作。OneWeb 星座构型方案如表 2 所示。

表2 OneWeb星座方案

参数	第一阶段		第二阶段		
轨道高度（km）	1200		1200		
卫星数量	716		6372		
单层架构卫星数量	588	128	1764	2304	2304
轨道面数	12	8	36	32	32
每轨卫星数	49	16	49	72	72
轨道倾角（°）	87.9	55	87.9	40	55

2.5 Telesat 星座

Telesat 系统是由 Telesat 公司提出的低轨互联网系统，是一种结合下一代技术的先进星座。该网络采用极轨和倾斜轨道的混合轨道，目标为提供一个类似于地面光纤网络的宽带服务。星地使用具有优先权的 Ka 频段 4GHz 带宽资源，星间采用高容量激光链路，能够为全球任意区域的固定用户和移动用户提供宽带服务。2017 年 11 月 3 日，Telesat 公司获得美国联邦通信委员会（FCC）的批准，其由低轨卫星组成的 Ka 频段卫星互联网系统进入美国宽带服务市场，成为继 OneWeb 公司之后，第二家进入美国宽带服务市场的公司。同时 Telesat 公司还拥有加拿大卫星互联网系统准入许可。

Telesat 公司的第一阶段 Lightspeed 星座由 298 颗卫星组成，其中 78 颗卫星将部署至 1015km 高度的近极地轨道，设置 6 个轨道平面，单轨道面 13 颗卫星；220 颗卫星将部署至 1325km 高度的倾斜轨道，设置 20 个轨道面，单轨道面 11 颗卫星。此外，Telesat 向 FCC 申请了第二阶段的“最终星座”，将在第一阶段“修改星座”的基础上增加倾斜轨道卫星的轨道面，将卫星总量增至 1671 颗。Telesat 一阶段星座构型方案如表 3 所示。

表3 Telesat一阶段星座方案

轨道类型	轨道面数	每轨卫星数	轨道高度（km）	卫星总数
近极地轨道	6	13	1015	78
倾斜轨道	20	11	1325	220

2.6 Kuiper 星座

2019 年 7 月 4 日，美国亚马逊公司向美国 FCC 提交了一组审查文件，用于申请一个巨型低轨通信星

座“Kuiper”在美国境内的商业运营权[12]。Kuiper 星座预计由 3236 颗低轨宽带通信卫星构成，在轨设计寿命 7 年。Kuiper 系统空间段包括在 3 个不同轨道高度和倾角的轨道面上的 3236 颗先进非地球同步轨道（NGSO）卫星。Kuiper 星座构型方案如表 4 所示。

表4　Kuiper星座方案

轨道面数	每轨卫星数	轨道高度（km）	轨道倾角（°）	卫星总数
34	34	630	51.9	1156
36	36	610	42	1296
28	28	590	33	784

Kuiper 系统的分层轨道设计很好地满足了客户在全星座部署时的容量和覆盖范围，通过使用不同倾角的重叠高度轨道面，星座设计最大限度地减少了在地理纬度上均匀分布覆盖所需的卫星总数，并在一颗卫星与其他系统发生内联干扰事件时提供链路多样性。

2.7　小结

通过对比分析典型低轨通信星座可以看出，低轨通信星座大多由数百甚至上万颗卫星组成，采用不同轨道高度、不同轨道倾角组成的混合星座进行组网，频率主要采用 Ka 和 Ku 频段，可为用户提供更低时延、更高带宽的高速卫星互联网接入。

3　星座覆盖仿真与分析

3.1 星座设计

基于 OneWeb 星座和铱星星座构型设计启发，本文设计了一种由近极轨道星座和倾斜轨道星座组成的混合星座。其中近极轨道星座轨道高度设计为 1200 公里，轨道倾角 86.4 度，分布在 6 个轨道面上，每个轨道面上部署 11 颗星；倾斜轨道星座轨道高度设计为 1200 公里，轨道倾角为 55 度，分布在 18 个轨道面上，每个轨道面上部署 12 颗星。星上载荷利用先进的相控阵波束成形和数字处理技术，为简化仿真操作，假设每颗卫星传感器均为圆锥形波束，半圆锥波束角为 55° 。星座构型参数如表 5 所示。

表5　星座构型设计方案

星座类型	倾斜轨道星座	近极轨道星座
	216 星	66 星
轨道高度	1200 km	1200 km
轨道倾角	55°	86.4°
轨道面数	18	6
每轨卫星数	12	11
对地覆盖角	±55°	±55°

星座全球分布态势示意图如图 1 所示。

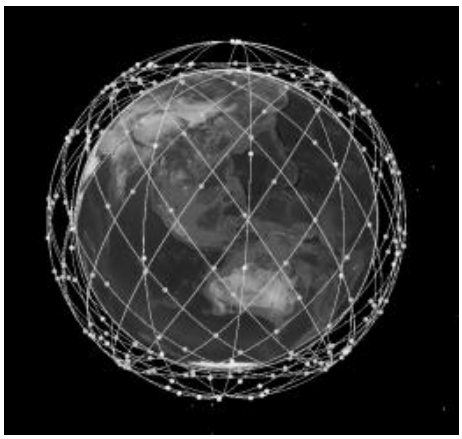

图1　星座全球分布态势示意图

3.2 覆盖分析

本文所设计的混合星座，其中近极轨道星座主要用于实现移动通信，在仿真分析中最低通信仰角设置为 10°；倾斜轨道星座主要用于实现宽带通信，最低通信仰角分别设置为 20°和 30°进行仿真分析。本节主要针对混合星座的全球覆盖性、典型位置覆盖性和区域覆盖性进行了仿真分析，其中覆盖性能指标主要为同一时刻典型位置和目标区域内可视卫星数量。

3.2.1 全球覆盖仿真分析

采用 STK 软件的覆盖分析模块，针对本文所设计的星座进行全球覆盖仿真。考虑到星座对地覆盖具有南北对称性，且倾斜轨道卫星倾角为 55°，因此仿真中仅分析近轨轨道星座在北纬 0°- 90°、倾斜轨道星座在北纬 0°- 65°范围内的覆盖情况，仿真结果如图 2 至图 4 所示。

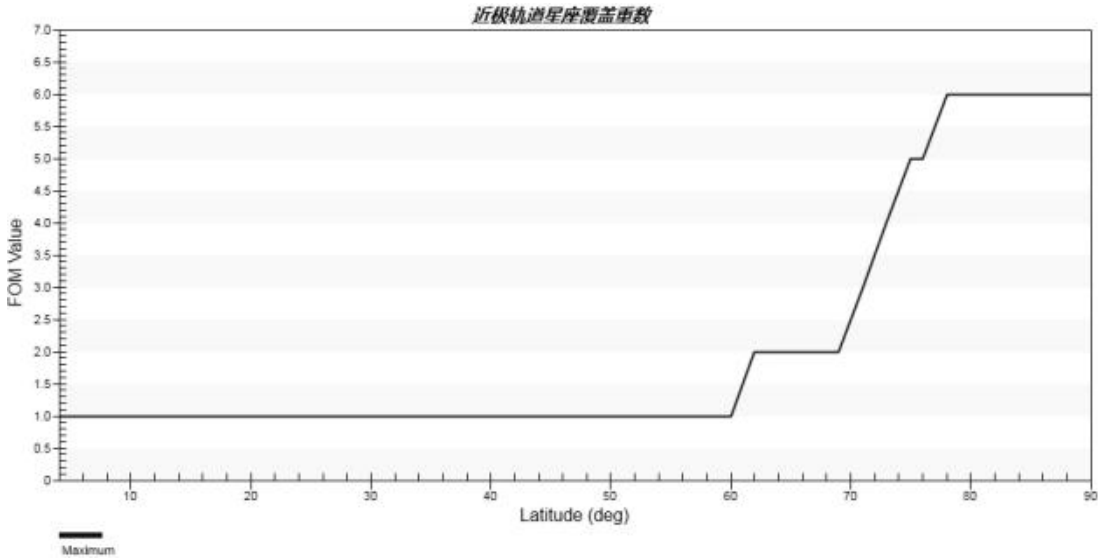

图 2　近极轨道星座覆盖性（10°仰角）

图 2 仿真结果表明，66 颗近极轨道星座卫星在 10°通信仰角的情况下，可实现全球 1 重以上覆盖，

在南北纬 62°－90°范围内区域可实现 2 重以上覆盖，最大覆盖重数为 6 重。

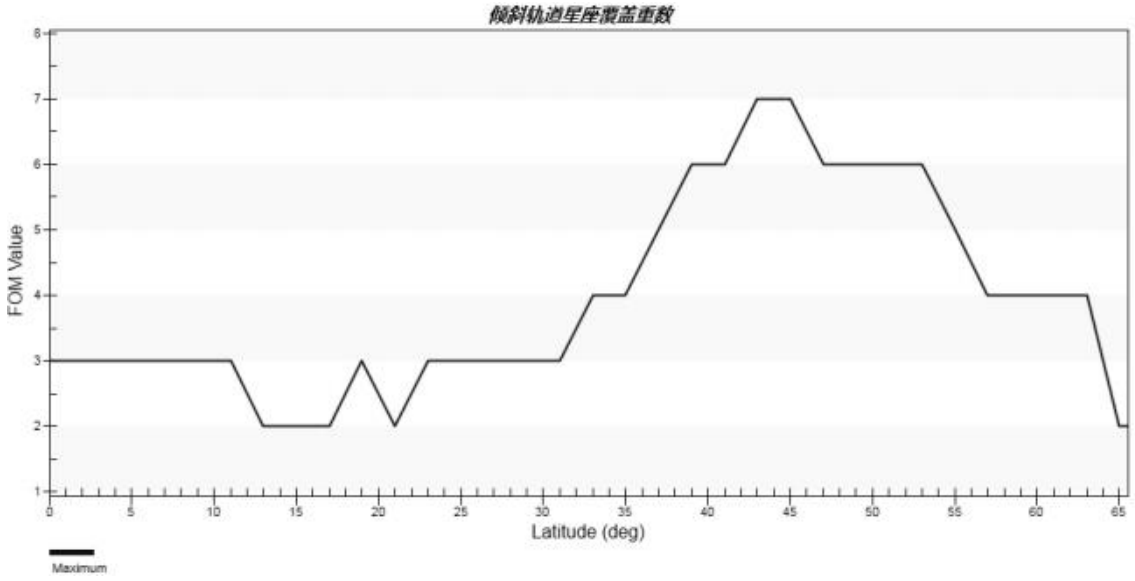

图 3　倾斜轨道星座覆盖性（20°仰角）

图 3 仿真结果表明，216 颗近极轨道星座卫星在最低通信仰角 20°的情况下，可实现南北纬 0°- 65°范围内区域 2 重以上覆盖，最大覆盖重数为 7 重。

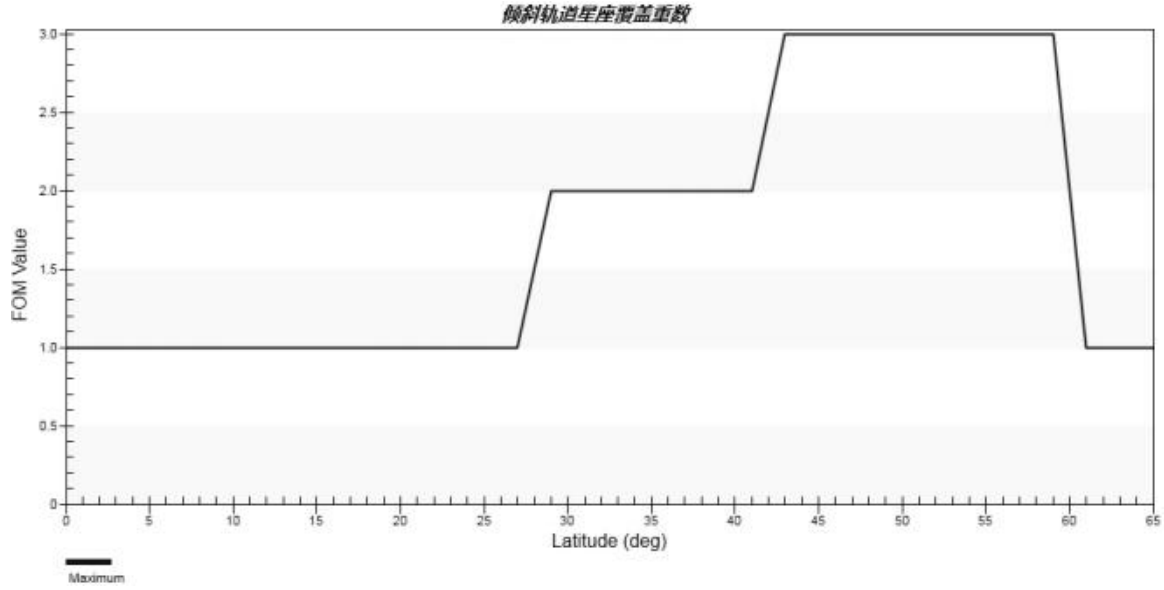

图 4　倾斜轨道星座覆盖性（30°仰角）

图 4 仿真结果表明，216 颗近极轨道星座卫星在最低通信仰角 30°的情况下，可实现南北纬 0°- 65°范围内区域 1 重以上覆盖，最大覆盖重数为 3 重。图 4 与图 3 对比可以看出，随着最低通信仰角的增加，星座覆盖重数不断减少，这是由于随着通信仰角的不断增加，对空可视范围逐渐缩小，导致可视卫星数量不断减少。

3.2.2 典型位置覆盖仿真分析

在我国南部、东北和西北各选择一个典型参考点，分别选择三亚（北纬 18.2°，东经 109.5°）、佳木斯（北纬 46.8°，东经 130.4°）、库尔勒（北纬 41.8°，东经 85.7°）作为具体分析对象，仿真分析一天时间内该地区对倾斜轨道星座可视卫星数量，仿真结果如图 5 至图 10 所示。

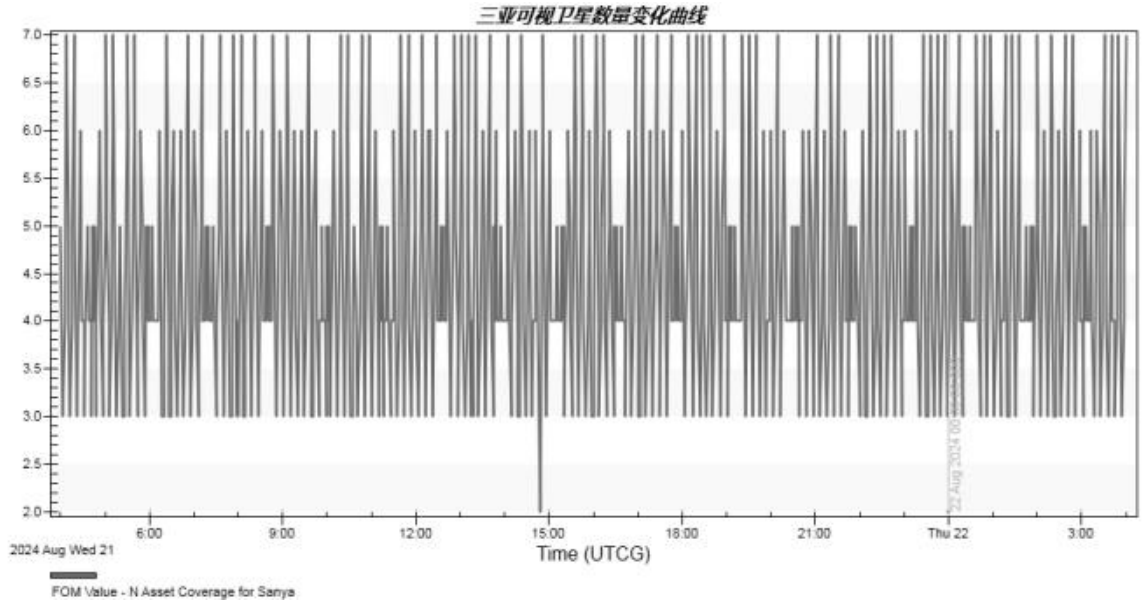

图 5　三亚地区可视卫星数量变化曲线（20°仰角）

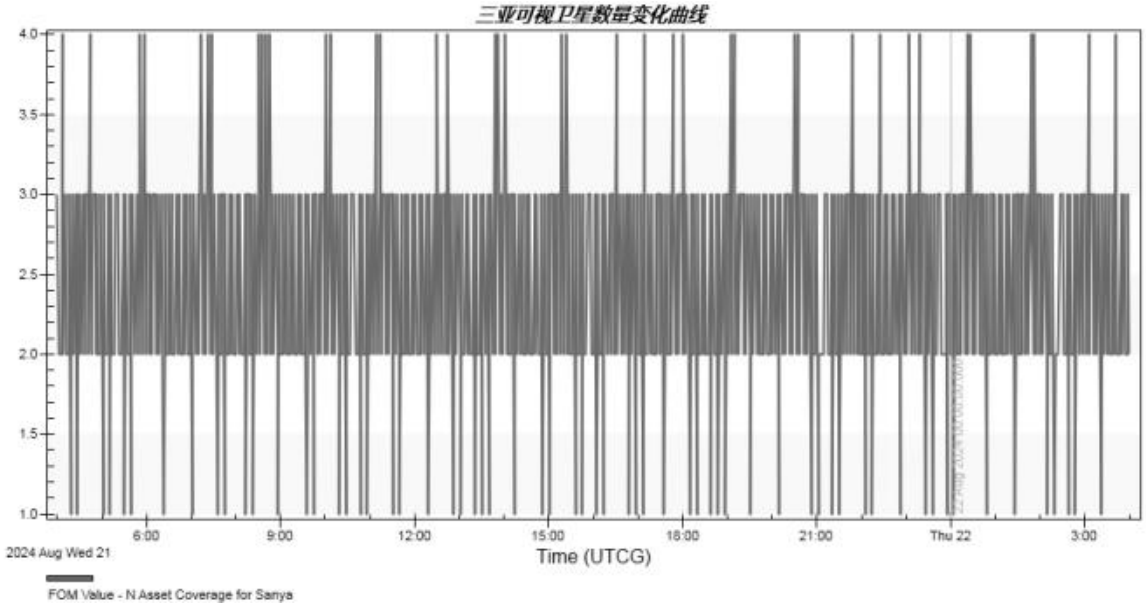

图 6　三亚地区可视卫星数量变化曲线（30°仰角）

图 5 和图 6 仿真结果表明，一天时间内，三亚地区在 20°通信仰角情况下，可视卫星数量在 2-7 之间；在 30°通信仰角情况下，可视卫星数量在 1-4 之间。

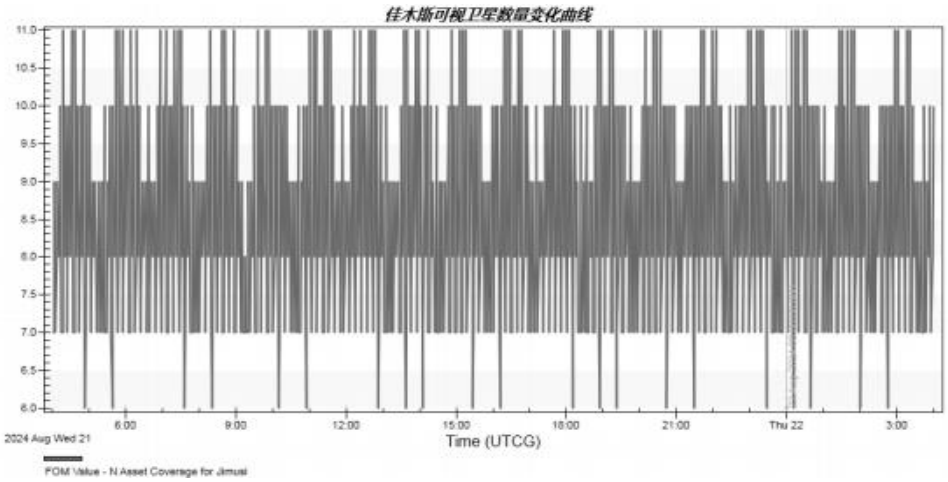

图 7　佳木斯地区可视卫星数量变化曲线（20°仰角）

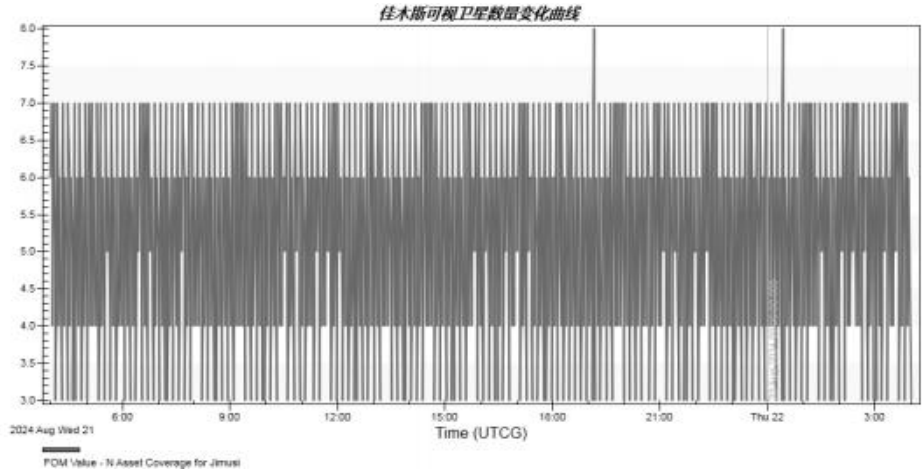

图 8　佳木斯地区可视卫星数量变化曲线（30°仰角）

图 7 和图 8 仿真结果表明，一天时间内，佳木斯地区在 20°通信仰角情况下，可视卫星数量在 6-11 之间；在 30°通信仰角情况下，可视卫星数量在 3-8 之间。

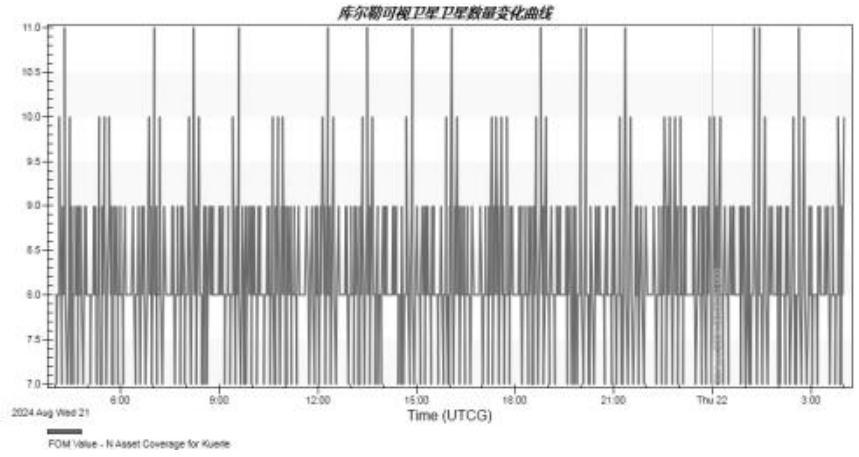

图 9　库尔勒地区可视卫星数量变化曲线（20°仰角）

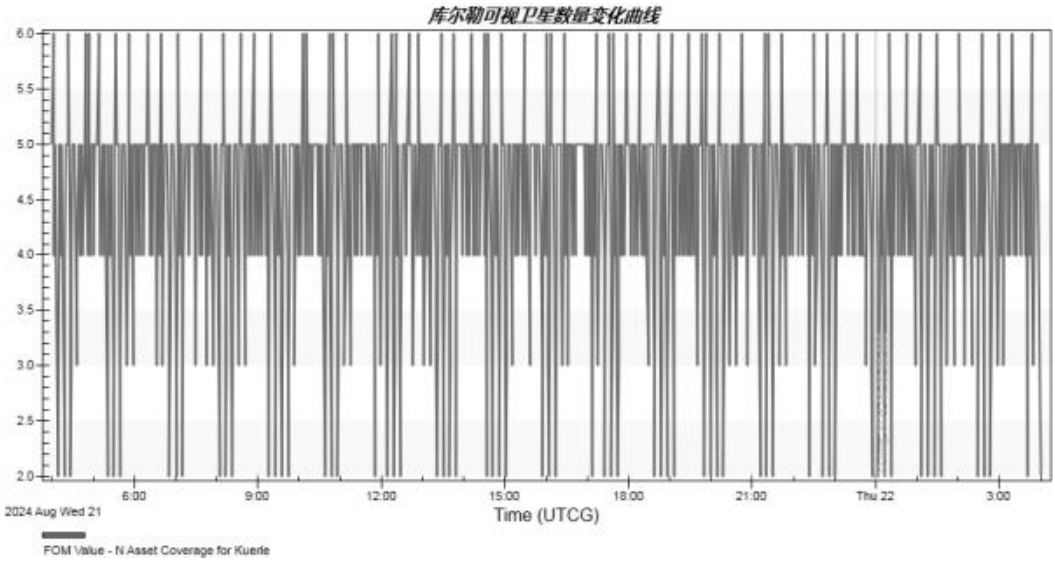

图 10　库尔勒地区可视卫星数量变化曲线（30°仰角）

图 9 和图 10 仿真结果表明，一天时间内，库尔勒地区在 20°通信仰角情况下，可视卫星数量在 7-11 之间；在 30°通信仰角情况下，可视卫星数量在 2-6 之间。

分别统计三亚、佳木斯、库尔勒三个典型位置仅可视 1 颗星、2 颗星、3 颗星、4 颗星和 5 颗星及其以上的时间占比，统计结果如表 6 所示。

表6　典型位置覆盖性分析

地点	通信仰角	可视卫星数量	仅可视 1 星占比	仅可视 2 星占比	仅可视 3 星占比	仅可视 4 星占比	可视 5 星及以上占比
三亚	20°	2-7	0%	0.01%	18.03%	42.69%	39.27%
	30°	1-4	4.55%	49.53%	43.445	2.485	0%
佳木斯	20°	6-11	0%	0%	0%	0%	100%
	30°	3-8	0%	0%	9.865	19.135	71.01%
库尔勒	20°	7-11	0%	0%	0%	0%	100%
	30°	2-6	0%	5.19%	6.15%	22.43%	66.23%

通过对比三亚、佳木斯、库尔勒三个位置可视卫星数量时间占比可以看出，同一位置情况下，通信仰角越大，可视卫星数量越少；同一通信仰角情况下，纬度越低，可视卫星数量越少，且可视卫星数量少的时间占比越长，这是由卫星对地可视范围不变，地理位置纬度越低，经纬网格所跨的经纬度数相同的情况下，面积就越大，因此导致低纬度地区可视卫星较高纬度地区少。

3.2.3 典型区域覆盖仿真分析

在前一节典型位置覆盖仿真分析基础上，以三亚、佳木斯和库尔勒为中心，分别计算区域半径在 200km、500km 和 1000km 情况下可视卫星数量，仿真结果如表 7 所示。

表7　典型区域覆盖性分析

地点	星座构型		通信仰角	区域可视卫星数量		
				200km	500km	1000km
三亚	近极轨道	66 星	10°	1-4	1-4	2-5
	倾斜轨道	216 星	20°	3-8	5-9	8-14
			30°	2-4	2-7	5-9
佳木斯	近极轨道	66 星	10°	2-5	2-6	2-7
	倾斜轨道	216 星	20°	7-11	9-14	12-18
			30°	4-8	6-11	9-13
库尔勒	近极轨道	66 星	10°	1-5	1-5	2-6
	倾斜轨道	216 星	20°	8-12	9-13	13-18
			30°	3-8	6-11	9-13

仿真结果表明，仿真区域面积一致情况下，仿真位置纬度越低，可视卫星数量越多；同一仿真位置情况下，仿真区域面积越大，可视卫星数量越多；对于近极轨道星座，受限于星座规模，随着仿真区域面积增大，可视卫星数量增加较少。

3.2.4 仿真小结

通过对星座全球覆盖性、典型位置覆盖性和区域覆盖性仿真结果进行对比可以看出，星座覆盖性能与星座规模大小、通信仰角、位置区域等因素密切相关。对于本文所设计的混合星座，同等情况下，通信仰角越大，可视卫星数量越少；仿真位置纬度越低，可视卫星数量越少；仿真区域面积越大，可视卫星数量越多。

4 结束语

本文首先梳理了具有代表性的6个低轨星座的研究现状。受此启发，设计了一个混合星座，包括一个66星组成的近极轨道星座和一个216星组成的倾斜轨道星座，并采用STK软件对星座的全球覆盖性、典型位置覆盖性和区域覆盖性进行了仿真分析。仿真结果表明，本文所设计的星座可实现全球覆盖，但在高通信仰角情况下，可视卫星数量较少，尤其是在三亚等中低纬度区域覆盖重数有限，需进一步增加星座规模，增强系统网络韧性。

参考文献：

[1] 王勇, 龙定央, 骆盛, 等. “星链”系统星座覆盖及应用分析[J]. 中国航天, 2021(8): 43-47.
WANG Y, LONG D Y, LUO S, et al. Analysis of constellation coverage and application of the "Starlink" system [J]. Aerospace China, 2021(8): 43-47.

[2] 余南平, 严佳杰. 国家和国家安全视角下的美国“星链”计划及其影响[J]. 国际安全研究, 2021, 39(5): 67-91.

YU N P, YAN J J. The US "Starlink" program and impact from the perspective of national security[J]. Journal of International Security Studies, 2021, 39(5): 67-91.

[3] 王迪, 骆盛, 毛锦, 等. Starlink 卫星系统技术概要[J]. 航天电子对抗, 2020, 36(5): 51-56.
WANG D, LUO S, MAO J, et al. Overview of Starlink satellite system technology[J]. Aerospace Electronic Warfare, 2020, 36(5): 51-56.

[4] 黄志澄. 从美国国防太空战略看“星链”的军事应用[J]. 太空探索, 2021(11): 68-73.
HUANG Z C. The military application of "Starlink" from the perspective of US defense space strategy[J]. Space Exploration, 2021(11): 68-73.

[5] 苗青, 蒋照菁, 王闯. 下一代铱系统发展现状与分析[J]. 数字通信世界, 2019(7): 21-23.
MIAO Q, JIANG Z J, WANG C. Development situation and analysis of the Iridium next system [J].Digital Communication World, 2019(7): 21-23.

[6] 李殷乔, 熊玮, 孙治国. 中国高轨移动通信卫星系统发展的机遇与挑战[J]. 国际太空, 2020(4): 36-41.
LI Y Q, XIONG W, SUN Z G. Opportunities and challenges for the development of China's high earth orbit mobile communication satellite system[J]. Space International, 2020(4): 36-41.

[7] 李博, 杜丹, 赵惠惠, 等. “一网”星座卫星研制情况简析[J]. 国际太空, 2021 (9): 62-65.
LI B, DU D, ZHAO H H, et, al. Analysis of the development of the "One Web" constellation satellite[J]. Space International, 2021 (9): 62-65.

[8] 白雪, 王丹丹, 白照广, 等. 低轨大规模星座概念研究与分阶段部署方案[J]. 南京航空航天大学学报, 2022, 24(S1): 1-8.
BAI X, WANG D D, BAI Z G, et, al. Conceptual study on low orbit large scale constellation and its phased
deployment scheme[J]. Journal of Nanjing University of Aeronautics & Astronautics, 2022, 24(S1): 1-8.

[9] 崔瑞飞, 赵治, 陈治科, 等. 低轨巨型星座正在深刻影响世界航天[J]. 国际太空, 2022 (11): 42-46.
CUI R F, ZHAO Z, CHEN Z K, et, al. LEO mega constellation is deeply changing space activities of the world[J]. Space International, 2022 (11): 42-46.

[10] 陈全, 杨磊, 郭剑鸣, 等. 低轨巨型星座网络: 组网技术与研究现状[J]. 通信学报, 2022, 43(5): 177-189.
CHEN Q, YAGN L, GUO J M, et, al. LEO mega-constellation network: networking technologies and state of the art[J]. Journal on Communications, 2022, 43(5): 177-189.

[11] 王韵涵, 李博, 刘咏. 国外低轨卫星互联网发展最新态势研判[J]. 国际太空, 2022(3): 7-12.
WANG Y H, LI B, LIU Y. Research and judgment on the latest development trend of foreign low earth orbit satellite internet[J]. Space International, 2022(3): 7-12.

[12] 纪凡策. “柯伊柏”星座介绍及与其他星座对比分析[J]. 国际太空, 2020(12): 27-31.
JI F C. Introduction to the "Kuiper" constellation and comparative analysis with other constellations[J]. Space International, 2020(12): 27-31.

[作者简介]

刘二江（1991—），男，博士，工程师。主要研究方向：卫星通信。

徐潇审（1985—），男，博士，高级工程师。主要研究方向：卫星通信。

王　良（1983—），男，博士，高级工程师。主要研究方向：卫星通信。

Relaying In Cislunar Telemetry and Telecommand Communication: An Information Value Loss Guided Scheduling Mechanism For Multiple Time-Delay Control Systems

Zhouyong Hu[1], Afang Yuan[1], Qinyu Zhang[1,2], Zhihua Yang*[1,2]

***Abstract*—In the lunar missions, relay satellites on the various orbits play critical roles in the cislunar communications, i.e. telemetry and telecommand to the probers on the far side of moon, which could help achieving the constant visibility between the actuator and the controller. However, huge time span in the end-to-end communication incurs obvious delay during the controlling loop which current controller design could not deal with effectively. In this work, therefore, we propose a Greedy Algorithm-based Scheduling Mechanism (GASM) for multiple time-delay control systems through the cislunar relay communication. In particular, we develop a novel metric of Information Value Loss (IVL) to measure the utility of the proposed GASA by considering the timeliness of telemetry and telecommand data on the control loop. The simulations show that the proposed GASM could achieve excellent control stability and timeliness of data compared with typical scheduling algorithms based on Age of Information (AoI).**

***Keywords*—Cislunar Communication, Time-Delay Control, Age of Information, Scheduling**

This work is supported in part by the National Natural Science Foundation of China under Grant 62371158 and Grant 62027802, and in part by the Major Key Project of PCL (PCL2024A01).

1 Zhouyong Hu, Afang Yuan, Qinyu Zhang, Zhihua Yang, Harbin Institute of Technology (Shenzhen), Shenzhen, Guangdong, 518055, China (e-mail:huzhouyong@stu.hit.edu.cn, yuanaf@stu.hit.edu.cn, yangzhihua@hit.edu.cn, zqy@hit.edu.cn).

2 Qinyu Zhang, Zhihua Yang, Pengcheng National Laboratory, Shenzhen, Guangdong, 518055, China.

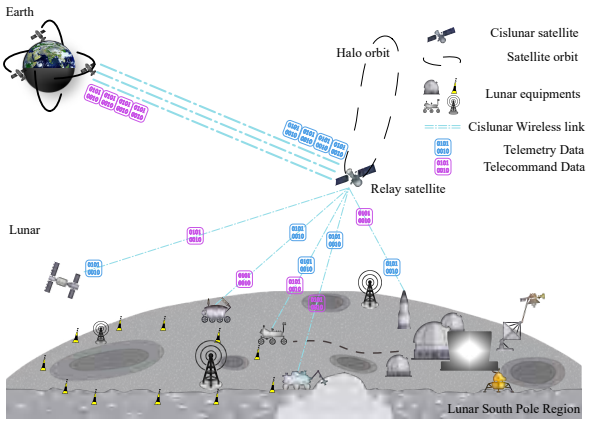

Figure 1 The Proposed Cislunar Relay-Based Control System.

I INTRODUCTION

The study of cislunar communications has assumed paramount importance as countries and prominent space agencies hasten their Earth-Moon exploration undertakings. As depicted in Figure 1, with the rapid progression of lunar exploration by diverse nations and the relentless advancement of aerospace technology, a multitude of equipment, including repeaters, orbiters, probes, flybys, and rovers, will be integrated into future lunar exploration missions. However, unique characteristics of long-distance propagation delays and relay communications in cislunar space introduce significant constraints to typical ground control processes. In the nascent stages of space exploration, telemetry and telecommand technologies are evolved independently. This kind of multifaceted joint measurement and control process inherently brings a series of challenges, such as resource allocation, transmission

scheduling, protocol interaction, etc. Emerging technologies, such as the Unified Carrier TTC System (UCTTCS) and the Unified Space Data Link Protocol (USLP) system as promulgated by Consultative Committee for Space Data Systems (CCSDS), are facilitating the convergence of measurement and control data transmission. Furthermore, the Earth-Moon communication environment's specific traits profoundly impact the measurement and control process, notably with a marked decline in data timeliness due to extensive propagation distances. Outdated data can compromise control performance [1], as a challenge exacerbated by the integration of measurement and control data transmission for multiple targets. A moderate amount of time-lag is allowed in the control process, and the relevant time-lag control system technology can reduce the harm brought about by this communication time delay [2-4], thus providing operational leeway for deploying various target measurement and control processes within the Earth-Moon environment's constrained communication resources. However, optimization of time-lag control has an upper performance limit, necessitating the optimization of the communication process within the permissible bounds of the control process. This requirement diminishes the efficacy of general communication optimization methods based on time delay. Consequently, it is imperative to further investigate the timeliness requirements of measurement and control data within the communication system. Typically, telemetry data and telecommand data may simultaneously focus on both timeliness and utility values. Data proximate to the moment of measurement is conducive to more effective decision-making, while a period of availability exists for measured data, after which it may become obsolete and unusable for analysis. Remote control telecommand data shares similar characteristics. That is, the stability of the control process is intimately linked to the timeliness of measurement data.

Imperfect communication links carrying the feedback loop add layers of complexity, as data delays and loss can negatively impact performance and potentially destabilize the system [5][6]. The lunar exploration measurement and control mission's control process demands high stability, high accuracy, and high timeliness. Most of typical control system performance indicators abstract the impact of data transmission into parameters such as communication delay and packet loss rate, modeling the control system in a black-box manner, which makes it difficult to analyze and evaluate the factors affecting time-sensitive performance of measurement and control data. Given that the timeliness of data significantly influences the stability and other performance aspects of the measurement and control process, the transmission scheduling mechanism in the relay or multi-hop communication link play critical role in the entire control system's operation. In this paper, therefore, we attempt to solve the transmission requirements of multiple measurement and control processes by investigating the relay scheduling mechanism on simultaneous cislunar telemetry and telecommand data. In particular, we will propose a time-effective scheduling strategy to meet the performance needs of various measurement and control process data. The main innovations are summarized as follows:

- We develop a novel metric, IVL, for evaluating the timeliness of telemetry and telecommand data in the cislunar time-lag control system. This metric considers the effect of the measurement and control data on the control loop after experiencing significant delay. Compared to the traditional Age of Information (AoI) [7], IVL better reflects the impact of communication delays on control performance, thereby aligning the communication optimization directly with the control performance requirements.
- We propose a Greedy Algorithm-based Scheduling Mechanism (GASM) based on IVL minimization, which adeptly utilizes the relay's storage and transmission resources to manage multiple control processes. This algorithm, in contrast to typical scheduling algorithms based on AoI [8], ensures the stable operation of multiple control processes simultaneously given the constrained relay resources.
- Simulation results underscore the proposed scheduling algorithm's distinct advantages over the typical AoI minimum scheduling algorithm in terms of control performance and timeliness.

II RELATED WORKS

The timeliness of measurement and control data significantly influences the performance of the control process, including its stability. The literature [1] delves into the hazards associated with stale information on control system performance, defining the maximum degree of staleness that can be tolerated to maintain specified stability, thereby underscoring the critical importance of information timeliness for control system stability. In the field of information timeliness research, AoI as a novel metric in real-time networked systems has emerged as a novel metric, guiding the optimization of systems' ability to transmit fresh data by quantifying the age of data. As evidenced by the works [9,10], AoI is extensively employed for system optimization in scenarios involving just-in-time transmission or wireless network control. The simplicity of the definition has led to a plethora of AoI-related studies [11,12] proposing various AoI-derived metrics. However, these metrics are largely independent of the control system, rendering the co-optimization of control and communication systems unattainable. Additionally, some studies as highlighted in [13], demonstrate that minimizing the average freshness of information does not necessarily ensure satisfactory control performance for individual systems and may re-

sult in subpar collective performance. This illustrates that the aggregation of numerous communication control subsystems hinders AoI from fulfilling stability requirements essential for the control process. Literature [14] seeks to stabilize multiple control systems by introducing AoI to optimize the transmission of multiple system control processes. It formulates an optimization problem aimed at minimizing the estimation error induced by the network on the controllers and determines the optimal transmission scheduling for each link. Literature [15] introduces a delay-dependent Value of Information (VoI) metric based on a trade-off analysis that quantifies the value of transmitted packets. However, the metric characterizes the final target cost function in the form of a simple summation of control and communication costs, which does not match in a physical sense, leading to results that deviate from the true optimal performance of the system. In order to solve the mismatch problem in the sense of control and transmission dimensions, literature [16] proposes a joint control and transmission design architecture based on Full Loop Age of Information (FL-AoI) for integrating multi-sub-system ICPSs in multi-hop networks. By introducing the this new cost metric, it solves the dimensional mismatch problem brought by the weighted summation form of control and transmission costs, and provides a new usable metric for the joint optimization of network and control systems.

III problem formulation

A System Models

Lunar missions are increasingly focused on regions such as the lunar back and south pole, and the special characteristics of these regions require that cislunar communication must rely on the participation of relay satellites. In the cislunar relay communication for the measurement and control scenario shown in Figure 1, the Earth $\mathfrak{E}$ or the Moon $\mathfrak{M}$ sends telemetry and telecommand packets to the relay satellite $\mathfrak{R}$ forwarding the packets to the other end.

Relay Model: As shown in Figure 2, the periodic task generates periodic state packets, so it is assumed that the packets arrive at a fixed frequency, by which each source generates packets at a time interval of T_i. The size of each arriving packet is randomized. However, given that the USLP can support a maximum of 65536 byte transmission frames, individual packets can all be encapsulated in a single spatial transmission frame. The data processing capacity of the relay node is set to a fixed value, i.e., it can only process p packets at the same time, and the propagation delay of the two links is set to T_{m2e} and T_{e2m}. The life cycle of a series of measurement and control packets generated by each measurement and control process is a function of time, which is set to be $C_i(t)$. In

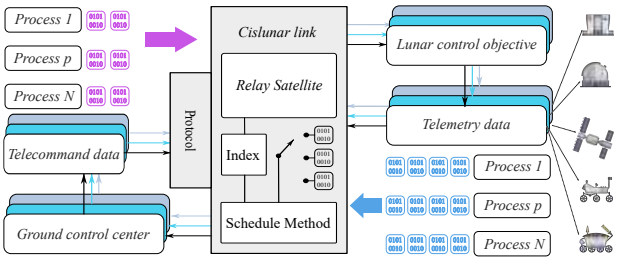

Figure 2 The Cislunar Relay Model on Telemetry and telecommand Data.

addition, the moment of generation of each measurement and control packet is set to be $u_i(t)$, and the time of expiration of the packet is set to be $d_i(t)$, then $C_i(t) = d_i(t) - u_i(t)$. Multiple packets generated by different measurement and control processes arrive at the relay satellite through the lunar relay link and wait in the cache queue of the relay satellite for scheduling and forwarding. Let the moment of the data packet k generated by the i source application be noted as $u_{i,k}$, the life cycle of the measurement and control data $C_{i,k}$ is encapsulated in the data packet as meta-information and decoded in the relay satellite to obtain the expiration time of the data packet $d_{i,k}$. Then, all the measurement and control packets are forwarded by the relay satellite based on the scheduling policy, and finally the data packet arrives at the destination at the $r_{i,k}$th moment. The relay satellite forwards all the measurement and control packets according to the scheduling policy, and finally the data packets arrive at the destination at the time of $r_{i,k}$. Assume that the queuing delay of the k-th data packet generated in the measurement and control process i in the cache queue is $\tau^w_{i,k}$, let $\tau^p_{i,k}$ represents the two-hop spatial wireless link propagation delay of the data packet, $\tau^t_{i,k}$ represents the transmission delay, $\tau^o_{i,k}$ represents other processing delays respectively, that is, the delay deviation value is:

$$\Delta\tau_i = \tau^p_{i,k} + \tau^w_{i,k} + \tau^t_{i,k} + \tau^o_{i,k}. \tag{1}$$

Then the arrival moment of the packet can be expressed as:

$$r_{i,k} = u_{i,k} + \Delta\tau_i. \tag{2}$$

In this case, the computational process latency of a general device is much smaller than the latency generated by the communication process, so the effect of $\tau^o_{i,k}$ will be ignored subsequently, i.e., $\tau^o_{i,k} = 0$. In the design of controllers with constant time deviation $\Delta\tau$, it is required that the time-lag of the data is constant, but in practice, due to the design of the communication network, the use of protocols, interference packet loss, and other phenomena occur, resulting in the time delay of the data transmission is not a controllable constant. However, one effective way is to set up buffers at the controller side and at the actuator side respectively, so that the stability of the control system can be ensured as long as at least one available sampling data is guaranteed during the control

sampling period. This design is simple and efficient: on the one hand, it can be applied to multiple control objects without the need to design separate controllers for each control object; on the other hand, it simplifies the design of communication protocols, and only needs to calibrate the maximum constant transmission delay for each data. Based on the stability requirements of different control systems, there is a maximum sampling period for sampling the state data, which is set as $T_{i,max}$. The design of the controlled object controller requires a certain sampling frequency, i.e., the sampling period determines the latency of the data transmission. For example, the sum $\Delta\tau_i$ of the delay deviation value of the state data and control data must satisfy the relation

$$\Delta\tau_i < T_{i,max}. \tag{3}$$

The relation (3) also specifies the expiration time of the data. The sensing data must reach the controller before the next sampling data is generated, otherwise the controller can not make a decision. At the same time, the actuator input signals generated by the controller need to arrive at the actuator and complete the transfer of the state before the next sampling comes, otherwise the stability of the control system may be affected. In this way, the expiration time of the data $d_i(t)$ is calibrated according to the maximum sampling period $T_{i,max}$ of different control systems. There can be many ways to calibrate the data, and different channel resources can be assigned different constant time-lags. Therefore, if the upstream channel (i.e., the Earth-side to the relay satellites to the Lunar-side) has a better communication condition, then it can be assigned a smaller constant time-lag. The downstream channel with a poor communication condition should be able to be assigned a larger constant time-lag. While, the channel with worse communication conditions should be able to allocate more constant time-lag. More specific settings should be set in conjunction with a variety of specific control systems. In this paper, upstream and downstream channel communication link parameters are the same to continue the next study as:

$$d_{i,max}(t) = u_i(t) + \Delta\tau_{i,max}, \tag{4}$$

where $u(t)$ denotes the time of data output, $\Delta\tau_{i,max} = \frac{T_{i,max}}{2}$.

Control Model The end-to-end delay in a wireless system consists of several components, i.e., over-the-air propagation delay, queuing delay, processing/computation delay, and additional delay due to retransmission. In particular, increase in one or more of these delays will be reflected as in the end-to-end delay [17]. A time-lag system captures how the dynamic error between the actual state and the target state of a motion planner design changes over time under the influence of wireless factors such as delay. As shown in Figure 3, in the measurement and control loop model [18], in the reference signal input, is the output state of the controlled object expected in

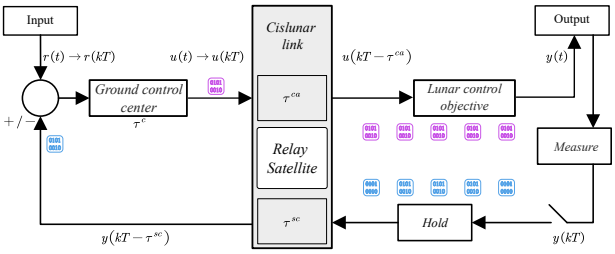

Figure 3 The Proposed Remote Control Loop Model.

the measurement and control mission, for example, the destination coordinates of the lunar rover operation. The actual output signal denotes the output state of the control object in the measurement and control mission, for example, the coordinates that the lunar rover is currently arriving at. The general automated control process is described as follows: first, in the feedback control loop, a measurement tool (e.g., a telemetry satellite) measures the output state of the control object (e.g., the actual positional coordinates of the lunar rover), and samples the continuous physical signals over a T time interval to obtain $y(kT)$. The sampled signal is delayed to reach the controller after transmission through the zero-order keeper and the communication network, i.e., the state signal of the input control object at the controller's end is the signal $y(kT-\tau^{sc})$ at the past moment $kT-\tau^{sc}$. The controller analyzes the desired reference input signal $r(kT)$ and the current feedback past state signal $y(kT-\tau^{sc})$ to calculate the desired execution input signal $u(kT)$. Because of the network communication delay, the execution signal input to the detector at moment t is also the signal $u(kT-\tau^{sc})$ of the past moment $kT-\tau^{ca}$, and the detector changes its state and outputs a state signal when it finishes execution. Currently in the control field to deal with this time-lag control system using a controller with a constant time-lag $\Delta\tau$ [18], this controller is designed based on the premise that the feedback data has a constant time delay for the design, and the determination of the constant time delay value can be realized by the time-lag control system into a general control system.

For the measurement and control process consisting of two transmission links, measurement and control constituting a loop structure, the constant time-lag upper limit is able to measure the utility value of data. The controlled object i generates new telemetry data $x_{i,k}$ after a certain processing delay $\tau^a_{i,k}$ during the execution of the control packet $u_{i,k}$ and then transmits it to the control destination. The console is analyzed and after a certain processing delay $\tau^c_{i,k}$, new control data $u_{i,k+1}$ with a defined life cycle $C_{i,k+1}$ is generated. After a certain communication delay, the data reaches the execution side to update until the application is completed.

B Problem Description

Definition 1 Remaining age of Information: $RoI = d(t) - t$ is the lifetime of the latest packet that is available at destination at moment t, i.e., the data expiration time $d(t)$ minus the current time t.

Definition 2 Value of Information:

$$V : indicator \mapsto value, \tag{5}$$

denotes that information is mapped to a specific form of value representation through the corresponding application indicator. The timeliness indicator, $AoI = t - u(t)$, can be mapped to a value by $v_{AoI} = v(t - u(t))$. The usefulness indicator, $RoI = d(t) - t$ can be mapped t oa value by $v_{RoI} = v(d(t) - t)$.

Definition 3 Loss fuction:

$$l(t) = l(v_m(t)), m = 1, 2, , M, \tag{6}$$

where M denotes the total number of indicators participating in the evaluation of information value, $v_m(t)$ denotes the information value characterized by indicator m, and l is the functional relationship between indicator values. Thus, Information Value Loss (IVL) is defined as a functional mapping of AoI and RoI,

$$IVL = V(AoI, RoI). \tag{7}$$

The purpose of this paper is to study the scheduling mechanism of the communication for all the measurement and control packets, i.e., how the transmission order of the measurement and control packets should be assigned, while meeting the timeliness requirements of the measurement and control process. Then we have

$$\pi_k = \underset{i \in 1, \cdots, N}{\operatorname{argmin}} \mathscr{L}(i, k), \tag{8}$$

where $\mathscr{L}$ characterizes the loss of information value generated by the transmission in the communication system.

IV ALGORITHM DESCRIPTION

A AoI&RoI

To construct a two-hop transmission scheduling model, define the source-relay-destination model as: the source sends data packets continuously to the destination in a certain time. In particular, the parameter of each data packet is defined as $[u_k, r_k, d_k]$, in which u_k, r_k, d_k are denoted as the generating moment, the arriving moment, and the expiration moment of the packet, respectively. Assuming that $u_k < r_k < d_k$ and $r_{k-1} < r_k$, then the AoI and RoI of the destination packet are shown in Figure 4. The closed expression of AoI is applied in the relay measurement and control model. The meaning of the

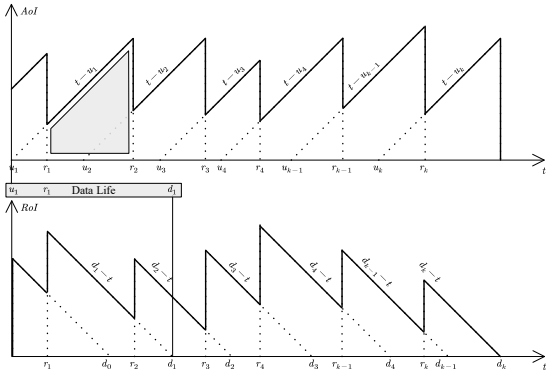

Figure 4 AoI and RoI.

basic AoI formula $AoI = t - u(t)$ is the age of the most recent packet available at destination at moment t, i.e., the current time t minus the time of birth $u(t)$, which is a typical segmentation function segmented by the range of time t:

$$AoI = t - u(t) = \begin{cases} t - u_1 & \text{if } r_1 \leqslant t < r_2 \\ t - u_2 & \text{if } r_2 \leqslant t < r_3 \\ \cdots & \text{if } \cdots \\ t - u_{k-1} & \text{if } r_{k-1} \leqslant t \leqslant r_k. \end{cases} \tag{9}$$

Examine the cumulative AoI of k packet transmissions in the time period $[r_1, r_k]$, set to $\Delta_{AoI}(k)$:

$$\Delta_{AoI}(k) = \int_{r_1}^{r_k} t - u(t)\mathrm{d}t = \begin{cases} \int_{r_1}^{r_2} t - u_1 \mathrm{d}t + \\ \int_{r_1}^{r_2} t - u_2 \mathrm{d}t + \\ \cdots \\ \int_{r_{k-1}}^{r_k} t - u_{k-1} \mathrm{d}t. \end{cases} \tag{10}$$

Then we have

$$\Delta_{AoI}(k) = \sum_{i=1}^{k-1} u_i (r_i - r_{i+1}) + \frac{1}{2}(r_k^2 - r_1^2), \tag{11}$$

which is a typical segmentation function segmented by a range of time t:

$$RoI = d(t) - t = \begin{cases} d_1 - t & \text{if } r_1 \leqslant t < r_2 \\ d_2 - t & \text{if } r_2 \leqslant t < r_3 \\ \cdots & \text{if } \cdots \\ d_{k-1} - t & \text{if } r_{k-1} \leqslant t \leqslant r_k. \end{cases} \tag{12}$$

Examine the cumulative RoI of k packet transmissions in the time period $[r_1, r_k]$, set to $\Delta_{RoI}(k)$:

$$\Delta_{RoI}(k) = \int_{r_1}^{r_k} d(t) - t\mathrm{d}t = \begin{cases} \int_{r_1}^{r_2} d_1 - t \mathrm{d}t + \\ \int_{r_1}^{r_2} d_2 - t \mathrm{d}t + \\ \cdots \\ \int_{r_{k-1}}^{r_k} d_{k-1} - t \mathrm{d}t. \end{cases} \tag{13}$$

Then we have

$$\Delta_{RoI}(k)=\sum_{i=1}^{k-1}d_i(r_{i+1}-r_i)+\frac{1}{2}(r_1^2-r_k^2). \tag{14}$$

B IVL

Based on the aforementioned metrics analysis requirements, this paper defines IVL expressions as

$$\begin{aligned} l(t) &\triangleq \exp(\frac{v_{AoI}-v_{RoI}}{d(t)-u(t)}\ln\alpha) \\ &\triangleq \exp(\frac{v[t-u(t)]-v[d(t)-t]}{d(t)-u(t)}\ln\alpha) \\ &\triangleq \exp(\frac{2t-[u(t)+d(t)]}{d(t)-u(t)}\ln\alpha), \end{aligned} \tag{15}$$

where α is the information indicator value coefficient, characterizing the rate of change of the value of information with the performance indicator parameters. $d(t)-u(t)$ denotes the information life cycle , which characterizes the length of the full utility period of information since its generation. This definition is used to characterize the accumulation of the age of information and the decrease of the remaining survival time of data during the transmission process. $l(t)$ characterizes the rate of reduction of information value in different time scales, and in a period of time $[t_a,t_b]$, the Cumulative Information Value Loss (CIVL) can be defined. Information Value Loss (CIVL) can be defined as

$$\begin{aligned} L &= \int_{t_a}^{t_b} l\,(t)\,dt \\ &= \int_{t_a}^{t_b} \exp(\frac{2t-[u(t)+d(t)]}{d(t)-u(t)}\ln\alpha)dt. \end{aligned} \tag{16}$$

Indicates the cumulative degree of loss of information value of consecutively arriving packets during the examined time period, and can be used to reflect the magnitude of the transmission system's ability to retain information value. Let $t_a=u(t),t_b=t$, then the cumulative information value loss as a function of time t can be obtained:

$$\begin{aligned} L(t) &= \int_{u(t)}^{t} l\,(\tau)\,d\tau \\ &= \int_{u(t)}^{t} \exp(\frac{2\tau-[u(\tau)+d(\tau)]}{d(\tau)-u(\tau)}\ln\alpha)d\tau. \end{aligned} \tag{17}$$

Let the value loss coefficient of the information index of the i-th application process be α_i, then its loss function is also a segmented function:

$$l_i(t)=\begin{cases} \exp(\frac{2t-[u_1+d_1]}{d_1-u_1}\ln\alpha_i) & \text{if } r_1\leqslant t<r_2 \\ \exp(\frac{2t-[u_2+d_2]}{d_2-u_2}\ln\alpha_i) & \text{if } r_2\leqslant t<r_3 \\ \cdots & \text{if } \cdots \\ \exp(\frac{2t-[u_{k-1}+d_{k-1}]}{d_{k-1}-u_{k-1}}\ln\alpha_i) & \text{if } r_{k-1}\leqslant t\leqslant r_k. \end{cases} \tag{18}$$

Algorithm 1 IVL based GASM.

Input: Number of processes N and time stages K
Output: Optimal policies Π^*
$\pi \leftarrow$ perms(N) `/* All possible strategies. */`
for $k=1:K$ **do**
  if $k=1$ **then**
    $\pi^*\leftarrow\pi[1]$ `/* Initial strategy` $\pi[1]$`. */`
  else
    for $j=1:length(\pi)$ **do**
      $L_{NIVL}^k(\pi[j])=\sum_{i=1}^{N}\Delta_{l_i(t)}(k)$
      $L\leftarrow\sum^k L_N^k(\pi[j])$
    end
    $\pi^*\leftarrow$ argmin$_\pi(L)$ `/* Find optimal strategy` π^*`. */`
  end
  $\Pi^*[k]\leftarrow\pi^*$
end

Examine the cumulative transmission loss of k packet transmissions in the time period $[r_1,r_k]$, set to $\Delta_{l_i(t)}(k)$:

$$\Delta_{l_i(t)}(k)=\begin{cases} \int_{r_1}^{r_2}\exp(\frac{2t-[u_1+d_1]}{d_1-u_1}\ln\alpha_i)\mathrm{d}t+ \\ \int_{r_1}^{r_2}\exp(\frac{2t-[u_2+d_2]}{d_2-u_2}\ln\alpha_i)\mathrm{d}t+ \\ \cdots \\ \int_{r_{k-1}}^{r_k}\exp(\frac{2t-[u_{k-1}+d_{k-1}]}{d_{k-1}-u_{k-1}}\ln\alpha_i)\mathrm{d}t, \end{cases} \tag{19}$$

where $f(j)=\int_{r_j}^{r_{j+1}}\exp(\frac{2t-[u_j+d_j]}{d_j-u_j}\ln\alpha_i)\mathrm{d}t$. Then we have

$$\Delta_{l_i(t)}(k)=\sum_{j=1}^{k-1}\frac{d_j-u_j}{2\ln\alpha_i}\left(\alpha_i^{\frac{2r_{j+1}-(d_j+u_j)}{d_j-u_j}}-\alpha_i^{\frac{2r_j-(d_j+u_j)}{d_j-u_j}}\right), \tag{20}$$

$$L_N^k(\pi(k))=\sum_{i=1}^{N}\Delta_{l_i(t)}(k). \tag{21}$$

C Greedy Algorithm Scheduling Mechanism

Based on (21) as a metric and optimization model for scheduling, at each moment k the scheduler always adopts the policy of the smallest L_N of the current N measurement and control packets as follows:

$$\pi^*(k)=\underset{\pi(k)\in\Pi(k)}{\operatorname{argmin}}\,L_N^k(\pi(k)), \tag{22}$$

where $L_N^k(\pi(k))$ is given by (20) and (21). The algorithm for GASM is given in Algorithm 1. The greedy algorithm always makes the choice that looks best at the moment. By calculating the CIVL value of the destination, GASM schedules packets based on the current optional decision $\pi[j]$. Then it determines the current optimal decision π^* based on the smallest

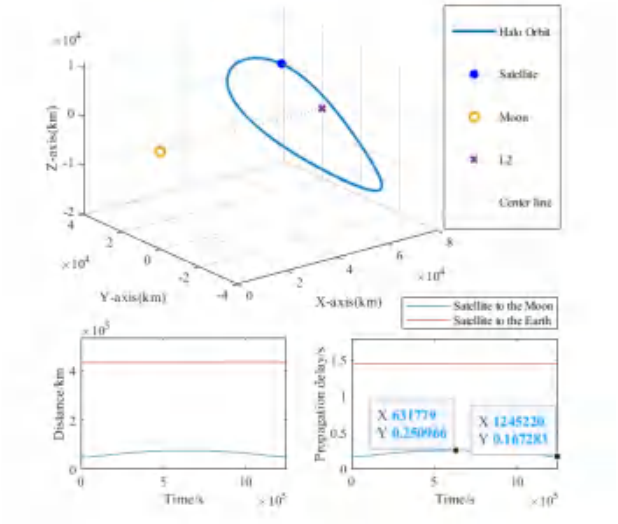

Figure 5 Halo Orbit Satellite.

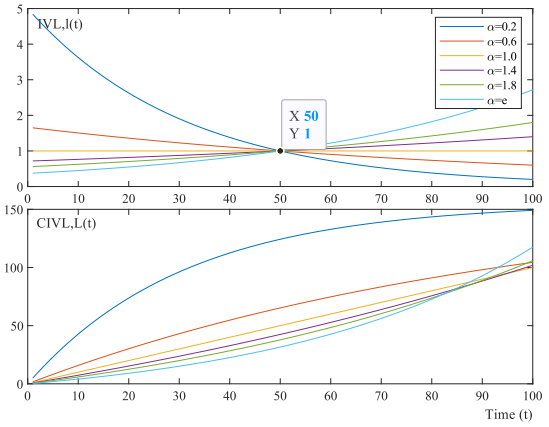

Figure 6 IVL and CIVL.

CIVL taken at each sub-stage, and finally the decision at each sub-stage is the final scheduling optimal decision Π^*. The time complexity analysis of the GASM algorithm is $O(N)$, where N is the number of the measurement and control processes, i.e., the number or length of measurement and control data to be processed. This is because the greedy algorithm usually requires only one traversal of the data and takes only a constant amount of time in selecting the optimal solution each time. Therefore, the time complexity of the entire algorithm can be expressed as $O(N)$.

V SIMULATION RESULTS

In the USLP protocol of CCSDS, the maximum length of transmission frame is 65536 bytes, considering that the data transmission rate of space conventional communication satellites is 10Mbps and is used for 100 communication virtual channels, so that a single application process is assigned a data transmission rate of 100 Kbps.

A Halo Orbit Relay Satellite

In this work, we employ a Halo-orbit satellite in the earth-moon system as the relay in the cislunar communication. As shown in Figure 5, the satellite in Halo orbit at the L2 point needs to schedule and forward all the arriving measurement and control data within the given visibility window. Figure 5 gives two curves, the spatial distance with propagation delay curves between the Halo relay satellite and the lunar surface, and the spatial distance with propagation delay curves between the satellite and the Earth, where the difference in propagation delay between the farthest and the closest point is about 84ms.

B IVL

Setting the parameters $u(t) = 0$s , $d(t) = 100$s, Figure 6 shows the theoretical IVL curve based on the given IVL metrics (15). The curve of IVL with time t for different Lossrates α is shown in Figure 6.

For any $t > 0$ moment, $l(t) > 0$, indicating that IVL always exists and accumulates over time t. IVL is referenced at $\alpha = 1$, when there is $l(t) = 1$, indicating that information occurs at a rate of one unit of value lost per unit of time. The curves for different α values all intersect at the same point $(\frac{d(t)+u(t)}{2}, 1)$, implying that the midpoint of age is the point at which the IVL rates are equal in the timeliness system characterized by the two indicator variables $u(t)$ and $d(t)$. The meaning of equality here means that the growth rate of IVL governed by $t - u(t)$ and $d(t) - t$ is equal at per time unit. In details, when

Table 1 Simulation parameters

Parameter	Value	Symbol
Data Package Size (Byte)	$0 \sim 65535$	
Cislunar Link Bandwidth (Mbps)	10	
Lunar-Terrestrial Distance (km)	384400	
Halo Satellite Orbital Amplitude	13000	
Halo Satellite Orbital Period (s)	1.277×10^6	
Number of Processes	4	N
Sampling Frequency (s)	1	T_i
Time Range (s)	$101 \sim 200$	T
Number of Stages	100	K
Lossrate	$0 \sim \infty$	α
Max Sampling Frequency (s)	$15, 10, 8, 6$	$T_{i,max}$

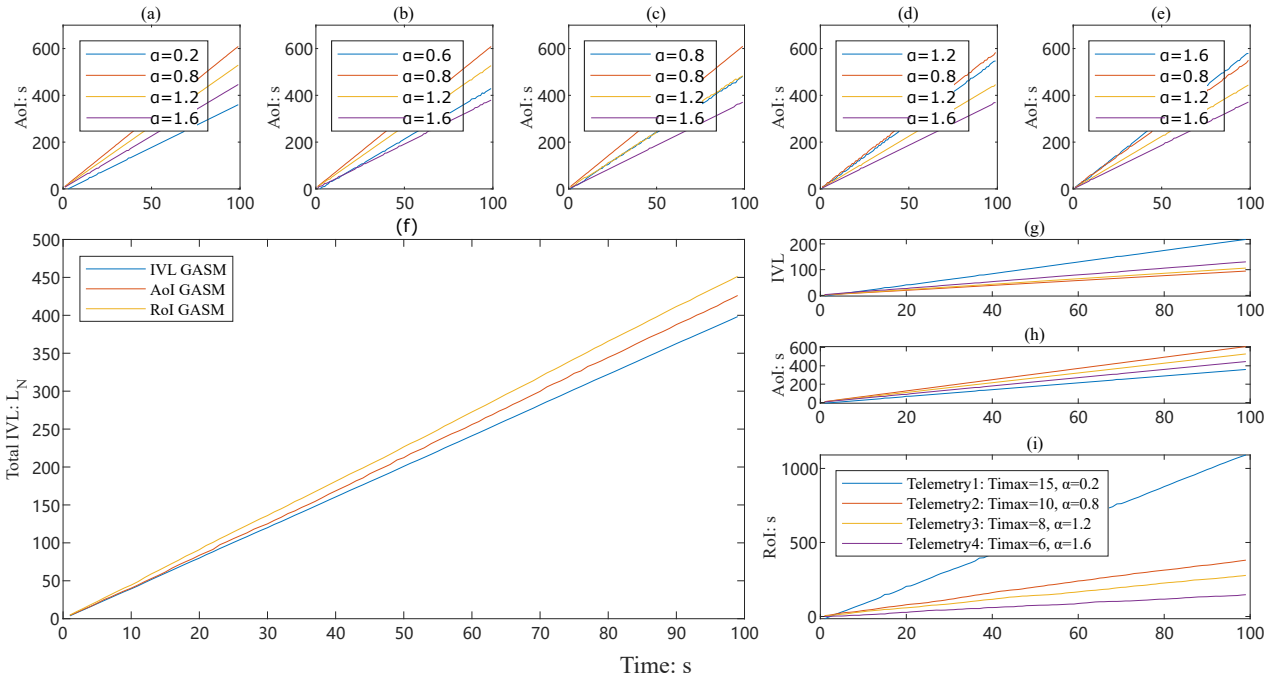

Figure 7　Simulation Performance.

the measurement and control data is more dependent on the timely arrival of the data, this type of data in the initial stage $u(t)$ will have a huge loss of value over time, the optimization model will give priority to this type of measurement and control data for scheduling in order to minimize the IVL of the system, and this type of data needs a smaller α, respectively. When the measurement and control data puts emphasis on the destructive nature of data expiration data, such data will not produce explosive value loss until close to the expiration time $d(t)$. The optimization model, in order to ensure that the IVL of the system is minimized, likewise, needs to ensure that this type of data can be transmitted within the validity period. In general, by setting the appropriate value of information loss, coefficient α value can allow different application processes in the system to realize the jointed optimization of multiple measurement and control data.

C　Performance of Algorithms

The receiving data bandwidth of the relay satellite is much larger than the sending data bandwidth, so the data from multiple sources are directly received into the data buffer after being sent to the relay satellite. After the packet forwarding protocol reads the necessary information of each application program packet, such as data expiration time $d(t)$ and generation time $u(t)$, it enters the queuing and forwarding queue to wait for the scheduler to send it to the Earth control destination. Since the space link propagation delay $\tau_{i,k}^{p} = 1.4s$ sent to the

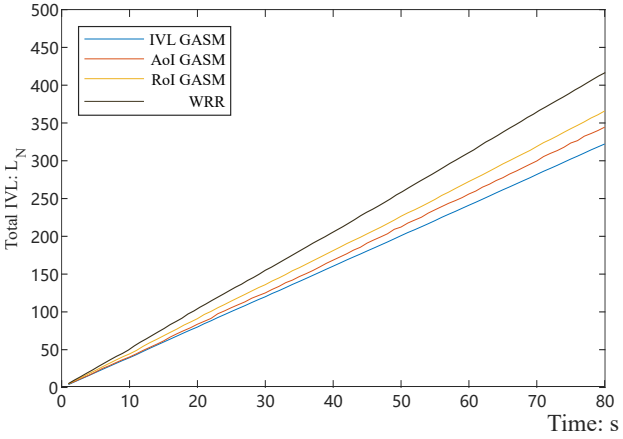

Figure 8　Performance of different algorithms.

Earth's control end is basically a fixed value, the relay satellite scheduler can perform scheduling based on calculating the information value transmission loss of the packets arriving at the Earth's end. As Figure 7 shows the simulation results under different scheduling methods. Here Figure 7 (a)∼(e) show the result of AoI value in different loss rates α. AoI (via the blue curve) becomes larger when the loss rate of Temetry1 becomes larger. For example, when the loss rate α of the other three measurement and control processes are $0.8, 1.2$ and 1.6 respectively, the α of the measurement and control process represented by the blue curve increases from 0.2 to 1.6. As loss rate α increase, the scheduling process will ignore the

timeliness of data, which will lead to an increase in the AoI of the data. Figure 7 (f) shows the performance improvements of IVL based GASM in the multi-measurement and control processes. Under the IVL-based GASM algorithm, with the passage of time, the total value loss L_N of all measurement and control processes grows the smallest, indicating that the performance improvement of the entire stage is the greatest. Compared with the algorithms based on AoI or RoI, the performance improvement is about 10%. Figure 7 (g)∼(i) further shows the variation of different indicators under IVL-based GASM. The parameters of the four telemetry processes are shown in the figure, with Telemetry 1 having a maximum sampling delay of $T_{max} = 15$ and a minimum loss rate $\alpha = 0.2$. A larger sampling delay indicates that the data is less time-sensitive and therefore produces a larger IVL for all telemetry processes, while a smaller $\alpha = 0.2$ results in a smaller AoI but a larger RoI for the data. The performance comparison between the GASM algorithm and the Weighted Round Robin (WRR) scheduling algorihm is added in Figure 8. The WRR algorithm does not take into account the AoI or RoI of the data, and is a deterministic scheduling mechanism based on the pre-set scheduling weights, so the value loss of the measurement and control processes under the GASM algorithm are all less than the WRR algorithm.

VI CONCLUSION

In the multi-mission measurement and control data transmission in cislunar communication, this paper proposes the IVL index of information value transmission loss and derives the closed expression of cumulative transmission loss CIVL during Earth-Moon relay communication. Based on it, we construct an optimization model for multi-measurement and control data communication, and propose a GASA scheduling algorithm. The final simulation results show that the newly proposed timeliness indexes satisfy the requirements of multi-task measurement and control. Compared with the general AoI and other timeliness indexes, is able to effectively reduce the value loss of the information transmission, and realize optimal scheduling of multiple measurement and control processes.

References

[1] T. Soleymani, J. S. Baras, and K. H. Johansson, 'Stochastic control with stale information Part I: Fully observable systems', in 2019 IEEE 58th conference on decision and control (CDC), Dec. 2019, pp. 4178–4182. doi: 10.1109/CDC40024.2019.9029447.

[2] E. Nuno, R. Ortega, N. Barabanov, and L. Basanez, 'A Globally Stable PD Controller for Bilateral Teleoperators', IEEE Trans. Robot., vol. 24, no. 3, pp. 753–758, Jun. 2008, doi: 10.1109/TRO.2008.921565.

[3] D. Lee and M. W. Spong, 'Passive Bilateral Teleoperation With Constant Time Delay', IEEE Trans. Robot., vol. 22, no. 2, pp. 269–281, Apr. 2006, doi: 10.1109/TRO.2005.862037.

[4] C.-C. Hua and X. P. Liu, 'Delay-Dependent Stability Criteria of Teleoperation Systems With Asymmetric Time-Varying Delays', IEEE Trans. Robot., vol. 26, no. 5, pp. 925–932, Oct. 2010, doi: 10.1109/TRO.2010.2053736.

[5] J. Nilson, "Real-time control systems with delays," Ph.D. dissertation, Dept. Autom. Control, Lund Inst. Technol., Lund, Sweden, 1998.

[6] O. Ayan, S. Hirche, A. Ephremides, and W. Kellerer, 'Optimal Finite Horizon Scheduling of Wireless Networked Control Systems', IEEE/ACM Trans. Networking, pp. 1–16, 2024, doi: 10.1109/TNET.2023.3300949.

[7] S. Kaul, M. Gruteser, V. Rai, and J. Kenney, "Minimizing age of information in vehicular networks," in Proc. 8th Annu. IEEE Commun. Soc. Conf. Sensor, Mesh Ad Hoc Commun. Netw., Jun. 2011, pp. 350–358.

[8] Q. He, D. Yuan, and A. Ephremides, 'On optimal link scheduling with min-max peak age of information in wireless systems', in 2016 IEEE international conference on communications (ICC), 2016, pp. 1–7. doi: 10.1109/ICC.2016.7511331.

[9] B. Buyukates, A. Soysal, and S. Ulukus, "Age of information in multihop multicast networks," J. Commun. Netw., vol. 21, no. 3, pp. 256–267, Jun. 2019.

[10] Z. Li, L. Xiang, and X. Ge, 'Age of information modeling and optimization for fast information dissemination in vehicular social networks', IEEE Transactions on Vehicular Technology, vol. 71, no. 5, pp. 5445–5459, May 2022, doi: 10.1109/TVT.2022.3154766.

[11] X. Zheng, S. Zhou, and Z. Niu, "Urgency of information for contextaware timely status updates in remote control systems," IEEE Trans. Wireless Commun., vol. 19, no. 11, pp. 7237–7250, Nov. 2020.

[12] Y. Sun, E. Uysal-Biyikoglu, R. D. Yates, C. E. Koksal, and N. B. Shroff, "Update or wait: How to keep your data fresh," IEEE Trans. Inf. Theory, vol. 63, no. 11, pp. 7492–7508, Nov. 2017.

[13] O. Ayan, M. Vilgelm, M. Klügel, S. Hirche, and W. Kellerer, ’Age-of-Information vs. Value-of-Information Scheduling for Cellular Networked Control Systems’, Mar. 13, 2019, arXiv: arXiv:1903.05356. Accessed: Jul. 18, 2024. [Online]. Available: http://arxiv.org/abs/1903.05356

[14] O. Ayan, S. Hirche, A. Ephremides, and W. Kellerer, ‘Optimal Finite Horizon Scheduling of Wireless Networked Control Systems’, IEEE/ACM Trans. Networking, pp. 1–16, 2024, doi: 10.1109/TNET.2023.3300949.

[15] S. Wang, Q. Liu, P. U. Abara, J. S. Baras, and S. Hirche, ‘Value of information in networked control systems subject to delay’, Dec. 29, 2021, arXiv: arXiv:2104.03355. Accessed: Jul. 18, 2024. [Online]. Available: http://arxiv.org/abs/2104.03355

[16] X. Lu et al., ‘Full-loop AoI-based joint design of control and deterministic transmission for industrial CPS’, IEEE Transactions on Industrial Informatics, vol. 19, no. 11, pp. 10727–10738, Nov. 2023, doi: 10.1109/TII.2023.3241590.

[17] B. Han, M.-X. Sun, L.-K. Muk, Y.-F. Li, and H. D. Schotten, ‘Flexible and dependable manufacturing beyond xURLLC: A novel framework for communication-control co-design’, in 2022 IEEE 22nd International Conference on Software Quality, Reliability, and Security Companion (QRS-C), Guangzhou, China: IEEE, Dec. 2022, pp. 562–568. doi: 10.1109/QRS-C57518.2022.00090.

[18] Mo-Yuen Chow and Yodyium Tipsuwan, ‘Network-based control systems: a tutorial’, in IECON’01. 27th Annual Conference of the IEEE Industrial Electronics Society (Cat. No.37243), Denver, CO, USA: IEEE, 2001, pp. 1593–1602. doi: 10.1109/IECON.2001.975529.

Zhouyong Hu received the B.Eng. degree from Harbin Institute of Technology (Shenzhen) of Communication Engineering in 2021. where he is currently working toward the Ph.D. degree of Information Telecommunications. His current research inter-ests include satellite communication Networks theory and technology.

Afang Yuan received the M.S. degree in communication engineering from the Harbin Institute of Technology, Shenzhen, China, in 2022, where she is currently working toward the Ph.D. degree. Her current interests include DTN, Earth-Moon Relay Communication, scheduling strategy and space information networks.

Qinyu Zhang received the bachelor’s degree in communication engineering from the Harbin Institute of Technology (HIT),Harbin, China, in 1994 and the Ph.D. degree in biomedical and electrical engineering from the University of Tokushima, Tokushima, Japan, in 2003. From 1999 to 2003, he was an Assistant Professor with the University of Tokushima. From 2003 to 2005, he was an Associate Professor with the Shenzhen Graduate School, HIT, and was the Founding Director of the Communication Engineering Research Center, School of Electronic and Information Engineering (EIE). Since 2005, he has been a Full Professor and the Dean of EIE School, HIT. He is also a Professor with Peng Cheng Laboratory, Shenzhen, China. His research interests include aerospace communications and networks, wireless communications and networks, cognitive radios, signal processing, and biomedical engineering. Dr. Zhang has been a TPC Member for the Infocom, IEEE ICC, IEEE Globecom,IEEE Wireless Communications and Networking Conference, and other flagship conferences in communications. He was the Associate Chair for Finance of the International Conference on Materials and Manufacturing Technologies 2012,the TPC Co-chair of the IEEE/CIC ICCC 2015, and the Symposium Co-chair of the CHINACOM 2011, and the IEEE Vehicular Technology Conference 2016(Spring). He was the Founding Chair of the IEEE Communications Society Shenzhen Chapter. He is on the Editorial Board of some academic journals, such as Journal of Communication, KSII Transactions on Internet and Information Systems, and Science China Information Sciences.

Zhihua Yang [corresponding author] received the Ph.D. degree in communication engineering from the Harbin Institute of Technology (HIT), Harbin, China, in 2010. He is currently a Professor with the Department of Electrical and Information Engineering, Shenzhen Graduate School, HIT. His current interests include deep space communications and networking, DTN, and wireless communications.

卫星物联网通信下基于双相关算子的极简同步方案

余忠洋[1,2]，闫玉倩[2,1]，朱海[1]，许蒙蒙[1]，王园园[1]，徐恒舟[1]
（1. 河南工程学院计算机学院，河南郑州 451191；2. 河南工业大学信息科学与工程学院，河南郑州 450001）

摘要：在卫星物联网通信中，导频资源和存储资源均受到了一定的限制，使得传统同步方案及其硬件实现面临着很大的挑战。为此，本文提出了一种基于双相关算子的极简同步方案，包括频相解耦合估计和分块相关数据补偿两部分。其中，频相解耦合估计部分提供了一个对莱斯衰落鲁棒的自相关频偏估计器和一个抗频偏能力强的低复杂度相偏估计器；分块相关数据补偿部分只需要使用基于互相关算子的少量数据补偿值便可以显著降低残留频偏的影响。仿真结果表明，在有限的导频开销下，所提的极简同步方案能够实现频偏对相偏的解耦合，同时获得比传统同步方案更少的存储空间占用和接近的误码性能，有利于工程实现。

关键词：导频资源；存储资源；双相关算子；分块补偿；卫星物联网通信
中图分类号：TN911.23
文献标志码：A

A minimal synchronization scheme based on double correlation operators for satellite IoT communications

Zhongyang Yu[1,2], Yuqian Yan[2,1], Hai Zhu[1], Mengmeng Xu[1], Yuanyuan Wang[1], Hengzhou Xu[1]

(1. School of Computer Science, Henan University of Engineering, Zhengzhou 451191, China; 2. College of Information Science and Engineering, Henan University of Technology, Zhengzhou 450001, China)

Abstract: In satellite Internet of Things (IoT) communications, both pilot and storage resources are limited such that conventional synchronization scheme and its hardware implementation have faced great challenges. To this end, this paper proposes a minimal synchronization scheme based on double correlation operators, including an auto-correlation based frequency-phase decoupled estimation and a cross-correlation based crorelation blockwise data compensation. In specific, the former provides an auto-correlation frequency offset estimator robust to the Rice fading and a low-complexity phase offset estimator with a strong ability of anti-frequency offset; the latter uses a small amount of cross-correlation based data compensation values to greatly lower the impact of residual frequency offset. Simulation results show that with the limited pilot overhead the proposed minimal synchronization scheme can implement the frequency-to-phase decoupling, and achieve less storage space occupation and near error performance compared with the conventional synchronization scheme.

Keywords pilot resource; storage resource; double correlation operators; blockwise compensation; satellite IoT communications

卫星物联网通信逐渐应用到地质监测、应急通信、海上通信等通信领域[1-3]。然而，有限的导频资源和存储资源将会给传统同步方案及其硬件实现带来很大的挑战。因此，如何在资源受限条件下设计一种极简同步方案来支持可靠的卫星物联网通信具有非常高的研究价值。

对于使用低成本振荡器的卫星物联网通信系统，相应的收发端会遭受到较大载波频偏和相偏的影响，从而导致传统同步方案在少量导频辅助下对应的频偏估计会严重影响相偏估计且后续的数据补偿会占用较大的存储空间。文献[4]针对短突发成形偏移正交相移键控（SOQPSK）传输系统提出了一种导频辅助的载波同步方案。考虑 LoRa 协议中的前导结构，文献[5]给出了一种联合时延、载波频偏和相偏的同步方案。针对宽带线性调频雷达系统，Yuan 等人以包络互相关的频率峰值作为输入设计了一种有效的联合频偏和相偏估计[6]。考虑低轨卫星正交时频空调制（OTFS）系统，Li 等人利用导频辅助完成了对载波频相偏的准确估计[7]。此外，针对低轨卫星通信系统中存在的大多普勒频移和相偏问题，文献[8]设计了一种导频辅助的载波同步方案。然而，这些传统同步方案都采用了所谓的频相耦合估计，即频偏估计器在

基金项目：国家自然科学基金（62201198，62172457），河南省科技攻关（242102210200，242102220030），河南省高校重点科研项目（24A510003，24A520010）

相偏估计器之前执行，则相偏估计器的性能依赖于频偏估计器精度，这就是频偏对相偏的耦合作用。为了减弱该耦合作用，传统同步方案往往需要使用较大的导频开销，但这不利于卫星物联网通信。在文献[9]中，Rice 指出在频相耦合估计中，只要初始采样时刻设置在前导结构中间位置时，频偏估计的克拉美罗界（CRB）会与相偏估计的 CRB 解耦合。但由于接收端不知道初始采样时刻位置，故无法人为设置该初始位置。另一方面，在频相耦合估计之后，传统同步方案大多会采用连续时刻数据补偿，即对接收数据进行逐时刻的频相偏补偿[4-8], [10-12]。这种数据补偿方式可以获得良好的解调性能，但缺点是需要占用较大的存储空间（与传输的数据长度成正比），这势必会加剧卫星物联网通信系统的硬件实现难度。

鉴于传统同步方案中频相耦合估计和连续时刻数据补偿的缺点，设计了一种基于双相关算子的极简同步方案。该方案包含频相解耦合估计和分块相关数据补偿两部分：第一部分包括对衰落不敏感的自相关频偏估计和低复杂度且抗大频偏的最大似然相偏估计；第二部分可显著降低存储空间占用并大大降低每个数据块中由残留频偏带来的最大累积相位。通过仿真验证了所提极简同步方案的有效性。

1 系统模型

对于窄带低速率卫星物联网上行通信，考虑莱斯平坦衰落信道下的单载波通信系统。则基于波特采样的接收信号可以表示为：

$$r(k)=h\cdot s(k)e^{\mathrm{j}(2\pi f_d T_s k+\theta)}+n(k),\ k\in\kappa_{\mathrm{p}}\bigcup\kappa_{\mathrm{d}} \tag{1}$$

式中，h 表示信道增益，其幅度服从由莱斯因子 K 决定的莱斯分布，f_d 和 θ 分别表示载波频偏和相偏，$s(k)$ 表示能量归一化的调制信号，$n(k)$ 表示均值为 0、方差为 σ_n^2 的复高斯随机变量，$\kappa_{\mathrm{p}}=\{\kappa_{\mathrm{p}_i},1\le i\le m\}$ 为图 1 所示的数据帧结构[13]中所有导频采样索引集合，$\kappa_{\mathrm{d}}=\{\kappa_{\mathrm{d}_j},1\le j\le m-1\}$ 为所有数据采样索引集合（其中 m 为导频块个数，$m-1$ 为数据块个数），且 κ_{p_i} 和 κ_{d_j} 的具体形式分别由式(2)和式(3)给出：

$$\kappa_{\mathrm{p}_i}=\left\{k:0\le k\le L_{\mathrm{p}_1}-1,i=1\right\}\bigcup\left\{k:\sum_{l=1}^{i-1}\left(L_{\mathrm{p}_l}+L_{\mathrm{d}_l}\right)\le k\le\sum_{l=1}^{i-1}\left(L_{\mathrm{p}_l}+L_{\mathrm{d}_l}\right)+L_{\mathrm{p}_i}-1,i>1\right\} \tag{2}$$

$$\kappa_{\mathrm{d}_j}=\left\{k:L_{\mathrm{p}_1}\le k\le L_{\mathrm{p}_1}+L_{\mathrm{d}_1}-1,j=1\right\}\bigcup\left\{k:\sum_{l=1}^{j-1}\left(L_{\mathrm{p}_l}+L_{\mathrm{d}_l}\right)+L_{\mathrm{p}_j}\le k\le\sum_{l=1}^{j}\left(L_{\mathrm{p}_l}+L_{\mathrm{d}_l}\right)-1,j>1\right\} \tag{3}$$

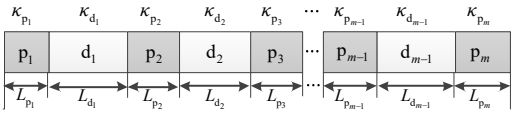

图 1 数据帧结构

2 基于双相关算子的极简同步方案

图 2 展示了基于双相关算子的极简同步方案的实现流程，包括去调制操作、一般化相关操作以及由此产生的频相解耦合估计和分块相关数据补偿。首先介绍去调制操作与一般化相关操作的基本原理。

2.1 去调制操作与一般化相关操作

所谓的去调制操作就是利用已知导频调制信号的共轭形式与接收导频信号相乘，从而消除其调制信息，进而获得去调制信号 $v(k)$。

$$\begin{aligned}v(k)&=r(k)\cdot\left[s(k)\right]^*\\&=h\cdot e^{\mathrm{j}(2\pi f_d T_s k+\theta)}+n'(k),\ k\in\kappa_{\mathrm{p}}\end{aligned} \tag{4}$$

式中，$n'(k)=n(k)s(k)^*$ 仍是高斯噪声，这是因为 $s(k)$ 是一个确知的导频信号。显然，去调制信号 $v(k)$ 的可靠性不仅受到噪声项 $n'(k)$ 的影响，还取决于信道增益 h。进一步地，当 k 遍历 κ_{p} 时，便可以获得一个去调制序列集合 $\mathbf{v}=\{\mathbf{v}_i,i=1,2,\ldots,m\}$，其中，$\mathbf{v}_i=\{v(k),k\in\kappa_{\mathrm{p}_i}\}$ 表示对应于第 i 个导频块 p_i 的去调制序列。

所谓的一般化相关操作就是自相关操作和互相关操作的统称。它可以利用这两种相关操作估计出附加了任意相偏的载波频偏。前提是使用一个相关值集合 $\mathbf{R}(\boldsymbol{\beta}\,|\,\tilde{\mathbf{v}})=\{R(\beta_{1i}\,|\,\mathbf{v}_{1i}),i=1,2,\ldots,m\}$，其中 $\boldsymbol{\beta}=\{\beta_{1i},i=1,2,\ldots,m\}$ 表示第 1 个导频块和第 i 个导频块之间的自/互相关延迟长度 β_{1i} 的集合，$\tilde{\mathbf{v}}=\{\mathbf{v}_{1i},i=1,2,\ldots,m\}$ 表示第 1 个去调制序列和第 i 个去调制序列的并集 $\mathbf{v}_{1i}$ 的集合，即 $\mathbf{v}_{1i}=\mathbf{v}_1\bigcup\mathbf{v}_i$。特别地，当 $i=1$ 时，$\mathbf{v}_{11}$ 简记为 $\mathbf{v}_1$，那么基于式(4)，可以定义一个相关算子 $R(\beta_{11}\,|\,\mathbf{v}_1)$，且具有如下表示形式：

$$\begin{aligned}R(\beta_{11}\,|\,\mathbf{v}_1)&=\frac{\sum_{k=0}^{L_{\mathrm{p}_1}-\beta_{11}-1}\left[v(k)^*\cdot v(k+\beta_{11})\right]}{L_{\mathrm{p}_1}-\beta_{11}}\\&=\psi\cdot e^{\mathrm{j}2\pi f_d T_s\beta_{11}}+\xi(\beta_{11})\end{aligned} \tag{5}$$

由于上式仅使用了第一个导频块 p_1，所以该相关算子称作自相关算子[14-16]。在式(5)中，$\beta_{11}\in(0,L_{\mathrm{p}_1}-1]$ 表示自相关延迟长度，

$\psi = \mathbb{E}\{|h|^2\}$ 表示接收导频信号的等效平均能量，$\xi(\beta_{11})$ 为噪声项且由式(6)给出。

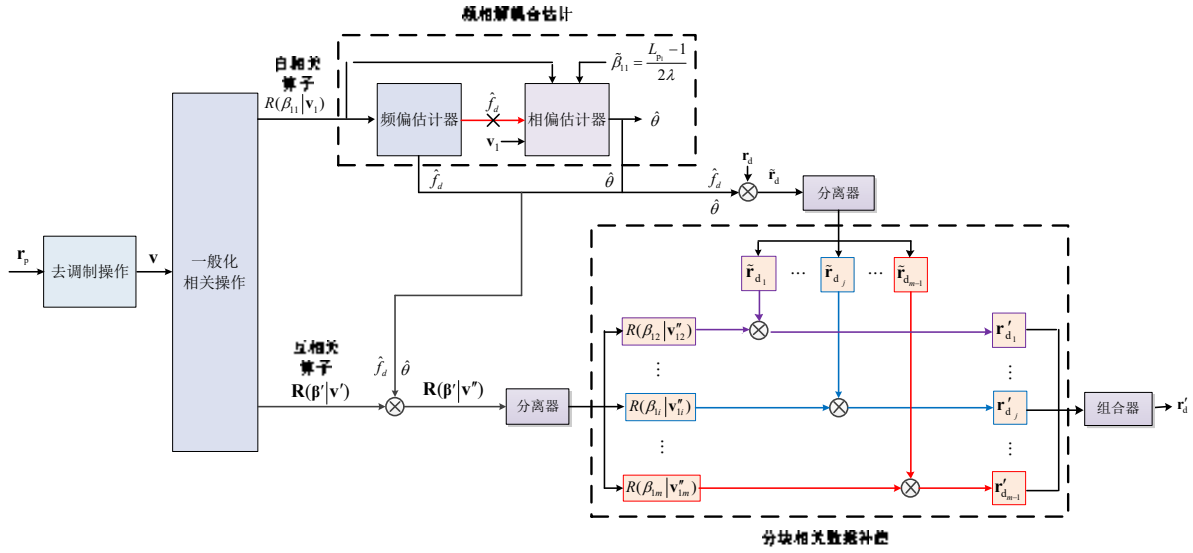

图 2 基于双相关算子的极简同步方案的实现流程框图（其中 ⊗ 表示共轭相乘）

$$\xi(\beta_{11})=\frac{1}{L_{p_1}-\beta_{11}}\sum_{k=0}^{L_{p_1}-\beta_{11}-1}\left[he^{j[2\pi f_d T_s(k+\beta_{11})+\theta]}n'(k)^*+he^{-j(2\pi f_d T_s k+\theta)}n'(k+\beta_{11})+n'(k+\beta_{11})n'(k)^*\right] \tag{6}$$

另一方面，当 $i>1$ 时，同样基于式(4)，还可以定义另一个相关算子 $\mathbf{R}(\boldsymbol{\beta}'|\mathbf{v}')$ 且 $\boldsymbol{\beta}'=\{\beta_{1i}, i=2,\ldots,m\}$，$\mathbf{v}'=\{\mathbf{v}_{1i}, i=2,\ldots,m\}$，如下式所示：

$$\begin{aligned}R(\boldsymbol{\beta}'|\mathbf{v}')&=\frac{1}{L_{p_1}}\sum_{k=0}^{L_{p_1}-1}\left[v(k)^*\cdot v(k+\beta_{1i})\right]\\&=\psi\cdot e^{j2\pi f_d T_s\beta_{1i}}+\xi(\beta_{1i}),\ i=2,\ldots,m\end{aligned} \tag{7}$$

由于该相关算子利用了多个不相交的导频块 $p_1\sim p_m$，故称为互相关算子[16-18]。式(7)中，$\beta_{1i}=\sum_{l=1}^{i-1}(L_{p_l}+L_{d_l})$ 表示互相关延迟长度，$\xi(\beta_{1i})$ 是噪声项，且具有类似于式(6)的表达形式：

$$\xi(\beta_{1i})=\frac{1}{L_{p_1}}\sum_{k=0}^{L_{p_1}-1}\left[he^{j[2\pi f_d T_s(k+\beta_{1i})+\theta]}n'(k)^*+he^{-j(2\pi f_d T_s k+\theta)}n'(k+\beta_{1i})+n'(k+\beta_{1i})n'(k)^*\right] \tag{8}$$

接下来，根据图 2，基于双相关算子即式(5)和式(7)，我们将详细阐述极简同步方案中频相解耦合估计和分块相关数据补偿两部分的具体实现步骤。

2.2 极简同步方案之频相解耦合估计

借助式(5)的自相关算子，设计一种频相解耦合估计模块，包括一个自相关频偏估计器和一个基于特定自相关值的最大似然相偏估计器。下面先给出该模块的实现步骤。

步骤 I：基于自相关算子 $R(\beta_{11}|\mathbf{v}_1)$，可以得到一个自相关频偏估计器，其频偏估计值为 $\hat{f}_d$，即

$$\begin{aligned}\hat{f}_d&=\frac{1}{2\pi T_s\beta_{11}}\arg\left\{R(\beta_{11}|\mathbf{v}_1)\right\}\\&=\frac{1}{2\pi T_s\beta_{11}}\arg\left\{\frac{\sum_{k=0}^{L_{p_1}-\beta_{11}-1}\left[v(k)^*\cdot v(k+\beta_{11})\right]}{L_{p_1}-\beta_{11}}\right\}\\&=\frac{1}{2\pi T_s\beta_{11}}\arg\left\{\psi\cdot e^{j2\pi f_d T_s\beta_{11}}+\xi(\beta_{11})\right\}\end{aligned} \tag{9}$$

其估计范围为 $[-0.5,\ 0.5]/(\beta_{11}T_s)$，$\xi(\beta_{11})$ 亦为噪声项，其形式见式(6)。特别地，当 $\beta_{11}=1$ 时，该自相关频偏估计器可以估计出接近于符号速率 $1/T_s$ 一半的频偏。由上式可知，在平坦衰落信道下，自相关频偏估计器的估计精度仅受到噪声项 $\xi(\beta_{11})$ 的影响。

步骤 II：考虑一个特定的自相关值 $R(\tilde{\beta}_{11}|\mathbf{v}_1)$（其中 $\tilde{\beta}_{11}=(L_{p_1}-1)/(2\lambda)$，$\lambda$ 称作解耦合系数），将其共轭形式带入到最大似然相偏估计器中，可以得到无频偏补偿下的相偏估计值 $\hat{\theta}$：

$$\hat{\theta}=\arg\left\{\underbrace{\left(\sum_{k=0}^{L_{\mathrm{p}_1}/\lambda-1}v(k)\right)\cdot R\left(\frac{L_{\mathrm{p}_1}-1}{2\lambda}\,|\,\mathbf{v}_1\right)^*}_{1\text{次复乘}}\right\} \tag{10}$$

$$=\arg\left\{\psi h\cdot e^{\mathrm{j}\left[\theta+\pi f_dT_s\left(\frac{1}{\lambda}-1\right)\right]}\frac{\sin\left(\pi f_dT_s\dfrac{L_{\mathrm{p}_1}}{\lambda}\right)}{\sin\left(\pi f_dT_s\right)}+\xi\right\}$$

$$\approx\theta+\pi f_dT_s\left(\frac{1}{\lambda}-1\right),\ |f_d|\le\frac{\lambda}{L_{\mathrm{p}_1}T_s} \tag{11}$$

需要说明的是，当莱斯因子 K 和信噪比 $\mathrm{SNR}\triangleq\psi/(2\sigma_n^2)$ 适中时，有 $\mathrm{Im}\{h\}\approx0$ 和 $\mathrm{Im}\{\xi\}\approx0$，且考虑 $|f_d|\le\lambda/(L_{\mathrm{p}_1}T_s)$，那么式(11)成立，否则，需要引入信道均衡来消除信道增益 h 的影响。在上式中，ξ 为噪声项，且具有如下形式：

$$\xi=\sum_{k=0}^{L_{\mathrm{p}_1}/\lambda-1}\left[he^{\mathrm{j}(2\pi f_dT_sk+\theta)}\xi\left(\frac{L_{\mathrm{p}_1}-1}{2\lambda}\right)^*+n'(k)\xi\left(\frac{L_{\mathrm{p}_1}-1}{2\lambda}\right)^*\right. \tag{12}$$
$$\left.+\psi e^{-\mathrm{j}\pi f_dT_sk\left(L_{\mathrm{p}_1}-1\right)/\lambda}n'(k)\right]$$

同时讨论以下两种情况：

1） 当 $\lambda=1$ 时，在较大频偏范围 $|f_d|<1/(L_{\mathrm{p}_1}T_s)$ 内，均有 $\hat{\theta}\approx\theta$ 且满足 $|\theta|<\pi$；

2） 当 $\lambda>1$ 时，在更大频偏范围 $|f_d|<\lambda/(L_{\mathrm{p}_1}T_s)$ 内，有 $\hat{\theta}\approx\theta+\pi f_dT_s(1/\lambda-1)$ 且满足 $|\theta|<\pi-\pi(\lambda-1)/L_{\mathrm{p}_1}$。

相较于第 1 中情况，第 2 种情况下的最大似然相偏估计器会牺牲一些估计范围但获得了成倍增加的抗频偏范围。实际上，第 2 中情况下真正的相偏估计值可以由下式给出：

$$\hat{\theta}'\approx\hat{\theta}-\pi\hat{f}_dT_s\left(\frac{1}{\lambda}-1\right) \tag{13}$$

式中，$\hat{f}_d$ 和 $\hat{\theta}$ 分别可以从式(9)和式(11)中得到。

另一方面，对于式(11)，如果频偏超过了约定范围即 $|f_d|>\lambda/(L_{\mathrm{p}_1}T_s)$，可以通过选择自相关延迟长度满足 $\beta_{11}\ll L_{\mathrm{p}_1}/(2\lambda)$ 的频偏估计器来保证所设计的频相解耦合估计的可靠性。

为了比较起见，再介绍下传统同步方案中频相耦合估计的实现流程，如图 3 所示。

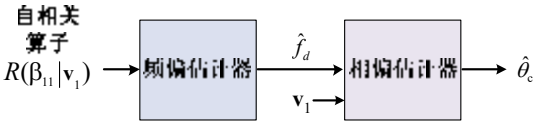

图 3 传统同步方案之频相耦合估计的实现流程框图

同样，其频偏估计器也是基于式(9)给出的自相关算子的。不同于上文的频相解耦合估计，该估计需要先将得到的频偏估计值按照第 1 个导频采样索引集合 $\kappa_{\mathrm{p}_1}=\{k:0\le k\le L_{\mathrm{p}_1}/\lambda-1\}$ 依次补偿到对应的去调制信号中，然后再进行最大似然相偏估计，即

$$\hat{\theta}_{\mathrm{c}}=\arg\left\{\underbrace{\sum_{k=0}^{L_{\mathrm{p}_1}/\lambda-1}\left[v(k)\cdot e^{-\mathrm{j}2\pi\hat{f}_dT_sk}\right]}_{L_{\mathrm{p}_1}/\lambda\text{ 次复乘}}\right\} \tag{14}$$

$$=\arg\left\{h\cdot e^{\mathrm{j}\left[\theta+\pi\Delta f_dT_s\left(\frac{L_{\mathrm{p}_1}}{\lambda}-1\right)\right]}\frac{\sin\left(\pi\Delta f_dT_s\dfrac{L_{\mathrm{p}_1}}{\lambda}\right)}{\sin\left(\pi\Delta f_dT_s\right)}+\xi_{\mathrm{c}}\right\}$$

$$\approx\theta,\ |\Delta f_d|\approx0 \tag{15}$$

式中，$\Delta f_d\triangleq f_d-\hat{f}_d$ 为估计补偿后的剩余频偏，$\xi_{\mathrm{c}}\triangleq\sum_{k=0}^{L_{\mathrm{p}1}/\lambda-1}n'(k)e^{-\mathrm{j}2\pi f_dT_sk}$ 为噪声项。上式的成立条件类似于式(11)的成立条件。但区别在于该最大似然相偏估计要求剩余频偏 Δf_d 接近于 0，也就是说，传统同步方案中（最大似然）相偏估计器的性能很大程度上依赖于自相关频偏估计器的估计精度。

另外，除了解耦合特性外，观察式(10)和式(14)可以发现，对应于极简同步方案中的最大似然相偏估计器仅需要 1 次复乘运算，而对应于传统同步方案中的最大似然相偏估计器则需要 L_{p_1}/λ 次复乘运算。这是所提同步方案的“极简”体现之一。

2.3 极简同步方案之分块相关数据补偿

根据图 2，需要先将在频相解耦合估计中得到的估计值 $\hat{f}_d$ 和 $\hat{\theta}$ 考虑到分块相关数据补偿中。这么做有两个目的：一是用来补偿接收数据序列 $\mathbf{r}_{\mathrm{d}}$ 得到 $\tilde{\mathbf{r}}_{\mathrm{d}}$；二是用来校正式(7)中的互相关值序列 $\mathbf{R}(\boldsymbol{\beta}'|\mathbf{v}')$ 获得 $\mathbf{R}(\boldsymbol{\beta}'|\mathbf{v}'')$，其中，$\mathbf{v}''$ 为 $\mathbf{v}'$ 经频相偏估计值补偿后的结果。接着再利用 $\tilde{\mathbf{r}}_{\mathrm{d}}$ 和 $\mathbf{R}(\boldsymbol{\beta}'|\mathbf{v}'')$ 便可以实现分块相关数据补偿。对应的实现步骤如下：

步骤 I：补偿数据序列 $\tilde{\mathbf{r}}_{\mathrm{d}}$ 的分离：$\tilde{\mathbf{r}}_{\mathrm{d}}$ 分离成 $m-1$ 个数据块即 $\{\tilde{\mathbf{r}}_{\mathrm{d}_j}\}$（$j=1,2,\ldots,m-1$），其中，$\tilde{\mathbf{r}}_{\mathrm{d}_j}\triangleq\{r'(k),\ k\in\kappa_{\mathrm{d}_j}\}$ 且 $r'(k)$ 具有如下形式：

$$\begin{aligned} r'(k) &= r(k)\cdot e^{-\mathrm{j}\left(2\pi\hat{f}_d T_s k+\hat{\theta}\right)} \\ &= hs(k)\cdot e^{\mathrm{j}\left[2\pi\left(f_d-\hat{f}_d\right)T_s k+\left(\theta-\hat{\theta}\right)\right]}+n(k)e^{-\mathrm{j}\left(2\pi\hat{f}_d T_s k+\hat{\theta}\right)} \\ &= hs(k)\cdot e^{\mathrm{j}(2\pi\Delta f_d T_s k+\Delta\theta)}+n''(k) \end{aligned} \tag{16}$$

式中，$n''(k)=n(k)e^{-\mathrm{j}(2\pi\hat{f}_d T_s k+\hat{\theta})}$ 仍是一个高斯噪声，$\Delta\theta\triangleq\theta-\hat{\theta}$ 为剩余相偏。

步骤 II：补偿互相关值序列 $\mathbf{R}(\boldsymbol{\beta}'\,|\,\mathbf{v}'')$ 的分离： $\mathbf{R}(\boldsymbol{\beta}'\,|\,\mathbf{v}'')$ 分离成 $m-1$ 个互相关值即 $R(\beta_{1i}\,|\,\mathbf{v}''_{1i})$（$i=2,3,\ldots,m$），其中 $\mathbf{v}''_{1i}\triangleq\mathbf{v}''_1\cup\mathbf{v}''_i$，且 $R(\beta_{1i}\,|\,\mathbf{v}''_{1i})$ 可以表示为：

$$\begin{aligned} R\left(\beta_{1i}\left|\mathbf{v}''_{1i}\right.\right) &= \frac{1}{L_{\mathrm{p}_1}}\sum_{k=0}^{L_{\mathrm{p}_1}-1}\left[\left(v(k)\cdot e^{-\mathrm{j}\left(2\pi\hat{f}_d T_s k+\hat{\theta}\right)}\right)^*\cdot\right. \\ &\quad\left.\left(v\left(k+\beta_{1i}\right)\cdot e^{-\mathrm{j}\left[2\pi\hat{f}_d T_s\left(k+\beta_{1i}\right)+\hat{\theta}\right]}\right)\right] \\ &= \psi\cdot e^{\mathrm{j}2\pi\Delta f_d T_s\beta_{1i}}+\xi\left(\beta_{1i}\right) \end{aligned} \tag{17}$$

式中，$\xi(\beta_{1i})$ 也是噪声项，其形式类似于式(8)。

步骤 III：互相关值分块补偿到数据块中： $\mathbf{r}'_{\mathrm{d}_j}=\tilde{\mathbf{r}}_{\mathrm{d}_j}\cdot R(\beta_{1i}\,|\,\mathbf{v}''_{1i})^*=\{r'(k)\cdot R(\beta_{1i}\,|\,\mathbf{v}''_{1i})^*\triangleq\tilde{r}(k),\ k\in\kappa_{\mathrm{d}_j}\}$（$j=i-1\in\{1,2,\ldots,m-1\}$），且 $\tilde{r}(k)$ 可以由下式给出：

$$\begin{aligned} \tilde{r}(k) &= r'(k)\cdot R\left(\beta_{1i}\left|\mathbf{v}''_{1i}\right.\right)^* \\ &= \psi h\cdot s(k)e^{\mathrm{j}\left[2\pi\Delta f_d T_s\left(k-\sum_{l=1}^{j}\left(L_{\mathrm{p}_l}+L_{\mathrm{d}_l}\right)\right)+\Delta\theta\right]}+\xi' \\ &= \psi h\cdot s(k)e^{\mathrm{j}[2\pi\Delta f_d T_s k'+\Delta\theta]}+\xi' \end{aligned} \tag{18}$$

式中，$k'=k-\sum_{l=1}^{j}(L_{\mathrm{p}_l}+L_{\mathrm{d}_l})\in\{k':-L_{\mathrm{d}_j}\le k'\le -1\}$ 为新的数据采样时刻索引，$\xi'=n''(k)\psi e^{-\mathrm{j}2\pi\Delta f_d T_s\beta_{1i}}+n''(k)\xi(\beta_{1i})^*+hs(k)\xi(\beta_{1i})^*\cdot e^{\mathrm{j}(2\pi\Delta f_d T_s k+\Delta\theta)}$ 为一个叠加噪声项，因而会对所提的分块相关数据补偿有较大影响。需要通过以下两种方式来降低这个影响：方式一是在保持较小的导频块长度 L_{p_i} 下增加导频块个数 m；方式二是考虑较少的导频块个数 m 而增大每个导频块长度 L_{p_i}。

步骤 IV：二次校正数据信号 $\mathbf{r}'_{\mathrm{d}_j}$ 的组合： 将 $\{\mathbf{r}'_{\mathrm{d}_j}, j=1,2,\ldots,m-1\}$ 组合成完整的数据序列 $\mathbf{r}'_{\mathrm{d}}$。

结合式(3)对每个数据采样索引集合的定义，便可以从式(18)中发现，所提的分块（互）相关数据补偿能够显著降低每个数据块 $\tilde{\mathbf{r}}_{\mathrm{d}_j}$ 的最大累积相位（$j=1,2,\ldots,m-1$），其原因在于新数据采样时刻索引 k' 的范围已经由原来的 $[\sum_{l=1}^{j-1}(L_{\mathrm{p}_l}+L_{\mathrm{d}_l})+L_{\mathrm{p}_j},\sum_{l=1}^{j}(L_{\mathrm{p}_l}+L_{\mathrm{d}_l})-1]$ 减少到 $[-L_{\mathrm{d}_j},-1]$。

为了比较起见，再介绍下传统同步方案中连续时刻数据补偿的实现流程。在执行频相耦合估计之后，连续时刻数据补偿需要先对式(17)进行取幅角操作再利用 $m-1$ 个两两导频块求和取平均操作得到剩余频偏 Δf_d 的估计值 $\Delta\hat{f}_d$，即

$$\begin{aligned} \Delta\hat{f}_d &= \frac{\frac{1}{m-1}\sum_{i=2}^{m}\arg\left\{R\left(\beta_{1i}\left|\mathbf{v}''_{1i}\right.\right)\right\}}{2\pi T_s\beta_{1i}} \\ &= \frac{\frac{1}{m-1}\sum_{i=2}^{m}\arg\left\{\psi\cdot e^{\mathrm{j}2\pi\Delta f_d T_s\beta_{1i}}+\xi\left(\beta_{1i}\right)\right\}}{2\pi T_s\beta_{1i}} \end{aligned} \tag{19}$$

其估计范围为 $[-0.5,\ 0.5]/(\beta_{1m}T_s)$，显然取决于第一个导频块 p_1 和最后一个导频块 p_m 之间的互相关延迟长度 β_{1m}。

然后，再利用获得的估计值 $\Delta\hat{f}_d$ 按照连续时刻遍历整个数据采样索引集合 κ_{d} 方式补偿到式(16)中，即

$$\begin{aligned} \tilde{r}_{\mathrm{ct}}(k) &= r'(k)\cdot e^{-\mathrm{j}2\pi\Delta\hat{f}_d T_s k} \\ &= \left[hs(k)e^{\mathrm{j}(2\pi\Delta f_d T_s k+\Delta\theta)}+n''(k)\right]\cdot e^{-\mathrm{j}2\pi\Delta\hat{f}_d T_s k} \\ &= hs(k)e^{\mathrm{j}\left[2\pi\left(\Delta f_d-\Delta\hat{f}_d\right)T_s k+\Delta\theta\right]}+n'''(k),\ k\in\kappa_{\mathrm{d}} \end{aligned} \tag{20}$$

式中，$n'''(k)=n''(k)e^{-\mathrm{j}2\pi\Delta\hat{f}_d T_s k}$。与所提数据补偿相比，连续时刻数据补偿所需要的补偿值数量为 $L_{\mathrm{d}_1}+L_{\mathrm{d}_2}+\cdots+L_{\mathrm{d}_{m-1}}$（与传输数据符号个数有关），即补偿值 $\{e^{-\mathrm{j}2\pi\Delta\hat{f}_d T_s(L_{\mathrm{p}_1}+1)},e^{-\mathrm{j}2\pi\Delta\hat{f}_d T_s(L_{\mathrm{p}_1}+2)},\ldots,e^{-\mathrm{j}2\pi\Delta\hat{f}_d T_s[\sum_{l=1}^{m-1}(L_{\mathrm{p}_l}+L_{\mathrm{d}_l})-1]}\}$。显然，传输数据符号个数要远远大于数据块个数（$m-1$），因此所提的分块（互）相关数据补偿可以大大减少对补偿值的存储空间。此外，它仅需要 $m-1$ 个互相关值就可以完成整个接收数据序列的相位补偿。这是所提同步方案的另一个“极简”体现。

3 仿真分析

本节将要比较极简同步方案与传统同步方案中频相解耦合估计和频相耦合估计的估计性

能，以及分块相关数据补偿和连续时刻数据补偿的存储空间占用及误码性能。

仿真条件一：正交相移键控（QPSK）调制，符号周期 $T_s = 50\ \mu s$，第 1 个导频块长度 $L_{p_1} = 11$，信噪比 $\mathrm{SNR} = 0:5:25$ dB，莱斯因子 $K = 0,\ 5,\ 10$ dB。

仿真条件二：QPSK 调制，符号周期 $T_s = 50\ \mu s$，（执行频相解耦合估计或频相耦合估计之后的）剩余频偏 $\Delta f_d = 200$ Hz，莱斯因子 $K = 5$ dB，导频块个数 $m = 3$（则数据块个数 $m-1 = 2$），数据符号长度为 150，导频符号长度分别为 3、6、9。需要说明的是，当导频长度为 3 时，需要使用第 1 个导频块中的 1 个导频符号，且设置第 2 个和第 3 个导频块长度均为 1，类似地，当导频长度为 6 和 9 时，需要使用第 1 个导频块中的 2 个和 3 个导频符号，且设置第 2 个和第 3 个导频块长度均为 2 和 3。

3.1 频相解耦合估计和频相耦合估计的比较

考虑仿真条件一，根据式(11)、式(13)及讨论的两种情况可知，对于频相解耦合估计下的最大似然相偏估计器，当 $\lambda = 1$ 时，它可以在 $|f_d| \le 1800$ Hz 内捕获到 $[-\pi, \pi)$ 范围内的相偏；当 $\lambda > 1$ 时，以 $\lambda = 2$ 为例，它可以在 $|f_d| \le 3600$ Hz 内估计出 $[-10\pi/11,\ 10\pi/11)$ 范围内的相偏。

1）自相关频偏估计器的估计性能：假设频偏 $f_d = 1600$ Hz（在 $\lambda = 1$ 时频相解耦合估计对应的最大似然相偏估计器的抗频偏范围内）。图 4 给出了自相关频偏估计器的均方误差（mean square error, MSE）性能。

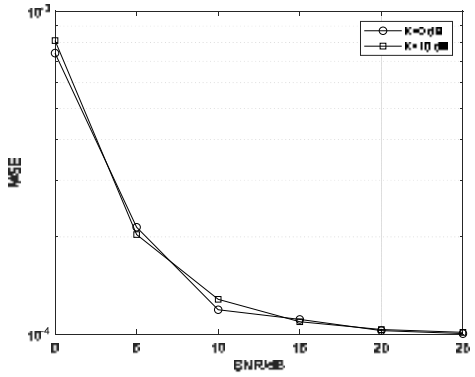

图 4 自相关频偏估计器的估计性能

由上图的仿真结果可知，对于 $K = 0$ dB 和 $K = 10$ dB，自相关频偏估计器均能够取得较好的 MSE 性能。其原因在于式(9)中的 ψ 是一个正实数，从而不会影响其取幅角操作。当 $\mathrm{SNR} \ge 25$ dB 时，自相关频偏估计器的 MSE 会小于 1×10^{-4}。从统计平均角度来看，剩余频偏 $\Delta f_d \le \sqrt{1\times10^{-4}}/T_s = 200$ Hz。这一数值就是仿真条件二中剩余频偏 $\Delta f_d = 200$ Hz 的来源。

2）最大似然相偏估计器的抗频偏性能：考虑 $\mathrm{SNR} = 20$ dB。图 5 展示了频相解耦合估计和频相耦合估计下最大似然相偏估计器的 MSE 性能。可见，只要频偏取值在约定的范围内即 $|f_d| < \lambda/(L_{p_1} T_s)$，不管解耦合系数 λ 和莱斯因子 K 如何，频相解耦合估计下的最大似然相偏估计器就可以获得比频相耦合估计下的最大似然相偏估计器更好的性能。这是因为在自相关算子中选择一个特定的延迟长度 $\tilde{\beta}_{11} = (L_{p_1} - 1)/(2\lambda)$ 不仅可以减少相偏估计的复乘运算次数，还可以降低较大频偏对相偏估计的影响。此外，由于莱斯因子 K 的增加会使信道增益 h 的虚部趋近于 0，因而对应的最大似然相偏估计器性能就越好，因此 $K = 10$ dB 的相偏估计性能要优于 $K = 5$ dB 的相偏估计性能。

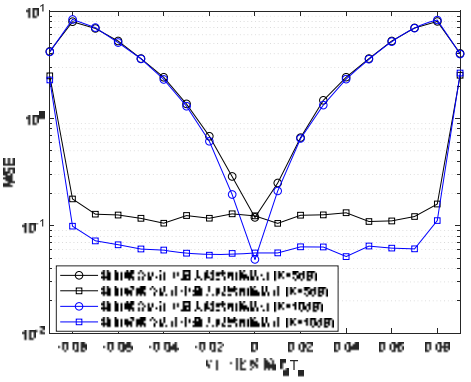

（a）$\lambda = 1$

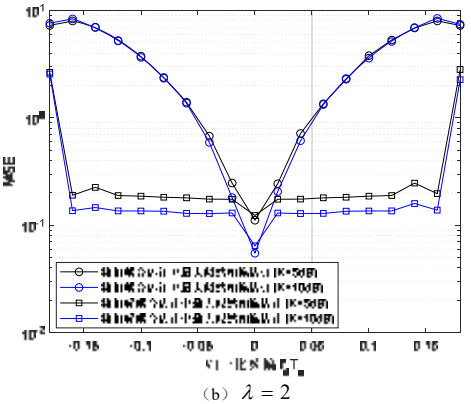

（b）$\lambda = 2$

图 5 最大似然相偏估计器的抗频偏能力

3.2 分块相关数据补偿和连续时刻数据补偿的比较

考虑仿真条件二，接下来从存储空间占用和误码性能两方面比较分块相关数据补偿和连续时刻数据补偿。

1）存储空间占用：从卫星物联网通信应用的角度来说，其硬件实现的存储资源是相当宝贵的。因此，评估这两种数据补偿的存储空间占用很有必要。基于上述的条件可知，连续时刻数据补偿的存储空间占用可视为传输的数据长度，即 150；而所提分块相关数据补偿的存储空间占用仅与使用的数据块个数有关，即 2。显然，在数据补偿的过程中，后者对补偿值的存储空间占用极少。

2）误码性能：图 6 给出了这两种数据补偿的误比特率（bit error rate，BER）性能。可以发现，当剩余频偏存在时，不作频偏补偿的 QPSK 系统无法正常工作；但采用了分块相关数据补偿和连续时刻数据补偿后，对应的系统性能均会有不同程度的改善，且导频块长度越大，相应的性能改善程度就越明显。这是因为导频块长度的增加会平滑分块相关数据补偿中式(18)中的噪声项 ξ' 和改善连续时刻数据补偿中式(19)中的估计值 $\Delta\hat{f}_d$。总体上，所提数据补偿的性能与连续时刻数据补偿的性能是相似的。不过在高信噪比区域（比如 SNR > 21 dB ）且使用很少导频（比如小于 6 个）时，所提数据补偿要比连续时刻数据补偿差 1 个多 dB。其原因是在高信噪比下后者的噪声方差会更小些。

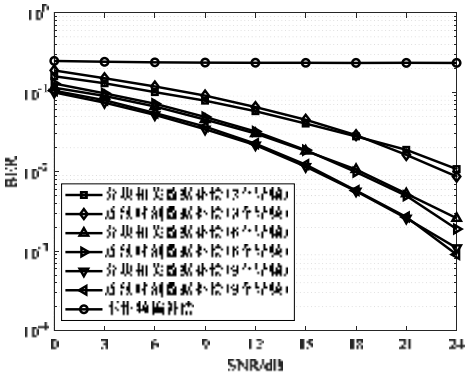

图 6 两种数据补偿的性能比较

4 结论

针对卫星物联网通信导频资源和存储资源双重受限下传统同步方案存在频相估计耦合及数据补偿占用存储空间大的问题，本文提出了一种基于双相关算子的极简同步方案。该方案包括频相解耦合估计和分块相关数据补偿两部分。具体地，对于频相解耦合估计部分，给出了一种对莱斯 K 因子不敏感的自相关频偏估计器和一种对抗频偏能力强的低复杂度最大似然相偏估计器；对于分块相关数据补偿部分，利用少量的等效数据补偿值便可以降低频相解耦合估计下残留频偏对数据解调的影响和连续时刻数据补偿过程中的存储空间占用，从而有助于工程实现。

参考文献：

[1] FRAIRE J, IOVA O, VALOIS F. Space-terrestrial integrated Internet of Things: Challenges and opportunities[J]. IEEE Communications Magazine, 2022, 60(12): 64-70.

[2] 王宏超, 屈杰. 基于 GEO 卫星的 IoT NTN 系统设计及实践[J]. 通信技术, 2023, 56(06): 786-791.

[3] 柴瀛. 海洋物联网中的卫星通信[J]. 物联网技术, 2022, 12(03): 28-30.

[4] HOSSEINI E, PERRINS E. Burst-mode synchronization for SOQPSK[J]. IEEE Transactions on Aerospace and Electronic Systems, 2019, 55(6): 2707-2718.

[5] TAPPARAL J, AFISIADIS O, MAYORAZ P, et al. An open-source LoRa physical layer prototype on GNU radio[C]// IEEE 21st International Workshop on Signal Processing Advances in Wireless Communications (SPAWC 2020), Atlanta, 2020.

[6] YUAN M, HE L, ZHANG Y, et al. Instantaneous velocity estimation based on envelope cross correlation and joint frequency-phase estimation for wideband LFM radar[J]. IEEE Sensors Journal, 2024, 24(9):14471-14481.

[7] LI S, ZHANG M, JU C, et al. Downlink carrier frequency offset estimation for OTFS-based LEO satellite communication system[J]. IEEE Communications Letters, 2024, 28(1): 163-167.

[8] 张嘉怡, 余忠洋, 朱敏, 等. 低轨卫星通信中 SCMA 系统载波同步算法设计[J]. 系统工程与电子技术, 2021, 43(5): 1354-1360.
ZHANG J, YU Z, ZHU M, et al. Design of carrier synchronization algorithm for SCMA system in LEO satellite communication[J]. Systems Engineering and Electronics, 2021, 43(5): 1354-1360.

[9] RICE F. Carrier-phase and frequency-estimation bounds for transmissions with embedded reference symbols[J]. IEEE Transactions on Communications, 2006, 54(2): 221-225.

[10] ZHANG X, LI H, LIU J, et al. Joint delay and Doppler estimation for passive sensing with direct-path interference[J]. IEEE Transactions on Signal Processing, 2016, 64(3): 630-640.

[11] YU Z, SUN J, BAI B, et al. A phase increment-based frequency

estimator for general PSAM in burst communications[C]// IEEE 83rd Vehicular Technology Conference (VTC 2016-Spring), Nanjing, 2016:1-5.

[12] DUNCAN J C M, MARRERO L M, QUEROL J, et al. A remote carrier synchronization technique for coherent distributed remote sensing systems[J]. IEEE Journal of Selected Topics in Applied Earth Observations and Remote Sensing, 2021, 14: 1909-1922.

[13] YAN Y, YU Z, XU M, et al. Efficient frame optimization scheme for PSAM assisted transmission over Rician fading channel[C]// 2024 4th International Conference on Information Communication and Software Engineering (ICICSE), Beijing, China, 2024: 147-152.

[14] ZHANG Q, YU Z Y, BAI B M. Carrier synchronizator in nonbinary LDPC coded modulation systems[C]// 12th EAI International Conference on Communications and Networking in China (Chinacom 2017), Xi’an, 2017.

[15] MEI R, WANG Z, HU W. Design and implementation of a low-complexity and reconfigurable carrier frequency synchronizer for satellite communications[J]. IEEE Communications Letters, 2022, 26(10): 2435-2439.

[16] MENGALI U, ANDREAL A N. Synchronization Techniques for Digital Receivers[M]. New York: Plenum Press, 1997.

[17] WANG S, TANG X, LEI J, et al. High-precision Doppler frequency estimation based positioning using OTFS modulations by red and blue frequency shift discriminator[J]. China Communications, 2024, 21(2): 17-31.

[18] ZHANG J, HE Q, YU Z, et al. Low-complexity coherent iterative receiver for SCMA-based LEO satellite communications[C]// IEEE Global Communications Conference (Globalcom 2019), Hawaii, 2019.

[作者简介]

余忠洋（1989—），男，博士，河南工程学院计算机学院科研办主任，讲师，主要研究方向：新一代移动通信技术、卫星通信技术、物联网通信技术等。

通信作者 E-mail：xd_yzy2013@sina.com

闫玉倩（2001—），女，在读硕士生，主要研究方向：物联网通信。

朱海（1978—），男，博士（后），教授，主要研究方向：新型网络计算与通信、人工智能优化算法。

许蒙蒙（1987—），男，博士，讲师，主要研究方向：物联网技术。

王园园（1991—），男，博士，讲师，主要研究方向：人工智能、工业视觉检测。

徐恒舟（1987—），男，博士，副教授，主要研究方向：信道编码与组合设计理论。

Performance Analysis of Satellite-Terrestrial Communication Networks Based on Stochastic Geometry Theory

QU Fangxin[1], LU Shuyuan[1], XU Guanjun[2*], CUI Junjun[2], SONG Zhaohui[2]

[1]School of Communication and Electronic Engineering, East China Normal University, Shanghai 200241, China
[2]Space Information Research Institute, and Zhejiang Key Laboratory of Space Information Sensing and Transmission, Hangzhou Dianzi University, Hangzhou 310018, China
*Corresponding author: gjxu@hdu.edu.cn

***Abstract*—The stability of satellite-terrestrial link communications is essential for ensuring high-quality satellite network performance. However, the complex environment of satellite-terrestrial links under high-speed satellite movement introduces new challenges to the reliability and anti-interference capabilities of communications between the mega satellite constellation and the terrestrial users. In this paper, we model low Earth orbit (LEO) satellite constellation and terrestrial users as a Poisson Point Process (PPP), incorporating two distinct channel states and establishing them as a two-state Markov process model. Combined with large-scale fading and small-scale fading of the communication link, we derive a closed-form expression for the outage probability of the satellite-terrestrial link. Additionally, we perform a numerical analysis of co-channel interference caused by adjacent satellites within this framework and assess the coverage performance of mega satellite constellations. Simulation results for the derived outage probability validate the accuracy of our proposed expression.**

***Keywords* — LEO satellite constellation, stochastic geometry, Markov model, co-channel interference, outage probability**

I. INTRODUCTION

With the rapid development of satellite communication technology, LEO satellites have become integral to global communications and earth observation due to their ability to provide low-latency and high-bandwidth data transmission. In recent years, countries have been deploying dense satellite networks in space, including G60, OneWeb, Starlink, and Kuiper. These satellite constellations expand internet coverage and specifically target users in remote and underdeveloped regions, effectively filling the gaps left by traditional terrestrial networks [1,2,3]. By expanding network connectivity, these constellations play a crucial role in enhancing global information exchange.

To achieve higher-quality satellite-terrestrial link communication, improvements must be made to the coverage and anti-jamming capabilities of the satellite constellation. Research on the communication performance of satellite-terrestrial links has garnered considerable interest. Existing studies [4,5] simulated the satellite network coverage based on deterministic

This work was supported in part by the National Natural Science Foundation of China under Grant 62271202, 61831008.

satellite constellation data. The literature [6] focuses on the Iridium constellation and analyzes the interruption probability of large LEO constellations from multiple dimensions, accompanied by simulation validation.

However, the studies are primarily based on existing satellite constellations' networks and data, making it difficult to ensure that the channel models apply to other constellations. Researchers have introduced stochastic geometry into the modeling of LEO satellite constellations. [7,8] have modeled satellites using stochastic geometry, deriving the angle distribution or distance distribution between satellites and terrestrial stations, and providing key performance metrics for satellite-terrestrial communication systems. The mainstream stochastic geometric modeling methods currently include the Binomial Point Process (BPP) and the Poisson Point Process (PPP). [9,10] have modeled the positions of satellites as BPP and analyzed the downlink coverage between satellites and terminal devices under a single channel state.

Although BPP effectively simulates uniformly distributed satellites on a spherical shell, its application in modeling satellite networks is limited due to its reliance on extensive prior knowledge and complex parameter settings, making it unsuitable for large satellite constellations. In contrast, PPP describes the number of visible satellites using a Poisson distribution, offering greater flexibility and universality. Moreover, the communication environment between satellites and terrestrial stations is quite complex in high-dynamic scenarios. The performance of the satellite-terrestrial link is significantly affected by environmental scattering and shadowing effects. The link state continually switches between direct line-of-sight and shadowed conditions, affecting signal quality. A single channel state cannot accurately capture the channel fading characteristics induced by the dynamic changes of satellites. Furthermore, variations in satellite-terrestrial link distance lead to fluctuations in signal attenuation and multipath effects, impacting system coverage. Additionally, significant interference between adjacent satellites can further degrade communication performance.

This paper establishes a comprehensive model of a mega LEO satellite-terrestrial communication system using stochastic geometry to address these challenges. We model the satellites and terrestrial users as PPP and account for dynamic changes in satellite-terrestrial link communication scenarios. The satellite network model incorporates a two-state Markov process for the satellite-terrestrial communication channel. The two primary states—direct line-of-sight and shadowed link—are modeled using the Rician distribution and Shadowed-Rician (SR) distribution, respectively. We derive a closed-form expression for the outage probability of the satellite-terrestrial communication system, considering both small-scale and large-scale random variations in the presence of adjacent satellite interference. We confirmed the accuracy of the proposed outage probability expression through extensive simulations and conducted a comprehensive analysis of the key performance metrics that impact the system's communication effectiveness.

II. FRAMEWORK FOR THE MODEL

A. SYSTEM MODEL

The model studied in this paper is a giant LEO constellation consisting of N satellites, as shown in Fig. 1. We assume that the Earth’s radius is R_e, and the users are distributed on the Earth's surface following a homogeneous PPP with intensity λ_U. Additionally, we assume that the satellites orbit at a height h above the Earth's surface, distributed on a spherical shell with radius R_e+h according to a homogeneous PPP with intensity λ_S. According to the Slivnyak theorem [11], for a stationary point process, the distribution of points around an observation point is independent of the location of the observation point. This means that the

representative of those experienced by any user within the point process. Therefore, we select a typical user on the Earth's surface for analysis.

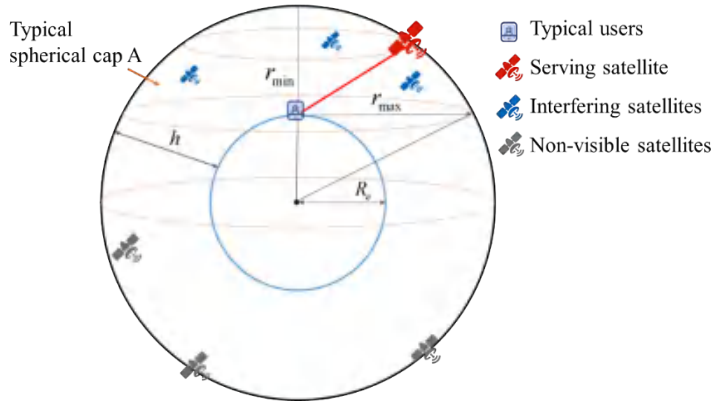

Figure 1. The LEO communication system.

Assuming that the typical user is connected to the satellite that provides the maximum average received power, we define this satellite as the service satellite. We assume that only satellites within the visible range of the typical user (i.e., above the typical user's horizon) can establish a communication link with the user. We denote the distance between a satellite and the typical user as R_n, where n=0, 1, …, N−1, and the maximum distance between the satellite and the typical user as r_{max}. Communication can only occur when at least one satellite is within the satellite's visible region, meaning that the distance between the satellite and the user must satisfy $R_n \le r_{max}$. The satellite's visible region is represented as a spherical cap above the typical user's horizon, as shown in Fig. 1. We model the satellite constellation using a homogeneous PPP, and the number of satellites within the visible region A is a random variable that follows a Poisson distribution with intensity $\lambda_S = \dfrac{N}{4\pi\left(r_{\min}+R_e\right)^2}$. Thus, the probability of having k satellites in region A, where k=0, 1, …, ∞, can be expressed as:

$$P\left(N(A)=k\right)=\frac{\left(\lambda_S|A|\right)^k}{k!}e^{-\lambda_S|A|}, \tag{1}$$

where $|A|$ denotes the surface area of the spherical cap A in the visible region of the satellite. According to Archimedes' Hat-Box theorem, $|A|=2\pi h\left(R_e+h\right)$.

B. Path Loss and Channel Model

The wireless channel consists of large-scale fading and small-scale fading. For simulating the large-scale fading, we adopt a classical path loss model, which quantifies the attenuation based on the distance between the service satellite and the typical user. The path loss factor $L(R)$ is given by:

$$L\left(R\right)=L_0R^{-\alpha}, \tag{2}$$

where R is the distance between the service satellite and the typical user, L_0 is the path loss constant ($L_0=\left(\dfrac{c}{4\pi f_c\sqrt{k_BT_nB_c}}\right)^2$), $c\approx3\times10^8$m/s is the speed of light, f_s is the carrier frequency of the satellite communication system, k_B=1.38×10^{-23}J/K is the Boltzmann constant, T_n is the noise temperature of the LEO satellite, B_c is carrier bandwidth, and α is the path loss exponent which is set to α=2 in this work.

The distance from the satellite to a typical user and the corresponding antenna gain are denoted by R_n and G_n, respectively. The distance from the serving satellite to the typical user and the corresponding antenna gain are denoted by R_0 and G_0, respectively. The received power at the serving satellite from the typical user can be expressed as:

$$P_s^r=P_tG_{Tol}L(R_0)\left|h_{SU}\right|^2, \tag{3}$$

where P_t is the satellite transmission power, G_{Tol} is the total antenna gain (G_{Tol}= $G_r G_t$), G_r is the user's receiving antenna gain, and G_t is the satellite's transmitting antenna gain, $|h_{SU}|^2$ is the channel fading coefficient of the satellite-terrestrial link.

We assume that the receiver is affected by additive white Gaussian noise (AWGN) with a mean of 0 and variance σ^2. Then, the signal-to-interference-plus-noise ratio (SINR) at the receiver can be expressed as:

$$SINR = \frac{P_s^r}{I+\sigma^2} = \frac{\bar{\gamma} G_{Tol} L(R_0) |h_{SU}|^2}{\gamma_{INR}+1}, \tag{4}$$

where P_s^r represents the received power of the typical user as given in (3), $\bar{\gamma} = \frac{P_t}{\sigma^2}$ denotes the average signal-to-noise ratio (SNR), $\gamma_{INR} = \frac{I}{\sigma^2}$ is the interference-to-noise ratio (INR), and I represents the co-channel interference caused by neighboring satellites. The interference I at the typical user can be expressed as:

$$I = \sum_{j=1}^{N_I} P_k G_{Tol,j} L(R_j) |h_j|^2, \tag{5}$$

where N_I is a random variable representing the number of interfering satellites, P_k is the power of the satellite, j denotes the j-th interfering satellite.

Therefore, for the INR, we have:

$$\gamma_{INR} = \frac{I}{\sigma^2} = \overline{\gamma_{INR}}\,\overline{G_{Tol}}\,\overline{L(R)} \sum_{i=1}^{N_I} |h_i|^2 = \sum_{i=1}^{N_I} \gamma_i, \tag{6}$$

where $\overline{\gamma_{INR}} = \frac{P_k}{\sigma^2}$ is the average INR, $\overline{G_{Tol}}$ is the average total antenna gain, $\overline{L(R)}$ is the average path loss. Assuming that the channel coefficients of the interference satellite-to-user link follow an exponential distribution, it can be seen from the above expression that γ_{INR} is the sum of N_I independent and exponentially distributed random variables. According to literature [12], we have the PDF of $\overline{\gamma_{INR}} \sum_{i=1}^{N_I} |h_i|^2$, then the probability density function (PDF) of γ_{INR} can be obtained as follows:

$$f_{\gamma_{INR}}(\gamma) = \frac{\overline{G_{Tol}}\,\overline{L(R)}}{\Gamma(N_I)} \left(\frac{1}{\overline{\gamma_{INR}}}\right)^{N_I} \gamma^{N_I-1} \exp\left(-\frac{\gamma}{\overline{\gamma_{INR}}}\right), \tag{7}$$

By integrating (7), the cumulative distribution function (CDF) of γ_{INR} can be further obtained as:

$$\begin{aligned} F_{\gamma_{INR}}(\gamma) &= 1 - \int_{\gamma}^{\infty} f_{\gamma_{INR}}(\gamma_{INR}) d\gamma_{INR} \\ &= 1 - \overline{G_{Tol}}\,\overline{L(R)} \exp\left(-\frac{\gamma}{\overline{\gamma_{INR}}}\right) \sum_{t=0}^{N_I-1} \frac{1}{t!} \left(\frac{\gamma}{\overline{\gamma_{INR}}}\right)^t, \end{aligned} \tag{8}$$

To facilitate the analysis of interference, we can obtain the average power of γ_{INR}:

$$\mathrm{E}[\gamma_{INR}] = \int_0^{\infty} x f_{\gamma_{INR}}(x) dx = \overline{\gamma_{INR}} N_I \overline{G_{Tol}}\,\overline{L(R)}, \tag{9}$$

We utilize a two-state Markov model to model the channel to accurately describe the small-scale fading and shadowing effects encountered in the communication link. This model captures the channel dynamics across two distinct states:

State One: In open areas or scenarios with minimal obstructions, the satellite-terrestrial link encounters minimal scattering and no significant blockage, leading to a solid direct signal component.

State Two: The satellite-terrestrial communication link experiences pronounced shadowing effects in scenarios with numerous obstacles.

To characterize State One and State Two, we employ the Rician distribution and the SR distribution, respectively. The Rician distribution, which models the presence of a solid direct path, is appropriate for State One. In this state, the PDF of the channel fading factor $|h_{SU}|_R^2$ can be expressed as:

$$\begin{aligned} f_{|h_{SU}|_R^2}(x) = (1+K) \exp\left[-K-(K+1)x\right] \\ \times I_0\left(2\sqrt{K(K+1)x}\right) \end{aligned}, \tag{10}$$

where K represents the Rician factor and $I_0(\bullet)$ represents

the zero-order modified Bessel function of the first kind. By integrating (10), we get the CDF of $|h_{SU}|_R^2$:

$$F_{|h_{SU}|_R^2}(x)=1-Q_1\left(\sqrt{K},\sqrt{2x(K+1)}\right), \quad (11)$$

The SR distribution accurately captures the effects of multipath and shadowing, offering a realistic model for signal attenuation in the environment described in State Two, the PDF and CDF of the channel fading factor $|h_{SU}|_{SR}^2$ are given by:

$$f_{|h_{SU}|_{SR}^2}(x)=ae^{-bx}\,{}_1F_1(m;1;\delta x), \quad (12)$$

$$F_{|h_{SU}|_{SR}^2}(x)=a\sum_{k=0}^{\infty}\frac{(m)_k\,\delta^k}{(k!)^2\,b^{k+1}}\gamma(k+1,bx), \quad (13)$$

where $a=\frac{1}{2n}\left(\frac{2nm}{2nm+\Omega}\right)^m$, $\delta=\frac{\Omega}{2n(2nm+\Omega)}$, $b=\frac{1}{2n}$. Ω denotes the average power of the LOS component in the satellite-terrestrial link, $2n$ is the average power of the multipath component, m represents the Nakagami parameter which indicates the degree of shadowing affecting the channel. ${}_1F_1(\cdot;\cdot;\cdot)$ and $\gamma(\cdot,\cdot)$ represent the confluent hypergeometric and the lower incomplete gamma functions, respectively.

Combining (10) and (12), the PDF of the overall channel fading coefficient $|h_{SU}|^2$ of the satellite-terrestrial link can be expressed as:

$$f_{|h_{SU}|^2}(x)=pf_{|h_{SU}|_R^2}(x)+(1-p)\,f_{|h_{SU}|_{SR}^2}(x), \quad (14)$$

By integrating (14), the CDF of $|h_{SU}|^2$ can be obtained:

$$F_{|h_{SU}|^2}(x)=pF_{|h_{SU}|_R^2}(x)+(1-p)F_{|h_{SU}|_{SR}^2}(x), \quad (15)$$

where p is the probability that a satellite at a distance r from a typical receiver communicates with a terrestrial user through a path that is not blocked by shadow and is used to simulate the randomness of small-scale channel fading [13]:

$$p(r)=exp\left(-\beta cot\left(arcsin\left(\frac{(R_e+h)^2-R_e^2)}{2rR_e}-\frac{r}{2R_e}\right)\right)\right), \quad (16)$$

where $\beta\geq 0$ is a constant related to the geometry of the urban environment.

III. PERFORMANCE ANALYSIS

In this section, we discuss the downlink performance of communication between LEO constellations at various altitudes and terrestrial users under the proposed system and channel models. Using stochastic geometry, we express the outage probability as a function of critical parameters, such as the satellite constellation altitude h and the number of satellites N. We derive an exact expression for the outage probability, accounting for interference from adjacent satellites.

As indicated by (2), the path loss of the satellite-terrestrial link is primarily determined by the distance. Therefore, to calculate the system's outage probability, it is essential to understand the distribution of the shortest distance between satellites and users. In satellite constellations, significant research has been conducted on the statistical characteristics of the distance distribution from satellites to typical users. When satellites are uniformly distributed with a given intensity λ_S, the PDF of the service distance r_0 can be expressed as [14]

$$f_{R_0}(r_0)=\frac{Nr_0}{2\mathrm{R_e}(r_{\min}+\mathrm{R_e})}\times\exp\left(-N\left(\frac{r_0^2-r_{\min}^2}{4\mathrm{R_e}(r_{\min}+\mathrm{R_e})}\right)\right), \quad (17)$$

where $r_0\in[r_{\min},r_{\max}]$, $r_{\max}=\sqrt{(\mathrm{Re}+h)^2-\mathrm{Re}^2}$, and $r_{min}=h$. Integrating (17), the CDF of the service distance can be obtained as:

$$F_{R_0}(r_0)=1-\exp\left[-N\left(\frac{r_0^2-r_{\min}^2}{4\mathrm{R_e}(\mathrm{R_e}+r_{\min})}\right)\right], \quad (18)$$

The outage probability is defined as the probability

that the SINR at the receiver falls below the minimum threshold required for successful data transmission, given that a communication link is established. Consequently, the outage probability of the LEO constellation's communication link can be expressed as:

$$\begin{aligned} &P\{SINR<\tau|r_0\} \\ &=P\left\{\frac{\bar{\gamma}G_{tol}L(R_0)|h_{SU}|^2}{\gamma_{INR}+1}<\tau\middle|r_0\right\} \\ &=\int_{r_{\min}}^{r_{\max}}F_{|h_{SU}|^2}\left(\frac{\tau x^2\left(\frac{I}{\sigma^2}+1\right)}{\bar{\gamma}G_rG_tL_0}\right)f_{R_0}(x)dx \end{aligned} \quad , \quad (19)$$

where τ is the SINR threshold. Combining (15) and (17), the exact expression of the outage probability can be obtained (20), where B=i+1, C=i+j+2, D=s+t+2,

$$\Xi=\frac{N}{4\mathrm{Re}\left(r_{\min}+\mathrm{Re}\right)},\quad \zeta=\frac{\tau\left(\gamma_{INR}+1\right)}{\bar{\gamma}G_{tol}L_0}.$$

IV. SIMULATION ANALYSIS

In this section, we configure the SINR threshold τ=7, the frequency f_S=9GHz, the path loss index α=2, the Rice factor K=2, and the SR parameters to n=0.158, m=19.4, Ω=1.29. By varying these parameters, we investigate the impact of the parameters of the satellite constellation (including the number of constellation satellites N, the constellation altitude h), the co-channel interference of adjacent satellites, and different channel states on the performance of the proposed model.

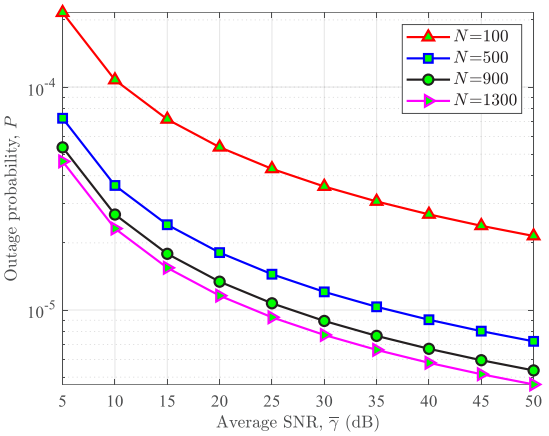

Figure 2. Outage probability vs ASNR for different numbers of satellites.

Fig. 2 illustrates the relationship between the average signal-to-noise ratio (ASNR) and the outage probability under different numbers of satellites. The more satellites there are, the lower the outage probability. As the number of satellites increases, the improvement in outage probability diminishes. Taking ASNR=10 dB as an example, when there are 100, 500, 900, and 1300 satellites in the constellation, the outage probabilities are 1.076×10^{-4}, 3.62×10^{-5}, 2.68×10^{-5}, 2.319×10^{-5}, respectively. This is because, as the number of satellites increases, users have more options for establishing a connection, reducing the outage probability. Notably, once the number of satellites reaches a certain threshold, further increases yield diminishing returns in coverage improvement. This is because, once global coverage is nearly complete, additional satellites contribute only marginally to enhancing coverage. Consequently, as the satellite count increases, the impact on communication quality becomes less pronounced, and the rate of change in outage probability slows.

$$\begin{aligned} P\{SINR<\tau|r_0\}&=p\Xi\exp\left(\Xi h^2-K\right)\sum_{i=0}^{\infty}\sum_{j=0}^{\infty}\frac{K^i(\zeta B)^{C-1}}{(\zeta B+\Xi)^C}\frac{\Gamma\left(C,(\zeta B+\Xi)h^2\right)-\Gamma\left(C,(\zeta B+\Xi)\left(h^2+2h\mathrm{Re}\right)\right)}{\Gamma(C)\Gamma(B)} \\ &+(1-p)a\sum_{s=0}^{\infty}\sum_{t=0}^{\infty}\frac{(-1)^t b^t\delta^s(m)_s}{t!(s!)^2(D-1)}\left(\frac{\zeta}{\Xi}\right)^{s+t+1}\left[\Gamma\left(D,\Xi h^2\right)-\Gamma\left(D,\Xi r_{\max}^2\right)\right] \end{aligned} \quad . \quad (20)$$

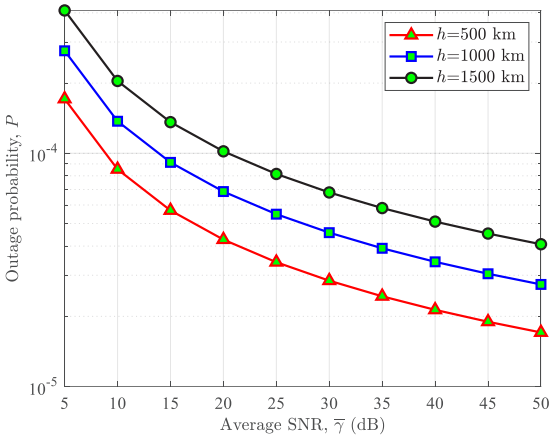

Figure 3. Outage probability vs ASNR for different constellation heights.

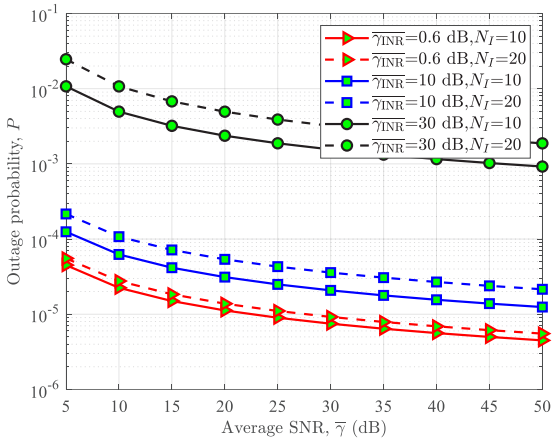

Figure 4. Outage probability vs ASNR under different interference.

Fig. 3 describes the relationship between the ASNR and the outage probability under different heights h of the satellite constellation. The figure indicates that a higher constellation altitude for a fixed number of satellites results in an increased outage probability. For instance, at an average SNR of 20 dB, the outage probabilities for constellation heights of 500 km, 1000 km, and 1500 km are 4.264×10^{-5}, 6.852×10^{-5}, 1.019×10^{-4}, respectively. This phenomenon occurs because an increase in altitude enlarges the distance of the satellite-terrestrial transmission link. According to the path loss in (2), the path loss is proportional to the square of the distance, leading to significant signal attenuation by the time it reaches the ground. Given the limited sensitivity of terrestrial receivers, an increased distance can result in received signal strength falling below the receiver's noise threshold, thereby degrading communication quality.

Fig. 4 examines the impact of adjacent interfering satellites on the system outage probability, including the number of interfering satellites N_I and the INR. This figure reveals that the outage probability rises as the number of adjacent interfering satellites increases. Similarly, an increase in INR correlates with a higher outage probability, with the rate of increase tapering off at a high average SNR. This is because more interfering satellites generate additional interference, diminishing the SINR of the target satellite's signal. As interference increases, INR also rises, exacerbating the relative interference compared to the noise signal. While high SNRs reduce the impact of noise, they do not significantly mitigate interference, causing only limited improvement in system performance despite increased SNR. Thus, the system's outage probability change becomes more gradual at higher SNR.

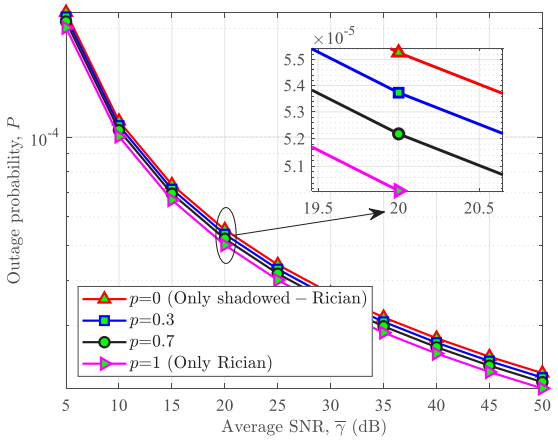

Figure 5. Outage probability vs ASNR under different communication environments.

Fig. 5 illustrates the effect of varying shadowing scenarios on the outage probability of the satellite-terrestrial communication link. The parameter p represents the probability that the channel is in the “no shadow occlusion” state. When p=0, the satellite-

terrestrial communication channel is heavily shadowed and described only by SR distribution. When p=1, the channel experiences minimal shadowing, and only the Rician distribution exists. The figure demonstrates that higher values of p correspond to lower outage probabilities. A higher p indicates less shadowing and fewer obstructions, resulting in less signal attenuation and reduced multipath effects, contributing to higher and more stable signal quality. The subplot shows the effect of p on outage probability at an average SNR of 22 dB. For p=0, 0.3, 0.7, and 1, the outage probabilities are 5.527×10^{-5}, 5.373×10^{-5}, 5.218×10^{-5}, 5.013×10^{-5}. The results suggest that the outage probability lies between those for p=0 and p=1. This variability reflects that in practical satellite-terrestrial links, the channel state is dynamic rather than constant, alternating between “good” and “poor” conditions. Modeling the channel state as a Markov process allows for a more accurate representation of these dynamic conditions than a static state model.

V. CONCLUSION

In this paper, we model a giant LEO network using stochastic geometry and analyze the communication performance of satellite-terrestrial downlinks based on a two-state Markov model. Accounting for environmental variations and the distance changes between satellite-terrestrial links due to the rapid movement of satellites, we account for both large-scale and small-scale fading effects in our analysis of the proposed system's performance. We employ a comprehensive path loss model. The channel state of the satellite-terrestrial link is modeled using a two-state Markov model, with the Rician and SR distributions characterizing the two states, respectively. Additionally, we address co-channel interference from adjacent satellites and quantify its average power. Finally, we derive the outage probability expression and conduct a simulation analysis. Our findings indicate that modeling the satellite-terrestrial link as a two-state Markov process offers a more accurate representation of real-world conditions than single-state models, thereby providing a more precise assessment and prediction of communication system performance. The outage probability expression derived in this study also offers essential guidance for developing satellite deployment strategies in complex environments.

References

[1] Del Portillo I, Cameron B G, Crawley E F. A technical comparison of three low earth orbit satellite constellation systems to provide global broadband[J]. Acta astronautica, 2019, 159: 123-135.

[2] Ma R, Zhang Z. A Case Study of Starlink and 5G in Future Space based Internet Services[C]//2022 4th International Symposium on Smart and Healthy Cities (ISHC). IEEE, 2022: 64-67.

[3] Wang N, Xu X, Zhang C, et al. Assumption and Key Technologies of Next Generation Satellite Network[C]//2023 15th International Conference on Communication Software and Networks (ICCSN). IEEE, 2023: 414-418.

[4] Vatalaro F, Corazza G E, Caini C, et al. Analysis of LEO, MEO, and GEO global mobile satellite systems in the presence of interference and fading[J]. IEEE Journal on selected areas in communications, 1995, 13(2): 291-300.

[5] Seyedi Y, Safavi S M. On the analysis of random coverage time in mobile LEO satellite communications[J]. IEEE Communications Letters, 2012, 16(5): 612-615.

[6] Ganz A, Gong Y, Li B. Performance study of low Earth-orbit satellite systems[J]. IEEE Transactions on Communications, 1994, 42(234): 1866-1871.

[7] Bliss M A, Block F J, Royster T C, et al. Orchestrating Heterogeneous NTNs: from Stochastic Geometry to Resource Allocation[J]. IEEE Transactions on Aerospace and Electronic Systems, 2024.

[8] Choi C S. Modeling and analysis of downlink communications in a heterogeneous LEO satellite network[J].

IEEE Transactions on Wireless Communications, 2024.

[9] Wang X, Deng N, Wei H. Coverage and rate analysis of leo satellite-to-airplane communication networks in terahertz band[J]. IEEE Transactions on Wireless Communications, 2023, 22(12): 9076-9090.

[10] Dwivedi A K, Chaudhari S, Varshney N, et al. Performance analysis of LEO satellite-based IoT networks in the presence of interference[J]. IEEE Internet of Things Journal, 2023.

[11] François B, Bartłomiej B. Stochastic geometry and wireless networks: Volume i theory[J]. NoW Publishers Breda, 2009, 55.

[12] Yang L, Hasna M O, Gao X. Performance of mixed RF/FSO with variable gain over generalized atmospheric turbulence channels[J]. IEEE Journal on Selected Areas in Communications, 2015, 33(9): 1913-1924.

[13] Al-Hourani A. An analytic approach for modeling the coverage performance of dense satellite networks[J]. IEEE Wireless Communications Letters, 2021, 10(4): 897-901.

[14] Okati N, Riihonen T. Coverage and rate analysis of mega-constellations under generalized serving satellite selection[C]//2022 IEEE Wireless Communications and Networking Conference (WCNC). IEEE, 2022: 2214-2219.

About the authors

QU Fangxin was born in Heilongjiang province. She received the B.E. degree in electronic information science and technology from Nanjing Agricultural University, Nanjing, China, in 2022. She is now pursuing the master's degree in East China Normal University, Shanghai, China. Her research interests are satellite network communication systems.

(Email: 51265904001@stu.ecnu.edu.cn)

LU Shuyuan was born in Zhejiang province. She received the B.E. degree in electronic information science and technology from Northwest University, Xian, China, in 2022. She is currently working toward the Ph.D degree with the School of Communication and Electronic Engineering, East China Normal University, Shanghai, China. Her research interests include the multi layer satellite network communication system and the Nonorthogonal multiple access technology.

(Email: 52275904002@stu.ecnu.edu.cn)

XU Guanjun was born in Anhui province. He is a professor in the Space Information Research Institute, Hangzhou Dianzi University, China. He has received his B.E. degree in electronic engineering from Chaohu University, Hefei, China, in 2010, his M.E. degree in communication and information systems from Southwest University of Science and Technology, Mianyang, China, in 2013, and his Ph.D. degree in information and communication engineering from Harbin Institute of Technology, China, in 2017. After that, he was a associate professor and full professor at East China Normal University, China until 2023. His research interests include radio wave propagation over fading channels, wave scattering in random media, optical wireless communications, and deep space communication.

(Email: gjxu@hdu.edu.cn)

CUI Junjun was born in Henan province. He is now pursuing the master's degree in Hangzhou Dianzi University, Hangzhou, China. His research interests are space information network and transmission.

(Email: cjj03202002@163.com)

SONG Zhaohui was born in Heilongjiang province. He received the B.S. degree, M.E. degree, and Ph.D. degree from the Harbin Institute of Technology, Harbin, China, in 1992, 1998, and 2006, respectively. He has been a professor at the Harbin Institute of Technology. He has been a professor at Hangzhou Dianzi University since 2022. His research interests mainly focus on antenna theory and technology, microwave circuits and systems, electromagnetic wave propagation theory, space information perception, and transmission.

(Email: songzh@hdu.edu.cn)

广义巨型星座体系架构研究

费立刚，常呈武，王瑛*，徐潇审，吕非超

（中国人民解放军 32039 部队 北京 102300）

摘　要：巨型星座是国家太空战略体系的关键支撑。本文在对美国“星链”等巨型星座发展趋势分析的基础上，提出了打造我国广义巨型星座的构想，从服务保障、空间布势、业务功能、运维管控和融合应用等维度设计了体系架构，并给出典型应用模式和后续发展建议。研究结果为我国广义巨型星座建设提供了借鉴参考，对空间信息网络创新发展具有推动作用。

关键词：巨型星座；体系架构；太空战略；空间信息网络

Research on System Architecture of Generalized Mega Constellation

Fei Ligang, Chang Chengwu, Wang Ying, Xu Xiaoshen, Lv Feichao

(Unit 32039 of the Chinese People's Liberation Army, Beijing 102300)

Abstract: Mega constellations constitute a pivotal support for the national space strategy system. Drawing upon the analysis of the development trend of constellations such as US “Starlink”, this paper introduces the concept of establishing a generalized mega constellation for China. The system architecture is crafted from multiple dimensions, encompassing service assurance, spatial deployment, business functionalities, operation and control, as well as integrated applications. Furthermore, typical application scenarios and suggestions for future development are presented. These research findings serve as a valuable reference for the construction of China’s generalized mega constellations and foster innovative advancements in space information networks.

Key words: mega constellation; system architecture; space strategy; space information network

1　引言

巨型星座是指由数千颗以上卫星在太空组成的规模庞大的卫星系统[1]。“星链”系统是全球领先的巨型星座。2015 年，美国宣布推出“星链”计划[2]，旨在开发全球卫星互联网系统。目前在轨已超 5900 颗、20 重覆盖，在 70 余个国家商业应用、超 230 万用户。此外，2022 年，美国启动“星盾”计划[3]，将继承“星链”卫星的技术和发射能力，设计“星链”的军用版本。

美国正在统筹军商盟力量，构建高中低轨结合、通导遥一体的广义巨型星座，具体发展趋势如下。

收稿日期：2024-08-30；改回日期：2024-10-12
*通信作者： 王瑛 duvin103time@163.com

- 构建巨型星座，打造混合太空架构[4]。将“星链”、“Skysat”[5]、“黑杰克”[4]、“鹰眼 360”[6]等新兴的卫星星座与传统的太空系统相集成，通过使用“可变信任”网络框架保证快速数据交换安全性[7]，实现军商盟在情报监视侦察、卫星通信、定位导航授时、态势感知等方面的资源共享。
- 突出军用特点，打造核心专用星座。为了突出抗毁保底的军事应用特点，美国在“星链”技术资源基础上建设“星盾”军事专用星座，还通过“黑杰克”项目构建出具有超高性价比、高度弹性化的军用低轨星座，实现卫星通信、遥感探测、预警侦察、导航定位、电子对抗、太空打击等应用。与此同时，美国在传统通导遥系统基础上，也加紧建设 AEHF 通信卫星[8]、下一代铱星系统[9]、“锁眼”[10]、“FIA”遥感卫星[11]等军事专用卫星，实现“军用核心层+民商增强补充层”的弹性体系。
- 多域信息融合，构造信息支援一体化体系。美国在“黑杰克”项目中融合军事通信、导航、侦察、预警等功能，并将技术成果应用到“扩散作战人员太空架构”[12]，实现了多域信息融合。同时，美国在强化低成本、规模化卫星制造等技术优势基础上，加紧开展星上边缘计算和人工智能、超大规模星群智能协同、星座自主运控等前沿技术开发，为信息支援一体化奠定基础。

我国现有的百余颗卫星均为单系统、小规模组网运用，不同系统间技术体制差异显著、互联互通手段匮乏，不具备以全域持续存在、海量泛在联接、通导遥算一体等为主要特征的巨型星座能力。目前，我国在建的卫星互联网[13]具有向巨型星座演进的基础，但仍处于起步阶段，规模能力与美国差距明显。同时，各类民商通信星座和民商遥感星座都在快速发展建设。上述系统如果能够在频段、协议、应用和终端等方面开展综合设计，可望在现有系统基础上实现融合应用，打造属于我国的广义巨型星座。

2 广义巨型星座体系架构设计

2.1 总体设计

充分利用我国本土信息网络优势和各空间层平台的驻留特性，以地面网云支撑为基础、以低轨卫星为主体、以中高轨卫星为支柱、以海空平台为补充，通导遥统筹建设、融合应用，打造全球广域覆盖、区域敏捷增强、跨域共享共用的中国特色广义巨型星座。

在规划上统筹设计、建设上分域实施、应用上强化融合，大力推动体系融合，采用载荷搭载、软件无线电、多模终端、网云一体处理、统一技术规范等多种方式，构建动态开放、创新迭代、弹性灵活的混合巨型星座架构，实现通导遥有机统一，提升整体应用效能。

通过多维度综合设计，广义巨型星座体系构架主要包括服务保障、空间布势、业务功能、运维管控和

融合应用等 5 个维度。

2.2　服务保障维度

构建“核心层+增强层+补充层”的服务型巨型星座，如图 1 所示。核心层为提供快响保底能力的专用系统，增强层为提供弹性增强能力的专用载荷或共用载荷及应用系统，补充层为以采购等方式提供专用服务的商用载荷及应用系统。

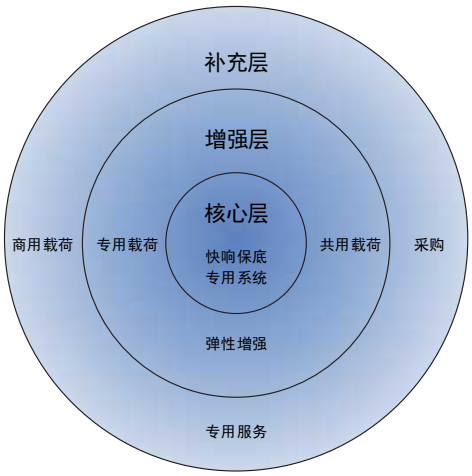

图1　服务保障维度示意图

2.3　空间布势维度

构建“天临空地一体”布势的弹性巨型星座，如图 2 所示。高中轨道以通信卫星、北斗导航卫星、遥感探测和民商高通量等为基础，适度发展中轨星座；低轨以卫星互联网为基础，拓展民商星座资源，增加卫星规模数量；高中低空敏捷部署驻留式网云节点和无人机探测体系；地面部署空地通信基站，海上固定/机动平台按需补充网络覆盖；频轨空间统筹规划高中低轨卫星以及 6G、手机宽带直连等天地网络频段，加强 30GHz 以上高频段，以及极低轨、中轨等频轨资源储备。

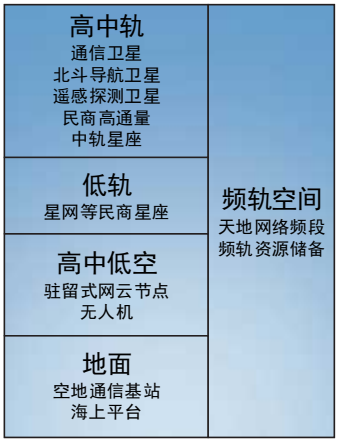

图2　空间布势维度示意图

2.4 业务功能维度

构建“通+导+遥”一体化服务的巨型星座，如图 3 所示。通信业务提供宽带、窄带、移动等通信服务并支持手机直连，导航业务提供复杂条件下定位、导航及授时服务，遥感业务提供气象观测、资源考察、地图测绘等服务。

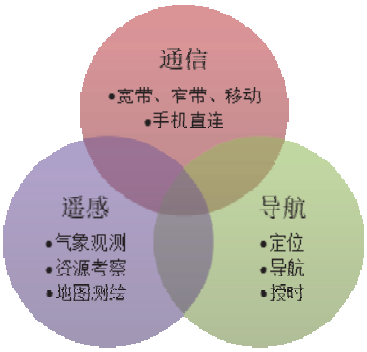

图3 业务功能维度示意图

2.5 运维管控维度

构建“联合+统一”的巨型星座运维管控系统，支持专管专用、联合管控、管用分离和整体纳管等多种运维管控方式，如图 4 所示。通用功能以资源提供方为主管控、为使用方按优先级提供服务保障，专用功能以使用方为主管控、资源提供方支撑保障，兼顾重要性层级、时序紧迫性和效能最大化设计优先级，借鉴“可变信任”网络框架确保数据交换安全，有效推进卫星资源、数据和地面网络、站点共享共用。

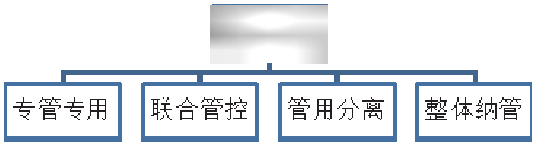

图4 运维管控维度示意图

2.6 融合应用维度

构建“分域+体系”融合的巨型星座，如图 5 所示。分业务领域推进协议融合、终端融合和地面融合。协议融合方面，通信领域向卫星波形、5G/6G 等协议融合发展，导航领域使用信号体制兼容的导航信号，遥感领域规范设计多载荷类型数据格式协议，提高系统互联互通能力。终端融合方面，通信和导航领域研制多频段多模终端，实现通信星座、导航星座的多模集成，提升系统弹性服务能力。地面融合方面，建设地面网云数据一体化处理系统，融入人工智能和边缘计算技术，高效实现数据地面交换和数据专业处理。同步推进不同业务领域之间体系融合，通过搭载频谱监测载荷，实现对通导遥等频段的全球监测；利用通信链路，支持导航增强和遥感数据传输。

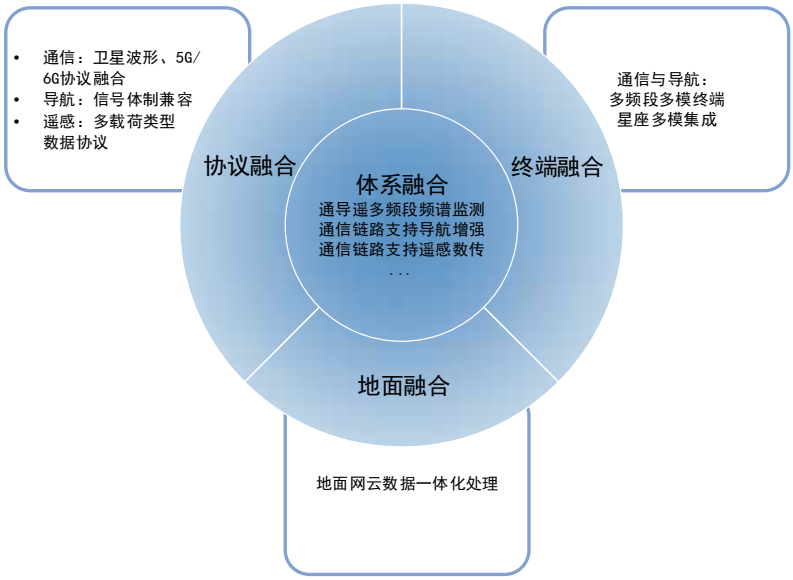

图5　融合应用维度示意图

3　广义巨型星座典型应用

广义巨型星座集成了通信、导航和遥感技术，打破传统星座系统界限，构建全方位、高性能的空间信息服务体系，其融合应用的典型模式如下。

- 通导遥集成搭载。在满足体积、重量、功耗及电磁兼容等约束条件的前提下，在轨卫星可按需搭载通信、导航和遥感等多种不同载荷，导航增强载荷实现导航信号增强，通信载荷为导航增强载荷产生的导航增强信息电文提供传输通道、为遥感载荷获取与处理的观测数据提供传输通道，频谱监测载荷实现对通导遥等频段的全球频谱态势实时监测。
- 通信信号导航定位。利用低轨卫星通信信号，实现基于多普勒频移的定位功能，以及基于载波相位的定位功能。通信信号导航定位发挥低轨卫星通信网络信号强、覆盖重数多的优势，仅需要升级现有通信终端兼容导航功能，即可在北斗系统不可用的情况下提供高性能导航定位服务。进一步地，还可实现北斗导航信号和低轨通信信号融合定位。
- 地面多源信息融合。构建地面网云数据一体化处理系统，引接各类卫星系统获取的对地观测数据、海洋探测数据、气象数据以及其它开源数据，开展多源产品融合处理、多域数据关联分析，提供标准化信息服务和融合态势信息产品。

4　广义巨型星座体系发展举措

广义巨型星座建设投入大、运维成本高，过硬的应用需求是现有星座体系聚优的主要动力，良好的商用市场是星座未来可持续发展的重要支撑。在保障用户的基础上，开拓培育民商产业生态，主要发展举措

如下。

- 需求统领政策引导。聚焦维护海外利益等战略需求，兼顾国民经济发展需要，通过在国家层面明确有关政策制度，引导各方力量协调一致，加快形成广义巨型星座能力。
- 卫星发射能力提升。加强海量卫星发射能力，具备更高的一箭多星发射运载能力，以及应急情况下快速发星补网能力。加大商用发射场支持力度，为卫星多工位发射、应急备份发射创造条件。
- 技术体制通用兼容。统一卫星载荷搭载、星间数据传输、星地业务管控接口协议，推进卫星平台和基站设备通用化、系列化、标准化，任务载荷模块化、板卡化、芯片化，支撑按需灵活搭载专用载荷，打牢系统互联互通和业务融合基础。

5 结束语

作为空间信息网络的重要形态，巨型星座正在加速战略布局，大国博弈竞争势头突显。本文提出的广义巨型星座体系架构，通过共享共融、以融增效，推进精细化、弹性化、体系化、智能化服务能力的迭代更新，力争在全球范围内达成战略平衡。

参考文献

[1] 张佳鑫, 常朝阳, 张易隆, 等. 巨型星座路由技术综述[J]. 天地一体化信息网络, 2024, 5(1): 2-13.
Zhang Jiaxin, Chang Zhaoyang, Zhang Yilong, et al. Survey on routing technology of mega constellation[J]. Space-Integrated-Ground Information Networks, 2024, 5(1): 2-13.

[2] Dominic Gates. Elon Musk touts launch of “SpaceX Seattle”[EB/OL].(2015-01-16)[2024-8-23]. https://www.seattletimes.com/business/elon-musk-touts-launch-of-lsquospacex-seattlersquo/.

[3] Mike Wall. SpaceX reveals “Starshield” satellite project for national security use[EB/OL]. (2022-12-7)[2024-8-23]. https://www.space.com/spacex-starshield-satellite-internet-military-starlink.

[4] 胡敏, 张锐, 徐灿. 太空信息支援发展现状及趋势分析[J]. 中国电子科学研究院学报, 2023, 18(3): 270-273.
Hu Min, Zhang Rui, Xu Can. Development status and trends of space information support[J]. Journal of China Academy of Electronics and Information Technology, 2023, 18(3): 270-273.

[5] 周宇, 王鹏, 傅丹膺. SkySat 卫星的系统创新设计及启示[J]. 航天器工程, 2015, 24(5): 91-98.
Zhou Yu, Wang Peng, Fu Danyin. System innovation and enlightenment of SkySat[J]. Spacecraft Engineering, 2015, 24(5): 91-98.

[6] 郝才勇. 鹰眼 360 天基无线电监测系统综述[J]. 中国无线电, 2023(1): 52-54+62.

Hao Caiyong. A Survey of Hawkeye 360 Satellite-based Radio Monitoring System[J]. China Radio, 2023(1): 52-54+62.

[7] Small Satellite Conference. Hybrid Space Architecture Statement of Principles[EB/OL]. (2020-9-30)[2024-8-24].https://smallsatalliance.org/wp-content/uploads/2020/09/Hybrid-Architecture-Statement-of-Principles-v21.pdf.

[8] 崔潇潇, 钟江山, 赵炜渝, 等. 美国“先进极高频”军用通信卫星系统现状及其应用[J]. 国际太空, 2021(5): 48-52.

Cui Xiaoxiao, Zhong Jiangshan, Zhao Weiyu, et al. Current status and application of US “AEHF” military communication satellite system[J]. Space International, 2021(5): 48-52.

[9] 苗青, 蒋照菁, 王闯. 下一代铱系统发展现状与分析[J]. 数字通信世界, 2019(7): 21-22+47.

Miao Qing, Jiang Zhaojing, Wang Chuang. Development situation and analysis of the Iridium next system[J]. Digital Communication World, 2019(7): 21-22+47.

[10] 李爽. 美军锁眼侦察卫星计划分析及展望[J/OL]. 武汉大学学报(信息科学版), 1-11(2023-9-5)[2024-8-24]. https://doi.org/10.13203/j.whugis20230128.

Li Shuang. Analysis and prospect of the U.S. Army’s decrypted keyhole satellite program[J]. Geomatics and Information Science of Wuhan University, 1-11(2023-9-5)[2024-8-24]. https://doi.org/10.13203/j.whugis20230128.

[11] 徐冰. 美国新一代成像侦察卫星概况[J]. 国际太空, 2011(11): 47-50.

Xu Bing. Review of the US New Generation of Imaging Reconnaissance Satellites[J]. Space International, 2011(11): 47-50.

[12] 许连杰, 刘亮亮, 庞鸿锋, 等. 美国“扩散型作战人员太空架构”系统建设进展及关键技术分析[J]. 中国航天, 2023(9): 47-54.

Xu Lianjie, Liu Liangliang, Pang Hongfeng, et al. Progress and key technology analysis of the US “Proliferated Warfighter Space Architecture”[J]. Aerospace China, 2023(9): 47-54.

[13] 中国政府网. 王勇出席中国卫星网络集团有限公司成立大会并讲话[EB/OL]. (2021-04-29)[2024-8-24]. https://www.gov.cn/guowuyuan/2021-04/29/content_5604037.htm.

Chinese government website. Wang Yong attended the founding ceremony of China Satellite Network Group Co., Ltd. and delivered a speech[EB/OL]. (2021-04-29)[2024-8-24]. https://www.gov.cn/guowuyuan/

2021-04/29/content_5604037.htm.

[作者简介]


费立刚（1968.12—），男，博士，正高级工程师，研究方向为卫星通信与航天测控。


常呈武（1969.10—），男，硕士，正高级工程师，研究方向为卫星通信。


王瑛（1981.11—），男，博士，高级工程师，研究方向为卫星通信与卫星导航。


徐潇审（1985.8—），男，博士，高级工程师，研究方向为卫星通信与航天测控。


吕非超（1994.11—），女，硕士，助理工程师，研究方向为太空安全与卫星通信。

低轨卫星数据链直连应用的移动性管理方法

李靖 高凌云 傅裕

天津七一二通信广播股份有限公司北京研发中心（北京华龙通科技有限公司）

摘 要：通过在低轨卫星上搭载数据链载荷，能够实现地面数据链直连卫星，是对常数据链通信的有效拓展。然而卫星的高速移动导致地面终端用户需要频繁切换卫星信号，对移动性管理技术提出了挑战。为实现数据链直连低轨卫星应用，在分析数据链直连低轨卫星的网络架构的基础上，设计了移动性管理流程，可以在不改变原地面数据链端机状态的条件下，实现在切换过程中提供数据链应用层会话的连续保持。

关键词：低轨卫星；数据链；移动性管理

Handover Management in Direct Data-Link Applications of LEO Satellites

JingLi LingyunGao YuFu

Tianjin 712 Communication & Broadcasting Co.,Ltd Beijing R&D Center

（Beijing Hualongtong Science & Technology Co.,Ltd）

Abstract: By equipping data link payloads on LEO satellites, it is possible to establish direct satellite-to-ground Data-Link, which effectively expand conventional data link communications. However, the high-speed movement of satellites leads to the need for ground terminal users to frequently switch satellite signals, posing a challenge to mobility management technology. To achieve direct data link applications with LEO satellites, a mobility management process has been designed based on the network architecture of LEO satellites. This process enables the continuous maintenance of data link applications during satellite switching.

Key words: LEO Satellites, Data-Link, Handover Management

1 引言

数据链是适应现代战争的需要和信息技术的发展而产生的一种用于在指挥控制系统、传感器和武器平台之间进行数据传输与交换的战术信息系统[1]。其典型代表就是美军的 Link-16 数据链[2,3]，广泛应用于美国军队和北约盟国的通信系统，旨在提供高效的战场情报共享和指挥控制能力。通过 Link-16 数据链，作战人员可以实时地获取和共享战场情报，从而提高作战效率和战场指挥的能力。美军作战模式，从“平台中心战”向“网络中心站”的转变过程中，所依托的就是数据链技术的发展，并且在此基础上，提出了战术星座网的建设计划[4]，利用卫星覆盖范围广，传输信号稳定等特点，进一步拓展了数据链的投送能力。

在轨卫星按运行轨道高度由高到低分为地球同步轨道卫星（GEO）、中轨卫星 MEO）和低轨卫星（LEO）[5]。相对于中高轨卫星，低轨卫星在轨高度较低，可以为星地间的数据传输提供较小的延时和更高的吞吐

量，空间链路传输损耗也相对较小，具备在地面终端不改变波形体制的情况下，直接接入低轨卫星的能力。但是，由于低轨卫星的波束范围覆盖区域较小，因此需要多颗的卫星来实现全域覆盖 [6]，同时由于低轨卫星过境速度较快，对于地面用户而言，单颗卫星的业务覆盖时间较短，为了保障用户业务的长时间进行，需要多颗卫星协同工作，不间断的为用户提供数据链服务，这种面向大规模低轨星座的链路切换管理为卫星通信系统的设计提出了苛刻的要求。需要在不改变已有的单兵、车载、船载、机载、弹载等装备平台数据链端机的前提下，实现天基站点的快速接入和切换，保持与指挥所和数据链组网中心之间实现无缝的数据交互。本文分析了数据链直连低轨卫星的星地网络通信的主要网元功能及接口关系，提出了一种基于数据链载荷端机身份识别策略的数据链的切换方式，可以在数据链直连低轨卫星的应用场景下，实现切换过程中应用层会话的连续保持。

2 低轨卫星切换管理研究进展

在低轨卫星星座的建设过程中，星地链路间的切换管理问题吸引了大量的专家学者展开研究。早期的研究中，卫星的接入和切换主要从用户角度展开，当用户需要发起数据业务通信时，根据当前区域的卫星仰角、信号强度等条件进行筛选，寻找最优的卫星接入星上载荷，当快速移动的卫星即将过境时，通过查阅星历，寻找下一颗可接入卫星继续业务通信[7,8]。这种基于用户终端搜星的方式进行链路切换，缺少对卫星实际运行状态的考虑，比如星上负载、波束覆盖时间等问题，导致链路切换频繁，产生大量的用户与卫星间的交互信令，影响通信服务质量，也造成不必要的信道浪费。在低轨卫星发展的过程中，另一种思路是通过确定用户活动区域，预先对过境卫星进行业务规划，不间断的为用户获取区域提供数据链服务，从而减少用户频繁发起的信令交互，缓解信令交互的压力[9]。但低轨卫星的过境时间很短，依然需要用户参与不断的链路切换。由此，一些研究希望在通信任务过程中，将用户的会话层业务与链路层业务进行解耦，通过一定的编址策略，使得用户不需要具体感知为其提供服务的卫星信息，只需在服务区域内向指定的编码地址发起通信业务即可[10,11]，星地组网策略交付给地面组网中心，不再需要用户和卫星的直接参与。在数据链终端直连应用上，其移动性管理方式应更趋向于后者。

3 数据链终端直连低轨卫星的移动性管理方法

3.1 网络架构

低轨卫星数据链直连网络主要由“天基承载网”和“地面承载网”两部分组成。数据链端机工作在低轨卫星上，借助于卫星构建天基数据链传输网络，实现装备平台、地面承载网的数据互通。地面承载网络由地面信关站、数据链组网中心、卫星互联网控制中心、任务中心、指挥所共同构建，通过地面信关站与卫星建立数据链路。整个网络的链路接口关系如图 1 所示。

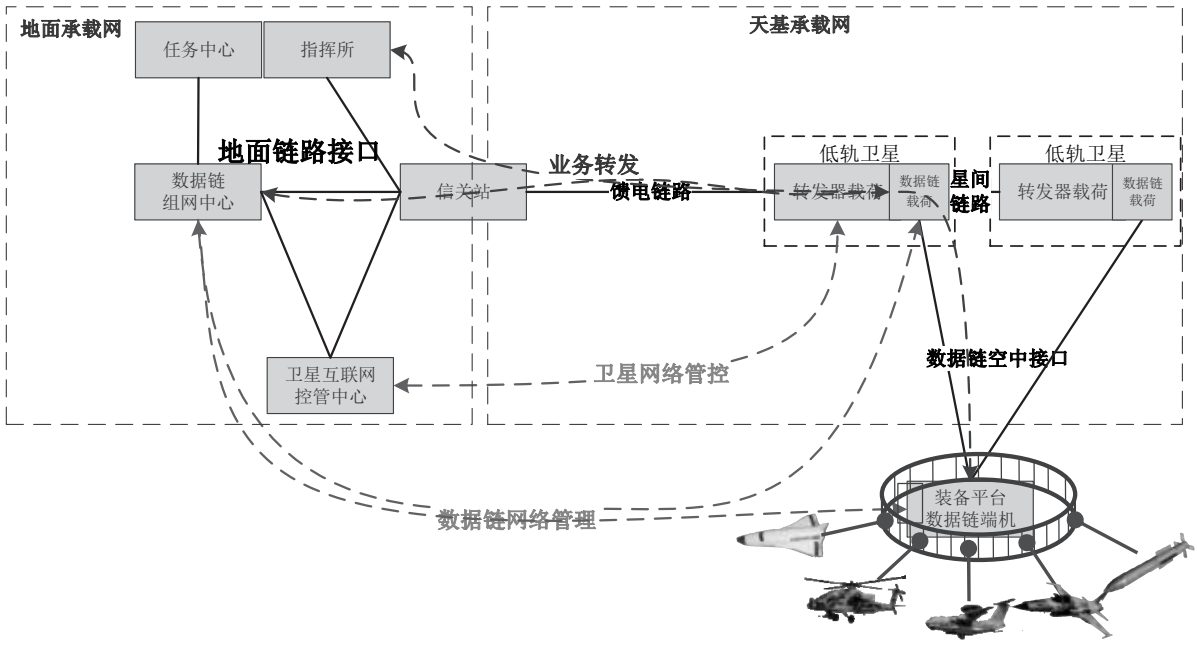

图 1 低轨卫星数据链终端直连网络系统架构

低轨卫星：天基承载网组成核心，用于承载数字转发器、以及数据链端机等各种通信链路载荷；

信关站：用于与卫星交互专用数据的地面站点；

卫星互联网控管中心：用于卫星星座的管理控制，包括卫星星座轨道管理、卫星健康管理、重构处理等。在本应用的移动性管理方面，主要依据全网数据转发规则，完成数据链数据在天基承载网络转发时的移动性管理；

数据链组网中心：根据任务需求和卫星信息（星历、波束、数据链载荷时频资源等），规划星载数据链任务，包括各种网络参数，并负责部分数据链信息的处理和交互转发。在移动性管理方面，主要完成数据链业务层面的移动性管理；

任务中心：根据作战需求，生成任务类型、区域和时段；

指挥所：数据链业务态势和指控数据的生成、处理和使用单位，配备有数据链数据的解析处理机；

装备平台数据链端机：已有的单兵、车载、船载、机载、弹载等装备平台数据链端机的用户。

3.2 网元与身份识别信息

为了实现应用业务与载荷平台的功能解耦，本文为天基数据链载荷端机设计了三层身份识别标识，分别为载荷端机的 IP 地址，虚拟平台编址（网络规划号）和载荷平台编址。三种编址识别方式的服务对象不同，IP 地址用于天基网络的规划寻址，虚拟平台编址（网络规划号）在用户层面为链路通信服务，载荷平

台地址具体参与数据链的业务传输。

IP 地址：该 IP 地址用于经数据链载荷在低轨卫星网络内做路由转发时识别数据源/目身份。每个数据链载荷端机在正常工作状态下，只有一个 IP 地址。该 IP 地址遵循低轨卫星载荷的统一编址规则，其数据的路由规划，接受卫星互联网控管中心的统一管理。

虚拟平台编址号：该虚拟编址号用于某次任务中，站点与装备平台的数据链端机和组网中心、指挥所的数据链信息格式化消息交互的身份识别。该虚拟平台编址号是数据链组网中心根据任务规划为数据链载荷端机分配的身份识别信息。当某任务开始后，所有服务当前任务的卫星数据链载荷均使用一个相同的虚拟平台编址号，从而使其他装备平台的数据链端机能够无感的工作在不同的卫星服务区内。数据链载荷可拥有多个虚拟平台编址号，能够支撑不同数据链子网同时工作。

载荷平台编址号：数据链载荷的唯一身份识别号，用于在数据链业务层面，组网中心或指挥所与其完成数据交互。该平台编址号是数据链组网中心根据数据链载荷实际的在轨情况为为数据链载荷端机分配的身份识别信息。一般的，一个数据链载荷使用一个平台编址号。

3.3 移动性管理流程设计

数据链直连低轨卫星的移动性管理流程如下图所示，可分为用户入网阶段和切换阶段。

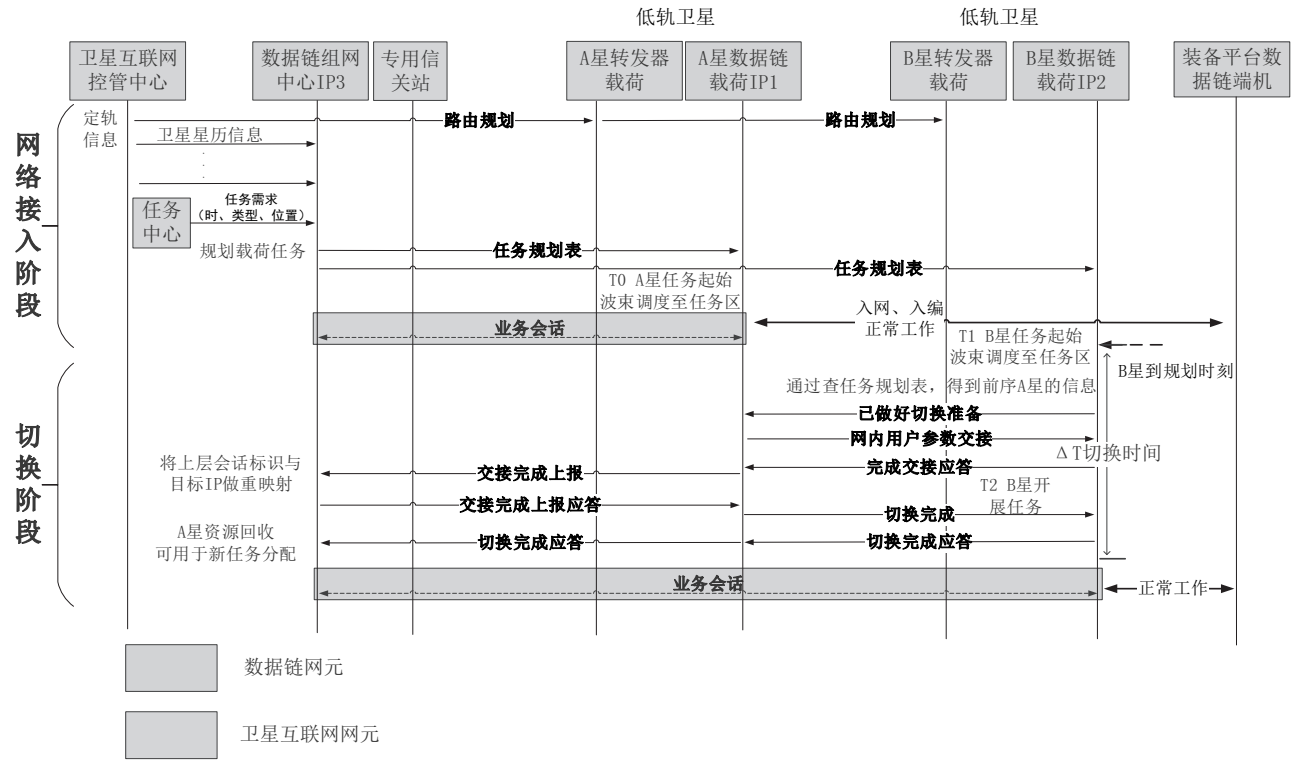

图 2 数据链端机移动性管理各阶段流程图

（1）网络接入流程

卫星数据链载荷端机为了正常工作，一方面需要在卫星互联网管控中心的管理下能够完成数据的转发，另一方面需要在数据链组网中心的管理下，按任务完成数据链网络参数的配置。其中，卫星数据链载荷端机的 IP 地址遵循卫星互联网管控要求，一般在正常工作状态使用固定分配的 IP 地址。卫星互联网管控中心接收数据链组网中心的任务上报，根据卫星星座的构型做需相关卫星数据链载荷端机与地面网络的路由规划，并经卫星网络管控接口完成对卫星、信关站等天基承载网络数据路由转发节点的路由规划更新。

地面终端接入卫星的方法有随域接入和按规划接入等方式。由于数据链应用的特殊性，现阶段一般采用预先规划的方式实现接入过程。

首先，数据链组网中心定期接收卫星互联网管控中心下发的卫星星历信息（轨道外推结果），当接收到任务中心下发的任务后，根据任务的类型、时段、区域，规划服务该次任务的低轨卫星数据链载荷。任务规划信息经数据链网络管理接口下发给各相关卫星数据链载荷端机，卫星数据链载荷端机将得到该次任务的“虚拟平台编址号”，在哪个圈次开始工作，以及波束照射的位置信息。若该卫星在不同时段服务多个数据链子网，则其拥有多个“虚拟平台编址号”，按当前服务的任务确定其当前的“虚拟平台编址号”。

当卫星运行到规定的圈次位置时，按要求将服务波束指向规定位置，并在运行过程中，根据自身的位置和姿态，令照射满足服务要求。装备平台的数据链端机到达任务区后，即可开始正常工作，实现装备平台的数据链端机的按时隙要求完成卫星接入。

卫星数据链载荷端机将把完成接入的装备平台的数据链端机计入本站点服务的端机列表，并按数据链规则上报数据链组网中心，中心获取当前装备平台的数据链端机的位置和接入所用站点完成接入流程。

（2）卫星的切换流程分析

现有条件下由于低轨卫星波束数量和照射范围有限，为了持续服务任务区域，地面需要规划一系列卫星，实现对某区域（凝视固定位置）或该航迹（跟随移动目标）的连续覆盖，按照一下步骤完成切换流程。

根据数据链组网中心的任务规划，在前序卫星 A 星移出服务区前，后序卫星 B 星将提前开机并将波束照射到服务区域。B 星的数据链载荷端机此时使用与卫星 A 相同的数据链网络参数，以及相同的“虚拟平台编址号”。

B 星完成上述操作后，向 A 星发送“READY”指令，告知 A 星自身已具备工作状态；A 星将当前接入其站点该子网的装备平台的数据链端机的用户信息，发送给 B 星；B 星向 A 星回复确认应答；A 星收到 B 星的确认应答后，向数据链组网中心发送切换交接完成上报。

数据链组网中心根据站点 IP 的变化，向管理数据链会话与 IP 地址映射的网络设备发送会话 IP 重映射

的设置信息，在全网范围完成该数据链子网的会话指向 IP 的更新；数据链组网中心完成会话的映射更新后，向 A 星发送交接完成上报应答；A 星接收到数据链组网中心发来的交接完成上报应答后，向 B 星发送切换完成指令；B 星收到切换完成指令后，按数据链网络规划要求开始正常工作和数据转发，并向 A 星发送切换完成应答；A 星收到切换完成应答后，停止工作，并向数据链组网中心发送切换完成应答；数据链组网中心接收后，回收 A 星资源，用于其他任务分配。

至此，完成 A 星和 B 星的切换，该过程中，装备平台的数据链端机无感。

4 结束语

通过低轨卫星搭载数据链载荷可以扩展数据链投送范围，是未来广域作战的发展方向。解决用户终端与卫星间的切换问题是数据链低轨卫星关键问题之一。本文初步描述了简单场景的数据链直连卫星应用的移动性管理的相关流程。后续的主要工作为针对实际的卫星星座场景开展直连数据链应用的切换仿真，并针对该流程仿真测试其切换时延，给出切换策略的约束要求。后续还将研究基于广域覆盖情况下，数据链随域接入卫星网络的可行性。

参考文献：

[1] 赵文栋,张磊,彭来献,刘熹,徐正芹,徐任晖,王向东.战术数据链[M].北京:清华大学出版社,2019.

[2] 孙召,陶孝锋.低轨卫星 Link16 数据链关键技术研究[J].空间电子技术,2021,18(03):64-69.

[3] 文猛,王俊毅,胡汭等.美军数据链最新发展及趋势研究[J].军事通信技术,2016,37(04):86-91.

[4] 杜利刚,田万勇,潘积远.天地一体化数据链网络架构研究[J].现代导航,2016,7(06):418-421.

[5] 苏昭阳,刘留,艾渤等.面向低轨卫星的星地信道模型综述[J/OL].电子与信息学报,2024,1-19.

[6] 柯知非,黄石生,李玉良等.低轨大型遥感星座发展现状及其关键技术[J].航天返回与遥感,2023,44(01):93-101.

[7] 聂敏,车俊丽,杨光等.基于可变仰角阈值的低轨道量子卫星切换策略及性能分析[J].现代电子技术,2018,41(17):1-5+10.

[8] Papapetrou E , Karapantazis S , Dimitriadis G ,et al.Satellite handover techniques for LEO networks[J]. International Journal of Satellite Communications and Networking, 2004

[9] 刘田,谢岸宏,李刚磊等.一种缓解低轨卫星馈电切换中用户群切换的算法[J].电讯技术,2021,61(06):697-702.

[10] 苏国强.LEO 卫星网络的移动 IP 管理与切换策略研究[D].国防科技大学,2017.

[11] Zhang, Z., Guo, Q. An IP mobility management scheme with dual location areas for IP/LEO satellite

network.　J. Zhejiang Univ. - Sci. C　13, 355－364 (2012).

[作者简介]

李靖　（1983～）男，硕士研究生，高级工程师，主要从事卫星通信系统设计和相关设备的研发工作

高凌云（1977~），女，博士，部长/工程师，主要从事卫星通信、卫星导航的系统设计和相关设备研制工作。

傅裕（1991~），男，硕士，工程师，主要从事卫星通信系统软件设计和相关研制工作。

基于天地一体化的中国深空测控系统

王振河，王冬冬，汤允昭，李超

（北京遥测技术研究所 北京 100094）

摘要：对于中国后续发展的以国际月球科研站为代表的载人深空航天器，地面中心与其保持全时无缝测控通信导航将是重要需求。中国当前的地基深空测控系统，不能满足该需求。在借鉴天链中继卫星系统和北斗卫星系统成功应用基础上，提出先后按天链深空、地月深空两个阶段论证建设天基深空测控系统。在中国地面中心统一控制下，通过综合发挥地基深空测控系统、天基深空测控系统的天地一体化测控优势，提高中国深空测控系统的可用性，满足以载人月球探测为代表的载人深空探测全时无缝测控通信导航需求。此外，该设想可进一步促进中国地基测控网、天基测控网和深空测控网的融合创新。

关键词：深空测控系统；天链中继卫星；地月平动点中继卫星；载人月球探测

China′s Deep Space TT&C System Based on Space-earth Integration

WANG Zhenhe，WANG Dongdong，TANG Yunzhao，LI Chao

（Beijing Research Institute of Telemetry, Beijing 100094, China）

Abstract: For China’s subsequent development of manned lunar exploration as a representative of the deep space spacecraft,the ground center and its full-time seamless communication and navigation will be an important demand.China’s current ground-based deep space TT&C system can not meet the needs.On the basis of the successful applicationof TDRSS and BEIDOU satellite system,the space-based deep space TT&C system is demonstrated in two phases:deep space of TDRSS and deep space of Earth-moon.Under the unified control of China ground center,the usability of China’s deep space TT&C system is improved by taking full advantage of the space-ground integration of ground-based and space-based TT&C system,to meet the requirements of the full-time seamless TT&C navigation for deep space exploration represented by manned lunar exploration. In addition,the concept can further promote the integration and innovation of China's ground-based network、space-based network and deep space TT&C network.

Key words: Deep space TT&C system；Tianlian TDRSS; Lunar relay satellite; Manned lunar exploration

1 引言

深空测控系统是对执行深空探测任务的航天器进行跟踪测量、监视控制和信息交换的专用系统，其在深空探测任务中具有不可替代的重要地位和作用[1]。

美国NASA深空网是目前世界上能力最强、规模最大的深空测控系统,主要包括美国戈尔德斯通、西班牙马德里和澳大利亚堪培拉三个深空站，属地基深空测控系统。该系统始建于1958年，在全球范围内基本按经度间隔120°规则均匀布站，可实现对深空航天器的连续跟踪、100%测控覆盖。随着时间推移，美国NASA深空网沿着该技术路线迭代发展，终成现在规模。

中国深空测控系统是伴随着探月工程“绕”“落”“回”三步走的战略步伐逐步建设和发展起来的。主要包括国内佳木斯、喀什和阿根廷萨帕拉三个地基深空站，三站位置在地球经度上分布不均匀，对深空航天器不能实现连续跟踪、测控覆盖率约90%左右[1][2]。

随着载人航天发展，载人航天器和地面中心间的全时无缝通信已成为关系航天员安全、任务成败的关键问题。基于此，人们开始思考体系结构和工作方式上的根本变化，提出了中继卫星系统概念，测控系统也逐步由地基测控系统向天地一体化测控系统演变。如20世纪80年代中期，美国跟踪与数据中继卫星系统(TDRSS)建成后，其载人航天器、中低轨卫星的测控任务逐步由中继卫星系统代替地面站完成，用于航天器运行段测控的地面站相继关闭或移作它用[3]。中国从2008年以来建设运行的天链中继卫星系统，具有为中低轨卫星、神舟飞船、中国空间站等航天器提供高可靠、实时和全球覆盖的天基测控与数据中继服务的能力，为多批次航天员/科学家在中国空间站的常驻发挥了重要的测控通信保障[4][5]，而过去由十几个国内外地面测控站和测量船组成的地基测控系统仅能实现18％左右的测控覆盖率。

中国当前的地基深空测控系统，为中国的嫦娥探月、火星探测等深空探测任务发挥了重要作用，持续做出了重要贡献，但当前任务均属非载人深空探测任务。随着以国际月球科研站为代表的载人深空探测任务的蓬勃发展，地面中心与其保持全时无缝测控通信导航将是重要需求，这就要求当前不具备100%测控覆盖、且国外站存在一定运行风险的中国深空测控系统，有必要发展完善、以适应未来载人深空探测任务需求。借鉴中国载人航天任务的发展历程和成功运行实践，天链中继卫星系统从无到有、从弱到强，推动中国航天测控系统由地基系统稳健发展为天地基一体化测控系统。当前，中国正面临着深空探测任务由无人向载人发展的关键期，迫切需要立足国家航天测控系统整体现状，参照现有的天地基一体化测控系统，采取继承发展、稳妥可靠、行稳致远的思路，通过重点拓展天链中继卫星系统的应用效能，探索建立发展天

地基一体化的深空测控系统，低成本高效益地满足未来载人深空探测任务需求。

2 空间探索任务及对深空测控系统的需求

2.1 空间探索任务

文献[6]中，包为民院士指出：世界航天科技发展迅速，载人空间站、太空旅游、载人月球探测等航天任务需求持续增长，月球、小行星等空间资源的开发利用、在轨制造已成为国际热点，世界航天已进入以大规模互联网星座、太空资源开发与利用、载人月球探测和大规模深空探测等为代表的新阶段[6]。中国在成功完成探月工程三期任务基础上，后续规划建设国际月球科研站/月球基地、载人月球探测、火星探测和小行星探测等重点任务[7][8]。

2.2 对深空测控系统的需求

包院士的论述，高屋建瓴，明确了中国后续的空间探索任务。分解到深空测控系统方面，可分析提炼出如下需求。

2.2.1 高精度的深空时频基准

这是深空探测对深空测控系统的基本要求。只有建立稳定的高精度深空时频基准，才能对深空探测器顺利实现测控通信导航。

2.2.2 更强的深空测控通信能力

为适应月球探测和遥远行星探测工程需要，需要深空测控系统具有更大的EIRP值、G/T值。主要技术途径：

1）增大收发天线增益G值。方法：增大天线口径D，如单天线口径直接增大、或天线组阵；或提高天线收发频率f。

2）研制更大功率P的发射机、更小T值的接收机。更小T值实现方式，减少天线和接收LNA间的损耗L、减小LNA的噪声系数F、采用低温LNA设备。

3）发展深空激光通信。激光链路在近地空间已开始应用，优势明显，后续需积极发展深空激光链路。

2.2.3 100%的测控通信覆盖

随着载人空间站、太空旅游、月球科研站/月球基地、载人月球探测等载人航天任务的持续增长。对

这些载人航天器/探测器稳定保持100%的测控通信覆盖已是必不可少的要求。

2.2.4 同时服务更多目标

适应航天器/探测器进入空间的大规模需求，要求测控系统同时对更多目标实施测控通信。此时，大口径窄波束的巨型天线同时对多目标航天器实施测控通信比较困难，而多天线、相控阵天线就表现出独特的优势。

2.2.5 高可用的深空测控系统

随着世界航天进入以大规模互联网星座、载人月球探测和大规模深空探测为代表的新阶段。对（深空）测控系统的长期稳定可靠性提出了更高的要求，系统的可用度必须满足新阶段航天测控需求。主要考虑两方面因素：

1）地球表面大气层对微波和激光信号传输产生的影响需要采取高性价比方式解决。这些影响主要包含：降雨衰减、大气湍流、降雨去极化衰减、大气吸收衰减、云雾衰减、沙尘暴衰减、闪烁衰减、法拉第旋转衰减等。

2）国外建站的风险不容忽视。当今世界百年未有之大变局正加速演进。国外建站，容易受国际关系、当地政局和治安影响，存在不能长期稳定由中国地面控制中心可靠使用的可能性，将降低测控系统长期运行的可靠性。

2.2.6 航天器间的实时通信

以载人航天为例。并行同时实施载人空间站、太空旅游、载人月球探测等载人航天任务时，载人航天器间的航天员/科学家实时交流是一个无法回避、必须解决的现实问题。如：2030年左右，航天员驻留国际月球科研站时，与LEO轨道中国空间站的航天员进行实时通信交流将是一件自然而然的事情。

3 国外深空测控系统应用现状

目前，美国、欧洲航天局、中国已建立了深空测控系统。俄罗斯、日本、印度等国家也研制建设了自己的深空测控设备，但并未形成完整的深空测控网。这些深空测控系统均属地基系统。文献[1]列出了全球深空测控设施布局，引用如图1所示[1]。

图1　全球主要深空测控设施布局

3.1 美国 NASA 深空测控网

美国NASA深空网由在全球基本均匀分布的三个深空通信综合设施组成，分别位于美国戈尔德斯通、西班牙马德里和澳大利亚堪培拉，深空网的操作控制中心位于美国加州帕萨迪纳的喷气推进实验室（JPL）。NASA深空网是目前世界上规模最大、能力最强的深空测控系统。该系统始建于1958年，建设背景是美苏太空竞赛，美国为顺利完成阿波罗登月任务，在全世界众多盟友国家范围内精选站址、全球均匀布局，以实现对深空航天器的连续跟踪、100%测控覆盖。1961年建成包括戈尔德斯通、澳大利亚伍默拉（Woomera）和南非约翰内斯堡（Johannesburg）3个深空站系统；之后在1965年新建了西班牙马德里和澳大利亚堪培拉两个深空站。直到1974年，马德里、堪培拉取代了伍默拉和约翰内斯堡（NASA关闭），形成了目前的三站格局。文献[1]列出了美国NASA深空网布局，引用如图2所示。

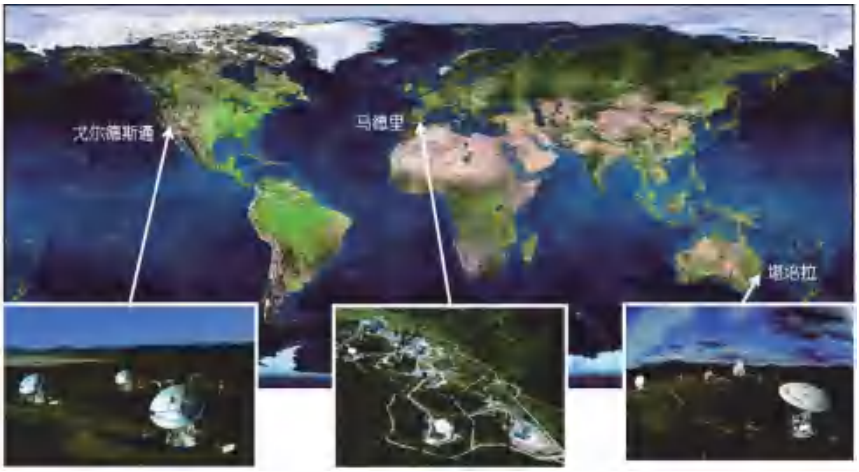

图2 美国NASA 深空网布局

戈尔德斯通深空通信综合设施，位于美国加州的莫哈维沙漠。建有70m天线1个，34m高效率（HEF）天线1个，34m波束波导（BWG）天线4个，正在新建1个34m BWG天线。

马德里深空通信综合设施，位于西班牙首都马德里以西60km。建有70m天线1个，34m高效率天线1个，34m波束波导天线2个，目前有2个34m波束波导天线在建。

堪培拉深空通信综合设施，位于澳大利亚首都堪培拉西南40km ，建有70m天线1个，34m高效率天线1个，34m波束波导天线2个，目前有2个34m波束波导天线在建。

3.2 ESA 深空测控网

ESA深空网的建设始于1998年，目前已经建成了全球分布的三个具有35m口径天线的深空站，分别是澳大利亚新诺舍站、西班牙塞弗雷罗斯站和阿根廷马拉圭站，三个深空站可以由位于德国达姆施塔特的欧洲空间操作中心（ESOC）进行远程操作控制。ESA是世界上第二个建成全球布站深空测控网的航天机构。

新诺舍深空站，位于澳大利亚西部珀斯市以北150km新诺舍镇以南8km，2003年建成。

塞弗雷罗斯深空站，位于西班牙马德里以西的埃维拉省塞弗雷罗斯城以南12km，2005年建成。

马拉圭深空站，位于南美洲阿根廷西部门多萨省马拉圭市以南30km，距离布宜诺斯艾利斯市1200km，2012年建成。

4 中国地基深空测控系统应用现状及优缺点分析

4.1 应用现状

中国深空测控系统分三个阶段建立。在探月工程一期中，利用中国服务于近地空间地球轨道卫星任务的航天测控网完成40万公里以远目标测控任务，实现了远距离测控技术的突破；在探月工程二期中，建设了国内2个深空站，即：佳木斯66m深空站、喀什35 m深空站，二者均于2013年建成，初步构建深空测控网，具备了独立实施深空探测任务测控支持的能力。在探月工程三期中，限于国力，不能象美国NASA、欧洲ESA深空网那样在全球范围内均匀布站，在阿根廷（萨帕拉）建设了35 m的第3个深空站，从而形成了全球布局、功能体系较完备的深空测控网。从整体布局而言，中国深空测控网并不是最优的全球布局，国内佳木斯、喀什两个深空站的经度差只有约54°，对月球及深空探测器的测控覆盖率约为60%，即每天平均约有9~10个小时不能对月球及深空探测器实施测控；喀什、阿根廷两个深空站的经度差约146°，可实现测控覆盖搭接；而佳木斯、阿根廷两个深空站的经度差达到160°，无法实现10°仰角的测控覆盖搭接。因此，中国深空测控网对深空航天器的测控覆盖率只能接近90%，即每天平均约有2~3个

小时不能对月球及深空探测器实施测控。文献[1-2]列出了3个深空站形成的对月球及深空探测器测控覆盖情况，引用如图3所示[1][2]。

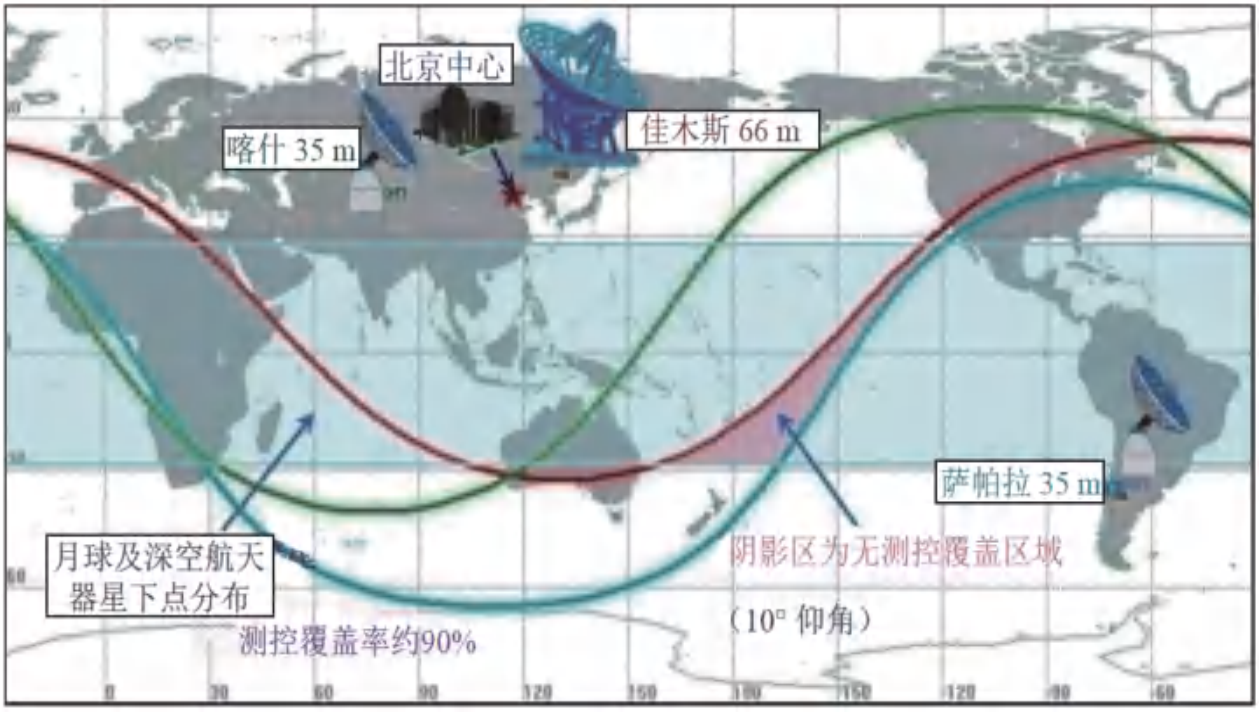

图3　中国深空网对月球及深空探测器覆盖率示意图

4.2 发展展望

文献[1-2]指明了中国地基深空测控网的后续发展方向。随着后续月球探测工程和行星探测工程的实施，中国地基深空测控网在规模和性能上都将会有大幅度的提升。文献[1-2]列出的主要技术发展路径为：

1）更强的深空测控通信能力。主要包括构建地基天线组阵系统、应用Ka频段测控通信、研制100KW级大功率发射机、发展深空光通信技术四个方面[1][2]。

2）更高的深空导航精度。主要包括构建相位参考干涉测量系统、发展地月空间长基线干涉测量技术。利用国内外深空站、中国VLBI（甚长基线干涉测量技术）天文观测网、甚至未来的月球VLBI天线，通过解算相位模糊度，可为后续深空探测任务提供更高精度的导航支持。

3）更多的科学探测应用。主要包括高精度时空基准测量、天体引力场测量、射电天文观测三个方面。

4.3 优缺点分析

对照2.2节分析提炼出的深空测控系统需求，发现地基深空测控系统存在如下特点。

4.3.1 优点

中国的地基深空测控系统，具有高精度的深空时空基准、强大的深空测控通信能力、成熟的工程建设运行实践，为中国的嫦娥探月、火星探测发挥重要作用,持续做出重要的贡献；随着后续系统的发展完善，将具有更高精度的深空时空基准、更强大的深空测控通信能力、更高的深空导航精度，将为中国后续的国际月球科研站/月球基地、载人月球探测、火星探测和小行星探测等重点任务持续发挥重要作用、继续做出重要贡献。

4.3.2 缺点

1）对月球及深空探测器不能实现100%的测控通信覆盖。由于中国深空测控站在全球布站不均匀，依靠国内佳木斯、喀什两个深空站时，对月球及深空探测器的测控覆盖率约为60%，即每天平均约有9~10个小时不能对月球及深空探测器实施测控；依靠国内外佳木斯、喀什、阿根廷三个深空站时，对月球及深空探测器的测控覆盖率约为90%，即每天平均约有2~3个小时不能对月球及深空探测器实施测控。

2）对航天器/探测器同时服务的目标较少。由于三个深空站的天线口径是35m、66m的大口径窄波束巨型天线，后续天线组阵的整体效果也与之等同，只能对同一波束内的多个目标实施测控服务。但由于波束窄、目标运动矢量差异大，将不可避免导致同时服务的航天器目标较少。

3）高可用性风险需持续关注。地球表面大气层客观存在，它对微波和激光信号传输产生的影响始终存在。如对微波信号传输而言，频率越高导致的降雨衰减就越大，示例如图4所示。若欲解决该问题，需要投入更多的资源、增加系统余量、以抵消这种影响,但费效比可能较差。另外，当今世界百年未有之大变局正加速演进。国外建站，容易受国际关系、当地政局和治安影响，存在不能长期稳定由中国地面控制中心可靠使用的可能性，将降低深空测控系统长期运行的可用性。

4）航天器间的实时通信不易实现。中国地基深空测控系统发展的一个重点方向是强化对单一深空航天器目标的测控通信能力，对于各种轨道航天器间的实时通信、或者异轨星座互联网构建着力不多，对以LEO轨道的中国空间站、月球科研站间航天员的实时通信交流为代表的典型通信需求缺乏实现手段。

后续，需大力深化完善中国地基深空测控系统优势，充分发挥地面大天线作用，有效满足深空探测器与地面中心间的高速率测控通信需求。同时，适应航天发展需要，扬长避短，充分发掘天基深空测控系统优势，天、地基融合发展、创新应用，通过综合发挥天地一体化深空测控系统优势，高费效比、高可用性、全时无缝满足中国未来空间探索航天任务需求。

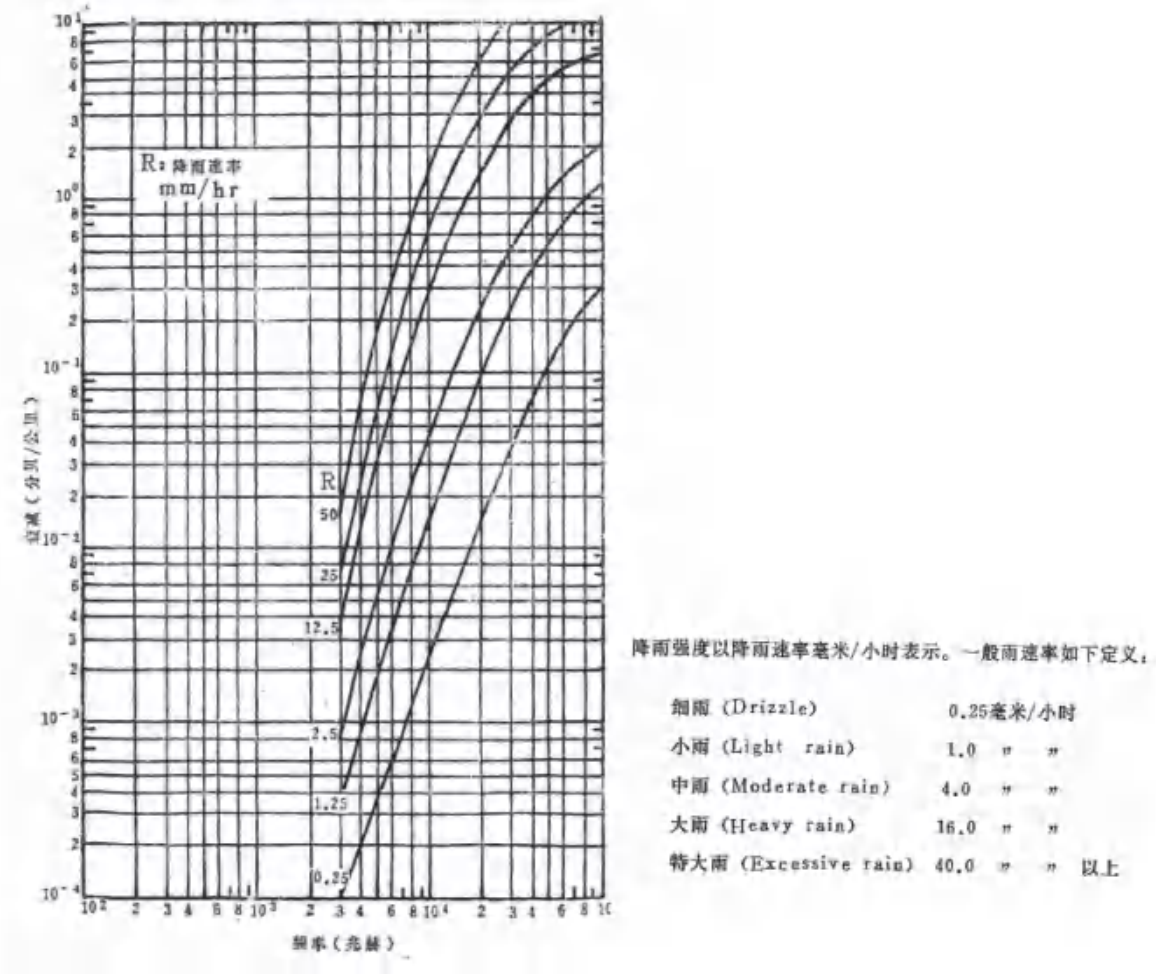

图4 地表附近降雨强度、公里雨衰和信号频率间关系示意图

5 天基深空测控系统发展建议

5.1 技术路线分析

文献[9]中，借鉴天链中继卫星系统的设计、建设、应用、发展实际，提出一个“鹊桥卫星-天链卫星”的星星双中继通信设想。从几何可见性角度进行多种条件的覆盖仿真分析，并从传输体制、链路设计、系统组成、捕获跟踪、工作流程、整体定位等多方面进行研究分析，完成了基于星星双中继的国际月球科研站全时无缝通信研究。在地面控制中心统一控制下，通过地面深空测控网、星星双中继的综合利用，国际月球科研站与地面控制中心间将具备全时无缝通信的技术能力。

文献[9]中，鹊桥卫星、国际月球科研站均属深空航天器。加装对天面天线的下代天链卫星，可以实现与下代鹊桥卫星的全时无缝通信。换言之，在忽略深空遮挡情况下，天链卫星自然也具备与其他深空航天器全时无缝通信的技术条件。其典型分析情况如下。

5.1.1 天链卫星覆盖鹊桥卫星仿真情况

仿真场景：

天链星：先采用当前天链星的三节点轨位；后增加第四节点，位置暂定在东、西节点外侧的中间位置。

鹊桥卫星：采用已到寿、轨道公开的地月拉格朗日L2点的halo轨道。卫星实际轨道可能由变化，不过与约45×10^4 km的星间距离相比，其轨道变化量为小量，对覆盖性仿真分析结果影响有限。

文献[9]列出了仿真情况，引用具体见表1。

表1 天链星覆盖鹊桥星仿真情况

天链星	当前在轨	加装对天载荷（三节点）		加装对天载荷（四节点）
星间天线	对地	对地+对天	仅对天	仅对天
假定天线转动范围	±45°圆锥角	±45°、±60°圆锥角	±60°圆锥角	±60°圆锥角
覆盖率	约75%	100%	约80%	100%
扩大天线转动范围	跟据实际情况确定	100%，重叠段增加	优于约80%，但小于100%	100%，重叠段增加，第四节点天链星轨位选择更灵活
应用分析	需大量挤占服务于中低轨航天器的天链星系统资源	需大量挤占服务于中低轨航天器的天链星系统资源	性能居中	对天星间天线服务深空航天器、对地星间天线服务地球中低轨航天器，均100%覆盖； 星间链路天地分开；同时又发挥天链星节点作用，准实时实现地基、近地、深空目标间的信息传递与交换。

5.1.2 天链—鹊桥星星双中继间星间微波链路预算情况

条件设定：

天链星对天天线口径为4.2m抛物面天线，鹊桥卫星对天链天线暂按1m抛物面天线设计。

Ka频段1m抛物面天线，按常规考虑，接收G/T值可取15dB·K^{-1}；发射EIRP值可取60dBW。

Ka频段4.2m抛物面天线，按常规考虑，接收G/T值可取27dB·K^{-1}；发射EIRP值取70dBW。

星星间传输的无线信号，需要星间天线动态跟踪，系统标校后存在剩余误差，导致天线不能完全对准，将由此导致跟踪误差，另外还有诸如极化损失等内容，所有这些均归算为信号电平损失，取值2.5dB。

通信质量，UQPSK调制解调体制，I路传输测量信息、Q路传输通信信息，按LDPC1/2编码方式，解调门限取值：1×10-7的误码率下，理论解调门限Eb/N0≤3.0dB；考虑解调损失，设计解调门限Eb/N0≤4.3dB。

设计采用UQPSK调制体制，信号能量主要集中于通信Q支路。星星双中继链路设计时，暂按Q支路占用全部EIRP进行设计。

文献[9]列出了预算情况，引用具体情况见表2。

表 2　星星双中继间星间微波链路预算

天链星	发信息 10 Mbit·s^{-1}	收信息 10 Mbit·s^{-1}
调制方式	UQPSK	UQPSK
编码方式	LDPC1/2	LDPC1/2
星间距离（Km）	450000	450000
工作频率（GHz）	Ka 频段	Ka 频段
信息速率（Mbit·s^{-1}）	10.0	10.0
[EIRP](dBW）	70.0	60.0
空间损耗(dB)	232.7	233.8
其他损耗（dB）	2.5	2.5
总传播损耗[L](dB)	235.2	236.3
[Gr/Tr]（dB·K^{-1}）	15.0	27.0
接收[Eb/N0]（dB）	8.4	9.3
理论解调门限（dB）	3.0	3.0
设计解调门限（dB）	4.3	4.3
设计余量（dB）	4.1	5.0

上述链路条件下，天链星向鹊桥卫星发送信息速率为10 Mbit·s^{-1}的前向信号，链路Eb/N0设计余量为4.1dB；天链星接收鹊桥卫星信息速率为10 Mbit·s^{-1}的返向信号，链路Eb/N0设计余量为5.0dB。该组双向链路均满足3dB余量条件，说明技术可行，具有实施性。

5.1.3 星星双中继通信链路情况

星星双中继通信设备主要包括：鹊桥卫星一体化通信终端、天链卫星一体化通信终端、星地通信链路设备、地面通信网和控制中心。文献[9]列出了国际月球科研站通信链路情况，引用如图5所示。

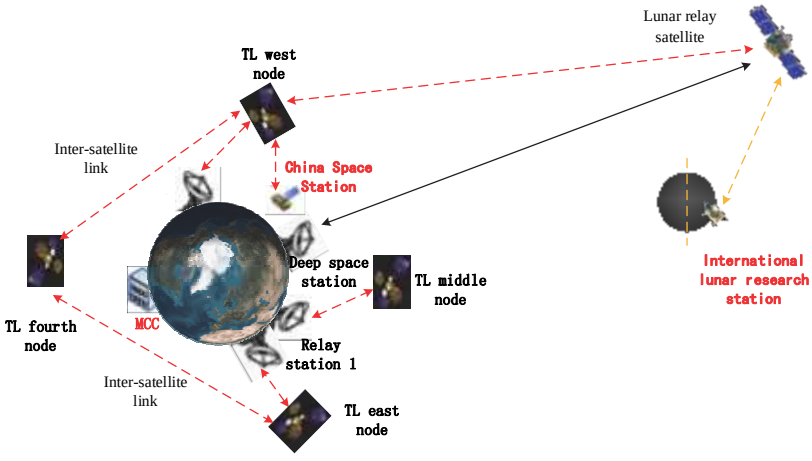

图5　国际月球科研站通信链路

5.2 北斗卫星支持

5.2.1 导航分析

文献[10]表明，北斗三号卫星星座由3类轨道卫星组成。第一类为GEO地球同步轨道，卫星3颗；第二类为IGSO地球倾斜同步轨道，卫星3颗；第三类为MEO中圆地球轨道，卫星24颗，均匀分布在3个轨道面上。星上配置了氢原子钟、铷原子钟、星间相控阵天线、收发信机、自主星历生成等软硬件，星间采用Ka频段星间链路实现星间通信和测距，各类收发信息通过星上数据处理、路由交换，将所有卫星和地面站相互连接，实现单个或多个北斗地面站对整个卫星系统的测控和业务管理。文献[10]中列出了北斗星座星间链路拓扑及相控阵天线示意，引用如图6所示。

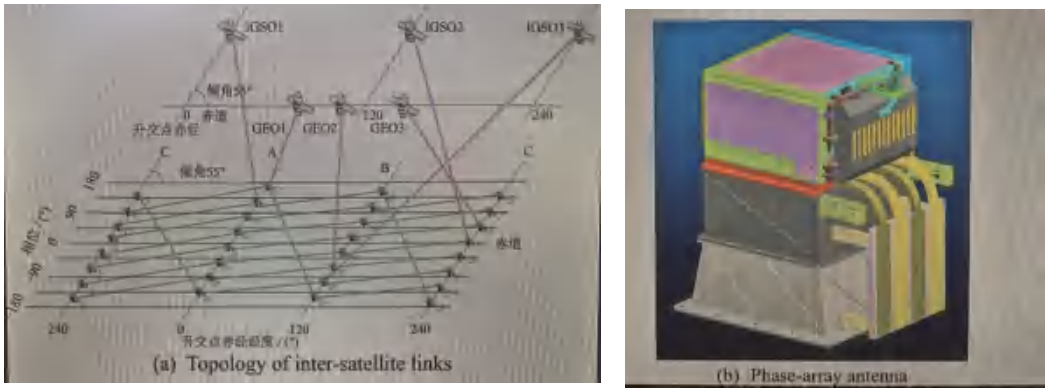

图6　北斗星座星间链路拓扑及相控阵天线示意

文献[11]表明，北斗三号卫星Ka频段星间相控阵载荷，在承载系统自身星间测量、数据传输等基础上，可将剩余链路、时隙等资源通过时分方式为高价值航天器用户提供测控支持服务。

根据文献[10-11]所述，结合天链星作用和贡献，可确认天链星为“高价值航天器”；据此，可将北斗三号星座的GEO卫星想定为“3+N”颗，其中“N”为天链星卫星颗数。后续天链星，严格按照北斗导航卫星系统协议，将与时频基准传递相关的北斗导航载荷纳入天链星中，并与天链星其他载荷开展整星一体化优化设计。天链星发射后，作为“准北斗”功能卫星，按协议要求与北斗卫星进行星间通信，实现时频基准由北斗卫星同精度传递到天链星、再通过天链星与深空航天器的星间链路，将时频基准传递到深空航天器上，最终实现深空航天器导航。

同时，时频基准由北斗卫星同精度传递到天链星后，天链星对地星间链路的时频基准也将同步提高，对地球中低轨航天器的服务效能也可得到显著改善。

5.2.2 第四节点天链星测控通信分析

1） 测控分析

第四节点天链星需布置在地球西半球GEO轨道的某定点附近，与国内任何地面站不能通视，国内地面站不能对该节点中继星实施测控通信；基于国外建站容易受国际关系、当地政局和治安等不利因素的影响，也不适合在国外建站对该节点中继星实施测控通信。基于上节导航分析，可基于北斗星座的强大功能，利用第四节点天链星与北斗卫星的星间链路，实现第四节点天链星的测控任务。基本流程如下：

返向遥测信息，由第四节点天链星通过星间链路，传递给某颗北斗卫星，通过北斗星座星间协议传递信息，将该遥测信息落地至北斗国内地面站，再通过地面中心间地地协议，经北斗地面中心将该遥测信息传递至天链地面中心，天链地面中心接收该遥测信息，经处理分析，掌握第四节点天链星状态。

前向控制信息，由天链地面中心产生，通过地面中心间地地协议，经北斗中心传递至北斗地面站，经星地链路信息上行传递至北斗卫星，通过北斗星座星间信息传递协议，将该控制信息传递至第四节点天链星。

在信息双向传递过程中，由于经历环节多，信息在信源、信宿间的传递时延可能较长，可能对信息传递实时性产生不利影响，需要在后续工作中论证设计解决。

2） 通信探讨

文献[11]表明，北斗卫星上已搭载了激光星间链路载荷，实施星间高速数传通信。受此启发，在后续各节点天链卫星上也搭载激光星间链路载荷，使第四节点天链星需转发的高速数据或深空航天器数据，通过激光链路传递至其它节点天链星，并通过天链星地链路数据落地，最终分发至各用户中心。

在星间激光通信工作期间，测控信息也可一并传递。

5.3 论证建设运行天链深空测控系统

5.3.1 目的

面向地月空间航天器，以航天员/科学家可能常驻的国际月球科研站/月球基地为典型测控通信目标，对地月空间航天器实现多目标、高可用、全时无缝测控通信导航。

5.3.2 建设内容

充分借鉴天链中继卫星系统和北斗卫星系统的成功建设应用实践[12-16]，融合创新，论证建设运行天链深空测控系统。主要内容如下：

1）深空测控通信。后续天链星采用四节点布置，采取当前成熟的Ka微波频段星间协议，星上均加装对天面深空大天线，如采用4.2m口径抛物面天线、或Ka频段大型相控阵多址KMA(Ka-band Multiple Access）

天线，以适应全时无缝、多目标的深空用户航天器需求[9]。

2）地月空间航天器导航。后续天链卫星上加装原子钟等时频设备[11]，且与北斗卫星建立星间链路[12]，进行星间测量通信[10]，将时频基准由北斗卫星同精度传递到天链星、再通过天链星与地月空间航天器的星间链路，将时频基准传递到地月空间航天器上，最终实现地月空间航天器导航[9]。

3）第四节点天链星测控通信。天链中心通过北斗卫星系统、利用天链/北斗星间链路实现对第四节点天链星的实时无缝测控；后续天链卫星上搭载激光星间链路载荷[17][18]，使第四节点天链星需转发的高速数据或深空航天器数据，通过激光链路传递至其它节点天链星，并通过天链星地链路数据落地，后分发至各用户中心。

4）建设运行天链星座骨干网。以四节点为骨架、星间激光为纽带、布置多颗天链星形成天链互联网星座（每个节点可布置数颗天链星）。每颗天链星上，舱内布置一体化终端，具备星上信号变换、数据处理、星间网络路由功能；舱外布置对天星间大天线、对地星间大天线和激光天线、对中继地面站星地天线、天链星间激光天线、对北斗星间天线等，具有Ka频段深空星间链、S/Ka微波与激光天基星间链、星地链、天链激光星间链、北斗星间链等。包含深空航天器在内的各类用户平台上安装相应的用户终端，接入天链星座骨干网，完成（深空）航天器多目标天基测控通信及星间协同任务。深空航天器可以灵活选择与天链中继星座、地面深空网通信。系统应用示意如图7所示。

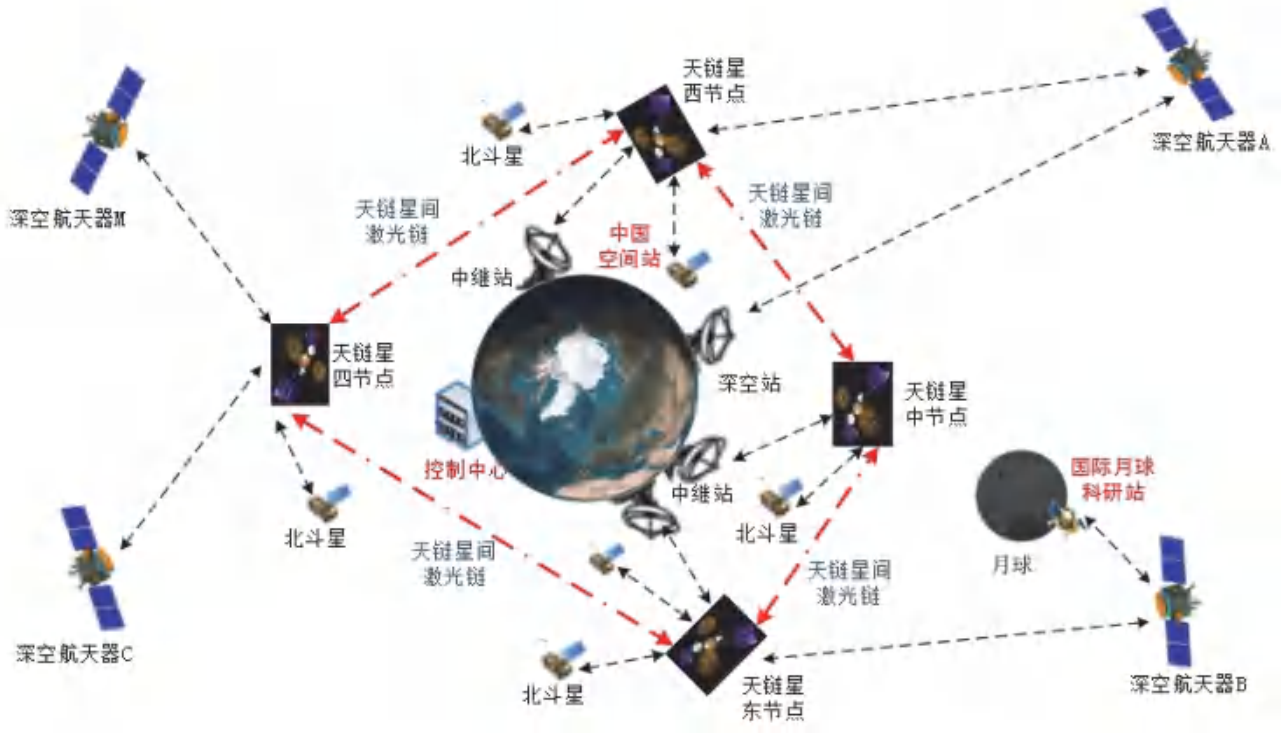

图7　基于天链深空的天地一体化测控系统应用示意

5）天地一体化深空测控系统融合应用。中国地面控制中心，实时无缝监控地面深空、天链深空测控系统，灵活调配二者资源，充分发挥天链深空、地面深空的天地一体化测控优势，满足以载人月球探测为代表的深空探测任务需求。

5.3.3 系统定位

天链深空、地面深空测控系统结合使用，可充分发挥天地一体化深空测控的综合优势：

1）地面中心可根据要求，灵活调配二者资源，制定二者有机结合的统一工作计划；

2）二者在深空航天器的共视覆盖范围内，都可以接收数据、传递至地面中心，从而实现数据接收的互为备份；向航天器发送控制信息时，可灵活在二者之间选择，增强系统工作稳健性；

3）天链深空星载天线口径比地面深空站小一个数量级，主要满足深空航天器全时无缝的高可用通信导航基本测控通信需求，如航天员/科学家与地面间工作生活的全时通信保障；对于面向各类科研试验任务的更高速率通信传输需求，需要由地面深空测控系统完成；

4）当仅处于天链深空的覆盖范围时，可充分发挥天链深空全时无缝覆盖的天基优势，高可靠、广覆盖完成地月空间航天器通信任务；

5）天链深空在轨应用之初，需在天地基的共视段落内，以地面深空系统为标尺，验证调校其通信性能；验证通过后，方可单独执行任务；长期在轨运行期间，天链深空状态发生较大变化后，仍需以地面深空系统为标尺，重新进行在轨测试，验证调校其通信性能。

5.3.4 主要性能比较

面向国际月球科研站、载人月球探测、载人火星探测及未来载人深空探测的多用户多种需求，从中国未来空天地综合测控网的系统实力、可用性、实时性、覆盖性、数传能力、同时服务深空用户数、性价比、航天器间的实时通信等多方面，对地基深空测控系统、天链深空测控系统及天地一体化深空测控系统的性能进行了性能比较。具体情况见表3。

表 3 系统性能比较

项目	地面深空测控系统	天链深空测控系统	天地一体化深空测控系统
系统实力	深空控制中心、国内深空站、国外阿根廷深空站	天链星系统、深空航天器配套的测控系统、北斗系统（支持）	深空控制中心、国内外深空站、天链星系统、北斗系统，由国内控制中心统一调配
可用性	大气层对地基站信号传输造成的多种衰减永久客观存在；且国外站受国际关	星间链路为真空、无大气层，信号没有如雨衰等各种大气衰减；	可用性高

	系影响存在运行风险	中国空间设施，由国内中心统一控制，可用性高	
实时性	国内站实时性强，国外站信息需通过卫通、跨洋通信传回国内，较弱	中国空间设施，由国内中心统一掌控，实时性强	实时性强
覆盖性	对深空航天器覆盖率上限约90%	天链星对天天线可100%覆盖深空航天器； 对天天线执行深空任务，对地天线执行常规天基测控任务	对深空航天器和中低轨航天器均有100%覆盖能力
数传能力	深空站天线口径大，数传速率可达数百兆bit·s-1。	近期星载天线尺寸小，数传速率可达十兆bit·s-1； 未来采用更高频率微波或激光传输，数传能力将逐步提高	高低数传速率按需传输，更好满足各类用户需求
同时服务能力	基本一天线跟踪一目标。同时服务用户数较少	一颗天链星含对天对地至少两幅星间天线，跟踪多目标的能力强。同时服务用户数较多	两系统结合，同时服务深空用户数多
性价比	深空站采用激光或更高微波频率信号，始终受大气影响，选址建设维护耗资巨大，性价比较弱	天链互联网中星间链路载荷一体化改造、系统综合利用，性价比高	性价比高
航天器间的实时通信	较难	通过天链/北斗互通、中低轨航天器天地一体化测控、天链卫星深空近地一体化测控，在实现高低轨航天器间准实时通信的同时，可促进我国地基测控网、天基测控网和深空测控网的融合发展，高效益助力国家空天地综合测控网的建设发展	

5.3.5 试验探索

1）开展更高频段深空星间链路试验探索应用工作，如频率70GHz左右的V频段、120GHz左右的D频段。充分发挥微波高频率带来的天线高增益、星间真空无大气层各种衰减的突出优势，在同样天线面积情况下，可有效提高深空测控的测控通信速率。相比Ka频段，同口径V频段天线的增益约提高10倍，在其他条件不变时，测控通信速率可提高10倍；相比X频段，同口径V频段天线的增益约提高近100倍，在其他条件不变时，测控通信速率可提高近100倍，效果显著。而地面深空站受大气层影响，效果将减弱。对星间V/D频段天线，可试验探索采用大口径抛物面天线、或大型相控阵多址VMA(V-band Multiple Access)/ DMA(D-band Multiple Access)天线，以适应深空用户航天器高速率、多目标测控通信需求。

2）开展深空激光链路的试验探索应用工作[17][18]。首先瞄准地月空间星间激光链路试验探索应用，实现地月航天器间的高速测控通信，早日实现工程化稳定应用。

5.4 适时论证建设地月深空测控系统

1）启动条件。更高微波频段星间链路实现工程化稳定应用；深空激光链路实现工程化稳定应用；基于天链深空的天地一体化深空测控系统稳定运行、持续完善；天链互联网中继星相继到达设计寿命，需要更新换代。

2）论证研制发射下一代天链互联网中继星。完成天链互联网星座平稳过度与更新，其星间载荷需进行适应性更新，至少增加：与地月平动点中继星互联的的激光天线；服务深空航天器的激光天线、V/D频段大型抛物面天线或相控阵天线。

3）论证研制发射新一代深空航天器。其星间载荷技术/进度要求与下一代天链互联网中继星、地月平动点中继星协调匹配，星间载荷主要包含激光天线、V/D频段小型抛物面天线或相控阵天线。深空航天器可以灵活选择与地月平动点中继星、天链中继星或地面深空网通信。

4）论证研制发射地月平动点中继星并接入天链互联网星座。首颗地月平动点中继星推荐发射运行在拉格朗日L2点附近，试验同时兼顾服务月球航天器。在地月平动点中继星上，舱内布置一体化终端，具备星上信号变换、数据处理、星间网络路由功能；舱外布置深空星间微波天线（如Ka/V/D频段）和激光天线、地月平动点星间激光天线、对天链激光天线、对地面深空站星地天线等，具有Ka/V/D微波和激光深空星间链、地月平动点间激光星间链、对天链激光星间链、对地面深空站星地链等。北斗卫星时频基准，基于天链互联网星座，通过天链激光天线同精度传递到地月平动点中继星上，再通过地月平动点中继星与深空航天器的星间链路，将时频基准传递到深空航天器上，最终实现深空航天器测控通信导航。

5）建设运行地月空间高低轨异构的中继星互联网星座[19]。在首颗地月平动点中继星成功接入天链互联网星座、圆满完成深空航天器测控基础上，对后续地月平动点中继星的设计研制进行优化完善后，陆续向其它地月平动点发星及功能验证，逐步建设运行地月空间高低轨异构的中继星互联网星座，并持续进行优化完善。最终形成：以GEO轨道的天链互联网星座为低轨星座、以地月平动点中继星座为高轨星座，在地月平动点各中继星之间、天链中继星之间、地月平动点中继星与天链星之间，搭建激光星间链路，形成地月空间高低轨异构的中继星互联网星座，最终组成地月深空测控系统。

6）下一代天地一体化深空测控系统融合应用。中国地面控制中心，实时无缝监控中国的地面深空、地月深空测控系统，灵活调配二者资源，制定二者有机结合的统一工作计划，充分发挥地月深空、地面深空的天地一体化测控优势，满足以载人月球/火星探测为代表的并行交叉、大规模深空探测任务需求。

系统应用示意如图8所示。

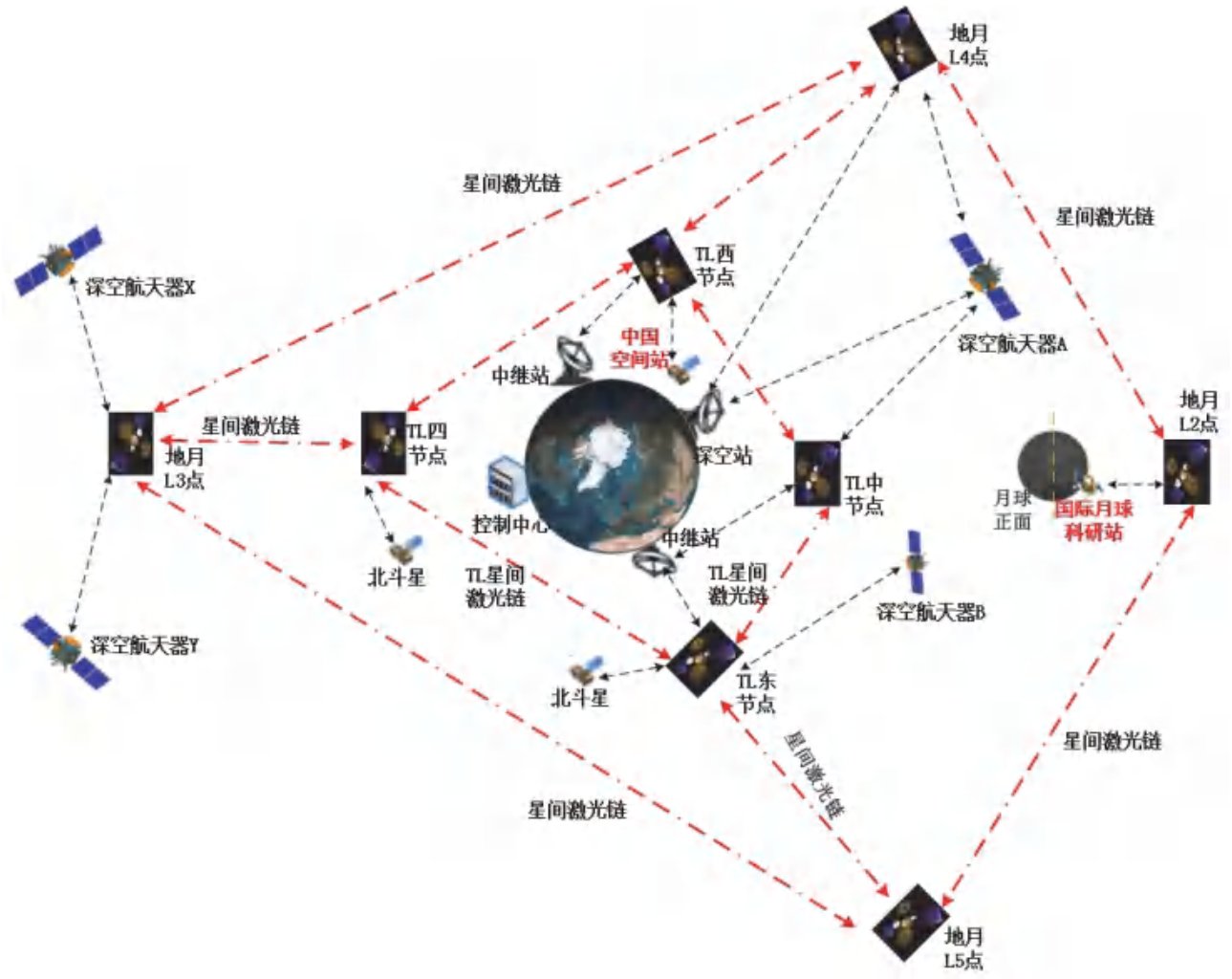

图8　基于地月深空的天地一体化测控系统应用示意

示例：深空航天器以V频段接入地月空间中继星互联网星座，中继星对天（深空）星载天线口径暂定5m，在其它条件不变情况下，地月深空测控系统与地面深空X频段测控系统的测控通信数传速率将基本相当。

6　结束语

中国的地基深空测控系统，在中国的嫦娥探月、国际月球科研站/月球基地、载人月球探测、火星探测及行星际探测，过去、现在、未来都将一直发挥重要作用、持续做出重要贡献。面向中国建设运行载人月球探测和大规模深空探测全时无缝测控通信导航的任务需求，本文提出先后按天链深空、地月深空两个阶段论证建设运行天基深空测控系统。在中国地面中心统一控制下，通过综合发挥地基深空、天基深空测控系统的天地一体化测控优势，提高中国深空测控系统的可用性，满足以载人月球探测为代表的深空探测高可用全时无缝测控通信导航需求。随着地月空间高低轨异构中继星互联网星座的持续应用完善，可进一步

促进地基测控网、天基测控网和深空测控网的融合发展，为建设“空天地”综合测控网发挥有益作用。

参考文献

[1] 吴伟仁, 李海涛, 李赞, 等. 中国深空测控网现状与展望. 中国科学: 信息科学, 2020, 50: 87-108.
Wu W R, Li H T, Li Z, et al. Status and prospect of China's deep space TT&C network (in Chinese). Sci Sin Inform,2020, 50: 87-108.

[2] 董光亮，李海涛，郝万宏，等. 中国深空测控系统建设与技术发展[J].深空探测学报，2018，5（2）：99-114.
DONG G L，LI H T，HAO W H，et al. Development and future of China’s deep space TT&C system[J]. Journal of Deep Space Exploration，2018，5（2）：99-114.

[3] 刘保国, 吴斌. 中继卫星系统在我国航天测控中的应用. 飞行器测控学报, 2012,31:1－5.
Liu B G, Wu B. Application of TDRSS in Chinese space TT&C (in Chinese). J Spacecraft TT&C Tech, 2012, 31:1－5.

[4] 李艳华，卢满宏. 天基测控系统应用发展趋势探讨. 飞行器测控学报, 2012, 31（4）：1－5.
LI Yanhua，IU Manhong. Trends of Applications of Space-Based TT＆C System. J Spacecraft TT&C Tech, 2012, 31（4）:1－5.

[5] 王磊,姬涛,郑军，范丹丹. 中继卫星系统发展应用分析及建议. 中国科学:技术科学,2022,52(2):303－317.
Wang L,Ji T,Zhen J,Fan D D,Investigations and proposals for data relay satellite systems. Sci Sin Tech,2022, 52(2):303－317.

[6] 包为民，汪小卫. 地月空间探索与开发的思考. 宇航学报, 2022（43）6：705-712.
BAO Weimin,WANG Xiaowei，Some Thoughts about Cislunar Exploration and Exploitation[J]. Journal of Astronautics，2022（43）6：705-712.

[7] 李春来，刘建军,左维，等. 中国月球探测进展(2011--2020). 空间科学学报, 2021, 41(1): 68-75.
LI Chunlai, LIU Jianjun, ZUO Wei, et al. Progress of China’s lunar exploration (2011–2020) (in Chinese).Chin. J. Space Sci., 2021, 41(1): 68-75.

[8] 裴兆宇,刘继忠,王倩,等.月球探测进展与国际月球科研站.科学通报, 2020, 65: 2577-2586.
PEI Zhaoyu, LIU Jizhong, WANG Qian, et al. Overview of lunar exploration and international lunar research station[J]. Chin. Sci. Bull., 2020, 65: 2577-2586.

[9] 王振河，孙宝升，刘永桦，等. 基于星星双中继的国际月球科研站的全时无缝通信. 空间科学学报, 2024, 44(3): 592-605.

WANG Zhenhe,SUN Baosheng,LIU Yonghua, et al. International Lunar Research Station Communication Based on Satellite Double Relay (in Chinese).Chin. J. Space Sci., 2024, 44(3): 592-605.

[10] 陈忠贵，武向军. 北斗三号卫星系统总体设计[J]. 南京航空航天大学学报, 2020, 52（6）: 835－845.
CHEN Zhonggui，WU Xiangjun. General design of the third generation BeiDou navigation satellite system［J］. Journal of Nanjing University of Aeronautics & Astronautics，2020，52（6）：835-845.

[11] 曹正蕊，张国亭，刘保国，等. 载人航天天基测控通信探析[J]. 遥测遥控, 2023, 44（5）：1－7.
CAO Zhengrui,ZHANG Guoting,LIU Baoguo,et al. Study on space-based TT&C and communication for manned space flight,Tracking and Command, 2023, 44（5）：1－7.

[12] 王家胜,齐鑫.为载人航天服务的中国数据中继卫星系统. 中国科学: 技术科学, 2014, 44: 235－242.
Wang J S, Qi X. China’s data relay satellite system served for manned spaceflight (in Chinese). Sci Sin Tech, 2014, 44: 235－242.

[13] 孙宝升.我国中继卫星系统在交会对接中的应用.飞行器测控学报,2014,33:183－187.
Sun B S. Application of China’s TDRSS in space rendezvous and docking missions (in Chinese). J Spacecraft TT&C Tech, 2014,33:183－187.
WANG Xiaobo,WANG Yi,LI Tie,et al. Research on application of digital multi-beam array antenna in aerospace TT&C system[J]. Journal of Telemetry,Tracking and Command, 2018 39(1):35-40.

[14] 黄惠明. 我国第一代中继卫星地面应用系统发展建设的思考. 飞行器测控学报, 2012, 31:1－5.
Huang H M. Reflections and development of the ground system of the first generation CTDRSS (in Chinese).Spacecraft TT&C Tech, 2012, 31:1－5.

[15] 王振河．TDRSS 航天器用户终端一体化设计初探[J]．飞行器测控学报，2009，28(5)：14—18.
wang Zhenhe．Research on Integrated Design of TDRSS Customer Spacecraft Terminals[J]．Journal of spacecraft TT＆.C Technology，2009，28(5)：14-18).

[16] 李于衡, 罗斌, 郭文鸽, 等. 中继卫星 Ka 频段支持飞船再入返回通信可行性分析. 载人航天, 2015, 21: 582－588.
Li Y H, Luo B, Guo W G, et al. Feasibility analysis of using Ka-band of TDRS to support wireless communication for spacecraft reentry (inChinese). Manned Spaceflight, 2015, 21: 582－588.

[17] 刘向南，王建军，李晓亮，等. 面向太阳系边际探测的激光通信方案研究[J]. 遥测遥控, 2022, 43（4）：62－69.

LIU Xiangnan, WANG Jianjun, LI Xiaoliang, et al. Laser communication proposal for solar system boundary exploration[J]. Journal of Telemetry, Tracking and Command, 2022, 43(4): 62-69.

[18] 罗彤, 王伟志, 薛佳音, 等. 深空光通信技术现状及发展趋势[J]. 遥测遥控, 2022, 43(4): 44-55.

LUO Tong, WANG Weizhi, XUE Jiayin, et al. Status and development trends of deep space optical communication[J]. Journal of Telemetry, Tracking and Command, 2022, 43(4): 44-55.

[19] 杨孟飞,彭兢,李炯卉,等.地月空间基础设施体系架构与发展设想[J].中国空间科学技术(中英文), 2024,44(3):1-14.

YANG M F,PENG J,LI J H ,et al.Architecture and development envision of cislunar space infrastructure[J].Chinese Space Science and Technology, 2024,44(3):1-14 (in Chinese).

[作者简介]

王振河（1970- ），男，硕士，高级工程师，主要研究方向为航天测控、卫星通信、空间信息网络技术等。

王冬冬（1982-），女，硕士，高级工程师，主要研究方向为卫星通信，卫星导航、空间信息网络等。

李超（1990-），男，硕士，工程师，主要研究方向为卫星网络通信、卫星导航等。

汤允昭（1987- ），男，硕士，工程师，主要研究方向为微波星间星地通信、北斗扩展用户接入、测定轨等。

Space-Based Multi-dimensional Spectrum Situation Online Completion via Time-Aware Tensor Factorization

XIAO Ruifeng, MA Yuan, ZHANG Xingjian

Abstract — Spectrum situation awareness by using low Earth orbit (LEO) satellites can comprehensively display current state and development trend of large-scale electromagnetic spectrum environment, thereby strengthening the overall control of electromagnetic space and the effective utilization of spectrum resources. However, the space-based electromagnetic spectrum monitoring system faces challenges such as limited computing, storage resources and long-distance transmission of satellite-ground links, which affect the integrity and timeliness of spectrum situation. To address these issues, this paper proposes a spectrum situation awareness scheme for space-based platforms based on multi-dimensional compressive sampling, in which a spatial spectrum situation online completion algorithm is designed via time-aware tensor factorization. The proposed scheme decomposes the high-dimensional spatial spectrum situation tensor into low dimensional temporal factor and non-temporal factors and iteratively update the low dimensional factor matrices in an online manner based on the spatiotemporal correlation, thereby achieving dynamic completion, anomalies correction, and real-time prediction of the spatial spectrum situation tensor. Simulation shows that the proposed algorithm can achieve reliable and efficient awareness of spatial spectrum situation.

Keywords — Spectrum situation awareness, wide-band compressive sampling, power spectrum reconstruction, online tensor completion

This work was supported in part by the National Natural Science Foundation of China under Grant 62101295; in part by the Young Elite Scientists Sponsorship Program by CAST under Grant 2023ONRC001 and 2020ONRC001; in part by the Shenzhen Natural Science Fund (Stable Support Program) under Grant GXWD20231129104413002; and in part by the Guangdong Office of Education under Grant 2023KTSCX229. (Corresponding author: Yuan Ma)

Yuan Ma and Ruifeng Xiao are with the State Key Laboratory of Radio Frequency Heterogeneous Integration, Guangdong Key Laboratory of Intelligent Information Processing, and the College of Electronic and Information Engineering, Shenzhen University, Shenzhen 518060, China. (e-mail: mayuan@szu.edu.cn; xiaoruifeng2022@email.szu.edu.cn).

Xingjian Zhang is with the Guangdong Provincial Key Laboratory of Aerospace Communication and Networking Technology, Harbin Institute of Technology (Shenzhen), Shenzhen 518055, China. (e-mail: x.zhang@hit.edu.cn).

I. INTRODUCTION

A. BACKGROUND

Compared to the limited coverage of ground-based electromagnetic spectrum monitoring systems [1][2], the space-based wideband spectrum monitoring system based on Low Earth Orbit (LEO) satellites can achieve continuous monitoring of the electromagnetic spectrum over a wide range. Therefore, to obtain a complete and continuous electromagnetic spectrum situation in time and space, relying on LEO satellites to build a space-based electromagnetic spectrum monitoring system is of great significance for the reconnaissance and identification of frequency equipment on a large scale.

At present, the space-based electromagnetic spectrum monitoring based on LEO satellites has received widespread attention. Current space-based electromagnetic spectrum monitoring systems mainly include the United States' HawkEye 360, Luxembourg's Kleos Space, France's UnseenLabs, etc [3], in which HawkEye 360 is the world's first commercial LEO satellite constellation and have achieved high-precision radio mapping by collecting radio uplink transmission signals worldwide. In order to further enhance real-time perception and effective control of electromagnetic space, China is actively deploying electromagnetic spectrum monitoring satellite constellations, including high-resolution series and remote sensing 30 satellites, to fully utilize the "high frontier" advantage of satellite systems to improve the control capability of electromagnetic space.

Although current multi-satellite system architecture and on-orbit processing and forwarding capabilities based on LEO satellites can achieve global networking and data exchange, bringing convenience to building a global spatiotemporal continuous spectrum situation, it is difficult to rely solely on the space-based spectrum monitoring system to construct large-scale and wide area situation data due to the limited in orbit computing capabilities of satellites. To address the limitations of processing and communication resources for lightweight and miniaturized LEO satellites, satellite-ground joint processing can be utilized to reduce the on-board payload constraint on the overall performance of LEO monitoring systems. Based on the spatiotemporal correlation characteristics and the powerful computing resources of ground fusion centers, it is expected to generate the multi-dimensional dynamic wide area spectrum situation through multi-source data fusion, thereby comprehensively displaying the current state, correlation situation, and development trend of the electromagnetic environment [4][5].

B. RELATED WORK

At present, spectrum situation generation can be mainly divided into two categories: model-driven and data-driven approaches:

The model-driven spectrum situation generation methods utilize prior information such as channel propagation models and radiation source locations to estimate spectrum situation parameters, therefore suitable for scenarios with few observations and insensitivity to location variations [6]. For example, [7][8] constructed the propagation channel model as a measurement matrix, and then used an algorithm based on compressive sensing. [9] constructed the generation mechanism of spectrum situation as a tensor decomposition model, and then used the structured

features combined with limited observations to estimate the actual physical components. However, in complex unknown electromagnetic environments, model-driven methods are difficult to obtain prior information and thus lack flexibility.

The data-driven generation methods are suitable for scenarios without prior information. Common methods include interpolation, matrix/tensor completion, and machine learning. The interpolation methods utilize the adjacent space and variational relationship between observations to interpolate and complete the spectrum situation. For example, in [10], based on Kriging interpolation, a small amount of observation data from mobile users were used to iteratively estimate the linear unbiased estimation of unobserved points to generate the accurate spectrum situation. In contrast, matrix/tensor completion is based on the low rank property of situation completion. For example, [11] used rank minimization and transformed it to its tightest convex surrogate, i.e., nuclear norm minimization to apply smoothness constraints for spectrum situation generation. Machine learning methods extract and learn spatiotemporal features from observation data to achieve completion. For example, in [12], a convolutional neural network and a residual network were used to predict the spatiotemporal spectrum situation within the perception area.

The above methods are batch processing optimization methods carried out under the fixed size of the spectrum situation. However, for the space-based spectrum monitoring system, the spectrum situation dynamically changes over time, which requires the algorithm to balance accuracy and real-time performance, and improve the efficiency of spectrum situation generation. [20] applied the online tensor completion method to spectrum prediction, utilizing a "predict first, complete later" approach to dynamically update tensor factors by integrating historical observation data, thereby efficiently and accurately predicting spectrum information. However, it didn’t reflect the real-time advantage of online methods compared to batch processing; Meanwhile, the online completion method adopted in the article is only applicable to three-dimensional tensors and has a high computational complexity. [21] proposed an incremental online tensor completion algorithm based on incremental update method, which reduced storage and computational burden and achieved real-time completion. However, the spectrum data in a single frequency band in 2-D space is used in the paper, without considering anomalies correction.

To meet the spectrum situation awareness requirements of space-based electromagnetic spectrum monitoring system under large-scale spatiotemporal coverage, this paper proposes a spectrum situation awareness scheme based on the multi-dimensional compressive sampling. To address shadow fading, interference and time delay caused by long-distance transmission of satellite-ground links, a spatial spectrum situation online completion algorithm is designed via time-aware tensor factorization, which decomposes the high-dimensional spatial spectrum situation tensor into low dimensional temporal factor and non-temporal factors, and then iteratively updates the low dimensional factor matrices in an online manner by mining temporal characteristics, thereby achieving dynamic completion, anomalies correction, and real-time prediction of the spatial spectrum situation.

C. PRELIMINARIES

In this subsection, some basic notations, operations and necessary definitions are presented, which are used throughout this paper.

1) Variable and its Elements:

Vectors are denoted by boldface lowercase letters, e.g., $\mathbf{a} \in \mathbb{R}^I$ and the i-th entry of it is denoted by a_i. Matrices are denoted by boldface capital letters, e.g., $\mathbf{A} \in \mathbb{R}^{I \times J}$ and the (i, j)-th element of it is $a_{i,j}$. The column vector of $\mathbf{A}$ is expressed as $\mathbf{a}_j^{(n)}$. So $\mathbf{A}$ is usually expressed as $\mathbf{A} = [\mathbf{a}_1, \cdots, \mathbf{a}_j, \cdots, \mathbf{a}_J]$. $\mathbf{A}$ is also written as $\mathbf{A} = [\mathbf{a}^T{}_1; \cdots; \mathbf{a}^T{}_i; \cdots; \mathbf{a}^T{}_I]$, where $\mathbf{a}^T{}_i$ is the i-th row vector of $\mathbf{A}$. Tensors are denoted by boldface Euler script letters, e.g., $\mathcal{A} \in \mathbb{R}^{I_1 \times I_2 \times \cdots \times I_N}$ and the $(i_1, i_2, \cdots, i_N)$-th of it is $a_{i_1, i_2, \cdots, i_N}$. Indices typically range from 1 to their capital version, e.g., $i = 1, \cdots, I$, and $i_n = 1, \cdots, I_n$, $n = 1, \cdots, N$. The Frobenius norm of the N-order tensor $\mathcal{A}$ which is represented as $\| \mathcal{A} \|_F$ is the square root of the sum of the squares of all its elements. $\| \mathcal{A} \|_0$ represents the ℓ_0-norm which calculates the number of non-zero elements in tensor $\mathcal{A}$. $\| \mathcal{A} \|_1$ represents the ℓ_1-norm which calculates the number of the magnitudes of $\mathcal{A}$.

2) Important Operations:

Matricization: Matricization is the process of reordering the elements of an N-order tensor $\mathcal{A}$ into a matrix and the mode-n matricization can be expressed as $\mathbf{X}_{(n)} \in \mathbb{R}^{I_n \times \Pi_{n \neq k} I_n}$.

Khatri-Rao product [13]: The Khatri-Rao product between a matrix $\mathbf{A} \in \mathbb{R}^{I_1 \times J}$ and another matrix $\mathbf{B} \in \mathbb{R}^{I_2 \times J}$ is $\mathbf{Y}_2 \in \mathbb{R}^{I_1 I_2 \times J}$, which is denoted by $\mathbf{Y}_2 = \mathbf{A} \odot \mathbf{B} = [\mathbf{a}_1 \otimes \mathbf{b}_1 \ \mathbf{a}_2 \otimes \mathbf{b}_2 \cdots \mathbf{a}_K \otimes \mathbf{b}_K]$, where $\otimes$ is the Kronecker product. The sequence of the Khatri-Rao products $\mathbf{A}^{(1)} \odot \cdots \odot \mathbf{A}^{(N)}$ is denoted by $\odot_{n=1}^{N} \mathbf{A}^{(n)}$. And $\odot_{n=1, n \neq l}^{N} \mathbf{A}^{(n)}$ denotes $\mathbf{A}^{(1)} \odot \cdots \odot \mathbf{A}^{(l-1)} \odot \mathbf{A}^{(l+1)} \odot \cdots \odot \mathbf{A}^{(N)}$.

Hadamard product [13]: The Hadamard product between a tensor $\mathcal{A} \in \mathbb{R}^{I_1 \times I_2 \times \cdots \times I_N}$ and another tensor with the same size $\mathcal{B} \in \mathbb{R}^{I_1 \times I_2 \times \cdots \times I_N}$ is $\mathcal{Y} \in \mathbb{R}^{I_1 \times I_2 \times \cdots \times I_N}$, which is denoted by $\mathcal{Y} \in \mathbb{R}^{I_1 \times I_2 \times \cdots \times I_N} = \mathcal{A} \circledast \mathcal{B}$. Hadamard product represents the multiplication of the corresponding elements of $\mathcal{A}$ and $\mathcal{B}$.

Outer Product and Rank-one Tensor [13]: The vector outer product between two vectors $\mathbf{a} \in \mathbb{R}^I$ and $\mathbf{b} \in \mathbb{R}^J$ is a rank-one matrix $\mathbf{Y}_4 \in \mathbb{R}^{I \times J}$, which is denoted by $\mathbf{Y}_4 = \mathbf{a} \circ \mathbf{b}$. It can also be extended to N-dimensional format which is expressed as $\mathcal{Y} = \mathbf{u}^{(1)} \circ \mathbf{u}^{(2)} \circ \cdots \circ \mathbf{u}^{(N)}$, where $\{\mathbf{u}_k \in \mathbb{R}^{I_k}\}_{k=1}^{N}$, and $\mathcal{Y} \in \mathbb{R}^{I_1 \times I_2 \times \cdots \times I_N}$ is called a rank-one tensor.

3) CP Factorization and Rank:

Tensor factorization [14] is the high-order extension of matrix decomposition, which is a technique for decomposing a high-order tensor into multiple lower-order components with the goal of simplifying data representation, extracting features, or performing data compression. CP (CANDECOMP/PARAFAC) decomposition is a classic decomposition model, which decomposes a tensor into a sum of component rank-one tensors. For a tensor $\mathcal{X} \in \mathbb{R}^{I_1 \times I_2 \times \cdots \times I_N}$, it can be written as $\mathcal{X} \approx \sum_{r=1}^{R} \mathbf{u}_r^{(1)} \circ \mathbf{u}_r^{(2)} \circ \cdots \circ \mathbf{u}_r^{(N)}$, where $\mathbf{u}_r^{(n)}$ is the r-th column vector of the factor matrix $\mathbf{U}^{(n)}$. If a weight λ_r is assigned to each rank one tensor to form a new tensor $\mathcal{X}'$, it can be expressed as $\mathcal{X}' \approx \sum_{r=1}^{R} \lambda_r \mathbf{u}_r^{(1)} \circ \mathbf{u}_r^{(2)} \circ \cdots \circ \mathbf{u}_r^{(N)}$, where $\boldsymbol{\lambda} \in \mathbb{R}^R$ is the weight vector. The rank of the tensor $\mathcal{X}$, denoted $\mathrm{rank}(\mathcal{X})$, is defined as the smallest number of rank-one tensors in its CP model.

II. SPATIAL SPECTRUM SITUATION AWARENESS SYSTEM MODEL

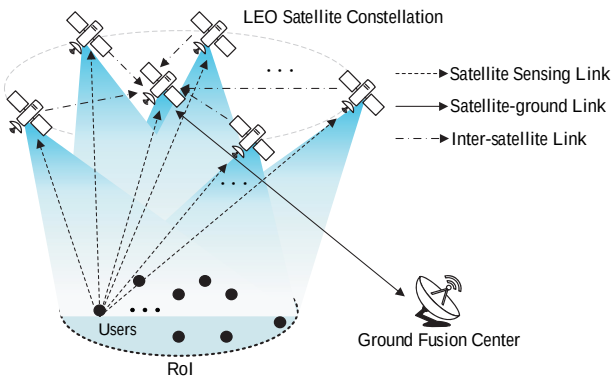

Figure 1 Schematic diagram of space-based electro-magnetic spectrum monitoring system.

A. REPRESENTATION

As shown in Figure 1, based on the on-orbit acquisition of electromagnetic signals within the Region of Interest (RoI), the LEO satellite constellation periodically transmits the observation data to the ground fusion center via the satellite-ground links. The ground fusion center fuses multi-source data and generates spatial spectrum situation in space, frequency, and time to visually display the spectral information such as spatial distribution of radiated signals in specific areas, spectrum occupancy and temporal changes in user frequency activities, thereby comprehensively analyzing and making decisions on the spatial spectrum situation.

The spectrum situation in three-dimensional (3D) space is the combination of multiple radiation sources within and around the RoI. Typically, the spatial spectrum situation is modeled as the Power Spectrum Density (PSD) of the received signals. According to the principle of spectrum situation superposition [15], spectrum situation can be viewed as a linear superposition of the PSD of different radiated signals across various spatial positions, frequencies, and time. As illustrated in Figure 2, the spectrum situation exhibits the spatial heterogeneity and approximate smoothness, where regions with a redder hue indicate higher spectrum occupancy, and greener regions suggest lower spectrum utilization. The time axis reflects the temporal variations of the spectrum situation.

The spatial spectrum situation, when discretized along the spatial, frequency, and temporal dimensions, can be represented as a tensor. The tensor-based discrete representation enables a more effective depiction of the structural information of the spatial spectrum situation across and within multiple dimensions. Specifically, in the space domain, the 3D space can be discretized into $I_1 \times I_2 \times I_3$ spatial grids with an equal interval d_θ, where I_1, I_2, and I_3 denote the grid number of the 3D space in x, y, z dimensions. In the time domain, the sensing interval which is assumed to be $T = [0, T_{tr}]$ can be discretized into T sensing durations with an equal interval I_T, i.e. $T_{tr} = I_T \cdot T$. I_T represents the smallest time interval during which changes in PSD are not significant, used to analyze the temporal variation patterns of the spectrum situation. In the frequency domain, the wideband spectrum $F = [f_1, f_2]$ to be monitored in a sensing duration can be discretized into N frequency points while the duration is discretized into N sampling points with the Nyquist sampling period $T_s = 1/f_s$ in the time domain, where $f_s = f_2 - f_1$. The relationship between T and N is shown in Figure 3.

Through the discretization, the spatial spectrum situation, the spatial transmission gain and the PSD of radiated signals can be represented in tensor forms, i.e. $X \in R^{I_1 \times I_2 \times I_3 \times N \times T}$, $H_r \in R^{I_1 \times I_2 \times I_3 \times N \times T}$, and $C_r \in R^{N \times T}$,

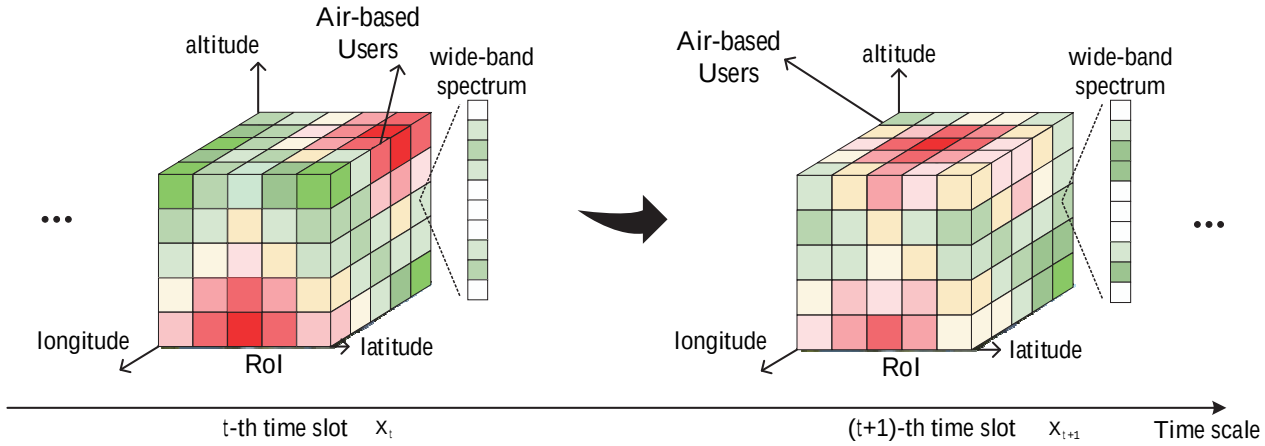

Figure 2 Schematic diagram of spatial spectrum situation tensor.

respectively. At any spatial grid (i_1, i_2, i_3), at any frequency point n and in any sensing duration t, the relationship among the elements of X, H_r and C_r can be represented as

$$x_{i_1,i_2,i_3,n,t} = \sum_{r=1}^{R_s} (h_r)_{i_1,i_2,i_3,n,t} \cdot (c_r)_{n,t}, \tag{1}$$

Where $(c_r)_{n,t}$ is expressed as the PSD of the r-th radiated signal at any frequency point n during the t-th sensing duration. The tensor-based representation described above can more effectively capture the higher-order structural information of the spatial spectrum situation across multiple dimensions. It facilitates the exploration of the correlations and structured features of spatial electromagnetic information in the spatial, frequency, and temporal dimensions.

The spatial transmission gain H_r of the radiated signals includes two components: the transmission gain from the radiation sources to different grids in the RoI, and the satellite-ground link transmission gain, which can be expressed as:

$$(h_r)_{i_1,i_2,i_3,n,t} = G_t \cdot G_r \cdot \underbrace{w(i_1,i_2,i_3) \cdot \left(\frac{d_0}{d}\right)^{\alpha} \left(\frac{c}{4\pi \cdot d_0 \cdot f_r}\right)^2}_{\text{Ground Transmission Gain}} \cdot \underbrace{\left(\frac{c}{4\pi \cdot 2h \cdot f_r}\right)^2 g^2}_{\text{Satellite-ground Transmission Gain}} \tag{2}$$

where G_t and G_r represent the transmission and reception gain of the antenna. The ground transmission gain can be modeled as the product of free path loss and shadow fading [9]. And the parameters d, α, c and f_r are transmitted distance, path loss exponent and the carrier frequency of the r-th radiated signal. Shadow fading w is typically modeled as a log-normal distribution with zero mean and a variance of σ_s. The satellite-ground transmission gain can be modeled as the product of satellite-ground path loss and channel fading g^2. And the parameter h is transmission distance of the satellite-ground Link. Considering that the received signal consists of both direct and multipath components, its envelope follows Rician distribution whose normalized probability density function is

$$P(x) = \frac{x}{\sigma_r^2} \exp\left(-\frac{x^2 + A^2}{2\sigma_r^2}\right) I_0\left(\frac{xA}{\sigma_r^2}\right), \tag{3}$$

where A and σ_r^2 represent the line-of-sight direct

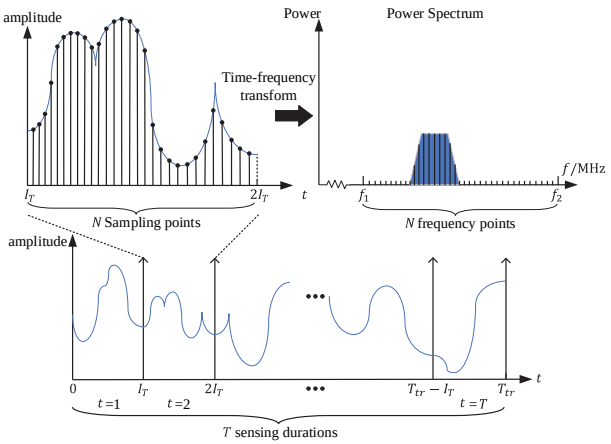

Figure 3 Discretization relationship diagram of time-frequency domain transformation

path envelope and the power of the multipath components, respectively. The Rician factor, denoted as $f_R = A^2 / 2\sigma_r^2$, indicates the proportion of the direct component; a larger value of f_R signifies a higher proportion of the direct component. $I_\theta(\cdot)$ represents the zeroth-order modified Bessel function of the first kind [16].

Due to the performance and power limitations of satellite payloads, high-speed wideband signal sampling is difficult to implement on LEO satellites. Therefore, this paper employs multicoset sampling [17] to perform low-speed sampling of wideband signals at rates far below than the Nyquist theorem. Multicoset sampling is a periodic, non-uniform sub-Nyquist sampling technique in the time domain, which can be implemented through a multi-channel parallel sampling architecture. Specifically, p parallel cosets are utilized, each of which takes uniform samples at time instants $(kL + c_i)T_s$, $i = 1, \ldots, p$, $k \in \mathbb{Z}$, via a decimated sampling rate $1/LT_s$ with a sampling time offset of $\tau_i = c_i T_s$, where $p \le L$. The result of multicoset sampling can be represented as

$$Y(f) = AS(f) + N, \quad f \in \left[0, \frac{1}{LT_s}\right), \tag{4}$$

where $A \in C^{p \times L}$ is random measurement matrix of multicoset sampling and its (i, j)-th element is

$$a_{i,j} = \frac{1}{LT_s} e^{j2\pi c_i (j-1)/L}. \tag{5}$$

$S(f)$ is the primary noise-free signal. Based on the low-rank property of the spatial spectrum, $S(f)$ exhibits joint sparsity property. Therefore, many common reconstruction algorithms can be used for its recovery, including greedy pursuit (GP), Multiple Signal Classification (MUSIC) reconstruction algorithms, sparse reconstruction algorithms based on ℓ_1-norm, and sparse Bayesian learning (SBL) algorithms. The sampling and reconstruction processes not only achieve compressed reconstruction of the spectrum situation in the time-frequency domain but also retain a substantial portion information of the frequency domain, thereby ensuring efficient generation even with a limited number of observations.

Based on the discrete estimates $\bar{S} \in \mathbb{C}^{L \times M}$ obtained from sparse reconstruction, where $M = N / L$, the average PSD of different channels can be further calculated, which can be expressed as

$$p_i = \frac{1}{BN} \left(r_{\bar{S}}\right)_{i,i}, \quad i = 1, 2, \ldots, L, \tag{6}$$

where p_i and B are the average PSD and the bandwidth of the i-th channel, respectively. $r_{\bar{S}}$ is the diagonal element of the discrete estimates signal auto-correlation matrix $R_{\bar{S}} \in C^{L \times L}$, which is also the sum of the energy across total frequency points in the i-th channel [18].

The PSD of primary wideband signals are reconstructed and combined with geographic and

temporal information to construct a multi-dimensional spatial spectrum situation tensor. However, due to constraints in data acquisition, computation, and communication resources of LEO monitoring satellites, the transmitted data to the ground exhibits characteristics of low spatial resolution and missing. Based on the low-rank property of the spatial spectrum situation tensor and the sparsity of anomalies, spectrum situation completion from incomplete and corrupted transmitted electromagnetic information can be formulated as a tensor completion problem, which can be described as follows:

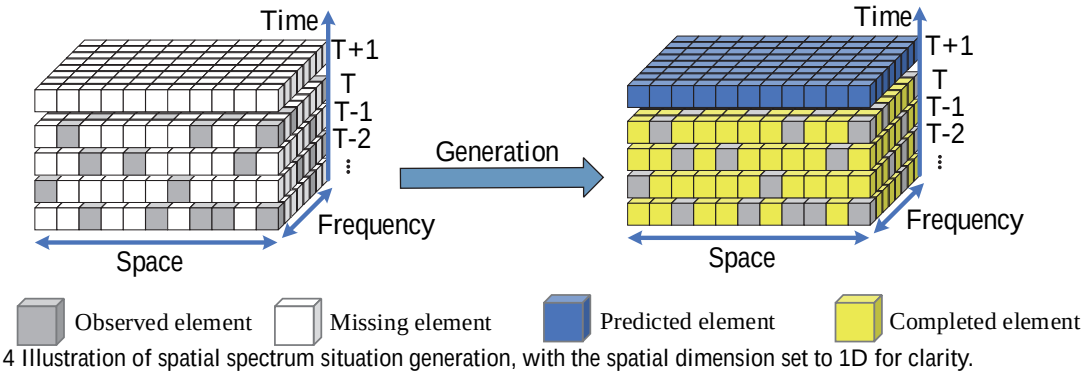

Figure 4 Illustration of spatial spectrum situation generation, with the spatial dimension set to 1D for clarity.

In practice, the ground fusion center processes the spectrum situation sub-tensor sequentially in time. Therefore, it's important to reconstruct the complete and clean spectrum situation sub-tensor X_t according to the measurement sub-tensor Y_t. Their relationship can be expressed as

$$\mathcal{Y}_t = \mathcal{O}_t \circledast \left(\mathcal{X}_t + \mathcal{A}_t + \mathcal{N}_t \right), \quad t = 1, 2, \ldots, T, \tag{7}$$

where $\mathsf{O}_t \in \mathbb{R}^{I_1 \times I_2 \times I_3 \times L}$ represents the binary observation sub-tensor, and the values at the observed and unobserved positions are set to 1 and 0, respectively. A_t and N_t represent sparse anomalies and noise sub-tensor. For the convenience of representation, all spectrum situation sub-tensors $\{\mathsf{X}_t\}_{t=1}^{T}$ within the interval $(1:T)$ can be expressed as a tensor $\mathsf{X}_{1:T} = \mathsf{X} \in \mathbb{R}^{I_1 \times I_2 \times I_3 \times L \times T}$.

As illustrated in Figure 4, this paper aims to obtain the complete and spectrum situation tensor X and predict the future spectrum situation sub-tensor X_{T+1} through anomalies correction and tensor completion.

$$\begin{aligned} &\min_{\mathcal{X},\mathcal{A}} \ \operatorname{rank}\left(\mathcal{X}\right) + \mu \left\| \mathcal{A} \right\|_0 \\ &\text{s.t.} \ \left\| \mathcal{O} \circledast \left(\mathcal{Y} - \mathcal{X} - \mathcal{A} \right) \right\|_{\mathrm{F}}^2 \le \varepsilon, \end{aligned} \tag{8}$$

where μ is the sparsity control parameter, and ε is the noise-related parameter. Table 1 summarizes several common tensor completion algorithms.

However, since the future spectrum situation sub-tensor X_{T+1} is unknown, the prediction problem cannot be directly solved by using tensor completion. To address this issue, this paper proposes an Online Spectrum Situation Generation algorithm via Time-aware tensor Factorization (OSSGTF), which performs the spatial spectrum situation by exploiting its temporal variation characteristics. The detailed algorithm will be introduced in the next section.

III. Online Spectrum Situation Generation Algorithm Based on Temporal Factors

As $\operatorname{rank}(\cdot)$ and ℓ_0-norm criteria are NP-hard, convex relaxation is performed and can be represented

Table 1 Comparison of Tensor Completion Algorithms

Algorithm	Anomalies fix	High order >3	Type	Rank prior	Additional Information
OLSTEC[19][20]	√	x	Online	√	BCD+RLS
ALS [22]	√	√	Batch process	√	ALS
BRTF[23]	√	√	Batch process	x	Variational Bayes
BRST[24]	√	√	Online	x	Streaming Variational Bayes

as

$$\min_{\mathcal{X},\mathcal{A}} \frac{1}{2}\left\|\mathcal{O}\circledast\left(\mathcal{Y}-\mathcal{X}-\mathcal{A}\right)\right\|_F^2+\mu\left\|\mathcal{A}\right\|_1 \quad \text{s.t. } \mathcal{X}=\sum_{r=1}^{R}u_r^{(1)}\circ\cdots\circ u_r^{(5)}. \tag{9}$$

Then, CP decomposition is introduced to decompose the spectrum situation tensor $\mathcal{X}$ into factor matrices, i.e., $\{U^{(n)}\}_{n=1}^{5}$, which encompasses five dimensions: three spatial dimensions, the frequency dimension, and the temporal dimension. The factors can further be divided into non-temporal factors $\{U^{(n)}\}_{n=1}^{4}$ and temporal factor $U^{(5)}\in\mathbb{R}^{T\times R}$. To address the incomplete and delayed perception results caused by sparse sampling on the satellite and long-distance data transmission, it is necessary to correct and complete the spatial spectrum situation tensor $\mathcal{X}$ based on the returned measurement tensor $\mathcal{Y}$ from T sensing durations and to predict the future spectrum situation sub-tensor $\mathcal{X}_{T+1}$. To achieve it, the proposed method completes, corrects and predicts the spatial spectrum situation sub-tensors by leveraging the temporal variation characteristics between consecutive spectrum situation sub-tensors in conjunction with the sensing data. The proposed online spatial spectrum situation generation algorithm can be divided into the following four steps:

A. INITIAL ESTIMATION

Traditional tensor completion algorithms require prior information about the rank. However, in the context of a complex and dynamic spatial spectrum environment, the tensor rank is unknown. Therefore, the proposed algorithm first utilizes a short segment of observation data $\mathcal{Y}_{1:t'}$ to perform an initial estimation, and t' is the number of durations for initial estimation. Since the temporal characteristics of the spectrum situation can be mapped onto the temporal factor, a smoothing constraint is applied to the temporal factors based on Equation (9) to fit the temporal characteristics of the spectrum situation. This approach not only helps improve the accuracy of spectrum situation restoration and completion but also lays the foundation for subsequent mining of temporal factor to capture temporal variations. The specific formulation is as follows:

$$\begin{aligned}\min_{\{U_{t'}^{(n)}\}_{n=1}^{4},U_{\text{init}}^{(5)}} &\frac{1}{2}\left\|\mathcal{O}_{1:t'}\circledast\left(\mathcal{Y}_{1:t'}-\mathcal{X}_{1:t'}-\mathcal{A}_{1:t'}\right)\right\|_F^2\\ &+\rho_1\left\|L_1U_{\text{init}}^{(5)}\right\|_F^2+\rho_s\left\|L_mU_{\text{init}}^{(5)}\right\|_F^2+\mu\left\|\mathcal{A}_{1:t'}\right\|_1\\ \text{s.t. }\ &\mathcal{X}_{1:t'}=\left[\!\left[U_{t'}^{(1)},U_{t'}^{(2)},U_{t'}^{(3)},U_{t'}^{(4)},U_{\text{init}}^{(5)}\right]\!\right],\\ &\left\|(u_{t'}^{(n)})_r\right\|_2=1,\ n=1,2,3,4,\end{aligned} \tag{10}$$

where $U_{t'}^{(n)}$ is the initial estimation of a non-temporal factor matrix and its r-th column vector is $(u_{t'}^{(n)})_r$. $U_{\text{init}}^{(5)}\in\mathbb{R}^{t'\times R}$ is the temporal factor matrix during the durations $(1:t')$. ρ_1 and ρ_s are smoothing control

parameters for $\mathbf{U}_{\text{init}}^{(5)}$ and $\mathbf{L}_i \in \mathbb{R}^{(T-i)\times T}$ represents a smoothness constraint matrix. As for [25], $\|\mathbf{L}_1\mathbf{U}_{\text{init}}^{(5)}\|_F^2$ represents the smoothing constraint for short-term similarity, and $\|\mathbf{L}_m\mathbf{U}_{\text{init}}^{(5)}\|_F^2$ represents the smoothing constraint for long-term periodicity. It's always larger than m for t' called the long-term temporal period. To achieve rapid initial estimation, an Alternating Least Squares (ALS) method in Table 1 is employed. This approach includes anomalies correction and factor matrices updating, enabling quick and effective completion of $\mathcal{Y}_{1:t'}$.

In the absence of rank prior, the above ALS optimization process requires determining the rank information through rank search step. A common method is to incrementally approach the true rank by gradually increasing the rank. After achieving convergence using the ALS algorithm, the rank is incremented by 1, and the R-th column vector of each factor matrix is initialized randomly to form a new factor matrix. The ALS optimization is then executed again, with this process being repeated until the residual change between two consecutive ranks is smaller than a predefined threshold, indicating convergence, which can be expressed as

$$\frac{\left|\Delta_R - \Delta_{R-1}\right|}{\left|\Delta_R\right|} < \text{tol}, \tag{11}$$

where Δ_R is the residual at rank R, which can be represented as $\Delta_R = \|\mathcal{O}_{1:t'} \circledast (\mathcal{Y}_{1:t'} - \mathcal{X}_{1:t'} - \mathcal{A}_{1:t'})\|_F^2$. tol is the pre-set discrimination threshold. Algorithm 1 summarizes the above optimization steps.

B. TEMPORAL ATTRIBUTES ANALYSES

To reliably generate the spatial spectrum situation, temporal analyses is crucial to explore long-term and short-term temporal trends in the spectrum situation. Therefore, in this section, the temporal factor matrix $\mathbf{U}_{\text{init}}^{(5)}$ obtained from the initial estimation is fitted to an additive Holt-Winters (HW) forecasting model [26]. These analyses lay the foundation for subsequent dynamic completion, anomalies correction and real-time prediction.

Based on the Holt-Winters model, the level $\mathbf{l}^T_t$, trend $\mathbf{b}^T_t$, and seasonal components $\mathbf{s}^T_t$, along with their corresponding smoothing parameters $\boldsymbol{\alpha}$, $\boldsymbol{\beta}$, $\boldsymbol{\gamma}$ are extracted from the row vectors $\mathbf{u}^{T(5)}_t$ of $\mathbf{U}^{(5)}_{\text{init}}$:

$$\begin{aligned}
\mathbf{l}^T_t &= \text{diag}(\boldsymbol{\alpha})(\mathbf{u}^{T(5)}_t - \mathbf{s}^T_{t-m}) \\
&\quad + (\mathbf{I}_R - \text{diag}(\boldsymbol{\alpha}))(\mathbf{l}^T_{t-1} + \mathbf{b}^T_{t-1}), \\
\mathbf{b}^T_t &= \text{diag}(\boldsymbol{\beta})(\mathbf{l}^T_t - \mathbf{l}^T_{t-1}) + (\mathbf{I}_R - \text{diag}(\boldsymbol{\beta}))\mathbf{b}^T_{t-1}, \\
\mathbf{s}^T_t &= \text{diag}(\boldsymbol{\gamma})(\mathbf{u}^{T(5)}_t - \mathbf{l}^T_{t-1} - \mathbf{b}^T_{t-1}) \\
&\quad + (\mathbf{I}_R - \text{diag}(\boldsymbol{\gamma}))\mathbf{s}^T_{t-m},
\end{aligned} \tag{12}$$

where $\text{diag}(\cdot)$ is a diagonal matrix generated from the input vector. Thus, the prediction of the temporal factor row vector is conducted based on (12). Specifically, the temporal factor vector for the future τ-th sensing duration is predicted using the level $\mathbf{l}^T_{t'}$ and the trend component $\mathbf{b}^T_{t'}$ from the t'-th duration, and the seasonal component $\{\mathbf{s}^T_t\}_{t=t'-m+1}^{t'}$ from the last tempo ral period. It can be expressed as

$$\hat{\mathbf{u}}^{T(5)}_{t'+\tau|t'} = \mathbf{l}^T_{t'} + \tau\mathbf{b}^T_{t'} + \mathbf{s}^T_{t'-m+\tau}. \tag{13}$$

C. DYNAMIC COMPLETION

To construct a high-precision multi-dimensional spatial spectrum situation, traditional tensor completion algorithms face challenges such as high computational complexity and low efficiency. It's considered that $\mathcal{Y}_t$ is dynamically input sequentially over time during the processing. Thus, the requirement of real-time processing capability drives

the updating of previously obtained factor matrices estimates, rather than recalculating new ones each time a new observation becomes available. Based on it, an online problem at the t-th duration can be modeled as

$$\begin{aligned}\min_{\{\mathbf{U}_t^{(n)}\}_{n=1}^4,\mathbf{u}_t^{T(5)}} &\sum_{\tau=t'+1}^{t}\Big[\left\|\mathcal{O}_\tau \circledast \left(\mathcal{Y}_\tau-\mathcal{X}_\tau-\mathcal{A}_\tau\right)\right\|_F^2+\rho_1\left\|\mathbf{p}_\tau\right\|_F^2\\ &+\rho_s\left\|\mathbf{q}_\tau\right\|_F^2+\mu\left\|\mathcal{A}_\tau\right\|_1\Big]\\ \text{s.t.}\quad &\mathcal{X}_\tau=\left[\!\left[\mathbf{u}_\tau^{T(5)};\mathbf{U}_\tau^{(1)},\mathbf{U}_\tau^{(2)},\mathbf{U}_\tau^{(3)},\mathbf{U}_\tau^{(4)}\right]\!\right]\\ &\left\|\mathbf{u}_r^{(n)}\right\|_2=1,\ n=1,2,3,4,\end{aligned} \tag{14}$$

where $t=t_0+1,t_0+2,\cdots,T$, $\mathbf{p}_\tau=\mathbf{u}_\tau^{T(5)}-\mathbf{u}_{\tau-1}^{T(5)}$ and $\mathbf{q}_\tau=\mathbf{u}_\tau^{T(5)}-\mathbf{u}_{\tau-m}^{T(5)}$. $\mathbf{U}_t^{(n)}$ represents the updated non-temporal factor matrix for the τ-th duration.

Based on the initially estimated temporal and non-temporal factor matrices, as well as the level, trend, and seasonal components obtained from the Holt-Winters model in the temporal attributes analyses, the observed spectrum situation sub-tensors $\{\mathbf{Y}_t\}_{t=t'+1}^{T}$ are incorporated to address the online optimization problem in (14).

This approach enables the online update of the factor matrices, facilitating the dynamic generation of the spectrum situation. This process can be divided into the following three parts:

1) Estimation of Anomalies Sub-tensor $\mathcal{A}_t$

The temporal factor vector for the t-th sensing duration is predicted according to (13), which is expressed as:

$$\tilde{\mathbf{u}}_{t|t-1}^{T(5)}=\mathbf{l}^T{}_{t-1}+\mathbf{b}^T{}_{t-1}+\mathbf{s}^T{}_{t-m}, \tag{15}$$

Subsequently, the vector $\tilde{\mathbf{u}}_{t|t-1}^{T(5)}$ and the non-temporal factor matrix $\{\mathbf{U}_{t-1}^{(n)}\}_{n=1}^4$ updated in the previous duration are computed through Kruskal operation to obtain the estimate of the spectrum situation sub-tensor $\tilde{\mathcal{Y}}_{t|t-1}$, or denoted as $\tilde{\mathcal{X}}_t$:

$$\begin{aligned}\tilde{\mathcal{Y}}_{t|t-1}=\tilde{\mathcal{X}}_t&=\sum_{r=1}^{R}(\tilde{\mathbf{u}}_{t|t-1}^{T(5)})_r\cdot(\mathbf{u}_{t-1}^{(1)})_r\circ(\mathbf{u}_{t-1}^{(2)})_r\circ(\mathbf{u}_{t-1}^{(3)})_r\circ(\mathbf{u}_{t-1}^{(4)})_r\\ &=\left[\!\left[\tilde{\mathbf{u}}_{t|t-1}^{T(5)};\mathbf{U}_{t-1}^{(1)},\mathbf{U}_{t-1}^{(2)},\mathbf{U}_{t-1}^{(3)},\mathbf{U}_{t-1}^{(4)}\right]\!\right].\end{aligned}$$

Algorithm 1: OSSGTF-Initialization

Input: $\mathcal{Y}_{1:t'}$, $\mathcal{O}_{1:t'}$, m, ρ_1, ρ_s, μ, tol
Output: $\mathcal{X}_{1:t'}$, $\{\mathbf{U}_{t'}^{(n)}\}_{n=1}^4$, $\mathbf{U}_{\text{init}}^{(5)}$, R

```
R = 1
Initialize {U_t'^(n) ∈ R^{I_n×R}}_{n=1}^4, U_init^(5), randomly
{X_1:t', {U_t'^(n)}_{n=1}^4, U_init^(5), A_1:t'}
        ← ALS{Y_1:t', O_1:t', R, {U_t'^(n)}_{n=1}^4, U_init^(5), ···}
Δ_R ← || O_1:t' ⊛ (Y_1:t' − X_1:t' − A_1:t') ||_F^2
repeat
    R = R + 1
    Initialize {u_R^(n)}_{n=1}^5, randomly
    {X_1:t', {U_t'^(n)}_{n=1}^4, U_init^(5), A_1:t'}
        ← ALS{Y_1:t', O_1:t', R, {U_t'^(n)}_{n=1}^4, U_init^(5), ···}
    Δ_R ← || O_1:t' ⊛ (Y_1:t' − X_1:t' − A_1:t') ||_F^2
until |Δ_R − Δ_{R−1}| / |Δ_R| < tol
```

(16)

The principle of online anomalies' correction involves comparing and identifying elements in $\tilde{\mathcal{Y}}_{t|t-1}$ that significantly differs from the actual observed sub-tensor $\mathcal{Y}_t$ to extract anomalies. The estimation of anomalies sub-tensor can be expressed as:

$$\hat{\mathcal{A}}_t=\mathcal{Y}_t-\tilde{\mathcal{Y}}_{t|t-1}-\Psi\left(\frac{\mathcal{Y}_t-\tilde{\mathcal{Y}}_{t|t-1}}{\hat{\Sigma}_{t-1}}\right)\circledast\hat{\Sigma}_{t-1}, \tag{17}$$

where $\Psi(\cdot)$ is a Huber Ψ-function that set a range $[-k,k]$, such that any element of the input tensor exceeding this range is defined as an anomaly and is automatically replaced with $-k$ or k. $\hat{\Sigma}_t\in\mathbb{R}^{I_1\times I_2\times I_3\times L}$ is an error scale tensor for each of whose entries are the scale of the forecast error in the corresponding entry. It's always defined as

$$\hat{\Sigma}_t=\phi\rho\left(\frac{\mathcal{Y}_t-\tilde{\mathcal{Y}}_{t|t-1}}{\hat{\Sigma}_{t-1}}\right)\circledast\hat{\Sigma}_{t-1}+(1-\phi)\hat{\Sigma}_{t-1}^2, \tag{18}$$

where $0 \le \phi \le 1$ is a smoothing parameter and $\rho(\cdot)$ is an elementwise biweight ρ-function which has a similar function with $\Psi(\cdot)$.

2) Update $\{U_t^{(n)}\}_{n=1}^4$:

Since the non-temporal factor matrix is updated based on previous updates, the proposed algorithm employs Stochastic Gradient Solvers to perform the update process. Based on this, we can focus solely on

Algorithm 2: OSSGTF-dynamic update

Input: (1) $\{Y_t, O_t\}_{t=t'+1}^{T}$, R, m, ρ_1, ρ_s, μ, μ_t, ϕ,
(2) $\{U_{t'}^{(n)}\}_{n=1}^4, \{u_t^{T(5)}\}_{t=t'-m+1}^{t'}$,
(3) $l^T_{t'}, b^T_{t'}, \{s^T_t\}_{t=t'-m+1}^{t'}$, $\boldsymbol{\alpha}, \boldsymbol{\beta}, \boldsymbol{\gamma}$
Output: $\{X_t\}_{t=t'+1}^{T}, \{U_T^{(n)}\}_{n=1}^4, u_T^{T(5)}, \tilde{X}_{T+1}$
Initialize $\hat{\Sigma}_{t'} \leftarrow \mu/100 \times I$
for $t = t'+1, t'+2, \cdots, T$
  estimate $\tilde{u}_{t|t-1}^{T(5)}$ using (15)
  estimate $\tilde{Y}_{t|t-1}$ using (16)
  estimate A_t using (17)
  update $\hat{\Sigma}_t$ using (18)
  update $\{U_t^{(n)}\}_{n=1}^4$ using (20)
  update $u_t^{T(5)}$ using (21)
  update l^T_t, b^T_t, s^T_t using (12)
  $X_t = [\![u_t^{T(5)}; U_t^{(1)}, U_t^{(2)}, U_t^{(3)}, U_t^{(4)}]\!]$
end for
Predict $\tilde{X}_{T+1}$ using (15) and (16)

the t-th summand of (14) which is defined as

$$\begin{aligned} & f_t(\{U^{(n)}\}_{n=1}^4, u^{T(5)}) \\ &= \left\| \mathcal{O}_t \circledast \left(\mathcal{Y}'_t - [\![u^{T(5)}; U^{(1)}, U^{(2)}, U^{(3)}, U^{(4)}]\!] \right) \right\|_F^2 \\ &\quad + \rho_1 \left\| u^{T(5)} - u_{t-1}^{T(5)} \right\|_F^2 + \rho_s \left\| u^{T(5)} - u_{t-m}^{T(5)} \right\|_F^2, \end{aligned} \tag{19}$$

where $Y'_t = Y_t - A_t$. The principle of the Stochastic gradient solvers is to use the sub-tensor $\tilde{X}_t$ predicted by Equation (16), substitute the corresponding factor $(\{U_{t-1}^{(n)}\}_{n=1}^4, \tilde{u}_{t|t-1}^{T(5)})$ into Equation (19), and solve for the gradient to guide the update direction of the corresponding factor. Here, a step size of μ_t is taken, and the specific update process is as follows:

$$\begin{aligned} U_t^{(n)} &= U_{t-1}^{(n)} - \mu_t \frac{\partial f_t(\{U_{t-1}^{(n)}\}_{n=1}^4, \tilde{u}_{t|t-1}^{T(5)})}{\partial U^{(n)}} \\ &= U_{t-1}^{(n)} + 2\mu_t R_{t(n)} \bigodot_{l=1, l\neq n}^{4} U_{t-1}^{(l)} \cdot \mathrm{diag}(\tilde{u}_{t|t-1}^{T(5)}), \end{aligned} \tag{20}$$

where $R_{t(n)}$ is the mode-n matricization of R_t, which is represented as $\mathcal{R}_t = \mathcal{O}_t \circledast (\mathcal{Y}_t - \mathcal{A}_t - \tilde{\mathcal{Y}}_{t|t-1})$.

3) Update $u_t^{T(5)}$:

Similar to the update of non-temporal factor matrices, the update of the temporal factor vector is as follows:

$$\begin{aligned} u_t^{T(5)} &= \tilde{u}_{t|t-1}^{T(5)} - \mu_t \frac{\partial f_t(\{U_{t-1}^{(n)}\}_{n=1}^4, \tilde{u}_{t|t-1}^{T(5)})}{\partial u^{T(5)}} \\ &= \tilde{u}_{t|t-1}^{T(5)} + 2\mu_t [(\bigodot_{n=1}^{4} U_{t-1}^{(n)})^T \cdot \mathrm{vec}(R_{t(n)}) \\ &\quad + \rho_1 u_{t-1}^{T(5)} + \rho_s u_{t-m}^{T(5)} - (\rho_1 + \rho_s) \tilde{u}_{t|t-1}^{T(5)}], \end{aligned} \tag{21}$$

where $\mathrm{vec}(\cdot)$ is the vectorization operator. Subsequently, the level, trend, and seasonal components of the temporal factor vector $u_t^{T(5)}$ within the current sensing duration are fitted based on (12), providing a foundation for the updates in subsequent sensing durations.

D. Forecast

Forecasting $\tilde{u}_{T+1|T}^{T(5)}$ using Equation (15), and then forecasting $\tilde{Y}_{T+1|T} = \tilde{X}_{T+1}$ using Equation (16). In summary, the temporal factor estimate $\tilde{u}_{t|t-1}^{T(5)}$ obtained from the sequential update of the temporal factor serves several functions: it provides the sub-tensor estimate for anomalies correction, helping to identify anomalies by combining with observed values; it offers gradients of various factors for the online completion of sub-tensors; and it supplies immediate temporal factor estimates for predicting spectrum situation sub-tensor in future durations.

Thus, OSSGTF effectively addresses the issues of incompleteness, reliability, and immediacy in

spectrum situation assessment, efficiently achieving dynamic completion, anomalies correction, and real-time prediction. The dynamic update process is summarized in Algorithm 2.

IV. EXPERIMENTAL EVALUATIONS

To validate the effectiveness of the proposed algorithm, a spatial spectrum situation model is first established based on the simulation parameters shown in Table 2. Next, the sensing process of a space-based electromagnetic spectrum monitoring system is simulated using multicoset sampling and spatial random sampling. Then, power spectrum recons-truction is performed using a reconstruction algorithm. Finally, the generation of the spatial spectrum situation is achieved using the proposed OSSGTF algorithm.

The simulation parameters setting is summarized in Table 2. The sensing interval is scaled to facilitate simulation, with I_T and T_{tr} only considered at the ‘μs’ level. It should be noted that, based on studies of the spatial distribution of radiation sources in real-world scenarios and time series data dominated by transmission power, the spatial distribution of radiation sources often exhibits significant regional clustering. This means that several radiation sources are typically located within a single grid in 3D space, making the actual number of spatial grids occupied by the radiation sources smaller than the number of radiated signals R_s. Furthermore, when simulating the transmission power of radiated signals, it follows long-term periodicity and short-term similarity trends in time variations. Based on these temporal characteristics, a transmission power time series is randomly generated with $m=10$. Then, according to the parameter settings in Table 2, the radiated signals and the true spectrum situation $X_{1:T+1}$ during the entire sensing interval are generated using the multi-dimensional spectrum situation repre-sentation model based on (1). Low rank property is a fundamental premise and core aspect of spectrum situation generation. To verify it, the tensor $X_{1:T+1}$ is evaluated across each dimension using the Pearson correlation coefficient [20] as a standard.

As shown in Figure 5, correlations can be observed in the three independent spatial dimensions, as well as across the overall spatial, frequency, and temporal dimensions of $X_{1:T+1}$, with particularly high correla-

Table 2 Simulation parameters setting

Variables/Parameters	setting	explanation
$I_1 \times I_2 \times I_3$	15×15×10km	3D spatial dimension size
T	200	The number of sensing durations
m	10	Long-term temporal period
N	10000	The number of sampling points in a duration
R_s	15	The number of radiated signals
α	$U(2,4)$	Path loss exponent
d_0	1km	Unit distance of the spatial grid
w	$\ln w \sim N(0,2)$dB	Shadow fading

$G_t \cdot G_r$	35.89dB	Transmission and reception gain of ground antenna
h	550km	Transmission distance of satellite-ground link
f_R	10dB	Rician factor
$[f_1, f_2]$	[500,1500]MHz	Spectrum monitoring range
f_s	1GHz	Frequency bandwidth
I_T	10μs	Time interval in a duration
T_{tr}	1ms	The whole sensing interval
B	20MHz	Channel bandwidth
L	50	The number of channels

tions in time domain. This demonstrates that the $X_{1:T+1}$ is indeed approximately low rank. Subsequently, random spatial sampling with a consistent proportion is performed sequentially in each sensing duration to simulate the loss of the spectrum data. Multiple measurement vector sampling and power spectrum reconstruction are applied to the sampled spatial signals. To improve reconstruction efficiency, an algorithm called Fast Marginalized Block Sparse Bayesian Learning (BSBL-FM) [27] is employed, which can restore most of the information in frequency domain at the measurement grids. The sparse anomalies are then added to this incomplete spectrum situation, with the magnitude of the anomalies set to twice the maximum value of $X_{1:T+1}$, and the positions of them distributed randomly. These anomalies are incorporated into the original spatial situation tensor as shown in (7), forming the measurement tensor Y.

To validate the effectiveness of the proposed OSSGTF algorithm, this section compares the scheme with those tensor completion algorithms summarized in Table 1. The performance is evaluated under different spatial missing rates using the logarithmic form of the Average Normalized Running Error - log(ANRE) and runtime, where log(ANRE) is expressed as:

$$\log\left(\mathrm{ANRE}\right) = \log\left(\frac{1}{T}\sum_{t=1}^{T}\frac{\left\|\hat{X}_t - X_t\right\|_F^2}{\left\|X_t\right\|_F^2}\right), \tag{22}$$

where X_t and $\hat{X}_t$ are ground truth and completed and corrected spectrum situation sub-tensor, respectively.

The algorithm parameters for OSSGTF are listed in Table 3. The simulation is configured with a sparse anomaly ratio of 20%, and each method listed in the table is executed 50 times to meet the requirements of Monte Carlo experiments. The actual missing rate is smaller than the spatial missing rate since BSBL-FM does not completely reconstruct the entire frequency band, but rather reconstructs narrowband channels with a high proportion of energy. It ensures good performance even under high missing rates.

Table 3 OSSGTF parameters setting

parameters	Setting
ρ_1	0.001
ρ_s	0.001
μ	10
ξ_1	0.001
ξ_2	0.01
d	0.85
tol	0.01
μ_t	0.1
ϕ	0.01

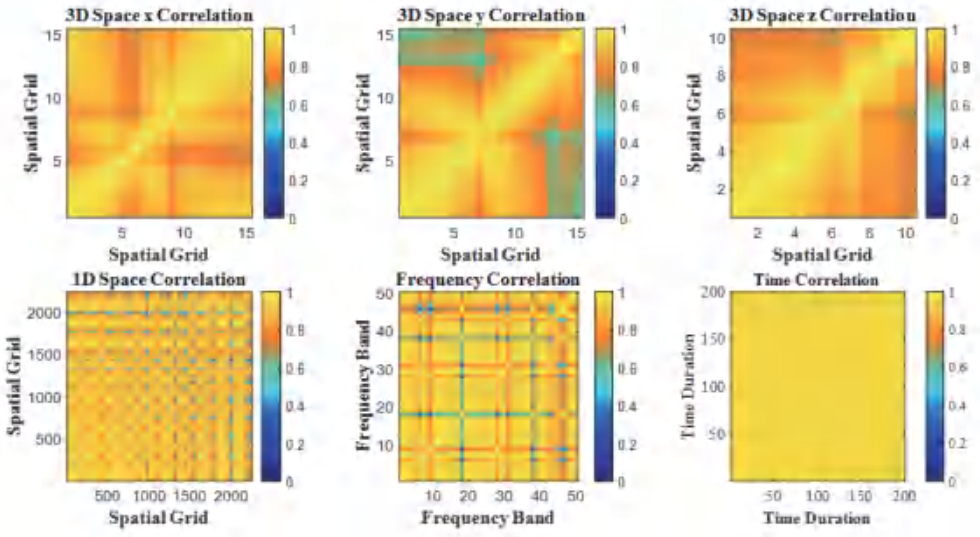

Figure 5 Correlation analyses of spatial spectrum situation in space, frequency, and time domains.

Figure 6 reveals the comparison curves of average completion error and running time at different spatial sampling rates. Compared to batch processing methods such as ALS and Bayesian Robust Tensor Factorization (BRTF), OSSGTF has shorter running time and higher completion efficiency. Although the error of OSSGTF is slightly higher the difference is only about 0.2%. This is because BRTF is based on Bayesian methods, with high computational complexity and a high number of iterations. ALS is the batch processing method, and as the temporal dimension increases, its running time will show exponential growth. The difference in accuracy is mainly due to OSSGTF using a threshold like method to correct anomalies. Compared to iterative methods, the accuracy is not high, and anomalies correction is one of the main factors affecting accuracy.

Compared to online completion methods such as Online Low-rank Subspace tracking by TEnsor CP decomposition (OLSTEC) and Bayesian Robust Streaming Tensor factorization (BRST), OSSGTF also demonstrate performance advantages of high efficiency and short running time. OLSTEC lacks inherent anomalies correction capability; however, when enhanced with ADMM-based anomalies correction, it demonstrates high performance. Not only that, as the missing rate increases, the error of OLSTEC also significantly increases. This is because it does not consider the smoothing constraint of temporal factor, thus ignoring the high correlation in the time dimension. In addition, OLSTEC only supports 3-D spectrum situation tensors. Therefore, it requires the 3-D space of the 5-D spectrum situation tensor to be vectorized, and then combined with the time and frequency domains to form a 3-D tensor. This approach does not meet the high-resolution requirements for generating the wide-area 3D spatial spectrum situation and ignores the correlation between different spatial dimensions.

Similar to BRTF, BRST based on Bayesian methods has the characteristics of high accuracy and complexity compared to OSSGTF. Figure 7 illustrates the normalized mean square error (NMSE) curves between the predicted sub-tensor $\hat{X}_{T+1}$ and the ground truth sub-tensor X_{T+1} under different

anomalies rates. Despite the high interference, OSSGTF is capable of accurately predicting the situation.

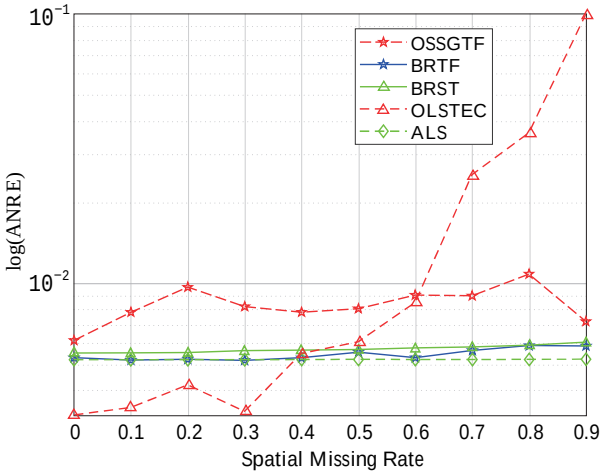

(a) Completion error vs. Spatial missing rate

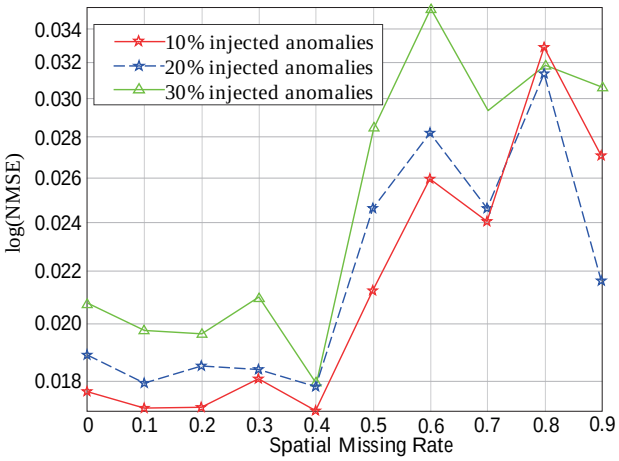

(b) Run Time vs. Spatial missing rate

Figure 6 Performance curve for spectrum situation. completion. completion in space, frequency, and time domains.

In summary, OSSGTF meets the scenario requirements for space-based spectrum situation awareness and achieves efficient generation of spectrum situations without compromising accuracy.

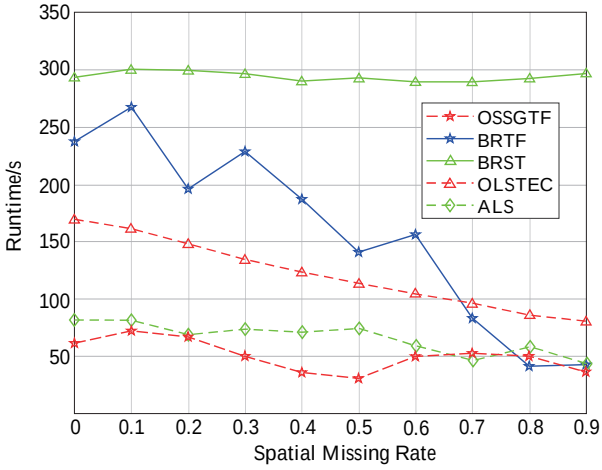

Figure 7 Prediction error vs. Spatial missing rate.

V. CONCLUSION

For spatiotemporal continuous spectrum situation awareness, this paper proposes a spectrum situation sensing model based on multi-dimensional compressive sampling and a spectrum situation generation algorithm via time-aware tensor factorization. Firstly, high-order structural information of the spatial spectrum situation is analyzed across multiple dimensions via tensor factorization to extract the correlation and structural characteristics of spatial electromagnetic information in the space, time, and frequency domains. Secondly, multi-dimensional compressive sampling is used to reduce the implementation cost of on-board broadband signal processing. Finally, by analyzing the temporal factor sequences from the situation decomposition, the proposed scheme simultaneously achieves anomalies correction, online completion, and situation prediction, thereby facilitating the efficient and reliable generation of the spatial spectrum situation.

References

[1] Yang Huang, Haoyu Cui, Yuqi Hou, Caiyong Hao, Wei Wang, Qiuming Zhu, Jie Li, Qihui Wu, Jiabo Wang. Space-Based Electromagnetic Spectrum Sensing and Situation Awareness[J]. Space Sci Technol, 2024, 4: 0109.

[2] Wu Q, Wang W, Li Z, et al. Spectrum Chain: A disruptive dynamic spectrum-sharing framework for 6G[J]. Science China Information Sciences, 2023, 66(3): 130302.

[3] Hao C, Wan X, Feng D, et al. Satellite-based radio spectrum monitoring: Architecture, applications, and challenges[J]. IEEE Network, 2021, 35(4): 20-27.

[4] Debroy S, Bhattacharjee S, Chatterjee M. Spectrum map and its application in resource management in cognitive radio networks[J]. IEEE Transactions on Cognitive Communications and Networking, 2015, 1(4): 406-419.

[5] Cai X, Wu C, Sheng J, et al. Spectrum situation awareness based on time-series depth networks for LTE-R communication system[J]. IEEE transactions on intelligent transportation systems, 2021, 23(7): 8629-8640.

[6] Bazerque J A, Mateos G, Giannakis G B. Group-lasso on splines for spectrum cartography[J]. IEEE Transactions on Signal Processing, 2011, 59(10): 4648-4663.

[7] Shen F, Ding G, Wu Q, et al. Compressed wideband spectrum mapping in 3D spectrum-heterogeneous environment[J]. IEEE transactions on vehicular technology, 2022, 72(4): 4875-4886.

[8] Wang J, Zhu Q, Lin Z, et al. Sparse Bayesian learning-based 3D radio environment map construction—Sampling optimization, scenario-dependent dictionary construction and sparse recovery[J]. IEEE transactions on cognitive communications and networking, 2023.

[9] Zhang G, Fu X, Wang J, et al. Spectrum cartography via coupled block-term tensor decomposition[J]. IEEE Transactions on Signal Processing, 2020, 68: 3660-3675.

[10] Y. Hu, R. Zhang. A spatiotemporal approach for secure crowdsourced radio environment map construction[J]. IEEE/ACM Transactions on Networking, 2020, 28(4):1790–1803.

[11] Schäufele D, Cavalcante R L G, Stanczak S. Tensor completion for radio map reconstruction using low rank and smoothness[C]//2019 IEEE 20th International Workshop on Signal Processing Advances in Wireless Communications (SPAWC). Cannes, France: IEEE, 2019: 1-5.

[12] Ren X, Mosavat-Jahromi H, Cai L, et al. Spatio-temporal spectrum load prediction using convolutional neural network and ResNet[J]. IEEE Transactions on Cognitive Communications and Networking, 2021, 8(2): 502-513.

[13] Kolda T G, Bader B W. Tensor decompositions and applications[J]. SIAM review, 2009, 51(3): 455-500.

[14] Sidiropoulos N D, De Lathauwer L, Fu X, et al. Tensor decomposition for signal processing and machine learning[J]. IEEE Transactions on signal processing, 2017, 65(13): 3551-3582.

[15] S. Bi, J. Lyu, Z. Ding, et al. Engineering radio maps for wireless resource management[J]. IEEE Wireless Communications, 2019, 26(2):133–141.

[16] Loo C. A statistical model for a land mobile satellite link[J]. IEEE transactions on vehicular technology, 1985, 34(3): 122-127.

[17] Ma Y, Gao Y, Liang Y C, et al. Reliable and efficient sub-Nyquist wideband spectrum sensing in cooperative cognitive radio networks[J]. IEEE Journal on Selected Areas in Communications, 2016, 34(10): 2750-2762.

[18] Yen C P, Tsai Y, Wang X. Wideband spectrum sensing based on sub-Nyquist sampling[J]. IEEE Transactions on Signal Processing, 2013, 61(12): 3028-3040.

[19] Kasai H. Online low-rank tensor subspace tracking from incomplete data by CP decomposition using recursive least squares[C]//2016 IEEE International Conference on Acoustics, Speech and Signal Processing (ICASSP). Shanghai, China: IEEE, 2016: 2519-2523.

[20] Li X, Wang X, Song T, et al. Robust online prediction of spectrum map with incomplete and corrupted observations[J]. IEEE Transactions on Mobile Computing, 2021, 21(12): 4583-4594.

[21] Zhang G, Wang J, Peng Q, et al. Tensor completion for dynamic spectrum cartography by canonical polyadic decomposition[C]//2021-IEEE International Conference on Communications (ICC). Montreal, Quebec, Canada: IEEE, 2021: 1-6.

[22] Lee D, Shin K. Robust factorization of real-world tensor streams with patterns, missing values, and outliers[C]//2021 IEEE 37th International Conference on

Data Engineering (ICDE). Chania, Greece: IEEE, 2021: 840-851.

[23] Zhao, Qibin et al. Bayesian Robust Tensor Factorization for Incomplete Multiway Data[J]. IEEE Transactions on Neural Networks and Learning Systems, 2014, 27: 736-748.

[24] Hawkins, Cole and Zheng Zhang. Variational Bayesian Inference for Robust Streaming Tensor Factorization and Completion[C]// 2018 IEEE International Conference on Data Mining (ICDM). Singapore, Singapore: IEEE, 2018: 1446-1451.

[25] Yokota T, Zhao Q, Cichocki A. Smooth PARAFAC decomposition for tensor completion[J]. IEEE Transactions on Signal Processing, 2016, 64(20): 5423-5436.

[26] Hyndman R J. Forecasting: principles and practice[M]. OTexts, 2018.

[27] Liu B, Zhang Z, Fan H, et al. Fast marginalized block sparse bayesian learning algorithm[J]. arXiv preprint arXiv:1211.4909.2012.

About the authors:

Ruifeng Xiao received the B.E. degree in communication engineering from Nanjing University of Post and telecommunications, Nanjing, China, in 2022. He is currently pursuing the M.S. degree in communication engineering in Shenzhen University, Shenzhen, China. His research interests include spatial spectrum situation awareness and space- based electromagnetic spectrum monitoring.

(Email: xiaoruifeng2022@email.szu.edu.cn)

Yuan Ma received the B.Sc. degree (First Class Hons.) in telecom-munications engineering from Beijing University of Posts and Telecom-munications, Beijing, China, in 2013, and the Ph.D. degree in electronic engineering from Queen Mary University of London, London, U.K., in 2017. She is currently an Associate Professor with the College of Electronic and Information Engineering, Shenzhen University, Shenzhen, China. Her research interests include cognitive communication networks, sparse signal processing, machine learning in communications, etc.

(Email: mayuan@szu.edu.cn)

Xingjian Zhang received the B.Sc. degree (First Class Hons.) in telecommunications engineering from Beijing University of Posts and Telecommunications, Beijing, China, and the Ph.D. degree in electronic engineering from Queen Mary University of London, London, U.K., in 2014 and 2018. He is currently an Associate Professor with the Department of Electronics and Information Engineering in the Harbin Institute of Technology (Shenzhen). His research interests include satellite communication, space-based wideband spectrum sensing and signal recognition.

(Email: x.zhang@hit.edu.cn)

面向超低轨通遥算一体化卫星星座的数传调度算法

李海，李勇军，王翔，宋鑫康，李信，李玉，赵尚弘

空军工程大学信息与导航学院 西安 710077

摘　要：超低轨通遥算一体化卫星星座具有建设成本低、重访周期短和观测分辨率高等优点，在应急救援和军事作战等关键领域发挥着重要作用。数传调度问题是影响超低轨通遥算一体化卫星星座效能发挥的关键问题。为了提高资源利用效率，针对超低轨通遥算一体化卫星星座的数传调度问题，在综合考虑直连卫星通信终端等多类型地面接收资源、差异化数传需求、遥感数据在轨处理和星间卸载传输等因素的基础上，建立了以最大化调度数传任务总收益为目标的约束满足模型。该数学模型的变量规模巨大且约束间相互耦合，难以直接进行求解，为此，提出了一种混合动态领域搜索算法和自适应大邻域搜索算法的两阶段数传调度算法（DNS-ALNS）。在第一阶段，通过动态邻域搜索算法对时延敏感型数传任务进行调度；在第二阶段，基于自适应大邻域搜索算法为时延容忍型数传任务分配数传资源；在两阶段迭代优化过程中，结合 Metropolis 准则来提高全局搜索能力。一系列仿真实验结果验证了 DNS-ALNS 算法相较于其他算法能够有效地提高数传收益。

关键词：超低轨；通遥算一体化；数传调度；动态邻域搜索；自适应大邻域搜索

Data transmission scheduling algorithm for Communication, remote sensing and computing integrated ultra-low orbit satellite constellation

LI Hai, LI Yongjun, WANG Xiang, SONG Xinkang, LI Xin, LI Yu, ZHAO Shanghong

School of Information and Navigation, Air Force Engineering University, Xi'an 710077, China

Abstract: Communication, remote sensing and computing integrated ultra-low orbit satellite constellation (VRC-USC) has the advantages of low construction cost, short revisit period, and high observation resolution, and plays an important role in key fields such as emergency rescue and military operations. The data transmission scheduling problem is a key issue that affects the effectiveness of the VRC-USC. In order to improve resource utilization efficiency, a constraint satisfaction model was established to maximize the total profit of scheduled data transmission tasks for the data transmission scheduling problem in the VRC-USC. This model takes into account multiple types of ground receiving resources such as direct satellite communication terminals, differentiated data transmission requirements, in orbit processing of remote sensing data, and inter satellite offloading and transmission. The variable scale of this model is huge and the constraints are coupled with each other, making it difficult to solve directly. Therefore, a two-stage data transmission scheduling algorithm (DNS-ALNS) combining

dynamic neighborhood search algorithm and adaptive large neighborhood search algorithm is proposed. In the first stage, delay sensitive data transmission tasks are scheduled using dynamic neighborhood search algorithms; In the second stage, data transmission resources are allocated for delay tolerant data transmission tasks based on adaptive large neighborhood search algorithm; In the two-stage iterative optimization process, the Metropolis criterion is combined to improve the global search capability. Extensive simulation experiments have verified that the DNS-ALNS algorithm can effectively improve data transmission profits compared to other algorithms.

Key words: ultra-low orbit; integration of remote sensing, communication and computing; data transmission scheduling; dynamic neighborhood search; adaptive large neighborhood search

1 引言

对地观测卫星通过其搭载的光学和微波等传感器，可有效地获取地球表面的空间信息数据，其已经在气象灾害预测、国土资源调查、生态环境保护等和军事侦察作战等领域发挥了关键作用[1-3]。超低轨通遥算一体化卫星星座具有效费比高、观测效果好、重访周期短和能耗低等优势，不仅可为边远地区的用户提供连续和稳定的通信服务，而且能够极大地提高卫星对地观测的分辨率，具有较高的战略价值和应用潜力[4-6]。尤其在救灾减灾和军事作战等关键应用领域，超低轨通遥算一体化卫星星座借助于星载智能处理，星间通信链路和星端直连等技术，可以实现观测数据直达用户通信终端，从而为用户提供准确和实时的高分辨遥感图像。

超低轨通遥算一体化卫星星座效能的发挥需要大规模卫星星座进行支撑，大规模卫星星座将产生海量的对地观测数据。同时随着对地观测卫星传感器观测精度的提升，超低轨通遥算一体化卫星星座产生的遥感数据规模越来越大。在超低轨通遥算一体化卫星星座中，观测数据通过星间通信链路和在轨数据处理等技术可提高数据回传的时效性和提高地面接收资源的利用效率，然而，由于我国地面站部署位置受限和星地通信链路容量有限等原因，如何将海量遥感数据及时回传到地面仍然面临着严峻的技术挑战[7-8]。因此，数传调度问题即在满足卫星资源约束和时间窗口约束的前提下，如何分配数据传输资源来最大化地面接收的遥感数据，成为了亟待解决的问题。

近年来，数传调度问题受到了广泛的关注和研究，文献[9]提出了一种可控粒子群调度算法，该调度算法设计了两种控制规则来自适应更新粒子的速度方向和尺度。文献[10]建立了一种考虑时间窗调整的数传调度模型，并且基于吱呀轮优化算法框架设计了一种多星数传调度算法。文献[11]建立了考虑风险控制的卫星数传模型，然后基于遗传禁忌求解算法提出了一种分布式并行求解策略。文献[12]提出了一种基于改进蚁群系统的卫星数传调度算法，该改进蚁群算法设计了一种蚂蚁探索概率自适应调整机制来提高算法的

性能。文献[13]在分析卫星数传资源筹划的特点基础上，提出了一种基于免疫遗传算法卫星数传资源规划方法，最后基于层次分析法设计了卫星数传资源筹划效能评估框架和流程。文献[14]基于自适应大邻域搜索（ALNS）框架提出了一种卫星数传调度问题求解算法，该算法结合卫星数传调度问题的启发式特征设计了 4 种摧毁算子和 3 种修复算子，通过摧毁算子和修复算子的迭代优化来搜索最优调度方案。文献[15]建立了一种考虑卫星数传等待时间的调度模型，并且基于模拟退火算法框架提出了一种两阶段调度策略，该算法在第一阶段为每个数传任务分配一个地面站用于接收其遥感数据，基于第一阶段的任务分配结果，在第二阶段，通过启发式策略为每个数传任务确定开始下传时间。

现有的针对数传调度问题的研究都只关注卫星和地面站之间通信链路的资源调度，没有充分考虑差异化数传需求、星间链路卸载传输、观测数据在轨处理和地面接收设备多样化等因素影响，这将导致现有的数传调度算法不能直接用于求解超低轨通遥算一体化卫星星座的数传调度问题。因此，为了提高卫星资源的利用效率，迫切需要针对超低轨通遥算一体化卫星星座设计一种高效的调度算法。

基于上述分析，本文针对超低轨通遥算一体化卫星星座的数传调度问题展开研究，主要工作和贡献介绍如下：

1）针对超低轨通遥算一体化卫星星座数传调度问题，建立了以最大化调度收益为目标的数学模型。该数学模型首次考虑了差异化的数传任务，多类型地面接收资源和观测数据在轨处理，并且包含了数传任务在星间卸载和星地下行传输过程中的多种约束条件。

2）提出了一种混合动态邻域搜索算法（DNS）和自适应大邻域搜索算法（ALNS）的两阶段数传调度算法（DNS-ALNS）。在第一阶段，设计了一种包含多个邻域结构的动态邻域搜索算法来调度时延敏感型数传任务；在第二阶段，在时延敏感型数传任务调度结果的基础上，针对时延容忍型数传任务调度问题，提出了一种基于自适应大邻域搜索算法的调度算法。在上述两阶段的迭代搜索过程中，引入 Metropolis 准则来提高算法全局搜索能力。

3）进行了一系列仿真实验，仿真实验结果验证了本文提出的 DNS-ALNS 算法的有效性。

2 系统模型

2.1 问题描述

在超低轨通遥算一体化卫星星座中，地面站和个人卫星通信终端均可接收遥感数据，地面站位置固定而个人终端的位置往往随机分布在地面网络覆盖不到的区域如高山和远海等。在超低轨通遥算一体化卫星星座中，每个卫星具有四条星间激光通信链路（反向缝两侧轨道面的卫星只有三条激光通信链路），波长是星间激光通信链路最小的频谱资源。卫星对地观测产生的遥感数据需要在给定的有效时间范围内下传给

地面站或个人卫星通信终端（将地面站和个人卫星通信终端统称为地面接收设备），遥感数据可通过星间激光通信链路卸载到其他卫星来实现实时下传，也可以先存储在星载内存中，等到卫星和地面站可见时，再通过卫星和地面站的通信链路进行下传。由于我国地面站部署位置受限，对时效性要求较高的遥感数据需通过星间通信链路将其卸载到和地面站可见的卫星才能实现实时下传。同时，卫星获取观测数据后可通过在轨数据智能处理来提高观测数据传输效率以及缩短传输时延。综上所述，超低轨通遥算一体化卫星星座的数传调度问题可概括为：通过合理分配星间通信链路的传输资源以及地面接收设备的接收资源，来最大化下传的观测数据的收益。为了简化描述，本文后续数传调度特指针对超低轨通遥算一体化卫星星座的数传调度。

为了使研究的问题更加聚焦，本章在合理概括数传调度问题实际情况和特点的前提下，做出如下假设：

- 只考虑卫星对地观测任务的观测数据的数据回传。
- 数传任务对应的遥感数据以整体的方式在星间和星地间进行传输。
- 假设下传给个人卫星通信终端的观测数据首先由其观测卫星进行数据处理然后再进行传输。
- 假设所有数传任务在调度周期开始前已经被确定，不考虑随机到达的动态任务。
- 假设每个通信天线一次只能建立一条通信链路，即任意一个卫星天线同一时刻只能和一个地面站天线建立通信链路，任意一个地面站天线同一时刻只能和一个卫星天线建立通信链路。
- 星间通信链路和星地通信链路在数据传输期间不允许被抢占；
- 数传任务在星间传输时只考虑传输时延，不考虑传播和处理等带来的延时，且每个数传任务在星间传输时只允许占用一个波长资源。

2.2 变量和符号定义

（1）数传任务集合$T=\{t_i \mid i \le n_t\}$，观测地面目标产生的待下传的观测数据被视作数传任务，每个数传任务对应一个观测目标的观测数据。数传任务根据时效性要求可分为时延敏感型和时延容忍型数传任务，时延敏感型数传任务具有较强的时效性，此类任务要求在较短的时限内完成观测数据的下传，而时延容忍型数传任务的有效下传时间较长，允许延迟一段时间再进行下传。此外，地面接收设备主要有地面站和直连卫星的个人终端如智能手机等，地面站位置是固定的，而个人终端的位置信息由用户位置决定，通常分布在地面网络无法提供泛在连接的区域。因此，本文根据地面接收设备和数传任务时效性要求将数传任务分为 3 类：1）个人终端时延敏感型数传任务；2）地面站时延敏感型数传任务；3）地面站时延容忍型数传任务；考虑到个人终端的数传任务往往对时效性要求较高，本文不考虑个人终端时延容忍型数传任务。综上所述，对于任意数传任务t_i，定义了以下任务属性：

- p_i 是数传任务 t_i 的单位数据收益，其反映了任务的重要性和紧急程度，不同类型任务的单位数据收益不同，第一类任务单位数据收益最高，第二类任务单位数据收益次之，第三类任务单位数据收益最低，
- d_i 是数传任务 t_i 的数据大小，数传任务必须在其有效时间窗口内下传到地面站，否则数传任务将失去其效用。
- $[fst_i, fet_i]$ 是数传任务 t_i 的有效时间窗口，有效时间窗口反映了任务对时效性的要求，数传任务必须在其有效时间窗口内下传到地面站，否则数传任务将失去其效用。时延敏感型任务的有效时间窗口较短，而时延容忍型任务的有效时间窗口较长。
- ids_i 为数传任务 t_i 所属的卫星标识。
- ξ_i^t 表示数传任务 t_i 的类型，$\xi_i^t = k$ 代表任务 t_i 是第 k 种类型任务。如果任务需下传给个人终端即 $\xi_i^t = 1$，则 pt_i 代表接收数传任务 t_i 的个人通信终端，pos_s^i 表示接收数传任务 t_i 的个人终端所在位置的经度、纬度和高度信息。此外，N_{ξ_1}、N_{ξ_2} 和 N_{ξ_3} 分别表示第一类、第二类和第三类任务的数量

（2）卫星集合 $S = \{s_j \mid j \le M\}$，其用于获取地面目标的观测数据以及将观测数据下传给地面站，其中 M 为对地观测卫星数量，对于任意对地观测卫星 s_j，定义了以下卫星属性：

- E_j 是卫星 s_j 的能量容量，卫星的能量容量表示在调度周期内卫星可消耗的能量的最大值。
- ξ_i^s 表示卫星 s_j 的类型，$\xi_i^s = 0$ 表示卫星 s_j 是通信卫星即只具备通信功能，反之，$\xi_i^s = 1$ 表示卫星 s_j 是通遥算一体化卫星即具备通信和遥感功能。
- E^i 表示卫星 s_j 的最大数传能量即在调度周期内允许用于执行数传任务而消耗的能量的最大值，通常通遥算一体化卫星执行数传任务可消耗的能量大于通信卫星。
- v_s^i、v_g^i 和 v_p^i 分别表示卫星 s_j 的星间通信链路、卫星与地面站的通信链路以及卫星与个人终端的通信链路的传输速率。

- e_s^i、e_g^i 和 e_p^i 分别表示卫星 s_j 的星间通信链路、卫星与地面站的通信链路和卫星与个人终端的通信链路的能量效率，通信链路的能量效率表示传输单位数据而消耗的能量。
- tr_s^i 为卫星 s_j 传输遥感数据到不同的地面接收设备所需要的转换时间。

（3）地面站集合 $G=\{g_k \mid k \le N\}$，其中 N 是地面站数量，对于任意地面站 g_k，定义以下地面站属性：

- pos_g^k 代表地面站 g_k 的位置信息，包含经度、维度和高度信息。
- tr_g^k 为地面站 g_k 接收来自不同卫星的遥感数据所需要的转换时间。

（4）$W_g=\{w_g^{jkl} \mid j \le M, k \le N, l \le L_g^{jk}\}$ 表示卫星和地面站间的可行传输时间窗口集合，其中 L_g^{jk} 表示卫星 s_j 和地面站 g_k 的可行传输窗口数量，卫星 s_i 和地面站 g_j 的第 k 个可行传输窗口 $w_g^{jkl} \in W_g$，可表示为对 $w_g^{jkl}=[st_g^{jkl}, et_g^{jkl}]$，其中 st_g^{jkl} 和 et_g^{jkl} 分别表示可行传输窗口 w_g^{ijk} 的开始时间和结束时间。

（5）$W_p=\{w_p^{jkl} \mid j \le M, k \le N_{\xi_1}, l \le L_p^{jk}\}$ 表示卫星和个人设备间的可行传输时间窗口集合，其中 L_g^{jk} 表示卫星 s_j 和接收任务 t_k 的个人终端 pt_k 之间的可行传输窗口数量，$\forall w_p^{jkl} \in W_p$，可表示为 $w_p^{jkl}=[st_p^{jkl}, et_p^{jkl}]$，其中 st_p^{jkl} 和 et_p^{jkl} 分别表示可行传输窗口 w_p^{jkl} 的开始时间和结束时间。

（6）$FS=\{fs_i \mid i \le N_{fs}\}$ 是为了保证遥感数据实时下传而预留的波长资源，N_{fs} 为预留的频隙资源数量。

（7）$OS_i=\{os_{ij} \mid j \le N_{os_i}\}$ 表示任务 t_i 的卸载卫星集合，任务 t_i 的卸载卫星集合由在任务 t_i 的有效时间窗口内与地面接收设备存在可行传输窗口的卫星组成。

（8）任务从其所属卫星通过星间激光通信链路传输到卸载卫星存在多条卸载路径，基于星间光网络拓扑结构和任务的卸载卫星集合，可计算出任务卸载路径集合 $R=\{r_i \mid i \le N\}$，其中任务 t_i 的卸载路径集合可表示为 $r_i=\{r_{ij} \mid r_{ij}, j \le N_{r_i}\}$，其中 N_{r_i} 为任务 t_i 的卸载路径数量，$\forall r_{ij} \in r_i$，$r_{ij}=[ids_i, r_{ij}^1, r_{ij}^l, \cdots, r_{ij}^e], l \le |r_{ij}|$，$r_{ij}$ 为任务 t_i 的第 j 条卸载路径，其中 $|r_{ij}|$ 为卸载路径 r_{ij} 包含的星间通信链路的数量，r_{ij}^k 表示卸载路径 r_{ij} 的第 k 跳卫星节点标识，r_{ij}^e 为卸载路径 r_{ij} 的下传卫星节点标识，下传卫星节点用于将任务下传给地面接收设备，其可以是任务 t_i 所属的卫星或其对应的卸载卫星。

$\varphi=\{\varphi_i \mid i \le N\}$ 表示考虑大众用户的卫星数传调度结果，其中 φ_i 为任务 t_i 的调度结果，可表示为：

$$\varphi_i = [x_i', X_i, Y_i, Z_i, TW_i, DW_{ii}] \tag{1}$$

其中 x_i' 为二进制变量，$x_i' = 0$ 表示任务 t_i 没有成功下传或任务 t_i 通过星间卸载的方式进行下传，$x_i' = 1$，表示任务 t_i 通过其所属卫星直接进行下传，$X_i = \{x_{ij} \mid j \le N_{r_i}\}$ 表示任务的 t_i 卸载路径选择结果，$x_{ij} = 1$ 代表任务 t_i 选择卸载路径 r_{ij} 进行传输；$Y_i = \{y_{ij}^{lnm} \mid j \le N_{r_i}, l \le N_{fs}, n \le M, m \le M\}$ 表示任务 t_i 的卸载路径传输结果，$y_{ij}^{lnm} = 1$ 代表任务 t_i 选择卸载路径 r_{ij} 以及基于频隙 fs_l 进行传输，并且卸载路径中包含卫星 s_n 到 s_m 的星间激光通信链路。Z_i 反映任务 t_i 下传到地面接收设备时选择的可行传输窗口，其可表示为：

$$Z_i = \begin{cases} \{z_g^{ijkl} \mid j \le M, k \le N, l \le L_g^{jk}\}, & \text{if } \xi_i \le 2 \\ \{z_p^{jil} \mid j \le M, l \le L_p^{ij}\}, & \text{if } \xi_i = 3 \end{cases} \tag{2}$$

$z_g^{ijk} = 1$ 和 $z_p^{ijk} = 1$ 分别表示在可行传输窗口 w_g^{ljk} 和 w_p^{ijk} 下传任务 t_i 到地面接收设备。$TW_i = [Tst_i, Tet_i]$ 为卸载传输时间窗口，其中 Tst_i 和 Tet_i 分别表示任务 t_i 在星间卸载传输时的开始时间和结束时间，DW_i 表示任务 t_i 的下传结果，其可以表示为:

$$DW_i = \begin{cases} \{dw_i^{jkl} \mid j \le M, k \le N, l \le L_g^{jl}\}, & \text{if } y_g^{iljk} = 1 \\ \{dw_i^{jl} \mid j \le M, l \le L_p^{jk}\}, & \text{if } y_p^{jil} = 1 \end{cases} \tag{3}$$

其中 $dw_i^{jkl} = [dst_i^{jkl}, det_i^{jkl}]$ 以及 $dw_i^{jk} = [dst_i^{jk}, det_i^{jk}]$，$dst_i^{jkl}$ (dst_i^{jl}) 和 det_i^{jkl} (det_i^{jl}) 分别表示任务 t_i 在可行传输时间窗口 w_g^{jkl} (w_p^{jik}) 内进行下传的开始时间和结束时间，其中 $det_i^{jkl} = dst_i^{jkl} + d_i / v_g^j$ 以及 $det_i^{jl} = dst_i^{jl} + d_i / v_p^j$ 。

2.3 约束满足模型构建

基于以上介绍，将面向超低轨通遥算一体化卫星星座的数传调度问题建模为约束满足模型。该模型的主要包括目标函数和约束条件，具体介绍如下：

2.3.1 目标函数

本文以数传收益最大化为目标即最大化成功调度的数传任务的收益之和，目标函数可表示为：

$$f: \max \sum_{i \le N} (x_i + \sum_{j \le N_{r_i}} x_{ij}) i p_i \tag{4}$$

2.3.2 约束条件

（1）数传任务唯一性约束：每个数传任务 t_i 可以通过其所属卫星直接下传或卸载到其他卫星进行下传，但只需要被执行一次。

$$x_i + \sum_{j \le N_{r_i}} x_{ij} \le 1, \forall i \le N \tag{5}$$

（2）数传任务下传时间窗口唯一性约束：每个数传任务 t_i 只能通过一个可行传输窗口下传到地面接收设备。

$$\begin{aligned} \sum_{j \le M, k \le N, l \le L_g^{jk}} z_g^{ijkl} \le 1, \forall i \le N, \quad \text{if } \xi_i \le 2 \\ \sum_{j \le M, l \le L_g^{ji}} z_g^{jil} \le 1, \forall i \le N, \quad \text{if } \xi_i = 3 \end{aligned} \tag{6}$$

（3）数传任务下传时间窗口相关约束：任务 t_i 的下传开始时间和结束时间必须在卫星和地面接收设备的可行传输时间窗口内。

$$st_g^{jkl} \le dst_i^{jkl} \le et_g^{jkl}, \forall i \le N, \text{if } \xi_i \le 2, z_g^{ijkl} = 1 \tag{7}$$

$$st_g^{jkl} \le det_i^{jkl} \le {}_g^{jkl}, \forall i \le N, \text{if } \xi_i \le 2, z_g^{ijkl} = 1 \tag{8}$$

$$st_p^{jil} \le dst_i^{jl} \le et_p^{jil}, \forall i \le N, \text{if } \xi_i = 3, z_p^{jil} = 1 \tag{9}$$

$$st_p^{jil} \le det_i^{jl} \le et_p^{jil}, \forall i \le N, \text{if } \xi_i = 3, z_p^{jil} = 1 \tag{10}$$

（4）星间激光通信链路的波长唯一性约束：星间激光通信链路的一个波长资源只能同时支撑一个数传任务在星间的卸载传输。

$$\begin{aligned} &[Tst_i, Tet_i] \cap [Tst_{i'}, Tet_{i'}] = \varnothing, \\ &\forall i, i' \le N, n, m \le M, \text{ if } y_{ij}^{lnm} \text{i} y_{i'j'}^{lnm} = 1 \end{aligned} \tag{11}$$

（5）卫星传输唯一性约束：卫星某一时刻只能和一个地面接收设备建立通信链路：

$$\begin{aligned} &[dst_i^{jkl}, det_i^{jkl}] \cap [dst_{i'}^{jk'l'}, det_{i'}^{jk'l'}] = \varnothing, \\ &\forall i, i' \le N_t, k, k' \le N, l \le L_g^{jk}, L' \le L_g^{jk'} \end{aligned} \tag{12}$$

$$[dst_i^{jl}, det_i^{jl}] \cap [dst_{i'}^{jl'}, det_{i'}^{jl'}] = \varnothing, \quad \forall i, i' \le N_t, l \le L_p^{ij}, L' \le L_p^{i'j} \tag{13}$$

$$[dst_i^{jkl}, det_i^{jkl}] \cap [dst_{i'}^{jl'}, det_{i'}^{jl'}] = \varnothing, \quad \forall i, i' \le N_t, k \le N, l \le L_g^{jk}, l' \le L_p^{i'j} \tag{14}$$

其中（15）和（16）分别表示卫星不能和地面站、个人终端同时保持 2 条通信链路，以及（17）表示卫星天线不能同时传输数据给个人终端和地面站。

（6）地面站传输唯一性约束：地面站某一时刻只能和一个卫星建立通信链路：

$$[dst_i^{jkl}, det_i^{jkl}] \cap [dst_{i'}^{j'k'l'}, det_{i'}^{j'k'l'}] = \varnothing, \quad \forall i, i' \le N, j, j' \le M, l \le K_g^{jk}, l' \le K_g^{j'k} \tag{15}$$

（7）卫星天线转换时间约束：卫星下传遥感数据给不同的地面设备需要一定的时间间隔来建立通信链路。

$$det_i^{jkl} + tr_s^j \le dst_{i'}^{jk'l'}, \forall i, i' \le N_t, k, k' \le N, \quad l \le L_g^{jl}, l' \le L_g^{j'l'}, \text{ if } dst_i^{jkl} \le dst_{i'}^{jk'l'} \tag{16}$$

$$det_i^{jl} + tr_s^j \le dst_{i'}^{jl'}, \forall i, i' \le N_t, \quad l \le L_p^{ij}, l' \le L_p^{i'j}, \text{ if } dst_i^{jl} \le dst_{i'}^{jl'} \tag{17}$$

$$det_i^{jkl} + tr_s^j \le dst_{i'}^{jl'}, \forall i, i' \le N_t, \quad l \le L_g^{jl}, l' \le L_p^{i'j}, \text{ if } dst_i^{jkl} \le dst_{i'}^{jl'} \tag{18}$$

其中（19）和（20）表示卫星下传遥感数据给两个不同的地面站和两个不同的个人终端时需要一定的转换时间，式（21）表示卫星下传遥感数据给不同类型的地面接收设备需要一定的转换时间。

（8）地面站天线转换时间约束：

$$det_i^{jkl} + tr_g^l \le dst_{i'}^{j'kl'}, \forall i, i' \le N_t, j, j' \le M, \quad l \le L_g^{jl}, l' \le L_g^{j'l'}, \text{ if } dst_i^{jkl} \le dst_{i'}^{jkl'} \tag{19}$$

（9）卫星能量约束：

$$\sum_{i\le N_t,k\le N_l,l\le L_g^{jk}} z_g^{ijkl}\,id_i\,ie_g^j+\sum_{i\le N_t,l\le L_p^{ji}} z_p^{jil}\,id_i\,ie_p^i+\sum_{i\le N_t,n\le N_{f_i},l\le N_{fs},m\le M} y_{in}^{ljm}\,ie_s^j\le E_j,\forall j\le M \tag{20}$$

3 两阶段数传调度算法

本节首先介绍两阶段数传调度算法框架，然后对框架的具体组成部分分别进行介绍。

§3.1 算法框架

传统的数传调度问题已经被证明是一个 NP-hard 问题[16-18]，其求解复杂度随问题规模增长呈指数型增长，是一个难以求解的复杂优化问题。超低轨通遥算一体化卫星星座的数传调度问题进一步考虑了多类型地面接收设备、差异化数传任务、数据在轨处理和星间卸载传输等因素，相互耦合的变量和复杂的约束条件使得该数传调度问题更加难以求解。针对此类解空间规模巨大且带有复杂约束条件的调度问题，难以设计精确求解算法，同时群智能优化算法如遗传算法等具有计算复杂度高和容易陷入局部最优解等缺点。启发式搜索算法在深入分析优化问题领域知识的基础上，通过在搜索过程中引入启发式信息来提高搜索效率，能够快速地找到最优解或近似最优解，尤其是针对大规模复杂优化问题，启发式搜索算法能够以较短的计算时间开销找到满意可行解，因此，综合考虑优化算法性能和求解速度，我们基于启发式搜索算法框架来设计数传调度算法。

分析三种数传任务特点可知：1）时延容忍型数传任务的单位数据收益低且数据量较大，其调度价值远小于时延敏感型数传任务；2）时延敏感型数传任务的有效时间窗口较短，难以直接通过其所属卫星下传给地面接收设备，往往需要通过星间卸载才能下传，时延容忍型数传任务的有效时间窗口较长，可下传时延容忍型数传任务的可行传输窗口数量较多，往往可通过其所属卫星直接下传。考虑到过度的数传任务需求和稀缺的数传资源之间的现实矛盾，单位数据收益较高的时延敏感型数传任务应该被优先调度，同时为了避免时延容忍型数传任务对数传资源的过度占有，单位数据收益较低的时延容忍型数传任务更适合通过其所属卫星直接下传而不采用星间卸载的方式进行下传。同时，在超低轨通遥算一体化卫星星座的数传调度问题的难点在于规模巨大的解空间以及相互耦合的变量和约束条件，为了降低求解难度，本文将超低轨通遥算一体化卫星星座架构下的数传调度分解为两个阶段：在第一个阶段，优先调度时延敏感型数传任务，时延敏感型数传任务可通过其所属卫星和地面接收设备的可行传输窗口直接下传或星间卸载的方式进

行下传。第二个阶段即时延容忍型数传任务调度阶段，对于时延容忍型数传任务，为了减少数传任务在星间卸载传输造成的资源浪费，只允许通过其所属卫星和地面接收设备的可行传输窗口直接进行下传。

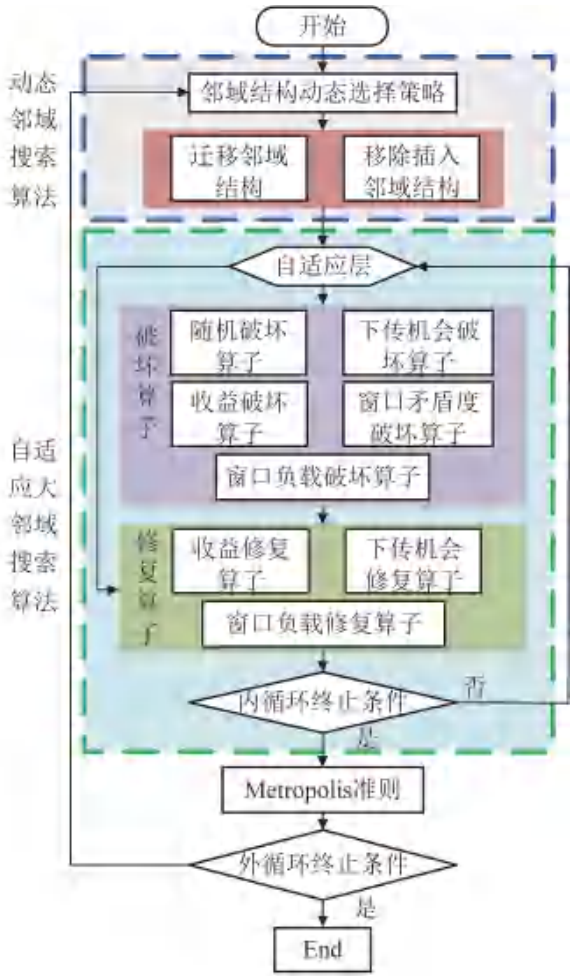

图1 DNS-ALNS算法框架图

基于上述分析，我们提出了一种混合动态邻域搜索算法（DNS）和自适应大邻域搜索算法（ALNS）的两阶段数传调度算法（DNS-ALNS），在 DNS-ALNS 算法的第一阶段，通过 DNS 算法对时延敏感型数传任务进行调度，在第二阶段，基于 ALNS 算法为非时延敏感型数传任务分配地面接收资源，执行完上述两阶段后，结合 Metropolis 准则来决定是否接受新产生的数传调度解，重复上述过程直到满足循环终止条件。具体来说，在 DNS 算法中，设计了迁移邻域结构和移除插入邻域结构两种邻域结构来拓展邻域搜索的范围，并且通过邻域结构动态选择策略提高邻域结构选择的针对性；在本文提出的 ALNS 算法中，根据非时延敏感型数传调度问题的启发式特征提出了 5 种破坏算子和 3 种修复算子，通过自适应层来动态更新破坏和修复算子的选择概率，在每次迭代过程中，自适应选择破坏算子和修复算子来进行邻域搜索，并且只贪婪地接受收益有改进的数传调度解。对于上述两阶段求出的数传调度解，根据 Metropolis 准则来判断

是否接受未改进的数传调度解，本文设计的 Metropolis 准则通过在温度衰减过程中引入概率升温策略来进一步提高算法的全局搜索能力。

§3.2 动态邻域搜索算法

针对时延敏感型数传任务调度问题，提出了一种动态邻域搜索算法（DNS），在 DNS 算法中，为了拓展邻域搜索的范围，设计了两种邻域结构，并且设计了一种邻域结构动态选择策略来实现邻域结构的自适应选择。

§3.2.1 迁移邻域结构

迁移邻域结构核心思想是将剩余可用能量较少的卫星上执行的数传任务迁移到剩余可用能量较多的卫星上。迁移邻域结构的伪代码如**算法** 1 所示：

算法 1 迁移邻域结构

初始化迁移任务比例 η_m、成功下传的任务数量 N_{sch}，卫星剩余可用能量 E_S^F；
for i=1:1: $\eta_m i N_{sch}$
  根据 E_S^F 选择剩余可用能量最少的卫星 s_L；
  提取通过卫星 s_L 下传的时延敏感型数传任务集合 T_{s_L}，对 T_{s_L} 按照数据量降序进行排序；
  for k=1:1: $|T_{s_L}|$
    计算 T_{s_L} 中第 k 个任务 $T_{s_L}^k$ 的卸载卫星集合 $OS_{T_{s_L}^k}$，对 $OS_{T_{s_L}^k}$ 按照剩余可用能量降序进行排序；
    for l=1:1: $OS_{T_{s_L}^k}$；
      尝试将任务 $T_{s_L}^k$ 卸载到卫星 $OS_{T_{s_L}^k}^l$ 来进行下传；
      if 任务 $T_{s_L}^k$ 卸载传输成功 do
        跳出循环，开始下一个任务的迁移操作
      end if
    end for
  end for
end for

迁移邻域结构的流程的简要描述如下：

第 1 行初始化迁移任务比例 η_m 等参数。

第 3~4 行首先筛选出剩余可用能量最少的卫星，然后将此卫星的调度数传任务序列中的时延敏感型数传任务按照数据量降序进行排序，即优先将数据量大的任务迁移到其他卫星进行下传。

第 6 行代表将待迁移任务 $T_{s_L}^k$ 的卸载卫星集合按照剩余可用能量降序进行排序。

第 7~12 行表示尝试将待迁移任务 $T_{s_L}^k$ 卸载到其他卫星进行下传。

§3.2.2 移除插入邻域结构

移除插入邻域结构通过移除任务和再插入任务来进行邻域搜索，具体来说，在移除操作中，首先从当前调度方案中移除收益能耗比低的时延敏感型数传任务，收益能耗比定义为：

$$\rho_i = p_i \Big/ \left(\sum_{j\le M,k\le N,l\le L_g^{jk}} z_g^{ijkl} ie_g^i + \sum_{j\le M,l\le L_g^{jk}} z_p^{jil} ie_p^i + \sum_{n\le N_{fj},l\le N_{fs},m\le M} y_{in}^{ljm} ie_s^j \right) \tag{21}$$

由式（23）可知，任务的收益能耗比大意味着下传此任务时，消耗单位能量和频谱等数传资源可带来较大的数传收益，因此，优先移除收益能耗比低的数传任务。在移除操作中，移除的数传任务占成功调度任务数量比例为 η_r，并且在后续的插入操作中，最后插入在当前迭代中移除的数传任务。在插入操作中，单位数据收益较高的个人时延敏感型数传任务被优先调度，并且按照数据量从大到小的顺序依次插入未调度的数传任务。对于每个未调度的数传任务，首先选择一条卸载路径以及分配相应的空闲频隙用于星间卸载传输，然后尝试在卫星和地面接收设备的可行传输窗口中进行下传。在插入未调度的数传任务时，计算每条卸载路径被选择时将消耗的能量，然后选择能量消耗最小的卸载路径进行传输。

§3.2.3 邻域结构动态选择策略

多种邻域结构组合搜索的方式可以避免算法由于搜索方向单一而陷入局部最优解，邻域结构的选择直接决定了邻域搜索的效率，为了实现邻域结构的自适应选择，提出了一种邻域结构动态选择策略。在邻域结构动态选择策略中，基于轮盘赌策略来选择邻域结构，并且邻域结构的选择概率根据其历史表现进行动态更新。具体来说，经过一定的迭代次数 ϑ_D 后，邻域结构的选择概率更新如下：

$$p_n^k = (1-\omega) \cdot p_n^k + \omega \cdot \frac{N_{imp}^k}{N^k}, k = 1,2 \quad (22)$$

$$p_n^k = \frac{p_n^k}{p_n^k + p_n^k}, k = 1,2 \quad (23)$$

其中 p_n^1 和 p_n^2 分别表示移除插入邻域结构和迁移邻域结构的选择概率，ω 是权重因子，反映了邻域结构最近的搜索表现对选择概率更新的影响程度，N_{imp}^k 表示选择第 k 个邻域结构成功提高数传收益的次数，N^k 表示在最近的 N_{ite} 次迭代更新中选择第 k 个邻域结构的次数。

§3.3 自适应大邻域搜索算法

算法 2 ALNS 算法

初始化非时延敏感型数传任务集合、可行传输时间窗口集合、卫星剩余能量、数传调度解 Sch_0；
初始化最佳调度解和当前调度解：$Sch_B \leftarrow Sch_0$，$Sch_N \leftarrow Sch_0$；
for ite=1:1: Ite_m
  基于破坏和修复算子的权重选择破坏算子 D_c 和修复算子 R_C；
  基于选择的破坏和修复算子 D_c 和 R_C 更新当前调度解 Sch_N；
  if Sch_N 的收益大于 Sch_B
    $Sch_B \leftarrow Sch_N$；
  else
    $Sch_N \leftarrow Sch_B$；
  end if
  if ite % ϑ_A ==1
    更新选择算子 D_c 和 R_C 的分数
  end if
end for

自适应大邻域搜索算法（ALNS）是大邻域搜索算法的改进版本，ALNS 通过设计多个破坏算子和修复算子来拓展邻域搜索的范围，并且通过破坏算子和修复算子的自适应组合来提高算法的搜索速度[32-34]，ALNS 算法相较于其他邻域搜索算法，搜索表现好而且求解速度快。本文基于 ALNS 算法对非时延敏感型任务进行调度，与经典的 ALNS 算法采用模拟退火准则接受较差解不同，为了提高 ALNS 算法的收敛速度，

本文提出的 ALNS 只接受收益有改进的解。ALNS 算法的伪代码如**算法** 2 所示，首先在时延敏感型数传任务调度结果的基础上，根据数据量从大到小的顺序，依次为非时延敏感型数传任务分配最早的下传时间，从而生成初始数传调度解 Sch_0，并且基于 Sch_0 来初始化最佳调度解 Sch_B 和当前调度解 Sch_C。然后开始 ALNS 算法的迭代搜索，在每一次迭代搜索过程中，ALNS 算法选择一个破坏算子和修复算子来进行邻域搜索，并且只贪婪地接受收益有改进的解，每次迭代之后根据算子的表现更新其分数，若干次迭代之后，基于算子的分数对权重进行更新。

§3.3.1 破坏算子

本文提出的 ALNS 算法包括了五种破坏算子：随机破坏算子、收益破坏算子、窗口破坏算子、窗口矛盾度破坏算子和任务矛盾度破坏算子。每个破坏算子移除的任务数量为 N_D，移除任务数量占所有已调度任务数量的比例为 R_D，为了避免对同一任务重复进行移除和插入操作，移除的任务在后续的修复算子中被禁止插入。

本章设计的 5 中修复算子定义如下：

（1）随机破坏算子：随机破坏算子是最简单的破坏算子，即在调度方案中随机移除 N_D 个非时延敏感型任务。

（2）收益破坏算子：在收益破坏算子中，贪婪移除 N_D 个收益最低的非时延敏感型任务。

（3）下传机会破坏算子：将任务的下传机会定义为可用于下传任务的可行传输窗口的数量，任务的下传机会越大，意味着该任务在当前调度解中被移除后再次下传的概率越大，因此，N_D 个下传机会大的任务被移除。

（4）窗口矛盾度破坏算子：卫星和地面站间的可行传输窗口的窗口矛盾度定义如下：

$$\psi_g^{jkl} = \frac{\sum_{w \in over(w_g^{jkl})} \sigma(w_g^{jkl}, w)}{et_g^{jkl} - st_g^{jkl}} \tag{24}$$

其中 ψ_g^{jkl} 是可行传输窗口 w_g^{jkl} 的窗口矛盾度，$over(w_g^{jkl})$ 代表与可行传输窗口 w_g^{jkl} 重叠的可行传输窗口集合，$\sigma(w_g^{jkl}, w)$ 为可行传输窗口 w 和 w_g^{jkl} 间的重叠时间长度。可行传输窗口的窗口矛盾度越大，则表明此窗口和其他可行传输窗口的重叠时间越长，在此窗口中下传的任务对其他未调度任务的下传影响越大，因

此，在窗口矛盾度破坏算子中，依次移除窗口矛盾度大的可行传输窗口中的所有任务，直至移除 N_D 个任务为止。

（5）窗口负载破坏算子：在可行传输窗口下传的任务越多，则此窗口阻塞后续未调度任务的可能性越大，因此，在窗口负载破坏算子中，依次移除下传的任务数据最大的可行传输窗口中下传机会最大的任务，直至移除 N_D 个任务为止。

§3.3.2 修复算子

针对破坏后的调度解，设计了三种修复算子用于插入未调度任务到数传调度解中，修复算子规定了未调度任务的插入顺序和插入未调度任务时其可行传输窗口的插入顺序。

（1）收益修复算子：按照收益从大到小的顺序对未调度任务进行排序，然后优先插入收益较大的未调度任务。在插入未调度任务时，优先选择在窗口矛盾度小的可行传输窗口中下传任务。

（2）下传机会修复算子：按照任务的下传机会进行排序，优先插入下传机会较少的任务。与收益修复算子类似，在插入未调度任务时，优先选择在窗口矛盾度小的可行传输窗口中下传任务。

（3）窗口负载修复算子：在窗口负载修复算子中，按照收益从大到小的顺序依次插入未调度任务，在插入未调度任务时，优先插入该任务到下传数据总量较小的可行传输窗口。

§3.3.3 自适应层

ALNS 算法通过自适应层来选择算子以及更新算子的选择概率，每个破坏算子和修复算子都对应一个权重 ϕ 和分数 φ，算子的分数在每一次迭代后进行更新：

$$\varphi = \begin{cases} \varphi + \beta_{1\prime} & \text{if } p_N \geq p_B \\ \varphi + \beta_{2\prime} & \text{if } p_N < p_B \end{cases} \tag{25}$$

其中 p_N 和 p_B 分别表示当前调度解的收益和全局最优调度解的收益，β_1 和 β_2 用于破坏和修复算子分数调整的系数，通常 $\beta_1 > \beta_2$，因此，当前调度解的收益有所改进时，对应的破坏算子和修复算子的分数将得到较大的提升。若干次迭代之后，基于算子的分数对权重进行更新并且重置算子的分数，算子的权重更新公式如下：

$$\phi_i = \lambda\phi_i + (1-\lambda)\varphi_i \Big/ \sum_{i \le N_o} \varphi_i \tag{26}$$

其中 ϕ_i 表示第 i 个破坏算子或修复算子的权重，N_o 为破坏算子或修复算子的总数，λ 是权重系数，其反映了算子最新的表现对算子权重的影响程度。ALNS 算法根据轮盘赌策略来选择算子，第 i 个破坏算子或修复算子的选择概率为：

$$pro_i = \phi_i \Big/ \sum_{i \le N_o} \phi_i \tag{27}$$

§3.3.4 Metropolis 准则

为了避免陷入局部最优调度解，DNS-ALNS 算法根据 Metropolis 准则来接受求解得到的较差调度解，在第 ite 次迭代中，接受新产生的调度解的概率为：

$$P_{acc} = \exp\left(\frac{p_{ite}^f - p_{ite}^s}{T_{ite}}\right) \tag{28}$$

其中 p_{ite}^f 和 p_{ite}^s 分别为第 ite 次迭代周期结束和开始时调度解的收益，T_{ite} 表示第 ite 次迭代周期的温度值。为了进一步提高 DNS-ALNS 算法的全局搜索能力，在温度衰减过程中引入概率升温策略，即在降温过程中温度以一定的概率升高，概率升温策略下温度更新公式如下：

$$T_{ite} = \begin{cases} T_{ite} \cdot \mu, \ if \ p_{ite}^f \ge p_{ite}^s \\ T_{ite} \cdot \mu, \ if \ p_R > \exp\left(\dfrac{p_{ite}^f - p_{ite}^s}{ite_m - ite}\right) \\ T_{ite} \Big/ \mu, \ if \ p_R \le \exp\left(\dfrac{p_{ite}^f - p_{ite}^s}{ite_m - ite}\right) \end{cases} \tag{29}$$

其中 μ 是温度衰减系数，p_R 是在[0,1]的随机数，ite_m 是最大迭代次数，根据公式（31）可知，求解得到收益较差的调度解时，温度升高的概率为：

$$P_T^{up} = \exp\left(\frac{p_{ite}^f - p_{ite}^s}{ite_m - ite}\right) \tag{30}$$

分析公式（31）可知，在算法迭代的中期，p_{ite}^f 和 p_{ite}^s 间差异较小，温度升高的概率变大，接受较差调度解的概率变大，这有助于算法跳出局部最优解。

4 仿真实验与分析

表 1 卫星轨道参数

卫星轨道参数	参数值
半长轴	6621（km）
偏心率	0.000627
轨道倾角度	86.4°
升交点赤经	$24° \times i$
近地点幅角	0°
真近地点	$4° \times i + 60° \times j$
E_{ij}，M_{ij}	150, 120
e_{ij}，m_{ij}	1, 1

仿真实验的数传调度周期设置为 2024/5/1 00：00：00—2024/5/1 23：59：59，仿真中采用的 10 个地面站均位于中国境内，分别位于北京密云、新疆喀什、海南三亚、云南昆明，陕西西安，山东青岛，江苏南京、湖北武汉、吉林长春和福建厦门，超低轨通遥算一体化卫星由 90 颗卫星组成，90 颗卫星均匀分布在 6 个轨道上，第 i 个轨道上的第 j 个卫星的轨道参数如表一所示。个人终端用户随机分布在 3° N-53° N、73° E-133° E 的区域。个人终端时延敏感型数传任务、地面站时延敏感型数传任务和地面站非时延敏感型数传任务的单位数据收益分别为 0.5，0.3 和 0.1，上述 3 种数传任务的数据大小分别均匀分布在[10, 30]、[20， 40]和[30, 50]。时延敏感型数传任务的有效时间窗口长度为 3600 秒，非时延敏感型数传任务的有效时间窗口长度随机分布在 14400-21600 秒范围内。通遥算一体化卫星的数传能量分别为 500，星间通信链路、卫星与地面站的通信链路以及卫星与个人终端的通信链路的能量效率为 3、3 和 1，单位波长上星间激光通信链路、卫星与地面站的通信链路和卫星与个人终端的通信链路的传输速率分别为 1、1 和 0.5，星间激光通信链路预留的最大波长数量为 8。

表 2 不同仿真场景下数传调度算法求解结果对比

调度场景	数传收益率（%）				数传数据比例（%）			
	DNS-ALNS	IALNS	GA-ALNS	G-ALNS	DNS-ALNS	IALNS	GA-ALNS	G-ALNS
s1	0.56	0.31	0.53	0.45	0.81	0.69	0.79	0.76
s2	0.62	0.41	0.59	0.53	0.86	0.77	0.84	0.82
s3	0.66	0.47	0.64	0.58	0.87	0.80	0.87	0.84
s4	0.70	0.53	0.68	0.63	0.88	0.83	0.87	0.86
s5	0.71	0.58	0.69	0.65	0.83	0.84	0.83	0.83

表 3 不同仿真场景下数传调度算法运行时间对比（秒）

调度场景	DNS-ALNS	IALNS	GA-ALNS	G-ALNS
S1	682.9	30.7	2350.8	31.9
s2	621.1	28.1	2219.2	26.8
s3	676.	29.1	2547.3	29.5
s4	726.	29.8	2819.0	31.7
s5	857.6	29.1	3271.5	32.0

为了验证 DNS-ALNS 算法的有效性，设计了 5 个不同规模的调度场景，5 个调度场景分别用 s1-s5 进行表示，每个调度场景中地面站时延敏感型业务和个人终端时延敏感型业务数量均为 300 和 400，地面站非时延敏感型业务数量均匀分布在 1000-3000 之间。表 2 和表 3 统计了 DNS-ALNS 算法、IALNS 算法、GA-ALNS 算法和 G-ALNS 算法在数传收益率、数传数据比例和运行时间上的性能表现。IALNS 算法是本文所提 ALNS 算法的改进版本，在 IALNS 算法中，禁止通过星间卸载的方式执行数传任务，时延敏感型数传任务和非时延敏感型数传任务均只能通过其所属卫星和地面站间的通信链路进行下传；GA-ALNS 算法和 GA-ALNS 算法均基于 DNS-ALNS 算法的框架而设计，在 GA-ALNS 算法中，通过遗传算法和本文所提 ALNS 算法分别求解时延敏感型数传任务调度问题和非时延敏感型数传任务调度问题；G-ALNS 算法以数据最快下传为准则贪婪地调度时延敏感型数传任务，同时基于 ALNS 算法为非时延敏感型数传任务分配数传资源。表 2 中的数传收益率和数传数据比例分别表示在收益和数据量上成功下传的数传任务占所有数传任务的比例。观察表 2 中数传收益率可知，相较于其他对比算法，在所有的仿真场景中，DNS-ALNS 算法可求出数传收益率最高的调度解，这证明了本文所提算法能够高效地求解超低轨通遥算一体化卫星星座架构下的数传调度问题；另外，DNS-ALNS 算法、GA-ALNS 算法和 G-ALNS 算法的数传收益率远大于 IALNS 算法，这是因为高收益的时延敏感型数传任务在超低轨通遥算一体化卫星星座架构下能够通过星间链路及时下传，这证明了超低轨通遥算一体化卫星星座有助于提高数传任务下传的时效性。同时容易发现数传收益率随着实验容忍型任务数量增加而升高，这是因为时延敏感型任务难以成功调度，而时延容忍型任务由于可行传输窗口较多从而容易被下传。由表 3 可知，DNS-ALNS 算法运行速度慢于 ALNS 算法和 G-ALNS 算法，远快于 GA-ALNS 算法，这是因为 ALNS 算法和 G-ALNS 算法无需耗时的算法迭代过程从而加快了求解速度，规模巨大的解空间和复杂的约束条件导致 GA-ALNS 算法需要较长的时间进行种群的编解码过程，从而导致了 GA-ALNS 算法的运行时间过长。综合分析表 2 和表 3 的仿真结果可知，DNS-ALNS 算法相较于其他对比算法能够以较短的时间求解出数传收益率最高的调度解，同时，对比分析 IALNS 算法和其他数传调度算法的仿真结果可知，超低轨通遥算一体化卫星星座在支撑高收益的时延敏感型数传任务的下传上具有较大的优势。

图 3 表示当调度场景中个人终端时延敏感型数传任务数量和地面站时延敏感型数传任务数量分别分布在[200 400]和[300, 500]范围时，DNS-ALNS 算法求解得到的调度方案的数传收益，其中图 3（a）和图 3

（b）分别表示地面站非时延敏感型任务数量为 1500 和 2500 时的仿真结果。观察图 3 可知，数传收益率随时延敏感型数传任务数量增加而降低，同时性能差距随时延敏感型数传任务数量增加而越来越小。

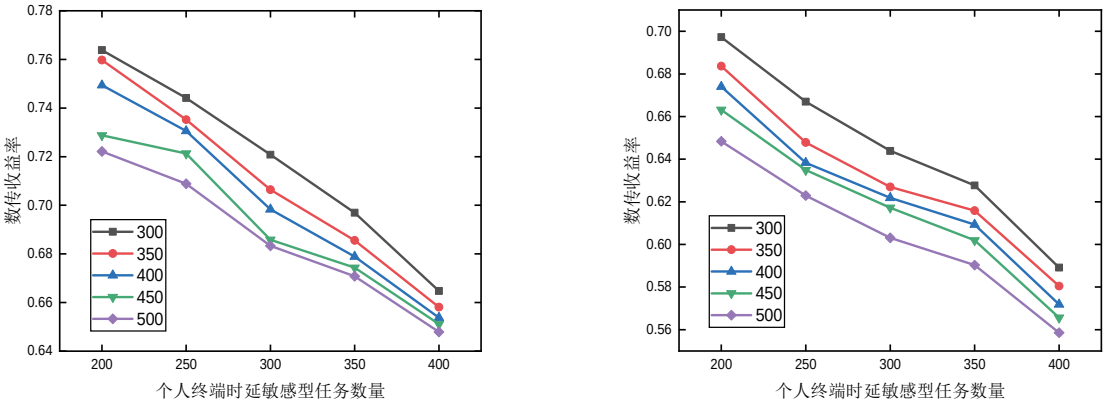

(a) 时延容忍型任务数量为 1500　　(b) 时延容忍型任务数量为 2500

图3 不同数量时延敏感型任务下数传收益率

5 结束语

本文针对超低轨通遥算一体化卫星星座的数传调度问题展开研究，考虑到多类型接收资源、星间卸载传输和差异化数传需求等因素，建立了以最大化数传收益为目标的调度模型，基于动态邻域搜索算法和自适应大邻域搜索算法提出了一个两阶段迭代数传调度算法。仿真实验结果表明，相较于其他对比算法，本文提出的两阶段迭代数传调度算法能够以较快的速度求解出数传收益最高的调度解，仿真实验结果也验证了超低轨通遥算一体化卫星星座在提高数传的时效性以及数传资源的利用效率上具有巨大的优势。

参考文献：

[1] 赵坚, 孟令杰, 王琦,等.我国高分辨率对地观测系统建设与发展[J].卫星应用,2022(11):8-13.
ZHAO J, MENG L J, WANG Q, et al. Construction and Development of High Resolution Earth Observation System in China [J]. Satellite Applications, 2022 (11): 8-13

[2] 孙伟伟,杨刚,陈超,等.中国地球观测遥感卫星发展现状及文献分析[J].遥感学报,2020,24(05):479-510.
SUN W W, YANG G, CHEN C, et al. Development Status and Literature Analysis of China's Earth Observation and Remote Sensing Satellites [J]. Journal of Remote Sensing, 2020, 24 (05): 479-510

[3] 李海,李勇军,刘元皓,等.基于 ESWO 的敏捷对地观测卫星任务调度算法[J].航空学报,2024,45(10):277-290.

Li H, Li Y J, Liu Y H, et al. A ESWO based task scheduling algorithm for agile earth observation satellites [J]. Acta Aeronautica at Chinese Sinica,2024,45(10):277-290.

[4] 吕久明,路建功,刁晶晶,等.超低轨道卫星技术发展现状及应用[J].国防科技,2020,41(01):33-37.
Lv J M, Lu J, Diao J, et al. Development Status and Application of Ultra Low Earth Orbit Satellite Technology [J]. National Defense Science and Technology, 2020, 41 (01): 33-37

[5] 袁春柱,张强,傅丹膺,等.超低轨道卫星技术发展与展望[J].航天器工程,2021,30(06):89-99.
Yuan C Z, Zhang Q, Fu D Y, et al. Development and Prospects of Ultra Low Earth Orbit Satellite Technology [J]. Spacecraft Engineering, 2021, 30 (06): 89-99

[6] 王世航.超低轨航天器轨道维持与星下点轨迹控制研究[D].哈尔滨工业大学,2021.
Wang Shihang. Research on Orbit Maintenance and Subsatellite Trajectory Control of Ultra Low Earth Orbit Spacecraft [D]. Harbin Institute of Technology, 2021.

[7] 李德仁,王密,沈欣,等.从对地观测卫星到对地观测脑[J].武汉大学学报(信息科学版),2017,42(02):143-149.
Li D R, Wang M, Shen X, et al. From Earth Observation Satellites to Earth Observation Brains [J]. Journal of Wuhan University (Information Science Edition), 2017, 42 (02): 143-149

[8] 张虹,陈林,薛嘉,等.航天测控网数传资源优化策略研究[J].航天器工程,2023,32(02):9-14.
Zhang H, Chen L, Xue J, et al. Research on Optimization Strategy of Data Transmission Resources in Aerospace Tracking and Control Network [J]. Spacecraft Engineering, 2023, 32 (02): 9-14

[9] 常飞,武小悦.卫星数传调度问题的速度可控粒子群优化算法[J].宇航学报,2010,31(08):2015-2022.
Chang F, Wu X Y. Speed controllable particle swarm optimization algorithm for satellite data transmission scheduling problem [J]. Acta Astronautica Sinica, 2010, 31 (08): 2015-2022

[10] 经飞,王钧,李军,等.基于吱呀轮优化的多卫星数传调度问题求解方法[J].宇航学报,2011,32(04):863-870.
Jing F, Wang J, Li J, et al. A solution method for multi satellite data transmission scheduling problem based on zigzag wheel optimization [J]. Acta Astronautica Sinica, 2011, 32 (04): 863-870

[11] 姜维,庞秀丽,李丽欣.卫星数传接收规划模型与算法研究[J].运筹与管理,2013,22(06):11-20.
Jiang W, Pang X L, Li L X. Research on Satellite Data Transmission Reception Planning Model and Algorithm [J]. Operations Research and Management, 2013, 22 (06): 11-20

[12] 黄双临,马冬青,方冬梅,等.基于改进蚁群算法的卫星数传调度[J].无线电工程,2015,45(07):27-38.
Huang S L, Ma D Q, Fang D M, et al. Satellite data transmission scheduling based on improved ant colony

algorithm [J]. Radio Engineering, 2015, 45 (07): 27-38

[13] 周毅荣. 卫星数传资源筹划关键技术研究[D].国防科学技术大学,2018.

Zhou Y R. Research on Key Technologies for Satellite Data Transmission Resource Planning [D]. National University of Defense Science and Technology, 2018

[14] Chen Y , Chen M , Wen J ,et al. An Adaptive Large Neighborhood Search Algorithm for the Satellite Data Transmission Scheduling Problem[J]. International Journal of Aerospace Engineering, 2020,1-12.

[15] Liu, Y.; Zhang, S.; Hu, H. A Simulated Annealing Algorithm with Tabu List for the Multi-Satellite Downlink Schedule Problem Considering Waiting Time [J]. Aerospace 2022, 9(5), 235.

[16] Barbulescu L, Watson J P, Whitley L D, et al. Scheduling Space–Ground Communications for the Air Force Satellite Control Network[J]. Journal of Scheduling, 2004, 7(1):7-34.

[17] Vazquez A J, Erwin R S. On the tractability of satellite range scheduling[J]. Optimization Letters, 2015, 9(2):311-327.

[18] Karapetyan D, Mitrovic Minic S, Malladi K T, et al. Satellite downlink scheduling problem: A case study[J]. Omega, 2015, 53:115-123.

[作者简介]

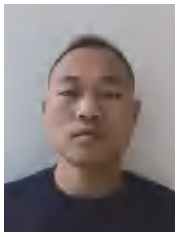

李海（1997-），男，博士研究生，主要研究方向：卫星互联网资源调度，对地观测任务资源调度。

通信作者 E-malil: hai_li@aliyun.com

李勇军（1979-），男，博士，教授，主要研究方向：卫星光网络路由算法、星地激光通信。

王翔（1984-），男，博士，副教授，主要研究方向：软件定义航空集群，算网融合。

宋鑫康（1997-），男，博士研究生，主要研究方向：机载光通信，射频/激光混合传输。

李信（1997-），男，博士研究生，主要研究方向：星地激光通信性能分析，射频/激光混合传输。

李玉（1984-），女，博士研究生，主要研究方向：空天地一体化网络资源管理和调度。

李勇军（1964-），男，博士，教授，主要研究方向：空间信息网络资源调度、微波光子、光通信。

天地一体化网络信息高速可靠传输系统设计

敦怡，徐潇审，王良，张画情

32039 部队，北京 100094

摘　要：在基于中继卫星的天地一体化网络中，受限于长时延、高误码及上下行链路带宽非对称等空间信息传输特性，地面网络传输中成熟应用的 TCP 协议不能在空间通信环境直接使用。为保障大容量数据的高速可靠传输，对 UDP 协议进行优化，设计了可靠 UDP 协议，增加了连接管理、差错处理、超时和确认重传、拥塞控制等多重机制，解决了可靠传输在高误码率、高网络带宽时延积信道下速率严重受阻的难题，突破了带宽不对称造成的传输瓶颈。经测试和试验表明，使用可靠 UDP 协议，可充分利用中继卫星信道带宽，实现了空间网络大容量数据的高速可靠传输。

关键词：天地一体化网络；中继卫星；空天信息；可靠传输；传输协议；可靠 UDP 协议

Design of High-speed and Reliable Transmission System for Space-ground Integrated Network information

DUN Yi, XU Xiao-shen, WANG Liang, ZHANG Hua-qing

32039 troops of PLA, Beijing 100094

Abstract: In order to solve the problem that reliable transmission protocols such as TCP, which have been mature and applied in ground network transmission, cannot be directly used in space communication environment due to the characteristics of space information transmission such as long delay, high bit error rate and asymmetric bandwidth of uplink and downlink, a space-ground network information system based on TDRSS is designed to ensure high-speed and reliable transmission of space network information. The UDP protocol commonly used in large-capacity and high-speed data transmission in terrestrial networks is optimized, and a reliable UDP protocol is designed, which adds multiple mechanisms such as connection management, error handling, timeout and acknowledgement retransmission, congestion control, etc., which solves the problem that the rate of reliable transmission is seriously hindered in the channel with high bit error rate and high network bandwidth delay product, and breaks through the transmission bottleneck caused by bandwidth asymmetry. Tests and experiments show that the reliable UDP protocol can make full use of the bandwidth of relay satellite channel and realize the high-speed and reliable transmission of large-capacity data in space network.

Key words: Space-ground integrated network; TDRSS; Space information; Reliable transmission; Transmission protocol; Reliable UDP protocol

1　引言

随着航天技术的快速发展，以组网和星座模式运行的航天器成为发展趋势。以往点对点封闭式数据传输的模式将难以满足空间网络和地面网络互联、多目标协同、天地间复杂互操作的需求，航天器与地面、航天器之间网络化互联成为必然，天地一体化网络信息传输需求益发迫切[1][2]。

空间通信环境下时，由于存在链路传播时延长、网络带宽时延积大、链路误码率较高、链路带宽不对称等问题，会导致传统地面网络成熟应用的可靠传输协议在空间卫星网络的应用面临严重挑战。因此在天地一体化网络体系下，数据端到端传输的可靠性以及端到端网络的高效利用，成为亟需解决的课题。

2　天地一体化网络信息传输

天体一体化信息网络由空间卫星节点互联组成的天基网络与地面网络构成的[3-6]，通过一体化的融合设计，为天、空、地、海不同应用场景用户提供全球泛在服务[7]。天基网络主要由中高低轨卫星构成，分布于不同的轨道面，需要具备全球覆盖、结构稳定、宽带承载、接入便捷，以及支持多类型业务接入和异构网络互联等方面的能力。

2.1　基于中继卫星的天地一体化系统

中继卫星系统因其高覆盖率、高传输速率和高动态适应性的特点，在空间信息传输方面发挥着巨大作用，是天地一体化网络中的重要骨干节点。基于中继卫星的天地一体化网络信息传输系统由用户目标、中继卫星、地面终端站、运管中心以及用户中心组成，如图 1 所示。其中，用户目标、中继卫星、地面站构成系统的空间段；地面站、控管中心和用户构成系统的地面段。用户目标是指信息获取平台，如卫星、飞机、运载火箭、舰船等，用户中心则为信息应用平台，即各类用户目标对应的地面应用中心[8]。具有内部子网的用户目标通过中继卫星星间和星地链路与地面系统构成天地一体化系统[9]。

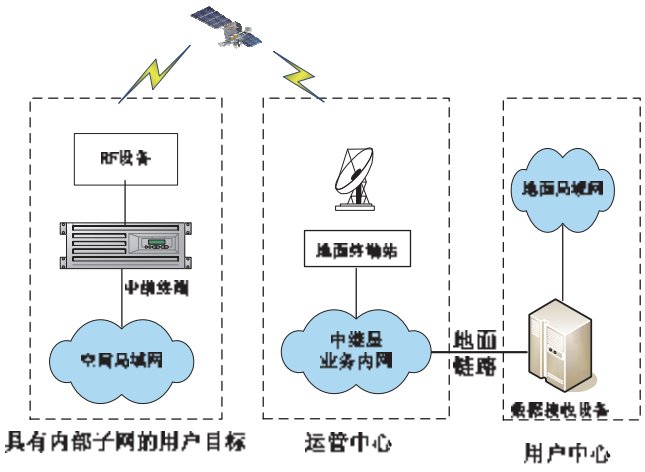

图1　基于中继卫星的天地一体化系统组成示意图

2.2 传输协议体系

目前可用于空间互联网的协议主要分为空间 IP、CCSDS 协议和 DTN 协议。其中，应用最广泛的是 CCSDS（空间数据系统咨询委员会）协议。协议针对空间信息网络节点动态性高及链路传输距离远、时延大、链路带宽不对称等特点进行了优化，借鉴了 OSI/RM 分层协议模型和 TCP/IP 体系的思想，设计了包含物理层、数据链路层、网络层、传输层和应用层的 5 层协议模型。物理层协议规定射频参数和调制格式，数据链路层协议有 TM、TC、AOS 等，网络层包括 SCPS-NP、IPv4/IPv6 等，高层协议包括 CFDP、SCPS-FP、SCPS-TP 等[7]。但由于 TCP 本身复杂的拥塞控制机制限制，使得基于 TCP 的增强或者改进的协议在中继卫星链路上传输性能仍然不够理想，尤其是高速数据传输的场景下，链路带宽不能充分利用，传输速率受限。

UDP 是基于帧的传输协议，具有开销小、速度快、效率高的特点，适用于高速传输和实时性要求较高的场景，但 UDP 协议下的数据传送是不可靠的传输，不适用于对传输可靠性要求高的场合。对于信息传输可靠性要求较高的场合，尤其是压缩文件或者加密文件传输，如果传输过程中数据丢失或发生错误，将导致后续内容、甚至整份文件解析失败，造成接收到的数据不可用，链路利用低效。因此，在对可靠性和高效性要求都较高的应用环境，需要对 UDP 协议进行改进，增加差错处理、拥塞控制和安全控制等机制[10]，通过增加差错处理机制，使得数据在传输过程中出错、或者丢失后能马上检测出来并被迅速地纠正或重传，解决传输的高速度和可靠性统一难题。

2.3 可靠 UDP 协议

可靠传输协议需要具有连接管理、超时和确认重传、拥塞控制等多重机制。可靠 UDP 连接控制处于 UDP 协议之上，在应用层实现协议的连接建立与终止、数据会话交互等处理。超时和确认重传一方面避免重复，另一方面解决分组丢失问题。在动态变化的链路环境中调整超时阈值是超时和确认重传机制保证传输效率的关键：阈值过小将造成不必要的重传，浪费时间和资源；阈值过大会导致响应时间延长、吞吐量降低。拥塞控制具备流量与速率双控策略，核心采用滑动窗口机制，由快速启动、拥塞避免、选择重传等部分组成，优化数据流的传输效率，使吞吐量持续稳定在高水平上。

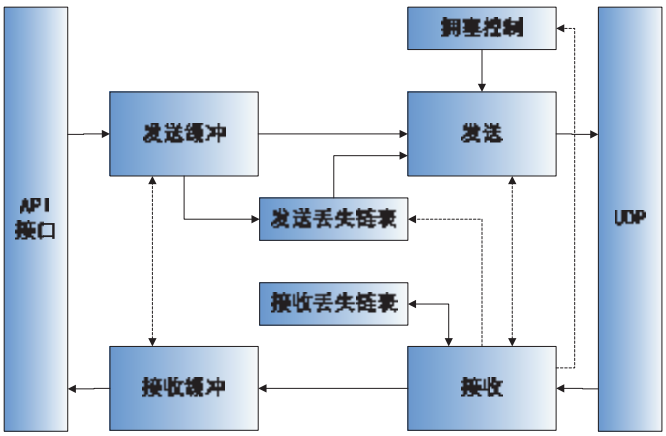

图2 可靠UDP协议逻辑结构示意图

2.1.1 拥塞控制算法

中继卫星链路往返时延（RTT）与普通卫星信道在同一量级，但信道带宽远大于后者，因此带宽时延乘积明显放大，具有非常显著的管道效应。UDP 协议是非可靠的无连接协议，没有拥塞控制，远比 TCP 简单，适用于高速传输，但为了在实现可靠传输的同时防止大容量传输导致的严重拥塞，必须加入拥塞控制机制。

可靠 UDP 的拥塞控制机制包括速率控制和窗口控制，其中速率控制是主要的，用于快速达到带宽的最大阈值、快速地丢包恢复；窗口控制采用递减式的窗口增加方式，帮助减少包的丢失和振荡，避免拥塞加剧。

可靠 UDP 协议中，通过测算链路带宽和往返时延，调整发送频率从而控制传输速度，调整窗口大小以控制发包数量。带宽估算时通常采用在发送端计算接收端反馈的 ACK 时间序列的方法，但由于中继卫星链路前、返向带宽的严重不对称，地面接收端生成的 ACK 容易暴发性地推送给空间发送端，根据这样的时间序列测算到的带宽误差较大，而地面接收端接收到的数据帧间隔更接近传输用时，通过记录数据帧的到达时间，结合上次记录可以更加准确地估算出链路带宽，并在 ACK 中进行反馈，因此本协议采用了在接收端估计带宽的方法。

在拥塞算法中，除了信道带宽，还必须考虑 RTT 指标。如果 RTT 是逐渐减小的，说明信道状况良好，否则，信道状态为拥塞的。与 TCP 协议采用 RTT 作为速度固定控制间隔不同，可靠 UDP 协议摒弃了基于目标值的窗口调节方式，采用延迟和报文丢弃一起作为信号，使得每个 RTT 内报文的增加速率更快，在收到拥塞信号后更加平滑地减小窗口，另外延迟的特性与信道容量成正比，因此更有助于提高传输稳定性。

2.1.2 选择重传机制

信道带宽的不对称性会对基于反馈机制的传输协议，如 TCP 协议产生明显影响，这是因为在数据发送方向有充裕的带宽，数据可以很快到达接收端，但接收信道带宽过低容易造成反馈消息的拥塞，导致发达端不能及时收到信息，也就无法准确判断下一步应该采取何种策略，从而造成整体传输性能的下降，在高误码率的信道环境下，这种影响尤其显著。

为了实现可靠传输，接收方应提供多类应答信息，如数据包的 ACK、连接会话中的握手包、会话保持的存活包等，一般都属于不可或缺的反馈数据。

由于中继卫星链路前、返向带宽的严重不对称，如果不对反馈机制进行合理设计，必然造成应答拥塞，进而导致返向传输速率下降。为了在不影响前向传输的前提下避免应答拥塞的发生，降低应答信息的频度和总量是解决问题的关键。

本协议设计了采用位向量标识接收到的报文段，用 1 表示正常报文段，用 0 表示需要重传的报文段，这样建立了位向量与报文段之间的映射关系，仅用一位就能标识一个报文段，其效率有了很大的提升。此

外，还对应答信息进行了适当的精简归并，将握手包、存活包以及 ACK 包等部分功能合一，减少传输频次，并且使用负向反馈数据压缩算法，将信息压缩后再回传给发送端，进一步降低应答数据频度和总量。

2.1.3 快启动和抖动抑制机制

在长时延信道环境下，TCP 协议的慢启动机制会造成数据传输速率增长非常缓慢，而信道的高误码率容易导致数据传输频繁进入慢启动环节，因此造成传输速率长时间处于低水平且抖动剧烈。为避免这种情形，本协议还设计了传输快速启动机制，一旦信道质量良好，就将发送速率快速提升至估计带宽，大幅减少收敛的绝对时间。

通常情况下，误码造成的数据包的丢失在传输中分布较为均匀，而拥塞引起的丢包则可能连续出现。根据理论推算和试验测试，中继卫星链路因误码造成的丢包远远多于因拥塞导致的丢包，而误码导致丢包发生时，单纯降低速度并不能减少丢包率，因此本协议中设计了传输抖动抑制机制，当传输过程中某拥塞周期内少量均匀丢包情况出现时，并不降低发送速度，仅在发生连续性的丢包或突发性大量丢包的情况下才降低速度以避免情况恶化。

2.4 端到端的可靠传输

用户目标空间局域网数据（即返向数据）在经空间信道传输前，首先要完成局域网数据链路层协议到 AOS 数据链路层协议的转换。返向数据经中继卫星信道传输到地面后，由中继卫星地面终端站接收后，通过地面链路传输至用户中心，用户中心对返向数据进行协议转换，得到用户目标局域网数据，实现了用户目标空间局域网数据到用户中心地面局域网的端到端传输。用户中心地面局域网数据（即前向数据）传输为上述过程的逆过程。

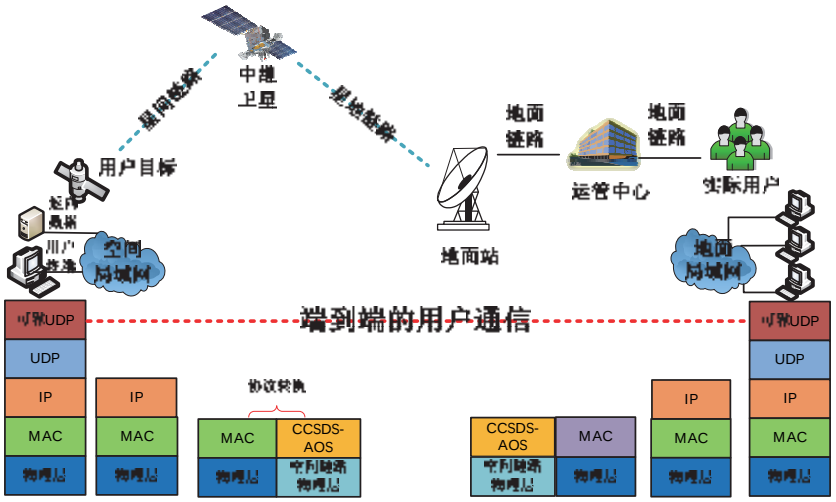

图3 端对端数据传输协议架构

3 试验验证

试验验证分为两个阶段，第一阶段是地面中频联试，第二阶段是大系统联试，即空间射频联试。

3.1 中频验证

地面中频联试设备连接如图 4 所示，采用 Iperf 测试软件与可靠 UDP 软件的测试结果进行比对。

首先测试带宽对传输性能影响。在 50M 带宽条件下，测试不同限速下的传输性能，结果如表 1 所示。测试结果表明：数据传输速率接近且略低于实际系统带宽时，传输效率最高。

后续测试中，为测试高速传输性能，设定为 150M 系统带宽。时延测试项目中，固定时延设置为 300ms，抖动时延设置为正态分布，最小 15ms，均值 30ms，标准差 20ms；误码乱序测试项目中，误码率设置为 10^{-6}、乱序概率设置为 10%。测试使用标准测试结果如表 1 所示。

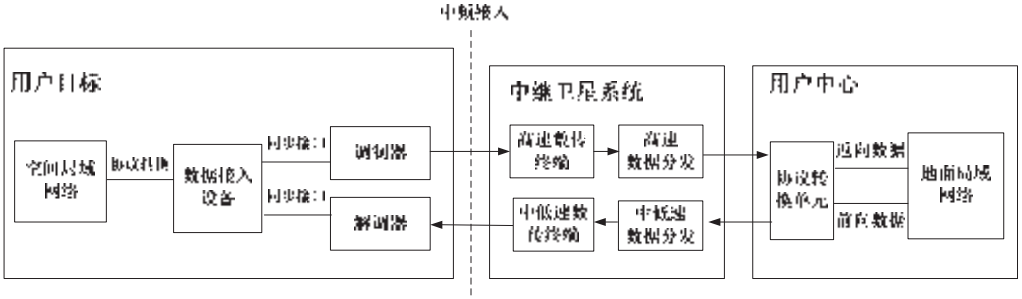

图4 中频联试设备连接示意图

表1 返向传输测试记录表

测试项目	**测试结果**	
	Iperf	**可靠** UDP
带宽影响（限定带宽 50M）	返向发 150Mbps，收方统计：均速 2.4Mbps，丢包率 98%，1168 包乱序	限速 150Mbps，均速 9.3 Mbps，无丢包
	返向发 80Mbps，收方统计：均速 12.4Mbps，丢包率 84%，1663 包乱序	限速 80Mbps，均速 11Mbps，无丢包
	返向发 50Mbps，收方统计：均速 45.4Mbps，丢包率 10%，1023 包乱序	限速 50Mbps，均速 28Mbps，无丢包
	返向发 40Mbps，收方统计：均速 39.9Mbps，丢包率 0%，无乱序	限速 40Mbps，均速 37.7Mbps，无丢包
固定时延影响	返向发 140Mbps，收方统计：均速 136Mbps，丢包率 0.009%，无乱序	返向发 1GB 文件，均速 137Mbps
抖动时延影响	返向发 140Mbps，收方统计：均速 137Mbps，丢包率 0.29%，无乱序	返向发 1GB 文件，均速 138Mbps
误码乱序影响	返向发 140Mbps，收方统计：均速 138Mbps，丢包率 0.02%，44291 包乱序；	返向发 1GB 文件，均速 118Mbps；

3.2 射频验证

射频联试设备连接如图 5 所示，测试结果表明，信道带宽利用率达到 80%以上，扣除协议开销等因素，信道带宽得到充分使用，实现了大容量数据的高速可靠传输。

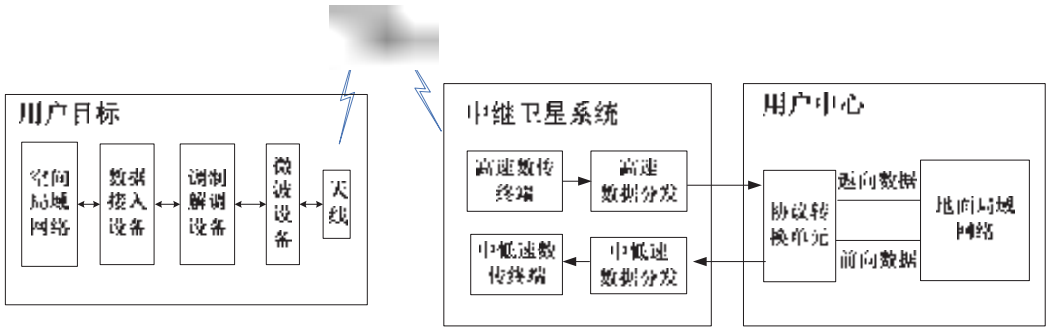

图5 射频联试设备连接示意图

表2 返向传输测试记录表

文件大小 （Byte）	用时 （s）	带宽 利用率
3981235678	261.54	81.19%
3024562387	199.31	80.93%
3415693126	225.98	80.61%
2645623857	174.26	80.97%

4 结束语

TCP 协议是当前地面网络中最为广泛应用的协议，TCP 协议面向连接，实现数据可靠传递主要采用 TCP 传输控制协议，但协议是针对地面有线网络进行设计的，直接应用于空间通信时，受限于空间数据传输误码率高、数据往返时延长及上下行链路带宽非对称等，会遇到诸多问题。对于中继卫星链路，其前、返向带宽严重不对称，加上延时大、误码率高，造成 BDP 很高，导致数据吞吐率低，即使采用多 TCP 流、加大发送窗口等方法，速率也远低于带宽容量，造成宝贵卫星资源的浪费。在基于中继卫星的天地一体化网络信息传输中，采用可靠 UDP 协议，提高了带宽和时延估计精度，随链路变化及时调整传输流量，在信道良好的情况下将速度迅速提升至上限，并根据 RTT 合理设置超时间隔，避免产生不必要的数据重传，使数据的吞吐率维持在高水平，显著节省了链路带宽资源，减少了重传的盲目性，克服了带宽不对称造成的传输瓶颈，快启动和抖动抑制机制，可实现传输速度快速收敛并能较长时间稳定在高水平，传输效率得到有效提升，为用户提供海基、天基、陆基的网络端到端无缝互联，用户可以通过网络直接进行数据传输和交互式操作，从而实现了中继卫星链路的高速、可靠传输。

参考文献：

[1] 沈荣骏 .我国天地一体化航天互联网构想[J]. 中国工程科学, 2006,8(10): 19-30.

SHEN R J .Some thoughts of Chinese integrated space-ground network system [J]. Engineering Science, 2006,8(10): 19-30.

[2] 吴巍. 天地一体化信息网络发展综述. 天地一体化信息网络[J], 2020, 1(1): 1-16

WU Wei. Survey on the Development of Space-Integrated-Ground Information Network. Space-Integrated-Ground Information Networks [J], 2020, 1(1): 1-16

[3] 蒋长林, 李清, 王羽, 赵丹, 赵达毅, 江勇, 徐明伟. 天地一体化网络关键技术研究综述[J]. 软件学报, 2024, 35(1): 266-287.

Jiang CL, Li Q, Wang Y, Zhao D, Zhao DY, Jiang Y, Xu MW. Survey on Key Technologies in Space-ground Integrated Network. [J] Journal of Software, 2024, 35(1): 266-287

[4] Li HW, Wu Q, Xu K, Wu JP, Yang ZY, Jiang Z, Zhu L. Progress and tendency of space and earth integrated network. [J] Science & Technology Review, 2016, 34(14): 95-106.

[5] Liang H, Chen FC, Ji XS, Lv P, Gao YZ. Development status and applied research on mimic technologies for space-ground integration information network. [J] SCIENTIA SINICA Informationis, 2019, 49(7): 799-818

[6] Wu W. Survey on the development of space-integrated-ground information network.[J] Space-Integrated-Ground Information Networks, 2020, 1(1): 1-16

[7] 汪春霆等.天地一体化信息网络架构与技术[M], 北京: 人民邮电出版社, 2022.

Wang Chunting. Space-ground Integrated Information Network Architecture and technology.[M] Beijing: People's post and telecommunications publishing house, 2022.

[8] 费立刚，范丹丹，寇保华，刘华峰，徐潇审. 基于中继卫星的天地一体化信息网络综合集成演示系统研究[J]. 中国电子科学研究院学报, 2015, 100(5): 479-484.

FEI Li-gang, FAN Dan-dan, KOU Bao-hua, LIU Hua-feng, XU Xiao-shen. Research on the Demonstration of Space Information Network Based on TDRSS [J]. Journal of China Academy of Electronics and Information Technology, 2015, 100(5): 479-484.

[9] 刘华峰，徐潇审，孙宝升，费立刚等. 基于同步骨干卫星的天地一体化 IP 网络互联模式设计及真星试验[J]. 中国电子科学研究院学报, 2018, 13(5): 532-538.

LIU Hua-feng, XU Xiao-shen, SUN Bao-sheng, FEI Li-gang, etc. Design and Verification of the Space-groud Integrated IP Network Interconnection Model Based on GEO [J]. Journal of China Academy of Electronics and Information Technology, 2018, 13(5): 532-538.

[10] 赵雄文 , 张钰 , 秦鹏 , 王晓晴 , 耿绥燕 , 宋俊元 , 刘瑶 , 李思峰. 空天地一体化无线光通信网络关键技术及其发展趋势[J]. 电子学报, 2022, 50(1): 1-17.

ZHAO Xiong-wen , ZHANG Yu , QIN Peng , WANG Xiao-qing , GENG Sui-yan , SONG Jun-yuan , LIU Yao , LI Si-feng. Key Technologies and Development Trends for a Space-Air-Ground Integrated Wireless Optical Communication Network[J]. Acta Electronica Sinica, 2022, 50(1): 1-17.

[作者简介]

敦怡（1973 年—），女，博士，高级工程师，研究方向为卫星通信

徐潇审（1985 年—），男，博士，高级工程师，研究方向为卫星通信

王良（1983 年—），男，博士，高级工程师，研究方向为卫星通信

张画情（1997 年—），女，本科，助理工程师，研究方向为卫星通信